Investigation on the Non-trivial Dielectric, Piezoelectric and Vibrational Properties of Some Lead-free Multifunctional Nanomaterials

Thesis submitted in 2023 to Jadavpur University
regarding partial fulfilment of the requirements for the degree of
Doctor of Philosophy (Science)

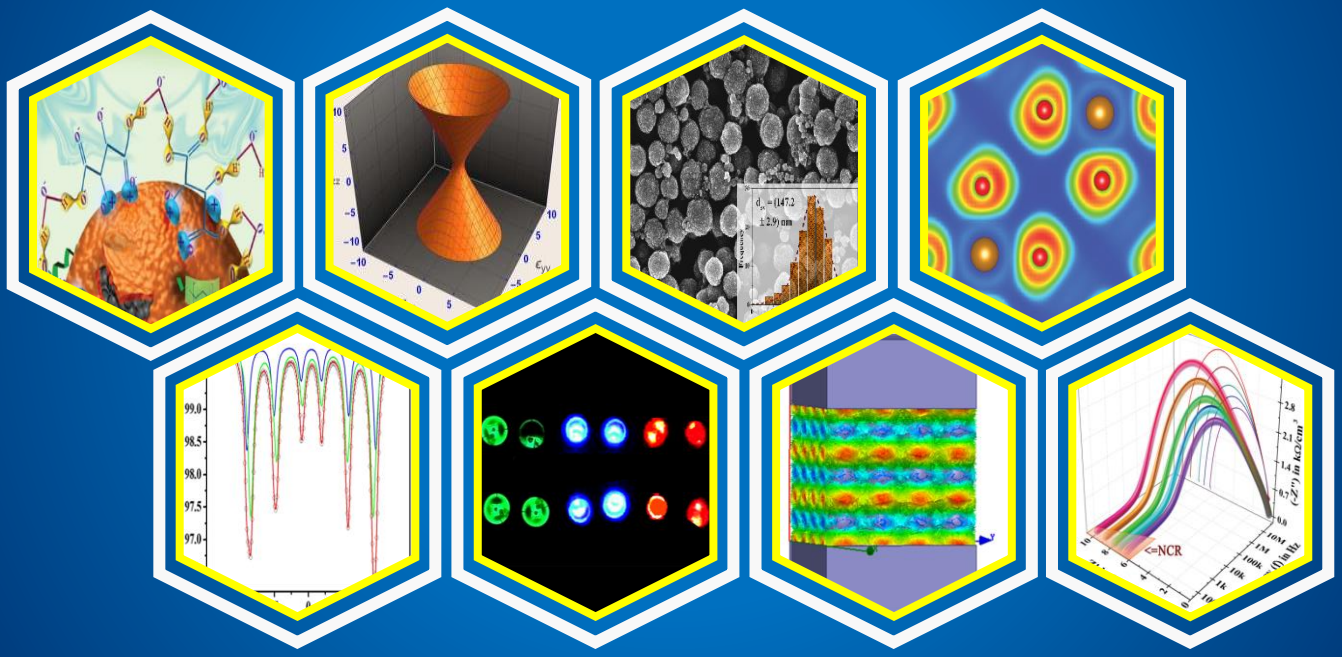

Souvik Bhattacharjee

Thin Film & Nanoscience Laboratory
Department of Physics, Faculty of Science
Jadavpur University, Kolkata – 700 032, India

Under the supervision of Prof. Kalyan Kumar Chattopadhyay

Index No. – 130/19/Phys./26 & Registration No. – SOPHY1113019

Investigation on the non-trivial dielectric, piezoelectric and vibrational properties of some lead-free multifunctional nanomaterials

Thesis submitted in 2023 to

Jadavpur University

regarding partial fulfilment of the requirements for the degree of

Doctor of Philosophy (Science)

by

Souvik Bhattacharjee

Thin Film & Nanoscience Laboratory
Department of Physics
Faculty of Science
Jadavpur University
Kolkata – 700 032, India

Name of the research scholar:	Souvik Bhattacharjee
Designation (while submitting the doctoral thesis):	Senior Research Fellow [CSIR(NET)-SRF]
Affiliation (while submitting the doctoral thesis):	Department of Physics Jadavpur University, Kolkata – 700 032 West Bengal, India
Index Number:	130/19/Phys./26
Registration Number:	SOPHY1113019
Date of Registration:	13th November, 2019
Tenure of doctoral research:	February 2018 – May 2023
Year of submission of the doctoral thesis:	2023 (June)
E-mail:	bhattacharjeesouvik083@gmail.com bsouvik_phy@zoho.com
ORCID:	https://orcid.org/0000-0003-0329-3171

= = = = = = = = = =

Name of the Ph.D. supervisor:
Prof. (Dr.) Kalyan Kumar Chattopadhyay

Designation and affiliation of the supervisor:
Professor and Head, Department of Physics
Ex-Director, School of Materials Science & Nanotechnology
Jadavpur University, Kolkata – 700 032
West Bengal, India

E-mail:
kalyan_chattopadhyay@yahoo.com
kkc.juphy@gmail.com

ORCID:
https://orcid.org/0000-0002-4576-2434

যাদবপুর বিশ্ববিদ্যালয়
কলকাতা - ৭০০ ০৩২, ভারত

Jadavpur University
Kolkata – 700 032, India

Certificate from the Supervisor

This is to certify that the thesis entitled "**Investigation on the non-trivial dielectric, piezoelectric and vibrational properties of some lead-free multifunctional nanomaterials**" submitted by **Sri Souvik Bhattacharjee**, who got his name registered on **13 / 11 / 2019** for the award of **Ph.D. (Science)** degree of **Jadavpur University**, is absolutely based upon his own work under the supervision of **Prof. (Dr.) Kalyan Kumar Chattopadhyay** and that neither this thesis nor any part of it has been submitted for either any degree/diploma or any other academic awards anywhere before.

Dated, 28.06.2023

Prof. Kalyan Kumar Chattopadhyay
Head, Department of Physics
Jadavpur University

Prof. Kalyan Kr. Chattopadhyay
Professor and Head
Department of Physics
Jadavpur University
Kolkata – 700 032

This page is intentionally left blank.

Statement of Originality

I, **Souvik Bhattacharjee**, registered on **13 / 11 / 2019**, do hereby declare that this thesis entitled "**Investigation on the non-trivial dielectric, piezoelectric and vibrational properties of some lead-free multifunctional nanomaterials**" contains literature survey and original research work done by the undersigned candidate as part of his Doctoral studies.

All information in this thesis have been obtained and presented in accordance with existing academic rules and ethical conduct. I declare that, as required by these rules and conduct, I have fully cited and referred all materials and results that are not original to this work.

Also, it has not been submitted for any degree or examination in any other university. I further declare that all the resources I have used or quoted have been indicated and acknowledged by complete references.

Souvik Bhattacharjee.

Dated, 28/06/2023.

Mr. Souvik Bhattacharjee

(The Doctoral Candidate)

This page is intentionally left blank.

This work is devoted to my parents. Their unconditional love, selfless sacrifice, and unwavering encouragement have been my guiding light.

This page is intentionally left blank.

Acknowledgements

This is a descent opportunity to thank all the people, who made invaluable contributions in my research works directly or indirectly by their generous presence in my life and by sharing their inherent wisdom and experiences with me. These are the people, who enriched me as a person and as a researcher, and made my doctoral journey a memorable one.

First and foremost, I would like to express my deep gratitude towards my Ph.D. supervisor, Prof. (Dr.) Kalyan Kumar Chattopadhyay, who invited me in the diversified research community under the Thin Film and Nanoscience Laboratory, Jadavpur University (JU). I particularly appreciate three important and rare characteristics of his guidance. First, he always treats his Ph.D. students as a fellow researcher and motivates them in every possible opportunity so that, one can convert initial failures in experimental trials to a prolong and sustained success. Second, he has setup a remarkable lab with multifaceted research facilities under one roof by years of hard work and dedication; via utilizing various project funds in the most economical way possible. Third, he gives as much liberty as possible to every member of his research group to promote original thoughts and individual interests. This includes utmost freedom to access a facility at any moment–day or night, discuss particulars of research works with any senior researcher or fellow lab-mate, and organize the initial draft of manuscripts with appropriate structure and co-authors. From the very initial days of my research carrier, I was interested in multiple fields under condensed matter physics, materials science and nanotechnology facilitating a mixed (experimental/computational/theoretical) framework, which he always supported. I certainly do not claim that I have made a remarkable contribution to my fields of research, nevertheless whatever insights I could realize, would not have been possible without Prof. Chattopadhyay's congruous guidance and encouraging supervision.

A major part of the knowledge that I accumulated throughout the past few years in terms of operating research instruments, acquiring an authentic set of data, synthesizing nanomaterials, and fabricating thin films were because of the generous help of Dr. Karamjyoti Panigrahi, Mr. Saikat Sarkar and Dr. Nilesh Mazumder. They supplied the initial fuel for the progression of my research journey. I do not consider them just as senior colleagues, rather they are more like my loving elder brothers and well-wishers. I have also learnt many useful instrumental and analytical techniques from Dr. Biswajit Das, Dr. Nirmalya Sankar Das, Dr. Subhajit Saha, Dr. Rajarshi Roy, Dr. Soumen Maiti, Dr. Pulak Pal, Dr. Partha Bairi, and Dr. Supratim Maity. They are not just exceptionally helpful seniors, but also have enriched our lab for more than a decade with their passion and dedication towards research.

Next, I would love to thank my closest friends (and partners in crime) from the lab, that include Mr. Anibrata Banerjee, Ms. Dimitra Das, Dr. Bikram Kumar Das, Mr. Arnab Das and Mr. Saikat Sarkar. These people must be acknowledged from the bottom of my heart. First, Anibrata is such a friend who keeps his own first author works aside to prioritize the computational support required for my experimental papers. He is the guy, who roams with me throughout Kolkata even at midnight to find out my missing mobile phone. And he is such a person, who humbly tries to help almost everyone around him (and sometimes starts exceptionally long conversations out of thin air) with a smile in the face. Next, I must mention the soul of our group, without whom life would have been different (by different, I mean pathetic) for all of us. I always wanted an elder sister, Dimitra'di filled that vacancy in my life within a very short time. She supported me in every possible way whether it is her experience in research, or her sweet and kind words in difficult times, or her selfless support to help me get abroad for attending an international conference for the first time in life. For her beautiful personality, almost every junior instantly starts considering her a beloved didi (elder sister)! However, I will always have this pity, that the amount of money she wasted in offering us (and an additional gang of juniors) tea, biscuit, and snacks almost every evening for years, has ruined the possibility of a big, fat mutual fund. Next, I would like to thank Bikram'da, who has significant contributions in setting up the present computational facilities of our lab. He not only helped in every DFT-based work as an experienced senior whenever Anibrata and I got stuck, but also have been a loving, kind and happy guy who I believe will make significant progress in life in spite of failing to be the greatest Dictator of this century. I also wish Bikram'da and Dimitra'di a beautiful and prosperous life together. I have already acknowledged the support of Saikat'da, here I would like to add, how much I value the small talks on physics that I had with him, throughout the past few years, especially during our failed attempts to run our old physical properties measurement system (PPMS). Finally, I must mention Arnab, he has such a free spirit and inadvertent personality, that I sometimes envy. I truly believe, people need an attitude like him to find true happiness in today's hectic and mechanical life. Another person I must mention is Ms. Barni Banerjee, who technically could be excluded from this present list, because I met her when half of my thesis was already complete. But she deserves to be named here for her impactful role in my life within a very short span of time. Last, but not the least, I would like to acknowledge Mr. Arya Ray, Mr. Jyotipriya Roy and Dr. Chitrak Bhadra; who have been loving friends and helpful companions beyond our lab. Every Ph.D. scholar has his own moments of frustration, because of repeated failures in experiments, sudden technical faults in instruments, limitations in funding or due to rejection of a paper. To survive, one needs a mechanism to drain out the growing anxiety and frustration on a regular basis, which in my case was assured by the generous presence of this group.

Next, I would like to acknowledge my close collaborators and colleagues from the lab. In our lab, there is a very nice culture of co-working in particular projects to efficiently utilize the expertise and interests of distinct scholars in order to faster achieve the desired goals. That's why, many scholars have been the co-authors of my first author papers, similarly I have got the opportunity to contribute in their works as well. While doing so, I have had prolonged discussions with these people that enriched my vision and concepts manifold. They are: Mr. Anibrata Banerjee, Dr. Nilesh Mazumder, Mr. Kausik Chanda, Mr. Saikat Sarkar, Mr. Suvankar Mondal, Mr. Suvankar Poddar, Dr. Soumen Maiti, Dr. Tufan Paul, Dr. Subhasish Thakur, Dr. Partha Bairi, Dr. Karamjyoti Panigrahi, Ms. Dimitra Das, Mr. Dipayan Roy, Mr. S. Najes Riaz, Dr. Ratna Sarkar, Mrs. Suvra Pal, Ms. Dipanwita Mitra, Ms. Ankita Chandra, Dr. Antika Das, Ms. Moumita Ghosh, Dr. Pulak Pal, Dr. Bikram Kumar Das, Dr. Mississippi Missouri Bhunia, Mr. Nripen Besra, Mr. Kausik Sardar, Mr. Anjan Das, and Dr. Madhupriya Samanta. I would like to acknowledge Prof. Paramita Chattopadhyay, Dr. Sourav Sarkar, and Dr. Chandan Kumar Ghosh as well in this regard. Among all my co-authors and collaborators, I would like to specially acknowledge the Suvankar duo and Dipayan. I had got the opportunity to work with Suvankar'da and Suvankar Poddar in some really interesting and impactful works in the last couple of years, and probably we will work together in future as well. I appreciate their positivity and the undivided aim of publishing in high-impact journals. On the other hand, I admire the knowledge and expertise of Dipayan in different fields of chemistry. I and Dipayan joined Prof. Chattopadhyay's lab on the same date (3rd January 2018), and instead of having completely different fields of interest, have always enjoyed working together in any opportunity. Whenever, I needed any advice in chemistry, I have consulted with Dipayan, and he had helped me. I also tried to return the favour with some inputs of physics, whenever possible. Furthermore, I must also mention some other seniors, with whom I had occasional discussion regarding research *viz*., Dr. Uttam Kumar Ghorai, Dr. Anuradha Mitra, Dr. Rituparna Chatterjee, Dr. Brahami Das, Dr. Dipayan Sen, Dr. Pranab Kumar Sarkar, Dr. Biplab Kumar Chatterjee, Dr. Samrat Sarkar, Mr. Prasanta Mandal, Dr. Rimpa Khan, Dr. Shrabani Ghosh, and Dr. Anup Debnath. Their inputs have also helped to re-shape the path of my research.

Over and above, I would also like to express my sincere thanks to my friends from JU and high school, well-wishers, and teachers. They have always encouraged and supported me in different circumstances of life. It is very difficult to mention all of them, but I would certainly mention at least a few of them such as Mr. Subhajit Mandal, Mr. Arghya Sil, Mr. Sudip Chakraborty, Mr. Mayukh Mukherjee, Mr. Rounak Sarkar, Ms. Mouli Choudhury, Mr. Sandipan Mohanta, Mr. Nirmalya Chakraborty, Mr. Pinaki Ranjan Kundu, Dr. Anan Bari Sarkar, Dr. Nirman Chakraborty, and Dr. Abhishek Maiti. I would also like to acknowledge the Department of physics, JU for providing the infrastructure, different instrumental facilities, and a healthy,

interactive research environment. In this regard, I especially express my deep gratitude towards Prof. Sanjay Kumar (and his Ph.D. scholars), Prof. Sukhen Das, Prof. Debasish Lohar, Prof. Ruma Ray, and Prof. Asim Kumar Ghosh. I also thank various M.Sc. and M.Tech. students (especially, Ms. Sampurna Mukherjee, Mr. Mousom Roy, and Mr. Pratik Chattopadhyay) of our lab and my juniors who are currently pursuing their Ph.D. such as Mr. Pulok Das, Ms. Nabamita Chakraborty, Ms. Piyali Dey, Ms. Sreya, Mr. Abhirup, and Ms. Nabanita Sen. Apart from our lab, there are many other scholars in our department, with whom I completed my course-work in 2021 or operated different instruments like the vibrating sample magnetometer (VSM). I thank them all for their valuable contribution in sustaining a solid research culture and friendly atmosphere in JU.

I heartily thank the University Grants Commission (UGC), the Government of India for the 'University with Potential for Excellence (UPE-II)' scheme [Grant No. F-1-10/12(NSPE)] & TEQIP programmes, and the Department of Science and Technology (DST) for Nanomission project. I am grateful to the Council of Scientific and Industrial Research (CSIR), the Government of India for awarding me junior and senior research fellowships [File No. 09/096(0946)/2018-EMR-I] for a total of five years' tenure. Due to this financial assistance, I could successfully submit my doctoral thesis. I also thank the DST-SERB (Science and Engineering Research Board), the Government of India for providing financial assistance under the ITS scheme, that helped me to present one of my published research works in the 8th Nano Today Conference in April 2023 at the Paradise Point, San Diego, CA, USA.

Finally, I express my deepest love and gratitude to my parents, who affectionately raised me, enlightened me with proper education and moral values, and also motivated me to pursue research in physics. To felicitate their unconditional love and kindness, I dedicate this thesis to my parents. An authentic appreciation also extends to the passionate souls who tirelessly devote themselves to the noble pursuit of serving humanity, persistently seeking enlightenment, and understanding science. I salute them all, because their unwavering determination triumphs over life's countless challenges and hardships, illuminating a path of indomitable will and resilience.

Souvik Bhattacharjee
Thin Film & Nanoscience Laboratory
Department of Physics
Jadavpur University
Kolkata – 700 032, India

Dated,
14th June 2023

Table of Contents

Preface

Recently, the pursuit of lead-free, non-toxic, and environment-friendly nanomaterials has emerged as a crucial objective in scientific research, driven by the increasing awareness of the adverse effects associated with the traditional lead-based counterparts. Factually, many lead-based perovskites and other materials exhibit appreciable ferroelectric, piezoelectric, mechanical and multiferroic properties, that find applications across different industries. It will not be misleading to claim that, the 20th century could be recognized as the century of lead-based materials, where research around physical and chemical properties of such compounds, their utilization in electrical and electronic gadgets, and the associated lead-pollution touched the peak in the history of humankind. Lead (Pb), a highly toxic heavy metal, has been widely used in various industries for about a couple of centuries. However, its detrimental effects on human health and the environment have become evident over time, leading to regulatory actions and a shift towards lead-free alternatives. The presence of lead in consumer products and its potential for contamination in ecosystems has raised concerns about long-term environmental sustainability. Therefore, there is an urgent need to develop lead-free nanomaterials that can replace their lead-based counterparts, ensuring safety, sustainability, and a healthier environment for future generations. At the same time, the properties of the new materials should be good enough to maintain the same standards. This doctoral thesis, entitled "Investigation on the non-trivial dielectric, piezoelectric and vibrational properties of some lead-free multifunctional nanomaterials" aims to address this pressing need by exploring the fascinating realm of condensed matter physics, materials sciences and nanotechnology to uncover desirable multifunctional properties in some lead-free nanomaterials.

In addition to addressing the environmental challenges, the exploration of multifunctional nanomaterials opens up exciting opportunities for advancements in various fields, including energy harvesting, energy storage, electronics, sensors, and biomedical applications. Nanomaterials exhibit unique properties and functionalities, enabling their integration into diverse technological applications. The ability to understand, manipulate, and optimize their properties is paramount in harnessing their full potential for practical applications. The depletion of fossil fuels and the adverse effects of greenhouse gas emissions have prompted a global shift towards renewable and sustainable energy sources. To emphasize the importance of developing sustainable energy technologies, let us consider some statistical data. According to the International Energy Agency (IEA), global energy demand is projected to increase by approximately 25% between 2020 and 2040. This growth is primarily driven by population expansion, urbanization, and rising living standards in developing countries.

Consequently, the need for alternative energy sources and efficient energy storage technologies becomes even more critical to meet this escalating demand while mitigating the environmental impact. Consequently, alternative energy technologies, such as solar cells, thermoelectric devices, and piezoelectric energy harvesters having large relative permittivity and breakdown strength, have gained considerable attention. These technologies offer the promise of clean, abundant, and renewable energy generation, but their efficiency and reliability heavily rely on the properties of the materials employed. Nanomaterials have emerged as key components in energy harvesting and storage devices due to their remarkable characteristics at the nanoscale. Enhanced charge transport, high surface-to-volume ratio, increased reactivity, and tuneable energy bandgaps are just a few of the advantages exhibited by nanomaterials, making them highly desirable for energy-related applications. By concentrating on various dielectric, piezoelectric, and vibrational properties at the nanoscale, this thesis aims to contribute to the development of efficient energy conversion and storage systems.

Experimental techniques play a crucial role in understanding the behaviour of nanomaterials at the sub-microscopic level. In this thesis, comprehensive experimental investigations are conducted to elucidate the crystallographic, structural, morphological, compositional, dielectric, piezoelectric, transport, and vibrational properties of particular nano-systems. By systematically varying composition, processing parameters, particle-size, and nanostructure, the relationships between the structure, composition, and functional properties of these materials can be established. For doing so, advanced crystallographic, spectroscopic and microscopic techniques, such as X-ray diffraction (XRD), field emission scanning electron microscopy (FESEM), transmission electron microscopy (TEM), Fourier-transform infrared spectroscopy (FTIR), Raman spectroscopy, X-ray photoelectron spectroscopy (XPS), energy dispersive X-ray (EDX) analysis, UV-Vis-NIR absorbance and diffuse reflectance spectroscopy (DRS), *etc*. have been employed.

Complementing the experimental investigations, theoretical methods based on density functional theory (DFT) are employed to unravel the underlying quantum mechanical principles governing distinct properties of the materials. DFT provides a powerful computational framework for calculating electronic structure, vibrational modes, optical parameters, mechanical, and thermal properties at the atomic level. By utilizing first principles simulations, the energetics, electronic band structures, and phonon dispersion can be accurately predicted, providing valuable insights into their electrical, electronic, piezoelectric, and vibrational attributes. Furthermore, there are finite element simulations that can illustrate the electric fields and energy densities around different nanostructures. An appropriate amalgamation of the experimental and theoretical results leads to a highly accurate and holistic understanding of materials physics and chemistry.

This doctoral thesis aims to contribute not only in extending the existing body of knowledge by providing a comprehensive investigation of the electrical, electronic, optical, magnetic and vibrational properties of the lead-free multifunctional nanomaterials, but also the research outcomes shed light on their potential applications in energy harvesting and storage technologies. To achieve the desired research objectives, this thesis is organized in the following manner. First, an introductory chapter is provided including the key-concepts, motivation and objectives. The 2nd chapter includes a comprehensive review of the relevant scientific literature as well as a collection of background theories required to understand the principal subject matter of this thesis. It also highlights the knowledge gaps and research opportunities that drive the investigations undertaken. The 3rd chapter mainly describes distinct experimental facilities and techniques, which are employed to characterize and analyse different properties of the materials under investigation. Relevant data analysis techniques, and computational/theoretical methods are included as well. In the 4th to 8th chapter, five of my published research works have been delineated with all the associated data and relevant inferences have been dropped. The details of my works, the background theory, motivation, and comprehension are stated in the successive chapters, which I am not repeating here. In the 9th and final chapter of this thesis, a summary of all the conclusions from my doctoral research are presented, followed by a basic scheme and future plan of the forthcoming projects.

Throughout this thesis, I have tried to provide an organised and refined version of most of the knowledge and experience that I gained in my doctoral journey. Still, I understand, there could be scope for human errors. I will always happily welcome any kind of constructive criticism or feedback and will be available for debates or discussion through my personal email id, as provided in the beginning of this thesis. I will consider this thesis a great success, if it helps even a single researcher or adds some value to the future research community. Thank you, very much and happy reading.

Souvik Bhattacharjee
Thin Film & Nanoscience Laboratory
Department of Physics
Jadavpur University
Kolkata – 700 032, India

Dated,
14th June 2023

List of Publications

My publications as the first author are enlisted below in chronological order. All works discussed in this thesis are based on selected research articles from the following list.

1. Souvik Bhattacharjee, Anibrata Banerjee, Nilesh Mazumder, Kausik Chanda, Saikat Sarkar, and Kalyan Kumar Chattopadhyay, Negative capacitance switching in size-modulated Fe_3O_4 nanoparticles with spontaneous non-stoichiometry: confronting its generalized origin in non-ferroelectric materials, ***Nanoscale***, 12(3), 1528-1540 (2020), DOI: https://doi.org/10.1039/C9NR07902E
2. Souvik Bhattacharjee, Suvankar Mondal, Anibrata Banerjee, and Kalyan Kumar Chattopadhyay, Dielectric and piezoelectric augmentation in self-poled magnetic Fe_3O_4/poly (vinylidene fluoride) composite nanogenerators, ***Materials Research Express***, 7(4), 044001 (2020), DOI: https://doi.org/10.1088/2053-1591/ab87d6
3. Souvik Bhattacharjee, Nilesh Mazumder, Suvankar Mondal, Karamjyoti Panigrahi, Anibrata Banerjee, Dimitra Das, Saikat Sarkar, Dipayan Roy, and Kalyan Kumar Chattopadhyay, Size-modulation of functionalized Fe_3O_4: Nanoscopic customization to devise resolute piezoelectric nanocomposites, ***Dalton Transactions***, 49, 7872-7890 (2020), DOI: https://doi.org/10.1039/D0DT01167C
4. Souvik Bhattacharjee, Anibrata Banerjee, and Kalyan Kumar Chattopadhyay, Field-enhanced polarization in polytype ferric oxides: confronting anisotropy in dielectric ellipsoid dispersion, ***Journal of Physics D: Applied Physics***, 54(29), 295301 (2021), DOI: https://doi.org/10.1088/1361-6463/abf806
5. Souvik Bhattacharjee, Ratna Sarkar, Pratik Chattopadhyay, Anibrata Banerjee, Nirmalya Sankar Das, Dimitra Das, and Kalyan Kumar Chattopadhyay, Manipulating dielectric relaxation via anisotropic field deviations in perovskite titanate grain–grain boundary heterostructure: a joint experimental and theoretical venture, ***Applied Physics A***, 128(6), 1-20 (2022), DOI: https://doi.org/10.1007/s00339-022-05638-2
6. Souvik Bhattacharjee, and Kalyan Kumar Chattopadhyay, Laser-induced Fano asymmetry, electron-phonon coupling, and phase transition in lanthanide sesquioxide (Ln_2O_3; Ln = Eu, Gd, Dy) nanoparticles: A Raman spectroscopic investigation, ***Journal of Applied Physics***, 132(21), 215107 (2022), DOI: https://doi.org/10.1063/5.0123854
7. Souvik Bhattacharjee, and Kalyan Kumar Chattopadhyay, Laser-induced Fano interference subsumed by electron-phonon coupling in orthorhombic $KNbO_3$ nano-bricks: An *ab-initio* vibrational and Raman spectroscopic investigation, ***Journal of Raman Spectroscopy*** (2023), DOI: https://doi.org/10.1002/jrs.6567

Apart from the above works, I also collaborated with other researchers from my lab and outside Jadavpur University. This facilitated the following works, where I served as a co-author. Although the current thesis is not directly associated with these works, they helped in my expanision of knowledge and experience throughout my Ph.D. tenure.

8. Suvra Pal, Nirmalya Sankar Das, Souvik Bhattacharjee, Subhadipta Mukhopadhyay, and Kalyan Kumar Chattopadhyay, Bias-tuned dielectric properties and Non-Debye relaxation in vanadium doped $BaSnO_3$ nanocubes, ***Materials Research Express***, 6(10), 105029 (2019), DOI: https://doi.org/10.1088/2053-1591/ab3750
9. Dipanwita Mitra, Souvik Bhattacharjee, Nilesh Mazumder, Bikram Kumar Das, Paramita Chattopadhyay, and Kalyan Kumar Chattopadhyay, Strain-induced partial phase transition in TiO_2 nanoparticles manifesting frequency dispersive pseudo-inductive switching of capacitance, ***Ceramics International***, 46(12), 20437-20447 (2020), DOI: https://doi.org/10.1016/j.ceramint.2020.05.138
10. Mississippi Missouri Bhunia, Karamjyoti Panigrahi, Chandra Bindu Naskar, Souvik Bhattacharjee, Kalyan Kumar Chattopadhyay, and Paramita Chattopadhyay, 2D square nanosheets of Anatase TiO_2: A surfactant free nanofiller for transformer oil nanofluids, ***Journal of Molecular Liquids***, 325, 115000 (2021), DOI: https://doi.org/10.1016/j.molliq.2020.115000
11. Nripen Besra, Kausik Sardar, Nilesh Mazumder, Souvik Bhattacharjee, Anjan Das, Bikram Kumar Das, Saikat Sarkar, and Kalyan Kumar Chattopadhyay, $CH_3NH_3PbI_3$ as a radio frequency decoupling capacitor: interplay between Maxwell–Wagner polarization and a pseudo inductive response, ***Journal of Physics D: Applied Physics***, 54(17), 175105 (2021), DOI: https://doi.org/10.1088/1361-6463/abdd66
12. Dipayan Roy, Karamjyoti Panigrahi, Bikram Kumar Das, Uday Kumar Ghorui, Souvik Bhattacharjee, Madhupriya Samanta, Sourav Sarkar, and Kalyan Kumar Chattopadhyay, Boron vacancy: a strategy to boost the oxygen reduction reaction of hexagonal boron nitride nanosheet in hBN–MoS_2 heterostructure, ***Nanoscale Advances***, 3(16), 4739-4749 (2021), DOI: https://doi.org/10.1039/D1NA00304F
13. Suvankar Mondal, Soumen Maiti, Tufan Paul, Aditi Sahoo, Souvik Bhattacharjee, Nirmalya Sankar Das, and Kalyan Kumar Chattopadhyay, All-inorganic halide perovskite tuned robust mechanical-energy harvester: Self driven posture monitor and power source for portable electronics, ***Applied Materials Today***, 26, 101385 (2022), DOI: https://doi.org/10.1016/j.apmt.2022.101385
14. Suvankar Mondal, Subhasish Thakur, Soumen Maiti, Souvik Bhattacharjee, and Kalyan Kumar Chattopadhyay, Self-Charging Piezo-Supercapacitor: One Step Mechanical-

Energy Conversion and Storage, ***ACS Applied Materials & Interfaces***, 15(6), 8446-8461 (2023), DOI: https://doi.org/10.1021/acsami.2c17538

15. S. Najes Riaz, Dipayan Roy, Souvik Bhattacharjee, Ankita Chandra, Kalyan Kumar Chattopadhyay, and Sourav Sarkar, Exploring the interfacial behavior of SiNWs/Sulphur and Nitrogen-doped carbon dot based heterostructure for near-infrared photodetection application, ***Materials Letters***, 134458 (2023), DOI: https://doi.org/10.1016/j.matlet.2023.134458
16. Dipanwita Mitra, Kausik Chanda, Souvik Bhattacharjee, Partha Bairi, Kalyan Kumar Chattopadhyay, and Paramita Chattopadhyay, Enhanced interfacial evaporation and desalination by solar heat localisation using nitrogenated Graphitic Carbon and Co_3O_4 nanorods, ***Solar Energy Materials and Solar Cells***, 257, 112361 (2023), DOI: https://doi.org/10.1016/j.solmat.2023.112361

List of Participations in National and International Conferences

All of my participations in various national and international scientific conferences are enlisted below, chronologically. In these conferences, I have exhibited some selected works of mine (as mentioned in the publications) as oral or poster presentations. I also had the glorious opportunity to meet many renowned scientists and to understand their field of research in their own words.

Sl. No.	Name of the conference	Venue and dates	Subject of presentation	Mode of presentation
1.	National Conference on Recent Developments in Nanoscience & Nanotechnology (NCRDNN)	Jadavpur University (JU), Kolkata, India. 29th to 31st January 2019.	Microwave-assisted one-step polyol synthesis of monodispersed and highly water dispersible Fe_3O_4 nanoparticles having wide size tunability to investigate size-dependent properties.	Poster
2.	2nd International Conference on Nanoscience and Nanotechnology (ICNAN'19)	Vellore Institute of Technology (VIT), Vellore, India. 29th November to 1st Decmber 2019.	Magnetite / Poly(Vinyledene Fluoride) Based Piezoelectric Nanogenerator Having Electromagnetic Interference Shielding Capability.	Oral
3.	International Conference on Nano Science and Technology (ICONSAT-2020), organised by SNBNCBS and DST	Biswa Bangla Convention Centre, Kolkata, India. 5th to 7th March 2020.	Negative capacitance switching in size-modulated Fe_3O_4 nanoparticles with spontaneous non-stoichiometry: confronting its generalized origin in non-ferroelectric materials.	Poster

4.	6th International Conference on Nanoscience and Nanotechnology (ICONN-2021)	Virtual conference organized by SRM Institute of Science and Technology. 1st to 3rd February 2021.	Laser-power Dependent Fano Asymmetry in Raman modes of Rare Earth Oxides.	Poster
5.	Young Scientists' Colloquium 2022 (YSC-2022), organised by the Materials Research Society of India (MRSI) – Kolkata Chapter	CSIR – Central Glass and Ceramic Research Institute (CGCRI), Kolkata, India. 16th December 2022.	Negative capacitance switching in size-modulated Fe_3O_4 nanoparticles with spontaneous non-stoichiometry: resolving ubiquities and confronting its generalized origin in non-ferroelectric materials.	Oral
6.	8th Nano Today Conference (An Elsevier Conference, jointly organised by Nano Today and Materials Today journals)	Paradise Point, San Diego, CA, USA. 22nd to 25th April 2023.	Negative capacitance switching in size-modulated Fe_3O_4 nanoparticles with spontaneous non-stoichiometry: resolving ubiquities and confronting its generalized origin in non-ferroelectric materials.	Oral

The certificates of participation in all of the enlisted conferences are attached below in chronological order.


National Conference on Recent Developments in Nanoscience & Nanotechnology,
29th -31st January 2019

NCRDNN

This is to certify that Souvik Bhattacharjee of Jadavpur University has participated/presented a paper as oral/poster presentation in the National Conference on Recent Developments in Nanoscience & Nanotechnology, 29th -31st January 2019, organized by the School of Materials Science and Nanotechnology, Jadavpur University.

31.1.2019
Prof. Kalyan Kumar Chattopadhyay
Convener


VIT
Vellore Institute of Technology
INSTITUTION OF EMINENCE

CNR

ICNAN'19
INTERNATIONAL CONFERENCE ON NANOSCIENCE AND NANOTECHNOLOGY

Certificate
of Presentation

This is to certify that

Dr./Mr./Ms. SOUVIK BHATTACHARJEE
has presented a paper (oral/~~poster~~) at the 2nd International Conference on Nanoscience and Nanotechnology (ICNAN '19) organized by the Centre for Nanotechnology Research (CNR), Vellore Institute of Technology, Vellore, India during 29th November – 1st December 2019.

Title of the paper:
" Magnetite/Poly(Vinylidene Fluoride) Based Piezoelectric Nanogenerator Having Electromagnetic Interference Shielding Capability"

Dr. Raja Sellappan
Convener

Vellore
1st December 2019

Dr. A. Nirmala Grace
Organizing Chair


Supported by
Department of Science & Technology Government of India

Organized by
S. N. Bose National Centre for Basic Sciences

ICONSAT

International Conference on Nano Science and Technology
5 - 7 March, 2020
Kolkata

Certificate of Participation

This certificate is awarded to
Souvik Bhattacharjee
of
Jadavpur University
for Oral Presentation / Poster Presentation / Participation in the International Conference on Nano Science and Technology (ICONSAT-2020) held during March 5-7, 2020 at Biswa Bangla Convention Centre, Kolkata.

Prof. Samir Kr. Pal
Jt. Convenor
ICONSAT-2020

Prof. Anjan Barman
Jt. Convenor
ICONSAT-2020

Prof. Samit Kr. Ray
Chair
ICONSAT-2020


SRM

6th International Conference on Nanoscience and Nanotechnology
(Virtual Conference)

SRM Institute of Science and Technology
Kattankulathur - 603203

ICONN 2021

Certificate

This is to certify that Mr. / Ms. / Dr. Souvik Bhattacharjee has participated and presented a paper entitled Laser-power Dependent Fano Asymmetry in Raman Modes of Rare Earth Oxides in the International Conference on Nanoscience and Nanotechnology (ICONN 2021) organized by Department of Physics and Nanotechnology, SRM IST, India during February 01 – 03, 2021, in association with Shizuoka University, Japan; National Chiao Tung University, Taiwan; GNS, New Zealand; University of Rome Tor Vergata, Italy; RMIT University, Australia; Tata Institute of Fundamental Research, India. The Asian Consortium on Computational Materials Science (ACCMS); Indian Physics Association (IPA); Material Research Society of India (MRSI), Indian Carbon Society, Council of Scientific & Industrial Research (CSIR), Indian Science Congress Association (ISCA), Department of Science & Technology (DST) and Springer Nature.

ICONN-2021

Head
Department of Physics and Nanotechnology
SRM IST

Chairperson
School of Applied Sciences
SRM IST


Materials Research Society of India (MRSI)
(Kolkata Chapter)

Certificate of Participation

This is to certify that Souvik Bhattacharjee of Jadavpur University (JU) has participated at the

"Young Scientists' Colloquium 2022"

Organised by
Materials Research Society of India (MRSI), Kolkata Chapter
On Friday, December 16, 2022
at CSIR-Central Glass and Ceramic Research Institute, Kolkata

Dr. Jui Chakraborty
Secretary, MRSI, Kolkata

Dr. Mrinal Pal
Chairman, YSC 2022

Prof. N. R. Bandyopadhyay
Chairman, MRSI, Kolkata

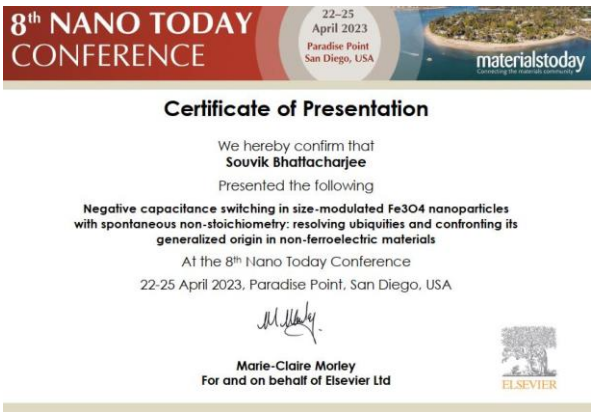
8th NANO TODAY CONFERENCE

22–25 April 2023
Paradise Point
San Diego, USA

materialstoday

Certificate of Presentation

We hereby confirm that
Souvik Bhattacharjee
Presented the following

Negative capacitance switching in size-modulated Fe3O4 nanoparticles with spontaneous non-stoichiometry: resolving ubiquities and confronting its generalized origin in non-ferroelectric materials

At the 8th Nano Today Conference
22-25 April 2023, Paradise Point, San Diego, USA

Marie-Claire Morley
For and on behalf of Elsevier Ltd

ELSEVIER

There are numerous other online/offline events and webinars, that I attended or participated in my Ph.D. tenure. Some of the relevant certificates are attached here.

Indian National Young Academy of Sciences (INYAS)
Flagship Event for Post-PhD Opportunities

PRAYOJAN
(23rd-24th April 2022)

CERTIFICATE
OF PARTICIPATION

This is to certify that:
Souvik Bhattacharjee

has participated online in the Post-Phd: Research, Academia and IndustrY Opportunities, Science Journalism, GrAnt writing and Networking (PRAYOJAN) workshop organized by INYAS during 23rd-24th April 2022

Event Conveners:

Dr. Prashant Kumar, Member, INYAS
Dr. Akshai Kumar, Member, INYAS
Dr. Praveen Kumar, Member, INYAS
Dr. Rajendra S. Dhaka, Chair, INYAS, New Delhi, India

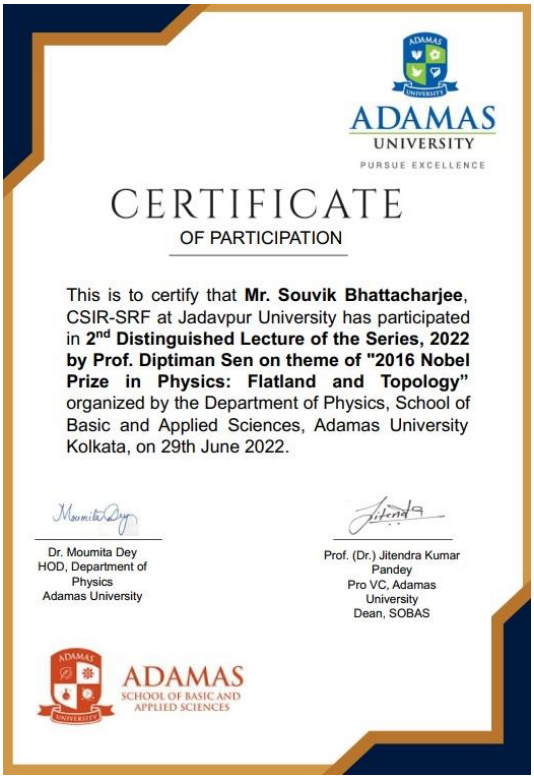

ADAMAS UNIVERSITY
PURSUE EXCELLENCE

CERTIFICATE
OF PARTICIPATION

This is to certify that **Mr. Souvik Bhattacharjee**, CSIR-SRF at Jadavpur University has participated in **2nd Distinguished Lecture of the Series, 2022 by Prof. Diptiman Sen on theme of "2016 Nobel Prize in Physics: Flatland and Topology"** organized by the Department of Physics, School of Basic and Applied Sciences, Adamas University Kolkata, on 29th June 2022.

Dr. Moumita Dey
HOD, Department of Physics
Adamas University

Prof. (Dr.) Jitendra Kumar Pandey
Pro VC, Adamas University
Dean, SOBAS

ADAMAS
SCHOOL OF BASIC AND APPLIED SCIENCES

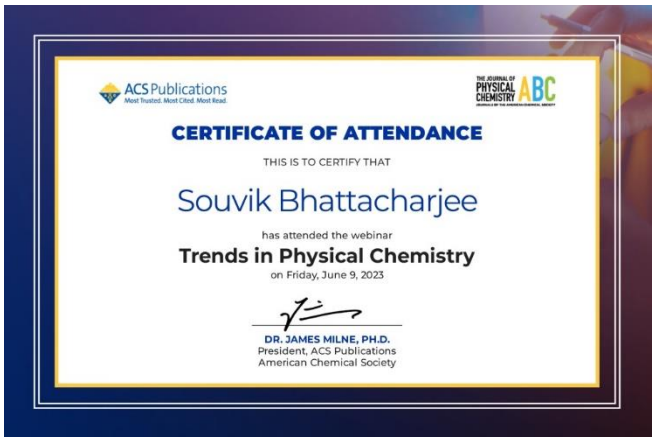

ACS Publications
Most Trusted. Most Cited. Most Read.

THE JOURNAL OF PHYSICAL CHEMISTRY ABC

CERTIFICATE OF ATTENDANCE

THIS IS TO CERTIFY THAT

Souvik Bhattacharjee

has attended the webinar

Trends in Physical Chemistry

on Friday, June 9, 2023

DR. JAMES MILNE, PH.D.
President, ACS Publications
American Chemical Society

1 INTRODUCTION AND OBJECTIVES

1.1 Introduction to nanomaterials and nanoscience

Nanomaterials are materials having at least one dimension in the nanometric scale, typically between 1 – 100 nm in size. Over the past few decades, their captivating surface, and remarkable electronic, optical, and catalytic properties have made them the centrepiece of leading-edge research.[1,2] At this scale, materials often exhibit unique physical and chemical properties that differ from those of their bulk counterparts. These have opened up new avenues for the development of novel technologies and applications. One of the most interesting features of nanomaterials is their large surface area-to-volume ratio. This means that at the nanoscale, materials have a much larger surface area per unit of mass than they do in bulk form, that leads to noteworthy implications like high reactivity and adsorption.[1,2] For example, nanoscale catalysts can exhibit much higher activity than bulk catalysts, due to their increased surface area. Another key property of nanomaterials is their size-dependent optical properties.[3] At the nanoscale, materials can exhibit quantum confinement of electronic states (and even phonons), which results in discrete energy levels, higher optical bandgap, and absorption spectra. So, nanomaterials can be tailored to exhibit fascinating optical properties, making them useful for a variety of applications, such as in solar cells and light-emitting diodes. Furthermore, nanomaterials can have unique electrical (because of smaller mean free path) and magnetic properties (such as superparamagnetism). Additionally, nanomaterials can also be engineered to have specific shapes, sizes, and surface functionalities. Besides, low dimensional materials can be of different genre as shown in Figure 1.1 *viz*., 0D (quantum dot or QD, tiny nanoclusters), 1D (nanowires, nanorods, *etc*.), 2D (ultrathin films, nanoflakes, nanoplatelets, *etc*.), and 3D (nanoparticles, nanoclusters, *etc*.). Thus, researchers can design and synthesize nanomaterials with specific applications in mind, such as photocatalysis, drug delivery, sensing, lighting, energy harvesting, and many more.[1-4]

In 1959, Richard Feynman delivered a compelling lecture titled, “There's plenty of room at the bottom”, in which he presented ground-breaking ideas for controlling and exploiting atomic-scale phenomena. Feynman's thought-provoking questions, such as 'What could we do with layered structures with just the right layers?' and 'What would the properties of materials be if we could really arrange the atoms the way we want them?' laid the groundwork for the

development of nanotechnology. His vision for successful manufacture and manipulation of materials at lower dimensions has transformed the field of physics and led to significant advancements in numerous industries, from electronics to medicine. Materials like carbon nanotubes (CNT), QD, graphene, MXenes, *etc*. have turned the 21st century into the era of nanotechnology.

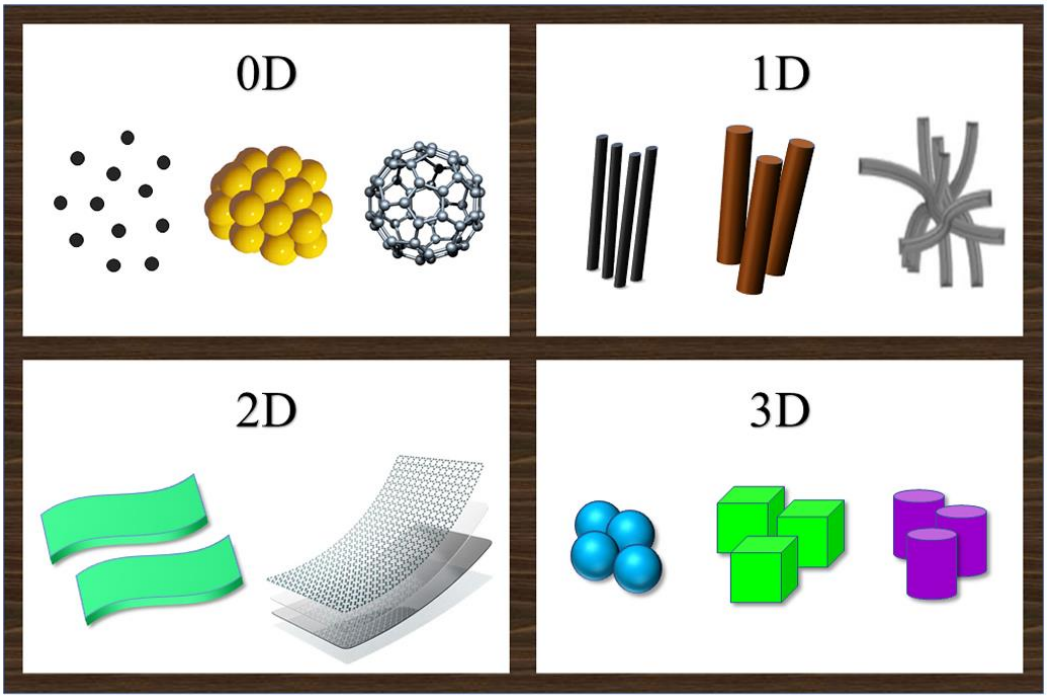

Figure 1.1 Schematics showing different form of low dimensional nanomaterials *viz*., 0D, 1D, 2D, and 3D nano-systems.

Despite their many promising applications, there are also concerns about the potential health and environmental impacts of nanomaterials. Due to high reactivity, nanomaterials could be more toxic than their bulk counterparts. As a result, researchers are actively studying the behaviour of nanomaterials in different environments, as well as developing methods to mitigate any negative impacts. In summary, nanomaterials offer many unique properties and opportunities for technological development. By engineering nanomaterials with specific properties, researchers can create materials with a wide range of applications in fields such as electronics, medicine, and energy.[1-5] However, it is also important to study the potential risks associated with the use of nanomaterials and to take steps to mitigate any negative impacts.

1.1.1 Synthesis of nanomaterials: top-down and bottom-up approach

The fabrication of nanomaterials can be achieved through two broad approaches: the top-down and the bottom-up methods.[6] Till date, most methods can be classified as to fall within one of these two categories, see Figure 1.2.

(i) ***The top-down approach*** involves the breaking down of bulk materials to obtain nanoscale materials. This method involves the use of mechanical, chemical, and thermal treatments to carve out structures at the nanoscale. Examples of the top-down method include lithography, where a pattern is first created on a substrate and then etched to create nanoscale features. In another example, ball milling is used to grind down bulk materials into nanoparticles. However, this creates many unwanted defect-states at the surface of nanomaterials. Moreover, the morphology of the nanostructures cannot be controlled, and agglomeration of grains is inevitable.

(ii) On the other hand, ***the bottom-up approach*** involves the assembly of smaller building blocks, such as atoms or molecules, to create the desired structure. This method can be achieved through chemical and biological methods. Examples of bottom-up approaches include the sol-gel method, where a solution of precursor molecules is hydrolysed and condensed to form a solid nanostructured material. Similarly, the self-assembly method is used to create ordered arrays of nanoparticles. Besides, common wet chemical methods including the hot injection method, one-pot synthesis routes, hydrothermal and solvothermal techniques *etc*. are all examples of the bottom-up category.

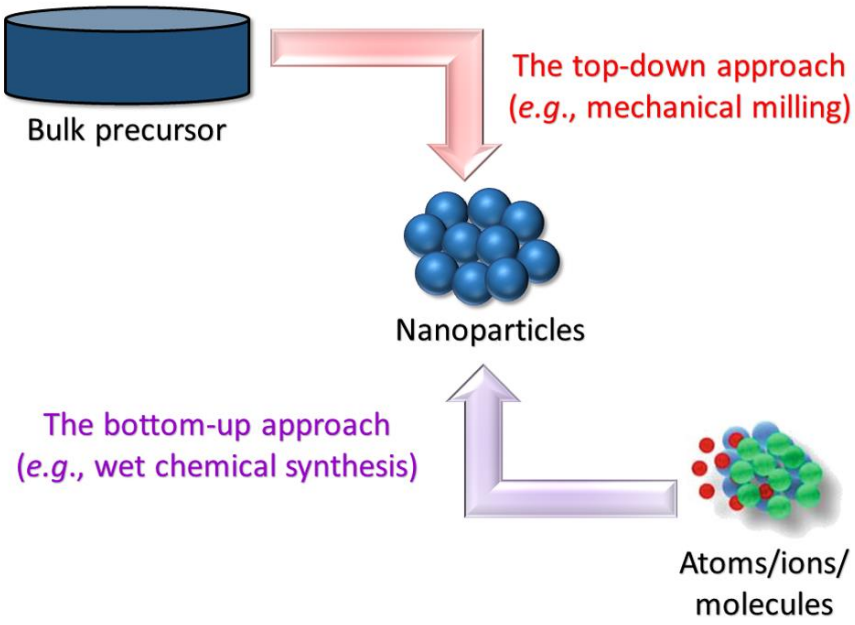

Figure 1.2 Schematics showing the top-down and bottom-up approach of synthesizing nanoparticles.

Both of these approaches have their own advantages and limitations. The top-down method is suitable for producing large quantities of nanomaterials with desirable sizes. However, this method can be costly (as per lithography is concerned), irregular (in case of ball-milling) and is limited in terms of the range of materials that can be processed. The bottom-up

approach, on the other hand, is better suited for creating complex nanoscale structures with greater control over their properties. However, this method can be challenging to scale up and may require specialized equipment. In summary, the choice of top-down or bottom-up approach depends on the specific requirements of the application, the desired properties of the nanomaterial, and the available resources. Both methods have contributed significantly to the development of nanotechnology and have led to numerous applications in fields ranging from electronics to medicine.

1.1.2 Size-dependent properties

Among the size-dependent properties, the magnetic, optical, thermal, chemical, and electrical properties have received considerable attention due to their fundamental scientific importance and potential technological applications.[3,7-9] One notable size-dependent property in nanomaterials is their magnetic behaviour. At the nanoscale, magnetic properties are influenced by surface effects and quantum confinement, resulting in distinct magnetic properties such as increased magnetization and superparamagnetism. These properties are of great interest for magnetic data storage, magnetic resonance imaging (MRI), and magnetic hyperthermia for cancer treatment. The optical properties of nanomaterials are also significantly influenced by their size. As the size of the material decreases, quantum confinement effects cause the energy levels to become discrete, leading to size-dependent changes in absorption and emission spectra. The change in optical bandgap as a function of size is usually described by the Brus equation.[10] The tunability of the optical properties of nanomaterials has significant implications for applications such as colour-tuneable displays, optical sensors, and biomedical imaging.[3] Thermal properties of nanomaterials, such as thermal conductivity, are also subject to size-dependent effects.[9] The increased surface area to volume ratio in nanomaterials results in more pronounced interfacial thermal resistance and phonon confinement, leading to lower thermal conductivity compared to bulk materials. However, the presence of defects and impurities can also have a significant impact on the thermal conductivity of nanomaterials. In the chemical domain, the size-dependent properties of nanomaterials can be exploited for a wide range of applications such as catalysis, gas sensing, and energy storage. The high surface area to volume ratio of nanomaterials enables higher reactivity, selectivity, and stability in catalytic reactions. In addition, the size-dependent chemical reactivity can be exploited for gas sensing, where the small size of nanoparticles enhances the surface adsorption of gas molecules. Finally, the electrical properties of nanomaterials also exhibit significant size-dependent effects. For example, the bandgap of semiconducting nanoparticles varies with size, enabling the tuning of their electrical conductivity and optical properties. The size-dependent electrical properties of nanomaterials have potential applications in electronic and optoelectronic devices, such as

transistors, solar cells, and light-emitting diodes. In summary, the size-dependent properties of nanomaterials exhibit fascinating and complex phenomena that have significant scientific and technological implications. Understanding and controlling these properties are critical for developing advanced materials with tailored properties and functions, and for enabling a wide range of applications in various fields.

1.1.3 Lead-free materials: Significance and future outlook

Lead-based perovskites and other materials have been widely researched for their exceptional dielectric, piezoelectric and photovoltaic properties for a long time. However, the use of lead in these materials raises concerns about their environmental and health impact.[11-13] Some key-issues are enlisted below.

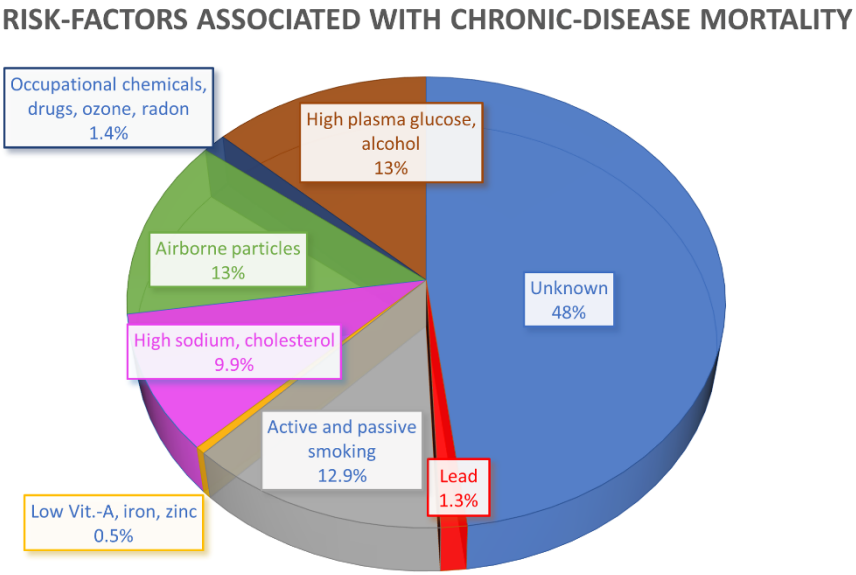

Figure 1.3 The chart presents the risk factors that lead to exposures which contribute to chronic-disease mortality. The data used to compile the chart were based on World Health Organization (WHO) estimates of exposures that contributed to the deaths of 50 million individuals globally in 2010.[11]

(i) ***Health risks:*** Lead is a toxic heavy metal that can cause serious health problems when it enters the human body. It can damage the brain, nervous system, kidneys, and reproductive system, and can also lead to hypertension, anemia, high blood pressure, immunotoxicity, and other health issues.[11-13] In fact, according to a data published by the World Health Organisation (WHO), approximately 1.3% of all chronic health mortality is caused directly or indirectly by lead pollution and contamination,[11] see Figure 1.3. Furthermore, some other data based on the US population within 1988 to 2011 directly shows how concentration of lead in blood abruptly increases the risk of serious health-

hazards and probability of death at an early age, see Figure 1.4.[14] This shows the severity of the concerns.

(ii) ***Environmental pollution:*** Lead can also harm the environment when it is released into the air, water, or soil. This can result in contamination of natural resources, and can affect the health of animals and plants.[12,13]

(iii) ***Electronic waste:*** Electronic waste is a growing problem, and lead-based materials are a significant contributor to this issue. When electronic devices containing lead are discarded, the lead can leach into the soil and water, causing environmental damage and potential health risks.

(iv) ***Regulatory compliance:*** Many countries have regulations in place that limit or ban the use of lead-based materials in technology. Failure to comply with these regulations can result in fines, legal action, and damage to a company's reputation.

(v) ***Recycling challenges:*** Lead-based materials can also make it more difficult to recycle electronic devices, as the lead needs to be properly removed and disposed of in a safe and environmentally friendly way.

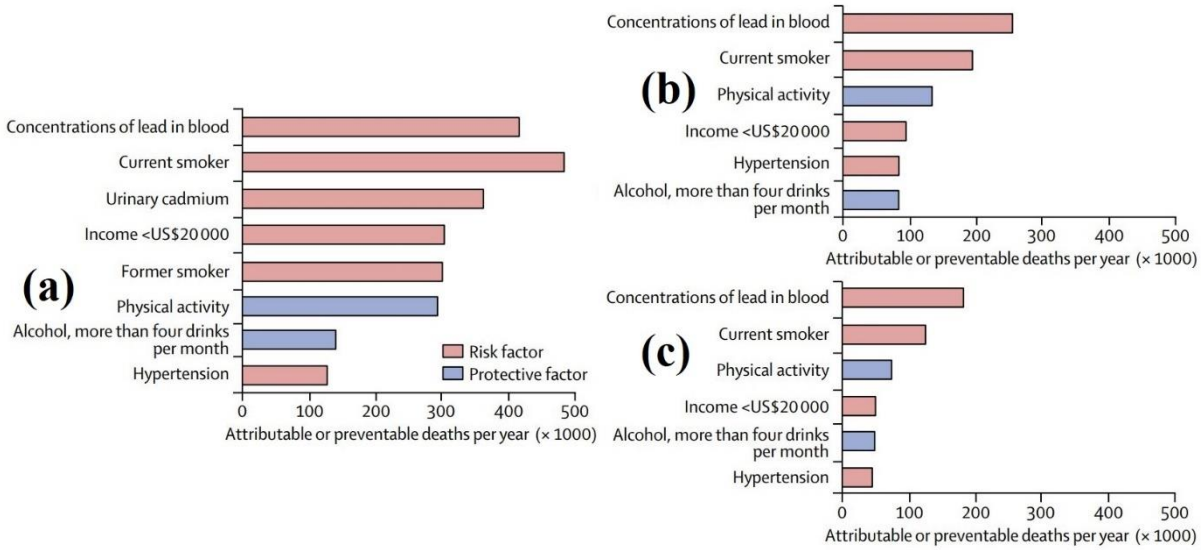

Figure 1.4 The panels illustrate the number of deaths caused by (a) all factors; (b) cardiovascular disease; and (c) ischaemic heart diseases in the US population during 1988 to 2011, that are attributed to certain modifiable risk factors. The concentration of lead in blood is provided in each graph. Reproduced and reformatted with permission from Ref. 15.

Overall, the use of lead-based materials in technology can have serious health and environmental consequences, and there are a variety of regulatory and practical challenges associated with their use and disposal. To address these concerns, researchers have turned their attention to lead-free materials. These materials have shown great potential for use in solar cells, offering comparable photovoltaic properties as lead-based perovskite materials

without the toxicity concerns. For example, tin-based perovskite materials have been developed and have shown remarkable stability and efficiency in solar cell applications. Moreover, lead-free perovskite materials have also been investigated for their potential use in light-emitting diodes (LEDs), as well as in optoelectronic devices. For instance, researchers have developed halide double perovskite materials, which offer a high degree of tunability of their optical and electronic properties. In summary, lead-free perovskite materials represent a promising alternative to lead-based perovskite materials, especially in the development of sustainable and environmentally friendly electrical, mechano- and optoelectronic devices.

1.2 Emerging energy crisis in the 21st century and its potential solutions

Throughout history, humanity has relied on fossil fuels as a primary source of energy. Since the industrial revolution, the demand for energy has increased, resulting in a higher dependence on fossil fuels. With the world's population growing at an accelerated rate, the demand for energy will continue to rise. As of 2018, almost 85% of the world's energy resources were derived from fossil fuels, with coal accounting for 27%, petroleum for 34%, and natural gas for 24%. In 2018, worldwide energy consumption increased by 2.9%, almost double the average of the previous decade and the highest since 2010. Electricity production accounted for nearly 20% of the world's total energy consumption, with demand for electricity continuing to increase. The global electricity demand grew by 4% in 2018 to more than 23,000 TW h, resulting in a further depletion of the earth's non-renewable energy resources, see Figure 1.5. Fossil fuels, which take billions of years to form, are being consumed at a much faster rate than they are being generated, making them a non-renewable resource.

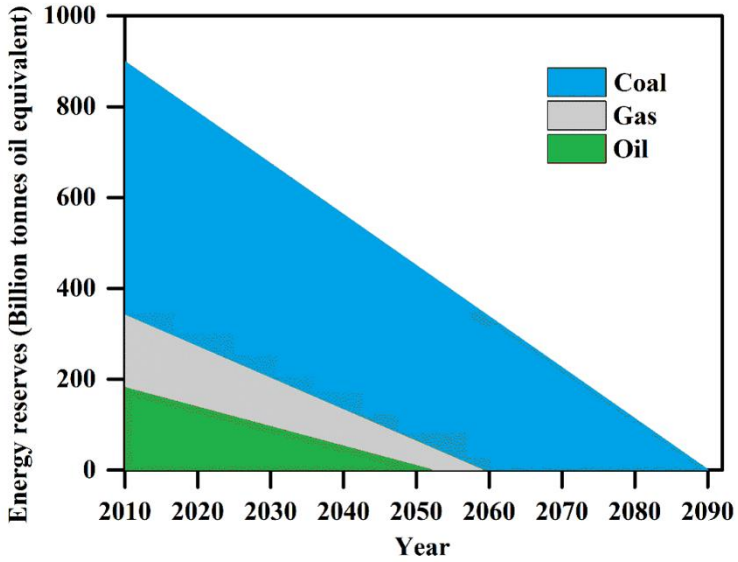

Figure 1.5 An estimated life span of different global fossil fuel energy reserves in 2023.

According to the 2019 Annual Energy Outlook, global GDP growth between 2017 and 2040 is expected to average 3.4%, with energy demand projected to increase by 1/3rd of the current value by 2040, driven by the increase in population and transportation consumption in China, India, and other parts of Asia. If this trend continues, it will lead to an unprecedented catastrophe worldwide, as we are depleting the earth's resources at an unsustainable rate. To address this issue, the world must shift to alternative and renewable energy resources. Currently, only 15% of global energy demand is met by renewable energy sources. To ensure the sustainability of humanity, we must increasingly utilize renewable energy resources to satisfy our ever-increasing demand for energy. It is crucial that appropriate measures be taken to mitigate this impending crisis before it is too late.

Aside from the threat of depleting fossil fuel reserves, the burning of these fuels poses a significant risk to the environment. While the use of fossil fuels has improved the standard of living worldwide since the industrial revolution, their combustion has severe environmental impacts that extend beyond those who use them. As fossil fuels burn, they release carbon dioxide (CO_2) into the atmosphere. It accelerates global warming, greenhouse effect, and climate change. The specific harmful effects depend on the type of fuel being burned, with coal, petroleum, and natural gas releasing particulate matter into the atmosphere that can cause smog and acid rain. The release of CO_2 and other greenhouse gases through the burning of fossil fuels is the main cause of climate change. Figure 1.6 illustrates the cumulative emission of greenhouse gases from 1850 to 2019 in different regions of the globe.

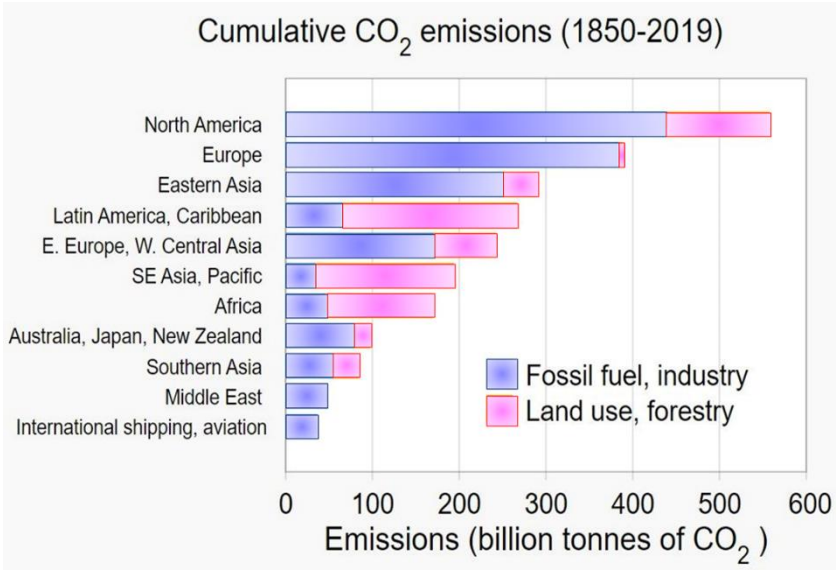

Figure 1.6 Bar chart showing the cumulative greenhouse gas emissions at different regions of the globe (based on WikiMedia commons data, IPCC AR6 WG3) between 1850 to 2019.

These emissions have led to accelerated global warming, resulting in the melting of glaciers, rising sea levels, and the extinction of many species. The impact of climate change on

biodiversity has been devastating, with many species disappearing in recent centuries, and the situation only worsening with time. The loss of species also impacts food production, exacerbating the problem of hunger. It is crucial to recognize the severe environmental impact of burning fossil fuels, and to shift towards more sustainable and environment-friendly energy sources. This will require significant effort and investment, but it is a necessary step to mitigate the ongoing climate crisis and ensure a sustainable future for all.

The burning of fossil fuels not only causes a depletion of reserves, but also generates nitric and sulfuric acids that lead to acid rain, which has adverse effects on both the environment and marble structures due to the dissolution of marble in acids. In addition, fossil fuels contain radioactive elements that are released into the atmosphere during combustion. For example, in 2000, coal burning worldwide released approximately 12,000 tonnes of thorium and 5,000 tonnes of uranium. Besides these detrimental effects, the combustion of fossil fuels is the primary cause of the global increase in air pollution. Due to the expansion of the transportation industry, which relies almost entirely on fossil fuels, air quality has significantly degraded in many large cities around the world, with severe impacts on human health such as premature death, acute respiratory illness, aggravated asthma, chronic bronchitis, and decreased lung function. The annual death toll caused by air pollution worldwide is approximately seven million.

It is essential to address not only the depletion of fossil fuel reserves but also the severe impacts caused by their combustion. Failure to do so could result in a global environmental catastrophe as demand for energy and usage of fossil fuels continue to increase. The scientific community must work towards developing efficient, pollution-free, and cost-effective alternative renewable energy resources. Responsibility for creating a sustainable future rest on both individuals and governments worldwide, who must rely more on these alternatives to meet their energy demands.

1.3 Alternative sources of energy

Nearly 77% of total energy demand is met by non-renewable sources like coal, petroleum, and natural gas. However, coal consumption contributes to climate change by releasing CO_2 and other toxic gases, causing air pollution and the greenhouse effect. Furthermore, these non-renewable sources took billions of years to form, making energy generation while maintaining the environment a significant challenge. Despite this, finding a renewable energy source that can serve as an alternative to petroleum and gas is necessary for our future security. Renewable energy sources, such as the sun, wind, hydro, and geothermal energy, provide endless energy and may be appropriate substitutes for non-renewable sources like coal and petroleum.[15] Over the past decade, global electricity generation has grown from

20% to 28%, with renewable energy contributing more than 20%. While electrical power generation from sunlight and wind has increased from 2% to 10%, these sources have lower efficiency and cost-effectiveness. Renewable energy resources are those that are sustainable and can provide an endless supply of energy without causing significant carbon emissions. Currently, renewable energy resources account for 15% of the world's energy supply, but according to the International Energy Agency (IEA), this number is expected to rise to 30% by 2024. In order to ensure a sustainable future, it is crucial that we increasingly satisfy our energy demands through the use of alternative renewable energy resources.

Renewable energy sources are ***sustainable*** and ***green*** because they do not deplete natural resources or harm the environment. These sources of energy rely on renewable resources that are continuously replenished, such as wind, solar, and water. In contrast, non-renewable sources of energy like fossil fuels are finite and take millions of years to form, and their extraction and consumption cause harm to the environment through carbon emissions and other pollutants. Renewable energy sources produce little to no greenhouse gas emissions or other pollutants, making them a more sustainable and cleaner alternative to traditional energy sources.[15] For instance, solar power generates electricity from the sun's energy, and wind power uses wind to spin turbines that generate electricity. Both of these sources of energy do not produce any greenhouse gas emissions, and their impact on the environment is minimal. In addition, renewable energy sources also help to reduce dependence on foreign oil, create jobs in the clean energy industry, and have the potential to lower energy costs over time. Moreover, using renewable energy helps to reduce our overall carbon footprint and can mitigate the effects of climate change. As we continue to address the challenges of climate change, renewable energy is becoming increasingly essential to building a sustainable future. Some sources are discussed below in detail.

(i) ***Solar energy*** is an abundant and free source of energy that supplies more energy in one hour than the world needs in a year. However, its availability depends on the location and weather conditions, making it difficult to be universally used. Furthermore, the efficient conversion of solar power into electricity is still lacking, hindering its full commercialization.

(ii) ***Wind energy*** is a clean source of energy that uses turbines to generate electricity for power grids. While domestic wind turbines are available, they may not be suitable everywhere.

(iii) ***Hydro energy*** is a well-developed renewable energy source, with dams and reservoirs being used to produce power that can be stored and supplied as needed.

(iv) ***Geothermal energy*** harnesses natural heat below the earth's surface, providing heat and electricity to homes, but its viability depends on location and environment.

(v) ***Biomass energy*** involves the conversion of waste into fuels, generating electricity at a lower environmental and economic cost.

(vi) ***Chemical energy***, such as hydrogen gas, is considered a clean energy source for the future. It is used in rechargeable batteries, hydrogen generators, and fuel cells. Fuel cells directly convert chemical energy into electrical energy, and they have been used to power automobiles on a small scale.

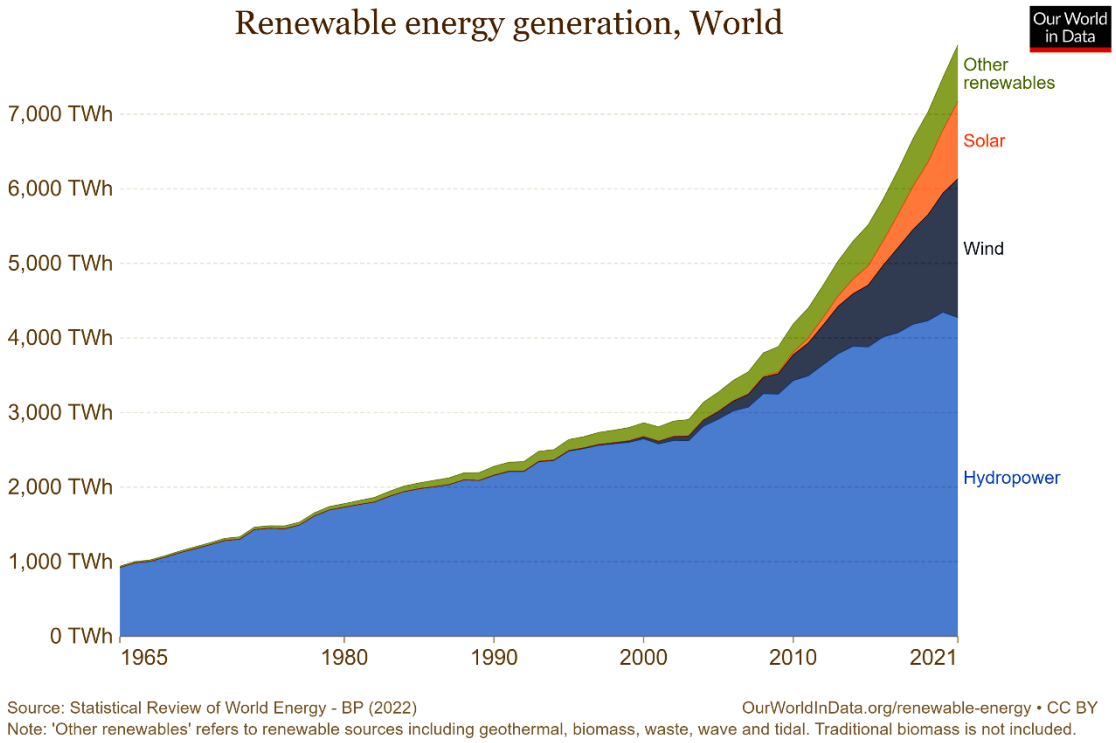

Figure 1.7 Statistical data on generation of different forms of renewable energy throughout the globe over the past few decades.

Although there exist various sources of renewable and green energies, they are still not applied on large scale due to the lack of proper and efficient technologies and fuel materials. Figure 1.7 shows the share of various renewable energy resources in generating electrical power. The maximum contribution is from hydro energy as already discussed. Nevertheless, to have a future where most of the global energy demands are satisfied from the renewable energy resources instead of fossil fuels, we need other reliable energy resources to be applied in large scale. To overcome these challenges, ***mechanical energy harvesting using piezoelectric transduction*** has gained attention. The ***piezoelectric nanogenerator*** is an efficient technology that can convert mechanical/vibrational energy into electrical energy, making it an ideal alternative to bulky batteries for powering smart, portable electronic gadgets. According to a report, the efficiency of the piezoelectric nanogenerator could be as high as 66%.

1.4 Energy harvesting, conversion, and storage

Energy harvesting, conversion, and storage are emerging fields that have gained significant attention in recent years.[16] The concept of energy harvesting involves capturing wasted energy from the surrounding environment and converting it into usable electrical power. This energy can be stored for future use, making it a sustainable and cost-effective solution for powering electronic devices. There are several types of energy harvesting devices that can be used to capture and convert wasted energy. One of the most common devices is the solar cell, which converts solar energy into electrical power. Solar energy can come in various forms such as solar photovoltaic, solar heat, solar heating, solar thermal, and photo-catalysis. The use of solar cells has been widely adopted as a sustainable alternative to traditional sources of energy.[17]

Another type of energy harvesting device is the ***thermoelectric generator***, which converts heat energy into electrical power.[18] This technology is widely used in applications where there is a large amount of wasted heat energy, such as in industrial processes or internal combustion engines. Pyroelectric generators can also be used to capture and convert heat energy. Mechanical energy harvesting is another alternative to electrical energy, which involves using piezoelectric nanogenerators. These devices convert mechanical energy into electrical power and can be used to power wireless, self-powered devices for a longer period. Extraction of wind and water energy using turbines and windmills has already been explored.

A ***transducer*** is an electronic device that converts energy from one form to another. The process of converting energy from one form to another is known as ***transduction***. Some common examples of transducers include loudspeakers, microphones, thermometers, and LEDs. Transducers are often employed at the boundaries of automation, measurement, and control systems, where electrical signals are converted to and from other physical quantities *e.g.*, energy, force, torque, light, motion, position, *etc*. On the other hand, research on storage of energy is primarily associated with batteries (lithium and sodium ion batteries) and supercapacitors (electrical double-layer capacitance or EDLC and pseudo-capacitance).[19]

The use of energy harvesting, conversion, and storage technologies has several advantages over traditional sources of energy. It is a sustainable and cost-effective solution for powering electronic devices, reducing the dependency on non-renewable sources of energy. It can also lead to the development of self-powered devices that do not require batteries or external power sources, making them more portable and convenient to use. So, energy harvesting, conversion, and storage are innovative fields that have the potential to revolutionize the way we use and consume energy. With the development of new and more efficient technologies, it is possible to harness wasted energy from the surrounding environment and convert it into usable electrical power, leading to a sustainable, eco-friendly future.

1.5 Piezoelectricity

Piezoelectric materials are unique materials that possess a specific structural conformation which generates electrical potential when subjected to mechanical stimuli. When the molecular structure of these materials deforms, a molecular dipole is formed, causing a shift in the positive and negative charge centres of the unit cell, leading to the creation of an external electric field. It occurs in non-centrosymmetric materials. One of the distinct features of piezoelectric materials is their reversibility. The ***direct piezoelectric effect*** produces an electric response under mechanical stress, while the ***reverse piezoelectric effect*** results in mechanical deformation under an applied electric field. Mathematically, the piezoelectric effect is described by the equation,

$$\sigma = d \times E + e \times D, \tag{1.1}$$

where, σ is stress (or strain), d is the piezoelectric stress constant, E is the applied electric field, e is the piezoelectric strain constant, and D is the electric displacement. On the other hand, ***electrostriction*** refers to the change in dimensions of certain dielectric materials when an electric field is applied. It occurs in centrosymmetric materials. In electrostriction, the strain or change in dimension is described by the equation,

$$\varepsilon = Q \times E^2. \tag{1.2}$$

Here, Q is the electrostrictive coefficient. Both effects involve the interaction between electric fields and material properties but arise from different crystal structures and mechanisms.

The direct and indirect piezoelectric effects have been utilized in many applications such as the development of piezoelectric nanogenerators, which can power various sensors, small electronics, Internet of Things (IoT) technologies, and other applications. The piezoelectric effect has also been used to create several industrial and scientific instruments, including atomic force microscopy (AFM) and scanning tunnelling microscopy (STM). In addition to these advanced applications, piezoelectric materials have also found their way into everyday objects such as lighters, baby-shoes *etc*., demonstrating their versatility and widespread use in modern society.

1.5.1 Evolution of piezoelectric materials and nanogenerators

The term "Piezoelectric" has its roots in the Greek word "piezein", meaning "to press tightly". This phenomenon involves an electrochemical interaction between mechanical domains and electrical domains. In 1880, the Curie brothers, Pierre and Jacques, were the first to observe the direct piezoelectric effect.[20] Initially, they discovered the direct piezoelectric behaviour of quartz and Rochelle salt crystals, with the inverse piezoelectric effect remaining unexplored. However, Lippmann mathematically realized the inverse piezoelectric effect in 1881, and in the same year, Curie experimentally established the inverse piezoelectric effect.[20]

The Curie brothers also demonstrated the piezoelectric effect of other materials, including tourmaline, topaz, cane sugar, and Rochelle salt crystals. In 1910, Woldemar Voigt published a book on the elastic behaviour of crystals, where he used tensor analysis to describe the characteristics of piezoelectric crystals.[21,22] During World War I, French scientist Paul Langevelt and his colleagues invented sonar using quartz crystal in 1917, marking the first practical application of the piezoelectric property of materials.[22]

In the following years, researchers discovered and established many more piezoelectric materials, and new applications were demonstrated. During World War II, researchers worldwide focused on developing new piezoelectric materials like barium titanate ($BaTiO_3$) and lead zirconate titanate ($PbZr_xTi_{1-x}O_3$) or PZT, which possess higher piezoelectric constants than natural materials. These materials have specific characteristics that are efficient for practical device applications. In 2008, Professor Z. L. Wang introduced the concept of self-powering, leading to the invention of piezoelectric nanogenerators (PENGs) that utilize the piezoelectric effect of ZnO nanowires.[23] This discovery became a milestone for self-powered device applications. Extracting mechanical energy from our surroundings and converting it into electrical energy is a valuable approach to meeting our energy needs.

1.5.2 Development of new-age piezoelectric nanogenerators (PENGs)

The development of PENGs based on ZnO nanowires (NWs) has been a significant milestone in the field of piezoelectricity.[23] The coupling between the semiconducting and piezoelectric properties of the vertically aligned ZnO NWs generates an electric signal when an AFM tip sweeps across them.[23] This discovery has spurred extensive research on piezoelectricity, leading to significant advancements in related applications. In the early stages of research, the unique physical and chemical properties of 1-D nanostructures of ZnO, such as nanorods, nanowires, nanotubes, and nanobelts, made them crucial semiconductor materials. Thereafter, Z. L. Wang *et al*. proposed an innovative idea for small-scale mechanical energy harvesting using a piezoelectric nanogenerator based on ZnO nanowire arrays. The nanogenerator produces an output signal under ultrasonic wave stimulation. The discovery of piezoceramic $BaTiO_3$ has played a significant role in the evolution of the piezoelectric field among stable inorganic oxides.[24] The unique structure of the unit cells and high piezoelectric coefficient of piezoceramics make them attractive materials for research. The direct piezoelectric effect has also been demonstrated in single crystal $BaTiO_3$ nanostructures under low-frequency mechanical stress. The fact that the output voltage is directly proportional to the applied strain rate, helped to develop a necessary circuit diagram for a piezoelectric nanowire-based sensor under low-frequency operation. Many perovskite piezoceramics, such as PZT, $ZnSnO_3$, $KNbO_3$, $LiNbO_3$, and $PbTiO_3$, have been well established in this field. PZT has gained the

most attention due to its large piezoelectric coefficient value. Several compositions of PZT-based piezoceramics have been studied, and the d_{33} value varies from 300 to 1000 pC N^{-1}. High quality PZT NW array-based PENGs have been tested for potential applications in mobile powering and daily use electronic gadgets. However, concerns about the presence of toxic lead have raised questions about the application of PZT. Several piezoelectric polymers such as PVDF have garnered significant attention in this field due to their flexibility, non-reactivity, and high piezoelectric coefficient. In the past decade, power density, durability and overall performance of PENGs composed of various nanomaterials and nanocomposites have improved manifold due to explicit research all over the world.

1.5.3 Electrostatics of PENGs

The fundamentals of a piezoelectric nanogenerator can be described starting from the Maxwell's equations in the free space and in material medium, as enlisted in the respective columns.[25,26]

$\vec{\nabla}.\vec{E} = \frac{\rho}{\varepsilon_0}$	(1.3A)	$\vec{\nabla}.\vec{D} = \rho_f$	(1.3B)
$\vec{\nabla} \times \vec{E} = -\frac{\partial \vec{B}}{\partial t}$	(1.4A)	$\vec{\nabla} \times \vec{E} = -\frac{\partial \vec{B}}{\partial t}$	(1.4B)
$\vec{\nabla}.\vec{B} = 0$	(1.5A)	$\vec{\nabla}.\vec{B} = 0$	(1.5B)
$\vec{\nabla} \times \vec{B} = \mu_0 \vec{J} + \mu_0 \varepsilon_0 \frac{\partial \vec{E}}{\partial t}$	(1.6A)	$\vec{\nabla} \times \vec{H} = \overrightarrow{J_f} + \frac{\partial \vec{D}}{\partial t}$	(1.6B)

Here, $\vec{E}$ and $\vec{B}$ respectively indicate the electric and magnetic fields, $\vec{D} = \varepsilon_0 \vec{E} + \vec{P} = \varepsilon \vec{E}$ is the electric displacement vector, $\vec{H} = \frac{\vec{B}}{\mu_0} - \vec{M} = \frac{\vec{B}}{\mu}$ is the magnetic intensity, ε is permittivity (for free space, a zero is added in the suffix), μ is permeability, ρ is charge-density (for free charge, an 'f' is added in the suffix), and $\vec{J}$ is current-density. Furthermore, $\vec{P}$ and $\vec{M}$ are the polarization and magnetization vectors.

In the presence of a transient external stress, electric field inside a piezoelectric material change, that leads to a displacement current given by,

$$\overrightarrow{J_D} = \varepsilon_0 \frac{\partial \vec{E}}{\partial t}. \tag{1.7}$$

This transforms equation 1.6A to a more compact form: $\vec{\nabla} \times \vec{B} = \mu_0 \left(\vec{J} + \overrightarrow{J_D}\right)$. On the other hand, in 2006, Prof. Z. L. Wang introduced an additional term, $\overrightarrow{P_s}$, to the polarization. This term represents the polarization resulting from electrostatic surface charge caused by mechanical response in the medium, which is distinct from the polarization $\left(\vec{P}\right)$ of the medium under an external electric field. Thus, we can revise the expression for displacement current as follows,

$$\vec{D} = \varepsilon_0 \vec{E} + \vec{P} + \vec{P_s}. \tag{1.8}$$

When a force is applied along the z-axis, the resulting polarization also occurs along the z-axis, and can be expressed as $\vec{P_s} = \vec{P_z} = \vec{\sigma_P}(z)$. Using this relationship, the displacement current density due to stress-induced polarization can be represented by the following equation,

$$\vec{J_P} = \frac{\partial \vec{P_z}}{\partial t} = \frac{\partial \vec{\sigma_P}(z)}{\partial t}. \tag{1.9}$$

So, here, $\vec{P_z}$ is the stress-induced polarization that changes over time.

- ***Open circuit voltage*** ($\boldsymbol{V_{OC}}$) is the voltage generated by a PENG when there is no external load connected to its output. In other words, it is the maximum voltage that the generator can produce when it is not connected to any load. This occurs because the piezoelectric material produces an electric charge in response to the mechanical stress applied to it, and this charge accumulates on the surface of the material, creating a voltage potential between the two electrodes of the generator. Now, we can determine the open-circuit voltage magnitude of the piezoelectric nanogenerator by using the equation,

  $$V_{OC} = \frac{t_z \sigma_P}{\varepsilon}. \tag{1.10}$$

  Here, t_z represents the thickness of the piezoelectric material along z-axis, σ_P is the magnitude of surface-charge owing to stress-induced polarization, and ε is the permittivity of the material.
- ***Short circuit current*** ($\boldsymbol{I_{SC}}$) is the current that flows through a PENG when its output is connected directly to a short circuit, *i.e.*, a load with zero resistance. In this scenario, the current flows freely through the load, and the voltage across the load is zero. The short circuit current is the maximum current that can be generated by the piezoelectric nanogenerator when it is connected to a load with zero resistance. This occurs because the piezoelectric material produces an electric current in response to the mechanical stress applied to it, and this current flows freely through the load when there is no resistance. Both V_{OC} and I_{SC} are idealistic parameters, but associate vital information regarding the performance of a PENG.
- However, the as-delivered power density provides a more consolidated information. The instantaneous power can be obtained from the product of the instantaneous voltage and current.

1.5.4 Operating principle of PENGs

The piezoelectric effect in solid materials is closely related to the polarizability of molecular dipoles or ions within the crystal lattice, which have unevenly distributed charge environments.[27] The crystal's net dipole moment can be determined by adding up the dipole moments per unit cell. Typically, these dipoles are arranged randomly in Weiss domains, but

under mechanical pressure, they tend to align in the direction of stress. A piezoelectric nanogenerator can be created by placing the piezoelectric material between two electrodes, where it is normally in a balanced state, with no net dipole moment. However, when mechanical stress is applied, the atomic dipoles align with the force, creating an internal electric field that induces opposite charges on both electrodes, creating a potential difference and causing an electric current to flow through the external circuit. Upon release, the electric field dissipates, causing a current to flow in the opposite direction, resulting in an AC current during a complete pressing and releasing cycle. The direction of current flow is schematically shown in Figure 1.8 during the press and release action over a piezoelectric crystal.

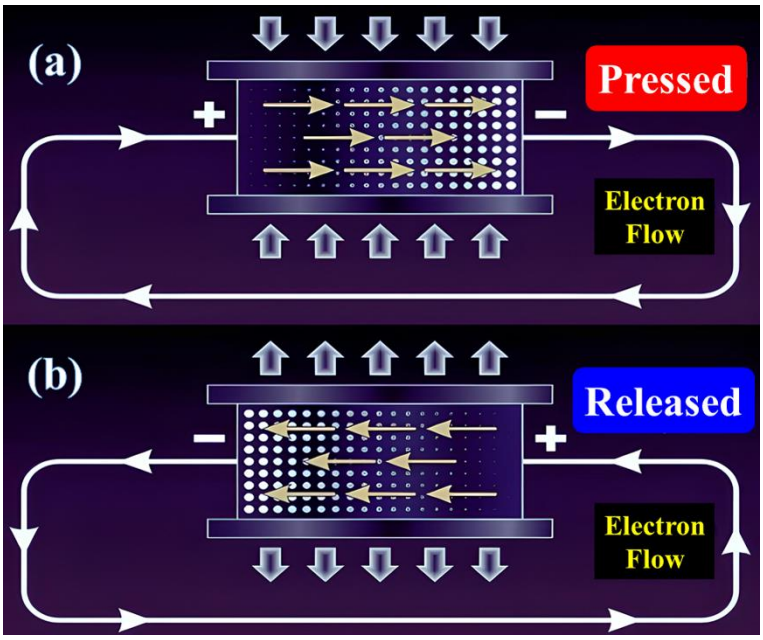

Figure 1.8 The direction of polarisation and electron flow when the piezoelectric crystal is (a) pressed or compressed; and (b) released or decompressed.

1.6 Dielectrics

Dielectrics are materials that are considered to be non-ideal insulators or poor electrical conductors. Even though most materials, including living organisms and agricultural products, can conduct electric currents to some degree, they are still classified as dielectrics due to their low conductivity.[28] The electrical properties of each material vary depending on its dielectric properties, and this information is crucial for researchers and engineers in designing and characterizing materials or monitoring process quality. Both polar and non-polar materials, which show some sort of polarization under an external electric field can be considered as dielectrics.

The primary parameter for dielectric properties is the complex permittivity, which describes a material's behaviour when subjected to an electromagnetic field.[28] A material that

can store electrostatic energy when an external electric field is applied is classified as a dielectric. The complex relative permittivity or dielectric function is expressed as, $\hat{\varepsilon}_r = \varepsilon_r' - i\varepsilon_r'', i = \sqrt{-1}$. Here, ε_r' is the real part, that represents the storage of the electric field, and ε_r'' is the imaginary part related to the dielectric loss factor, that represents the measure of energy dissipating or how lossy a material is to an external electric field. Conductivity (σ) measures a material's ability to conduct an electric current. The dielectric constant is associated with a material's capacitance, which is its ability to store energy or polarization when an electric field is applied. The ratio between the imaginary and real parts corresponds to another parameter, the dissipation factor, or loss tangent ($\tan\delta$). It represents the ratio of energy lost to energy stored per cycle.

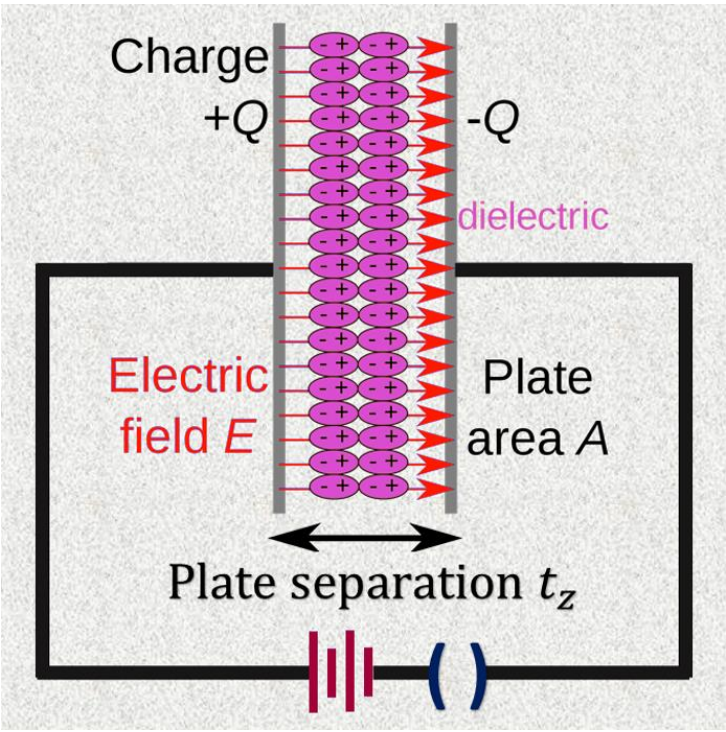

Figure 1.9 Schematics of a parallel plate capacitor with a dielectric material inserted between the plates, connected to a battery.

1.6.1 Dielectric capacitor

A capacitor is a device that contains two conductor plates with a dielectric material in between them. It is usually in the form of parallel plates, as shown in Figure 1.9. The primary function of a capacitor in electronic devices is to store electrical energy. Capacitance is the ability of a capacitor to store energy and is determined by the physical dimensions of the conductors and the permittivity of the dielectric material between the plates, regardless of the potential difference and total charge on the conductors. Capacitance is directly proportional to the overlap area and the relative permittivity of the dielectric, and inversely proportional to the

separation distance between the plates. The formula for capacitance of a parallel-plate capacitor is given by,

$$C = \frac{\varepsilon_0 \varepsilon_r' A}{t_z}. \tag{1.11}$$

Here, A is the effective area of overlap between the plates, and t_z is the thickness between the plates (say, along the z −axis), see Figure 1.9.

When an external voltage is applied to the capacitor, the plates become electrically polarized, causing positive and negative charges to accumulate on the two plates, respectively. This is known as the charging process of the capacitor, which is completed when the electrical potential caused by the accumulated charge Q on both plates equals the external applied voltage V. The charge on the capacitor is equal to the capacitance times the voltage, $Q = CV$. The capacitance may vary if the relative permittivity of the dielectric changes due to an external bias, in which case the capacitance is defined in terms of differential change *i.e.*, $C = \frac{dQ}{dV}$. During the charge process, work must be done to move charges between the conductor plates, and electric energy is stored in the dielectric material.[29] The amount of stored energy (W) can be calculated using the formula, $W = \frac{Q^2}{2C} = \frac{1}{2}CV^2 = \frac{1}{2}QV$. This formula expresses the relationship between capacitance, charge, and voltage, and shows that the stored energy is proportional to the square of the voltage or charge on the capacitor.

1.6.2 Measurement techniques

In the field of dielectric measurement, no single technique can fully characterize all materials over the entire frequency band. Accurately measuring both lossy and low-loss materials present a challenge, as each frequency band and loss type requires a different method.[30] Moreover, there is always uncertainty in dielectric measurements while characterizing materials. Several significant factors impact these measurements, including frequency, required accuracy, temperature, material nature, sample size/thickness, contacting/non-contacting measurement, destructive/non-destructive testing, and cost.

In light of the aforementioned factors, selecting the appropriate measuring technique requires considering the testing frequency and the type of test material. Additionally, the selection of measurement equipment and sample holder design must be based on frequency and the material being tested. Dielectric measurement techniques can be broadly categorized into two main categories: resonant and non-resonant.[30] Resonant methods can characterize the material at single or discreet frequency points. In this method, a dielectric material is used as a resonant element, but it is limited to low-loss test samples. Examples of resonant methods include dielectric, planar, and split resonator methods. The perturbation method is another method in which a sample is placed into a resonant cavity that causes the perturbation,

resulting in resonant frequency shift. This method is suitable for lower and moderate-loss samples.

On the other hand, non-resonant methods can measure over a broad range of frequencies. This method can categorize the material by determining the reflection and transmission coefficients that cause changes in characteristic impedance and wave velocity. Among the various techniques, some of the most popular and essential methods for dielectric measurements are coaxial probe method, transmission line method (waveguide), free space method, resonant cavity method, parallel plate (electrode) method, planar transmission line method, *etc*.[30]

The parallel plate (electrode) method involves sandwiching a thin sheet sample of a dielectric material between two electrodes to form a capacitor. Measurements can be taken using an LCR meter or impedance analyser and a dielectric fixture. Typically, low frequencies (sub-1 GHz) are used for this method. Parallel plate test parameters are derived by considering the dimensions of the material and by measuring its capacitance and dissipation factor. To measure the dielectric constant, a dielectric sample is placed into a sample holder, and the capacitance value is used to calculate the permittivity. This method has high measurement accuracy (about $\pm 1\%$ for ε_r' and $(5 \pm 0.005)\%$ for $\tan\delta$) and involves very simple sample preparation and setup, typically with a frequency range from 20 Hz to 1 GHz. However, the air gap and its effects can cause significant error if not considered and calibrated. Additionally, spurious measurements due to electrode polarization effect can lead to poor results, which can be mitigated by using electrodes with large, microscopic surface or by using higher frequencies as the effect is reduced rapidly with increasing frequency.

1.6.3 Energy storage density of dielectric materials

The energy stored per unit volume of a dielectric, known as energy storage density (J) is commonly used for research purposes to enable convenient comparison. J values can be obtained using two methods: static and dynamic.[28,29] In the static method, the sample capacitor is first charged by an external bias, and the electric energy is stored in the dielectric. The capacitor is then connected to the load R to complete a circuit using MOSFET switching, and a part of the stored energy is discharged along with a transient current formed in the closed circuit. The discharged energy can be obtained using the formula,

$$W = \int I^2(t) R dt. \tag{1.12}$$

Here, R is the resistance of the load, and t is the discharge time. Finally, the energy density J can be calculated by using the ratio between W and the volume of the capacitor. It is important to note that the obtained J value using this method is the recoverable energy storage density, as some of the stored energy is lost during the charge and discharge process.

In the dynamic method, the energy storage density can be induced easily. The charge density $\left(\frac{Q}{A}\right)$ on the conductor plate of a capacitor is equal to the electrical displacement, $D = \varepsilon E$ in the dielectric. Therefore, the energy storage density can be expressed as,

$$J = \frac{W}{At_z} = \int E_{max} D dE. \tag{1.13}$$

Here, the external applied electrical field, $E = \frac{V}{t_z}$, and the other letters are defined as before. For dielectrics with a high permittivity, the electrical displacement is very close to their electrical polarization. Therefore, $J \approx \int E_{max} P dE$. Based on this, the J value of the dielectric can be easily obtained by numerical integration of the area between the polarization and the curves of the electric field-polarization $(P - E)$ loops. During the discharge process from E_{max} to zero, the recoverable electrical energy density J_{reco} is released. This means that part of the stored energy is exhausted during the depolarization process due to hysteresis loss. Based on these results, the energy storage efficiency η can be defined as,

$$\eta = \frac{J_{reco}}{J_{store}} \times 100\%. \tag{1.14}$$

Also, the formula, $J = \int E_{max} \varepsilon E' dE'$ for dielectrics with a linear permittivity is independent of the external applied field. In this case, we effectively get,

$$J = \int E_{max} P dE = \frac{1}{2} \varepsilon E^2. \tag{1.15}$$

This result indicates that the energy storage density for linear dielectric materials is directly proportional to the relative permittivity of the dielectrics and to the square of the operating field. It should be noted that the J value obtained using the dynamic method is usually larger than that obtained using the static method.[29,30]

1.6.4 Effect of temperature and DC bias on relative permittivity

The relative permittivity, also known as the dielectric constant, is an important electrical property of materials, describing their ability to store electric charge in an electric field. It is defined as the ratio of the capacitance of a capacitor filled with a material, to the capacitance of the same capacitor with a vacuum or air filling. The relative permittivity of a material depends on various factors, including temperature, pressure, frequency, and DC bias.[31-34]

Temperature is one of the most important factors affecting the relative permittivity of materials. The temperature-dependence of permittivity is related to the thermal vibrations of atoms and molecules in the material. As temperature increases, the thermal motion of atoms and molecules also increases, leading to a decrease in the density of the electric dipoles in the material, and hence a decrease in the relative permittivity.[31,32] This effect is more significant in materials with high polarizability, such as ferroelectrics.

DC bias is another important factor affecting the relative permittivity of materials. When a DC bias voltage is applied to a material, it causes a shift in the centre of the electric dipoles, resulting in a change in the relative permittivity of the material.[33,34] The magnitude and direction of the DC bias-dependence of permittivity depend on the orientation of the electric dipoles in the material with respect to the applied DC bias field. A DC bias can also create space charge regions and affect the electronic properties of the material, leading to changes in the dielectric constant and dielectric loss. These changes can be used to understand the electronic properties of the material and the mechanism of charge transport.[33,34] It can have important implications for the performance of electronic devices, especially capacitors and insulators. For example, in high-frequency applications, the capacitance of a capacitor may vary with frequency due to the frequency-dependence of permittivity. Similarly, in high-voltage applications, the breakdown voltage of an insulator may depend on the DC bias voltage, due to the DC bias-dependence of permittivity.

1.7 Vibrational properties

Vibrational properties of nanomaterials play a crucial role in determining their physical, chemical, and electronic properties. The vibrations of atoms in nanomaterials can be described as phonons, which are quantized units of lattice vibrations. Vibrational spectroscopy techniques such as Raman spectroscopy and Fourier-transform infrared (FTIR) spectroscopy are widely used to study the vibrational properties of nanomaterials.

1.7.1 Raman and FTIR spectroscopy

Raman spectroscopy is a powerful technique for studying the vibrational properties of nanomaterials. In Raman spectroscopy, a laser is used to excite the vibrational modes of a material, and the scattered light is analysed to obtain information about the vibrational frequencies and modes. Raman spectroscopy is sensitive to both symmetric and asymmetric stretching modes, as well as bending and scissoring modes.[35] The Raman spectrum can provide information about the size, purity and crystallinity of nanoparticles, the nature of the chemical bonds, and the presence of defects or impurities in the material.

FTIR spectroscopy is another widely used technique for studying the vibrational properties of nanomaterials. In FTIR spectroscopy, infrared radiation is used to excite the vibrational modes of a material, and the absorption or transmission of the radiation is analysed to obtain information about the vibrational frequencies and modes. FTIR spectroscopy is sensitive to both symmetric and asymmetric stretching modes, as well as bending and scissoring modes. The FTIR spectrum can provide information about the chemical composition, purity, and functional groups of nanomaterials.

1.7.2 Phonon dispersion and density of phonon states

In all vibrational aspects, study of phonon dispersion plays a crucial role. The phonon dispersion of a material is a plot of the energy and momentum of its phonon modes.[36] In nanomaterials, the phonon dispersion is influenced by the size, shape, and surface structure of the material. The phonon dispersion can be calculated using first-principles calculations based on density functional theory (DFT) or measured experimentally using techniques such as inelastic neutron scattering (INS) or Raman spectroscopy. The resemblance of phonon dispersion between bulk and nanomaterials is important to understand the effect of size on the vibrational properties of nanomaterials.[36,37]

The density of phonon states (DOPS) can be defined mathematically as the derivative of the total number of phonon modes with respect to the phonon frequency. In other words, the DOPS represents the number of phonon modes per unit energy interval per unit volume of the crystal. Mathematically, the DOS can be expressed as,

$$\mathrm{DOS}(\omega) = \frac{V}{2\pi^2\omega^2}\sum j\delta(\omega - \omega_j). \tag{1.16}$$

Here, $\mathrm{DOS}(\omega)$ is the density of phonon states at frequency ω, V is the volume of the crystal, ω_j is the frequency of the j^{th} phonon mode, and $\delta(\omega - \omega_j)$ is the Dirac delta function, which is zero unless $\omega = \omega_j$. The summation is taken over all phonon modes. The DOS is an important quantity in the study of the vibrational properties of materials and is used to calculate various thermodynamic properties such as specific heat and thermal conductivity.[36,37]

1.7.3 Exploration and applications of molecular vibrations

The vibrational modes of nanomaterials can be classified into several types, including symmetric stretching, asymmetric stretching, bending, scissoring, and others. Symmetric stretching involves the stretching of two or more atoms in a molecule in a symmetric manner. Asymmetric stretching involves the stretching of two or more atoms in a molecule in an asymmetric manner. Bending involves the bending of two or more atoms in a molecule, while scissoring involves the motion of two atoms in opposite directions. The vibrational modes of nanomaterials can provide important information about their chemical and physical properties.[38,39]

The study of vibrational properties of nanomaterials is of great importance in various fields such as nanoelectronics, catalysis, and nanomedicine. The vibrational properties of nanomaterials can be used to tune their electronic, optical, and catalytic properties. For example, the size and shape-dependent vibrational properties of metal nanoparticles can be used to tune their plasmonic properties, which find applications in sensing, imaging, and energy conversion. In addition, the vibrational properties of nanomaterials can be used to understand

the interaction of nanoparticles with biological systems, which find applications in drug delivery and imaging. Furthermore, the interference of vibrational energy levels with other energies leads to many remarkable physical outcomes.[38,39]

1.7.4 The Fano effect

Fano interference, ***Fano resonance***, and ***Fano asymmetry*** are related phenomena that can be observed in a variety of physical systems, including Raman spectroscopy and electron-phonon coupling. Fano interference refers to the interference between a discrete state and a continuous spectrum of states.[40] This interference results in a characteristic asymmetric line-shape in the spectrum, known as a ***Breit-Wigner-Fano (BWF) line-shape***.[41] This is different from the traditional symmetric profiles, such as Gaussian or Lorentzian distributions. The BWF line-shape is characterized by a sharp peak, or resonance, superimposed on a broad background. Mathematically it is described by a line-shape parameter or Fano asymmetry parameter, q. The peak position and line-shape are determined by the relative strength and phase of the coupling between the discrete and continuous states. Fano resonance refers to the sharp peak in the Fano line-shape, which is caused by the constructive interference between the discrete state and the continuum of states.[40] This also defines the resonance energy, or the energy position of the peak. Such asymmetric profile can be used to extract information about the coupling strength, energy level structure, density of states, optical transition strength, and the nature of the discrete state.

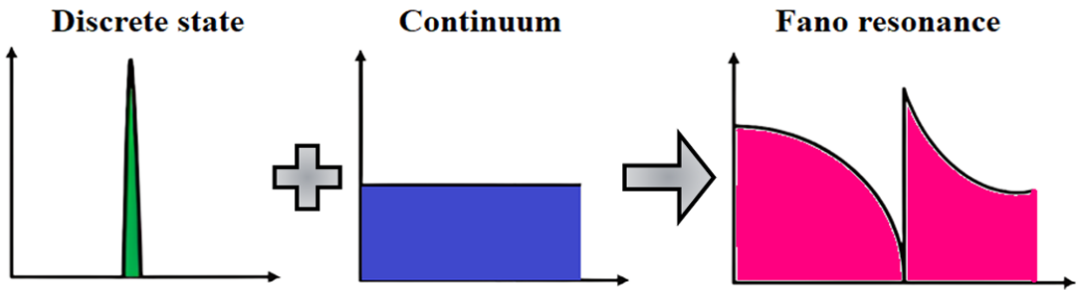

Figure 1.10 Schematics showing Fano resonance from the interference of a discrete state with a continuous background.

Fano interference can be observed in the Raman spectra of certain materials, particularly those with discrete vibrational states that are strongly coupled to a continuum of electronic states.[40-42] The Fano line-shape of Raman peaks can provide information on the nature of the electronic or vibrational states, as well as the coupling strength between them. In regard to charge-phonon coupling, Fano interference can be observed in the electronic spectra of materials with strong electron-phonon, hole-phonon, or exciton-phonon interactions.[40,41] The nature of the electronic states and the strength of the coupling to the phonons can be related to

the electronic transport and thermal properties of the materials. Besides, quantum confinement of phonons in ultrasmall nanoparticles, quantum dots or ultrathin films can also cause Fano asymmetry in Raman modes.[42] The Fano interference, Fano resonance, and Fano asymmetry are complex phenomena that are influenced by various factors, such as the energy levels of the discrete states, the density of states in the continuum, and the coupling strength between the discrete and continuous states, which is unique for every material. Exploring these phenomena can provide valuable insights and rich physics regarding the properties of a wide range of materials and physical systems.

1.7.5 Fano Resonance: A retrospective and prospective view

In 1947, Ugo Fano published a seminal paper titled "Effects of Configuration Interaction on Intensities and Phase Shifts", where Fano introduced a theoretical framework to describe the interference between a discrete bound state and a continuum of states.[43] He demonstrated that this interference leads to characteristic line shapes in atomic and molecular spectra, which are now known as Fano profiles or Fano resonances. Fano's theoretical formulation provided a powerful tool to analyse and interpret experimental observations, revolutionizing the field of atomic and molecular physics. Fano resonance was found to play a crucial role in a wide range of phenomena, including photoionization, Auger processes, and autoionization. By studying the asymmetries and line shapes observed in the spectra, scientists gained insights into the underlying atomic and molecular dynamics and electronic structure. Fano's work laid the foundation for the understanding of complex quantum systems and became an essential tool in spectroscopy.

Over the years, Fano resonance has also found applications in solid-state physics and nanoscience. The unique interference effects associated with Fano resonance have been observed in various systems, including quantum dots, plasmonic nanoparticles, and metamaterials.[44,45] By engineering the geometries and properties of these nanostructures, researchers can control and manipulate the Fano resonances, leading to applications in sensing, energy harvesting, and information processing. Fano resonance has proven particularly useful in enhancing light-matter interactions at the nanoscale and achieving subwavelength control of electromagnetic fields. In recent years, the study of Fano resonance has expanded to other fields, such as optics, acoustics, and metamaterials.[44,45] Researchers have explored new materials and systems, including graphene, topological insulators, and photonic crystals, to observe and harness Fano resonances for various applications. Additionally, the integration of Fano resonance with other phenomena, such as plasmonics, has opened up new possibilities for designing novel devices with enhanced functionalities, such as ultrasensitive sensors and efficient light-emitting diodes (LEDs).

1.8 Aims and objectives

Although the goal of the as-conducted research has always been gaining multifaceted knowledge in the concerned domains, the broad aims and objectives of the current thesis can be summarized as the following.

- First and foremost, we try to identify and synthesize some fundamentally interesting and technologically sound, durable lead-free nanomaterials (predominantly oxides), that can offer interesting electrical, optical, vibrational, or magnetic properties. Some proposed materials are, (i) Fe_3O_4, (ii) Fe_3O_4–PVDF nanocomposite, (iii) α and γ phases of Fe_2O_3, (iv) $ATiO_3$; A = Ca, Sr, Ba, and (v) Ln_2O_3; Ln = Eu, Gd, Dy.
- Fe_3O_4, a half-metallic electret material with its unique electrical properties, assumes compelling negative capacitance (NC) attributes. The effect of particle size and external bias-field has hardly been explored over non-ferroelectric NC dispersions in literature. Therefore, the objective here is to identify the origin of non-ferroelectric NC, controlling the same by internal/external parameters such as grain size and DC bias, and thereby propose some generalized model applicable for a variety of nano-systems.
- To investigate size-dependent physiochemical properties, an enormous variation in particle dimensions via a single reproducible method is pre-requisite and core-shell structured magnetite nanoparticles can take up an archetypical testbed in such a study. Furthermore, Fe_3O_4 can be incorporated as a nanofiller with different size and loading %age within PVDF-based standalone films to enhance the electroactive phases by charge transfer through ion-dipole interactions. To cherish the enhanced piezo-, ferro- and dielectric properties, piezoelectric nanogenerators (PENGs) can be devised with optimum performance.
- DC bias-dependent impedance, admittance, dielectric, and modulus studies and proper interpretation of the frequency dispersive data by fitting with suitable relaxation models, equivalent circuit analysis, or scaling laws reveal a lot about the core electrical properties of nanomaterials. Therefore, we wish to study two representative nano-systems, say ferric oxide polymorphs (binary oxides) and perovskite titanates (ternary oxides) on this ground, and extend our understanding of anisotropic deviations due to grain core-boundary heterostructure as well as the intrinsic crystal conformation with theoretical/computational methods like DFT and finite element simulations.
- Laser power dependent Raman spectroscopy is a powerful tool to understand the coupling of electronic continuum and discrete phonon modes in terms of Fano interference amid photo-excited electron plasma. This methodology has the potential to uncover the yet unexplored physics of lanthanide sesquioxides by modelling Raman line-shape asymmetry, charge-phonon coupling constant, anharmonic phonon life time, *etc*. as a function of lattice temperature against focussed laser irradiation.

❑ ***Strategy and implementation:***

- ✓ At first, we need to synthesize the materials under interest in pure phase and in a facile, but efficient and reproducible bottom-up technique. Good crystallinity is a priority as well.
- ✓ Next, executing structural, crystallographic, morphological, electrical, electronic, optical, thermal, and vibrational characterization of the as-synthesized nanomaterials according to the requirements of a particular project is important for a holistic understanding of the physiochemical properties.
- ✓ We opt to start our research with iron oxide nanoparticles, which reportedly has at least 16 different polymorphs. Magnetite (Fe_3O_4), a representative relaxor multiferroic material, possesses fundamentally appealing multifaceted size-dependent properties. However, varying particle size using a single wet chemical method, from micro particles to ultrasmall nanoparticles (quantum confinement regime) could be challenging. Achieving so, investigation of its numerous size-dependent optical (such as bandgap, crystal field energies, *etc*.), electrical, lattice-vibrational, and magnetic properties can be interesting. This may lead to a precise control over these attributes by a systematic tuning of particle size distribution, which is a prior goal in the field of nanoscience.
- ✓ As an electret material, magnetite nanoparticles can be incorporated into PVDF to fabricate Fe_3O_4–PVDF nanocomposite-based thin films to devise PENGs. The anticipated charge-transfer between the PVDF matrix and filler nanoparticles should enhance the electroactive β −phase. Studying the piezoelectric response, scrutinizing the strength of ion-dipole or dipole-dipole interactions, and optimization of open-circuit voltage, short-circuit current, dielectric function, and the as-delivered power for energy harvesting applications could be some prior objectives in this work.
- ✓ Speaking of non-trivial dielectric properties, Fe_3O_4 can be an interesting candidate to explore the frequency dispersive NC phenomenon and Delta function like dielectric loss peaks with varying DC bias. The double-well energy landscape in Landau description of ferroelectrics predicted mathematical possibility of NC, which today has been well-implemented in overcoming fundamental limits of power dissipation suggested by Boltzman tyranny. However, classical electrodynamics do not include any theory related to NC in non-ferroelectric materials. Absence of strong and pre-defined theoretical grounds compelled researchers to explain their observations using versatile and apparently uncorrelated ideas. So, there ought to be some generalized mechanisms associated, which we will attempt to explore. Also, we need to find a new model that can describe the entire positive to negative capacitance regime by a single equation.
- ✓ Apart from Fe_3O_4, ferric oxide polymorphs are very interesting and useful materials for various electric and magnetic applications. Among these, hematite ($\alpha -Fe_2O_3$) and

maghemite ($\gamma -Fe_2O_3$) are the two most important phases. In scientific literature, temperature-dependent dielectric properties have been sufficiently investigated, but DC bias-dependent studies are quite rare. Therefore, we would like to explore DC bias-dependent frequency dispersions of various dielectric parameters and fit the data with relaxation models like Cole-Cole, Cole-Davidson, Havrialiak–Negami, Kohlrausch–Williams–Watts (KWW) and/or Jonscher model (whichever applicable), and also conduct equivalent circuit analysis. Besides, materials can hold built-in anisotropic deviations, that may manifest via the dielectric ellipsoid dispersions. DFT can be a useful tool to explore it.

- ✓ Next, instead of the above-mentioned binary oxides, we can try some ternary lead-free oxides as well, such as perovskite titanates. $ATiO_3$ (A = Ca, Sr, Ba) are noteworthy dielectric materials. DC bias-dependent impedance, admittance, dielectric, and modulus studies in a comparative way can add a shiny feather in the wide literature of these materials. The analysis suggested in the previous paragraph can be adopted here as well. Additionally, we can use finite element simulations to understand the anisotropic deviations of electric fields and displacement vectors around the grain cores immersed in the grain boundary matrix.
- ✓ Very often, electrical, and electronic properties are correlated with vibrational attributes (as discussed in section 2.6). For probing different vibrational features and phonon properties, Raman spectroscopy can be a convenient tool. In general, for understanding the fundamentals of various vibrational properties, the effect of size, temperature, pressure, laser-induced local heating, electron-phonon coupling *etc*. on it are analysed very often. Lanthanide sesquioxides are an important testbed for conducting laser power-dependent Raman spectroscopic analysis. Furthermore, this can cherish photoexcited electron plasma, that eventually leads to the Fano interference between discrete phonon modes and the electronic continuum. In literature, already there are different models like of Allen and Hui. Fitting the as-obtained spectral data with suitable models can help to scrutinize the charge-phonon coupling constant or anharmonicity (if present).
- ✓ Besides, DFT-based first principles prophecy can be united with the various experimental results for precise and in-depth understanding of the nanometric physical properties of condensed matter in a comprehensive manner.
- ✓ Finally, we wish to utilize the as-gained physical knowledge of structural, dielectric, piezoelectric, optical, and lattice vibrational properties of the lead-free materials under investigation in suitable energy harvesting, conversion, and storage-related applications to ensure sustainable development and growth.

The pieces of work that will be presented in the 4th to 8th chapter of this thesis are aligned with the aforementioned goals and objectives.

References

1. J. K. Patel, A. Patel and D. Bhatia, in *Emerging technologies for nanoparticle manufacturing*, Springer, 2021, pp. 3-23.
2. M. Fazal-ur-Rehman, *J. Basic Appl. Sci. Res.*, 2018, **8**, 1.
3. R. Lopez, L. C. Feldman and R. F. Haglund Jr, *Phys. Rev. Lett.*, 2004, **93**, 177403.
4. V. Bhardwaj and A. Kaushik, *Journal*, 2017, **8**, 298.
5. L. Zhang and M. Fang, *Nano Today*, 2010, **5**, 128-142.
6. P. Iqbal, J. A. Preece and P. M. Mendes, *Supramolecular chemistry: from molecules to nanomaterials*, 2012.
7. K. Jagiello, B. Chomicz, A. Avramopoulos, A. Gajewicz, A. Mikolajczyk, P. Bonifassi, M. G. Papadopoulos, J. Leszczynski and T. Puzyn, *Struct. Chem.*, 2017, **28**, 635-643.
8. E. Roduner, *Chem. Soc. Rev.*, 2006, **35**, 583-592.
9. Z. Zhang, Y. Ouyang, Y. Cheng, J. Chen, N. Li and G. Zhang, *Phys. Rep.*, 2020, **860**, 1-26.
10. M. L. Steigerwald and L. E. Brus, *Annu. Rev. Mater. Sci.*, 1989, **19**, 471-495.
11. S. M. Rappaport, D. K. Barupal, D. Wishart, P. Vineis and A. Scalbert, *Environ. Health Perspect.*, 2014, **122**, 769-774.
12. R. Zhang, V. L. Wilson, A. Hou and G. Meng, *International Journal of Health, Animal Science and Food Safety*, 2015, **2**.
13. S. Y. Njati and M. M. Maguta, *Environ. Pollut.*, 2019, **249**, 1091-1105.
14. B. P. Lanphear, S. Rauch, P. Auinger, R. W. Allen and R. W. Hornung, *The Lancet Public Health*, 2018, **3**, e177-e184.
15. N. L. Panwar, S. C. Kaushik and S. Kothari, *Renewable Sustainable Energy Rev.*, 2011, **15**, 1513-1524.
16. A. Thakur and P. Devi, *Nano Energy*, 2022, 106927.
17. N. Asim, K. Sopian, S. Ahmadi, K. Saeedfar, M. A. Alghoul, O. Saadatian and S. H. Zaidi, *Renewable Sustainable Energy Rev.*, 2012, **16**, 5834-5847.
18. W. He, G. Zhang, X. Zhang, J. Ji, G. Li and X. Zhao, *Appl. Energy*, 2015, **143**, 1-25.
19. X. Gao, Y. Dong, S. Li, J. Zhou, L. Wang and B. Wang, *Electrochem. Energy Rev.*, 2020, **3**, 81-126.
20. G. G. Guilbault, J. M. Jordan and E. Scheide, 1988.
21. J. Tichý, J. Erhart, E. Kittinger and J. Privratska, *Fundamentals of piezoelectric sensorics: mechanical, dielectric, and thermodynamical properties of piezoelectric materials*, Springer Science & Business Media, 2010.
22. S. Katzir, *The Beginnings of Piezoelectricity: A Study in Mundane Physics*, 2006, 15-64.
23. Z. L. Wang, *Adv. Funct. Mater.*, 2008, **18**, 3553-3567.

24. M. Acosta, N. Novak, V. Rojas, S. Patel, R. Vaish, J. Koruza, G. A. Rossetti Jr and J. Rödel, *Appl. Phys. Rev.*, 2017, **4**, 041305.
25. J. C. Maxwell, *The London, Edinburgh, and Dublin Philosophical Magazine and Journal of Science*, 1861, **21**, 161-175.
26. Z. L. Wang, *Mater. Today*, 2017, **20**, 74-82.
27. J. Zhang, Y. He, C. Boyer, K. Kalantar-Zadeh, S. Peng, D. Chu and C. H. Wang, *Nanoscale Adv.*, 2021, **3**, 5465-5486.
28. R. Coelho, *Physics of Dielectrics for the Engineer*, Elsevier, 2012.
29. X. Hao, *J. Adv. Dielectr.*, 2013, **3**, 1330001.
30. M. T. Khan and S. M. Ali, *International Journal of Information Technology and Electrical Engineering*, 2012, **1**.
31. F. Haberey and H. P. J. Wijn, *Phys. Status Solidi B*, 1968, **26**, 231-240.
32. G. A. Samara, *Phys. Rev. B*, 1983, **27**, 3494.
33. C. Ang, A. S. Bhalla, R. Guo and L. E. Cross, *J. Appl. Phys.*, 2001, **90**, 2465-2468.
34. J. W. Liou and B. S. Chiou, *J. Am. Ceram. Soc.*, 1997, **80**, 3093-3099.
35. V. Chiş, *Chem. Phys.*, 2004, **300**, 1-11.
36. H. Bilz and W. Kress, *Phonon dispersion relations in insulators*, Springer Science & Business Media, 2012.
37. P. Y. Yu, M. Cardona, P. Y. Yu and M. Cardona, *Fundamentals of Semiconductors: Physics and Materials Properties*, 2010, 107-158.
38. E. B. Wilson, J. C. Decius and P. C. Cross, *Molecular vibrations: the theory of infrared and Raman vibrational spectra*, Courier Corporation, 1980.
39. G. Zerbi, *Appl. Spectrosc. Rev.*, 1969, **2**, 193-261.
40. A. Ueda and M. Eto, *Phys. Rev. B*, 2006, **73**, 235353.
41. S. D. M. Brown, A. Jorio, a. P. Corio, M. S. Dresselhaus, G. Dresselhaus, R. Saito and K. Kneipp, *Phys. Rev. B*, 2001, **63**, 155414.
42. R. Gupta, Q. Xiong, C. K. Adu, U. J. Kim and P. C. Eklund, *Nano Lett.*, 2003, **3**, 627-631.
43. U. Fano, *Phys. Rev*., 1961, **124**(6), 1866.
44. M. F. Limonov, M. V. Rybin, A. N. Poddubny and Y. S. Kivshar, *Nat. Photon.*, 2017, **11**(9), 543-554.
45. B. Luk'Yanchuk, N. I. Zheludev, S. A. Maier, N. J. Halas, P. Nordlander, H. Giessen and C. T. Chong, *Nat. Mater.*, 2010, **9**(9), 707-715.

2 BACKGROUND THEORY AND LITERATURE REVIEW

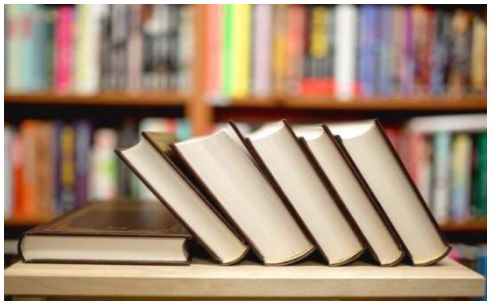

2.1 Electric polarization and transport properties

Development of electrical polarization and transport properties are fundamental concepts in materials science and physics. Electrical polarization refers to the separation of positive and negative charges within a material. When a material is subjected to an electric field, the electrons in the material experience a force that causes them to move. The movement of electrons can lead to a separation of charges within the material, creating a net dipole moment. The magnitude of the dipole moment is proportional to the strength of the applied electric field and the distance between the separated charges. This concept relies in presence of external electric field, whether the material is composed of polar or non-pole molecules.

The ability of a material to conduct electricity or heat is determined by its transport properties. Transport properties depend on a variety of factors, including the structure and composition of the material, as well as external factors such as temperature and pressure. In general, materials with high electrical conductivity tend to have low resistivity, which allows for efficient flow of electrons. However, DC conductivity and AC conductivity are quite different in nature. The former is related to the drift velocity of carriers, while the latter is frequency dispersive and associated with relaxation phenomena. Conversely, materials with high thermal conductivity tend to be good conductors of heat.

The relationship between electrical polarization and transport properties is complex and depends on the specific material being studied.[1,2] In some materials, electrical polarization can enhance transport properties by creating a more efficient pathway for the flow of charge carriers. For example, in ferroelectric materials, the spontaneous polarization can create domains that act as channels for the flow of electrons, leading to increased conductivity. On the other hand, electrical polarization can also impede the flow of charge carriers in some materials. This is often the case in insulating materials, where the strong polarization of the atoms and molecules can create a barrier to the flow of electrons. Similarly, in materials with high dielectric constants, the strong polarization can lead to a drop in the mobility of charge carriers. This is because polarization is associated with bound carriers, while conductivity is related with the availability of free carriers. Often, dielectric breakdown strength also depends on them. A

comprehensive understanding of the relationship between electrical polarization and transport properties is critical to the development of new materials with enhanced electrical and thermal conductivity.

2.2 Classification of materials based on electric polarization, transport, and associated characteristics

In materials science and physics, materials are classified based on their ability to conduct electricity. Materials can be broadly categorized as conductors, semiconductors, and insulators. Conductors, such as metals, are materials that allow electric current to flow through them easily. In conductors, the outer electrons of the atoms are free to move, and an electric field applied to the material can cause these electrons to move and create a current. Metals such as copper, silver, and gold are good conductors of electricity due to their high number of free electrons. Ideal conductors have zero resistance to the flow of electrical current, meaning that they allow for a perfect flow of electricity without any loss of energy. ***Superconductors*** are a special class of materials that exhibit zero electrical resistance and perfect conductivity at extremely low temperatures. Superconductors were discovered in 1911 by Heike Kamerlingh Onnes, who found that the electrical resistance of mercury disappeared at temperatures close to absolute zero (~4.2 K).[3] Superconductors are characterized by the ***Meissner effect***, which indicates the total expulsion of a magnetic field from the material when it is cooled below its critical temperature. This is different from the like ideal conductors. And more important, superconductivity is completely a quantum phenomenon. High temperature superconductivity in Type-II superconductors is a topic of active research.[4]

Insulators, also known as non-conductors, are materials that do not allow electric current to flow through them easily. In insulators, the outer electrons of the atoms are tightly bound to the nucleus and do not have the ability to move freely. As a result, insulators have high resistivity and low conductivity. Materials such as rubber, glass, and plastic are good insulators. Ideal insulators have an infinite resistance to the flow of electrical current, meaning that they do not allow any current to flow through them. Apart from these, there are ***Mott insulators*** that behave like that because of strong electron-electron interactions.[5] Semiconductors are materials that have electrical conductivity between that of a conductor and an insulator. Silicon (Si) and germanium (Ge) are two of the most commonly used ***intrinsic semiconductors***. The formation of electrons and holes in semiconductors; and the associated mechanism of conduction is mostly correlated with the ***band theory of solids***.[6] The conductivity of semiconductors can be enhanced by doping, a process of introducing impurities into the material to add excess electrons (n-type) or holes (p-type) and thus changing its electrical properties. In semiconductors, the movement of electrons is restricted, but they can still move through the

material. This makes semiconductors useful in electronic devices such as transistors and diodes. Semiconductors are often considered as dielectrics, although at higher temperatures, their DC conductivity increases due to generation of higher number of electrons and holes.

In summary, materials can be classified as conductors, semiconductors, or insulators based on their ability to conduct electricity. Conductors allow current to flow through them easily, while insulators do not allow current to flow through them easily. Semiconductors have intermediate conductivity and can be controlled by doping. Ideal conductors have zero resistance, while ideal insulators have infinite resistance. Superconductors exhibit zero resistance and perfect conductivity at extremely low temperatures, and they are characterized by the Meissner effect. Here, we enlist a few classes of materials, which have certain similarities and a number of differences, based on the nature of electric polarization.

2.2.1 (Sub)linear dielectric and paraelectric materials

Linear dielectrics, also known as normal or trivial dielectrics, are materials that exhibit a linear relationship between the applied electric field and the polarization they induce *i.e.*, the polarization is directly proportional to the electric field. Linear dielectrics follow the principle of superposition, meaning that the total polarization of the material is the sum of individual polarizations caused by each component of the applied electric field.

Paraelectric materials are a class of ***sublinear dielectric materials*** that do not exhibit spontaneous polarization in the absence of an external electric field. This is in contrast to ferroelectric materials, which do exhibit spontaneous polarization even in the absence of an external field. The term "paraelectric" is derived from the Greek word "para", meaning "alongside", indicating that paraelectric materials exist alongside ferroelectric materials in terms of their electrical properties. Paraelectric materials can still be polarizable in the presence of an external electric field. However, this polarization disappears when the external field is removed, and the material returns to its non-polarized state. Examples of paraelectric materials include many ceramics, semiconductors, biomaterials, and certain polymers. The lack of spontaneous polarization in paraelectric materials is due to the fact that their crystal structure is symmetrical, and the positive and negative charges are evenly distributed throughout the material. Or sometimes, there could be local dipoles.[7] But due to thermal agitation and arbitrary direction of the dipoles, there is no net spontaneous polarization. In other words, there is no preferred direction of polarization at a global level in the absence of an external electric field, either the molecules or unit cells are polar or non-polar in nature. If dielectrics can store charge temporally, they are sometimes called ***electrets***.[8] These materials may have non-zero polarization for some short time even after suspension of external field, which is useful in particular applications.

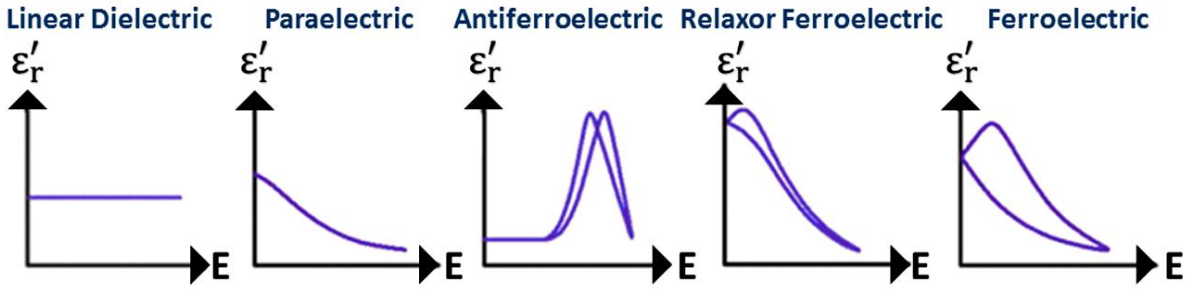

Figure 2.1 The dielectric function (real part) versus external electric field dependence for linear dielectric, paraelectric, antiferroelectric, relaxor ferroelectric, and normal ferroelectric materials.

Paraelectric materials have a number of important practical applications. For example, they are commonly used in the fabrication of capacitors, where they serve as the dielectric material between the two metal plates. In this application, the paraelectric material can be polarized by an external electric field, allowing it to store electrical charge. When the field is removed, the paraelectric material returns to its non-polarized state, and the stored charge is not retained. Another important application of paraelectric materials is in the development of ferroelectric materials. By doping paraelectric materials with specific impurities, it is possible to promote non-centrosymmetric crystal structure and induce spontaneous polarization, that transforms them into ferroelectric materials. This process is known as ***ferroelectric doping*** and is an important technique for developing new materials with tailored electrical properties.

2.2.2 Pyroelectricity: effect of temperature

Pyroelectricity is a phenomenon in which certain materials develop a temporary electrical charge when exposed to a change in temperature. The term "pyroelectricity" is derived from the Greek word "pyr", meaning "fire", and refers to the fact that the effect was first observed with crystals that were heated or cooled by a flame. Pyroelectric materials are typically composed of crystals that possess a non-centrosymmetric crystal structure, meaning that their arrangement of atoms lacks a centre of symmetry. This non-centrosymmetry leads to an asymmetry in the distribution of positive and negative charges within the material, which can give rise to a net electric polarization in the presence of a temperature gradient.

When a pyroelectric material is heated or cooled, its initial crystal structure undergoes a change that causes the polarization of the material to shift, resulting in the development of an electric charge on its surface. The magnitude and direction of the charge depend on the rate and direction of the temperature change.[9] For example, a material may develop a positive charge when it is heated, and a negative charge when it is cooled. Pyroelectric materials have a number of important practical applications. For example, they are commonly used in infrared detectors, where they can convert changes in temperature into changes in electric charge. When infrared

radiation is absorbed by the material, it heats up, causing a change in temperature and the development of an electric charge. This charge can be measured and used to detect the presence of infrared radiation. Pyroelectric materials are also used in ***thermoelectric generators***, which convert heat directly into electrical energy.[10] In these devices, a temperature gradient is applied across the pyroelectric material, causing a net electric polarization and the development of an electric charge. This charge can be collected and used as an electrical power output.

2.2.3 Piezoelectricity and electrostriction: effect of mechanical strain

Piezoelectricity and electrostriction are both phenomena that involve the interaction between electrical and mechanical energy in certain materials. While they share some similarities, there are also distinct differences between the two concepts.[11] Piezoelectricity refers to the ability of certain crystals, ceramics, and polymers to generate an electric charge in response to applied mechanical stress. Conversely, when an electric field is applied to these materials, they undergo mechanical deformation. This reciprocal relationship between mechanical stress and electric charge is a unique characteristic of piezoelectric materials. Examples of piezoelectric materials include quartz, tourmaline, and certain ceramics. Piezoelectricity finds applications in various fields such as sensors, actuators, ultrasound devices, and energy harvesting systems.

On the other hand, electrostriction refers to the phenomenon where a material changes its shape or size when subjected to an applied electric field. Unlike piezoelectricity, electrostrictive materials do not generate an electric charge when mechanically stressed. Instead, they exhibit a change in their physical dimensions when an electric field is applied. Electrostriction is observed in materials such as ferroelectric ceramics and polymers. This property is utilized in applications like microelectromechanical switches (MEMS), precision positioning systems, and optical devices.

Although both piezoelectricity and electrostriction involve the coupling between mechanical and electrical energy, the underlying mechanisms differ. Piezoelectricity relies on the asymmetric crystal structure of certain materials, which creates a separation of charges in response to stress. In contrast, electrostriction arises from changes in the material's polarization distribution due to an applied electric field.

2.2.4 Ferroelectrics and relaxors

Ferroelectricity is a phenomenon in which certain materials exhibit spontaneous polarization that can be reversed by applying an external electric field. Ferroelectric materials are typically crystals that possess a non-centrosymmetric crystal structure and have a dipole moment that can be oriented in different directions throughout a domain.[12] The term "ferroelectricity" is derived from the Latin word "ferro", meaning "iron", and is a reference to

the similarities between the behaviour of ferroelectric materials and ferromagnetic materials, which exhibit a similar phenomenon known as ferromagnetism.

Ferroelectric materials have two important properties: ***coercivity*** and ***remanence***.[12] Coercivity is the amount of electric field required to switch the polarization of the material from one direction to another. Remanence is the amount of polarization that remains in the material even after the external electric field is removed, see Figure 2.2. The ***domain theory of ferroelectricity*** explains how ferroelectric materials exhibit spontaneous polarization that can be reversed by an external electric field.[13] The theory proposes that ferroelectric materials have small regions called domains, each of which has a net dipole moment oriented in a particular direction. In the absence of an external electric field, these domains are randomly oriented, leading to a net polarization of zero. However, when an external electric field is applied, the domains begin to align, leading to a net polarization in the direction of the field. The coercive field required to reverse the polarization is related to the energy barrier between the different domain orientations. Understanding the domain theory of ferroelectricity is essential for designing and optimizing ferroelectric materials for various applications.

Ferroelectric materials have a number of important practical applications. For example, they are commonly used in electronic devices such as capacitors, memory devices, and sensors. In capacitors, ferroelectric materials can be used as the dielectric material between the two metal plates. When an electric field is applied, the material becomes polarized, allowing it to store electrical charge. When the field is removed, the material retains its polarization, and the stored charge is retained. In memory devices, ferroelectric materials can be used to store information by polarizing the material in different directions. This polarization can be read out by measuring the electrical charge stored in the material. A related optimistic goad is to build ***four-state memory devices*** with ***electric-writing, magnetic-reading*** capability.[14] Ferroelectric materials are also used in sensors, where they can convert changes in temperature, pressure, or other physical parameters into changes in electric charge.

Relaxor ferroelectric materials or simply relaxors are a special class of ferroelectric materials that exhibit unique electrical properties, particularly in terms of their polarization response and temperature dependence.[15] Normal ferroelectrics exhibit a well-defined and sharp transition from a non-polar phase to a polar phase at a specific temperature, called the ***Curie temperature*** ($\boldsymbol{T_C}$). Below T_C, the ferroelectric material possesses a spontaneous polarization that can be switched and reversed by an external electric field. In contrast, relaxor ferroelectrics do not possess a distinct phase transition and exhibit a broad and diffuse transition.[15] Their polarization response is not as well-defined as in normal ferroelectrics. Instead of having a single Curie temperature, relaxor ferroelectrics have a temperature range known as the relaxor phase, over which their polarization behavior is more complex and diffuse.

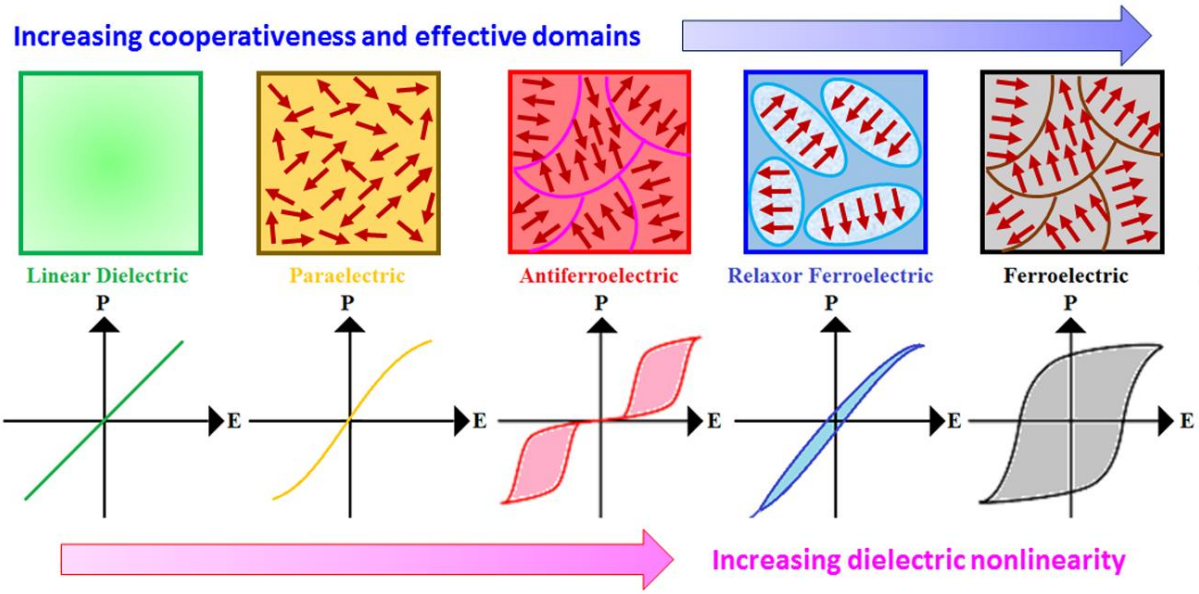

Figure 2.2 Schematics showing distribution of microscopic dipoles and the polarisation versus external electric field plot for linear dielectric, paraelectric, antiferroelectric, relaxor ferroelectric, and normal ferroelectric materials (last three cases manifest hysteresis).

Relaxor ferroelectrics show a phenomenon known as the frequency-dependent permittivity, where the dielectric constant peak versus temperature varies significantly with the frequency of the applied field. This frequency dispersion is a characteristic feature of relaxor materials and is associated with the presence of ***polar nanoregions (PNRs)*** within the material.[15,16] Relaxors are characterized by a high degree of chemical disorder at the atomic level, particularly in the arrangement of their cations. This disorder leads to the formation PNRs within the material. PNRs are regions of locally distorted polarization that fluctuate on a nanoscale level. These PNRs do not possess long-range order like the domains found in normal ferroelectrics. The presence of PNRs and their dynamic behavior contribute to the diffuse phase transition and frequency dispersion observed in relaxor ferroelectrics. Relaxors often possess high piezoelectric coefficients, making them suitable for use in transducers and sensors. They also exhibit excellent electromechanical coupling properties and are used in ultrasound transducers, actuators, and other devices that require efficient energy conversion between mechanical and electrical domains. Potassium sodium niobate ($K_{0.5}Na_{0.5}NbO_3$) and bismuth sodium titanate ($Bi_{0.5}Na_{0.5}TiO_3$) are two popular relaxors. Even magnetite (Fe_3O_4) has been identified as a relaxor multiferroic material at a certain temperature range.

2.2.5 Ferrielectric and antiferroelectric materials

Ferrielectric materials exhibit a coexistence of two or more ferroelectric phases with different polarization directions. These phases can exist at different temperatures, compositions, or under the influence of external parameters like stress or electric field. The

polarization in ferrielectric materials is non-zero even in absence of external electric field and can switch between different domains with distinct orientations, leading to hysteresis behaviour.

Antiferroelectricity is a related phenomenon in which certain materials exhibit an antiparallel alignment of their dipole moments.[17] This leads to zero net polarization in absence of external electric field, see Figure 2.2. Antiferroelectric materials are typically crystals that possess a centrosymmetric crystal structure and have a dipole moment that can be oriented in different directions. Like ferroelectrics, antiferroelectric materials can also have domains. Some popular examples are lead zirconate ($PbZrO_3$), ammonium dihydrogen phosphate or ADP ($NH_4H_2PO_4$), and sodium niobate ($NaNbO_3$). Antiferroelectric materials have a number of important practical applications. For example, they are commonly used in energy storage devices, such as capacitors and batteries. In capacitors, antiferroelectric materials can be used to store electrical charge due to their high energy density. In batteries, they can be used as electrode materials due to their high energy storage capacity.

2.3 Progress and recent advances in dielectrics

In this section, we will discuss different types of dielectric materials with examples, their properties, characterization techniques, some important dielectric relaxation models, and applications.

2.3.1 Linear and nonlinear dielectrics

The behaviour of dielectrics under the influence of an electric field can be classified as linear or nonlinear. Linear dielectrics are materials whose response to an electric field is directly proportional to the applied electric field. The relationship between the polarization and the electric field can be described by the following equation.

$$P = \varepsilon_0 \chi_e E. \tag{2.1}$$

Here, P is the polarization, E is the electric field strength, ε_0 is the permittivity of free space, and χ_e is the electric susceptibility of the material. In linear dielectrics, χ_e is constant, and therefore, the relationship between P and E is linear. Examples of linear dielectrics include air, vacuum, and most ceramic materials.

Nonlinear dielectrics, on the other hand, are materials whose response to an electric field is not proportional to the applied electric field. In nonlinear dielectrics, the electric susceptibility is not constant, but depends on the strength of the electric field. The relationship between the polarization and the electric field can be described by a power series of the electric field. The simplest form of this power series is,

$$P = \varepsilon_0 \left\{ \chi_e^{(1)} E + \chi_e^{(2)} E^2 + \chi_e^{(3)} E^3 + \cdots \right\}. \tag{2.2}$$

Here, $\chi_e^{(1)}, \chi_e^{(2)}, \chi_e^{(3)}, \ldots$ *etc*. are the first, second, third and higher order susceptibilities of the material, respectively. In nonlinear dielectrics, the polarization response increases nonlinearly with the strength of the electric field. Examples of nonlinear dielectrics include barium titanate ($BaTiO_3$), potassium dihydrogen phosphate (KDP), lithium niobate ($LiNbO_3$), *etc*. Basically, ferro-, ferri-, and antiferroelectric materials are highly nonlinear in nature. Nonlinear dielectrics have important applications in optical communications, optical computing, and nonlinear optics. For example, KDP crystals are used in frequency doubling of lasers, while lithium niobate is used in electro-optic modulators.

2.3.2 Homogeneous versus inhomogeneous dielectrics

Dielectrics can be classified into two categories based on their internal structure and properties *viz*., homogeneous, and inhomogeneous dielectrics. Homogeneous dielectrics are materials that have uniform electrical properties throughout their volume. In other words, they have the same dielectric constant, or relative permittivity, at every point inside the material. Examples of homogeneous dielectrics include air, vacuum, and many types of plastics. Inhomogeneous dielectrics, on the other hand, are materials that have non-uniform electrical properties throughout their volume. This can happen when the dielectric constant varies in different regions of the material, or when there are different types of dielectric materials present in the same volume.[18] Inhomogeneous dielectrics can be further divided into two types: ***composite*** and ***graded***.

Composite dielectrics are materials made up of different types of dielectric materials that are combined to create a new material with specific electrical properties. An example of a composite dielectric is a ceramic capacitor, which is made up of alternating layers of ceramic and metal to create a high-capacitance device with a specific voltage rating. Graded dielectrics are materials in which the dielectric constant varies continuously across the material. This can be achieved by using materials with different dielectric constants in different regions of the material, or by changing the structure of the material in a controlled way. An example of a graded dielectric is a high-voltage cable, where the insulation material has a varying dielectric constant to optimize its performance.

2.3.3 Isotropic versus anisotropic properties

Dielectric materials can also be classified based on their directional response to electric fields, as isotropic or anisotropic dielectrics. Isotropic dielectrics are materials that exhibit the same electrical properties in all directions. In other words, their electrical properties, such as permittivity and conductivity, are independent of the direction of the electric field. For isotropic materials, the polarizability tensor (a 2nd rank tensor) is generally a scalar multiplied by a unit matrix. Examples of isotropic dielectrics include air, vacuum, and many types of plastics.

Anisotropic dielectrics, on the other hand, are materials that exhibit different electrical properties in different directions. In these materials, the dielectric constant, conductivity, and other electrical properties can vary depending on the direction of the applied electric field.[18,19] Anisotropic dielectrics can be further divided into two categories: ***uniaxial*** and ***biaxial***. Uniaxial anisotropic dielectrics have a single axis of symmetry, where the electrical properties are the same in two perpendicular directions but different in a third direction. This can be seen in crystals like quartz, where the electrical properties vary depending on the direction of the electric field. Biaxial anisotropic dielectrics have two axes of symmetry, where the electrical properties are different in three perpendicular directions. This can be seen in materials like mica, where the electrical properties vary in all directions. Not only the elements present in the principal diagonal of the polarizability tensor, but also other elements are usually non-zero and sometimes unequal for anisotropic materials. This is different from the polarizability tensor of the isotropic materials, where the off-diagonal elements are usually zero. Anisotropic dielectrics have important applications in many fields, such as optics and electronics. For example, liquid crystal displays (LCDs) use anisotropic dielectrics to control the polarization of light, while some types of semiconductors have anisotropic electrical properties that allow for more efficient electronic devices.

2.3.4 Noteworthy dielectric materials and their crystal structure

There are many dielectric materials, which show impressive dielectric constant, high breakdown strength, great thermodynamic stability, and also offers cost-effective production, abundance, and purity. Some of them are mentioned below.

i. ***Silicon dioxide (SiO_2):*** This is a widely used dielectric material in semiconductor technology, with typically a quartz crystal structure. Its static dielectric constant is around 3.9 at room temperature. Silicon dioxide is used as an insulator in integrated circuits and other electronic devices.

ii. ***Silicon nitride (Si_3N_4):*** This is a ceramic material with a wurtzite crystal structure and space group $P\,63/m$. Its static dielectric constant is around 8 at room temperature. Silicon nitride is used as an insulating material in electronic components, such as power electronics, microprocessors, and sensors.

iii. ***Polyethylene:*** This is a common plastic material that has a simple, amorphous crystal structure. Its static dielectric constant is around 2.3 at room temperature. Polyethylene (also called polythene) is used as an insulating material in cables, capacitors, and other electrical applications.

iv. ***Polypropylene:*** This is a thermoplastic polymer material that has a simple, amorphous crystal structure. Its static dielectric constant is around 2.2 at room temperature.

Polypropylene is used as an insulating material in capacitors, cables, and other electrical appliances.

v. ***Aluminium oxide (Al_2O_3):*** This is a ceramic material with a corundum crystal structure and space group $R\bar{3}c$. Its static dielectric constant is around 9 at room temperature. Aluminium oxide is used as an insulating material in electronic components, such as power electronics, microprocessors, and sensors.

vi. ***Hafnium oxide or hafnia (HfO_2):*** This is a metal oxide material that has many crystal structures. Two important ones are monoclinic and orthorhombic structure with space groups $P\,21/c$ and $Pbca$. Its static dielectric constant is around 25 at room temperature. Hafnium oxide is used as a high-k dielectric material in metal-oxide-semiconductor (MOS) devices, such as transistors and memory cells, due to its high dielectric constant, good thermal stability, and compatibility with silicon-based technology.

vii. ***Zirconium oxide or zirconia (ZrO_2):*** Zirconia has similar crystal structure like hafnia and it is also used in MOS devices. Hafnium zirconium oxide ($Hf_xZr_{1-x}O_2$) is another commonly used material in this industry.

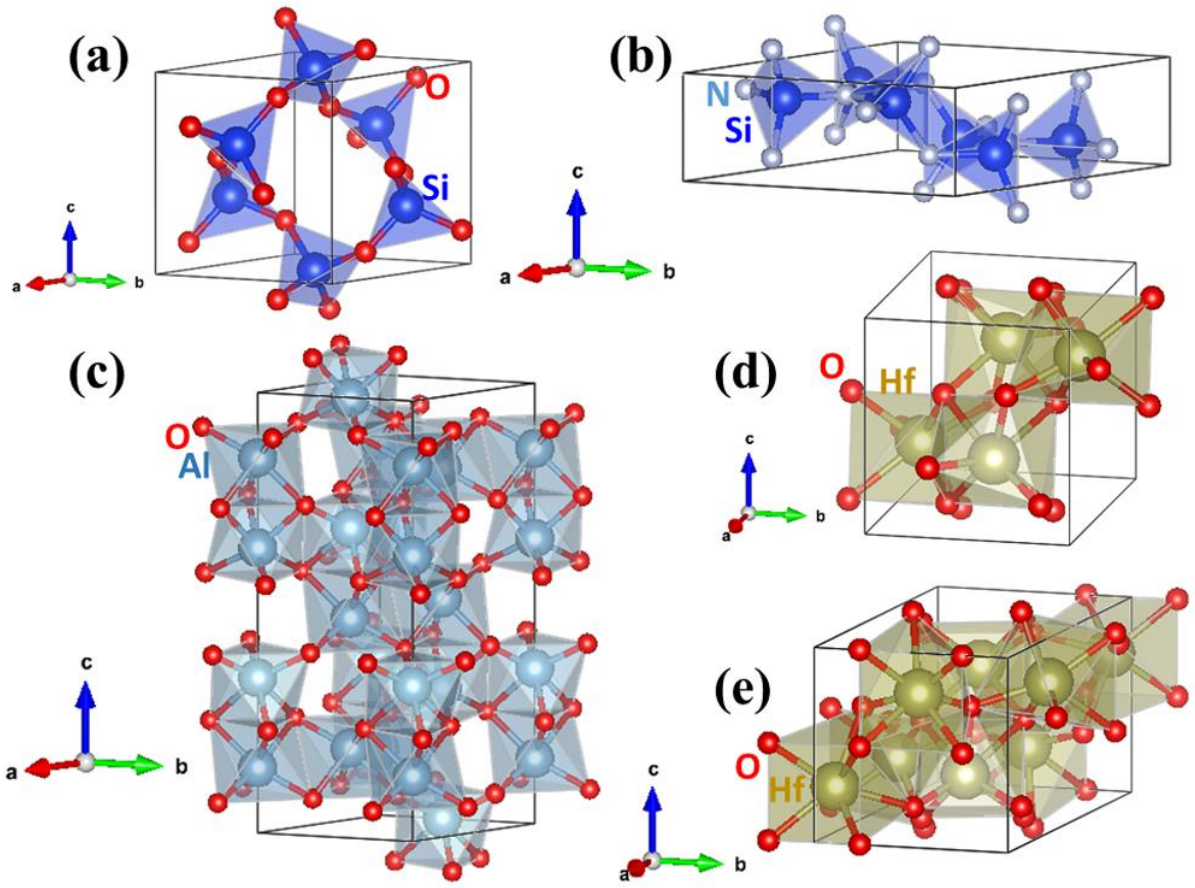

Figure 2.3 Conventional unit cells of some popular dielectric materials: (a) SiO_2; (b) Si_3N_4; (c) Al_2O_3; (d) HfO_2 (monoclinic); and (e) HfO_2 (orthorhombic).

2.3.5 Impedance, admittance, dielectric, and modulus spectroscopy

Impedance, admittance, dielectric, and modulus spectroscopy are experimental techniques that are used to study the electrical properties of materials, particularly dielectric materials. These techniques involve measuring the response of a sample to an applied electrical field or frequency, and can provide information about the dielectric constant, dielectric loss, AC conductivity, and other properties of the material over a range of frequencies or temperatures.

Impedance spectroscopy measures the complex impedance of a material, which (in simple language) is the ratio of the applied voltage to the resulting current. The impedance has both magnitude and phase components and can be represented as a complex number in the form $\hat{Z} = Z' + jZ''$ $\left(j = \sqrt{-1}\right)$, where Z' is the gross resistance (or real part) and Z'' is the reactance (or imaginary part). This technique is commonly used in materials science, electrochemistry, and biophysics, among other fields.[20-22] Admittance spectroscopy is similar to impedance spectroscopy, but instead measures the complex admittance of a material, which is the reciprocal of the impedance. The admittance has both magnitude and phase components and can be represented as a complex number in the form $\hat{Y} = G + jB$,, where G is the conductance (or real part) and B is the susceptance (or imaginary part). Admittance spectroscopy is often used to study the electrical properties of semiconductor materials, such as defects and impurities.[20,21]

Dielectric spectroscopy measures the complex permittivity of a material, which is a measure of its ability to store electrical energy in an applied field. The permittivity has both real and imaginary components and can be represented as a complex number in the form $\hat{\varepsilon} = \varepsilon' - j\varepsilon''$, where ε' is the real permittivity (or dielectric constant) and ε'' is the imaginary permittivity (or dielectric loss). Dielectric spectroscopy is often used to study the dynamics of molecular motions in polymers, proteins, and other soft materials, as well as the electrical properties of ceramics and other solid materials.[20-22] Modulus spectroscopy is similar to dielectric spectroscopy, but instead measures the complex modulus of a material, which is the ratio of the complex stress to the complex strain in an applied field. The modulus has both real and imaginary components and can be represented as a complex number in the form $\widehat{M} = M' - jM''$, where M' is the storage modulus (or elastic modulus) and M'' is the loss modulus (or viscous modulus). Modulus spectroscopy is often used to study the mechanical and electrical properties of materials, such as polymers and gels, as well as the glass transition temperature and other relaxation processes.

Despite their differences, these spectroscopy techniques share several similarities. They are all non-destructive, non-invasive, and can be performed over a range of frequencies, DC bias, or temperatures.[20-22] They also provide information about the electrical properties of materials, including dielectric constant, conductivity, and other parameters, that can be used to study the

structure and dynamics of nanomaterials (both semiconductors and insulators), as well as to develop and optimize new materials for various applications.

2.3.6 Distinct polarization mechanisms

Polarization is a fundamental concept that explains the electrical behaviour of dielectric materials. It occurs due to the displacement of charges in response to an applied electric field and it is measured as net dipole moment per unit volume. The various mechanisms of polarization in dielectric materials are given below.

- ***Maxwell-Wagner interfacial polarization*** occurs at the interface between two materials, typically a dielectric material and a conductor, due to the accumulation of charges at the interface. The accumulation of charges occurs due to the difference in conductivity between the two materials, leading to the formation of an internal electric field that opposes the external electric field.[23,24] In polycrystalline materials, polarization can occur due to the presence of grains and grain boundaries. This is because, grains are considered as good conductors, while the grain boundaries are insulators. Their overall contribution decides the electrical property of the material. The polarization is a result of the displacement of charges at the grain boundaries and within the grains. The polarization due to grain and grain boundary dynamics is dependent on the frequency of the applied electric field.[23,24] At low frequencies, the polarization is due to the motion of charged defects within the grains, while at high frequencies, the polarization is due to the motion of charged defects at the grain boundaries.
- ***Dipolar relaxation*** occurs in polar dielectric materials due to the realignment of dipoles in response to an applied electric field. The mechanism behind dipolar relaxation is the energy dissipation due to the reorientation of dipoles, which is manifested as a dielectric loss.[25] The frequency at which dipolar relaxation occurs is dependent on the strength of the dipole and the electrical viscosity of the medium.
- ***Ionic polarization*** occurs in materials containing ionic species, such as salts, in which the polarization is due to the displacement of ions under the influence of an applied electric field. The mechanism behind ionic polarization is the formation of ionic dipoles due to the separation of charges within the material. The frequency at which ionic polarization occurs is dependent on the mobility of the ions.
- ***Electronic polarization*** occurs in materials containing covalent bonds, in which the polarization is due to the displacement of electrons under the influence of an applied electric field. The associated mechanism involves the deformation of the electron cloud around the atoms due to the applied electric field. The frequency at which electronic polarization occurs is dependent on the energy required to deform the electron cloud.

The polarization mechanisms of dielectric materials are dependent on the frequency of the applied electric field. At low frequencies, the polarization is primarily due to the interfacial polarization, grain and grain boundary dynamics mechanisms. At high frequencies, the polarization is due to the dipolar relaxation, ionic polarization, and finally, electronic polarization mechanisms. The frequency range at which each mechanism is significant varies depending on the material properties.

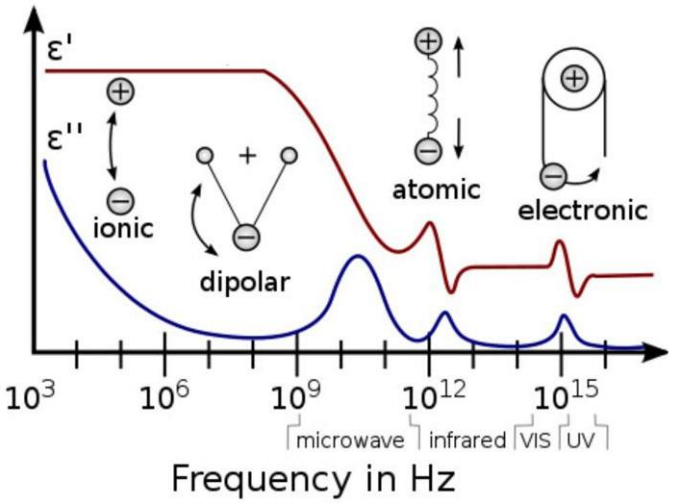

Figure 2.4 Schematic presentation of the typical frequency dispersions of real and imaginary dielectric function under different polarization mechanisms. This image is collected from WikiMedia commons and has been slightly modified.

In addition to polarization mechanisms, dielectric materials can also exhibit conduction mechanisms such as ***small and large polaron hopping conduction***. Small polaron hopping conduction occurs due to the hopping of electrons between sites within the material.[26] Large polaron hopping conduction occurs due to the motion of polarons,[27] which are quasiparticles formed due to the coupling between electrons and lattice vibrations, which should be considered when designing dielectric materials for specific applications.

2.3.7 Some popular dielectric relaxation models

Dielectric relaxation is a phenomenon that occurs in dielectric materials when they are subjected to an alternating electric field. In this process, the dipoles or charges within the dielectric material respond to the applied field, leading to a temporary polarization of the material. Owing to this alternating electric field, the polarization also alternates. This leads to a time-dependent dynamics of the charges that can be characterized by the frequency-dependent dielectric response of the material. There are several interesting models that have been developed to explain the dielectric relaxation phenomena. Some of the popular models are described below.

- ***Debye model:*** This is a simple model that assumes that the dielectric material consists of a large number of electric dipoles that are uniformly distributed throughout the material.[28] The model assumes that each dipole is attached to a spring, which enables it to oscillate in response to the applied electric field. The response of the material is then characterized by a single relaxation time, which is related to the viscosity and temperature of the material. Basically, it describes a system of ideal non-interacting dipoles. The associated equations are given below.

$$\hat{\varepsilon}(\omega) = \varepsilon'(\omega) - j\varepsilon''(\omega) = \varepsilon_\infty + \frac{\Delta\varepsilon}{1 + j\omega\tau}, \tag{2.3A}$$

$$j = \sqrt{-1}, \Delta\varepsilon = \varepsilon_s - \varepsilon_\infty = \varepsilon_{\substack{\omega\to 0 \\ T\to\infty}} - \varepsilon_{\substack{\omega\to\infty \\ T\to 0}}, \tag{2.3B}$$

$$\varepsilon'(\omega) = \varepsilon_\infty + \frac{\varepsilon_s - \varepsilon_\infty}{1 + \omega^2\tau^2}, \tag{2.3C}$$

$$\varepsilon''(\omega) = \frac{(\varepsilon_s - \varepsilon_\infty)\omega\tau}{1 + \omega^2\tau^2}, \tag{2.3D}$$

$$\tan\delta = \frac{\varepsilon''(\omega)}{\varepsilon'(\omega)} = \frac{(\varepsilon_s - \varepsilon_\infty)\omega\tau}{\varepsilon_s + \varepsilon_\infty\omega^2\tau^2}. \tag{2.3E}$$

Here, $j = \sqrt{-1}$, $\Delta\varepsilon$ is the amplitude of the dielectric response or the dielectric strength, τ is the relaxation time, $\omega = 2\pi f$ is the circular or angular frequency of the applied electric field, whereas f is the linear frequency in Hz.

- ***Cole-Cole model:*** This model extends the Debye model by including a distribution of relaxation times within the material. This distribution is described by the Cole-Cole function, which has a characteristic shape that can account for a broad range of relaxation times.[29] The Cole-Cole model is often used to analyse complex dielectric spectra, where symmetric broadening of dielectric loss-peaks or multiple relaxation processes are present. It is associated with a shape parameter α, which is a proper fraction. If $\alpha = 1$, the Cole-Cole model boils down to the Debye model. The associated equations are given below.

$$\hat{\varepsilon}(\omega) = \varepsilon'(\omega) - j\varepsilon''(\omega) = \varepsilon_\infty + \frac{\Delta\varepsilon}{1 + (j\omega\tau)^\alpha}, \tag{2.4A}$$

$$\varepsilon'(\omega) = \varepsilon_\infty + \frac{(\varepsilon_s - \varepsilon_\infty)\left\{1 + (\omega\tau)^\alpha \cos{}^{\alpha\pi}/_2\right\}}{1 + 2(\omega\tau)^\alpha \cos{}^{\alpha\pi}/_2 + (\omega\tau)^{2\alpha}}, \tag{2.4B}$$

$$\varepsilon''(\omega) = \frac{(\varepsilon_s - \varepsilon_\infty)(\omega\tau)^\alpha \sin{}^{\alpha\pi}/_2}{1 + 2(\omega\tau)^\alpha \cos{}^{\alpha\pi}/_2 + (\omega\tau)^{2\alpha}}, \tag{2.4C}$$

$$\tan\delta = \frac{\varepsilon''(\omega)}{\varepsilon'(\omega)} = \frac{(\varepsilon_s - \varepsilon_\infty)(\omega\tau)^\alpha \sin{}^{\alpha\pi}/_2}{\varepsilon_s + (\varepsilon_s + \varepsilon_\infty)(\omega\tau)^\alpha \cos{}^{\alpha\pi}/_2 + \varepsilon_\infty(\omega\tau)^{2\alpha}}. \tag{2.4D}$$

- ***Cole-Davidson model:*** The Cole-Davidson model is another important model used to describe dielectric relaxation in materials. It was first proposed by Cole and Davidson in 1941 and is based on the idea that the relaxation time of a dielectric material is related to

the distribution of activation energies within the material. This model assumes that the dielectric material consists of a distribution of relaxation times, which are related to the distribution of activation energies.[29] The activation energy distribution is then characterized by a broadening factor, β, which reflects the width of the distribution. The Cole-Davidson model is often used to analyse the dielectric spectra of polymers, glasses, and other materials that exhibit a broad range of relaxation times and asymmetric broadening of dielectric loss-peaks. The model has been shown to provide a good fit to experimental data and has been used to study the relaxation behaviour of materials over a wide range of frequencies and temperatures. One advantage of the Cole-Davidson model is that it provides a quantitative description of the distribution of activation energies within the material, which can be related to the microstructure and dynamics of the material. It is associated with the shape parameter β, which is a proper fraction. If $\beta = 1$, the Cole-Davidson model boils down to the Debye model. The associated equations are given below.

$$\hat{\varepsilon}(\omega) = \varepsilon'(\omega) - j\varepsilon''(\omega) = \varepsilon_\infty + \frac{\Delta\varepsilon}{(1 + j\omega\tau)^\beta}, \tag{2.5A}$$

$$\varepsilon'(\omega) = \varepsilon_\infty + (\varepsilon_s - \varepsilon_\infty)(cos\,\varphi)^\beta\, cos\,\beta\varphi, \tag{2.5B}$$

$$\varepsilon''(\omega) = (\varepsilon_s - \varepsilon_\infty)(cos\,\varphi)^\beta\, sin\,\beta\varphi, \tag{2.5C}$$

$$\tan\delta = \frac{\varepsilon''(\omega)}{\varepsilon'(\omega)} = \frac{(\varepsilon_s - \varepsilon_\infty)(cos\,\varphi)^\beta\, sin\,\beta\varphi}{\varepsilon_\infty + (\varepsilon_s - \varepsilon_\infty)(cos\,\varphi)^\beta\, cos\,\beta\varphi}, \tag{2.5D}$$

$$1 + j\omega\tau = e^{j\varphi}\sqrt{1 + \omega^2\tau^2} = \frac{e^{j\varphi}}{\cos\varphi}\ (\text{say}), \varphi = \tan^{-1}\omega\tau. \tag{2.5E}$$

- ***Havriliak-Negami model:*** This model also includes a distribution of relaxation times, but it uses a different function to describe the distribution. The Havriliak-Negami function has a more flexible shape than the Cole-Cole function and can better account for relaxation processes that are more complex than those described by the Debye model.[30] Partially symmetric and asymmetric broadening of loss-peaks are assessed in this model, and this comes from a merger of the Cole-Cole and Cole-Davidson models. It is associated with the shape parameters α & β, which are proper fractions. If $\alpha = \beta = 1$, the Havriliak-Negami model boils down to the Debye model. The associated equations are given below.

$$\hat{\varepsilon}(\omega) = \varepsilon'(\omega) - j\varepsilon''(\omega) = \varepsilon_\infty + \frac{\Delta\varepsilon}{\{1 + (j\omega\tau)^\alpha\}^\beta}, \tag{2.6A}$$

$$\varepsilon'(\omega) = \varepsilon_\infty + (\varepsilon_s - \varepsilon_\infty)\frac{cos\,\beta\varphi}{\left[1 + 2(\omega\tau)^\alpha\, cos\,{}^{\alpha\pi}/_2 + (\omega\tau)^{2\alpha}\right]^{\beta/2}}, \tag{2.6B}$$

$$\varepsilon''(\omega) = (\varepsilon_s - \varepsilon_\infty)\frac{sin\,\beta\varphi}{\left[1 + 2(\omega\tau)^\alpha\, cos\,{}^{\alpha\pi}/_2 + (\omega\tau)^{2\alpha}\right]^{\beta/2}}, \tag{2.6C}$$

$$\tan\delta = \frac{\varepsilon''(\omega)}{\varepsilon'(\omega)} = \frac{(\varepsilon_s - \varepsilon_\infty)\, sin\, \beta\varphi}{\varepsilon_\infty\left[1 + 2(\omega\tau)^\alpha\, cos\, {\alpha\pi}/{2} + (\omega\tau)^{2\alpha}\right]^{\beta/2} + (\varepsilon_s - \varepsilon_\infty)\, cos\, \beta\varphi}, \tag{2.6D}$$

$$1 + (j\omega\tau)^\alpha = e^{j\varphi}\frac{\sqrt{1 + 2(\omega\tau)^\alpha\, cos\, {\alpha\pi}/{2} + (\omega\tau)^{2\alpha}}}{1 + (\omega\tau)^\alpha\, cos\, {\alpha\pi}/{2}} = \frac{e^{j\varphi}}{\cos\varphi}\ \text{(say)},$$
$$\varphi = tan^{-1}\left[\frac{(\omega\tau)^\alpha\, sin\, {\alpha\pi}/{2}}{1 + (\omega\tau)^\alpha\, cos\, {\alpha\pi}/{2}}\right]. \tag{2.6E}$$

- ***Jonscher model:*** This model is a semi-empirical model that combines a Debye-like response with a power-law response.[31] The model assumes that the dielectric material consists of a distribution of relaxation times, and that the response of the material is characterized by both a Debye relaxation process and a power-law process. The Jonscher model is often used to analyse dielectric spectra of materials that exhibit a broad range of relaxation times and frequencies. We shall use Jonscher's power law (JPL) with a $\sim\omega^n$ dependence to fit AC conductance data in chapters 6 and 7, where a robust discussion on it will be added.

These models and others have helped researchers to understand and delineate the dielectric relaxation phenomenon in a variety of materials, including polymers, glasses, ceramics, and biological tissues. Understanding the dielectric response of materials is important for a range of applications, including in the design and optimization of electronic devices, as well as in the study of biological systems and materials science.

2.3.8 Applications

In this section, we mention just a few examples of the many uses of dielectric materials in various fields. The unique dielectric properties of these materials make them highly useful in a wide range of technological and scientific applications.

i. ***Capacitors:*** Dielectric materials are commonly used in capacitors, which are electronic components that store electrical energy. When a voltage is applied to the plates, the dielectric material becomes polarized, creating an electric field that stores electrostatic energy.

ii. ***Insulators:*** Dielectric materials with high breakdown strength are often used as insulators in electrical equipment to prevent the flow of electric current. Examples include the insulation used in power cables, transformers, and electrical motors.

iii. ***Piezoelectric devices:*** Certain dielectric materials, such as quartz and barium titanate, exhibit the piezoelectric effect, which means that they can convert mechanical energy into electrical energy and vice versa. These materials are used in a variety of applications, including ultrasound imaging, vibration sensors, transducers, and actuators.

iv. ***Microwave devices:*** Dielectric materials are used in microwave devices, such as filters, resonators, and antennas. These materials can be designed to have specific dielectric properties that enable them to manipulate microwave signals in various ways.

v. ***Energy storage:*** Dielectric materials can also be used for energy storage in applications such as high-energy density capacitors and batteries.

vi. ***Biomedical applications:*** Dielectric materials are used in biomedical applications such as tissue engineering, drug delivery, and biosensors. For example, some polymers are used as scaffolds for tissue engineering, while others are used as drug delivery vehicles. Additionally, the dielectric properties of biological tissues are often used in medical imaging techniques such as magnetic resonance imaging (MRI) and electrical impedance tomography (EIT).

2.4 The notion of negative capacitance (NC)

The phenomenon of negative capacitance refers to a situation in which the capacitance of a material decreases with an increase in the applied voltage. In other words, when a voltage is applied to a material exhibiting NC, the energy stored in the material decreases instead of increasing, as is the case with conventional capacitors. The phenomenon of negative capacitance has been observed in both ferroelectric and non-ferroelectric materials.

2.4.1 Ferroelectric class of NC

The Landau description of ferroelectricity associates a double well energy landscape. The maximum involves an unstable state, that can be related with NC. The free energy (U) of a ferroelectric material can be expressed as a function of the charge (Q), as given below.[32,33]

$$U(Q) \cong \alpha Q^2 + \beta Q^4 + \gamma Q^6, \alpha < 0. \quad (2.7)$$

Here, α, β & γ are anisotropy constants. The typical graph of $U(Q)$ has two minima and one maximum, as shown in Figure 2.5.

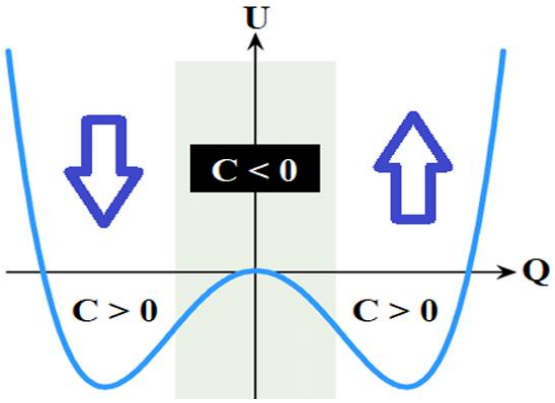

Figure 2.5 Schematically demonstrated double well energy landscape of a Landau ferroelectric material and the negative/positive capacitance regime.

In polycrystalline ferroelectric materials, NC arises due to the presence of the domain wall, which acts as a charge capacitor.[34] When an external voltage is applied, the domain walls move, and the polarization direction changes, leading to a decrease in the stored energy and, thus, negative capacitance.[32-34] This phenomenon is called the 'domain wall' negative capacitance. Another mechanism of negative capacitance in ferroelectrics is based on the idea of 'bulk' negative capacitance. In this mechanism, the internal electric field within the ferroelectric material opposes the external field, leading to a reduction in the polarization and negative capacitance.

2.4.2 NC in non-ferroelectric materials and devices

In non-ferroelectric materials, negative capacitance is generally attributed to the presence of an energy barrier between the polarization states. This energy barrier can arise due to a variety of factors, such as bandgap engineering or the formation of a heterojunction. When an external voltage is applied, the energy barrier is lowered, and the polarization direction changes, leading to a decrease in the stored energy and, thus, negative capacitance. In general, the mechanism of low frequency NC in non-ferroelectric materials is more complicated and versatile than in ferroelectric materials.[36-38] In literature, it has been explained with phenomena like space-charge propagation, mixed electronic and ionic polarization, slow transients, presence of defects, heavy dipoles, minority charge effects, uneven heating, extrinsic or doping effects, *etc*. However, at higher frequencies, pseudo-inductive effects sometimes generate similar observations, which is fundamentally different and a trivial concept. The negative capacitance in non-ferroelectric materials is typically a result of the interplay between various factors such as electronic structure, charge density, and interface engineering.[36-38] In fact, it is an 'extraordinary' and non-trivial dielectric feature, that very often comes with a delta function like dielectric loss at the capacitive transition point.

2.4.3 Applications

Negative capacitance in ferroelectric materials has several potential applications, as discussed below.

- ***Energy-efficient transistors:*** Negative capacitance can be utilized to design low-power transistors. By placing a ferroelectric material in the gate oxide of a metal oxide semiconductor field-effect transistor (MOSFET), the negative capacitance effect can overcome the thermodynamic limit of the subthreshold swing given by the Boltzmann tyranny, leading to an enhanced energy efficiency.[35,39]
- ***Steep slope devices:*** Negative capacitance can enable the development of many other steep slope electronic devices, which have the potential to overcome the limitations of conventional transistor scaling. Steep slope devices can achieve a subthreshold swing

smaller than the fundamental limit of 60 mV/decade, allowing for improved performance and reduced power consumption.

- ***Memory devices:*** Negative capacitance can be employed in non-volatile memory devices to enhance their energy efficiency and performance.[39] By utilizing the NC effect, it becomes possible to reduce the energy required for writing and reading operations in memory cells.
- ***Solid state NC supercapacitors:*** Ferroelectric NC material together with an ordinary dielectric (positive) capacitor leads to an overall positive energy density.[40] However, the series equivalent capacitance of the duo can be extremely high. This kind of systems are very stable, free of electrolytes, durable, and can have ultrahigh energy and power densities.

Regarding non-ferroelectric materials, as of now, there is limited scope of specific applications, because the associated understanding is still at an early level and requires a lot of further elucidation. The as-reported investigations involve utilizing certain material properties or device architectures to induce an NC response, that are directly or indirectly related with some device application. For example, NC has been detected in solar cells, photodiodes, quantum well photodetectors, LEDs, *etc*. However, the research in this area is still in its early stages, and the practical applications of NC in non-ferroelectric materials are not yet well-established.

2.5 A brief review on the recent developments in piezoelectrics

Piezoelectric materials refer to a class of materials that exhibit a unique property of developing an electrical charge on their surface when subjected to mechanical stress. This phenomenon arises due to the non-centrosymmetric crystal structure of piezoelectric materials, which results in the displacement of positive and negative charges upon mechanical deformation. Piezoelectric materials can be classified as either naturally occurring or synthetic. Synthetic piezoelectric materials such as piezo-ceramics and piezo-perovskites exhibit stronger piezoelectric characteristics than natural materials. The piezoelectric nature of a material can be characterized by its piezoelectric coefficient, which is commonly denoted as d_{33} or d_{31}. In the d_{33} mode, the potential developed in the material is along the direction of the applied strain, while in the d_{31} mode, the potential is developed perpendicular to the applied strain. Typically, the d_{33} value is greater than the d_{31} value. The piezoelectric effect is a crucial property for various applications, including sensors, actuators, and energy harvesting devices.

2.5.1 Electromechanical coefficients

Piezoelectric ceramics are anisotropic materials, and physical constants describing their properties are dependent on both the direction of the applied mechanical or electric force and the directions perpendicular to it. As a result, each constant typically has two subscripts to indicate the directions of the two related quantities, such as stress (force on the ceramic

element per unit surface area of the element) and strain (change in length of element divided by original length of element) for elasticity. In a rectangular system of x, y & z axes, the direction of positive polarization is usually aligned with the z −axis (as shown in Figure 2.6). The directions x, y & z are represented by the subscripts 1, 2, and 3, respectively, while shear about one of these axes is represented by the subscripts 4, 5, or 6, respectively.

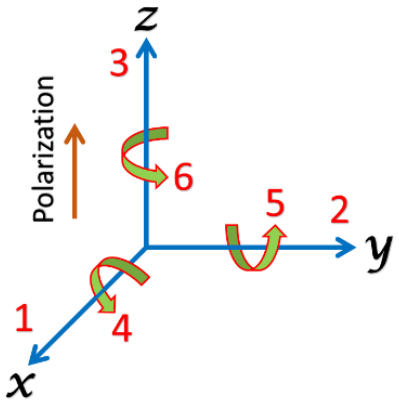

Figure 2.6 Direction and orientation of different forces that influence a piezoelectric element.

So, here we provide a summary of the definitions of the most frequently used constants and equations for determining and interrelating these constants. Basically, all of them are 2nd rank tensors. It is important to note that the piezoelectric charge constant, d_{ij}, the piezoelectric voltage constant, g_{ij}, and the permittivity, ε_{ij}, are temperature-dependent factors.

- ***Piezoelectric charge constant:*** Piezoelectric materials generate a polarization in response to a mechanical stress, which can be quantified by the piezoelectric charge constant, d_{ij}. Alternatively, d_{ij} can be described as the mechanical strain induced by an electric field. The first subscript of d indicates the direction of polarization generated when the electric field is zero or the direction of the applied field strength. The second subscript denotes the direction of the applied stress or the induced strain. The suitability of a material for strain-dependent applications (such as actuators) can be assessed by its value of d_{ij}. Specifically, the induced strain in a piezoelectric material is proportional to the product of the electric field and d_{ij}. The most important piezoelectric charge constant can be expressed as d_{33}, which represents the induced polarization in direction 3 (parallel to the direction of polarization in the ceramic element) per unit stress applied in the same direction. Similarly, d_{31} represents the induced polarization in direction 3 per unit stress applied in direction 1 (perpendicular to the direction of polarization). Finally, d_{15} represents the induced polarization in direction 1 (perpendicular to the direction of polarization) per unit shear stress applied about direction 2 (perpendicular to both the direction of polarization and direction 1).

- ***Piezoelectric voltage constant:*** The piezoelectric voltage constant, g_{ij}, describes the electric field generated by a piezoelectric material in response to a mechanical stress or the mechanical strain experienced by the material in response to an electric displacement. The first subscript of g_{ij} indicates the direction of the generated electric field or the applied electric displacement, while the second subscript represents the direction of the applied stress or induced strain. In sensing (sensor) applications, the value of g_{ij} is important for evaluating the suitability of a material. Specifically, the induced electric field produced by a piezoelectric material in response to a physical stress is proportional to the product of the applied stress and g_{ij}. The piezoelectric voltage constant can be expressed as g_{33}, which represents the induced electric field in direction 3 (parallel to the direction of polarization in the ceramic element) per unit stress applied in the same direction. Similarly, g_{31} represents the induced electric field in direction 3 per unit stress applied in direction 1 (perpendicular to the direction of polarization). Finally, g_{15} represents the induced electric field in direction 1 (perpendicular to the direction of polarization) per unit shear stress applied about direction 2 (perpendicular to the direction of polarization, as well as with direction 1).
- ***Young's modulus:*** The Young's modulus, denoted as Y, is a measure of the stiffness or elasticity of a ceramic material. This parameter is calculated by dividing the stress applied to the material in a specific direction by the resulting strain in the same direction. The higher the Young's modulus value, the stiffer or less deformable the material is in response to an applied stress.
- ***Dielectric coefficient:*** The dielectric coefficient $(\varepsilon_{r,ij})$ represents the electric displacement that occurs in the direction of the i −axis in response to an applied electric field along the j −axis. It is worth noting that for most piezoelectric materials, the electric displacement occurs only along the direction of the applied field (*i.e.*, j −axis) to achieve maximum effect. Additionally, the relative dielectric constant is defined as the ratio of the permittivity of a material to the permittivity of free space. This parameter provides information on the extent to which an electric field can be stored in the material for a given electric flux density.
- ***Piezoelectric coupling coefficient:*** The effectiveness of piezoelectric materials is commonly assessed using the piezoelectric coupling coefficient (k_{ij}), which quantifies their ability to convert mechanical energy into electrical energy. The subscript 'i' indicates that the electrodes are perpendicular to the i −direction, while mechanical stress is applied in the j −direction. For example, if a piezoelectric material is stretched mechanically along the 1-direction and develops a piezoelectric potential in the 3-direction, the ratio between transformed mechanical energy and electrical energy can be expressed as κ_{13}^2.

$$\kappa_{13} = \sqrt{\frac{W_{elec}}{W_{mech}}}. \tag{2.8}$$

The piezoelectric coupling coefficient can also be expressed in terms of other piezoelectric coefficients, such as the Young's modulus (Y) and the piezoelectric charge constant (d_{ij}). The relation between these quantities is given below.

$$\kappa_{ij}^2 = Y g_{ij} d_{ij}. \tag{2.9}$$

2.5.2 Naturally available piezoelectric substances

Piezoelectric materials occur naturally in various forms, with single-crystal quartz being one of the first and most well-known examples. Other naturally occurring piezoelectric crystals, such as cane sugar, tourmaline, Rochelle salt, and topaz, have also been identified and studied. In addition, certain biological materials, such as bone, DNA, enamel, and dentin, exhibit the piezoelectric effect too.

- ***Quartz***, for example, is a continuous framework of SiO_2 that displays a piezoelectric coefficient (d_{33}) of approximately 3 pC/N. This property makes it useful for a range of applications, including crystal oscillators, quartz clocks, and other electronic devices.
- ***Topaz***, which has a general chemical formula of $Al_2SiO_4(F,OH)_2$, exhibits an orthorhombic crystal structure having $Pbnm$ space group.
- ***Rochelle salt***, also known as potassium sodium tartrate tetrahydrate, is a double salt of tartaric acid. Its piezoelectric effects were first demonstrated by Sir David Brewster in 1824, and it has since been used in various electronic appliances such as speakers and microphones.
- ***Biological materials*** such as bone and teeth display piezoelectric properties due to the highly oriented and patterned structure of collagen, which responds to mechanical stress. enamel and dentin, for instance, exhibit piezoelectric behaviour due to the presence of hydroxyapatite. The piezoelectricity of hydroxyapatite in enamel is lower than that in dentin, with a d_{33} value of approximately 0.003 pC/N.

Figure 2.7 Images of certain piezoelectric crystals: (a) quartz; (b) topaz; (c) Rochelle salt; and (d) hydroxyapatite (present in enamel and dentin). All images are collected from the internet.

- ***Sugarcane***, on the other hand, is a bio-composite material. Its main component is strontium titanate ($SrTiO_3$) having a simple cubic ($Pm\bar{3}m$) crystal structure.

2.5.3 Popular binary and ternary piezoelectric oxides/ceramics

Piezoelectric ceramics are a class of materials that generally possess ferroelectric properties due to their polycrystalline structure, which are typically composed of perovskite, tetragonal, or rhombohedral crystals. At temperatures above the Curie temperature, these materials mostly exhibit a centrosymmetric cubic structural symmetry where the centre of positive and negative charges coincide, resulting in no electric dipoles. However, below the Curie temperature, the cubic structure distorts, and electric dipoles arise from the displacement of charge centres. Realignment of neighbouring dipoles leads to the formation of Weiss domains. This is when piezoelectricity is observed in these materials. In general, ferroelectrics are a subset of pyroelectrics, which is again a subset of piezoelectrics, and finally all of these materials are dielectric for obvious reasons. The hierarchy is shown in the following figure.

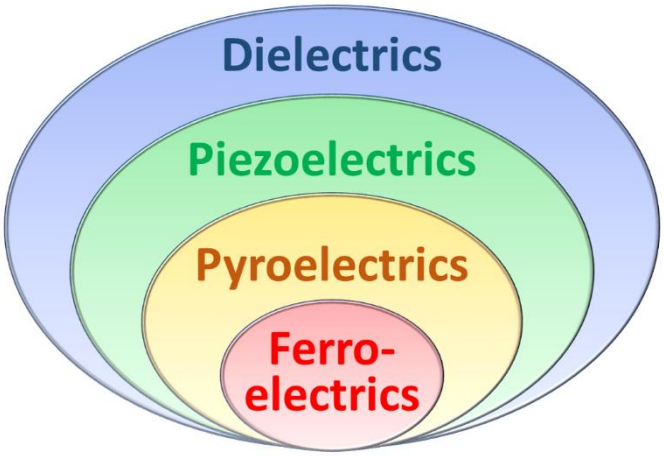

Figure 2.8 The hierarchy of dielectrics, piezoelectrics, pyroelectrics, and ferroelectrics.

Some commonly available, popular inorganic piezoelectric materials and their basic details are enlisted below.

- Zinc oxide (ZnO) exists in two forms: hexagonal wurtzite and cubic zincblende structures. Both structures lack inversion symmetry, making them piezoelectric. The hexagonal crystal structure has a d_{33} value of 3.62 ± 0.5 pC/N.
- Titanium dioxide (TiO_2) is a commonly used binary oxide in various applications due to its excellent electrical, optical, and mechanical properties. It has commonly a tetragonal crystal structure with space group $P4mm$, and it exhibits piezoelectricity along the c −axis.
- Barium titanate ($BaTiO_3$) is the first discovered polycrystalline ceramic material that exhibits piezoelectricity. It possesses two crystal structures *viz*., cubic ($Pm\bar{3}m$) and tetragonal ($P4mm$) perovskite structure with a piezoelectric coefficient of ~500 pC/N.

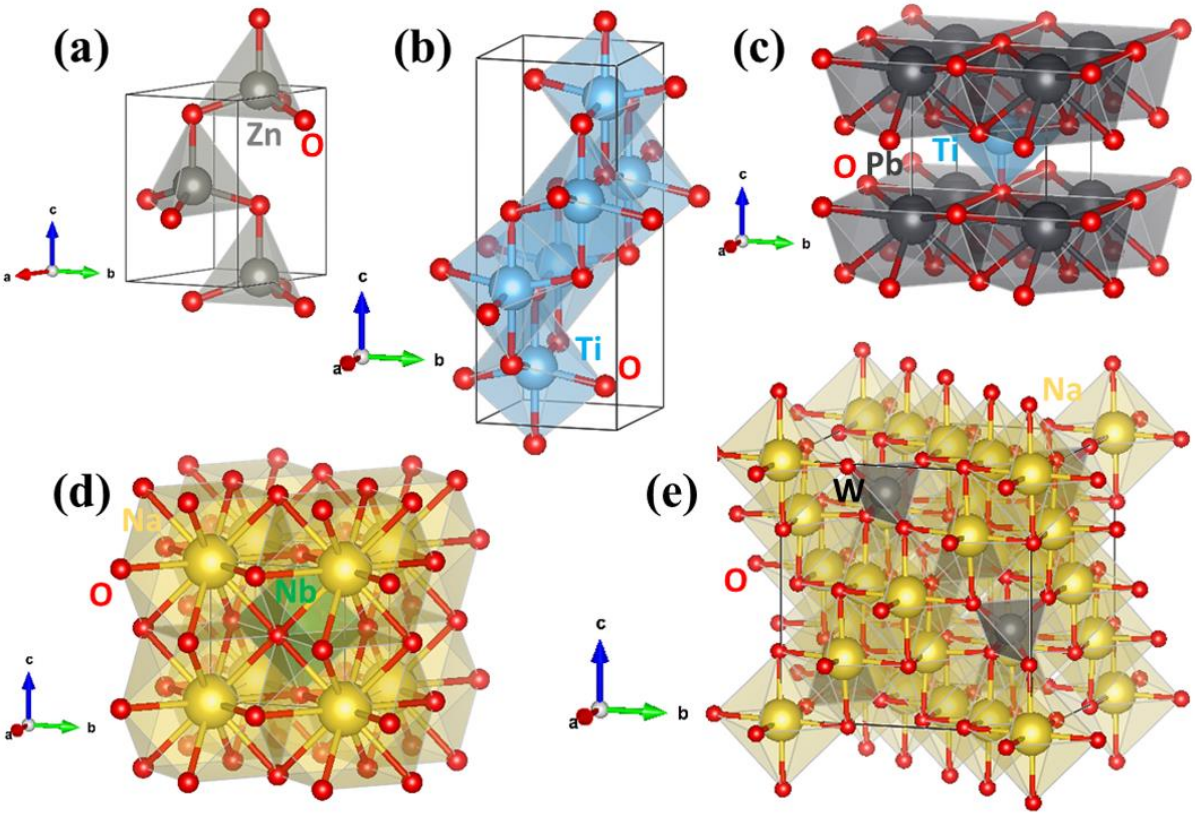

Figure 2.9 Conventional unit cells of some popular piezoelectric materials: (a) ZnO; (b) TiO_2; (c) $PbTiO_3$; (d) $NaNbO_3$; and (e) Na_2WO_4.

- Lead titanate ($PbTiO_3$) is a well-known lead-based inorganic perovskite compound that shows a d_{33} value of 110 pC/N.
- Lead zirconate titanate or PZT is the most widely used inorganic perovskite piezoelectric compound, with a chemical formula of ($PbZr_xTi_{1-x}O_3$) with $0 \leq x \leq 1$. PZT exhibits a superior piezoelectric effect compared to other materials, with a d_{33} value of ~245 pN/C. It is commonly used in ultrasonic transducers, piezoelectric nanogenerators, and scientific instruments such as scanning tunnelling microscopes (STM) and piezo-response force microscopy (PFM).
- Potassium niobate ($KNbO_3$) is an inorganic lead-free perovskite compound that exhibits a piezoelectric effect. It belongs to the orthorhombic system, with the $Amm2$ space group.
- Sodium niobate ($NaNbO_3$) is piezoelectric. Its crystal structure belongs to the perovskite family, and its space group is $R3c$.
- Lithium niobate ($LiNbO_3$) is a manmade salt of niobium and lithium that belongs to the trigonal crystal system with the $R3c$ space group. The absence of inversion symmetry in this structure makes it piezoelectric.
- Sodium tungstate (Na_2WO_4) is an inorganic compound that exhibits the piezoelectric effect. It crystallizes in the cubic $Fd\bar{3}m$ space group.

2.5.4 Piezoelectric polymers

Over the years, researchers have taken a keen interest in polymeric piezoelectric materials due to their flexible, durable, lightweight, and promising potential in energy storage applications.[41] In contrast, perovskite piezoceramics are limited in their application area due to their brittle nature. The piezoelectric effect in polymers is a result of the molecular dipoles present in the polymer chain, which reorient themselves along the direction of stress under mechanical stress. Piezo-polymers generally have a moderate piezoelectric coefficient value of $20 - 30$ pC/N, but they exhibit higher piezoelectric stress constants, making them more suitable for sensor applications than other piezoelectric materials. Moreover, polymers generally have a higher dielectric breakdown strength and can endure higher working electric fields than piezoceramics. Well-established piezo-polymers include poly(vinylidene fluoride) or PVDF, poly(vinylidene fluoride-hexafluoropropylene) or PVDF-HFP, poly(vinylidene fluoride-tetrafluoroethylene) or PVDF-TFE, poly(vinylidene fluoride-trifluoroethylene) or PVDF-TrFE, poly(L-lactic acid) or PLLA, polyurea, among others.[41] To be piezoelectric, semi-crystalline polymers must have a polar crystalline phase, with crystallites existing within the amorphous region. The mechanical properties of the polymer are determined by the glass transition temperature, which depends on the amorphous region, while the melting temperature *i.e.*, maximum used temperature is dependent on the crystalline region. The degree of crystallinity of the polymer is influenced by the preparation method, and various processes, such as mechanical stretching, thermal annealing, electric poling, electrospinning, and filler insertion, are used for phase transformation from non-polar to polar.

2.5.5 Crystal structure of PVDF and its advantages

In 1969, the phenomenon of piezoelectricity was first observed in poly(vinylidene difluoride) or poly(vinylidene fluoride) polymer or PVDF and since then, interest in these materials has grown rapidly. PVDF is a polymer that exhibits a large piezoelectric coefficient (d_{33}) of $\mathbf{6 - 7}$ $\boldsymbol{pC\ N^{-1}}$, which is approximately an order greater than most other polymers. The unique electromechanical response of PVDF is mainly due to the orientation of the hydrogen and fluorine atoms in the polymer chain. Additionally, pristine PVDF exhibits a relative dielectric permittivity of about 10, which is much higher than most piezopolymers, making it an interesting material for device implementation.

Amorphous PVDF has a ***glass transition temperature of*** $\mathbf{-35}$ °C, which is below room temperature, giving it a highly flexible character at ambient conditions. Depending on the synthesis procedure, the amount of crystallinity in PVDF can be enhanced up to 90%. PVDF typically possesses ***five crystal phases:*** $\boldsymbol{\alpha, \beta, \gamma, \delta}$, ***and*** $\boldsymbol{\varepsilon}$.[42] Among these, the first three phases are more abundantly obtained and considered for device-based applications, check Figure 2.10.

The α −phase is thermally stable and exhibits a nonpolar ***TGTG'*** conformation of the polymer chain. The β −PVDF shows piezoelectric nature due to its all-trans (***TTTT***) chain conformation, while the γ −phase exhibits a highly polar character due to its semi-crystalline ***T_3GT_3G'*** chain conformation. In the β −phase, a polar monomer unit (—CH_2—CF_2—) perpendicular to the chain axis is repeated in the PVDF matrix to form a linear fluorinated hydrocarbon that possesses a high dipole moment of $\sim \mathbf{7 \times 10^{-30}}$ ***C m***. Pristine PVDF is mostly composed of α −phase, and after poling, the molecular dipoles are rotated to form a crystalline structure.[42] Recently, researchers and scientists have established the polarization stability of PVDF and its copolymers, which are related to Coulombic interactions between the surface charge of some filler materials and oriented molecular dipoles in the crystals. As a result of these interactions, the molecular dipoles are trapped, and the orientation of the dipoles is locked, stabilizing the crystalline phases.

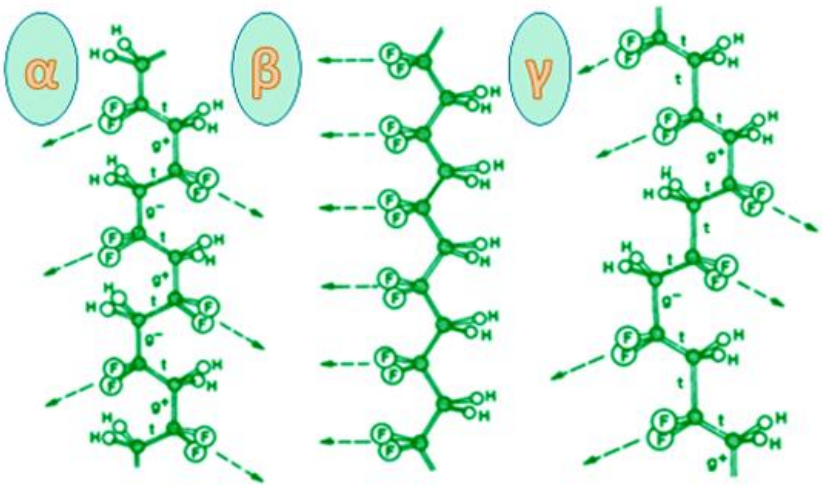

Figure 2.10 Chemical structures of the common polymorphic phases (α, β & γ) of PVDF.

2.5.6 Polymeric piezoelectric nanogenerators (PPNGs)

Although piezoelectric polymers exhibit lower piezoelectric strain constants (d_{31}) than piezoelectric ceramics, their piezoelectric stress constant (g_{31}) values are much higher than that of piezoelectric ceramic materials. PVDF exhibits different orientations in molecular chain conformation depending on the chain conformation linkages, that causes formation of the five polymorphic phases, described in the previous section. The α −phase is completely nonpolar (and thermodynamically most stable), while the β & δ −phases (known as ***electroactive phases***) exhibit spontaneous polarization and are desired for energy storage applications, sensors, biomedical applications, Internet of Things (IoT) technology, *etc*. PVDF and its copolymers have become prospective polymers for their high ferroelectric property, flexibility, negligible cytotoxicity, long-term stability, and non-reactivity. Various approaches have been introduced to enhance the electroactive β −phase, including direct-write piezoelectric

nanogenerator based on PVDF using electrospinning and PVDF-based piezoelectric nanogenerator that harvests mechanical energy from the human body. Additionally, copolymers of PVDF, such as PVDF-TrFE, PVDF-TFE, and PVDF-HFP exhibit a robust piezoelectric effect and can adopt an all-trans crystalline phase structure directly similar to the β −phase of PVDF.

Piezoelectric properties are not limited to PVDF and its copolymer, as other polymers like polypropylene, polystyrene, poly(methyl methacrylate), polyvinyl acetate, and odd-number nylons such as nylon-11 also exhibit such properties. In 2016, Sepúlveda *et al*. demonstrated the use of polypropylene as an active piezoelectric material in a flexible, efficient, and biocompatible piezoelectric nanogenerator device. They employed the finite element method (FEM) to elucidate the mechanism of mechanical to electrical energy conversion in their fabricated films, resulting in the development of a self-powered flexible/foldable keyboard. Furthermore, Asadi *et al*. and his colleagues presented evidence of piezoelectricity in a nylon-11 fibre, and their findings suggest that the device has the potential to scavenge energy from low-frequency mechanical vibrations.

Polyaniline (PANI) is a conducting polymer that possesses both electrical conductivity and piezoelectric properties. By integrating PANI into a nanogenerator structure, it is possible to generate electricity through mechanical deformation. PANI-based PPNGs have shown potential for applications in wearable electronics and self-powered sensors. Polyurethane (PU) is another versatile polymer that can be engineered to exhibit piezoelectric behaviour. PU-based PPNGs have been developed using various techniques, such as electrospinning or solution casting. These nanogenerators have demonstrated the ability to convert ambient vibrations into electricity, making them suitable for powering small electronic devices.

Cellulose is a renewable and biodegradable polymer that has recently gained attention for its piezoelectric properties. Cellulose-based PPNGs can be fabricated using cellulose nanocrystals or cellulose nanofibers. These nanogenerators have shown promise in harvesting energy from human motion or mechanical vibrations in the environment. Also, silk is a natural protein-based polymer known for its exceptional mechanical properties. Recent research has explored the piezoelectric characteristics of silk fibres and developed silk-based PPNGs. These nanogenerators can generate electricity from subtle mechanical stimuli, making them potentially useful in wearable electronics and biomedical devices. Thus, PPNGs offer a versatile and lightweight approach in harvesting mechanical energy for various applications.

2.5.7 Fabrication of PVDF-based PENGs via enhancement of the electroactive phase

PVDF films can be synthesized using various techniques such as melt casting, spin coating, film casting, and solution casting. Solution-based processing is typically done using polar solvents like N,N-dimethylformamide (DMF), dimethyl sulfoxide (DMSO), N-

methylpyrrolidone (NMP), dimethylacetamide (DMAC), and butanone. In 2006, Prevedouros *et al*. used the ionic form of Fluoro surfactant perfluorononanoic acid for aqueous emulsion polymerization. DMF (or DMSO) and acetone in a 3:2 ratio is commonly used to dissolve the PVDF pellets or powder, which is then stirred at ~60 ℃ for approximately 2 h. The prepared PVDF films are typically composed of the non-piezoelectric α −phase, and several methods such as electrospinning, mechanical stretching, and electric-poling process can be used to achieve a piezoelectric β −phase.

- The ***electrospinning technique*** has become a popular method to prepare highly polar PVDF films due to high reproducibility, simple and easy processing. Baek *et al*. demonstrated the electrospinning of carbon nanotube (CNT)-PVDF composite nanofiber mats in 2003, while Sheng *et al*. established PVDF nanofiber mats in 2006.[43]
- ***Application of mechanical stress/tension via stretching, bending, twisting, or pressing*** is also a useful approach to improve the piezoelectric and dielectric properties of the PVDF matrix. Nayak *et al*. reported that a stretching ratio of 2 achieved a maximum β −phase content of about 86%, while Mendez *et al*. examined the impact of temperature and stretching ratio on the PVDF matrix's phase transition from non-ferroelectric to ferroelectric phase.
- The most straightforward and effective method to polarize a nanocomposite is ***high electric field poling***. When an electric field is applied across a piezoelectric material, atomic dipoles align themselves along the field direction and the material becomes polar. Miranda *et al*. investigated the poling effect on PVDF in 1989 and reported a monotonically increasing behaviour in thermal diffusivity and dielectric constant with the poling field.[44]
- ***Incorporation of appropriate fillers (chemical method)*** in the polymer matrix is the most conventional and cost-effective way to increase the electroactive phase fraction of the PVDF matrix. This process is generally conducted under the ***self-poling*** framework.[45] When nanomaterials are inserted into the PVDF matrix as a filler, the surface charge of the filler interacts with the dipoles of the PVDF chain, resulting in the orientation of dipoles along a specific direction.[45] This happens when the entire system is left in a vibration free idle state, which allows the poling process on its own, called the self-poling process.
- Thin, uniform ferroelectric PVDF films with ordered β crystals can be fabricated using ***thermal annealing*** as well. Researchers like Park *et al*. have employed rapid thermal treatment to increase the amount of crystals in the film. The film is heated rapidly until it reaches a temperature just below the melting point of PVDF, causing residual DMF to flow down the film's normal. Fast thermal annealing can produce a film with over 90% crystal content.

2.5.8 Applications

PVDF-based PENGs have a wide range of potential applications. These devices have the potential to provide self-powered systems that can harvest energy from ambient mechanical sources, making them highly attractive for various applications. Further research and development in this area will likely lead to the development of new and innovative applications for this technology. Some of the presently explored applications are mentioned below.

i. ***Piezo-phototronics and photodetectors:*** The piezo-phototronic effect refers to the coupling between the piezoelectric and semiconductor properties of a material. By incorporating PVDF-based PENGs into photodetectors, the sensitivity and efficiency of the detectors can be enhanced by the piezoelectric effect. This technology has applications in imaging, sensing, and energy harvesting.

ii. ***Piezo-supercapacitors:*** Supercapacitors are energy storage devices that can charge and discharge rapidly, making them ideal for applications requiring high power output. By combining PVDF-based piezoelectric nanogenerators with supercapacitors, it is possible to develop self-powered systems that can harvest energy from ambient mechanical sources and store it for later use.

iii. ***Wearable electronics:*** PVDF-based piezoelectric nanogenerators can be integrated into clothing or accessories, such as shoes or backpacks, to generate power from the wearer's movement. This technology can also be used in medical devices, such as pacemakers or insulin pumps.

iv. ***Structural health monitoring:*** PVDF-based piezoelectric sensors can be used to monitor the health of structures such as bridges, buildings, and aircraft. The sensors can detect changes in strain or pressure, and the nanogenerator can provide power to the sensors, making them self-powered and wireless.

v. ***Water and air quality monitoring:*** PVDF-based PENGs can be used to power sensors that detect pollutants or contaminants in water or air. This technology has applications in environmental monitoring, public health, and industrial process control.

vi. ***Self-powered wireless sensors:*** PVDF-based PENGs can be used to power wireless sensors for applications such as smart homes, smart cities, and IoT applications. The sensors can monitor various parameters, such as temperature, humidity, vibrations, and motion, and transmit data wirelessly without requiring an external power source. This makes the devices lightweight, portable, cost-effective, and durable.

vii. ***Human-machine interfaces:*** PVDF-based piezoelectric sensors can be used to develop touch-sensitive interfaces for electronic devices. The sensors can detect pressure, touch, or gesture, and the nanogenerator can provide power to the device, making it self-powered and wireless.

viii. ***Piezo-catalysis:*** The piezoelectric effect can enhance the performance of catalytic reactions by providing an electric field that promotes charge separation and facilitates the transfer of electrons between the reactants. This technology has applications in energy conversion and storage, as well as in environmental and biomedical fields.

2.6 Correlation between electrical and vibrational properties

The correlation between electrical polarization-related properties and vibrational properties arises due to the interaction between charged particles and lattice vibrations in materials. As mentioned earlier, the coupling between these properties can be attributed to the ***flexoelectric effect*** and ***phonon-induced polarization***, as well as ***charge-phonon coupling***.[46,47] The flexoelectric effect refers to the coupling between the polarization and the gradient of strain induced by phonons, while phonon-induced polarization is the displacement of charged particles induced by phonons. Charge-phonon coupling, on the other hand, refers to the interaction between the electronic and vibrational degrees of freedom in a material, which can affect the electronic band structure and polarization. The correlation between these properties can have a significant and complex impact on material properties. For example, the ferroelectric response of a material is closely related to its vibrational properties, such as phonon dispersion, density of states, and linewidth. In addition, the piezoelectric response of a material can also be affected by its vibrational properties, as changes in the phonon dispersion and density of states can lead to changes in the piezoelectric coefficient. Similarly, the electronic band structure and transport properties of a material can be affected by its vibrational properties through charge-phonon coupling.

The ability to control the electrical polarization and vibrational properties of materials is crucial for the development of new materials with desired technological properties. One way to control these properties is through the use of external stimuli, such as electric fields, mechanical strain, and temperature. For example, applying an electric field can induce a change in the polarization of a material, while applying mechanical strain can affect its vibrational properties. Another way to control these properties is through the use of doping and defect engineering. The introduction of dopants and defects can affect the electronic band structure and polarization of a material, which can in turn affect its vibrational properties. Similarly, the introduction of dopants or defects can also affect the phonon dispersion, density of states, and linewidth, which can alter the electrical polarization-related properties of the material. In addition, the correlation between these properties can be controlled through the use of heterostructures and interfaces.

The correlation between electrical polarization-related properties and vibrational properties can have a significant impact on material properties. For example, the ferroelectric

response of a material affects its piezoelectric and pyroelectric properties, as well as its capacitance and permittivity. Similarly, the vibrational properties of a material can affect its thermal conductivity, as well as its mechanical and optical properties. The ability to control the correlation between these properties can lead to the development of new materials with improved technological applications. For example, the use of heterostructures can lead to the development of materials with enhanced ferroelectric and piezoelectric attributes, as well as improved electronic and transport mechanisms.

In conclusion, the correlation between electrical polarization-related properties and vibrational properties is an important topic in materials science, with a significant impact on material properties and technological applications. The coupling between these properties can be controlled through external stimuli, doping and defect engineering, and the use of heterostructures and interfaces. The ability to control the correlation between these properties can lead to the development of new materials with tailored properties, such as enhanced ferroelectric and piezoelectric features, improved electronic and transport endeavor, and unique vibrational properties. The study of the correlation between electrical polarization and vibrational properties is essential for the development of new materials for various technological applications, such as sensors, actuators, and energy conversion devices.

2.7 Fano interference and Raman line-shape asymmetry

Fano interference is a quantum interference phenomenon that can occur in a variety of physical systems, including Raman scattering. In Raman spectroscopy, the Fano interference results in an asymmetric line-shape in the Raman modes, known as the Fano line-shape.[48] The Fano resonance arises when a narrow spectral feature, such as a phonon mode, is coupled to a continuum of electronic or vibrational states. The narrow feature and the continuum of states interfere, leading to an asymmetric line-shape in the Raman spectrum. The Fano line-shape can be described by the Breit-Wigner-Fano (BWF) formula, which relates the intensity of the Raman scattering to the frequency of the phonon mode and the coupling between the phonon mode and the continuum of states.[48,49] The BWF formula can be written simply as the following.

$$I = \frac{(q+\varepsilon)^2}{1+\varepsilon^2}. \tag{2.10}$$

Here, I is the intensity of the Raman scattering, q is the Fano interference parameter, which represents the strength of the interference between the narrow feature and the continuum of states, and ε is the detuning parameter, which represents the difference between the frequency of the phonon mode and the resonant frequency of the continuum of states. Further mathematical details are available in chapter 8. Thus, the Fano resonance can provide valuable insights about the coupled electronic states and phonon modes in a material.

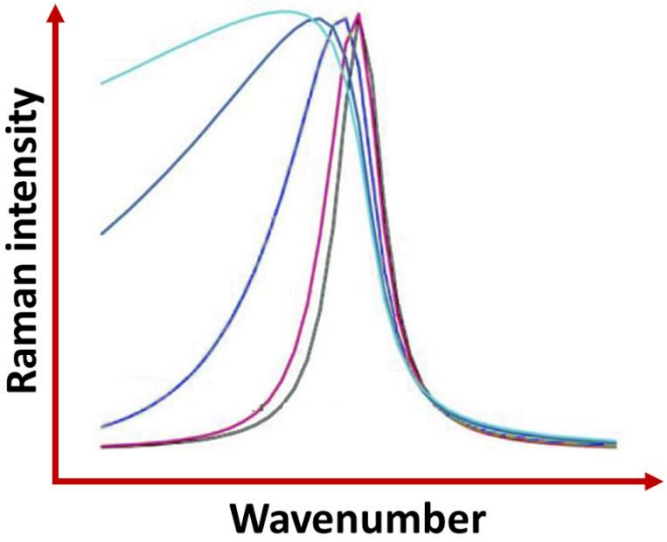

Figure 2.11 Symmetric Lorentzian versus asymmetrically broadened BWF line-profile (due to Fano interference) in a Raman mode.

The asymmetry of the Fano line-shape depends on the nature of the coupling between the phonon mode and the electronic or vibrational states. For example, if the coupling is strong and the continuum of states is dense, the Fano line-shape will be strongly asymmetric. On the other hand, if the coupling is weak and the continuum of states is sparse, the Fano line-shape will be weakly asymmetric. The Fano resonance has important applications in materials science and condensed matter physics. It can be used to study the electronic and vibrational properties of materials, such as semiconductors, metals, and superconductors. In addition, the Fano resonance can provide information about the symmetry and dynamics of phonon modes in materials.

2.7.1 Quantum confinement of phonon states

Phonons are quantized mechanical vibrations in a solid that result from the collective motion of atoms or molecules. In ultra-small nanoparticles and low-dimensional materials, the size of the material can be comparable to or smaller than the characteristic length scales of phonon modes. It leads to the quantum confinement of phonons, where the vibrational modes become restricted within a small region of space, leading to a quantization of the vibrational modes. The ***phonon confinement model (PCM)*** describes this phenomenon mathematically.[49,50] In this model, the phonon modes are confined within a region of width L, such as a nanowire or a thin film. The vibrational modes of the phonon are then quantized, with the wavevector $\vec{k}$ restricted to discrete values determined by the boundary conditions at the edges of the confined region. The energy levels of the confined phonon modes can be calculated using the wave equation for acoustic waves.

The phonon confinement energy depends on the size and shape of the confinement region, and it can be expressed as,

$$E_n = \hbar\omega \sqrt{\left(\frac{n_x}{L_x}\right)^2 + \left(\frac{n_y}{L_y}\right)^2 + \left(\frac{n_z}{L_z}\right)^2}. \tag{2.11}$$

Here, n_x, n_y, and n_z are the mode numbers in the x, y, and z directions, respectively. L_x, L_y, and L_z are the dimensions of the confinement region in those directions. This equation shows that the phonon energy levels depend on the confinement dimensions in all three dimensions, with the energy levels becoming more closely spaced as the confinement dimensions become smaller.[49,50] In ultra-small nanoparticles and low-dimensional materials, the confinement of phonons can have a significant impact on the thermal and mechanical properties of the material. For example, the thermal conductivity of a material can be reduced due to phonon confinement, which can be advantageous for thermoelectric applications. Phonon confinement can also affect the mechanical properties of a material, such as its elastic modulus and strength.

2.7.2 Charge-phonon coupling effect

The charge-phonon coupling effect refers to the interaction between the electronic charge density and the vibrational modes of the lattice in a material. This effect arises due to the fact that the movement of the atoms in the lattice affects the electronic structure, and vice versa. The coupling of charge and phonons can have significant consequences for the electronic and optical properties of a material.[46-48] There are two types of charge carriers in a semiconductor *viz*., electrons and holes. Both electrons and holes can couple to phonons, leading to electron-phonon coupling and hole-phonon coupling, respectively. In electron-phonon coupling, the electron density interacts with the vibrational modes of the lattice, while in hole-phonon coupling, the hole density interacts with the vibrational modes of the lattice. Under the ***Born–Oppenheimer approximation*** (states that, the electronic and nuclear motions in molecules can be separated), we may assume that the electrons instantaneously respond to the ionic motion. This allows the electron–phonon interaction Hamiltonian $\left[\hat{H}_{e-ion}\right]$ to be expressed as a Taylor series expansion of the electronic Hamiltonian $\left[\hat{H}_e\left(\vec{r_i}, \overrightarrow{R_J}\right)\right]$.[51]

$$\hat{H}_{e-ion}\left(\vec{r_i}, \delta\overrightarrow{R_J}\right) = \sum_j \left(\frac{\partial \hat{H}_e}{\partial \overrightarrow{R_J}}\right)\Bigg|_{\overrightarrow{R_{J0}}} . \delta\overrightarrow{R_J} + \cdots \tag{2.12}$$

In most cases, the electronic Hamiltonian is not known exactly. So, approximations are required to calculate the electron–phonon interaction. The ***charge-phonon coupling constant*** is a measure of the strength of the coupling between charge carriers and phonons in a material.[46-48] It quantifies the change in the energy of the electronic states due to a small change in the atomic positions. The coupling constant is related to the deformation potential, which is the change in

the electronic energy due to a change in the atomic positions at a fixed electronic state. In general, the coupling constant depends on the material properties, such as the band structure, the density of states, and the phonon dispersion. The coupling constant can also depend on the specific phonon mode that is being considered.

The effect of charge-phonon coupling can be seen in a variety of electronic and optical properties of materials. For example, in semiconductors, the coupling between electrons and phonons can lead to carrier scattering, which can affect the mobility and conductivity of the material. Furthermore, the coupling between electrons and phonons can affect the optical properties of a material, such as the absorption and emission spectra. In some cases, charge-phonon coupling can lead to novel phenomena, such as ***polaron*** formation.[52] A polaron is a quasi-particle that results from the coupling of an electron (or hole) with the phonons in the lattice. The formation of polarons can significantly affect the transport properties of a material, as well as its electronic and optical properties. Both electron-phonon coupling, and hole-phonon coupling can lead to significant changes in the properties of a material, and the coupling constant provides a measure of the strength of the coupling between charge carriers and phonons. Understanding the charge-phonon coupling effect is crucial for the design and optimization of materials for various applications, such as optoelectronics and energy conversion.

2.7.3 Effect of temperature, pressure, and phase transition

The Fano asymmetry in Raman spectroscopy can be affected by several factors, including temperature, pressure, and phase transition.[53,54] Temperature can influence the coupling between the phonon mode and the electronic or vibrational states, while pressure can change the phonon frequency and alter the electronic or vibrational states that couple to the phonon mode.[53] Phase transitions can lead to changes in the lattice structure and electronic properties, which can impact the Fano asymmetry.[54] Understanding these effects is important for the interpretation and analysis of Raman spectra, particularly in materials science and condensed matter physics.

Temperature can affect the Fano asymmetry in several ways. One effect is that the broadening of the phonon mode due to thermal motion can influence the shape of the Raman line. As the temperature increases, the phonon linewidth increases, which can reduce the contrast between the resonant and non-resonant contributions to the Raman signal, leading to a less pronounced Fano asymmetry. Here, we refer both the thermodynamic temperature of the sample, and the lattice-temperature. Another effect of temperature is that it can change the coupling between the phonon modes and the electronic or vibrational states. In some cases, the coupling strength also depends on the temperature, which can lead to a temperature-dependent

Fano asymmetry. For example, in graphene, the Fano asymmetry of the G-band Raman mode can change with temperature due to changes in the coupling between the phonon mode and the electronic states. Pressure can also affect the Fano asymmetry in Raman spectroscopy. The phonon frequency can vary under pressure due to the compression of the lattice, which can alter the resonance condition for the Raman scattering. In addition, pressure can affect the electronic or vibrational states that couple to the phonon mode, which can influence the Fano asymmetry. For example, in diamond, the Fano asymmetry of the Raman modes can change with pressure due to changes in the electronic structure of the material. Phase transitions can also have a significant role on the Fano interference in Raman spectroscopy. When a material undergoes a phase transition, the lattice structure and phonon modes change, which can alter the coupling between the phonon mode and the electronic or vibrational states. As a result, the Fano asymmetry profile changes across a phase transition. For example, in the perovskite oxide $SrTiO_3$, the Fano asymmetry of the Raman modes changes across the ferroelectric phase transition due to changes in the phonon modes and electronic structure. In chapter 8, we shall specifically discuss the effect of laser-induced local heating on the Fano interference of some lanthanide sesquioxides.

2.8 First principles calculations based on density functional theory (DFT)

Density functional theory (DFT) is a widely used computational method in quantum mechanics that has revolutionized materials science and condensed matter physics. The theory is based on the principle that ***the total energy of a system is a functional of the electron density***.[55,56] The ***electron density is the probability density of finding an electron in a given volume of space***. The theory is called 'density functional' because it is based on the functional relationship between the electron density and the total energy.[55,56] Loosely speaking, a functional means a function of another function. This approach efficiently simplifies an apparently impossible computational problem to a solvable one.

DFT is based on an electronic structure method that can be used to calculate the ground state electronic structure of materials, including atoms, molecules, solids, and surfaces. Given the ***crystallographic information file (CIF)*** of the material, it can also predict distinct properties of the system such as their optimized geometric and electronic structure, optical, mechanical, thermodynamic, vibrational, and magnetic properties. The basic idea behind DFT is that the properties of a system can be determined by solving the many-body ***Schrödinger equation*** for the system's electron density. The transformation of the many-body problem with a lot of Coulomb interactions to a much easier electron density-based problem is schematically shown in Figure 2.12, that empowers the DFT-based first principles techniques.

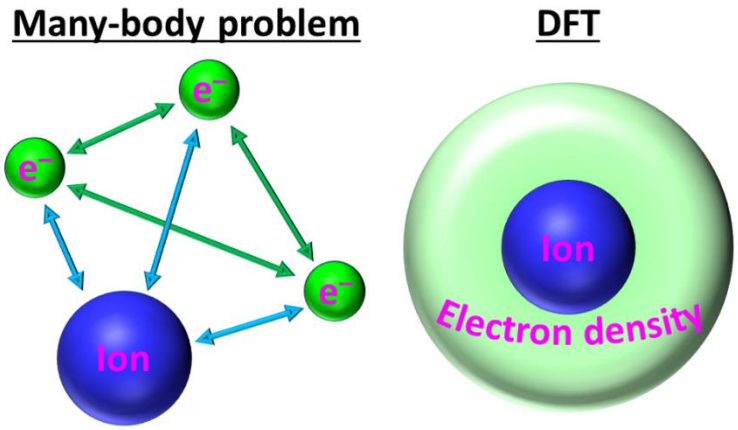

Figure 2.12 The fundamental approach of DFT to replace the individual effects of electrons with an electron density that spreads in three dimensions around the positive ion cores in the lattice.

2.8.1 Hohenberg-Kohn (HK) theorems & Kohn-Sham equations

The two ***Hohenberg-Kohn (HK) theorems*** form the foundation of DFT. ***The 1st HK theorem states that the ground state energy of a system is a unique functional of its electron density.*** On the other hand, the second theorem helps to identify the actual ground state energy. ***The 2nd HK theorem states that the electron density that minimizes the ground state energy is the true ground state density.*** These theorems provide a theoretical framework for the use of the electron density as the fundamental variable in DFT calculations. In practice, the ***Kohn-Sham equations*** are used to solve for the electron density.[55,56] These equations assume that the system under investigation can be described by a set of non-interacting electrons in an effective potential that is derived from the true potential. The Kohn-Sham equations are a set of self-consistent equations that determine the electron density $[\rho_e(\vec{r})]$ and the effective potential $[V_{eff}(\vec{r})]$. The principal mathematical equation is,

$$\hat{H}\psi_i(\vec{r}) = \left(-\frac{h^2}{2m_e}\right)\nabla^2\psi_i(\vec{r}) + V_{eff}(\vec{r})\psi_i(\vec{r}) = \varepsilon_i\psi_i(\vec{r}). \qquad (2.13)$$

Here, $\hat{H}$ is the Hamiltonian, $\psi_i(\vec{r})$ is the i^{th} single-particle wave function, ε_i is the corresponding eigenvalue (*i.e.*, energy), m_e is the electron mass, and h is the Planck constant. The Laplacian operator, ∇^2 represents the sum of the second partial derivatives of a function with respect to its three spatial coordinates, and it is used to describe the curvature or 'bending' of the wavefunction. The effective potential, $V_{eff}(\vec{r})$ is a combination of the external potential of the system (*e.g.*, due to atomic nuclei or external fields) and the ***Hartree potential***, which arises from the interaction between electrons. The Hartree potential is itself a functional of the electron density and is therefore obtained self-consistently by solving the Kohn-Sham equations iteratively until convergence. Later the ***Hartree-Fock approximation*** came with an updated scheme. These equations are solved with a finite number of iterations by adjusting the electron

density until the energy of the system is minimized. Such a self-consistent approach allows the Kohn-Sham equations to account for the complex interactions between electrons and the external potential in a computationally efficient manner.

2.8.2 Different codes and approximations

DFT faces a significant challenge regarding the precise functionals for exchange correlation, except in the case of the free-electron gas. Nonetheless, there are available approximations that enable accurate calculations of specific physical quantities. Among these approximations, the ***local-density approximation (LDA)*** is one of the simplest. In LDA, the exchange-correlation energy is typically separated into two parts: the exchange part and the correlation part. The ***local spin density approximation (LSDA)*** is an extension over the LDA methodology that can conceptually resemble UHF calculations, because it treats differently the electrons based on their spin projections. The LDA assumes uniform density throughout the system, which leads to an underestimation of the exchange energy and an overestimation of the correlation energy. However, the errors resulting from the exchange and correlation components tend to offset each other to some extent. To address this tendency, it is customary to expand the calculations based on the density gradient, which accounts for the non-uniformity of the actual electron density. These expansions are known as ***generalized gradient approximations (GGA)***.[57]

The most common and popular codes used for DFT calculations are ***VASP***, ***Quantum ESPRESSO***, and ***CASTEP***. VASP (Vienna *Ab initio* Simulation Package) is a commercial software package developed by the University of Vienna and is widely used in both academia and industry. CASTEP (Cambridge Sequential Total Energy Package) is another popular commercial software package developed by the University of Cambridge. On the other hand, Quantum ESPRESSO is an open-source and free code appreciated widely all over the world. VASP is based on a plane wave basis set and pseudopotentials. The plane wave basis set allows for the accurate representation of the wavefunctions of the electrons, while the pseudopotentials are used to approximate the core electrons. In our works, mostly the Perdew–Burke-Ernzerhof (PBE) potential is used together with the ***Hubbard U parameter*** in case of transition metal-based materials to account the onsite Coulomb potential. Apart from the ordinary 3D crystal structures, VASP is additionally well-suited for calculations on large systems and for the study of surfaces and interfaces. CASTEP is also based on a plane wave basis set but can use ultrasoft pseudopotentials instead of norm-conserving pseudopotentials. Ultrasoft pseudopotentials allow for a more efficient representation of the electron density and can lead to more accurate results. CASTEP is often used for the study of materials properties such as band structures, density of states, and optical properties. Basically, VASP and CASTEP are two widely used codes

for DFT calculations, each with their own advantages and limitations. In conclusion, DFT is a powerful tool for the study of electronic structure and properties of materials, which has been employed in almost all the works of this thesis to support and interpret experimental findings.

2.8.3 Properties to study

Here are some properties which can be theoretically investigated using DFT codes.

I. Crystallographic Properties:

- ***Lattice Parameters:*** DFT can predict the equilibrium lattice parameters, which are the lengths and angles defining the crystal structure of a material. These values can be obtained by minimizing the total energy of the system.
- ***Elastic Constants:*** DFT can calculate the elastic constants of a material, which describe its mechanical response to external stress or strain. These constants are essential for understanding material stability, deformation, and mechanical properties.

II. Electronic Properties:

- ***Band Structure:*** DFT can determine the electronic band structure of a material, which provides information about the energy levels and allowed electronic transitions. It helps to understand electrical conductivity, optical properties, and other electronic phenomena.
- ***Density of States (DOS):*** DFT allows the calculation of the electronic density of states, which describes the distribution of electronic states with respect to energy. The DOS helps to determine electronic properties like electrical conductivity, heat capacity, and magnetic behavior.

III. Thermodynamic Properties:

- ***Formation Energy:*** DFT can calculate the formation energy of materials, which provides insights into their thermodynamic stability and relative ease of formation. Similarly the formation energy of defects such as oxygen vacancies can be calculated from the energy of the pristine unit cell, defect-incorporated cell and chemical potential of the atom.
- ***Phase Diagrams:*** By comparing the total energies of different crystal structures and compositions, DFT can construct phase diagrams, which depict the stable phases of a material as a function of temperature, pressure, and composition.

IV. Magnetic Properties:

- ***Magnetic Moments:*** DFT can predict the magnetic moments associated with atoms or ions in a material. It provides information on the magnetic ordering and behavior, such as ferromagnetism, antiferromagnetism, or paramagnetism.
- ***Magnetic Anisotropy:*** DFT can calculate the magnetic anisotropy energy, which describes the dependence of magnetization on the orientation of the magnetic moments. It helps in understanding the stability of magnetization directions and magnetic storage devices.

V. Optical Properties:

- ***Dielectric Function:*** DFT can determine the dielectric function of a material, which describes its response to electromagnetic radiation. It provides information on optical properties such as absorption, reflection, refraction, energy loss spectrum, as well as energy band gaps.
- ***Refractive Index:*** By analyzing the dielectric function, DFT can predict the refractive index of a material, which governs the speed of light propagation and its interaction with the material.

These are just a few examples of the properties that can be explored theoretically using DFT in materials science. The accuracy and predictive power of DFT depend on various factors, including the choice of exchange-correlation functional and the treatment of electron-electron interactions. Nonetheless, DFT has proven to be a valuable tool for understanding and designing materials with tailored properties.

2.9 Motivation

The detailed discussion on the fundamental concepts and relevant background theories associated with electrical and vibrational properties of nanomaterials clearly indicate how rich physics is still buried deep. Also, the review of the already published papers reveals the importance and cutting-edge technological applications across different industries. So far, I also found some technologically sound nanomaterials like ferrous, ferric, and ferrosoferric oxides, PVDF, alkaline earth metal titanates, lanthanide oxides, potassium niobate, *etc*. These materials are interesting as well as lead-free. Hence, through this thesis, I have tried to add another small, but noteworthy pebble in the Everest of physical knowledge gained by the humankind.

References

1. S. S. Aplesnin, L. V. Udod, M. N. Sitnikov and O. B. Romanova, *Ceram. Int.*, 2021, **47**, 1704-1711.
2. M. Pollak, *Discuss. Faraday Soc.*, 1970, **50**, 13-19.
3. V. V. e. Schmidt, V. V. Schmidt, P. Müller and A. V. Ustinov, *The physics of superconductors: Introduction to fundamentals and applications*, Springer Science & Business Media, 1997.
4. P. B. Allen, F. D. Bedard, D. Belitz, J. E. Crow, R. A. Ferrell, J. W. Lynn, N. Ong, A. Santoro, R. N. Shelton and C. S. Wang, *High temperature superconductivity*, Springer Science & Business Media, 1990.
5. B. H. Brandow, *Adv. Phys.*, 1977, **26**, 651-808.
6. J. Singleton, *Band theory and electronic properties of solids*, Oxford University Press, 2001.

7. K. Zhou, S. A. Boggs, R. Ramprasad, M. Aindow, C. Erkey and S. P. Alpay, *Appl. Phys. Lett.*, 2008, **93**, 102908.
8. G. M. Sessler, *J. Electrost.*, 2001, **51**, 137-145.
9. R. W. Whatmore, *Rep. Prog. Phys.*, 1986, **49**, 1335.
10. D. Champier, *Energy Convers. Manag.*, 2017, **140**, 167-181.
11. D. Damjanovic and R. E. Newnham, *J. Intell. Mater. Syst.*, 1992, **3**, 190-208.
12. V. Fridkin and S. Ducharme, *Ferroelectrics*, 2014, **466**, 133-144.
13. Y. Ishibashi and Y. Takagi, *J. Phys. Soc. Jpn.*, 1971, **31**, 506-510.
14. M. Bibes and A. Barthélémy, *Nature Mater.*, 2008, **7**, 425-426.
15. L. E. Cross, *Ferroelectrics*, 1987, **76**, 241-267.
16. G. Xu, Z. Zhong, Y. Bing, Z. G. Ye and G. Shirane, *Nature Mater.*, 2006, **5**, 134-140.
17. K. M. Rabe, *Functional metal oxides: new science and novel applications*, 2013, 221-244.
18. W. C. Guest, N. R. Cashman and S. S. Plotkin, *Phys. Chem. Chem. Phys.*, 2011, **13**, 6286-6295.
19. M. Schadt, *J. Chem. Phys.*, 1972, **56**, 1494-1497.
20. M. Nakanishi, *Int. J. Spectrosc.*, 2014, **2014**.
21. Y. W. Hong and J. H. Kim, *Ceram. Int.*, 2004, **30**, 1307-1311.
22. D. P. Almond and A. R. West, *Solid State Ion.*, 1983, **11**, 57-64.
23. M. Samet, V. Levchenko, G. Boiteux, G. Seytre, A. Kallel and A. Serghei, *J. Chem. Phys.*, 2015, **142**, 194703.
24. T. Prodromakis and C. Papavassiliou, *Appl. Surf. Sci.*, 2009, **255**, 6989-6994.
25. R. M. Neagu, E. Neagu, A. Kyritsis and P. Pissis, *J. Phys. D: Appl. Phys.*, 2000, **33**, 1921.
26. G. N. Greaves, *J. Non-Cryst. Solids*, 1973, **11**, 427-446.
27. S. Singh, P. A. Jha, S. Varma and P. Singh, *J. Alloys Compd.*, 2017, **704**, 707-716.
28. P. Q. Mantas, *J. Eur. Ceram.*, 1999, **19**, 2079-2086.
29. K. S. Cole, *J. Chem. PIIys.*, 1941, **9**, 341-351.
30. A. S. Volkov, G. D. Koposov, R. O. Perfil'ev and A. V. Tyagunin, *Opt. Spectrosc.*, 2018, **124**, 202-205.
31. A. K. Jonscher, *Colloid Polym. Sci.*, 1975, **253**, 231-250.
32. M. Hoffmann, P. V. Ravindran and A. I. Khan, *Materials*, 2019, **12**, 3743.
33. M. Hoffmann, M. Pešić, S. Slesazeck, U. Schroeder and T. Mikolajick, *Nanoscale*, 2018, **10**, 10891-10899.
34. M. Hoffmann, A. I. Khan, C. Serrao, Z. Lu, S. Salahuddin, M. Pešić, S. Slesazeck, U. Schroeder and T. Mikolajick, *J. Appl. Phys.*, 2018, **123**, 184101.
35. A. G. Boni, R. Patru, L. D. Filip, C. Chirila, I. Pasuk, I. Pintilie and L. Pintilie, *ACS Appl. Energy Mater.*, 2022, **5**, 3307-3318.

36. I. Mora-Seró, J. Bisquert, F. Fabregat-Santiago, G. Garcia-Belmonte, G. Zoppi, K. Durose, Y. Proskuryakov, I. Oja, A. Belaidi and T. Dittrich, *Nano Lett.*, 2006, **6**, 640-650.
37. D. Korucu, Ş. Altindal, T. S. Mammadov and S. Özçelik, *J. Optoelectron. Adv. Mater.*, 2009, **11**, 192-196.
38. J. Panigrahi, R. Singh, N. Batra, J. Gope, M. Sharma, P. Pathi, S. K. Srivastava, C. M. S. Rauthan and P. K. Singh, *Sol. Energy*, 2016, **136**, 412-420.
39. M. Hoffmann, S. Slesazeck, U. Schroeder and T. Mikolajick, *Nature Electron.*, 2020, **3**, 504-506.
40. M. Hoffmann, F. P. G. Fengler, B. Max, U. Schroeder, S. Slesazeck and T. Mikolajick, *Adv. Energy Mater.*, 2019, **9**, 1901154.
41. J. S. Harrison, Z. Ounaies and D. M. Bushnell, 2001.
42. R. Gregorio and E. M. Ueno, *J. Mater. Sci.*, 1999, **34**, 4489-4500.
43. M. Naebe, T. Lin and X. Wang, *Nanofibers*, 2010, **11**, 8160.
44. A. H. Franzan, N. F. Leite and L. C. M. Miranda, *Appl. Phys. A*, 1990, **50**, 431-438.
45. J. Guo, M. Nie and Q. Wang, *ACS Sustain. Chem. Eng.*, 2020, **9**, 499-509.
46. A. Glamazda, K. Y. Choi, P. Lemmens, D. Wulferding, S. Park and S. W. Cheong, *Phys. Rev. B*, 2013, **87**, 144416.
47. F. Bussolotti, J. Yang, T. Yamaguchi, K. Yonezawa, K. Sato, M. Matsunami, K. Tanaka, Y. Nakayama, H. Ishii and N. Ueno, *Nature Commun.*, 2017, **8**, 173.
48. S. Satpathy, A. Roy and A. Mohapatra, *Eur. J. Phys.*, 2012, **33**, 863.
49. S. Bar-Ad, P. Kner, M. V. Marquezini, S. Mukamel and D. S. Chemla, *Phys. Rev. Lett.*, 1997, **78**, 1363.
50. K. Roodenko, I. A. Goldthorpe, P. C. McIntyre and Y. J. Chabal, *Phys. Rev. B*, 2010, **82**, 115210.
51. P. Y. Yu, M. Cardona, P. Y. Yu and M. Cardona, *Fundamentals of Semiconductors: Physics and Materials Properties*, 2010, 107-158.
52. A. S. Alexandrov and J. T. Devreese, *Advances in polaron physics*, Springer, 2010.
53. D. Marrocchelli, P. Postorino, D. Di Castro, E. Arcangeletti, P. Dore, M. C. Guidi, S. Ray and D. D. Sarma, *Phys. Rev. B*, 2007, **76**, 172405.
54. W. Qi, C. Xie, A. Hushur and S. Kojima, *Appl. Phys. Lett.*, 2023, **122**.
55. R. G. Parr, *Annu. Rev. Phys. Chem.*, 1983, **34**, 631-656.
56. E. Engel, *Density functional theory*, Springer, 2011.
57. J. P. Perdew, K. Burke and M. Ernzerhof, *Phys. Rev. Lett.*, 1996, **77**, 3865.

3 EXPERIMENTAL TECHNIQUES AND INSTRUMENTATION

Here, in this chapter, some common experimental methods and spectroscopic techniques are discussed, that have been adopted for different works elaborated in chapters 4 to 9. Also, a brief description of the as-used instruments and their specifications are stated.

3.1 Synthesis and fabrication-related equipment

3.1.1 Muffle furnace

A muffle furnace is a high-current system used for high-temperature applications that require controlled heating and insulation. It is named after the refractory material, called the muffle, that surrounds the heating element and prevents direct contact between the material being heated and the flame or electric heating element. This ensures that the material being heated is exposed only to the desired temperature and not to any potentially damaging gases or by-products of combustion.

Figure 3.1 Digital photograph of (a) heating system and (b) control unit of the alumina box-furnace (maximum temperature: 1000 ℃).

Muffle furnaces are commonly used in industries such as materials science, ceramics, metallurgy, and pharmaceuticals. They are often used for processes such as sintering, calcining, annealing, and heat treating, among others. Their operational temperature can be as high as 1800 ℃, depending on the design and construction of the furnace. They are available in various sizes and configurations, from bench-top models to larger industrial-sized furnaces. Our locally manufactured muffle furnaces are equipped with advanced features such as digital temperature control, programmable settings, and safety features that prevent overheating or overloading. This makes them more convenient and safer to use, while also providing more precise control over the heating process. It provides a controlled environment for heating materials, allowing for precise and consistent results. In our lab, we use both alumina box-furnace and quartz tube-furnace with open air heating system and gas purging arrangement, respectively. The maximum operational temperature of the instruments present in our lab varies between 900 – 1400 ℃. One commonly used programmable blue box-furnace is shown in Figure 3.1.

3.1.2 Hot-air oven and vacuum oven

A hot-air oven is a device that is commonly used for sterilization, drying, and curing of various materials, including glassware, metal equipment, and laboratory samples. The oven operates by heating the air inside the chamber to a set temperature, which then transfers heat to the materials being processed. Hot-air ovens are often used in scientific research, medical laboratories, and manufacturing processes.

Figure 3.2 Digital photograph of a hot-air oven (maximum temperature: 180 ℃).

The temperature of a hot-air oven can range from 50 °C to 300 °C, and it is generally controlled by a thermostat or a digital controller. Hot-air ovens are available in different sizes and capacities, and they can be made of different materials such as stainless steel, aluminium, or galvanized steel. In our lab, we have multiple hot-air ovens with distinct maximum temperatures and heating rates. These are principally used for hydrothermal and solvothermal reactions inside a Teflon-lined stainless-steel autoclave. One commonly used oven is displayed in Figure 3.2.

A vacuum oven is a type of drying oven that operates under reduced air-pressure to remove moisture and other volatile compounds from materials. The oven creates a rough vacuum environment by removing the air inside the chamber using a vacuum pump (oil rotary pump in our case). This allows for faster and more efficient drying, as the lower pressure helps to remove moisture from materials at a lower temperature. Vacuum ovens are commonly used in the laboratory for drying and curing of heat-sensitive materials such as powders, electronics, and polymers. The temperature of a vacuum oven can range from room temperature to ~220°C, and it is controlled by a thermostat or a digital controller. Vacuum ovens are available in different sizes and capacities, and they can be made of different materials such as stainless steel or aluminium. and one vacuum oven. The vacuum oven of our lab is shown in Figure 3.3.

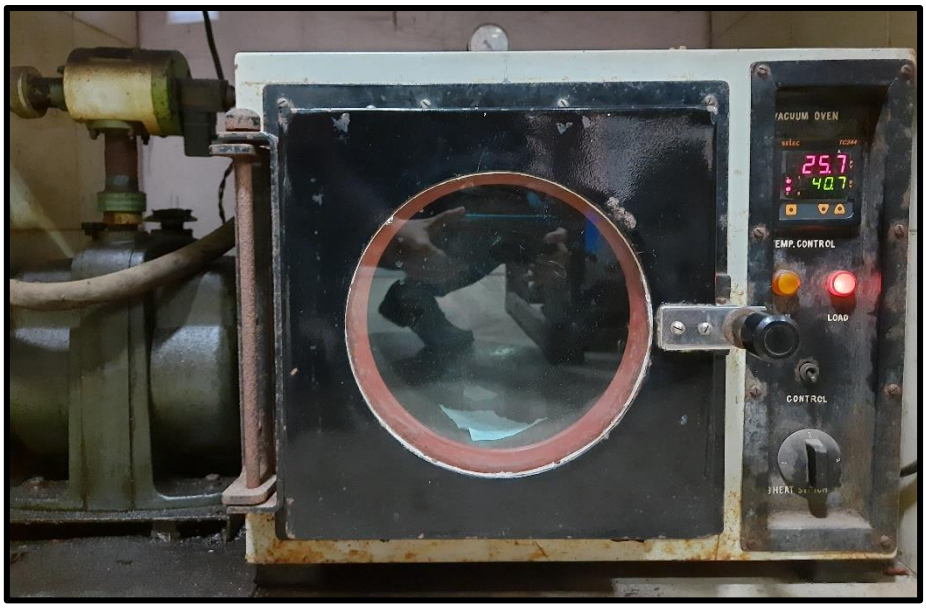

Figure 3.3 Digital photograph of the vacuum oven (maximum temperature: 120 °C).

3.1.3 Microwave synthesis reactor

A microwave synthesis reactor is a device used for chemical synthesis that employs microwave energy to heat the reaction mixture quickly and uniformly. Microwave synthesis has become an attractive technique in the field of synthetic chemistry due to its numerous advantages, such as shorter reaction times, higher yields, and the ability to perform reactions

under solvent-free conditions. This makes it an efficient alternative of the conventional hydrothermal or solvothermal reactions. In our lab, we have the Monowave 200 Model by Anton Paar, see Figure 3.4.

Figure 3.4 Digital photograph of the Monowave 200 microwave synthesis reactor from Anton Paar.

The Monowave 200 is a high-performance microwave synthesis reactor that is designed for efficient and precise synthesis of organic and inorganic compounds. The reactor is equipped with a temperature and pressure monitoring system that allows for accurate control of reaction conditions. The Monowave 200 can operate at temperatures up to 300°C and pressures up to 30 bars, making it suitable for a wide range of chemical reactions. The Monowave 200 features a compact design that includes a touchscreen interface for easy operation and monitoring of the reaction progress. The reactor is equipped with a reaction vessel made of high-quality materials such as Teflon or quartz, which ensures excellent chemical resistance and durability. Additionally, it has a built-in cooling system and compressor that allows for efficient cooling of the reaction mixture after the reaction is complete.

3.1.4 Magnetic stirrer cum heater

Magnetic stirrer cum heater, also known as a hot plate magnetic stirrer, is a laboratory device that is used for stirring and heating liquids or solutions, see Figure 3.5. The device consists of a flat plate that is made of a heat-resistant material such as aluminium or ceramic and is heated by an embedded heating element. A magnetic stir bar is placed in the liquid to be stirred, which is then rotated by a magnetic field generated by a rotating magnet located beneath the plate. The combination of magnetic stirring and heating provides several

advantages over traditional heating methods such as a Bunsen burner or a hot-air oven. Magnetic stirring ensures homogeneous mixing of the liquid or solution, which leads to a more uniform heating profile. Moreover, the heating temperature can be precisely controlled and adjusted based on the needs of the experiment, providing better reproducibility of results.

Figure 3.5 Digital photograph of the hot plate magnetic stirrer.

Magnetic stirrer cum heater is used in various scientific applications, such as in chemical synthesis, biological assays, and microbiology. It is particularly useful for preparing and heating solutions that require continuous stirring, such as solutions that contain solid particles or are prone to sedimentation. The device is also useful in applications that require accurate temperature control, such as enzymatic reactions, DNA denaturation, and protein unfolding studies. In our lab, it is used to mix the precursors within a suitable organic or inorganic solvent before hydrothermal, solvothermal, hot-injection or other wet chemical synthesis techniques.

3.1.5 Ultrasonic bath

An ultrasonicator or ultrasonic cleaning bath is a laboratory instrument that uses high-frequency sound waves to break down and disperse particles in a liquid. This process is known as ultrasonication, and it is a common technique used in various scientific fields, such as chemistry, biology, and material science. Ultrasonication works by creating high-frequency pressure waves in a liquid sample. These waves create tiny bubbles in the liquid, which then rapidly collapse, generating high levels of energy that can break apart particles in the liquid. The energy generated by ultrasonication can be adjusted by controlling the frequency and intensity of the sound waves, making it a versatile technique that can be used for a wide range of applications. One common application of ultrasonication is in the preparation of emulsions, where it is used to disperse and stabilize immiscible liquids. Ultrasonication can also be used to

break apart cells or other biological materials, making it a useful tool in fields such as cell biology and biotechnology. In material science, ultrasonication is used to disperse nanoparticles and improve the properties of materials. Thus, it is a powerful tool for the dispersion and processing of particles in liquids. Its versatility, ease of use, and its ability to generate high levels of energy without the need for harsh chemicals or high temperatures makes it an attractive alternative to other processing methods. The ultrasonicator used in our lab also accompanies heating facility, see Figure 3.6. For an even more powerful, ultrasonication, a probe-sonicator is used.

Figure 3.6 Digital photograph of the ultrasonic bath.

3.1.6 Centrifuge machine

A centrifuge machine is a laboratory instrument that separates particles in a liquid based on their density using the principle of centrifugal force. The machine spins the sample at high speeds, generating a force that causes the denser particles to move to the bottom of the sample tube. This helps to isolate specific components of a sample, such as proteins, DNA, or cells, for further study. In our lab, it is generally used to separate powder samples (nanoparticles) from the solvents and/or by-product solutions after synthesis and to wash the samples using de-ionized water, ethanol or acetone.

We have the SIGMA ANALYTICA 3-18KS model in our lab, see Figure 3.7. This high-speed centrifuge is designed for a wide range of applications in research, clinical, and industrial settings. The machine has a maximum speed of 12000 revolutions per minute (rpm) and can generate a maximum centrifugal force as high as $35000 \times g$. It also features a user-friendly interface with a touch screen display and intuitive controls. The machine has a built-in rotor recognition system that automatically detects the rotor and sets the appropriate speed and time

for the program. It has a variety of rotors available, including fixed-angle and swing-out rotors, allowing for flexibility in the types of samples that can be processed.

Figure 3.7 Digital photograph of the SIGMA centrifuge machine with built-in cooling facility.

3.1.7 Pelletizer

Pelletizers are used to compress powdered or granulated materials into pellets of uniform size and density. The process of pelletizing improves the compressive strength, durability, flowability, handling, and storage properties of the material, making it easier to use and process. The BDS Analytical standard pelletizer is a precision instrument designed for producing high-quality pellets with a uniform size and density, see Figure 3.8. The specifications of the BDS Analytical standard pelletizer are as follows:

- Maximum pressure: 20 tons
- Maximum diameter of pellets: 40 mm
- Pellet thickness: 1 to 20 mm
- Adjustable pellet height and diameter
- Customizable pressure and dwell time
- Compact and easy-to-use design

3.1.8 Spin-coater

Spin-coating is a commonly used technique in the field of material science and nanotechnology to deposit thin films onto a substrate. It involves spinning a liquid solution or suspension onto a substrate, which is then centrifuged to spread the solution evenly over the substrate's surface. The resulting thin film is then dried and annealed to create a solid film of uniform thickness. In our lab, we have the Apex Spin NXG-P1 spin-coater designed for precise and uniform thin film deposition, see Figure 3.9. It has a compact and easy-to-use design, making it suitable for use in research laboratories and small-scale production environments. To grab the substrate, suction using a small oil-free pump is used. The specifications of the Apex Spin NXG-P1 model are as follows:

Figure 3.8 Digital photograph of the BDS Analytical standard pelletizer.

Figure 3.9 Digital photograph of the Apex Spin NXG-P1 spin-coating unit.

- Maximum spin speed: 12000 rpm
- Maximum substrate size: 4 inches in diameter
- Programmable spin time: 1 – 999 s
- Programmable spin speed: 500 – 12000 rpm
- Digital display for spin speed and time
- Compatible with a wide range of solvents and solutions
- Compact and portable design
- Adjustable tilt angle for coating optimization

3.1.9 Thermal evaporation-based vacuum coating unit

Thermal evaporation is a commonly used, fast, and convenient physical vapor deposition (PVD) method for depositing uniform thin films of simple materials with precise melting and boiling points, such as metals, basic inorganic, and hybrid compounds. This method employs a resistive heat source to evaporate a solid material at high temperatures in high or ultra-high vacuum conditions, producing the required vapor pressure to coat the substrate. In our laboratory, we utilize the thermal evaporation technique using a HIND HIVAC (India) make vacuum coating unit (model: 12A4D) to deposit low boiling point metals (2200 – 2800 ℃), such as Al, Cu, Ag, Au, and simple compounds like copper (II) phthalocyanine onto various substrates, including glass, ITO/FTO-coated glass, Si, *etc*. We use one diffusion pump to evacuate the coating chamber (bell jar) to reach pressures up to 10^{-6} mbar with the aid of a primary rotary oil pump in backing mode. Pressure measurements are carried out using a Pirani and a penning gauge to read pressures as low as 10^{-3} and 10^{-6} mbar, respectively. We employ a tungsten basket or a molybdenum boat, which can withstand up to 200 A (DC), as the high resistance and high melting point holder to carry and heat up the source material. To prevent overheating, an external pump-chiller setup is used to circulate cold water in a closed cycle through the water-cooling coils incorporated in the vacuum chamber and the oil diffusion pump body. A quartz crystal oscillator circuit is used to digitally monitor the nanoscale thickness of the deposited film, which involves measuring the shift in resonant frequencies.

The thermal evaporator is a simple device based on the Joule heating principle, which enables the evaporation of low-boiling-point metals or non-metals, see Figure 3.10. This is achieved by placing the source material on a high-resistance and high-melting-point (~3000 ℃) metallic (*e.g*., W, Ta, Mo) or ceramic holder, under high-vacuum conditions to avoid oxidation of the generated vapour. The high melting point of the holder ensures that it reaches a temperature that completely evaporates the source material at a prescribed DC-intake. The vapour then moves upward, cools down and condenses onto a substrate. To ensure uniform deposition, the substrate is rotated slowly throughout the process. In some cases, the substrate may also be mildly heated to influence the nature and morphology of the deposited film. The thickness of the deposited film is measured using a quartz oscillator and the current is slowly tuned off once the desired thickness is achieved.

Figure 3.10 Digital photograph of the HIND HIVAC make thermal evaporation-based vacuum coating unit (model: 12A4D).

The thermal evaporation technique is limited in cases where the material to be deposited has a high boiling point, as there may be no feasible metal to work as the filament without melting at such high temperatures. In such cases, the electron-beam deposition technique is used, where a highly focused stream of high kinetic energy (~15 keV) electrons is imposed at a small patch of the target material. This portion is heated locally to a very high temperature and evaporates. The rest of the principle is similar to that of thermal evaporation. This technique can deposit almost any metal, regardless of its boiling point.

Thermal evaporation is commonly used to fabricate metallic contacts with nanoscopic attachments to the host material. It is useful for all sorts of electrical measurements and characterization of thin films, analysis of circuits or devices, especially where silver paint is difficult to apply. Vacuum coating technology is used to produce metallized paper, plastic film, and all-metal thin foils for packaging applications that largely employ substrates like PET or oriented polypropylene (OPP). Sometimes, beautiful patterns of uniform nanostructures are

generated by employing proper masking. For capacitor prefabrication, the substrate is typically used as a dielectric and the coating as an electrode. To achieve high capacitance, the distance between the electrodes needs to be very small, which is obtainable by a coating on thinner substrates. Co-deposition of multiple components is also possible by controlling the temperature of the crucible. Thermal evaporation is commonly applied to deposit metallic contact layers in multilayer thin-film devices such as OLEDs, solar cells, and MOSFETs. In fact, it has largely dominated commercial production of organic photodetectors, making it a well-known and widely adopted technology in organic optoelectronics. In addition to metallic films, charge extraction layers, transparent barrier coatings, and exciton blocking layers (EBLs) can also be evaporated, including small molecules, oxides, and salts like fluorides and carbonates. In some cases, thermal evaporation is used to produce specific polymeric coatings. Polymeric films such as PTFE and nylon in metal-polymer nanocomposite films have been successfully grown. However, this method has limitations, as it involves resistive heating of polymers, and most polymers have low thermal conductivity.

3.2 Crystallographic study

3.2.1 Powder X-ray diffraction (XRD)

Powder X-ray diffraction (XRD) is a widely used analytical technique for characterizing the crystal structure, crystallinity, and preferred orientation of powders and thin films. It works by illuminating a powder sample with a beam of X-rays, and then measuring the diffraction pattern created by the interactions of the X-rays with the electrons in the crystal lattice of the sample. The diffraction occurs because interplanar spacing or lattice constant of a typical crystal lattice is of the order of angstroms, that matches with the wavelength of the as-used X-rays.

The basic principle of XRD is based on the diffraction of X-rays by a crystal, which is governed by Bragg's Law,

$$2d_{hkl} \sin\theta = n\lambda, \tag{3.1}$$

where, n is the order of diffraction ($n = 1$ for first-order diffraction), λ is the wavelength of the X-ray beam, d_{hkl} is the distance between the consecutive Bragg (hkl) planes in the crystal lattice that are responsible for the diffraction, and 2θ is the angle between the incident and diffracted beams. Powder XRD is a non-destructive and sensitive technique, which can be used to analyse a wide range of materials, including metals, ceramics, nanoparticles, polymers, and biomaterials. It is particularly useful for identifying the phases present in a sample, determining the crystallinity and preferred orientation especially in case of single crystals or thin films, and measuring the lattice parameters (such as unit cell dimensions and angles) of the crystal structure.

In our lab, we have a Rigaku MiniFlex 600 powder X-ray diffractometer, see Figure 3.11. It is a benchtop mini-system that is widely used for qualitative and quantitative analysis of samples at room temperature. It operates with $40\ \text{kV} - 15\ \text{mA}$ constant power supply and draws 600 W electric power. A water chiller is used to regulate the temperature around $20 - 22\ ℃$ during data acquisition. The instrument features a rotating anode X-ray source (Cu-K_α line, $\lambda = 1.54059$ Å) and a high-resolution detector. It is capable of measuring powders and thin films over a wide range of 2θ angles ($3° - 90°$). It also features a user-friendly software, which allows for easy data acquisition and analysis. After recording a full range XRD data, it can be matched with the powder diffraction files (PDFs) available in the database of International Centre for Diffraction Data (ICDD) to identify the phase. Moreover, Scherrer's equation and Williamson-Hall analysis can be conducted to calculate the crystallite size or micro-strain of the nanoparticles. More on this can be found in the successive chapters. Overall, powder X-ray diffraction is a widely used analytical technique that provides valuable information on the crystal structure, crystallinity, purity of phase, crystallite-size, micro-strain, and preferred orientation of powders and thin films.

Figure 3.11 Digital photograph of the Rigaku MiniFlex 600 powder X-ray diffractometer.

3.2.2 Rietveld refinement

The Rietveld refinement method is a powerful tool in the field of crystallography, used to extract structural information from powder X-ray diffraction (PXRD) data. The method is based on a least-squares refinement of the crystal structure, where the calculated X-ray diffraction pattern is compared to the experimental one and the structural and instrumental

parameters are refined simultaneously to give the best agreement between the calculated and experimental pattern. Rietveld refinement can provide accurate lattice parameters, and can also detect the presence of small amounts of impurities and minor phases in a sample. It was developed by Hugo Rietveld in the 1960s and 70s, and has since become a standard method in the analysis of powder diffraction data.

The method involves the fitting of a structural model to the experimental diffraction pattern, optimizing a set of adjustable parameters to minimize the difference between the calculated and observed diffraction intensities. These parameters include the crystal structure parameters (unit cell dimensions, atomic positions, thermal parameters), the instrument parameters (wavelength, zero shift, peak shape), and the background parameters (linear or polynomial coefficients). The Rietveld's method is based on the full profile analysis, which means that it takes into account the entire diffraction pattern, including peak widths and shapes. The calculated intensity of each reflection is given by the sum of the intensity contributions from all atoms in the crystal structure, convoluted with the instrument function and the background function,

$$I(hkl) = K \sum j\left[P_j(hkl)F_j(hkl)B(hkl)\right]V, \tag{3.2}$$

where, $I(hkl)$ is the observed intensity of the reflection with Miller indices (hkl), K is a scaling factor, $P_j(hkl)$ is the profile function of the j^{th} atom, $F_j(hkl)$ is the structure factor, $B(hkl)$ is the background function, and V is the unit cell volume. The structure factor describes the scattering amplitude of the j^{th} atom at the position $\vec{r}_j$ in the crystal lattice. The profile function describes the shape of the diffraction peak, which depends on the crystal size, strain, and microstructure. The most commonly used profile function is the pseudo-Voigt function, which is a combination of Gaussian and Lorentzian functions:

$$P_j(hkl) = (1-\eta)G_j(hkl) + \eta L_j(hkl), \tag{3.3}$$

where, η is the mixing parameter, $G_j(hkl)$ is the Gaussian function, and $L_j(hkl)$ is the Lorentzian function.

The background function describes the non-diffracting signal, which includes contributions from incoherent scattering, fluorescence, and air scattering. It is usually modelled by a linear or polynomial function, which is fitted to the low-angle region of the diffraction pattern. The Rietveld refinement involves the minimization of the difference between the calculated and observed intensities, using a least-squares fitting procedure. The quality of the fit is assessed by several parameters, including the R-factor, the goodness-of-fit (GOF) parameter or χ^2, and the weighted profile R-factor. More details on the relevant formulae and their acceptable values are illustrated in the coming chapters, where Rietveld's method is used for crystallographic analysis of different synthesized powder samples (nanoparticles).

The Rietveld refinement has a wide range of applications in materials science, solid-state chemistry, and mineralogy, including the determination of crystal structures, phase quantification, and microstructural analysis. It can also be used to study the thermal and dynamic properties of materials, by analysing the changes in the crystal structure parameters as a function of temperature or pressure. The method is particularly useful for the analysis of complex multiphase samples, where several phases may overlap in the diffraction pattern. By fitting a structural model to the entire pattern, the Rietveld method can separate the contributions from each phase, and determine their respective phase fractions. This is known as quantitative phase analysis, and is often used in the analysis of geological and cementitious materials. The Rietveld method is also used in the determination of crystallographic disorder, such as the occupancy of a mixed site or the positional disorder of an atom. In such cases, the Rietveld refinement can provide insights into the local structure of the material, and the degree of order or disorder in the crystal lattice.

The Rietveld refinement method can be implemented using various software packages, with the Fullprof Suite (used in all the works discussed in this thesis) being one of the most popular.[1] Fullprof is a comprehensive software package for the analysis of PXRD data, developed by Juan Rodriguez-Carvajal in the 1990s. It includes modules for data reduction, structure solution, Rietveld refinement, and visualization of results. The Rietveld refinement module in Fullprof allows for the simultaneous refinement of multiple data sets, multiple crystal structures, and multiple phases. It includes options for the refinement of various parameters, such as cell parameters, atomic positions, thermal parameters, and peak shape parameters. It also includes several features for the analysis of the refinement results, including the calculation of various R-factors and χ^2; which can further be enhanced with artificial intelligence (AI).[2]

3.3 Spectroscopic investigation

Spectroscopy is the study of the interaction between light and matter. It involves the measurement and analysis of the electromagnetic radiation emitted, absorbed, or scattered by a sample, to provide information about its physical, chemical, or biological properties. Spectroscopy is used in a wide range of scientific fields, including chemistry, physics, biology, medicine, and materials science. The basic principle of spectroscopy is that different materials interact with light in different ways, depending on their chemical and physical properties. When a sample is illuminated with light, it can absorb, transmit, reflect, or scatter the light, depending on the wavelength and energy of the light and the properties of the sample. Different types of spectroscopies are based on different types of interactions between light and matter. The following subsections elaborate some useful spectroscopic techniques, that have been employed to probe the characteristics of distinct samples of this thesis.

3.3.1 X-ray photoelectron spectroscopy (XPS)

X-ray photoelectron spectroscopy (XPS), also known as electron spectroscopy for chemical analysis (ESCA), is a surface analysis technique that provides valuable information on the chemical and electronic state of the surface of a material. XPS measures the kinetic energy of photoelectrons emitted from the surface of a sample when irradiated with X-rays, which can be used to determine the chemical composition and electronic state of the surface. The kinetic energy of an electron emitted from a surface in XPS is given by the following formula,

$$E_K = h\nu - E_B - \Phi, \tag{3.4}$$

where, E_K is the kinetic energy of the electron, $h\nu$ is the energy of the incident photon, E_B is the binding energy of the electron to the atom, and Φ is the work function of the material.

The penetration depth of X-rays in XPS depends on the energy of the incident photons and the composition of the material being analysed. In general, X-rays used in XPS have energies ranging from a few hundred to a few thousand eV. The penetration depth of X-rays in XPS is typically on the order of a few nanometres to a few tens of nanometres. This means that X-rays can only penetrate the outermost few layers of atoms on the surface of a material, providing information about the surface composition and electronic structure. The penetration depth of X-rays in XPS can be increased by using higher-energy photons, but this can also cause damage to the material being analysed. In addition, the high-energy photons can also excite electrons in deeper layers of the material, leading to spectral contributions from deeper layers that can complicate the analysis. Therefore, XPS is best suited for the analysis of surface layers of materials and is not well-suited for the analysis of bulk materials or buried interfaces. Other techniques, such as Auger electron spectroscopy (AES) and X-ray absorption spectroscopy (XAS), can be used to probe deeper layers in materials. Additionally, satellite peaks can arise in photoelectron spectra, that often supplies important information regarding the multiplet structure of transition metals or heavy atoms.

In our lab, we use the SPECS HSA 3500 model (see Figure 3.12), which is a high-performance XPS system that uses a monochromatic Al-K_α X-ray source to provide high-energy photons for photoelectron excitation. It operates with $10\ kV - 15\ mA$ regulated power supply at ultra-high vacuum (UHV) conditions ($\leq 10^{-10}$ mbar). The system is equipped with a hemispherical analyser that can detect photoelectrons with high resolution and sensitivity. The system also includes a sample holder that can accommodate multiple samples and allows for automated sample exchange. The SPECS HSA 3500 model is capable of performing XPS measurements with high accuracy and precision, making it a valuable tool for surface analysis in a variety of fields, including materials science, chemistry, and physics. The system can be used to study a wide range of materials, including metals, semiconductors, polymers, and biomolecules.

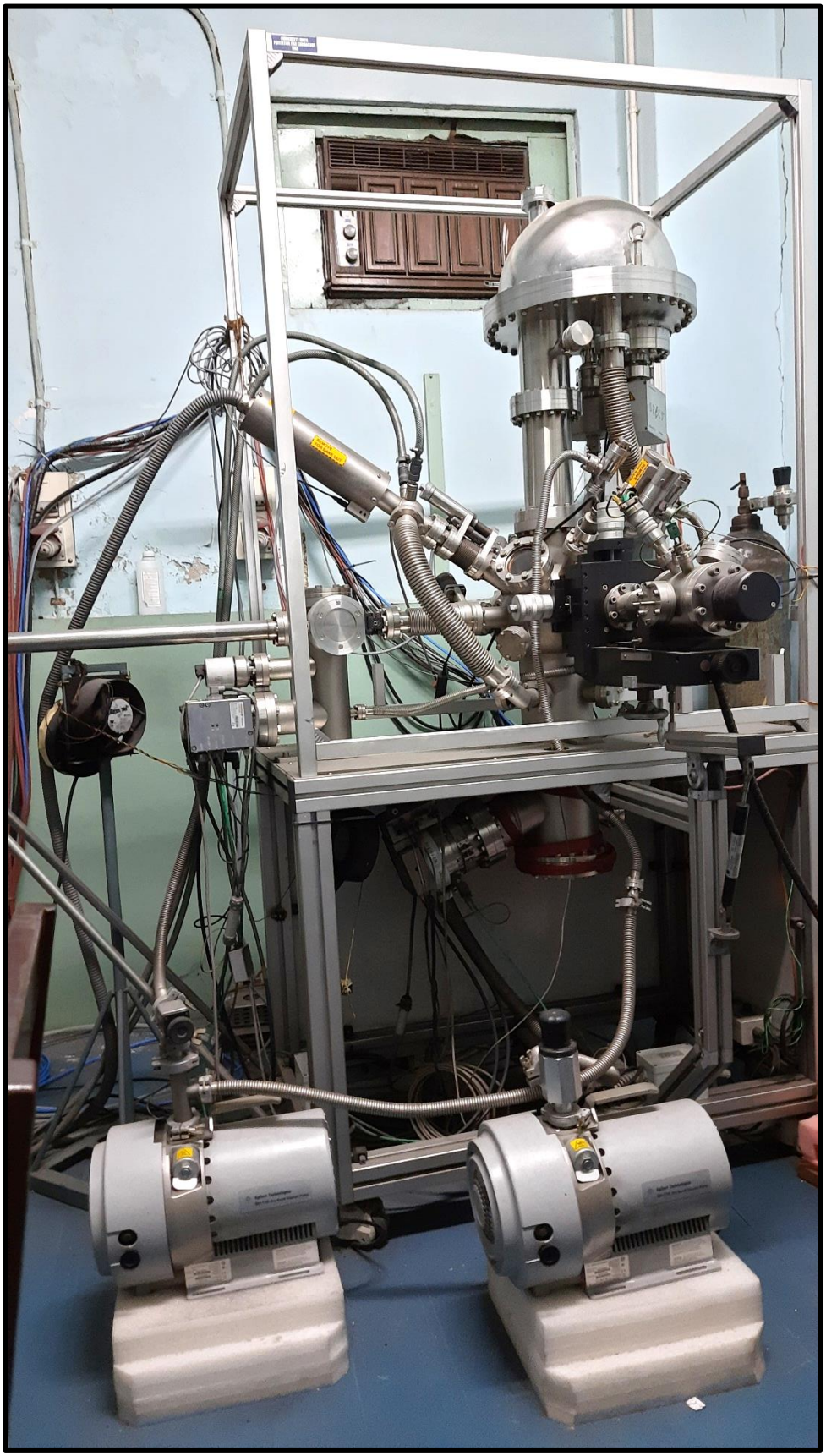

Figure 3.12 Digital photograph of the SPECS HSA 3500 X-ray photoelectron spectrometer and connected turbo molecular pumps.

Satellite peaks are additional peaks that appear on the high-energy side of the main photoelectron peaks in XPS spectra. They are often observed in XPS spectra of materials with high atomic number elements, such as metals or transition metal compounds. They arise from the multiplet splitting of the core-levels of the atoms in the material. This splitting is caused by the interaction of the core electrons with the valence electrons and the spin-orbit coupling of the electrons. The multiplet splitting results in several sub-levels of the core-level energy, which can be resolved in XPS spectra as satellite peaks. Satellite peaks are typically weaker than the main photoelectron peaks and are located at higher binding energies. Their intensity depends on the number of unpaired valence electrons in the atom and the strength of the spin-orbit coupling. Therefore, satellite peaks are more prominent for materials with high atomic number elements or for materials with unpaired electrons. Satellite peaks can provide additional information on the chemical and electronic state of the material. The presence and intensity of satellite peaks can be used to determine the valence state and the coordination geometry of the atoms in the material, as well as the nature of the chemical bonds.

The non-flat background intensity in XPS spectra is caused by several factors, including inelastic scattering, surface contaminants, and instrument settings.[3] These factors cause the background intensity to change with binding energy or kinetic energy, resulting in a sloping background. The main factor that contributes to the non-flat background intensity in photoelectron spectra is the inelastic scattering of the photoelectrons as they travel through the material before escaping from the surface. Inelastic scattering can cause a loss of energy for the photoelectrons, resulting in a broadening and tailing of the spectral peaks towards lower binding energies. This effect leads to an increase in the background intensity at lower binding energies, creating a sloping background. Another contributing factor is the presence of surface contaminants or adsorbates. These contaminants can absorb or scatter some of the emitted photoelectrons, leading to a reduction in the photoelectron intensity and contributing to the non-flat background. Generally, Shirley background is used to model this sloping background intensity, while fitting broad spectral peaks.[4] Using fitting of the peaks and comparison of the area under the curve, XPS can also be employed to derive an approximate composition of the material.

3.3.2 Energy dispersive X-ray (EDX) analysis

Energy-dispersive X-ray spectroscopy (EDS or EDX) is a technique used to obtain information about the elemental composition of a sample by detecting the characteristic X-rays emitted by the atoms in the sample. The technique involves the interaction of a high-energy electron beam with the sample, which results in the production of X-rays from the sample's constituent elements. In EDX analysis, a beam of high-energy electrons is directed onto the

surface of the sample being analysed. When the electrons collide with the atoms in the sample, they transfer energy to the electrons in the atom's inner shell, causing them to be ejected. The ejected electrons are replaced by outer-shell electrons, which emit X-rays in the process. The energy and frequency of these emitted X-rays are characteristic of the elements in the sample, providing information about the sample's elemental composition. EDX systems are generally integrated with electron microscopes, which will be discussed in section 3.4 of this chapter.

EDX analysis is used in a wide range of applications, including materials science, geology, environmental science, and forensic science. It is particularly useful in the characterization of thin films, surface coatings, and multi-layered structures, where the composition and thickness of individual layers need to be determined. In materials science, EDX analysis is used to identify the composition of alloys, ceramics, and polymers, and to study the structure and chemistry of materials at the nanoscale.

One of the main limitations of EDX analysis is its inability to detect light elements, such as hydrogen, helium, and lithium. This is because the X-rays emitted by light elements have very low energies, making them difficult to detect using standard EDX detectors. Additionally, light elements tend to have low X-ray yields, which means that the number of X-rays emitted from light elements is much lower than those emitted from heavier elements. As a result, light elements cannot be detected with high sensitivity using EDX analysis. Another limitation of EDX analysis is the potential for spectral overlap between X-rays emitted by different elements. This can make it difficult to accurately identify and quantify the elements present in a sample, particularly if the sample contains trace amounts of elements.

3.3.3 Raman spectroscopy

Raman spectroscopy is a non-destructive analytical technique used to study the vibrational modes of molecules. It is a powerful tool for the structural and chemical analysis of a wide range of materials, including gases, liquids, and solids. In Raman spectroscopy, a monochromatic light source, usually a laser, is used to illuminate the sample. The laser light interacts with the molecules in the sample, causing them to vibrate. This vibration leads to the emission of scattered light. A small fraction of the light scattered by the sample is shifted in frequency due to the vibrational motion of the molecules or atoms in the sample. This shift in frequency is known as the Raman shift, and it is specific to the chemical bond and vibrational mode of the molecule or atom. The Raman shift is given by the formula,

$$\Delta\nu = \nu_{vib} - \nu_{exc}, \tag{3.5}$$

where, $\Delta\nu$ is the Raman shift, ν_{vib} is the vibrational frequency of the molecule, and ν_{exc} is the frequency of the incident laser light. Although there are classical analogues using polarizability ellipsoids, this shift is a purely quantum mechanical phenomenon. The Raman shift can be

measured using a spectrometer, and the resulting spectrum can be used to identify the chemical composition and structural information of the sample.

Rayleigh scattering is the elastic scattering of light by particles in a medium, such as air or water. In Rayleigh scattering, the scattered light has the same frequency as the incident light, and the intensity of the scattered light is proportional to the fourth power of the frequency of the incident light. It is difficult to detect Raman scattering (inelastic) against Rayleigh scattering because Rayleigh scattering is much stronger (about a million times) than Raman scattering, and the scattered light is of the same frequency as the incident laser light. To detect Raman scattering, specialized equipment is required, such as a Raman spectrometer, which is designed to filter out the Rayleigh scattering and detect the much weaker Raman signal.

Stokes and anti-Stokes lines are the Raman-shifted lines in a Raman spectrum. Stokes lines are the lines that appear at lower frequencies than the incident laser light, while anti-Stokes lines are the lines that appear at higher frequencies than the incident laser light. Stokes lines result from the excitation of the molecule to a higher vibrational state, while anti-Stokes lines result from the relaxation of the molecule from a higher vibrational state to a lower one. The intensity ratio of the Stokes and anti-Stokes lines depends on the temperature of the sample and the energy of the incident laser light. At low temperatures, the intensity of the Stokes lines is much higher than that of the anti-Stokes lines, simply because the population of the ground state is much higher than the excited states owing to Boltzmann distribution. However, at high temperatures, the opposite can be true. The intensity ratio is also influenced by the polarization of the incident laser light and the molecular orientation in the sample. In fact, the sky and sea appear blue due to the Raman effect because the molecules in the atmosphere and water scatter the incoming light, causing it to shift slightly. This scattered light is predominantly in the blue region of the spectrum, giving the sky and sea their blue colour. This effect is known as the Raman scattering of light, and it is most effective for blue light because it has the shortest wavelength and is scattered the most.

In recent years, Raman spectroscopy has been increasingly used to study the properties of nanomaterials. The small size of nanomaterials and their unique optical properties can lead to enhanced Raman signals, which makes them amenable to study using Raman spectroscopy. It is particularly useful in characterizing the properties of carbon-based nanomaterials, such as carbon nanotubes and graphene. The Raman spectra of these materials show characteristic peaks that are related to their unique crystal structure, which can be used to distinguish between different allotropes. Furthermore, Raman spectroscopy can also be used to study the optical properties of semiconductor nanomaterials, such as quantum dots, and also utilized to investigate the properties of metal-based nanomaterials. The Raman spectra of these materials can provide information on their electronic and optical properties, such as bandgap, exciton

binding energy and plasmonic properties. Raman spectroscopy is also a valuable tool for studying biological nanomaterials. Raman spectroscopy can be used to study the structures of biological molecules, such as proteins and nucleic acids, as well as the interactions of these molecules with other biomolecules and with surfaces.

In our lab, we have the WITEC Alpha 300 RS confocal Raman spectrometer (see Figure 3.13), which is a high-performance instrument designed for the analysis of samples using Raman spectroscopy at room temperature. The instrument is equipped with an optical microscope, a monochromatic (532 nm) Nd:YAG laser, connected Peltier-cooled CCD-type detectors, and a power meter for precise laser power control. The whole system is mounted over a HOLMARK vibration-free platform. This spectrometer is designed to automatically filter out the Rayleigh line, as well as anti-Stokes lines. The confocal design of the instrument allows for the acquisition of high-quality Raman spectra with excellent spatial resolution. A collection of ZEISS lenses having $10\times, 20\times, 50\times$ & $100\times$ magnification is available for suitable focussing of the sample. This system has an additional built-in atomic force microscopy (AFM) facility.

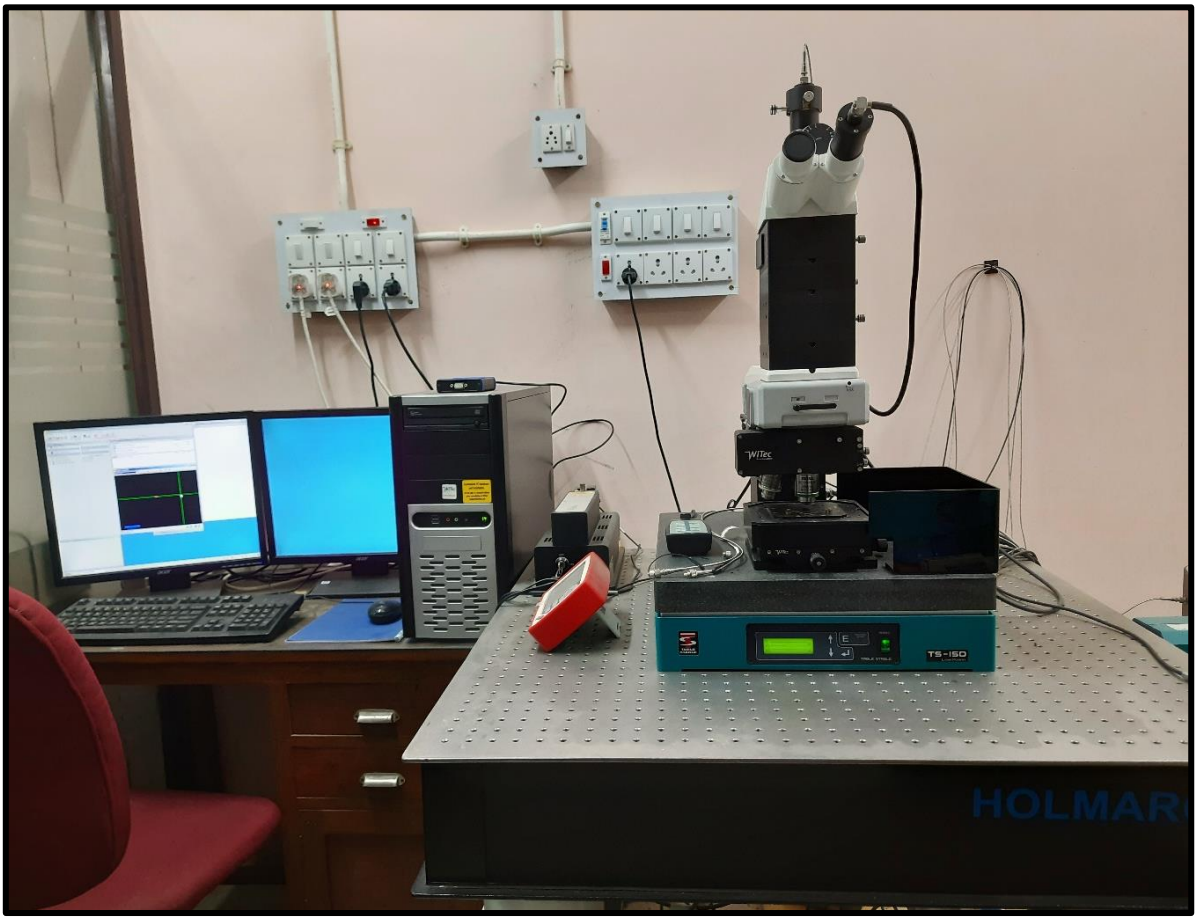

Figure 3.13 Digital photograph of the WITEC Alpha 300 RS confocal Raman spectrometer cum microscopy system with built-in Raman imaging and AFM facility.

There are some other branches of specialized Raman spectroscopy. ***Polarized Raman spectroscopy*** is a technique that uses polarized laser light to probe the orientation and symmetry of molecules in a sample. The scattered light from the sample is analysed in terms of its polarization and intensity, which can provide information about the molecular structure, orientation, and dynamics. This technique is particularly useful in studying materials such as crystals, polymers, and biological molecules. ***Surface-enhanced Raman spectroscopy (SERS)*** is a technique that enhances the Raman signal of molecules by several orders of magnitude by using a nanostructured surface as a substrate. The enhancement is due to the localized surface plasmons of the high curvature substrate that amplify the electric field of the incident laser. SERS is a highly sensitive technique that can detect single molecules and has applications in chemical sensing, bioimaging, and nanotechnology. ***Angle-resolved Raman spectroscopy (ARRS)*** is an expensive technique that analyses the scattering pattern of Raman light at different angles to extract information about the crystal structure and symmetry of materials. By measuring the polarization and intensity of the scattered light at different angles, ARRS can provide information about the phonon dispersion relations, lattice dynamics, band splitting, spin-orbit coupling, and electronic properties of materials.

3.3.4 Fourier-transform infrared spectroscopy (FTIR)

Fourier transform infrared (FTIR) spectroscopy is a technique used to identify and analyse the chemical composition of a sample by measuring the absorption or transmission of infrared radiation. The infrared spectrum of a sample can provide information about its functional groups, molecular structure, and chemical bonding by analysing the finger-print modes of vibration. There are several vibrational modes that can be observed in FTIR spectroscopy. These include,

i. ***Symmetric stretching:*** This is a mode of vibration where the atoms in a molecule move symmetrically in opposite directions along the bond axis.
ii. ***Asymmetric stretching:*** This is a mode of vibration where the atoms in a molecule move asymmetrically in opposite directions along the bond axis.
iii. ***Bending:*** This is a mode of vibration where the atoms in a molecule move perpendicular to the bond axis.
iv. ***Scissoring:*** This is a mode of vibration where the atoms in a molecule move towards each other in a scissoring motion.
v. ***Rocking:*** This is a mode of vibration where atoms in a molecule move back and forth on a plane perpendicular to the bond axis. Rocking vibrations are commonly observed in molecules having some sort of ring structure.

The Shimadzu FTIR-8400S model installed in our lab (see Figure 3.14), is a high-performance FTIR spectrometer with a range of advanced features. Some of the specifications of this model include:

- ***Spectral range:*** 7,800 - 350 cm^{-1}.
- ***Resolution:*** 0.5 cm^{-1}.
- ***Detector:*** DLATGS detector
- ***Sample compartment:*** Sealed and purgeable with temperature control
- ***Software:*** Spectra Manager Suite software with various analysis tools and libraries.
- ***Accessories:*** A range of accessories including ATR, transmission, and reflection measurement modules.

Figure 3.14 Digital photograph of the Shimadzu FTIR-8400S spectrometer.

Apart from fundamental investigations, FTIR spectroscopy has a wide range of applications in various fields including chemistry, biology, and medicine. Some of the applications include:

- ***Analysis of chemical composition:*** FTIR spectroscopy is used to identify and analyse the chemical composition of a sample, including the identification of functional groups and chemical bonding.
- ***Quality control:*** FTIR spectroscopy is used in the pharmaceutical and food industries for quality control and monitoring of manufacturing processes.
- ***Environmental monitoring:*** FTIR spectroscopy is used to analyse air, water, and soil samples for environmental monitoring and pollution control.
- ***Forensic science:*** FTIR spectroscopy is used in forensic science to analyse trace evidence such as fibres, paint chips, and drugs.

3.3.5 UV–Vis–NIR absorbance and diffuse reflectance spectroscopy (DRS)

UV–Vis–NIR absorption spectroscopy and diffuse reflectance spectroscopy (DRS) are two widely used techniques in the field of material science and analytical chemistry. These techniques provide important information about the electronic structure, optical properties, and chemical composition of materials. UV–Vis–NIR absorption spectroscopy is used to study the absorption of electromagnetic radiation by a sample in the ultraviolet (UV), visible (Vis), and near-infrared (NIR) regions of the electromagnetic spectrum.

When light is incident on a sample, it can be either absorbed, transmitted, or reflected. When the sample is exposed to suitable electromagnetic radiation, the electrons in the sample absorb energy and get excited to higher energy levels. The amount of energy absorbed depends on the electronic structure of the sample. This absorbed energy can be quantified using the Beer-Lambert law, which relates the absorbance of the sample to the concentration of the sample and the path length of the light through the sample. ***The Beer-Lambert law*** states,

$$\mathrm{A} = \varepsilon \mathrm{cL}, \tag{3.6}$$

where, A is the absorbance, ε is the molar absorptivity (also called the extinction coefficient), c is the concentration of the sample, and L is the path length of the light through the sample. The molar absorptivity is a measure of how strongly a sample absorbs light at a particular wavelength. The transmittance (T) and reflectance (R) of a sample can be related to its absorbance using the following equations.

$$\mathrm{T} = 10^{-\mathrm{A}}, \tag{3.7}$$

$$R = (1 - T)^2. \tag{3.8}$$

UV–Vis–NIR spectroscopy is widely used in many fields, including chemistry, physics, material science, and biology. It is used to study the electronic structure of molecules and materials, the kinetics of chemical reactions, the purity and concentration of solutions, and the properties of materials such as colour, transparency, and refractive index. DRS is a technique that is used to study the reflectance of a sample in the UV-Vis-NIR regions of the electromagnetic spectrum using a standard reference (white powder) like $BaSO_4$. The reflectance of a sample depends on its chemical composition, surface structure, and optical properties.

UV–Vis–NIR spectroscopy can also be used to determine the bandgap of a material. The bandgap is the energy difference between the highest occupied molecular orbital (HOMO) and the lowest unoccupied molecular orbital (LUMO) of a material or simply the gap between the conduction band minimum (CBM) and valence band maximum (VBM). ***Tauc's plot*** is a method used to determine the bandgap of a material from its absorption spectrum. The plot is created by plotting $(\alpha h\nu)^2$ versus $h\nu$ in case of direct gap, where α is the absorption coefficient and hν is the photon energy. The bandgap can be determined from the point where the plot intersects the x-axis. Relevant formulae for direct/indirect gap are discussed in the coming chapters.

The reflectance of a sample can be quantified using the Kubelka-Munk theory, which relates the reflectance of a sample to its absorption and scattering properties.[5] The theory is based on the assumption that the sample is a homogeneous, infinitely thick, and isotropic medium. The Kubelka-Munk equation is given by,

$$\left(R_\infty + \frac{K}{S}\right)^2 = R_\infty^2 + 2R_\infty(1 - R_\infty)\left(1 - \frac{K}{S}\right) + (1 - R_\infty)^2\left(\frac{2K}{S}\right). \quad (3.9)$$

Here, R_∞ is the reflectance of the sample in the absence of scattering, R is the reflectance of the sample, and k & s are the absorption and scattering coefficients of the sample, respectively. DRS is widely used in the analysis of powdered samples, such as pigments, minerals, and pharmaceuticals. It is also used to study the properties of surfaces, coatings, and thin films.

The Shimadzu UV-3600 UV-Vis-NIR spectrophotometer (see Figure 3.15) is used in our lab for the aforementioned experiments. It is equipped with a high-performance xenon lamp and a double-monochromator optical system, which provides high sensitivity and resolution in the UV-Vis-NIR regions (mainly $200 - 2200$ nm) of the electromagnetic spectrum. The instrument has a spectral bandwidth of 1 nm. It is also equipped with a diffuse reflectance accessory, which allows for the analysis of powdered samples. The instrument has a user-friendly interface and software, which enables easy data acquisition, analysis, and storage.

Figure 3.15 Digital photograph of the Shimadzu UV-3600 UV-Vis-NIR spectrophotometer.

3.4 Morphological investigation

3.4.1 Field emission scanning electron microscopy (FESEM)

The scanning electron microscope (SEM) is an important tool for morphological investigation in the field of nanotechnology, material science, biology and engineering. Among the different types of SEMs, field emission scanning electron microscope (FESEM) is one of the most advanced and versatile SEM that offers superior resolution, high magnification and high

surface sensitivity. The fundamental concept of FESEM is based on the interaction of a focused beam of electrons with the surface of a specimen. In FESEM, the electrons are generated commonly from a sharp tungsten filament (cathode) by applying a high voltage (up to 30 kV) and focused by electromagnetic lenses onto the sample surface. The electrons interact with the specimen and generate different signals such as secondary electrons (SE), backscattered electrons (BSE), X-rays and cathodoluminescence (CL). These signals are then detected by different detectors to generate high-resolution three-dimensional (3D) images and compositional information of the sample surface.

The working principle of FESEM is based on three fundamental components: electron source, electromagnetic lenses, and detectors. The electron source in FESEM is a field emission gun (FEG) that produces a beam of electrons with high brightness and low energy spread. The electron beam is then focused onto the sample surface by a set of electromagnetic lenses that work based on the principles of electrostatic and magnetic fields. The focused electron beam interacts with the sample surface and generates different signals that are detected by different detectors. The SE detector is used to generate high-resolution images of the sample surface, while the BSE detector is used to provide compositional information of the sample. The CL and X-ray detectors are used to study the optical and compositional properties of the sample.

FESEM has a wide range of applications in material science, nanotechnology, biology, and engineering. Some of the common applications of FESEM are as follows:

- ***Material Science:*** FESEM is used to study the microstructure and morphology of different materials such as metals, alloys, ceramics, polymers, and composites.
- ***Nanotechnology:*** FESEM is used to study the morphology, size, and shape of nanoparticles, nanofibers, and other nanomaterials.
- ***Biology:*** FESEM is used to study the surface morphology of biological samples such as cells, tissues, and organs.
- ***Engineering:*** FESEM is used to study the failure mechanism and deformation behaviour of different engineering materials such as metals, ceramics, and polymers.

The Hitachi S-4800 is a high-resolution FESEM that offers superior imaging capabilities and analytical capabilities. It is used in our lab as shown in Figure 3.16, and it accompanies an integrated EDX facility. The basic specifications of the Hitachi S-4800 are as follows:

- ***Electron source:*** Field emission gun (FEG) with a high-brightness electron beam
- ***Accelerating voltage:*** 0.3 to 30 kV
- ***Resolution:*** 0.8 nm (SE mode), 1.5 nm (BSE mode)
- ***Magnification:*** Up to 10^6 ×
- ***Detectors:*** SE, BSE, CL, and X-ray detectors
- ***Imaging modes:*** SE, BSE, and CL imaging modes

- ***Sample size:*** Up to 15 mm in diameter and 10 mm in height
- ***Sample stage:*** Five-axis motorized stage for precise sample positioning and tilting
- ***Imaging software:*** Proprietary imaging software with advanced image processing and analysis tools

Figure 3.16 Digital photograph of the Hitachi S-4800 FESEM and EDX facility.

3.4.2 High-resolution transmission electron microscopy (HRTEM)

Transmission electron microscopy (TEM) is a powerful tool used for studying the structure and properties of materials at the atomic and molecular scale. High-resolution transmission electron microscopy (HRTEM) and selected area electron diffraction (SAED) are advanced techniques used in TEM for studying crystal structures and defects. The fundamental concept of TEM is based on the interaction of a beam of electrons with a thin sample. The electron beam is generated by an electron gun, accelerated by an electric field, and focused by a series of magnetic lenses onto the sample. As the electrons pass through the sample, they interact with the atoms and produce different signals, such as transmitted electrons, diffracted electrons, and scattered electrons. These signals are detected by different detectors to generate high-resolution images and diffraction patterns of the sample. The transmitted electrons are detected by a fluorescent screen or a CCD camera to generate 2D images of the sample. The diffracted electrons are detected by a diffraction pattern detector to analyse the crystal structure of the sample.

HRTEM is an advanced TEM technique that uses a high-resolution electron microscope to image crystal structures at an atomic resolution. HRTEM works by focusing the electron beam onto a specific area of the crystal structure and detecting the scattered electrons using a high-resolution detector. This eventually generates a lattice fringe that can be matched with particular Bragg peaks for the crystal structure. Similarly, in SAED, a beam of electrons is focused onto a specific small area of the crystal, producing a diffraction pattern. The diffraction pattern is then analysed to validate the crystal structure of the material. TEM, HRTEM, and SAED have a wide range of applications in material science, nanotechnology, biology, and engineering that are similar to that of FESEM. Here, the advantage is a significantly higher resolution, generation of lattice fringe and SAED patterns. On the other hand, the limitation is a more difficult sample preparation method.

Figure 3.17 Digital photograph of the JEOL-JEM 2100 HRTEM system.

The JEOL-JEM 2100 is a high-resolution TEM that offers superior imaging and analytical capabilities. It is available as a central facility at Jadavpur University, see Figure 3.17. The basic specifications of the JEOL-JEM 2100 are as follows:

- ***Electron gun:*** Field emission gun (FEG) that produces a highly coherent and stable electron beam.

- ***Lenses:*** The JEOL-JEM 2100 has a series of magnetic lenses that provide high-resolution imaging and diffraction capabilities.
- ***Detectors:*** The JEOL-JEM 2100 has several detectors, including a high-resolution CCD camera, a diffraction pattern detector, and a STEM detector.
- ***Imaging resolution:*** High-resolution imaging capability of up to 0.19 nm.
- ***Accelerating voltage range:*** $80 - 200$ kV.
- ***Sample stage:*** The JEOL-JEM 2100 has a motorized sample stage that can rotate up to $\pm 70°$ and tilt up to $\pm 30°$.
- ***Analytical capabilities:*** The JEOL-JEM 2100 has advanced analytical capabilities, including energy dispersive spectroscopy (EDS) and electron energy loss spectroscopy (EELS). Although, EELS is not available in our set up.

3.5 Electrical characterization

3.5.1 Impedance and dielectric spectroscopy

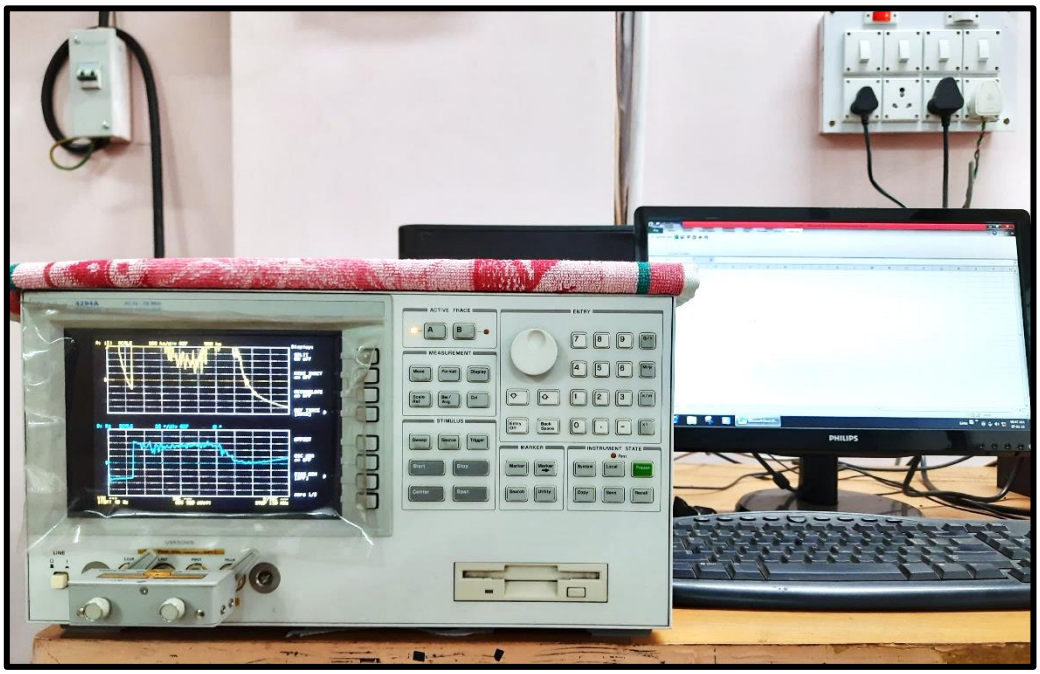

Figure 3.18 Digital photograph of the Agilent 4294A precision impedance analyser system; connected to a gold electrode sample holder.

Impedance is a measure of how much an electrical circuit resists the flow of current when a voltage is applied, while admittance is the inverse of impedance and measures how much current can flow for a given voltage. Dielectric spectroscopy measures the electrical response of materials to changes in frequency or temperature, while modulus spectroscopy measures the mechanical response of materials to the same stimuli. Being complex quantities,

all of them carry complementary information in the magnitude-phase or real-imaginary parts.[6,7] The basic concept of impedance, admittance, dielectric, and modulus spectroscopy is already delineated in section 2.3.5 of the last chapter. Hence, let us directly discuss the instrumental details.

The Agilent 4294A precision impedance analyser system, installed in our lab (see Figure 3.18), is a powerful tool for measuring a wide range of electrical parameters for materials and devices, including impedance, admittance, dielectric and modulus attributes. It offers a frequency range of 40 Hz to 110 MHz, with a measurement accuracy of 0.05% and a resolution of 0.001 degrees for phase measurements. It has a built-in oscillator for frequency accuracy and stability, and can measure both impedance and admittance in the range of 1 mΩ to 1 GΩ. The default amplitude of the input waves is 500 mV, which can be modified according to the requirement. Thus, apart from pellets, thin films can also be sampled using this system. It also offers five bandwidth settings. The system includes a variety of measurement modes, including sweep mode for frequency-dependent measurements, and time-domain mode for waveform analysis. It can also perform DC bias-dependent measurements for devices in the range $0 - 40$ V at room temperature.

3.5.2 Study of ferroelectric loop (P-E loop)

Ferroelectric loop tracing is a technique used to measure the polarization $(\vec{P})$ of a ferroelectric material as a function of an applied electric field $(\vec{E})$. Fundamentally, ferroelectric materials are characterized by their ability to spontaneously polarize when subjected to an electric field. This polarization is reversible and can be observed as a hysteresis loop in a graph of polarization versus electric field. The domain theory of ferroelectric materials suggests that the polarization arises due to the alignment of dipoles in the material. These dipoles are organized into domains, which are regions of the material where the dipoles are aligned in the same direction. When an electric field is applied, the domains align in the direction of the field, leading to a net polarization.

The ferroelectric hysteresis loop consists of four important parameters: remanence (P_r), coercivity (E_c), saturation polarization (P_s), and the shape of the loop itself. Remanence is the polarization that remains after the electric field has been removed, while coercivity is the minimum electric field required to switch the polarization direction. Saturation polarization is the maximum polarization that can be achieved in the material under an applied electric field.

The Radiant Precision Premiere II (see Figure 3.19) is an efficient device that can be used for ferroelectric loop tracing. It is a high-performance instrument capable of measuring the electrical properties of a wide range of materials (typically in pellet form), including ferroelectrics. The instrument has a frequency range of 10 μHz to 1 MHz, and can measure

impedances from 1 mΩ to 10 GΩ. It also includes a variety of measurement modes, including impedance, admittance, and conductance. It can also execute positive-up-negative-down (PUND) measurements. In our system, an amplifier and a safety unit are attached additionally, that can amplify the typical range of 0 − 100 V to as high as 10 kV.

Figure 3.19 Digital photograph of the Radiant Precision Premiere II ferroelectric loop tracer.

3.5.3 Digital storage oscilloscope, digital multi-meter, and associated electrical measurement systems

The KEYSIGHT InfiniiVision DSOX2012A digital storage oscilloscope can be used for a wide range of electrical measurements. It is used in our lab and is displayed in Figure 3.20(a). It offers two channels with a bandwidth of 100 MHz and a sampling rate of up to 2 GSa/s. Its advanced triggering capabilities, waveform analysis tools, and intuitive user interface make it a great choice for measuring open circuit voltage and short circuit current of piezoelectric nanogenerators (PENGs). To measure the open circuit voltage of a PENG, one channel of the DSOX2012A should be connected to the PENG's output while setting the trigger mode to auto. The DSOX2012A will capture the voltage waveform, which can then be analysed using its waveform analysis tools. To measure the short circuit current of a PENG, one can connect the PENG's output to a load resistor and connect the other end of the resistor to ground. Then, one can connect the other channel of the DSOX2012A to the load resistor and set the trigger mode to single. When the PENG is triggered, the DSOX2012A will capture the current waveform, which can be analysed using its waveform analysis tools.

A digital multi-meter (DMM) is a versatile tool used to measure various electrical quantities. The device typically measures voltage, current, and resistance. To measure voltage, the DMM connects to the circuit in parallel with the voltage source. For current measurements, the DMM connects to the circuit in series with the current source. The device measures the

resistance of a component by passing a small current through it and measuring the resulting voltage drop. Some DMMs can also measure frequency, capacitance, and temperature. Frequency measurement is done by measuring the number of cycles per second in an alternating current signal. Capacitance measurements are made by measuring the time it takes for the capacitor to charge or discharge to a certain voltage. Temperature measurement is done using thermocouples. DMMs also offer various features such as auto-ranging, which allows the device to automatically select the appropriate range for the measurement being taken. Some models also feature a data logging function that enables users to record measurements over time. I use the DT9205A model for various aforementioned measurements, as shown in Figure 3.20(b). It is also capable to check continuity in electrical circuits and determine various parameters of diodes and transistors.

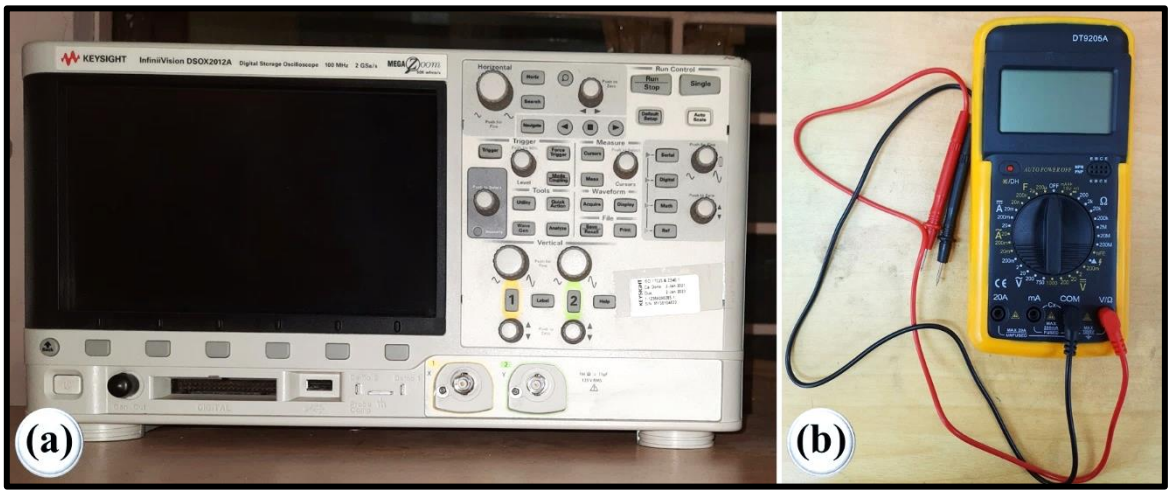

Figure 3.20 Digital photograph of (a) KEYSIGHT InfiniiVision DSOX2012A digital storage oscilloscope; and (b) DT9205A digital multi-meter (DMM).

In addition to these, electrometers can also be used to measure the open circuit voltage of a PENG, such as Keithley electrometer (Model 6514). An electrometer is a sensitive instrument that can measure very low currents and voltages. It is particularly useful for measuring the leakage current of PENGs, which can affect their performance.

References

1. J. Rodriguez-Carvajal, *Phys. B: Condens. Matter*, 1993, **192**, 55.
2. Z. Feng, Q. Hou, Y. Zheng, W. Ren, J.-Y. Ge, T. Li, C. Cheng, W. Lu, S. Cao and J. Zhang, *Comput. Mater. Sci.*, 2019, **156**, 310-314.
3. N. Pauly, F. Yubero and S. Tougaard, *Nanomaterials*, 2023, **13**, 339.
4. M. H. Engelhard, D. R. Baer, A. Herrera-Gomez and P. Sherwood, *J. Vac. Sci. Technol. A*, 2020, **38**.

5. A. A. Kokhanovsky, *J. Phys. D: Appl. Phys.*, 2007, **40**, 2210.
6. M. Nakanishi, *Int. J. Spectrosc.*, 2014, **2014**.
7. Y. Huang, K. Wu, Z. Xing, C. Zhang, X. Hu, P. Guo, J. Zhang and J. Li, *J. Appl. Phys.*, 2019, **125**, 084103.

4 SIZE-MODULATION OF FUNCTIONALIZED Fe_3O_4: NANOSCOPIC CUSTOMIZATION TO DEVISE RESOLUTE PIEZOELECTRIC NANOCOMPOSITES

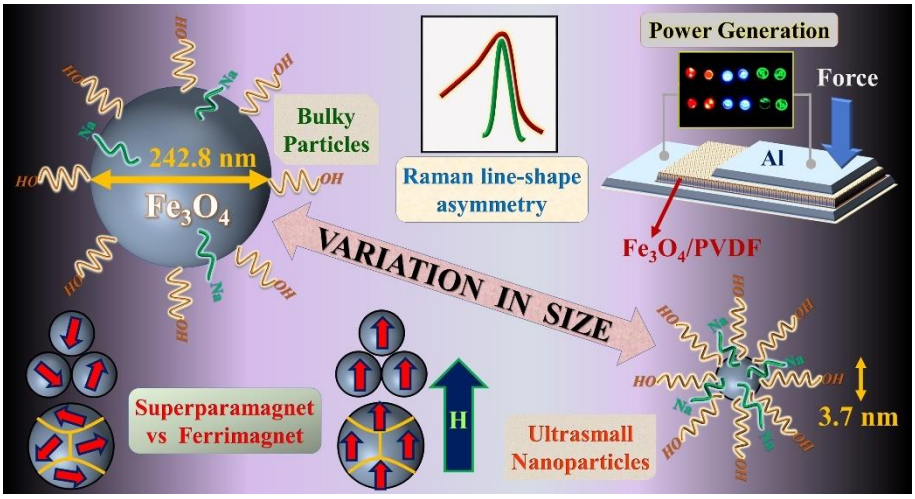

Abstract

Magnetite (Fe_3O_4), an archetypical relaxor multiferroic material, transpires to possess fundamentally appealing multifaceted size-dependent properties. To appraise such a prototype spinel transition metal oxide (STMO); monodispersed and highly water-dispersible spherical magnetite nanoparticles (MNPs) with enormous variation in size (3.7 – 242.8 nm) are synthesized by a persuadable microwave-assisted and polyol-mediated solvothermal approach at controlled temperature and pressure, using idiosyncratic crystallite growth inhibitors. An exalted long-term colloidal stability in polar environment together with Zeta potential insurgence conform the coordinative effect of carboxylate groups contriving the covalent surface functionalization; duly validated from FTIR spectra, TGA and XPS analysis. The optical band-gap (E_g) between crystal-field split-off bands, calculated from absorption spectra, increases gradually against size-contraction enfolding a broad UV-Vis range (1.59 – 4.92 eV). Red-shifting of asymmetric Raman peaks with smaller size and short-range electron-phonon coupling are explained from the modified phonon confinement model (MPCM); whereas ferrimagnetic nature rejigged by superparamagnetism is verified from Mössbauer analysis. These stoichiometric, non-toxic, polar and magnetic nanocrystals are not only ideal for biomedical applications, but also compliant with electroactive porous host-networks. Size-modulated MNPs are finally incorporated in poly(vinylidene floride) [PVDF]-based polytype nanogenerators as an electret filler to reinforce piezoelectric performance (V_{OC}~115.95 V, I_{SC}~1.04 μA), accompanied by substantial electromagnetic interference shielding.

4.1 Introduction

Recent understandings on charge-orbital ordering in low-temperature symmetries across Verwey transition[1-4] and associated relaxor multiferroicity[5,6] urge to critique the momentous attributes of the oldest known magnetic compound-magnetite. Its eccentric traits are nowadays being applied to numerous provinces; such as biomolecular separation, biological sensing or cell tracking, waste water purification, environmental remediation, etc; whereas superparamagnetic nanocrystals (SPNCs) are engaged in targeted drug delivery, magnetic fluid hyperthermia (MFH) treatment of tumour cells, gene delivery, and magnetic resonance imaging (MRI) as T_1/T_2 contrast agents.[7-16] Quantitative scrutiny of size-selective magnetic and electronic properties of magnetite nanoparticles (MNPs), having excellent biocompatibility and negligible toxicity can be technologically upbringing under a well-designed approach in synthetic chemistry.[9,13-16] In device-based applications, nanomaterials exhibiting narrow size-shape distributions with satisfactory colloidal stability and high crystallinity are required. However, a substantial reduction in particle-dimension leads to a dramatic increase in surface-energy and effective area-to-volume ratio $[\sim(\text{particle}-\text{size})^{-1}]$; leading to high defect-density, compromised crystallinity & stoichiometry, and substantial aggregation-tendency.[9,12-16] Therefore, to perpetuate stable nanosystems of high quality and to sustain essential physio-chemical characteristics; systematic reduction of size via appropriate surface-functionalization is requisite, which in turn regulates dispersity, band-gap, electron-phonon interactions, carrier-transport and magnetization to entreat particular devices.[9,14-16]

Out of sixteen different iron oxide/oxyhydroxide polymorphs; hematite (α-Fe_2O_3), maghemite (γ-Fe_2O_3), and magnetite (Fe_3O_4) ought to be most significant.[17] Bulk magnetite crystallizes in an inverse cubic-spinel structure: $(Fe^{3+})_A[Fe^{2+}Fe^{3+}]_B(O^{2-})_4$ [space group O_h^7 $(Fd3m)$]; comprising a close-packed O^{2-} FCC lattice.[18] It possesses a smaller unit cell than hematite and is free of vacancies unlike maghemite. There are two types of Fe atoms: the tetrahedrally coordinated A-sites (Wyckoff site: 8a; point group: $\bar{4}3m$) and the octahedrally coordinated B-sites (16d; $\bar{3}m$) with reference to the oxygen sublattice. Rapid hopping of an extra down-spin electron among B-sites builds up minority-spin polarized electronic conductivity, ascribing its room-temperature half-metallicity.[19] Consequently, Fe_3O_4 possesses one conducting and one semiconducting channel composed of respective minority/majority spins, resulting an absolute spin-polarization at the Fermi level; unfolding newer prospects in spintronics too. Magnetic properties of bulk magnetite with a multidomain structure are governed by two distinct mechanisms. Firstly, the anti-ferrimagnetic super-exchange interaction between the Fe_{Oct}^{3+} and Fe_{Tet}^{3+} sites coupling through the overlapping $2p$ orbital of intermediate oxygen.[20] Association of B-sites in a pyrochlore lattice with corner-sharing tetrahedra gives rise to a magnetic moment antiparallelly aligned with A-sites having unequal

magnitude. The second factor is the predominant double-exchange interaction between the Fe_{Oct}^{2+} and Fe_{Oct}^{3+} sites via hopping of spin-down electrons, upholding parallel alignment. Therefore, all Fe_{Oct}^{2+} ions contribute to the magnetic moment, while the two variants of Fe^{3+} ions counteract each other out. In fact, the B-site Fe^{3+} $3d^5$ ($S = \frac{5}{2}$) up-spins subsist twice the A-site down-spins, resulting a net non-vanishing magnetic moment ($\approx 4\mu_B$), entailing ferrimagnetism with a Curie temperature, T_c~858 K. As the size decreases below ~50 nm, the particles tend to attain a single-domain structure, where coercivity is maximized and T_c gets lowered. When the dimension further drops below 20 nm, the magnetization becomes randomized by thermal agitation, owing to superparamagnetic swapping between two stable magnetic orientations.

Low-dimensional materials and sub-80 nm particles not only call for fundamental and sceptic research-interests, but also possess unique electrical, optical, magnetic, and catalytic phenomena useful in optoelectronics and biotechnology; hard to be realized in their bulk counterparts. Quantum dots (QDs) are effectively zero-dimensional (typically < 10 nm) semiconducting nanocrystals, that exhibit quantum confinement of the electronic states, because of extreme limitations in size.[21] Their lattice parameters deviate from the bulk and long-range interactions are suspended unless explicit dense-packing. Colloidal dots are advantageous for attaining an immensely narrow size-distribution, resulting well-defined and finely tunable optoelectronic properties in terms of absorption, excitonic peaks, and photoluminescence; whereas QDs can also be nucleated inside a host matrix, commonly a nanoporous mesonetwork or a thin film. In this work, monodispersed and spherical core-shell MNPs having diameters from quantum regime to bulk order are synthesized via a cost-effective and highly reproducible microwave-assisted solvothermal technique to regulate versatile physio-chemical properties, meticulously. These functionalized particles with prescribed optical, electronic, and magnetic features can be more adaptive to develop certain nanocomposites, reconcilable with diverse set of applications; one of which is corroborated herein.

In the era of depleting fossil-fuel; scavenging alternative sources such as solar or fusion-energy and mechanical/chemical energy-harvesting or storage have topped the priorities of materials research. Since the nineties; polymers, 2D materials and different composites have been satisfactorily explored for enhancement of supercapacitor and nanogenerator-based applications. Use of electroactive polymers with high dielectric constant and their composites for cost-effective, flexible, wearable, biocompatible, self-powered nano-devices has truncated considerable attention in this regard. Among these, poly(vinylidene floride) [PVDF] and its copolymers, well-known for their promising piezo-, pyro- and ferroelectric response, have been classified as a model-system in fabrication of easily scalable high power-density devices with large breakdown strength and intrinsic reciprocal conversion capability.[22-26] PVDF, a semi-

crystalline fluoropolymer, comprises five different crystalline polymorphs *viz*. α, β, γ, δ, and ε-phase. While in ambient conditions, the thermodynamically favourable non-polar α-phase with alternate trans-gauche (TGTG') conformation is the predominant constituent; tensile stretching, high electric field poling or embedding polar nanoparticles can enhance the planer all-trans (TTTT) pseudohexagonal β-phase with largest spontaneous polarization.[22,23] To improve compatibility with smart textiles and electronic gadgets, these devices owe to have suitable magnetic and dielectric properties for built-in propensity of reducing electromagnetic interference (EMI). Fe_3O_4 is not only a superior magnetic material, but also acts as an electret *i.e*., can store charge temporally to enhance electroactive response of the system. Im and Park have recently fabricated mechanically robust magnetic Fe_3O_4/PVDF composite nanofibers by embedding commercial Fe_3O_4 powder to ameliorate its triboelectric performance.[25] However, inorganic compounds very often cease to exhibit high dispersibility, uniform layout and long-term stability; while being incorporated to organic medium in composite frameworks. To resolve such drawbacks and avoid unfavourable phase-separations, organic surface-coatings are essential around the inorganic nanocore. Thus, functionalized MNPs with high surface-charge can intensify the β-phase contributions as a filler. Numerous materials in different weight-ratios were incorporated in PVDF to fabricate composite piezoelectric nanogenerators (PENGs) in previous literature.[23-26] But here tinier lead-free additives are utilized to gradually enhance piezo-activity foremostly.

4.2 Methods and enumeration

4.2.1 Synthesis and experimental details

4.2.1.1 Reagents and materials

All reagents are of analytical grade (Assay ≥ 99.5%) and used directly without any further purification. Ethylene, diethylene, and polyethelene glycol (PEG-6000) are used to prepare the polyol solvent. Ferric chloride hexahydrate ($FeCl_3.6H_2O$) and anhydrous sodium acetate (CH_3COONa) with ≥ 99.9% purity are the principle precursors, purchased from SIGMA-ALDRICH. Hydrated disodium (+) tartrate [$(CHOH.COONa)_2.2H_2O$] is bought from LOBA Chemie. Absolute ethanol from Merck and deionised water (~18.2 MΩ) are used for washing. PVDF powder and N,N-dimethylformamide (DMF) used here; are also from SIGMA-ALDRICH.

4.2.1.2 Synthetic procedure

MNPs synthesized from polyol-mediated routes exhibit excellent stability and dispersibility in organic solvents due to intricate coating. However, such a coating is not covalently linked to the particle-surface and therefore achieves a relatively weak interaction

with polyol-molecules. While being used for *in vivo* applications, such nanoparticles usually lose stability owing to desorption of polyols and uptake by aggregated macrophages.[15] To conquer these problems, biocompatible carboxylic acid salts with coating tendency are used to develop long-term colloidal stability under physiological conditions. Shen *et al*.[15] have synthesized ultra-small, monodispersed and water-dispersible MNPs by using trisodium citrate to control growth, whereas Wang *et al*.[16] have produced even smaller nanoparticles via high-temperature co-precipitation approach using poly(acrylic acid) as a capping agent to control morphology.

In a typical synthesis of 3.7 nm MNPs, 0.35 g (1.29 mmol) $FeCl_3.6H_2O$ is first mixed vigorously in 25 mL solution of ethylene and diethylene glycol (1:4). Then 0.15 g (0.65 mmol) disodium tartrate is added, followed by 1.2 g (14.63 mmol) CH_3COONa and 1.6 g (0.27 mmol) PEG-6000. The resulting mixture is ultrasonicated for 10 min and magnetically stirred at 80 °C for half an hour to form a homogeneous dark yellow solution. Thereafter, 5 mL of this mixture is transferred into a 10 mL SiC vial (C10), closed in air and placed inside the single-mode Anton-Paar microwave synthesis reactor (Monowave 200) at 200 °C in a pressure-range: 8– 10 bar for 22 min with an additional ramp-up time of 5 min. For uniform reaction-dynamics, the solution is continuously stirred up by a magnetic bead at 1000 rpm. After cooling against a compressor, the dark black solution is collected and washed at least 10 times (≥ 10 min each) via centrifugation at 9000 rpm in 10 °C, being dispersed in an 80:20 mixture of absolute ethanol and deionized water. Finally, the obtained precipitate is dried at 60 °C for 5 h under rough vacuum to obtain fine Fe_3O_4 powder-sample.

The details of composition and synthesis-parameters are listed in Table 4.1. Samples of two batches: Series A & B are prepared at 220 and 200 °C respectively, maintaining a continuous decreasing size-profile via adjusting concentration of surfactants or coating agents. Because of a strong microwave dissipation at the as-used frequency (2.45 GHz), the microwave irradiation converts into heat, leading to the quick formation of MNPs. Since the thermal conductivity of SiC is significantly higher than glass/pyrex vials, substances within SiC vial would be partially shielded from the electromagnetic field and some heat-transfer would also occur via conduction through SiC walls. This dual heating mechanism causes the ultrafast generation of nano-seed crystals within a few minutes. Next, the growth-time is adjusted at a certain temperature and pressure to control particle size accordingly. The fast microwave-assisted route is specialized for synthesis of tiny nanoparticles and not suitable for synthesizing larger particles (≥ 80 nm), because increasing reaction-time indefinitely can compromise safety-issues governing microwave reactor. Hence, common solvothermal approach is used to synthesize larger particles, where a greater pressure (~30 bar) at elevated temperature plays key-role in the reaction-kinetics and particle size.

Table 4.1 Synthesis-parameters, particle dimensions, ZP-vales and optical band-gap for all samples

Reaction-temperature (°C)	Synthesis technique	Sample Code	Amount of reagents					Growth-time	Crystallite-size (d_{WH}) in nm from W-H plot	Hydrodynamic size (d_H) in nm from DLS	Average particle-diameter (d_{EM}) in nm from SEM/TEM	(-) Zeta Potential in mV	Optical Band-gap (E_g) in eV
			EG + DEG (ml)	$FeCl_3.6H_2O$ (gm)	Sodium tartrate (gm)	Sodium acetate (gm)	PEG - 6000 (gm)						
220 (Series – A)	Microwave assisted solvothermal	A1	25+0	0.50	0.02	1.75	1.00	2 h	50.3 ± 2.1	X	53.2 ± 1.1	10.7	2.61
		A2	20+5	0.40	0.03	1.60	1.20	1 h	38.9 ± 5.1	47.1 ± 1.4	39.8 ± 0.9	20.1	2.99
		A3			0.04	1.50	1.30	50 min	29.4 ± 2.6	X	33.0 ± 1.8	23.9	3.60
		A4	15+10		0.06	1.40	1.40	40 min	10.7 ± 3.0		11.9 ± 0.6	28.7	4.00
		A5	10+15		0.10	1.30	1.50	30 min	7.6 ± 3.2		7.9 ± 0.8	35.3	4.24
		A6	5+20	0.35	0.15	1.20	1.60	22 min	4.3 ± 3.0	9.2 ± 0.5	5.5 ± 1.0	38.3	4.78
200 (Series – B)		B1	25+0	0.50	0.02	1.75	1.00	2 h	45.0 ± 1.0	X	48.9 ± 0.7	X	2.72
		B2	20+5	0.40	0.03	1.60	1.20	1 h	32.2 ± 1.9		30.2 ± 1.2		3.67
		B3			0.04	1.50	1.30	50 min	15.1 ± 3.0	21.2 ± 0.9	16.0 ± 1.4		3.80
		B4	15+10		0.06	1.40	1.40	40 min	8.9 ± 2.9	X	9.1 ± 0.4		4.08
		B5	10+15		0.10	1.30	1.50	30 min	6.0 ± 3.4		7.0 ± 0.8		4.34
		B6	5+20	0.35	0.15	1.20	1.60	22 min	2.9 ± 2.2		3.7 ± 0.4		4.92
185 (Series – C)	Ordinary solvothermal	C1	30+10	1.00	0.05	4.00	1.00	32 h	202.0 ± 0.4	223.7 ± 6.9	242.8 ± 2.4		1.59
		C2	20+20	0.90	0.10	3.00	2.00	16 h	119.8 ± 0.4	X	127.1 ± 0.5		1.88
		C3	10+30	0.80	0.15	2.00	3.00	8 h	86.0 ± 1.9	88.8 ± 5.2	84.5 ± 1.2		2.26
S		Commercial powder purchased from SIGMA-ALDRICH							40.5 ± 0.3	X	43.9 ± 0.2		2.30

"X" means, experiment has not been conducted.

Similar precursor-mixture (as mentioned in Table 4.1) is put into a Teflon-lined stainless steel-autoclave with 50 mL capacity and maintained at 185 °C for $8-32$ h. After natural cooling the samples are washed and collected likewise. The as-synthesized MNPs (Series-C) might have a broader size-distribution and lesser sensitivity towards size, due to bulky nature. Commercial Fe_3O_4 powder (Sample-S) is also purchased from SIGMA-ALDRICH for an inclusive comparison.

4.2.1.3 Microwave synthesis reactor and its implications

Fe_3O_4 nanoparticles are synthesized in the single-mode Anton-Paar microwave reactor-Monowave 200. The system operates at a frequency of 2.45 GHz with a maximum power of 850 W. Pressure and temperature can be simultaneously monitored by an external infrared (IR) sensor and an internal fibre-optic (FO) probe. With this system, glass-vials of 2 different size (G10 & G30; the number represents the maximum capacity of the vial in mL) and one Silicon Carbide (SiC) vial (C10) are supplied. Only SiC vials are suitable for this synthesis protocol in order to prevent accidents during reactions at the maximum values of temperature ($T_{max} = 260$ °C) and pressure ($P_{max} = 30$ bar).

In traditional solvothermal routes, the precursor-solution is directly transferred to a Teflon-lined stainless still jacket and placed to be heated in a hot-air oven for hours or even days. However homogeneous and well-dispersed the precursors are, eventually undergoes some density distribution inside; besides due to finite thermal conductivity of the container as well as the precursor-medium, the part of the solution in direct touch with the Teflon-wall attains the required temperature first and then it slowly gets conducted to the interior region. Naturally, seed-crystals get created first at the exterior region, and by the time the interior-part reaches the set-temperature, the outer seeds already grow to a certain extent. Moreover, the growth-dynamics hugely depend on the local density of the precursors. Hence, particles of a broad size-distribution are formed, which is hardly suitable for size-dependent studies like this work. The best way to acquire uniform nucleation & growth is continuous stirring to cease any density or temperature-gradient; which is followed in one-pot, hot injection or reflux methods. In microwave synthesis reactor the magnetic bead can be rotated up to 1200 rpm, higher than that of the traditional one-pot set-ups; generating an extremely narrow size-distribution of the nanoparticles in a very short span of time.

4.2.1.4 Role of surfactants/capping agents in coating mechanism

In the synthesis and storage of multivariant transition metal oxides (TMOs); stability demands utmost attention. On exposure to ambient atmosphere, the surface of Fe_3O_4 crystallites is often covered with a few layers of Fe_2O_3, monolayer amounts of surface hydroxyls and physiosorbed H_2O. Very often, to passivate the nanoscopic surface during or after synthesis,

suitable organic coatings are employed, in absence of which, hydrophobic interactions promote interparticle aggregation and formation of large clusters in order to reduce surface area to volume ratio. The capping agents prevent arbitrary growth or agglomeration and are useful in regulating reactivity, imparting solubility and maintaining packing characteristics.[27] Surfactants are also used to control morphology and protect nanoparticles from deteriorating over time.

In this reaction, sodium acetate acts as a nucleating agent, that helps to partially reduce Fe^{3+} ions into Fe^{2+} in the polyol medium to form Fe_3O_4. The two principal surfactants are: (i) disodium tartrate, a bidentate carboxylic acid salt, having covalent linking capability to nanoscopic surfaces; and (ii) polyethylene glycol (PEG-6000), having long polymeric chains, whose layers can cover the nanoparticles and inhibit further growth. PEG not only functionalizes MNP-surface and acts as a stabilizer, but also dissipates heat energy from microwave to facilitate the reaction. Biocompatible sodium tartrate (a non-toxic salt, found in fruits like grapes, tamarind *etc*.) is chosen, as it can restrict crystal grain growth according to its concentration and thereby prepares ultra-small nanoparticles/QD compatible for biomedical applications. The two carboxylate groups of tartrate molecules have strong coordination affinity to Fe^{3+} ions and get attached to the surface of MNPs. It makes them intrinsically stabilized with a layer of hydrophilic ligands *in situ* to prevent aggregating into larger crystals, essential for their long-term aqueous stability. Hence, these two chemicals together can obstruct the growth-mechanism very efficiently; as the macromolecules of PEG-6000 envelope the synthesized MNPs very fast, and the tiny tartrate molecules link covalently to the surface of MNPs. Use of this novel dual-surfactant combination helped ultrasmall MNP-formation via a facile, cost-effective, fast, single-step and extremely reproducible method.

4.2.1.5 Chemical reactions

The polyol solvent supplies adequate amount of OH^- ions in the solution in presence of CH_3COONa. This makes up the required reducing environment for the nucleation of Fe_3O_4 nanocrystallites. In the first step iron hydroxides and goethite (α-FeOOH) form. Then Fe_3O_4 is generated by a solid-state reaction between them in definite temperature, pressure, reaction/crystal-growth time *etc*. The reactions follow:

$$FeCl_3 \rightarrow Fe^{3+} + 3Cl^-$$

$$Fe^{3+} + 3OH^- \rightarrow Fe(OH)_3$$

$$Fe^{3+} + e^- \rightarrow Fe^{2+}$$

$$Fe^{2+} + 2OH^- \rightarrow Fe(OH)_2$$

$$Fe(OH)_3 \rightarrow \alpha - FeOOH + H_2O$$

$$Fe(OH)_2 + 2\alpha - FeOOH \rightarrow Fe_3O_4(\downarrow) + 2H_2O$$

Different synthesis-parameters, concentration of precursor & surfactants and related details are listed in Table 4.1 for persistent reproduction of samples.

4.2.1.6 Fabrication of Fe_3O_4/PVDF PENGs

1.5 g PVDF powder along with particular amount of Fe_3O_4 are vigorously stirred in a solution of 12 mL acetone and 8 mL DMF at 80 °C for 2 h and thereafter transferred onto glass-slides homogeneously. The slides are put to drying at 70 °C in rough vacuum for 24 h without any mechanical disturbance. Finally, the dry stand-alone thin films are separated out of the slides and employed for fabrication of flexible PENGs with thin aluminium electrodes, deposited in top-bottom configuration.

4.2.2 Characterization techniques and specifications

The crystallographic phase composition of the as-synthesized samples is determined from X-ray diffraction using Rigaku Miniflex powder X-ray diffractometer; operated at 40kV–15mA. Data is acquired in steps of 0.02° at a rate 1°/min. Surface morphology and size-distribution of MNPs are analysed using a field emission scanning electron microscope (FESEM, JEOL 6340F FEG-SEM), whereas a high-resolution transmission electron microscope (HRTEM, JEOL-JEM 2100) operated at 200 kV; is employed to observe the ultra-small nanoparticles, analyse crystalline nature and unidirectional growth. Samples for FESEM and HRTEM are prepared by casting a drop of dilute dispersion in ethanol on Si wafer and Ted Pella carbon type-B support films (200 mesh grids) respectively, followed by fast evaporation.

The hydrodynamic particle-size (d_H) is determined from DLS-nano ZS90 (Zetasizer Nanoseries, Malvern Instruments) using a dilute solution (~0.1 g L^{-1}), prepared by ultrasonicating the powder-sample in distilled water. The incident laser is projected at an angle 173° for detecting backscattered photons and the average size is estimated from the autocorrelation function of the time-dependent fluctuation in scattered intensity. Particles in a colloidal dispersion scatter the incident laser, so the scattered intensity continuously fluctuates over time due to Brownian motion of the mobile particles and get detected in DLS instrument. Generally, particles having dimensions $\leq \frac{\lambda}{10}$, λ being the wavelength of the incident light, scatter light elastically and isotropically (Rayleigh scattering).[19] However, when the size exceeds this threshold of $\frac{\lambda}{10}$, Rayleigh scattering is dominated by anisotropic (preferably in forward and backward direction) Mie scattering. As particle-size further increases, Mie scattering predominantly takes place in the forward direction. Hence, by generating an autocorrelation function (ACF) based on time-variation of intensity and degree of anisotropy of the scattered light, number-distribution of particle-size is estimated in DLS. Both d_H and ζ-potential are evaluated by averaging five measurements against each sample.

The surface composition of PEG/tartrate coated MNPs is characterized by X-ray photoelectron spectroscopy (XPS) to investigate the nature of the chemisorbed surfactant molecules and to substantiate the effects of the capping agents on sample-quality, stability, and stoichiometry. Data is obtained using a SPECS XPS (monochromated Al K_α source; $h\nu = 1486.6$ eV) with hemispherical analyser (HSA 3500). The survey scans and high-resolution elemental scans for XPS analysis are carried out with pass energy of 160 eV in steps of 1 eV and 20 eV in steps of 0.1 eV respectively. The spectra are calibrated by C 1*s* peak with a binding energy of 284.8 eV. The coordinative effect of carboxylate groups in the surface-composition is further verified by FTIR spectra, collected from Shimadzu FTIR-8400S. To analyse thermal degradation behaviour of the core-shell MNPs; about 15 mg of four chosen powder-samples are elucidated by TGA-DTG (Perkin Elmer Diamond Pyris 480) in N_2-atmosphere from room-temperature to 1000°C in 2 h. As maghemite and magnetite exhibit almost similar XRD patterns because of lookalike spinel structure, the composition is further verified by Raman spectroscopy, capable of characterizing the finger-print modes of vibration. Micro-Raman (beam-diameter ≅ 1 μm) spectrum are recorded employing a solid-state Nd:YAG laser (532.3 nm) as the excitation source and analysed by a WITec ALPHA300 RS confocal spectrometer in backscattering configuration. Holographic supernotch filters are applied to reject the Rayleigh and anti-stokes lines without using polarizers. Data is acquired using a 20X Zeiss achromatic objective with 600 groove/mm grating (spectral resolution = 3.3 cm^{-1}) by averaging 12 spectral acquisitions with 5 s of integration-time each. Laser power and data acquisition time are restricted to avoid laser-induced partial oxidation of Fe_3O_4 into maghemite, followed by hematite. Absorption spectra of the as-prepared samples are collected using a stable aqueous dispersion by employing a Shimadzu UV 3600 UV-Vis-NIR Spectrophotometer, whereas diffuse reflectance spectrum (DRS) of the commercial sample (S) is obtained using $BaSO_4$ as a reflectance standard.

Zero-field Mössbauer absorption spectra are recorded at a maximum relative speed of 14 mm s^{-1} using a constant acceleration drive (CMTE-250), equipped with a 25 mCi ^{57}Co source diffused in Rh matrix. The instrument being placed in an indigenously made vibration-free stand; is calibrated with a natural iron-foil at room temperature. Using a closed cycle refrigerator (APD Cryogenics, USA), the measurement temperature is maintained to (300.0 ± 0.5) K. The as-obtained spectra are fitted with Recoil and Fit;o) program using Lorentzian profile. Hysteresis properties of polarization are found in the Precision Premier II ferroelectric tester (maximum voltage = 10 kV) from Radiant Technologies, Inc. using standard bipolar waveform. Data is recorded at different electric fields below the breakdown strength. A KEYSIGHT InfiniiVision DSOX2012A digital storage oscilloscope is employed for the electrical

data-acquisition of the as-fabricated nanogenerators. Dielectric measurements are done using an Agilent 4294A precision impedance analyser.

4.2.3 Computational details

In the density functional theory (DFT) calculations, as implemented in the Vienna *ab-initio* simulation package (VASP);[28,29] projector augmented wave (PAW) method[30] is used to represent the electron-ion interactions. All exchange-correlation terms are treated within the generalised gradient approximation (GGA) using the Perdew-Burke-Ernzerhof (PBE) functionals for both DFT and DFT+U approach.[31] We selected $U = 3.50$ eV for strongly correlated Fe 3d electrons based on previous reports.[32,33] All calculations are carried out in spin unrestricted manner and for dispersive force corrections, the PBE+D2 force field (Grimme's) method is considered.[34] The first Brillouin zone is sampled with a Γ-cantered k-point mesh of $(6 \times 6 \times 6)$ and $(3 \times 8 \times 1)$ during the geometrical optimization of pristine Fe_3O_4 and PVDF respectively, although for the larger Fe_3O_4/PVDF composite system, a minute $(1 \times 1 \times 1)$ mesh is used. The plane-wave basis set with cut-off energy 600 eV is used and the corresponding structures are allowed to be fully relaxed until the energy converges to 0.1 meV atom^{-1}.

4.3 Results and discussion

4.3.1 Bijective correlations of distinct physio-chemical characteristics with size of MNPs

4.3.1.1 Size-determination of Fe_3O_4 crystallites and nanoparticles

All diffraction peaks are indexed according to the inverse-spinel structure of magnetite (JCPDS card no. 85-1436) without detection of any additional peak, confirming purity of phase. The regular increase in full width at half-maximum (FWHM) with decreasing particle size is clearly visible in Figure 4.1(a). The average crystallite-size (d_{WH}) and strain (ε) are given by the Williamson-Hall equation considering spherical morphology:

$$\beta \cos\theta = 4\varepsilon \sin\theta + 0.89\frac{\lambda}{d_{WH}}, \tag{4.1}$$

where, β is the FWHM of Bragg peaks, θ is the diffraction-angle and $\lambda = 1.5406$ Å (Cu k_α). Depicting $\beta \cos\theta$ vs $\sin\theta$ plot, d_{WH} and ε are respectively obtained from the intercept and slope of the straight line. The values of d_{WH} are listed in Table 4.1 for all the samples. Changes in ε are negligible and random with size.

The mean size calculated from DLS is not only due to the particle itself, but also because of the hydrated/solvated corona formed at the surface; known as hydrodynamic size (d_H). It is defined as the diameter of a hypothetical hard sphere that diffuses with the same speed as the

particles assayed under DLS and hence seems larger always.[35] The joint effects of PEG-chain & tartrate ions increase solubility and stability in aqueous suspension by building a polar core-shell structure around MNPs, elaborated schematically in Figure 4.1(b). It causes an increment in d_H up to $10 - 15$ nm due to agglomeration of circumambient H_2O molecules.

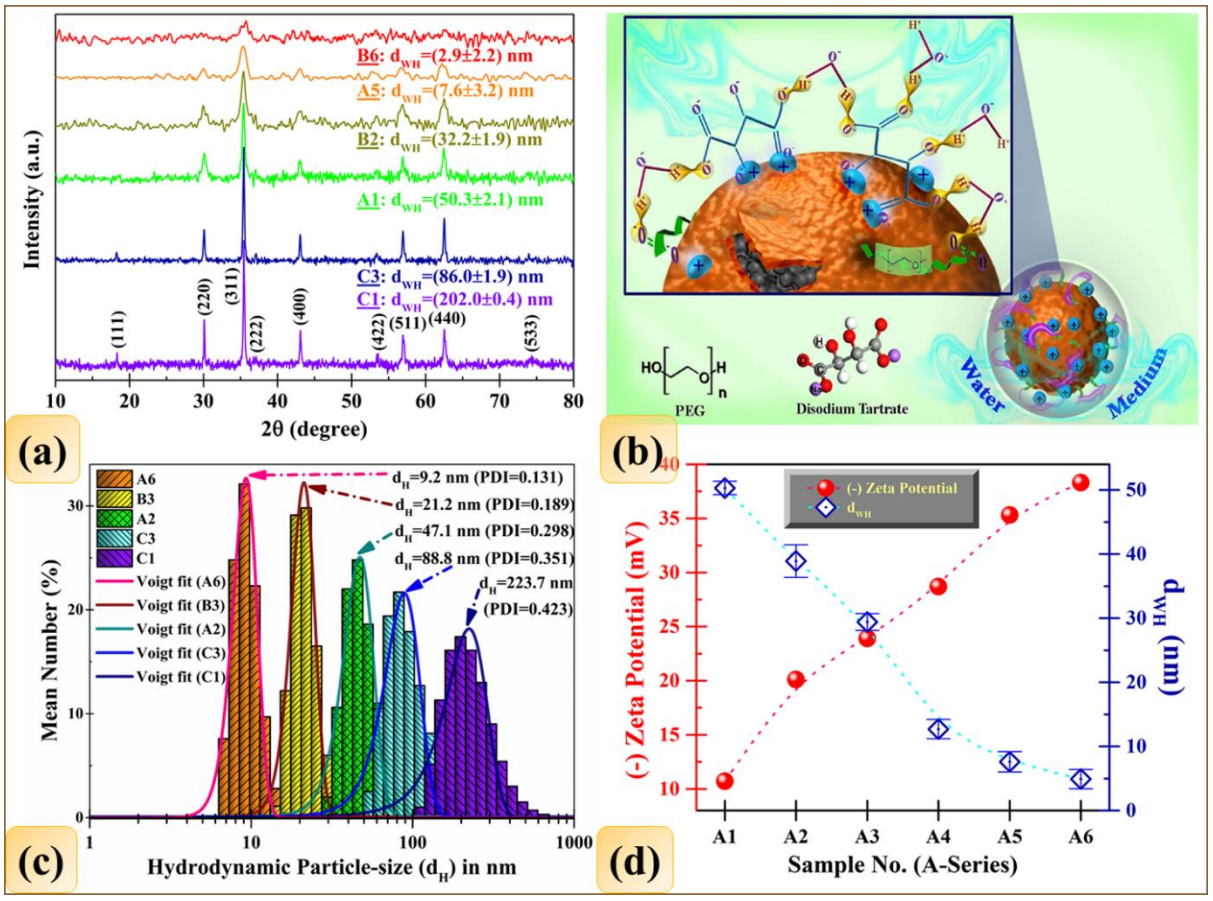

Figure 4.1 (a) X-ray powder diffraction pattern shown for six selected samples. The variation of FWHM of Bragg peaks is massive and used to determine the crystallite-sizes from Williamson-Hall equation; (b) Schematic: PEG chain and tartrate ions playing major role in polarizing the nanoscopic surface of Fe_3O_4; which promotes high water-dispersibility; (c) Number-distribution of hydrodynamic diameter of spherical nanoparticles in neutral pH shown for five samples, selected from all three series; (d) Variation of zeta potential and crystallite-size for the samples from A-series. Higher concentration of coating agent controls growth and also enhances surface-charge density. Dotted lines are guide to the eye.

In Figure 4.1(c), number-distribution of size-modulated particles for five selected samples is fitted with the Voigt function to estimate the most probable hydrodynamic size. This probability-distribution function is a convolution of Cauchy-Lorentz & Gaussian symmetries. Polydispersity Index (PDI), a measure of the distribution of molecular mass in a given sample, indicates the uniformity of colloidal dispersion. Generally, a dispersion with PDI ≤ 0.2 are likely

to be monodispersed, as observed for the smaller nanoparticles, see Figure 4.1(c). The decrease in FWHM & PDI for the smaller variants synthesized by microwave irradiation resembles monodispersity.

According to the synthesis protocol, the regular decrease in size is demonstrated in FESEM and HRTEM images, see Figure 4.2. The polycrystalline samples prevail spherical morphology, because of the tartrate ions in polyol environment. From the Voigt fit of particle size distribution, most probable size (d_{EM}) is determined, ranging between 3.7– 242.8 nm. The HRTEM images, exhibiting well-resolved lattice fringes with 0.25 nm interplanar spacing corresponding to the (311) plane and SAED patterns reveal high crystallinity.

4.3.1.2 Addressing surface-charge development due to functionalization

Zeta potential (ZP) i.e., an electro-kinetic potential at the shear/slipping plane around a colloid-particle moving under an electric field; specifies the surface-charge and estimates stability of the dispersion.[35] It is calculated by determining mobility using Debye's law:

$$\psi = \zeta e^{-\kappa r}, \tag{4.2}$$

where, $\psi =$ surface-potential, $\zeta =$ ZP, $\kappa =$ Debye-Hückel parameter; related to the ionic strength and $r =$ distance from the core-surface (Stern layer). Pure Fe_3O_4 does not dissolve/disperse in solvents like water, ethanol, chloroform, acetone *etc*. It only dissolves in acidic medium. Naturally, the magnitude of ZP in distilled water is only a few mV for pure Fe_3O_4. But after surface-functionalization, it hikes up to –38.3 mV, indicating formation of exemplary water-stable (for days) polar core-shell nanostructures. Figure 4.1(d) shows the continuous ZP increase of the A-series samples with higher concentration of surfactants and lower size in neutral pH. The negative surface-charge indicates formation of an outer layer, where the carboxylate (R–COO) groups grafted in tartrate and PEG are facing water molecules, providing hydrophilic properties to MNPs.

A thorough XPS survey for the sample-A2 detects Fe 2*s*, 2*p*, 3*s* and 3*p*-peaks along with an Auger peak; as well as peaks of 1*s* orbitals of C and O, see Figure 4.3. Using CasaXPS software, calculation of atomic percentage reveals synthesis of near-stoichiometric magnetite ($Fe_{2.97}O_4$), infrequent in scientific literature. The off-stoichiometry parameter (δ) for non-stoichiometric magnetite [$Fe_{3(1-\delta)}O_4$] has not exceed 0.025 for the tested samples of different size, which indicates that, the oxidation state of Fe remains unaffected by the change in surface-to-volume ratio, in accord with other reports.[32,36] The $2p_{3/2}$ peak of high-spin ferrous/ferric compounds undergoes broadening compared to metallic $Fe^{(0)}$ or low-spin Fe^{2+}. Gupta and Sen explained such broadness as an outcome of electrostatic interactions or spin-orbit coupling among the 2*p* core-hole and unpaired 3*d*-electrons inside the photoionized cation due to crystal-field interactions.[37]

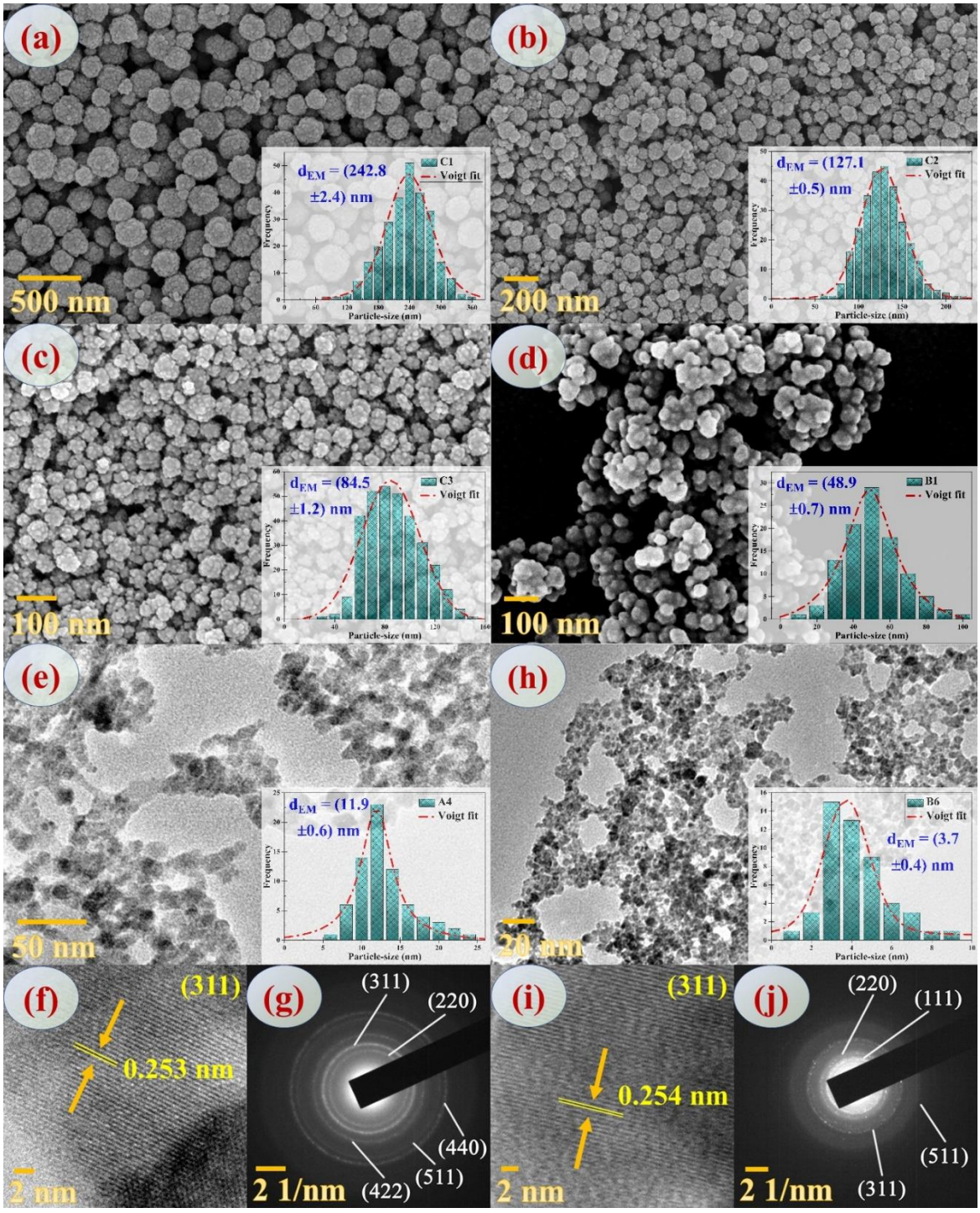

Figure 4.2 (a) – (d) FESEM micrographs for the samples C1, C2, C3 and B1 respectively. From the Voigt fit of particle size distribution, average size is determined; (e) TEM view of the sample A4 with particle size distribution; (f) HRTEM image of the lattice fringes for the sample A4, growth of the (311) plane is predominant; (g) SAED pattern for the same sample showing preponderance of a few lattice planes in the reciprocal space. Despite polycrystallinity, signatures of different lattice planes are well-resolved; (h) – (j) TEM, HRTEM and SAED results of the smallest sample (B6) with d_{EM} = 3.7 nm only. Growth of lattice planes is comparable to the previous sample.

While analysing high-pressure behaviour of magnetite, Bengtson *et al*. has established the spin-state of iron in Fe_3O_4 to be high based on *ab initio* calculations.[38] Moreover, partially filled *d*-orbitals initiate complex multiplet splitting, also contributing to the peak-structure. Thus, to pursue rigorous analysis, the high resolution XPS spectra of Fe $2p_{1/2}$ and $2p_{3/2}$ peaks are deconvoluted into three components each (keeping in mind, the simultaneous presence of 2+ and 3+ oxidation states with two species having tetrahedral and octahedral occupancies) along with 3 satellite peaks with a squared deviation of $\chi^2 = 0.98$ using Shirley background.

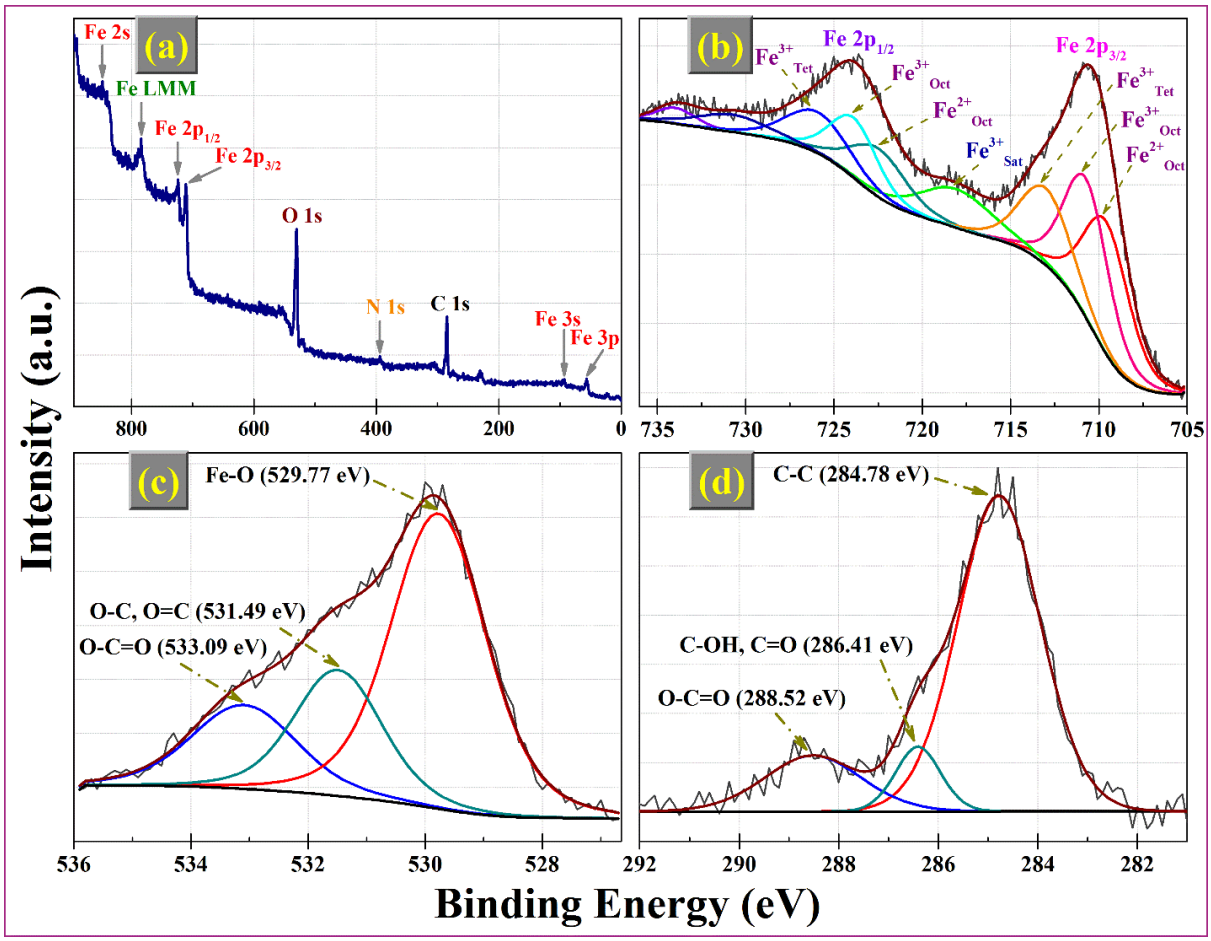

Figure 4.3 X-ray photoelectron spectra for the sample A2: (a) Elemental survey scanning. Trace of C, N, O, and Fe detected; (b) High resolution scan of Fe 2*p* band, deconvoluted into tetrahedral and octahedral contributions along with a Fe^{3+} satellite peak; (c) & (d) HR scans of O 1*s* and C 1*s* peaks and their deconvolution to distinguish the respective contributions of lattice bonds and capping agents. Signature of particular bonds present in carboxylate groups of PEG and tartrates are illustrated.

The $2p_{3/2}$ peak is a convolution of 3 components *viz*., 709.57 (Fe_{Oct}^{2+}), 710.71 (Fe_{Oct}^{3+}) and 713.01 eV (Fe_{Tet}^{3+}); whereas the $2p_{1/2}$ peak is resolved into components at 722.46 (Fe_{Oct}^{2+}), 723.88 (Fe_{Oct}^{3+}) and 725.93 eV (Fe_{Tet}^{3+}). These values are close to previous literature.[32,39] The

satellite at 718.08 eV is assigned to the surface-peak of γ-Fe_2O_3 due to unavoidable partial oxidation at the outer surface of MNPs, common in most TMO's. From CasaXPS, the ratio of relative intensities of the three iron species is found to be $Fe_{Oct}^{2+}: Fe_{Oct}^{3+}: Fe_{Tet}^{3+} = 1: 1.03: 0.77$, which is quite close to the predicted unity ratio. The little higher Fe^{2+}/Fe^{3+} ratio may be attributed to the surface reduction under ultrahigh vacuum conditions.

The O 1*s* XPS spectrum is fitted into three peaks having binding energies 529.77, 531.49 and 533.09 eV with a squared deviation of $\chi^2 = 0.91$. The most intense peak at 529.77 eV corresponds to the lattice oxygen in Fe_3O_4. The remaining two peaks result from oxygen atoms in mono/bidentate carboxylate groups present in the surfactants used. The high-resolution C 1*s* spectrum displays another three peaks at 284.78, 286.41 and 288.52 eV. The most intense one at 284.78 eV is assigned to the carbon atoms of aliphatic –C–C bonds, while the rest two are attributed to –C-OH, -C=O and –O-C=O groups present in PEG and tartrate ions respectively.

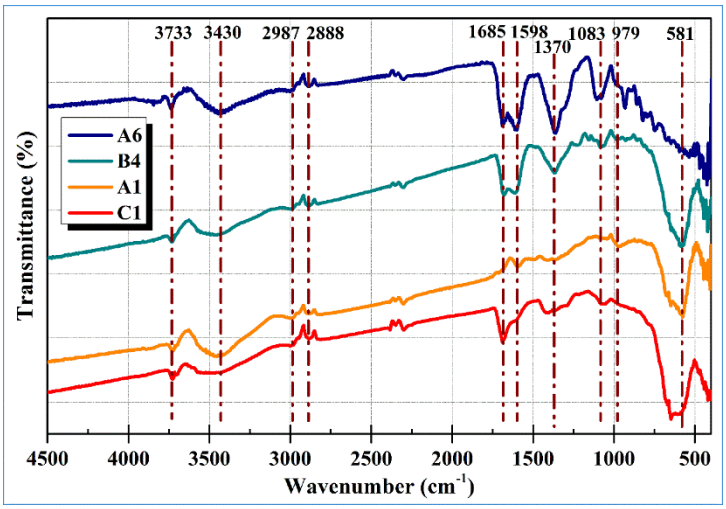

Figure 4.4 FTIR spectra for four selected samples. Lattice vibrations due to specific mono- and bidentate carboxylate groups are classified for all samples.

4.3.1.3 Fourier-transform infrared (FTIR) spectroscopy

The spectra show intense characteristic absorption peaks at 581 and 1370 cm^{-1} referring Fe-O bending & stretching vibrations respectively, see Figure 4.4.[40] The peak at 979 cm^{-1} arise due to the bending vibrations of =C-H & C-C-O groups and the 1083 cm^{-1} peak is assigned to C-O-C axial deformation and aliphatic bending vibrations. The bands at 1598 and 1685 cm^{-1} can be attributed to –COO– stretching, bending of water molecules absorbed on the surface of MNPs and C=O stretching. The symmetric/asymmetric stretching of the methylene (=CH_2) group and C-H stretching result the respective peaks at 2888 and 2987 cm^{-1}, whereas the bands near 3430 and 3733 cm^{-1} indicate stretching and bending vibrations of hydroxyl groups, which represent the characteristic peaks of PEG too.[40] Therefore, FTIR spectra confirms successful formation of tartrate-coated and PEGylated MNPs.

4.3.1.4 Thermogravimetric analysis (TGA) & difference thermogravimetry (DTG)

In presence of open air or oxygen, pure Fe_3O_4 gets easily oxidized under heat-treatment and generates Fe_2O_3 polymorphs. This process gets decelerated, acted by suitable organic coating or in presence of inert atmosphere. For a quantitative overview of the carboxylate groups bound to the surface, TGA is performed in N_2-atmosphere from room-temperature to 1000 °C in 2 h.

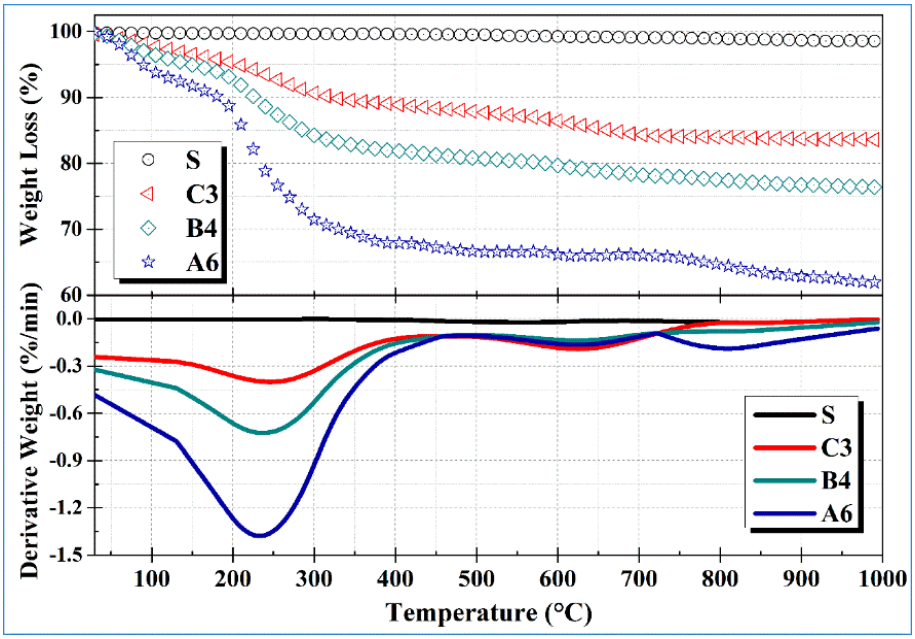

Figure 4.5 TGA-DTG results in inert atmosphere for three synthesized samples in comparison with the commercial sample (S) having no surface-coating. Growth of the smaller nanoparticles is restricted by thicker coating in the core-shell structure. The organic coating gets decomposed at high temperature resulting larger weight loss; whereas the commercial sample remains intact.

As depicted in Figure 4.5, a large weight loss up to 38 wt% is observed for the smallest MNPs. In contrast, much smaller loss is found for the solvothermally prepared sample (C3) with lesser amount of surfactants. The commercial sample (S) without surface-coating; produces almost no loss in N_2. It is thus demonstrated that considerable amount of carboxyl salt is bound to the surface of MNPs. The weight loss below 200 °C is attributed to the adsorbed water at the surface. The main weight loss at 200– 300 °C is due to the decomposition of tartrate, whereas PEG undergoes a slow and steady decomposition in the range 180– 900 °C.[21] The small peak near 630 °C might arise because of reduction to FeO, which is thermodynamically more stable than Fe_3O_4 above 570 °C in phase-diagram of Fe-O system. Another tiny derivative peak near 800 °C possibly signifies deoxidation of FeO in N_2 environment. FTIR and thermogravimetry altogether confirm successful formation of tartrate-coated and PEGylated MNPs.

4.3.1.5 Mössbauer analysis and size-controlled magnetic nature

The ^{57}Fe Mössbauer absorption spectra can efficiently designate size-dependent magnetic properties. The hyperfine magnetic field (HMF) and related parameters can be extracted without application of an external magnetic field, only by fitting the zero-field data using Recoil and Fit;o) software below the magnetic ordering temperature.[41] The refined values are enlisted in Table 4.2. Mössbauer spectra mainly incorporate three hyperfine interactions, having distinct origins *viz*. chemical/isomer shift (IS), quadrupole splitting (QS), and magnetic hyperfine interaction. The spectrum for the larger MNPs exhibit a superposition of two distinct hyperfine Zeeman sextets corresponding to the tetrahedral (A) and octahedrally coordinated (B) sites; whereas the smaller nanoparticles show only a single superparamagnetic quadruple doublet, depicted in Figure 4.6(a) – (b).

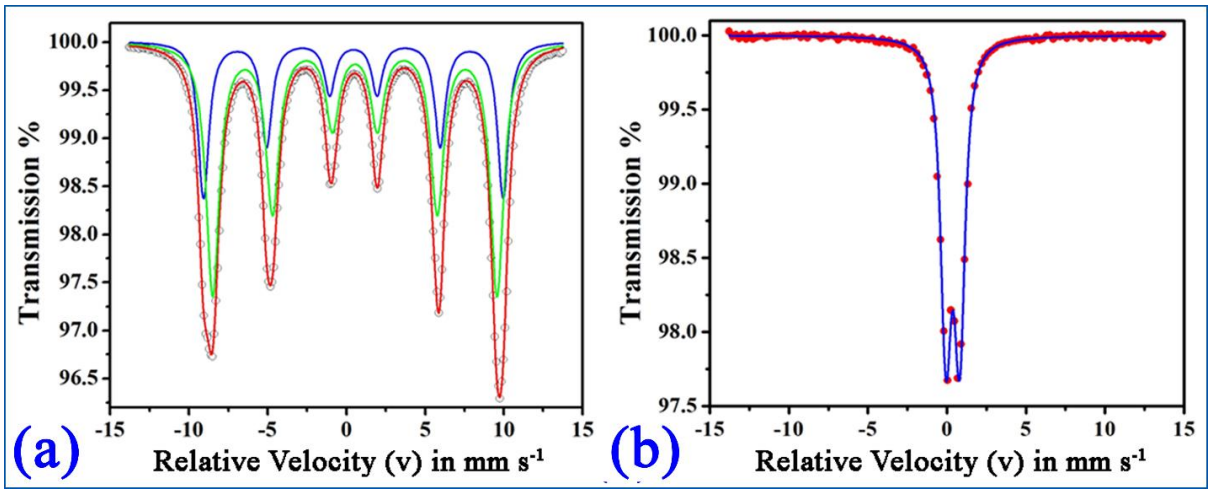

Figure 4.6 (a) Zero-field Mössbauer spectrum for bigger ferrimagnetic nanoparticles, recorded at 300 K. Open circles represent the experimental data and the continuous lines correspond to the computed Lorentzian fit of the Zeeman sextets; (b) Spectrum for the tiny nanoparticles. Pure quadrupole splitting ensures superparamagnetic nature.

IS-values vary between 0.37 – 0.55 mm s^{-1} within instrumental or computational error, suggesting the presence of high spin $Fe^{(III)}$ ions. There is a specific difference in the IS of the two cationic co-ordinations due to prior difference in the surrounding chemical environment of the interacting nuclei. In cubic spinel ferrites, the Fe 3*p* – O 2*p* bond-separation is larger for B-sites; resulting a smaller overlapping between orbitals and larger IS. Moreover, the IS-values hint at slight presence of maghemite in the composition of larger MNPs. The quadrupole splitting (QS) is found for the tiny nanoparticles, although for the larger MNPs splitting is either absent or undetectable due to the broadening of the sextet. In an ordered magnetic system, the intrinsic magnetic fields arise predominantly from the Fermi contact-interaction between the nucleus and the surrounding spin-polarized *s* electrons.[41] Thus, the nuclear magnetic field is

proportional to the atomic magnetic moments and the mean field for all the ions in a particular sub-lattice is proportional to the average magnetization.

Table 4.2 Refined hyperfine parameters obtained by fitting Mössbauer spectra

Sample	Nature of the spectra	IS (±0.03) [mm s^{-1}]	QS (±0.01) [mm s^{-1}]	HMF (±0.2) [T]	Width (±0.04) [mm s^{-1}]	Area fraction (±0.2) [%]
C1 ($\boldsymbol{D_{EM} = 242.8\ nm}$)	Sextet A	0.45	0.0	59.0	0.40	33.3
	Sextet B	0.55	0.0	56.0	0.50	66.7
A6 ($\boldsymbol{D_{EM} = 5.5\ nm}$)	Doublet	0.37	0.87	–	0.35	100

Bulk magnetite characteristically shows, two separate 6-line magnetic hyperfine patterns *viz*. sextet A and B, ideally in the ratio $\frac{I_A}{I_B} = 0.5$.[42] However, the actual ratio may be higher or lower due to different Mössbauer fractions of the respective sites and non-stoichiometry present in the system, respectively. For a material, that consists of particles having a wide range of dimensions, the sextet and quadrupole doublet area fractions inflict a signature of the respective population of larger ferrimagnetic and smaller superparamagnetic particles. The hyperfine interactions and splitting depend on three factors: (a) size of nanoparticles, (b) temperature and (c) time of observation/measurement. For C1, only two sextets are found implying absence of tiny superparamagnetic nanoparticles, whereas for A6 only quadrupole splitting is obtained indicating absence of large particles or congruent agglomeration. Samples with intermediate size should develop results in between. Inherent magnetic anisotropy in nanoparticles, redirects the magnetic moment to pursue only two stable orientations opposite to each other, separated by an energy barrier, which forms the magnetic easy axis. At a finite temperature, empowered by the thermal energy, the system possesses finite probability to change the orientation via jumping through the barrier. The average time between two successive jumps is the so-called Néel relaxation time (τ_N) of nuclear magnetic moment at HMF.[43] It depends on the average particle dimension (V), effective magnetic anisotropy energy-density (K_{eff}) and temperature (T); according to the Néel–Arrhenius equation:

$$\tau_N = \tau_0 exp\left(\frac{K_{eff}V}{k_B T}\right), \tag{4.3}$$

where, k_B is the Boltzman constant and τ_0 is the characteristic attempt period of the material. Now for any assembly of magnetic nanoparticles, the nature of the Mössbauer spectrum depends on the relation between τ_N and time of measurement (t_m), which is effectively same as

the Larmor precession time (τ_L). For ^{57}Fe Mössbauer spectroscopy, τ_L~1 ns. As τ_N is an exponential function of the grain-volume (V), the magnetic moment of smaller nanoparticles is more likely to encounter rapid flipping at a moderate temperature. If the duration of measurement, $t_m \gg \tau_N$ for a particular temperature, the magnetic moment can flip several times during the course of measurement, making its time-average drop to zero. However, an external magnetic field will develop a high magnetization and large susceptibility, implying the superparamagnetic state. Contrarily if $t_m \ll \tau_N$, the moment does not get enough room to flip around and the initial magnetic state of the system gets frozen or 'blocked'. During most experiments, t_m is kept fixed depending on the instrument and hence temperature or associated thermal fluctuations decide the superparamagnetic or blocked state of the magnetic system. Therefore, the temperature below which a particle becomes superparamagnetic *i.e.*, attains a steeper magnetization curve with large susceptibility and zero hysteresis area, is called the blocking temperature (T_B) and can be calculated from,

$$T_B = T|_{t_m \cong \tau_N} = \frac{K_{eff}V}{k_B \ln\left(\frac{t_m}{\tau_0}\right)} \approx \frac{K_{eff}V}{25k_B}. \quad (4.4)$$

The fluctuations in magnetization slower than the Larmor hyperfine frequency (ν_L) collapse the multiplet to a superparamagnetic doublet, suggesting T_B to be somewhat lower than the sample-temperature. The spectral peaks might broaden at a specific temperature, if the onset of superparamagnetic fluctuations overcomes the magnetic anisotropy barrier for the material. Hence, state of superparamagnetism is inevitable for smaller nanoparticles, higher temperature and longer duration of measurement. Keeping the last two factors fixed, size-dependent magnetic nature is ventured.

4.3.1.6 Raman spectroscopy and phonon dynamics

The three principal polymorphs of iron oxide can be obtained simply by heating magnetite in presence of oxygen to specific temperatures as:

$$Fe_3O_4 \xrightarrow{\geq 200°C} \gamma - Fe_2O_3 \xrightarrow{\geq 450°C} \alpha - Fe_2O_3$$

The laser-beam with micron-order diameter causes local heating at the point under observation, which makes it reach the threshold temperature for a phase-change. Shebanova and Lazor studied this laser-induced oxidation of Fe_3O_4 by varying laser-power and time of measurements.[44] Although it is observed that, samples with thicker surface-coating are less prone to thermal oxidation or compromised sample-quality in ambient atmosphere; laser-power is kept below 2 mW during measurements. According to the inverse spinel structure of Fe_3O_4, the irreducible normal modes of vibration at the first Brillouin zone-centre are given by, $\Gamma_{vib} = A_{1g} + E_{1g} + T_{1g} + 3T_{2g} + 2A_{2u} + 2E_u + 4T_{1u} + 2T_{2u}$.[32] The pronounced band at 670 cm^{-1} is assigned to the A_{1g} mode, whereas the features at 201, 318 and 542 cm^{-1} are quite weak for all

samples and are attributed to the three T_{2g} modes.[45] There is a clear red-shift of 13.48 cm^{-1} and higher degree of asymmetry in the A_{1g} peak with the decrease in particle size, as shown in Figure 4.7(a).

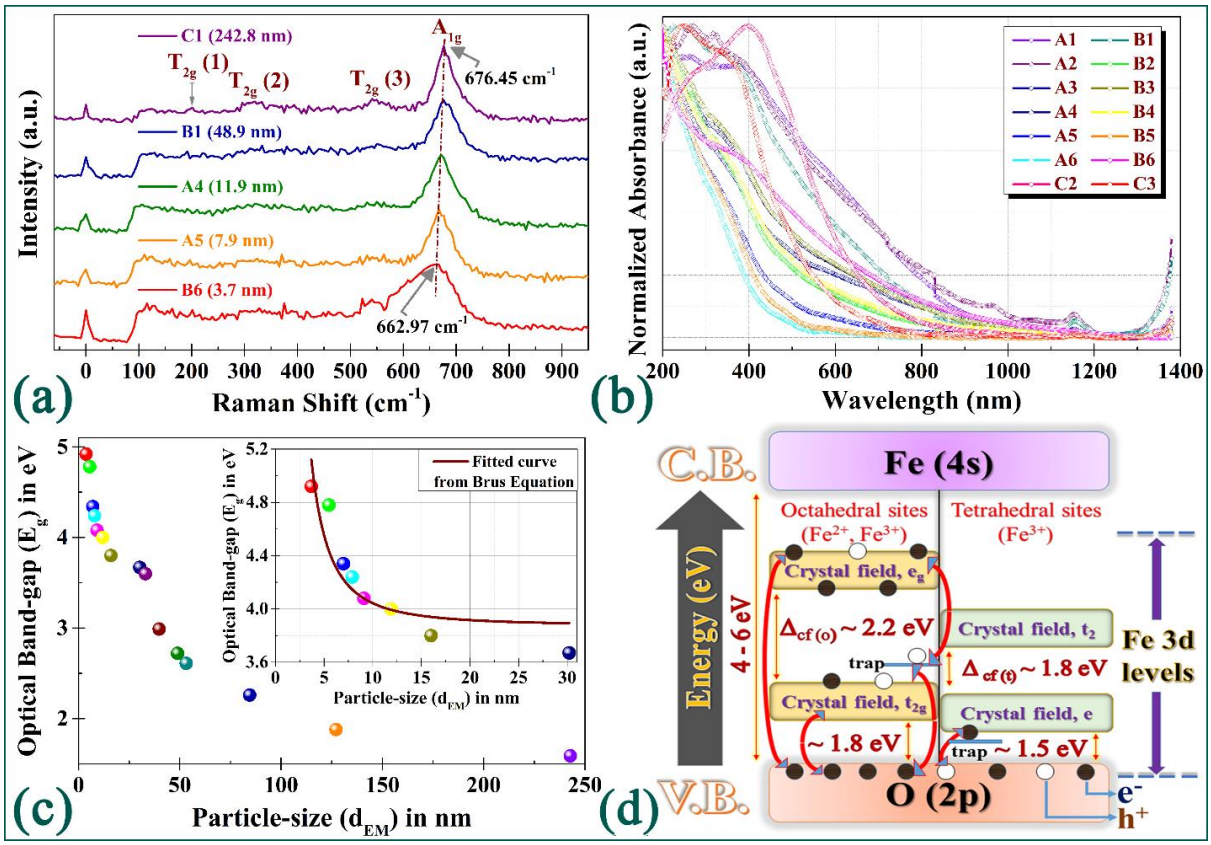

Figure 4.7 (a) Room-temperature Raman spectra for five selected samples. As size decreases below 20 nm, red-shifting and development of Fano asymmetry is clear in the A_{1g} peak; (b) Absorbance spectra in UV-Vis-NIR region for all samples; being dispersed in deionized water; (c) Band-gap vs particle size plot for all samples. Inset: fitting of the respective data near quantum regime using Brus equation to determine effective mass of electron-hole bound system; (d) Schematic of the energy bands generated as a result of crystal field splitting in nanoscale Fe_3O_4 system.

The Raman line-shape of A_{1g} mode for bulk sample is Lorentzian, but as the particle size outreaches < 15 nm, a thorough downshift and asymmetric broadening at the low-frequency side is observed, which can be better described by the Breit-Wigner-Fano (BWF) profile.[46] If the oscillators are interacting with another mode or a continuum of modes, the line-shape may be strongly altered, giving rise to the Fano asymmetry, as the actual spectral shape depends on the electron-phonon coupling strength. Such asymmetric peaks might appear for three reasons: (a) a laser heating effect causing Fano interference between optical phonons scattered from the $q = 0$ plane and electronic continuum scattering due to the laser-induced electrons in the

conduction band. Gupta *et al*. has described this effect on Si nanowire samples for > 3 mW laser power.[47] But certainly this is not our case, as to avoid oxidation the laser power is intentionally kept nominal; (b) Disorder effects leading to reduced phonon correlation length. In disordered systems, lack of translational invariance activates the forbidden modes. But, for surfactant-controlled orderly growth of magnetite, this possibility is crossed out; (c) Phonon confinement (quantization) effect: In Richter's phonon confinement model (PCM), the confined phonon wavefunction leads to a breakdown of selection rules at the Brillouin zone-centre ($q = 0$) as found in bulk material.[48] For such relaxation in selection rules due to confinement induced uncertainty, other phonons having different frequencies from the same branch are 'activated'. This leads to an asymmetric broadening and red-shifting of the Raman band as prescribed by Campbell and Fauchet's modified model (MPCM).[49,50] The Raman intensity as a function of frequency (ω) and crystallite size (d) can be expressed as:

$$I(\omega, d) = A\frac{\rho(\omega)}{d^3}\int_{2\pi-1}^{2\pi+1} \frac{4\pi q^2\left[\frac{\sin\left({}^{q}/_{2}\right)}{q(4\pi^2 - q^2)}\right]^2\left(\frac{\Gamma}{2}\right)}{[\omega - \omega'(q)]^2 + \left(\frac{\Gamma}{2}\right)^2} dq, \tag{4.5}$$

where, $\rho(\omega)$ corresponds to Bose-Einstein occupancy, Γ is the asymmetric linewidth i.e., the sum of symmetric and asymmetric half-widths, A is a constant and a suitable dispersion relation is required for $\omega'(q)$ depending on the material. Intensity is calculated by appropriately choosing weighing functions and integration limits on the wave-vector. In this model, the fundamental requirement of phonon confinement is, the phonon mean free path must be greater than the particle size, which is feasible for the smallest MNPs.

4.3.1.7 Size-dependent optical properties

The samples show a broad absorption pattern at 200-600 nm [Figure 4.7(b)], mainly in the UV-range, which is attributed to the *d*-orbital transitions of Fe_3O_4. Thereafter a steady downfall with increasing wavelength is captured, except for a small peak near 1150 nm, which can be ascribed to the electron-traps in the tetrahedral sites; originated because of oxygen-vacancies. The allowed direct optical bandgap (E_g) can be calculated using Tauc's equation:

$$(\alpha h\nu)^2 = A^2\left(h\nu - E_g\right), \tag{4.6}$$

where, α is the absorption coefficient, defined as 2.303 times absorbance per unit length and A is a proportionality constant. By plotting $(\alpha h\nu)^2$ vs $h\nu$, a straight line is obtained at the absorption band-edge, by extrapolating which, $E_g = h\nu|_{\alpha=0}$ is determined. A continuous increase in bandgap from 1.59 to 4.92 eV is observed with decreasing particle size from bulk to quantum regime. In bulk materials, bands encompass quasi-continuous energy levels of a large ($\sim 10^{23}$) number of atoms/molecules. As the particle size reaches nano-regime, where every particle consists of a tiny number of atoms/molecules, the overlapping of orbitals or energy

levels decreases, and the width of the band gets narrower. This causes an increase in energy-gap between the valence band and the conduction band, which explains the higher bandgap (E_g) in nanoparticles than its bulk counterpart. So, there is a blue-shift of absorption spectrum with decreasing particle size. As the width of the forbidden region increases, the electrons' motion gets more and more restricted. So, nanoparticles generally exhibit lower electrical conductivity than the bulk.

For ultra-small nanoparticles, quantum confinement and excitonic effects often play a key-role in optical properties at room-temperature in contrast to bulk semiconductors.[51] In the strong confinement regime, the electrons and holes are treated as individual particles and the Hamiltonian for such low-dimensional systems is given by,

$$H = -\frac{\hbar^2}{2m_e^*}\nabla_e^2 - \frac{\hbar^2}{2m_h^*}\nabla_h^2 + V_e + V_h - \frac{e^2}{4\pi\varepsilon|r_e - r_h|}, \tag{4.7}$$

where, effective masses of electrons and holes are m_e^* & m_h^* and ε is the permittivity. Nanda *et al.* have used the effective mass approximation (EMA) with finite-depth square-well potential to scrutinize the size-dependent bandgap (SDBG) for narrow and wide band-gap semiconductor candidates and found that EMA is more suitable for near-insulating materials having lower dielectric constant.[52] For semiconductors with larger dielectric constant and carrier-density, quantum effects can be estimated more precisely using the excitonic model and the Brus equation; given by,

$$E_g^{(nano)}(r) = E_g^{(bulk)} + \frac{h^2}{8r^2}\left(\frac{1}{m_e^*} + \frac{1}{m_h^*}\right) - \frac{1.786e^2}{4\pi\varepsilon r}, \tag{4.8}$$

$$\therefore \Delta E_g(d) = \frac{h^2}{2\mu^* d^2} - \frac{1.786e^2}{2\pi\varepsilon_0\varepsilon_r d}, \qquad \text{where } \frac{1}{\mu^*} = \frac{1}{m_e^*} + \frac{1}{m_h^*} \text{ and } \varepsilon_r = \frac{\varepsilon}{\varepsilon_0}, \tag{4.9}$$

for spherical particles of diameter $d = 2r$ and μ^* being the reduced effective mass of the electron-hole bound system or exciton. The first term in equation 4.9 represents the particle-in-a-box quantum localization energy ($\sim d^{-2}$), whereas the 2nd term describes the binding energy of an exciton due to Coulomb attraction ($\sim d^{-1}$). Materials like Fe_3O_4 having small carrier effective mass and large dielectric constant, the first term predominates. The optical bandgaps so obtained for the smaller MNPs are well-fitted with equation 4.9 for suitable values of $\mu^*(0.0219m_e)$ and $\varepsilon_r(\sim 10^2)$ [see Figure 4.7(c) and its inset], acceptable in accordance to preceding literature.[53]

Several researchers have probed the electronic bandgap (~0.1–0.3 eV) of halfmetallic magnetite above Verwey transition using both theoretical & experimental methods,[54,55] but the gap is too small to interfere with light of UV-Vis range. Hence, the optical bandgap determined from the absorption spectra is not the electronic gap between valence band maxima and conduction band minima, rather corresponds to particular optical transitions between crystal

field bands of the octahedral and tetrahedral sites, composed of 3d metal atomic orbitals. Jordan *et al.* employing scanning tunnelling spectroscopy on specific crystal planes of single crystalline magnetite have shown that, surface disorder and non-stoichiometry can alter the electronic signature of magnetite and calculated exchange energy (Δ_{ex}) between the crystal field levels of the associated majority and minority spins.[55] From laser-excited photoluminescence spectra; Sadat *et al.* proposed a model of Fe 3d levels sub-merged between the valence band of O 2p and empty Fe 4s levels, separated by an energy-gap of 4-6 eV.[56] Figure 4.7(d) shows the possible transitions in an approximate band structure of magnetite based on both experimental and theoretical DOS studies, which supports the range of band-gap so obtained with variation in size. The octahedral splitting energy ($\Delta_{cf\,(o)}$) is larger than the tetrahedral species ($\Delta_{cf\,(t)}$) due to its geometry and mainly contributes to the optical transitions [$e_g \leftrightarrow t_{2g} \leftrightarrow O(2p)$]. The splitting energies are size-dependent, and trap-states in between play a major role in the whole process.

The Urbach energy characterizes the extent of the exponential tail of the absorption edge and gives a measure of defect-density and trap-states present in the crystal that originates from thermal vibrations in the lattice, static/induced disorder & impurities.[56] Hence, it depends on temperature, strength of ionic bonds and average photon energies. But in crystalline materials, the principal factor that contributes to edge broadening is exciton-phonon coupling (dynamic disorder). Urbach energy (E_u) and the onset of exponential absorption tail (E_0) are given in accordance with the empirical relation between absorption co-efficient (α) and absolute temperature (T).

$$\alpha = \alpha_0 exp\left\{\frac{\sigma}{k_B T}(E - E_0)\right\} = \alpha_0 exp\left(\frac{E - E_0}{E_u}\right), \qquad \text{where } E_u = \frac{k_B T}{\sigma}. \tag{4.10}$$

$$\therefore \ln \alpha = \ln \alpha_0 + \frac{\sigma}{k_B T}(E - E_0). \tag{4.11}$$

Here, σ is the steepness parameter and k_B represents Boltzman constant. So, by plotting $\ln \alpha$ vs $E(=\frac{hc}{\lambda})$, we get a straight line with slope $=\frac{\sigma}{k_B T}$, the reciprocal of which determines Urbach energy.

The variation of E_u for a number of selected samples are shown in Figure 4.8. In our case, E_u depends on a number of competing factors such as crystal growth-time, concentration of surfactants, particle-size and surface to volume ratio. Decreasing reaction-time and increasing surface to volume ratio originates higher defect-density on the surface, whereas higher concentration of tartrate and PEG regularizes the growth-dynamics and controls defect-formation. Hence, although initially increases; an overall decreasing trend of E_u is observed with smaller size. On the other hand, E_0 does not explicitly depend on particle-size, but firmly reciprocates the crystal-field splitting energy of the Fe_{Oct} sites.

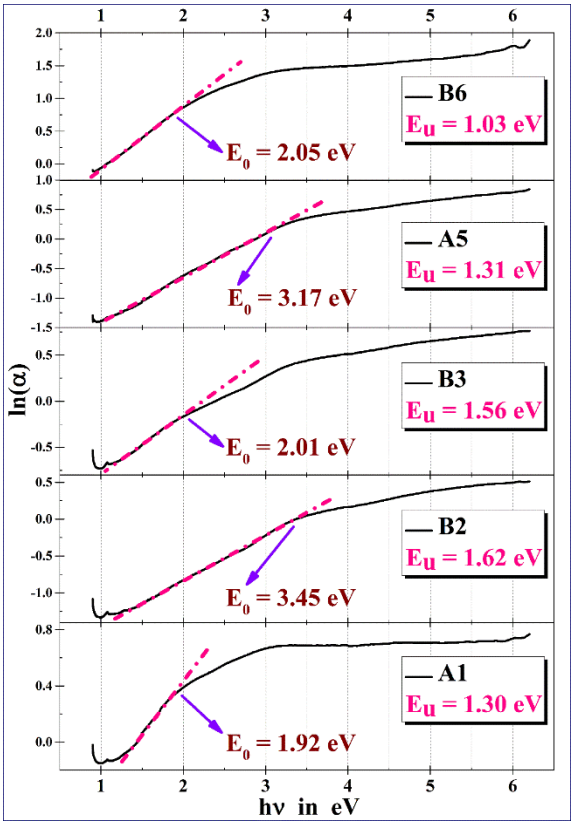

Figure 4.8 Determination of Urbach energy (E_u) and the extent of exponential absorption tail (E_0) from ln α vs excitation energy ($h\nu$) plots.

4.3.2 Fe_3O_4/PVDF nanocomposite-based self-poled PENGs

4.3.2.1 Quantitative structural assessment of polymorphic phases

MNPs of five different diameters (8.9, 30.2, 45.1, 78.6 and 149.0 nm) and three different amounts (4, 8 and 12 wt(%)) are chosen to produce 15 self-poled thin films by a simple solvent-casting technique and their piezoelectric performance is compared with the pure PVDF film. These films are way more uniform than that of commercial Fe_3O_4/PVDF.

The successful formation of Fe_3O_4/PVDF composite and quantitative analysis of the enhancement of β-phase with respect to α-phase are confirmed from XRD, FTIR and Raman spectra given in Figure 4.9(a)–(c) [for 30.2 nm particles]. XRD pattern of pure PVDF reveals the preponderance of α-phase with the characteristic (100), (110), (021) and (002) peaks at $2\theta = 17.99°, 19.90°, 26.56°$ and $39.03°$ respectively. Weak traces of γ [(020) & (002)] and β −phases are also detected, among which the (110) and (200) mixed planes at 20.28°, characteristic of β −phase are found to enhance vigorously with magnetite incorporation and for the 8 wt(%) film it dominates over the non-polar counterparts. Although it again gets suppressed a bit for higher concentration of magnetite. With increasing wt(%); (311), (220) and (111) planes of Fe_3O_4 develop gradually.

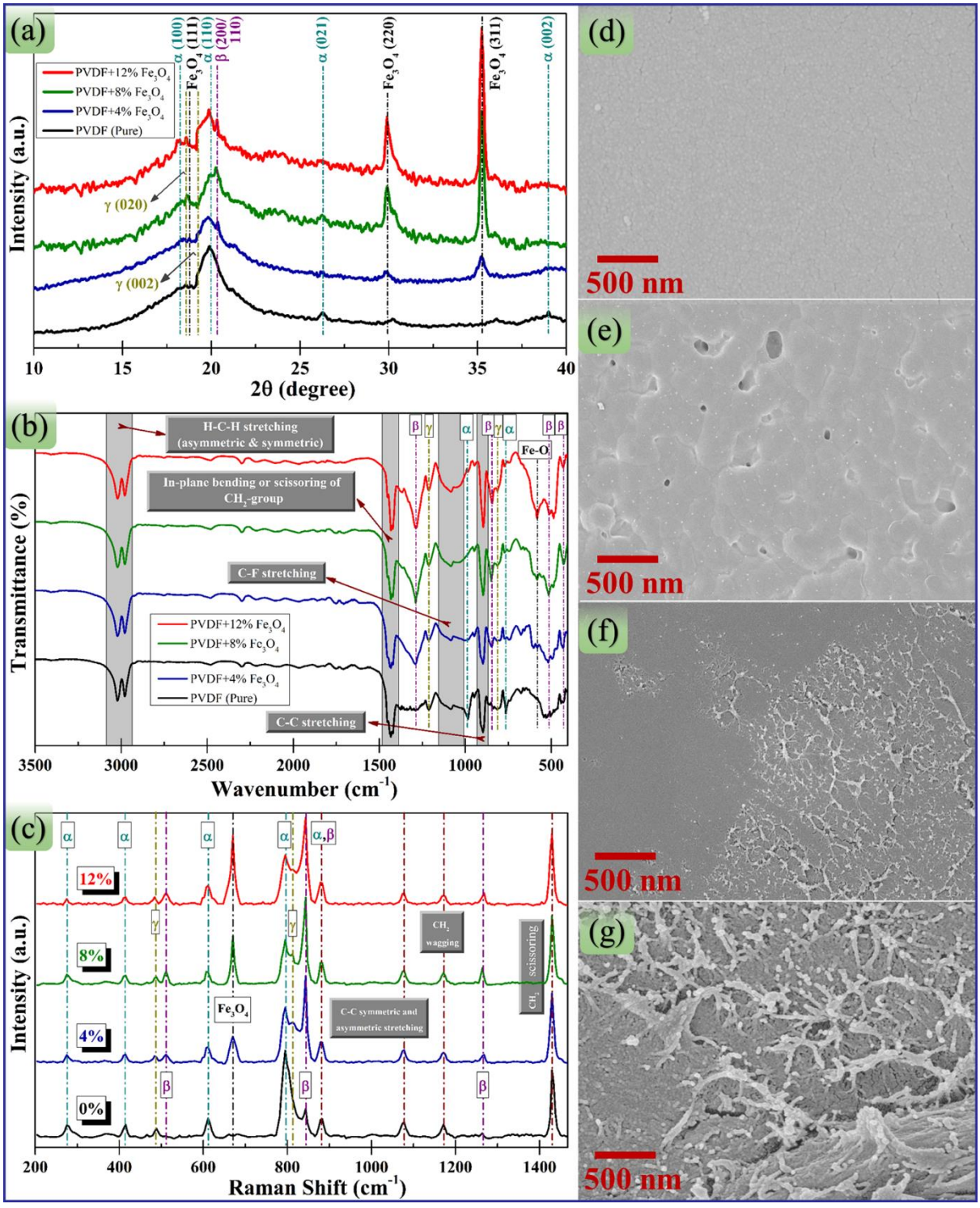

Figure 4.9 (a) – (c) XRD, FTIR and Raman spectra of the composite films with Fe_3O_4 nanoparticles of 30.2 nm average size embedded in PVDF matrix at different proportions. Signatures representing β-phase enhance with higher amount of magnetite incorporation in all cases, but suddenly drops for 12% film; (d) – (g) FESEM micrographs of the Fe_3O_4/PVDF nanocomposite films for 0, 4, 8 and 12 wt(%) magnetite (30.2 nm). For higher Fe_3O_4 concentration, traces of agglomeration and aggregation are found.

The key-features of PVDF and its composites can be distinguished on basis of the finger-print modes of molecular vibration using FTIR and Raman spectra.[57-60] There are some infrared active modes, which are common for all the PVDF polymorphs, such as in-plane bending, scissoring, symmetric & asymmetric stretching of CH_2-group and C-C or C-F stretching; whereas some characteristic modes of α, β and γ-phases can be useful in quantitative analysis, as shown in Figure 4.9(b). The successive augmentation of peaks at 844 and 1278 cm^{-1}; associated with the CH_2-wagging and CF_2-symmetric stretching vibrations; indicates formation of β −phase against the rise of Fe-O bending mode at 581 cm^{-1}. The evolution of β-bands at 445 & 510 cm^{-1} against declining α −bands at 764 & 976 cm^{-1} clearly indicates the change in relative proportions, although the γ −bands at 832 & 1234 cm^{-1} remain unaltered.

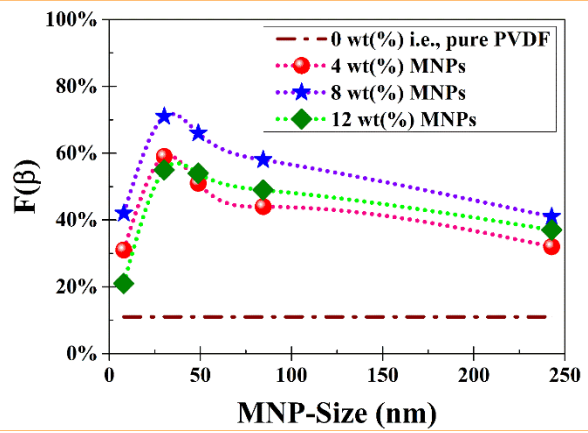

Figure 4.10 Quantitative comparison of β-phase content obtained from FTIR spectra for incorporation of MNPs with different size and weight ratio. The dotted lines are guide to the eye. The curves show, 30.2 nm MNPs at 8 wt(%) addition holds optimum results. Deviation from these parameters entails lesser enhancement.

FTIR analysis is the most abundantly used method to quantify all the electroactive phase-contents present in PVDF, although different researchers have performed such quantifications using versatile formulae following distinct distributions. As XRD and Raman spectra hint that, the γ −phase content is nominal and hardly differs against MNP-incorporation; the β −phase can be considered as the only major electroactive phase present in the system. Assuming that the FTIR absorption spectra follows the Beer-Lambert law, the following formula, used by several researchers is employed to calculate the relative fraction of the β −phase with respect to the non-polar α −phase.

$$F(\beta) = \frac{A_\beta}{\left(\frac{K_\beta}{K_\alpha}\right)A_\alpha + A_\beta} X100\%. \qquad (4.12)$$

Here, $F(\beta)$ is the exact β −content in percentage, A_α & A_β are the absorbance-values for the two phases and $K_\alpha (= 6.1 \times 10^4\ cm^2\ mol^{-1})$ & $K_\beta (= 7.7 \times 10^4\ cm^2\ mol^{-1})$ are the absorption

coefficients at the respective wavenumber of 764 & 844 cm^{-1}, which are the most prominent signatures of the associated phases. Using this formula, β −content is graphically presented as a function of both MNP-size and wt (%) in Figure 4.10. The results show high improvement in electroactive fraction (from 10.9% to 71.4%) against incorporation of MNPs, which is in agreement with the results obtained from the Raman analysis given in the main manuscript.

Another precise quantitative assessment of the relative proportions of different phases can be accomplished using the Raman spectra; as suggested by Barnakov and Ma *et al*.[59,60] The bands at 276, 413, 609 and 795 cm^{-1}; signifying CF_2 twisting/wagging, rocking, scissoring and CH_2 rocking vibrations, are characteristics of α-phase; whereas CF_2 scissoring, CH_2 rocking and C-C symmetric stretching & scissoring vibrations in the β-phase generate the bands at 511, 843 and 1272 cm^{-1}. Some weak bands at 485 and 812 cm^{-1} are also detected, confirming presence of γ-phase in a tiny proportion. The β-bands gain noticeable increment with magnetite's A_{1g} peak at 670 cm^{-1}. Among all these bands, 843 and 795 cm^{-1} are the most prominent and intense ones assigned for the β and α-phase respectively and their intensities can be employed to determine the relative proportion $\left(\frac{I_\beta}{I_\alpha}\right)$ of the two phases. For pure PVDF, the ratio is only 0.38, MNP-incorporation of suitable size and amount enhances it as high as 1.93. Besides, some other peaks arise because of the rocking, wagging and scissoring vibrations of CH_2-group and symmetric/asymmetric stretching of the carbon-chain; which are common for all the polymorphs. Embedding MNPs in PVDF matrix has left the less-polar γ −phase (T_3GT_3G') almost unaffected, as seen in all the basic characterizations.

4.3.2.2 First principles prophecy

In theoretical calculations, conventional cubic cell of pristine Fe_3O_4 with lattice parameter optimized to a = 8.398 Å and orthorhombic β −PVDF optimized lattice with parameters: a = 8.336, b = 4.910 and c = 2.583 Å are employed. For composite system, the PVDF chain is planted on the intense (311) diffraction-plane of Fe_3O_4. A vacuum slab of 2 nm is framed along 'c'-direction to avoid the interaction between periodic images. From the optimized structure [Figure 4.11(a)], the PVDF chain is observed to get bonded with the Fe_3O_4 surface via physisorption. The bond-length between the nearest Fe and F atoms are 2.43 and 2.44 Å as shown in the figure. Furthermore, charge-density difference and the planner average charge-density along c-direction of the composite system impart an insight to the interactions between Fe_3O_4 and PVDF. The charge exchange cloud demonstrates a significant charge-transfer from the Fe atom of Fe_3O_4 to the adjacent F atoms of PVDF. In the planner average charge-density calculation, contributions of average charge-density of Fe_3O_4 surface and PVDF are summed up individually and finally subtracted from the average density of the composite. As a result of the subsequent electrostatic interactions, a total of 0.104e charge is transferred from Fe_3O_4 (311)

plane to PVDF per formula unit [Figure 4.11(b)]. Bader charge analysis is another intuitive method of separating a molecule to its constituent atoms by simulating the 'zero flux' surfaces. To determine the total electronic charge cumulated by an atom, charge enclosed within the conventional 'Bader volume' can be a sufficiently good approximation. Therefore, to recognise the multipole moments in the Fe_3O_4/PVDF charge-ordered nanocomposite, this technique is utilized as well. Results generated so far are consistent with the Bader charge-analysis,[61] pertaining localized charge-accumulation in all atoms.

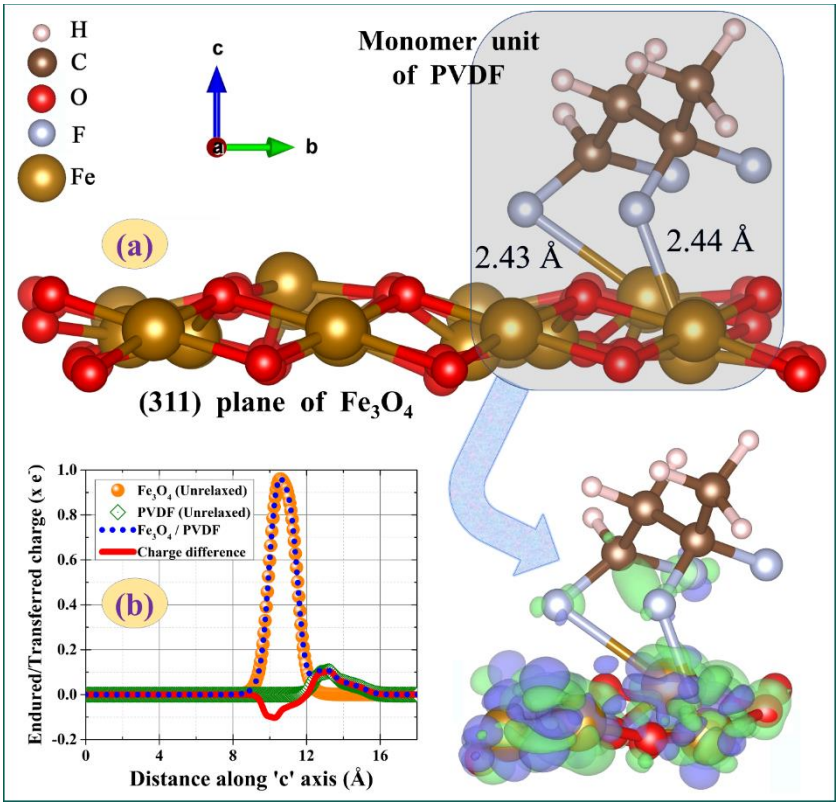

Figure 4.11 (a) Optimized structure for Fe_3O_4/PVDF composite. Formation of Fe-F bonds via physisorption facilitates transfer of charge between the vinylidene fluoride (monomer) unit & Fe_3O_4 (311) plane. In the immediate vicinity (shaded region), the charge-density difference (iso-surface value 0.0093) demonstrates notable charge-redistribution. Green & blue colour represents charge-gain and loss respectively; (b) Planner average charge-density reallocation in 'c'-direction.

4.3.2.3 Electrical characteristics and piezo-performance

The best overall piezoelectric gain is obtained for the 30.2 nm – 8 wt(%) film, for which rapid finger-tapping motion ($\leq 34\ kPa$) on a 4 cm² effective electrode-area can generate open-circuit voltage (V_{OC}) and short-circuit current (I_{SC}) as large as 115.95 V and 1.04 μA, which is nearly an order enhancement from the pure PVDF reference, see Figure 4.12.

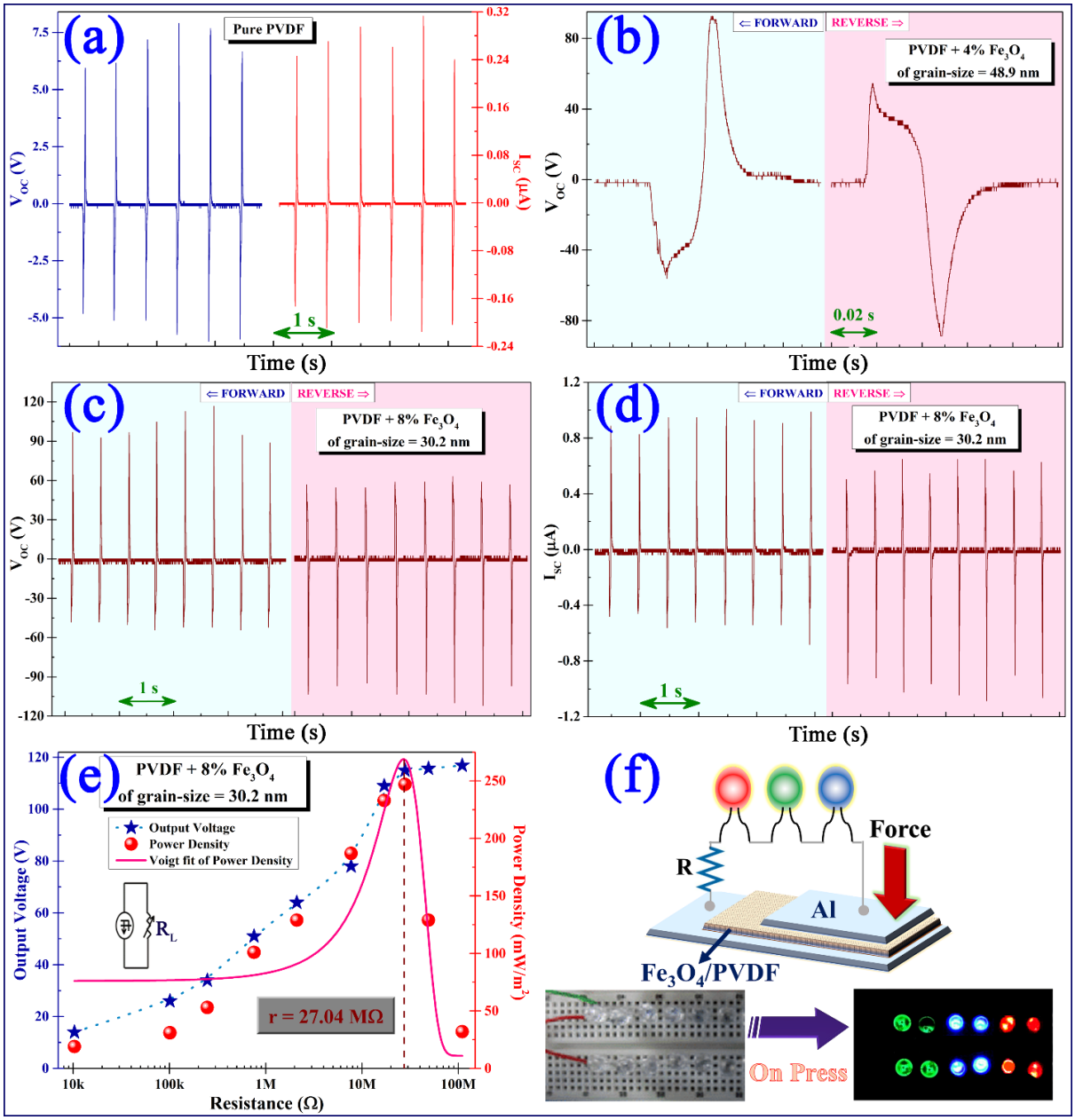

Figure 4.12 (a) Open-circuit voltage (V_{OC}) and short-circuit current (I_{SC}) for the pure PVDF nanogenerator against prompt finger-tapping sequence; (b) Charge gain & decay dynamics for a single press and demonstration of polarity-reversal in PENGs for exchanged electrode connections; (c) & (d) V_{OC} and I_{SC} for the best performing film [30.2 nm – 8 wt(%)] in forward and reverse connections; (e) Output voltage/power-density as a function of series-resistance and determination of the internal resistance of the system from a Voigt fit employing maximum power transfer theorem; (f) Schematic circuitry and snapshot of green, blue, and red commercial LEDs glowing from piezoelectricity.

During the press-action the electrons get accumulated at the film-electrode interface with a voltage-peak and no sooner the electrons start to balance with the piezo-potential causing the diminishing peak-shape. After the release, the accumulated free electrons get back

to the electrode and thereby giving an opposite signal. The polarity-inversion for the forward and reverse connections confirm the piezoelectric effect. An uneven voltage gain for the press and release action indicates different micro-strain association at the interface. Employing a number of load-resistances ($10^4 - 10^8 \Omega$), the internal resistance of the films is estimated from a Voigt fit of the power-distribution using the maximum power-transfer theorem.[62] The 30.2 nm – 8 wt(%) sample delivered output power density ~ 247.3 mW m^{-2} for a resistor close to its internal resistance i.e., 27.04 MΩ.

The enhancement of β −phase and piezo-response with the gradual incorporation of functional MNPs is governed by an ion−dipole electrostatic interaction, restraining the -CH_2-/-CF_2-molecular dipoles in the PVDF chain, via a sustained support from nanoscopic layers of oxo-, hydroxo- & carboxylate-groups on the surface of physisorbed Fe_3O_4. In fact, the organic coating *in situ* helps not only in acquiring better dispersibility and stability of the inorganic additives in midst of the polymeric chains, but also helps to build up the polar β −polytype. Moreover, the electret-doping effect strengthens the polarizability of the PVDF-matrix. As the size of the particles decreases according to the synthesis-scheme, the predeveloped surface-charge and contribution of polar functional groups at the surface evolve continuously. As a result, the parallelly aligned dipole moments associated with C–H & C–F bonds; perpendicular to the carbon backbone add up altogether to boost the net moment, stabilizing the electroactive β-phase. Besides tiny magnetic particles are more effective for EMI shielding. This trend is quite consistent up to 30.2 nm size. But, as the particle size gets smaller (approaching quantum regime); due to high surface-energy, the nanoparticles start to aggregate and form clusters causing blockage or discontinuity in the film. This degradation becomes massive for the 8.9 nm size and 12 wt(%) sample. This proposition is also supported by the FESEM images for different wt(%) films. The pure PVDF film is quite homogeneous and uniform, whereas in the 4% film, some smudges and tiny porous structures associated with MNPs develop. In the 8% sample, gradual aggregation of the nanoparticles initiates at random regions and for the 12% PENG, the MNPs exceed the bearing capacity of the PVDF network. Consequently, the agglomeration becomes severe enough to obstruct the continuity of the film, resulting degradation in piezo-performance.

The ferroelectric hysteresis loops at room-temperature for two field-strengths are shown in Figure 4.13(a). The electrical breakdown strength of the films varies in between 85 – 100 kV cm^{-1} and thus data is taken at lower fields. The bare PVDF, having a very small proportion of polar phases, produces a nominal hysteresis area, coercive field (E_c) and remnant polarization (P_r); whereas for the composite films, the parameters have enhanced to values as large as E_c~12.3 kV cm^{-1} and P_r~480 nC cm^{-2} against < 84 kV cm^{-1} external field. The increase in remanence *i.e.*, charge retaining capability after removal of the external field and loop-area,

compared to the neat PVDF film justify the enhancement in the piezoelectric properties of the composite films.

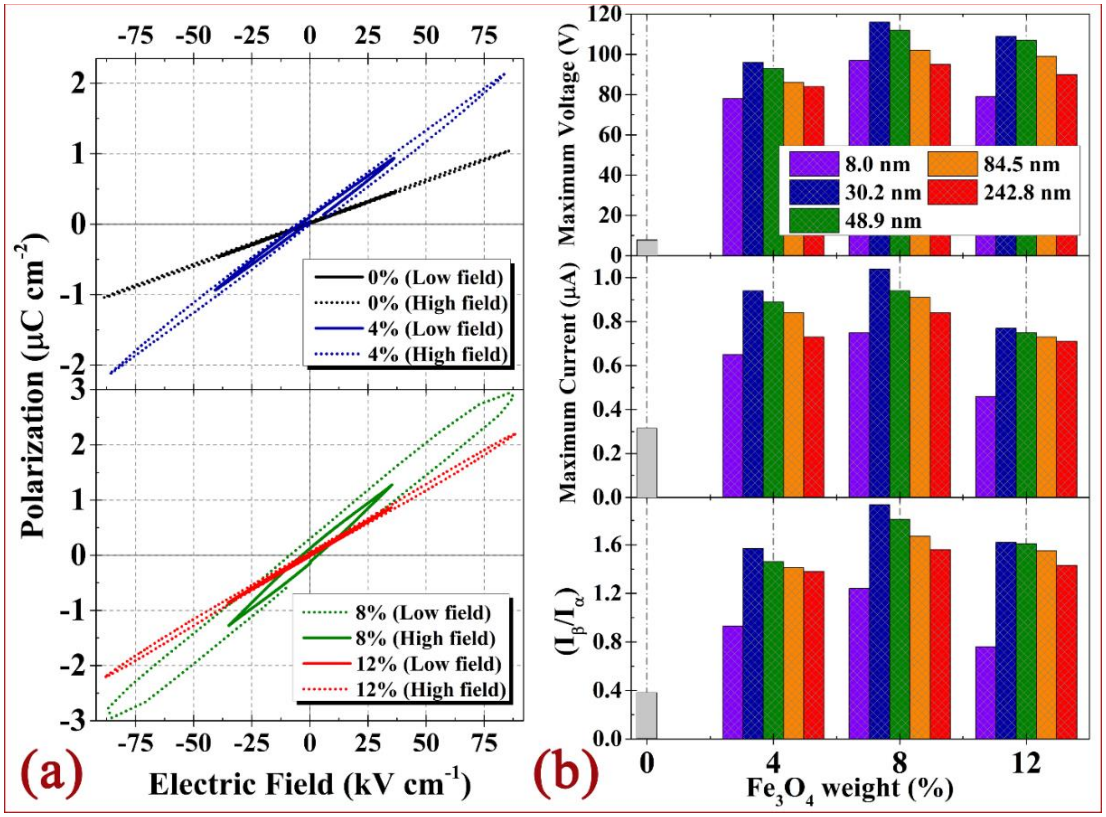

Figure 4.13 (a) Ferroelectric hysteresis loops for composite films with 30.2 nm particles in different amounts. Data is taken at two field-strengths: low filed ($\lesssim 30$ kV cm^{-1}) and high field ($\lesssim 84$ kV cm^{-1}). Fe_3O_4 incorporation up to 8% has increased the loop-area, remanence and coercivity; (b) Consolidated data of maximum voltage, current (at 34 kPa pressure) and ratio of β & α-phase proportions from Raman spectra to compare the overall piezo-profile of all nanogenerators.

Dielectric spectroscopy is a useful characterization tool to assess electrical energy storing capacity of a system. Frequency-dispersion of the real part of relative permittivity or dielectric function (ε_r) is obtained from the capacitance values (C), using the following formula,

$$\varepsilon_r = \frac{\varepsilon}{\epsilon_0} = \frac{Ct}{\epsilon_0 A}. \tag{4.13}$$

Here, t = thickness of the film, ϵ_0 = permittivity of vacuum = 8.854 × 10^{-12} F m^{-1} and A is the effective electrode area. As the MNPs are incorporated in PVDF, not only the dielectric constant (both static value and high frequency behaviour) enhances, but also the overall dipolar relaxation gets reshaped as shown in Figure 4.14. This signifies notable electroactive phase formation inside the nanocomposites. Therefore, dielectric dispersions also reveal the same trend of results as before.

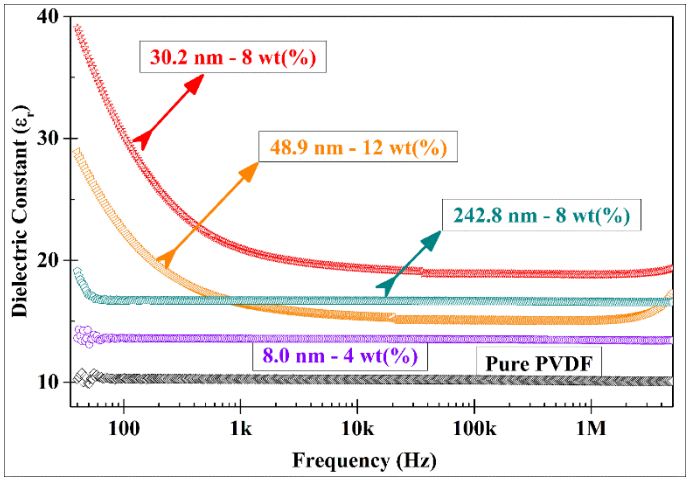

Figure 4.14 Dielectric dispersion for five selected samples, showing considerable increase in the polarization behaviour and dielectric constant.

Comparing the general trends of output voltage, current, maximum power delivered and I_β/I_α ratio; the 30.2 nm – 8 wt(%) PENG performs optimally [Figure 4.13(b)], which has further been employed to light up multicoloured LEDs by gentle press. A rough comparison of piezo-performance of some well-fabricated lead-free nanogenerators is provided in Table 4.3 to estimate the implication of our work, although the experimental conditions, applied force/pressure, effective area/thickness of films and load-resistance might vary a bit. Hence, it can be inferred, use of superparamagnetic polar nanoparticles with high dielectric constant and superior electret-properties can be assigned to polymer-based new-age piezo-, pyro- and triboelectric nanogenerators with high power-density.

4.4 Concluding remarks

In summary, size of Fe_3O_4 nanoparticles is varied systematically over an extensive range by regulating a number of guiding parameters via a perceptive microwave-assisted solvothermal strategy to collocate resourceful properties. By virtue of the as-used exotic coating agents, the resultant biocompatible nanoparticles develop an appreciably high surface-charge and abiding dispersibility due to covalent surface-functionalization; conforming ZP, FTIR, and TGA-DTG results. XPS analysis differentiates the binding energies of the tetrahedral and octahedrally co-ordinated Fe species and substantiates stoichiometry. Red-shifting and line-shape asymmetry of A_{1g} Raman mode for ultra-small nanoparticles are illustrated as per the phonon confinement effect. The optical bandgap (E_g) increases from 1.59 to 4.78 eV in a very regular fashion with decreasing size, which consents corresponding crystal field splitting energies. A minute Brus equation fit determines effective mass of the excitons and accounts for the drastic change in E_g with size. Next, these polar MNPs are incorporated in PVDF as an electret filler to boost up its electroactive β-phase, aptly validated from first principles studies.

Embedding MNPs of ferrimagnetic or superparamagnetic nature in suitable proportions would prevent electromagnetic flux to interfere with the electronic performance of smart devices and enhances piezo-activity by an order.

Table 4.3 Comparison of the PVDF-based surpassing PENGs from the literature

Composition	Structure	Maximum piezoelectric outputs			
		Open circuit voltage (V_{OC})	Short circuit current (I_{SC})	Power-density (P)	Applied Pressure
PVDF[63]	Fabric	14 V	29.8 μA	110 – 510 μW cm^{-2}	0.02 – 0.10 MPa
P(VDF-TrFE)[64]	Flat film	7 V	58 nA	–	–
P(VDF-TrFE)[65]	Curved film	120 V	700 μA	3.9 mW m^{-2}	–
Graphene - $BaTiO_3$ / PVDF[66]	Nanocomposite films	10 V	2.5 μA	5.8 μW	2 N
$BaTiO_3$ / PVDF[67]	Nanowire-grafted films	14 V	4 μA	1.5 μW	–
$Ba(Ti_{0.9}Zr_{0.1})O_3$ / PVDF[68]	Nanocube-grafted films	11.99 V	1.36 μA	0.2 – 15.8 nW (as sensors)	11 N
SnO_2 / PVDF[69]	Nanosheet-grafted films	45 V	6.25 μA cm^{-2}	4900 W m^{-3}	–
ZnO / PVDF[70]	Nanocomposite films	24.5 V	1.7 μA	32.5 mW cm^{-3}	28 N
ZnO / PVDF[71]	Nanowire-grafted films	6.9 V	0.96 μA	6.624 μW	–
NKNS-LT-BZ / PVDF[72]	Nanocomposite films	18 V	2.6 μA	–	50 N
NiO@SiO_2 / PVDF[73]	Nanocomposite films	53 V	0.3 μA cm^{-2}	685 W m^{-3}	0.3 MPa
AlO-rGO / PVDF[74]	Nanocomposite films	36 V	0.8 μA	2797 μW	31.19 kPa
PVDF[75]	Electrospun membrane	48 V	6 μA	51 μW	8.3 kPa
ZnO / PVDF[76]	Electrospun membrane	85 V	2.2 μA	–	–
Graphene / PVDF[77]	Composite nanofibers	7.9 V	–	–	–
MWCNTs / PVDF[78]	Electrospun composite nanofibers	6 V	–	81.8 nW	–
$NiCl_2 . 6H_2O$ / PVDF[79]	Electrospun mats	0.762 V	–	–	–
Fe_3O_4 / PVDF (Present Work)	Nanoparticle-embedded films	115.95 V	1.04 μA	247.3 mW m^{-2}	34 kPa

References

1. M. S. Senn, J. P. Wright and J. P. Attfield, *Nature*, 2012, **481**, 173.
2. R. Kukreja, N. Hua, J. Ruby, A. Barbour, W. Hu, C. Mazzoli, S. Wilkins, E. E. Fullerton and O. G. Shpyrko, *Phys. Rev. Lett.*, 2018, **121**, 177601.
3. S. Lim, B. Choi, S. Y. Lee, S. Lee, H.-H. Nahm, Y.-H. Kim, T. Kim, J.-G. Park, J. Lee and J. Hong, *Nano Lett.*, 2018, **18**, 1745-1750.
4. S. Borroni, G. Tucker, F. Pennacchio, J. Rajeswari, U. Stuhr, A. Pisoni, J. Lorenzana, H. Rønnow and F. Carbone, *New J. Phys.*, 2017, **19**, 103013.
5. M. Ziese, P. Esquinazi, D. Pantel, M. Alexe, N. Nemes and M. Garcia-Hernández, *J. Phys.: Condens. Matter*, 2012, **24**, 086007.
6. F. Schrettle, S. Krohns, P. Lunkenheimer, V. Brabers and A. Loidl, *Phys. Rev. B*, 2011, **83**, 195109.
7. J. Bao, W. Chen, T. Liu, Y. Zhu, P. Jin, L. Wang, J. Liu, Y. Wei and Y. Li, *ACS Nano*, 2007, **1**, 293-298.
8. S.-H. Kim, M.-J. Kim and Y.-H. Choa, *Mater. Sci. Eng., A*, 2007, **449**, 386-388.
9. D. Ling, N. Lee and T. Hyeon, *Acc. Chem. Res.*, 2015, **48**, 1276-1285.
10. Y. Zhu, Y. Fang and S. Kaskel, *J. Phys. Chem. C*, 2010, **114**, 16382-16388.
11. Y. Wu, J. Zhang, Y. Tong and X. Xu, *J. Hazard. Mater.*, 2009, **172**, 1640-1645.
12. M. Sadat, R. Patel, J. Sookoor, S. L. Bud'ko, R. C. Ewing, J. Zhang, H. Xu, Y. Wang, G. M. Pauletti and D. B. Mast, *Mater. Sci. Eng., C*, 2014, **42**, 52-63.
13. Y. Shen, J. Tang, Z. Nie, Y. Wang, Y. Ren and L. Zuo, *Sep. Purif. Technol.*, 2009, **68**, 312-319.
14. Y. Wang, X. Cao, G. Liu, R. Hong, Y. Chen, X. Chen, H. Li, B. Xu and D. Wei, *J. Magn. Magn. Mater.*, 2011, **323**, 2953-2959.
15. L.-h. Shen, J.-f. Bao, D. Wang, Y.-x. Wang, Z.-w. Chen, L. Ren, X. Zhou, X.-b. Ke, M. Chen and A.-q. Yang, *Nanoscale*, 2013, **5**, 2133-2141.
16. G. Wang, X. Zhang, A. Skallberg, Y. Liu, Z. Hu, X. Mei and K. Uvdal, *Nanoscale*, 2014, **6**, 2953-2963.
17. A. Navrotsky, L. Mazeina and J. Majzlan, *Science*, 2008, **319**, 1635-1638.
18. M. E. Fleet, *J. Solid State Chem.*, 1986, **62**, 75-82.
19. J. Coey and C. Chien, *MRS Bull.*, 2003, **28**, 720-724.
20. J. A. Cuenca, K. Bugler, S. Taylor, D. Morgan, P. Williams, J. Bauer and A. Porch, *J. Phys.: Condens. Matter*, 2016, **28**, 106002.
21. S. J. Rosenthal, J. C. Chang, O. Kovtun, J. R. McBride and I. D. Tomlinson, *Chem. Biol.*, 2011, **18**, 10-24.
22. H. Guo, M.-H. Yeh, Y. Zi, Z. Wen, J. Chen, G. Liu, C. Hu and Z. L. Wang, *ACS Nano*, 2017, **11**, 4475-4482.

23. N. Cui, J. Liu, L. Gu, S. Bai, X. Chen and Y. Qin, *ACS Appl. Mater. Interfaces*, 2015, **7**, 18225-18230.
24. W. Wu, S. Bai, M. Yuan, Y. Qin, Z. L. Wang and T. Jing, *ACS Nano*, 2012, **6**, 6231-6235.
25. J.-S. Im and I.-K. Park, *ACS Appl. Mater. Interfaces*, 2018, **10**, 25660-25665.
26. H. Xue, Q. Yang, D. Wang, W. Luo, W. Wang, M. Lin, D. Liang and Q. Luo, *Nano Energy*, 2017, **38**, 147-154.
27. W. Wu, Z. Wu, T. Yu, C. Jiang and W.-S. Kim, *Sci. Technol. Adv. Mater.*, 2015, **16**, 023501.
28. G. Kresse and J. Hafner, *Phys. Rev. B*, 1993, **47**, 558.
29. G. Kresse and J. Hafner, *Phys. Rev. B*, 1994, **49**, 14251.
30. P. E. Blöchl, *Phys. Rev. B*, 1994, **50**, 17953.
31. J. P. Perdew, K. Burke and M. Ernzerhof, *Phys. Rev. Lett.*, 1996, **77**, 3865.
32. S. Bhattacharjee, A. Banerjee, N. Mazumder, K. Chanda, S. Sarkar and K. K. Chattopadhyay, *Nanoscale*, 2020, **12**, 1528-1540.
33. H. Liu and C. Di Valentin, *J. Phys. Chem. C*, 2017, **121**, 25736-25742.
34. S. Grimme, *J. Comput. Chem.*, 2006, **27**, 1787-1799.
35. S. Bhattacharjee, *J. Control. Release*, 2016, **235**, 337-351.
36. J. Lee, S. G. Kwon, J.-G. Park and T. Hyeon, *Nano Lett.*, 2015, **15**, 4337-4342.
37. R. Gupta and S. Sen, *Phys. Rev. B*, 1975, **12**, 15.
38. A. Bengtson, D. Morgan and U. Becker, *Phys. Rev. B*, 2013, **87**, 155141.
39. D. Wilson and M. Langell, *Appl. Surf. Sci.*, 2014, **303**, 6-13.
40. V. Panwar, P. Kumar, A. Bansal, S. S. Ray and S. L. Jain, *Appl. Catal. A-Gen.*, 2015, **498**, 25-31.
41. B. K. Chatterjee, A. Dey, C. K. Ghosh and K. K. Chattopadhyay, *J. Magn. Magn. Mater.*, 2014, **367**, 19-32.
42. C. Johnson, J. Johnson, H. Hah, M. Cole, S. Gray, V. Kolesnichenko, P. Kucheryavy and G. Goloverda, *Hyperfine Interact.*, 2016, **237**, 27.
43. J. Gittleman, B. Abeles and S. Bozowski, *Phys. Rev. B*, 1974, **9**, 3891.
44. O. N. Shebanova and P. Lazor, *J. Raman Spectrosc.*, 2003, **34**, 845-852.
45. I. Chamritski and G. Burns, *J. Phys. Chem. B*, 2005, **109**, 4965-4968.
46. E. H. Hasdeo, A. R. Nugraha, M. S. Dresselhaus and R. Saito, *Phys. Rev. B*, 2014, **90**, 245140.
47. R. Gupta, Q. Xiong, C. Adu, U. Kim and P. Eklund, *Nano Lett.*, 2003, **3**, 627-631.
48. H. Richter, Z. Wang and L. Ley, *Solid State Commun.*, 1981, **39**, 625-629.
49. I. Campbell and P. M. Fauchet, *Solid State Commun.*, 1986, **58**, 739-741.
50. S. K. Gupta and P. K. Jha, *Solid State Commun.*, 2009, **149**, 1989-1992.
51. C. Vatankhah and A. Ebadi, *Res. J. Recent Sci. ISSN*, 2013, **2277**, 2502.

52. K. Nanda, F. Kruis, H. Fissan and S. Behera, *J. Appl. Phys.*, 2004, **95**, 5035-5041.
53. A. Zhou and W. Sheng, *Eur. Phys. J. B*, 2009, **68**, 233-236.
54. A. D. Rowan, C. H. Patterson and L. Gasparov, *Phys. Rev. B*, 2009, **79**, 205103.
55. K. Jordan, A. Cazacu, G. Manai, S. Ceballos, S. Murphy and I. Shvets, *Phys. Rev. B*, 2006, **74**, 085416.
56. M. Sadat, M. Kaveh Baghbador, A. W. Dunn, H. Wagner, R. C. Ewing, J. Zhang, H. Xu, G. M. Pauletti, D. B. Mast and D. Shi, *Appl. Phys. Lett.*, 2014, **105**, 091903.
57. X. Cai, T. Lei, D. Sun and L. Lin, *RSC Adv.*, 2017, **7**, 15382-15389.
58. P. Martins, A. Lopes and S. Lanceros-Mendez, *Prog. Polym. Sci.*, 2014, **39**, 683-706.
59. Y. A. Barnakov, O. Paul, A. Joaquim, A. Falconer, R. Mu, V. Y. Barnakov, D. Dikin, V. P. Petranovskii, A. Zavalin and A. Ueda, *Opt. Mater. Express*, 2018, **8**, 2579-2585.
60. J. Ma, Q. Zhang, K. Lin, L. Zhou and Z. Ni, *Mater. Res. Express*, 2018, **5**, 035057.
61. W. Tang, E. Sanville and G. Henkelman, *J. Phys.: Condens. Matter*, 2009, **21**, 084204.
62. S. Bhattacharjee, S. Mondal, A. Banerjee and K. K. Chattopadhyay, *Mater. Res. Express*, 2020, **7**(4), 044001.
63. N. Soin, T. H. Shah, S. C. Anand, J. Geng, W. Pornwannachai, P. Mandal, D. Reid, S. Sharma, R. L. Hadimani and D. V. Bayramol, *Energy Environ. Sci.*, 2014, **7**, 1670-1679.
64. Z. Pi, J. Zhang, C. Wen, Z.-b. Zhang and D. Wu, *Nano Energy*, 2014, **7**, 33-41.
65. W.-S. Jung, M.-J. Lee, M.-G. Kang, H. G. Moon, S.-J. Yoon, S.-H. Baek and C.-Y. Kang, *Nano Energy*, 2015, **13**, 174-181.
66. U. Yaqoob, A. I. Uddin and G.-S. Chung, *Appl. Surf. Sci.*, 2017, **405**, 420-426.
67. C. K. Jeong, C. Baek, A. I. Kingon, K. I. Park and S. H. Kim, *Small*, 2018, **14**, 1704022.
68. N. R. Alluri, B. Saravanakumar and S.-J. Kim, *ACS Appl. Mater. Interfaces*, 2015, **7**, 9831-9840.
69. E. Kar, N. Bose, B. Dutta, S. Banerjee, N. Mukherjee and S. Mukherjee, *Energy Convers. Manag.*, 2019, **184**, 600-608.
70. P. Thakur, A. Kool, N. A. Hoque, B. Bagchi, F. Khatun, P. Biswas, D. Brahma, S. Roy, S. Banerjee and S. Das, *Nano Energy*, 2018, **44**, 456-467.
71. B. Saravanakumar, S. Soyoon and S.-J. Kim, *ACS Appl. Mater. Interfaces*, 2014, **6**, 13716-13723.
72. C. Zhang, Y. Fan, H. Li, Y. Li, L. Zhang, S. Cao, S. Kuang, Y. Zhao, A. Chen and G. Zhu, *ACS Nano*, 2018, **12**, 4803-4811.
73. B. Dutta, E. Kar, N. Bose and S. Mukherjee, *ACS Sustain. Chem. Eng.*, 2018, **6**, 10505-10516.
74. S. K. Karan, R. Bera, S. Paria, A. K. Das, S. Maiti, A. Maitra and B. B. Khatua, *Adv. Energy Mater.*, 2016, **6**, 1601016.

75. K. Maity and D. Mandal, *ACS Appl. Mater. Interfaces*, 2018, **10**, 18257-18269.

76. J. Li, S. Chen, W. Liu, R. Fu, S. Tu, Y. Zhao, L. Dong, B. Yan and Y. Gu, *J. Phys. Chem. C*, 2019, **123**, 11378-11387.

77. M. M. Abolhasani, K. Shirvanimoghaddam and M. Naebe, *Compos. Sci. Technol.*, 2017, **138**, 49-56.

78. H. Yu, T. Huang, M. Lu, M. Mao, Q. Zhang and H. Wang, *Nanotechnology*, 2013, **24**, 405401.

79. D. Dhakras, V. Borkar, S. Ogale and J. Jog, *Nanoscale*, 2012, **4**, 752-756.

5 NEGATIVE CAPACITANCE SWITCHING IN SIZE-MODULATED Fe_3O_4 NANOPARTICLES WITH SPONTANEOUS NON-STOICHIOMETRY: CONFRONTING ITS GENERALIZED ORIGIN IN NON-FERROELECTRIC MATERIALS

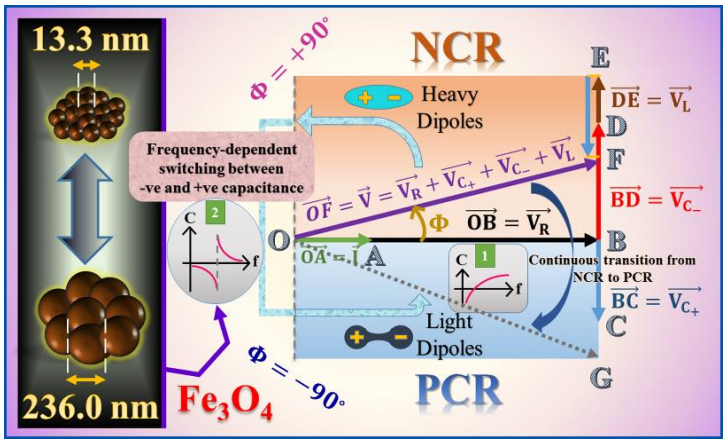

Abstract

A persistent low-frequency negative capacitance (NC) dispersion has been detected in half-metallic polycrystalline magnetite (Fe_3O_4) nanoparticles having a size-variation: 13 – 236 nm, under the application of moderate DC bias. Using Havriliak–Negami model, 3D Cole-Cole plot is employed to recapitulate the relaxation-time (τ) of the associated oscillating dipoles, related shape-parameters (α, β) and resistivity for different sizes. Universal Debye relaxation (UDR) theory requires a modification to address the shifted quasi-static NC-dispersion plane in materials showing both +ve and –ve capacitance about a transition/switching frequency (f_0). A consistent blue-shift of 'f_0' is observed with increasing external DC field and decreasing particle-size. Based on this experimental data, a generalized dispersion scheme is proposed to fit the entire positive and negative capacitance regime including the diverging transition point. In addition, a comprehensive model is discussed using phasor-diagrams to differentiate the underlying mechanisms of continuous transition from –ve to +ve capacitance concerning localized charge recombination or time-dependent injection/displacement currents; adequately explored in scientific literature and the newly proposed 'capacitive switching' phenomenon. An inherent non-stoichiometry due to iron-vacancies $[Fe_{3(1-\delta)}O_4]$, duly validated from first principles calculations; builds up p-type nature, which consequently promotes more covalent and heavier dipoles slowing down dipolar relaxations; incommensurate to Maxwell-Wagner

interfacial polarization (MWIP) dynamics. This combinatorial effect is apprehended for the sluggish response of the associated dipoles and stabilization of NC.

5.1 Introduction

Negative capacitance (NC) phenomena have been an exclusive paradigm of contemporary research, detected in an extensive variety of fields and materials *viz*. ferroelectric nanostructures,[1-4] thin films,[5-7] amorphous chalcogenides,[8,9] binary oxides,[10-12] perovskite solar cells,[13-15] electrorheological fluids,[16] organic/inorganic compounds,[17-25] composites and glass-alloys,[26-34] Schottky diodes,[35] heterojunctions,[36] biological membranes[37-40] etc. The manifestation of NC is theoretically a bit adequate for ferroelectric materials, based on Landau theory of ferroelectrics. It has further been implemented in MOSFET devices for matching the positive gate capacitance to overcome the Boltzman tyranny of 60 mV/dec subthreshold swing.[41-43] On the contrary, stable NC dispersion in non-ferroelectric substances/devices is explained from versatile (apparently uncorrelated) ideas including localization of charge in trap/interface states,[17,32] contact injection,[32] extrinsic[44] or doping effects,[45] space-charge propagation,[28] slower transients,[46] mixed ionic-electronic hysteresis in the current-voltage dependency,[47] minority carrier migration[17] etc. Hence, a generalized theory of NC for all the above-mentioned systems is imperatively required.

In a series R-L-C circuit, capacitance (C) and inductance (L) compete for the current variation to lead over and lag behind the applied voltage, respectively. Any real material can also be modelled as suitable series/parallel combinations of these passive circuit-elements. Positive capacitance in semiconductor/insulators are governed by the space-charge accumulation in the grain-grain boundary constitution causing Maxwell-Wagner interfacial polarization (MWIP)[48,49] and dipolar contributions as in Cole-Davidson theory.[50] On the other hand, steady and linear drift velocity of carriers do not produce inductance; although external field assisted hopping of delocalized charge-carriers to nonlinear localized sites might give rise to an inductive effect.[36] Phenomenologically, the interpretation of current lagging behind the voltage agitation can be associated with both +ve inductance and -ve capacitance. However, absence of considerable magnetic field in most materials hardly supports the inductive origin, resulting $O(L)$~pH only in standard polycrystalline pellets. Hence, the perception is carried forward with the notion of NC. By theory, NC is a consequence of depopulation of interface-states with stored charge or time-dependent trap-assisted carrier-recombination with increased potential. Detrapped or injected free carriers might cause polarization loss, but when the corresponding currents become time-dependent; the temporally diminishing polarization manifests frequency dispersive NC. Recently, Ebadi *et al.*[47] explained light-enhanced NC in perovskite solar cells as an outcome of slow transitory ion-displacement in forward diode-

current and consecutive negative gradient with voltage-change. They rather argued, this 'current retardation' barely signifies any converse charge accumulation or counter capacitive feature. Another analogous current-voltage phase relationship is observed in frequency-range greater than a few tens of MHz, where inductive effects start dominating, which is rarely correlated to 'quasi-static' or 'transient' NC. For example, in a series R-L-C circuit; reactance, $Z'' = \omega L - \frac{1}{\omega C}$; so, at sufficiently high frequencies $\left(\omega \gg {}^{R}/_{L}\right)$, inductive reactance $(\sim\omega)$ gets overestimated against the capacitive nature $\left(\sim {}^{1}/_{\omega}\right)$ and impedance ramps up; known as parasitic inductance[51-53] in capacitor prefabrication industries. This pseudo-inductive genre $\left(C_{eff} = -\frac{1}{\omega^2 L}\right)$ should not be confused with true NC, where NC regime (NCR) appears at lower frequency than positive capacitance regime (PCR).[24]

Out of more than 16 polymorphs[54] of iron oxide and oxyhydroxides; magnetite $\{(Fe^{3+})_A[Fe^{2+}Fe^{3+}]_B(O^{2-})_4\}$ with an inverse spinel cubic structure (point group: $Fd3m$) is contemplated as the most interesting and crucial one for over three centuries to theoretical as well as experimental condensed matter physicists and materials scientists; because of its unique electrical and magnetic properties. This half-metallic and ferrimagnetic material[55-57] has also been observed to act as a relaxor multiferroic[58] till 30 K, far below the Verwey transition (120-125 K);[59-61] which is still not completely understood. Moreover, the theoretically claimed 100% spin-polarized (at Fermi level) material[62] concerning double-exchange and super-exchange interactions;[63] gets converted to h-Fe_3O_4 with a normal spinel lattice on application of ≥ 10 GPa pressure.[64,65] Previously, many researchers recognized Fe/O stoichiometry, strain and grain-size to be the critical parameters, governing its electronic and magnetic properties.[58,64-67] Here we report, non-stoichiometric magnetite $\left[Fe_{3(1-\delta)}O_4\right]$ also shows a frequency-dependent –ve to +ve capacitive switching at room-temperature; adaptable via external DC bias. In the subsequent sections, first the nature and origin of non-stoichiometry in Fe_3O_4 are discussed; followed by duly investigated impedance and capacitive dispersions. Finally, a comprehensive model is proposed to establish the intrinsic connection between this structural orientation and transformed dipolar relaxation originating capacitive switching; and thereby classifying NC in distinct materials based on their qualitative root-mechanism. To the best of the authors' knowledge, this is the first time, nanoparticle size-effect on NC has been precisely ventured in non-ferroelectrics.

5.2 Methods & enumeration

5.2.1 Experimental techniques

Magnetite nanoparticles (MNPs) of different size (Sample: S1-S5, in decreasing order) are prepared via a facile one-step solvothermal technique by varying concentration of disodium

tartrate (coating agent) to control crystallite growth in polyol medium. Spherical MNPs are synthesized using analytical grade reagents (purchased from SIGMA-ALDRICH) without further purification. In a typical synthesis of 47 nm nanoparticles (S3), 1.50 g (5.55 mmol) $FeCl_3.6H_2O$ is mixed vigorously in a solution of 40 mL ethylene glycol and 40 mL diethylene glycol. Then, 0.35 g (1.52 mmol) hydrated disodium (+) tartrate is added; followed by 3.00 g (36.57 mmol) anhydrous sodium acetate and 3.50 g (0.58 mmol) polyethelene glycol (mol. wt. = 6000). This mixture is ultrasonicated for 10 minutes and magnetically stirred for an hour at 80 °C to form a homogeneous dark yellow solution. Thereafter it is put into a Teflon-lined stainless steel-autoclave with 100 mL capacity and maintained at 185 °C for 12 h. After natural cooling, the black product is precipitated with ethanol followed by thorough centrifugation, washing (in deionized water & ethanol) and vacuum-drying at 65 °C to acquire fine Fe_3O_4 powder. The amount of disodium tartrate and PEG-6000 is varied in between 0.05 – 0.65 and 3.00 – 4.00 g respectively to tune particle-size, which obstruct crystal grain growth and act as stabilizer.[1-3] A thicker coating around the tinier nanoparticles is apprehended in different surface-characterizations *viz*. XPS, FTIR and Raman spectroscopy.

To verify the crystallographic phase conformation, X-ray diffraction data is acquired in a 2θ range: 15° – 80° with 0.02° step-size at 1°/min scan-speed; by employing a Rigaku Miniflex powder X-ray diffractometer with Cu K_α source $(\lambda = 1.5406\ \text{Å})$; operated at 40 kV – 15 mA and the diffraction peaks are indexed from JCPDS card no. 85-1436. Absence of additional peaks confirmed purity of spinel phase. The dramatic hike in FWHM (β) of the Bragg-peaks from S1–S5 clearly demonstrate significant lowering of size. Employing Williamson-Hall equation: $\beta \cos\theta = 4\varepsilon \sin\theta + \frac{0.89\lambda}{d_{WH}}$, crystallite-size $(d_{WH}: 8.9 - 189.6\ nm)$ of the as-synthesized samples are estimated, as mentioned in Figure 5.1(a); although strain (ε) underwent a very nominal change with size. Surface-morphology and size-distribution of MNPs are obtained from a ZEISS Sigma field emission scanning electron microscopy (FE-SEM) system with a 5 kV electron-gun and 400 k× maximum zoom. From the Voigt fit of the particle-size distribution, average particle-diameter $(d_{SEM}: 13.3 - 236.0\ nm)$ is determined, which is found larger than d_{WH}, implying polycrystalline nature [see Figure 5.1]. X-ray photoelectron spectra is obtained using a SPECS XPS (monochromated Al K_α source; $h\nu = 1486.6\ eV$) with hemispherical analyser (HSA 3500). The survey and high-resolution elemental scans are carried out with pass energy of 160 and 20 eV; in steps of 1 and 0.1 eV, respectively. A high-resolution transmission electron microscope (HRTEM, JEOL-JEM 2100) operated at 200 kV; is employed to observe the smallest MNPs, analyse their crystalline nature and unidirectional growth. The S5 sample is dispersed in absolute ethanol and drop-casted on Ted Pella carbon type-B support films on 200 mesh grids for further TEM characterization to perceive their size and crystalline nature, see Figure 5.2.

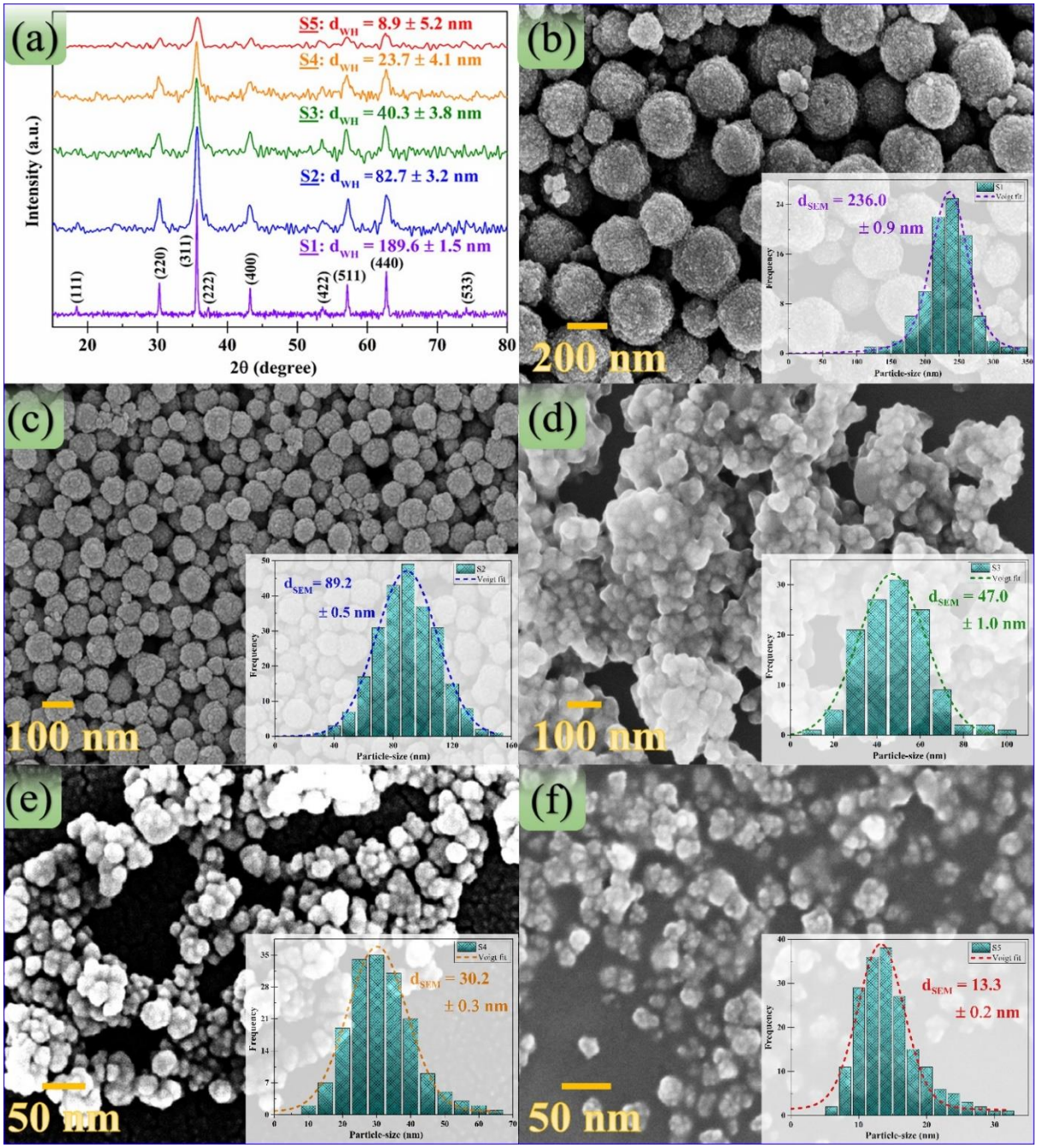

Figure 5.1 (a) XRD pattern for all samples and corresponding crystallite-sizes from W-H analysis; (b)-(f) FESEM micrographs and associated size-distributions (see the insets) for samples S1 to S5, respectively.

As magnetite (Fe_3O_4) and maghemite (γ-Fe_2O_3); having comparable spinel structure exhibit near-similar XRD patterns, the finger-print modes of vibration are further verified from FTIR and Raman spectra, see Figure 5.3. The coordinative effect of carboxylate groups in the surface-composition is found in FTIR spectra, collected using Shimadzu FTIR-8400S. Micro-Raman (beam-diameter ≅ 1 μm) spectra is recorded with ≤ 5 mW laser power and analysed by a WITec ALPHA300 RS confocal spectrometer in backscattering configuration. The UHTS 300

spectrograph is connected to a Peltier-cooled back-illuminated charge-coupled device (CCD), operated at –62°C with better than 90% QE in the visible excitation. A solid-state frequency doubled Nd:YAG laser (532.3 nm) is used as the excitation source, having a maximum power of 30mW. Data is acquired using a 50X (N.A. = 0.9) achromatic objective (Zeiss) with 600 groove/mm grating (spectral resolution = 3.3 cm^{-1}) by averaging 10 spectral acquisitions with 6 s of integration-time each to minimize background noise. The wavenumber error is considered ±1.5 cm^{-1} for our calculations. No polarizers are used, but holographic supernotch filters are employed to reject the Rayleigh and anti-stokes lines. The principal vibrational features of MNPs are already explained in detail in chapter 4, which are re-verified for the as-synthesized samples. Therefore, these attributes are not repeated in the current chapter.

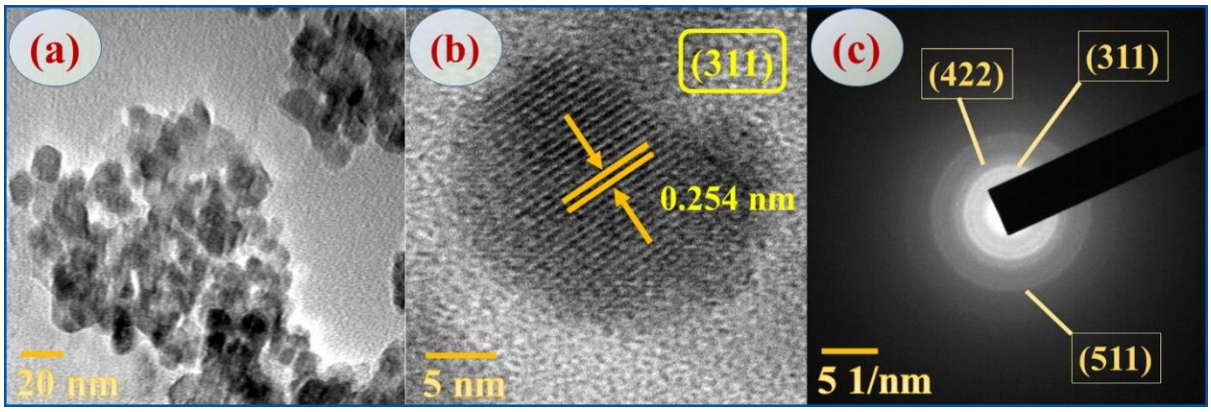

Figure 5.2 (a) TEM image showing the size-distribution of Fe_3O_4 nanoparticles and dispersion; (b) High resolution TEM image representing lattice fringes and inter-planer spacing of the (311) lattice plane; (c) Selected area electron diffraction (SAED) pattern showing polycrystalline nature of the nanoparticles and growth of particular lattice planes.

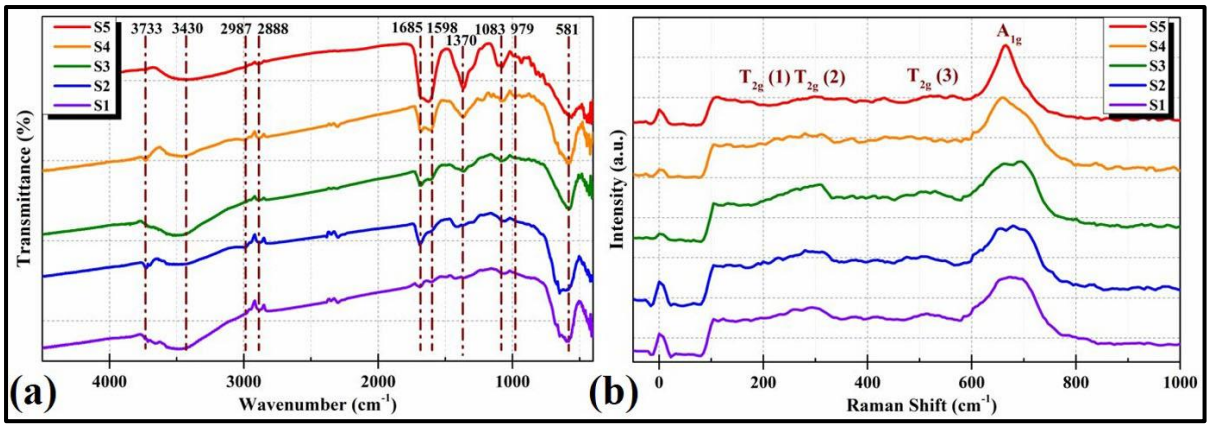

Figure 5.3 (a) FTIR spectra and (b) Raman spectra of tartrate coated and PEGylated Fe_3O_4 samples (S1 – S5). As shown in the FTIR spectra, the surfactant contributions get enhanced for smaller particles having wider shells around the core to control growth.

For dielectric spectroscopy, 0.45 g of each powder-sample is cold-pressed by applying 0.5 GPa pressure to prepare hard polycrystalline pellets of 1.8 mm thickness and 8.5 mm diameter, followed by electrode deposition covering full area in top-bottom configuration to attain MIM geometry.[5] An Agilent 4294A precision impedance analyser with a frequency range: 40 Hz – 110 MHz and variable external DC bias up to 42 V is employed for impedance spectroscopy. The density of the pellets may influence its dielectric properties, as lower density compared to the pristine density indicates presence of air-bubbles, pores, cracks and adsorbed moisture which might manipulate the broadband dielectric spectra and conductivity of the sample. But annealing is not a suitable option due to temperature-dependent phase change of magnetite to the thermodynamically favourable polymorphs of iron oxides e.g., α & γ-Fe_2O_3 and thermally induced agglomeration of nanocrystallites, which can cover up the true size-effects in the nano-regime. Instead, the samples are cautiously dried in vacuum at 75 °C before measurements to minimize experimental error. Additionally, it is assured that, the density of the used pellets is ≥ 90% of the pristine value, a vast majority of which comes due to the lower density of the as-used coating agents. Considering half-metallic system, the AC rms value and DC bias are kept limited to 500 mV and 1 V, respectively in order to exclude time-dependent leakage conductance and impact ionization.

5.2.2 Computational details

First-principles calculations are performed based on the spin polarized density functional theory (DFT) using the projector augmented wave (PAW) method;[68] implemented in the Vienna *ab initio* Simulation Package (VASP).[69-72] The Perdew-Bruke-Ernzerhof (PBE) pseudopotential of the generalized gradient approximation (GGA) is chosen as the exchange-correlation functional.[73] For strongly correlated systems, to avoid self-interaction errors in the standard GGA functional, the DFT+U approach is adopted to account for the on-site Coulomb interaction in the relevant d-orbitals. The PBE+U method used here; is a simplified rationally invariant formulation by Duadrev *et al.*,[74] where the on-site Coulomb parameter: U and exchange parameter: J are combined into a single parameter, $U_{eff} = U - J$ and varied in between 3.5 – 4.0 eV for strongly correlated Fe 3d electrons based on previous reports.[75-77] During the optimization of the crystal structure, ion positions are allowed to relax by applying a Gaussian-smearing approach with σ = 0.01 eV until energy converges to $\leq 10^{-4}$ eV atom^{-1}. The kinetic energy cut-off of wave-functions is set to 520 eV and a Γ-centered 6 × 6 × 6 k-mesh is used to sample the Brillouin Zone (BZ). To investigate the electron cloud delocalization effect near specific (vacancy) sites, electron localization function (ELF) has been depicted in the concerned Bragg planes.

5.3 Results and discussion

5.3.1 Addressing non-stoichiometry in Fe_3O_4

A thorough XPS survey reveals Fe 2*s*, 2*p*, 3*s*, and 3*p*-peaks along with an Auger peak; as well as signatures of 1*s* orbitals in C and O, see Figure 5.4(a). For high-spin ferrous/ferric compounds, the $2p_{3/2}$ peak undergoes broadening compared to metallic $\left[Fe^{(0)}\right]$ or low-spin Fe^{2+}.[78] Gupta and Sen[79] described this broadness as an outcome of electrostatic interactions and spin-orbit coupling among the 2*p*-core hole and unpaired 3*d* electrons inside the photoionized cation due to crystal field interactions. Moreover, partially filled *d*-orbitals cause complex multiplet splitting recasting the peak-structure. Crystallographically, magnetite $\left\{(Fe_A^{3+})\left[Fe_B^{2.5+}\right]_2(O^{2-})_4\right\}$ holds two kinds of cationic sites: one tetrahedral A-site and two octahedral B-sites per formula unit. Hence for rigorous analysis, the high resolution XPS spectra of Fe $2p_{1/2}$ and $2p_{3/2}$ peaks are further deconvoluted into two components against tetrahedral and octahedral occupancies along with a satellite peak [Figure 5.4(b)] with a squared deviation of $\chi^2 \leq 1.09$. The binding energies of the tetrahedral/octahedral components are comparable with previous literature.[80] The satellite near 718 eV is assigned to the surface-peak of maghemite (γ-Fe_2O_3) due to unavoidable partial oxidation on the outer surface of MNPs, common in most transition metal oxides (TMO).

The O 1*s* and C 1*s* spectra have been fitted into three components each; considering lattice oxygen, aliphatic C–C bonds and contributions from various groups located in the mono/bidentate carboxylates present in the coating agents, see Figure 5.4(c) & (d). The surfactant contributions get enhanced for smaller variants having wider shells around the core to control growth. Using CasaXPS software, atomic composition is determined considering Shirley background. The off-stoichiometry parameter (δ) per Fe-site varied in between 0.032– 0.041 for the tested samples of different size without any prior trend. Therefore, like many other multivalent TMO's, magnetite possesses an inherent non-stoichiometry independent of size,[81,82] manipulated solely by the synthesis protocol. As surface of smaller MNPs is prone to get oxidized partially, desiccated preservation is obligatory. The ratio of relative intensities of the two cationic sites (Fe_A:Fe_B) is found to vary in between 0.56– 0.61, which departs from the stoichiometric ratio of 0.50 significantly; inkling the presence of vacancy-defects in Fe_B sites – a probable origin of this non-stoichiometry. In Fe_3O_4, the nature of all possible point-defects is further explored scrupulously via first-principles calculations, that clarifies the situation in a better way.

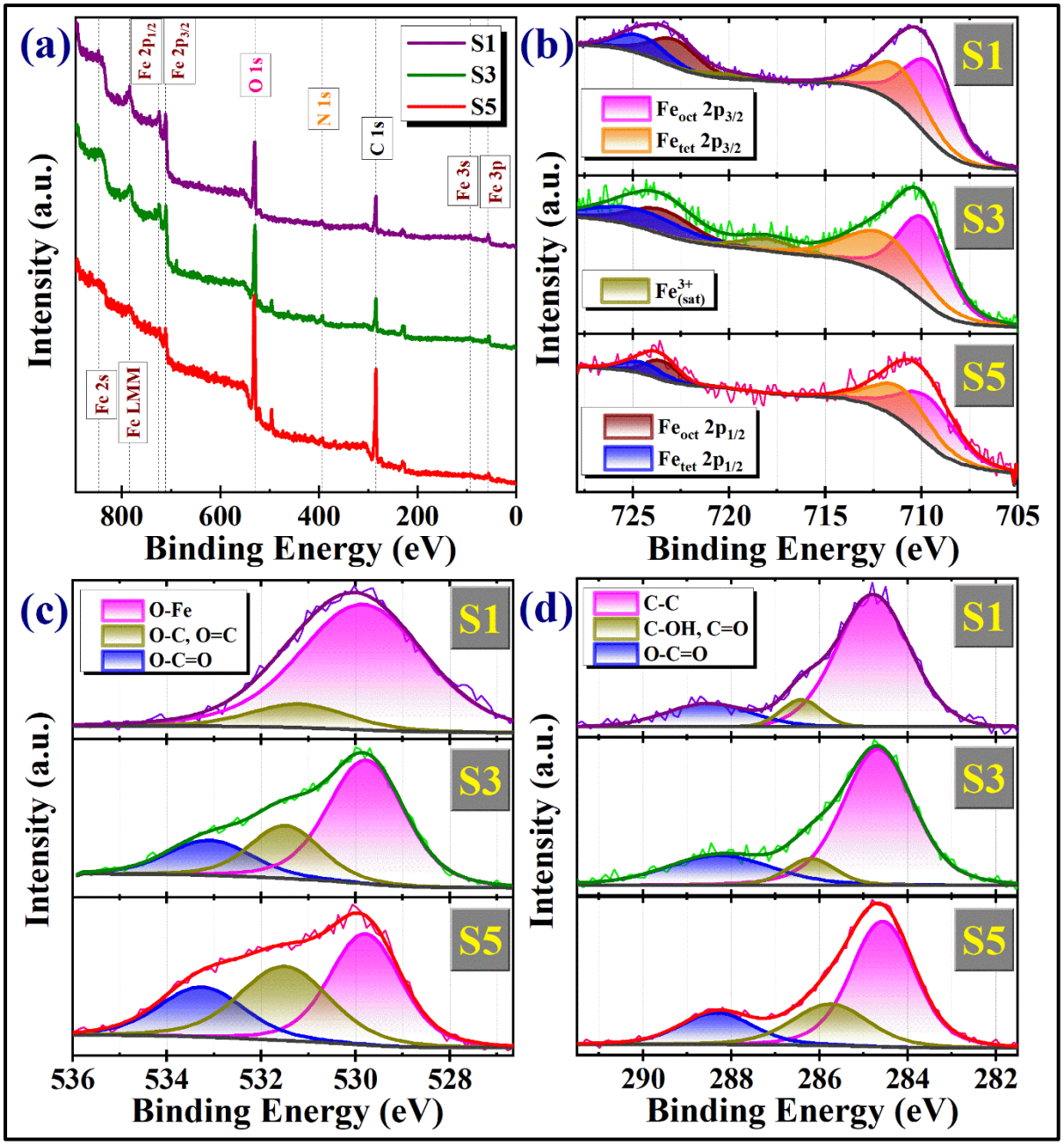

Figure 5.4 (a) XPS elemental survey scanning: trace of C, N, O and Fe; (b) High resolution scan of Fe 2*p* band and its deconvolution to tetrahedral and octahedral contributions along with a Fe^{3+} satellite peak; (c) & (d) HR scan of O 1*s* and C 1*s* peaks and their deconvolution to isolate lattice bonds and capping agent contributions. With thicker shells wrapping smaller MNP's; the O-C, O=C and O-C=O components gradually get intensified.

DFT calculations are performed on the conventional unit cell containing 56 atoms to determine vacancy formation energies (E_f) of one anionic and two cationic sites by removing corresponding atoms from the cell to build the mono-vacant structures from the equation: $E_f = E_v - E_p + \mu$, where E_v is the total energy of the optimized Fe_3O_4 structure with vacancy-defect, E_p is the total energy of pristine magnetite and μ is the chemical potential of the removed

atom.[83-85] The chemical potential of Fe atom is calculated from bulk Fe,[84] whereas for single oxygen atom; it is set with respect to the equilibrium gas state $\frac{1}{2}E_{O_2}$.[86-87] As DFT-GGA noticeably overestimates the binding energy of an O_2 molecule, a correction term must be added to the calculated O_2 energy, which we adopted from the reported O_2 total energy: – 8.50 eV for the PBE functional;[83,86] using the O PAW pseudopotential. This leads to the results of Table 5.1. Comparing the results, we get a prominent trend of least E_f for Fe_{oct} sites, making it the predominantly possible vacancy-defect in magnetite at ambient conditions; which consents XPS results. Now, the anti-ferrimagnetic super-exchange interaction between the Fe_{oct}^{3+} and Fe_{tet}^{3+} sites coupling through the overlapping O $2p$ orbital and the predominant ferromagnetic double-exchange interaction between the Fe_{oct}^{2+} and Fe_{tet}^{3+} sites establish ferrimagnetic alignment of dipoles.[63] Again, the minority spin-polarized electronic conductivity is governed by the hopping of an extra down-spin electron among the octahedral sites;[55-57,61,62] making Fe_B the most consequential co-ordination governing the electronic and magnetic properties of Fe_3O_4. Hence, point-defects in such sites can out-turn distinct properties dramatically.

Table 5.1 Formation energy in eV of neutral mono-vacancies in Fe_3O_4

Vacancy sites	$U_{eff} = 3.50\ eV$	$U_{eff} = 3.75\ eV$	$U_{eff} = 4.00\ eV$
$V_{Fe_{tet}}^{X}$	3.28	3.31	3.24
$V_{Fe_{oct}}^{X}$	2.54	2.41	2.38
V_{O}^{X}	3.53	3.17	3.40

The source of non-stoichiometry might be many-fold though. To minimize free energy ($F = U - TS$), materials often increase their entropy (S) via formation of point-defects. Besides, partial oxidation of surface-states,[80] dangling bonds and twin-defect[88,89] due to the absence of $[Fe^{2.5+}]_B$ interface-plane spontaneously promote non-stoichiometry driven p-type nature and a consequent electron cloud/hole delocalization panorama. This nonlinearity adds an additional term to the modulation conductance, which often lags the voltage sweep and at a limiting situation; might cause appearance of NC according to Shulman *et al*.[90]

5.3.2 Impedance Spectroscopy

The dielectric response of an ensemble of ideal non-interacting dipoles to an alternating electric field is usually expressed by the Debye relaxation (DR) theory.[91] But, considering feasible interactions with other dipoles and the environment, the relaxation mechanism for symmetrically and asymmetrically broadened loss-peaks are better represented by the Cole-Cole[92] & Cole-Davidson[50] equations with exponent cum shape-parameters α & β $(0 \leq \alpha, \beta \leq 1)$ respectively. These dynamics have been further merged by Harvriliak and Negami for

generalization,[93] which reduces to DR with a single relaxation time for $\alpha = \beta = 1$. For angular frequency; $\omega = 2\pi f$, complex permittivity $[\hat{\varepsilon}(\omega) = \varepsilon'(\omega) - j\varepsilon''(\omega), j = \sqrt{-1}]$ and the real and imaginary parts, entailing storage and dissipation/loss of energy; can be expressed as follows.

Table 5.2 Dipolar relaxation models

Debye Relaxation		**Havriliak-Negami (HN) Model**	
$\hat{\boldsymbol{\varepsilon}}(\boldsymbol{\omega}) = \boldsymbol{\varepsilon}_\infty + \dfrac{\Delta\boldsymbol{\varepsilon}}{\mathbf{1} + \boldsymbol{j\omega\tau}}$	(5.1A)	$\hat{\varepsilon}(\omega) = \varepsilon_\infty + \dfrac{\Delta\varepsilon}{\{1 + (j\omega\tau)^\alpha\}^\beta}$	(5.2A)
$\boldsymbol{\varepsilon}'(\boldsymbol{\omega}) = \boldsymbol{\varepsilon}_\infty + \dfrac{\boldsymbol{\varepsilon}_s - \boldsymbol{\varepsilon}_\infty}{\mathbf{1} + \boldsymbol{\omega^2\tau^2}}$	(5.1B)	$\varepsilon'(\omega) = \varepsilon_\infty + \dfrac{(\varepsilon_s - \varepsilon_\infty)\cos\beta\varphi}{\left[1 + 2(\omega\tau)^\alpha \cos {}^{\alpha\pi}/_2 + (\omega\tau)^{2\alpha}\right]^{\beta}/_2}$	(5.2B)
$\boldsymbol{\varepsilon}''(\boldsymbol{\omega}) = \dfrac{(\boldsymbol{\varepsilon}_s - \boldsymbol{\varepsilon}_\infty)\boldsymbol{\omega\tau}}{\mathbf{1} + \boldsymbol{\omega^2\tau^2}}$	(5.1C)	$\varepsilon''(\omega) = \dfrac{(\varepsilon_s - \varepsilon_\infty)\sin\beta\varphi}{\left[1 + 2(\omega\tau)^\alpha \cos {}^{\alpha\pi}/_2 + (\omega\tau)^{2\alpha}\right]^{\beta}/_2}$	(5.2C)

Here, ε_s is the static (saturated) permittivity, ε_∞ gives the high-frequency limit, $\Delta\varepsilon = \varepsilon_s - \varepsilon_\infty$ is known as the polarisation strength, $\varphi = \tan^{-1}\left[\frac{(\omega\tau)^\alpha \sin {}^{\alpha\pi}/_2}{1+(\omega\tau)^\alpha \cos {}^{\alpha\pi}/_2}\right]$ and τ is the characteristic relaxation time of the oscillating dipoles. These formulae retain similar form for analogous dielectric quantities such as impedance ($Z = Z' + jZ''$), admittance (Y), modulus (M) *etc*. To understand the complete impedance response, a 3D Cole-Cole curve is plotted for S1 and S5 with five bias voltages *viz.*, $V = 0.0, 0.1, 0.3, 0.6$ & 1.0 Volts as shown in Figure 5.5 and fitted with the HN equations; which leads to the extraction of the shape-parameters. The fitting parameters (α & β) in the Harvriliak-Negami model as obtained from the Cole-Cole plots of all the samples are listed in Table 5.3. Comparing the two extreme sizes, a little higher overall resistivity for the smaller variant is observed conforming general trends. The bent semicircles stabilized with a negative ($-Z''$) value, indicates NCR at lower frequencies. Although the sample S1 develops NC only on application of moderate bias-voltage (in the range of measurement), the smallest sample (S5) holds NC even without bias.

Table 5.3 Values of the fitting parameters (α & β) for all samples at different bias

	α					**β**				
Bias:	**0.0 V**	**0.1 V**	**0.3 V**	**0.6 V**	**1.0 V**	**0.0 V**	**0.1 V**	**0.3 V**	**0.6 V**	**1.0 V**
S1	0.985	0.985	0.986	0.988	0.990	0.692	0.693	0.699	0.703	0.708
S2	0.970	0.972	0.975	0.979	0.984	0.635	0.638	0.643	0.649	0.651
S3	0.975	0.976	0.979	0.982	0.988	0.561	0.565	0.569	0.572	0.577
S4	0.992	0.995	0.998	0.998	1.000	0.599	0.601	0.604	0.607	0.613
S5	0.990	0.991	0.996	0.997	0.999	0.617	0.620	0.621	0.623	0.624

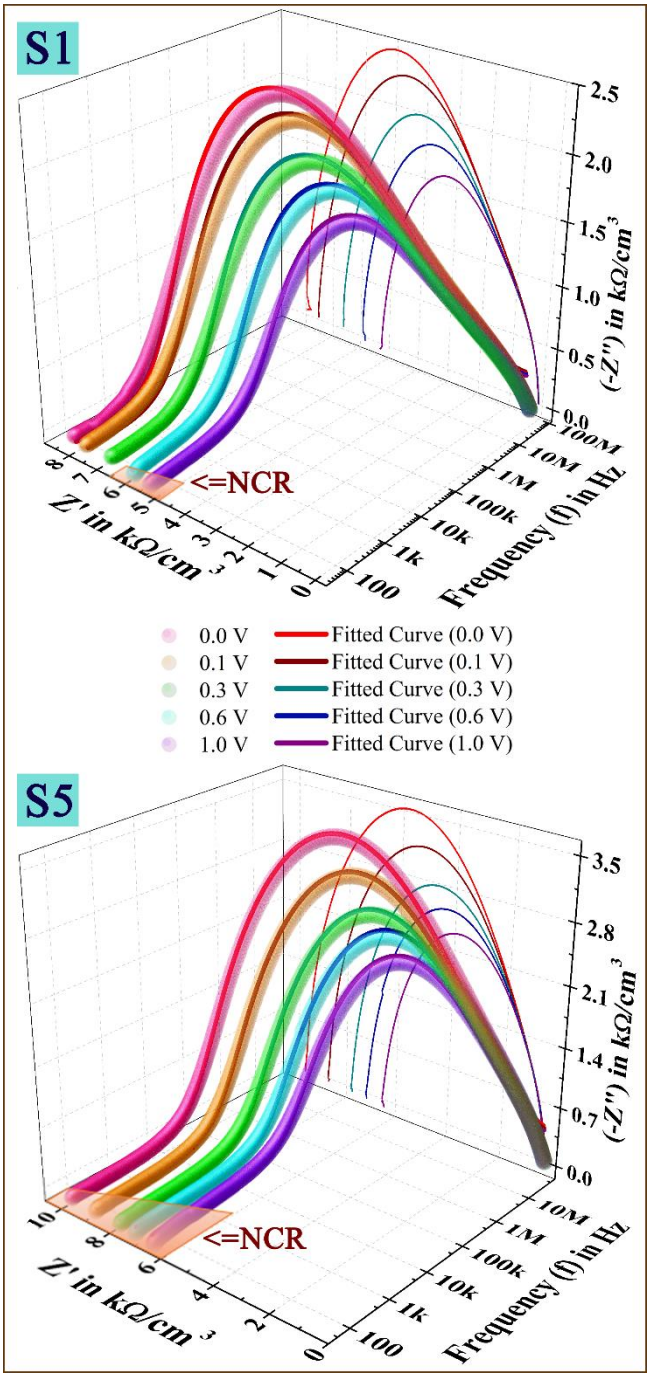

Figure 5.5 3D Cole-Cole plot fitting employing Havriliak-Negami model for the largest (S1) and smallest (S5) nanoparticles for various external bias and identification of stabilized NCR. The semi-transparent broad lines consist of experimental data-points and intense solid lines are the fitted curves. The $(-Z^{"})$ vs Z' projection entitles conventional 2D Cole-Cole curves.

For all the samples, α and β are found to vary in between 0.97– 1.00 and 0.56– 0.71 respectively; which imply small deviation from DR for such an archetypical ferrite compound.[58] Hence, time-dependent dielectric displacement vector $[\vec{D}(t)]$ varies with electric field $[\vec{E}(t)]$ and polarization vector $[\vec{P}(t)]$ in the usual way,

$$\vec{D}(t) = \varepsilon_s \left[\varepsilon_\infty \vec{E}(t) - (\varepsilon_s - \varepsilon_\infty) \int_{-\infty}^{t} \left\{ \frac{d}{dt'} \left(\frac{\vec{P}(t')}{\vec{P}(0)} \right) \right\} \vec{E}(t - t') dt' \right]. \quad (5.3)$$

In literature, ferrites are often seen to possess distinct grain-grain boundary resistance correlations. Their grains might deliver almost equal resistivity as the grain-boundaries.[94] The Cole-Cole curves show unclear dissociation between the grain and grain-boundary contributions, which reflects an identical situation ceasing MWIP. No prior electrode polarization effect is detected in the operating frequency range, which although might become significant at further lower frequencies.

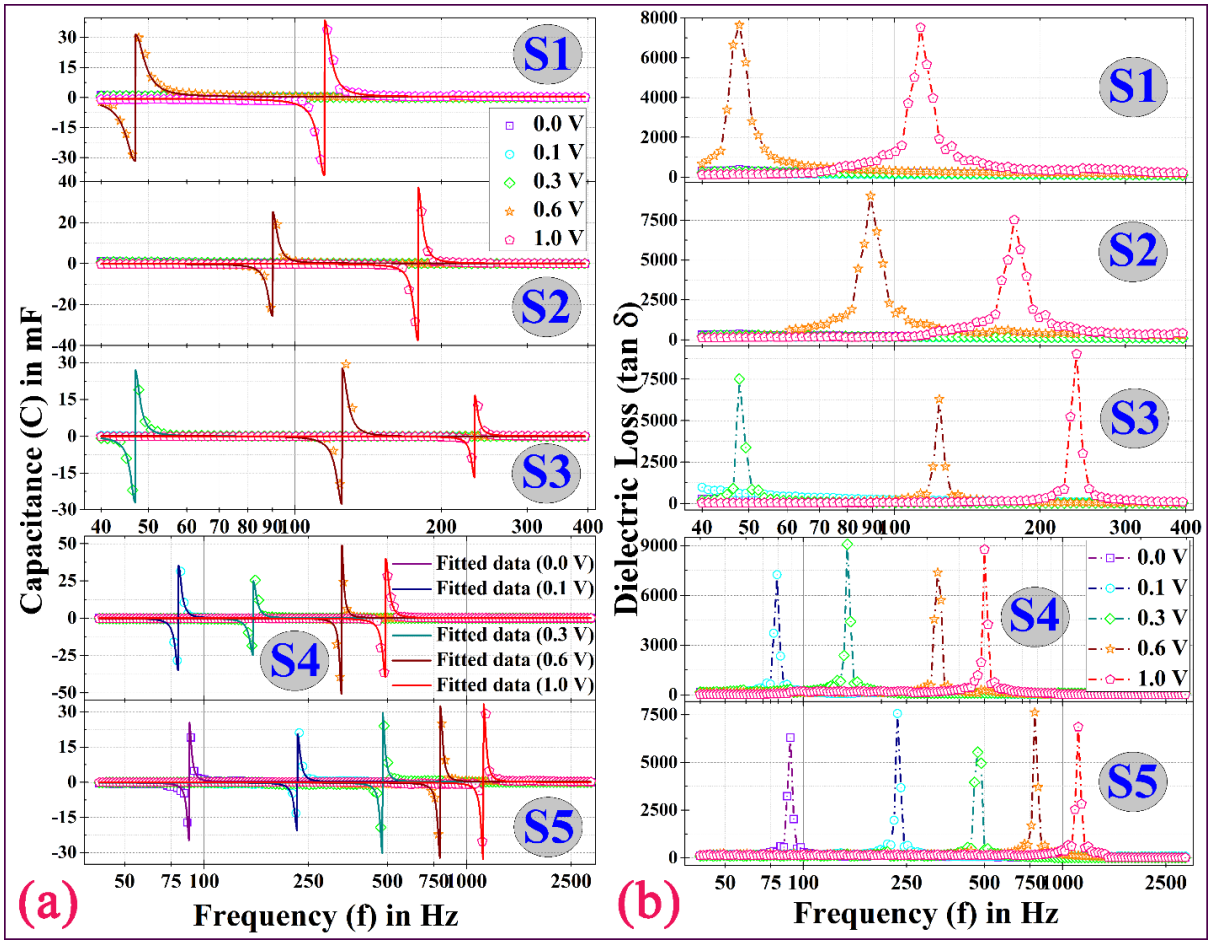

Figure 5.6 (a) Capacitive switching for all samples at different external field. From S1 – S5, capacitance switches in lower external bias. By fitting the line-shape with equation 5.5, related parameters are extracted; (b) dispersion of dielectric loss-tangent with subsequent delta-peaks.

The series-capacitance (C) demonstrates a striking and further insightful dispersion, see Figure 5.6(a). All the samples, except S5, persists only in PCR (~μF) in absence of DC field in the operating frequency-range. But application of specific bias inverts sign of capacitance. While switching at a suitable DC field, capacitance gets amplified to mF order at a characteristic frequency. The largest sample (S1) discloses NC at lower frequencies on application of ≥ 0.6 V

bias, which blueshifts for the smaller variant S2. For S3 and S4, NC is demonstrated successively at smaller bias-voltages; whereas the smallest variant S5 prevails NC at nil bias. It contradicts the generalized mechanism of NC suggested by Shulman *et al.*[90] in consequence of DC bias superimposed on AC input in a nonlinear media. Although considering non-stoichiometry induced quasi-Fermi levels (E_F) due to majority and minority carriers, an internal potential might develop between terminal contacts, $V_0 = -\frac{1}{e}\left(E_{F_n} - E_{F_p}\right)$ against differential carrier generation.[45] On application of DC field, the NCR extends to higher frequencies even up to kHz order for the smaller nanoparticles. The trend of data hints at the existence of NC for all the samples at lesser frequencies for smaller or even nil bias. So, the origin of NC could be collective, but the outcome is size-dependent. The transition-point between NCR and PCR holds a unique peak-shape (elaborated later), similar as reported by Mazumder *et al.*[45] Another resembling line-shape was reported by Kim *et al.*[95] in a slightly different context. In an $Al_2O_3/BaTiO_3$ bilayer structure, the variation of curvature of internal energy (U) vs polarisation (P) *i.e.*, $\left(\frac{d^2U}{dP^2}\right)^{-1}\Big|_{P=0}$ ($\propto C$), with the thickness of the dielectric layer attains this shape near a critical thickness, which indicates a frustration in NC due to an unstable competition comprising the capacitances of the ferroelectric and dielectric counterparts.

Dispersion-formula of capacitance ($\propto \varepsilon'$) can be adopted from UDR [Equation (5.1B)]. But for materials, that exhibit both +ve and –ve values of capacitance, this expression fails to fit the experimental data due to shifting of 'quasi-static' NC plane to a new frequency *viz.* f_0. Thus, to describe positive capacitance dispersion, the formula is modified as follows:

$$C_+(f) = C(\infty) + \frac{\Delta C_+}{1 + 4\pi^2(f - f_0)^2\tau^2}, C(\infty) > 0, \Delta C_+ = C_{s+} - C(\infty) \to 0_+ \qquad (5.4A)$$

Likewise, the negative capacitance dispersion can be formulated as:

$$C_-(f) = C(0) + \frac{\Delta C_-}{1 + 4\pi^2(f_0 - f)^2\tau^2}, C(0) < 0, \Delta C_- = C(0) - C_{s-} \to 0_- \qquad (5.4B)$$

Practically, $C(0)$ *i.e.*, the absolute DC capacitance is not negative, as the phase lead/lag is undefined for steady field. These two formulae can be merged to evaluate the complete dispersion by considering, $|C(\infty)| \cong |C(0)| = C_0$ (as the limiting value of the phase-lead or lag acquired by the associated dipoles; typically settles for the same order of magnitude) and $|\Delta C_+| \cong |\Delta C_-| = |\Delta C|$ via a step-function defined as: $\Theta(f, f_0) = -1\ for\ f < f_0\ and + 1\ for\ f > f_0$; but undefined at $f = f_0$; *e.g.*, $\frac{f - f_0}{|f - f_0|}$. So, the proposed modification of UDR is given by,

$$C(f) = \Theta(f, f_0)\left[C_0 + \frac{|\Delta C|}{1 + 4\pi^2|f - f_0|^2\tau^2}\right]. \qquad (5.5)$$

This new formalism matches that unique line-shape including the divergence and by fitting the full-range experimental data using equation 5.5, relaxation-time (τ) has been extracted, which

falls with increasing DC bias and decreasing particle-size as shown in Figure 5.7(d). Realization of a single relaxation time as well manifests absence of notable contact-dielectric interfacial polarization concerning a different characteristic time and ensures ohmic nature of the electrode connections. This precise fitting also suggests correlation of the underlying mechanism displaying NC with particular dipoles, elaborated in the next section. Correspondingly, dielectric loss-tangent $\left[\tan\delta = \frac{\varepsilon''(\omega)}{\varepsilon'(\omega)}\right]$ exhibits subsequent delta functions [Figure 5.6(b)] at the transition-frequencies; which indicates the maximum phase lag between oscillating dipoles and sweeping waveform. The switching-point undergoes blue-shifting with higher external field and smaller size.

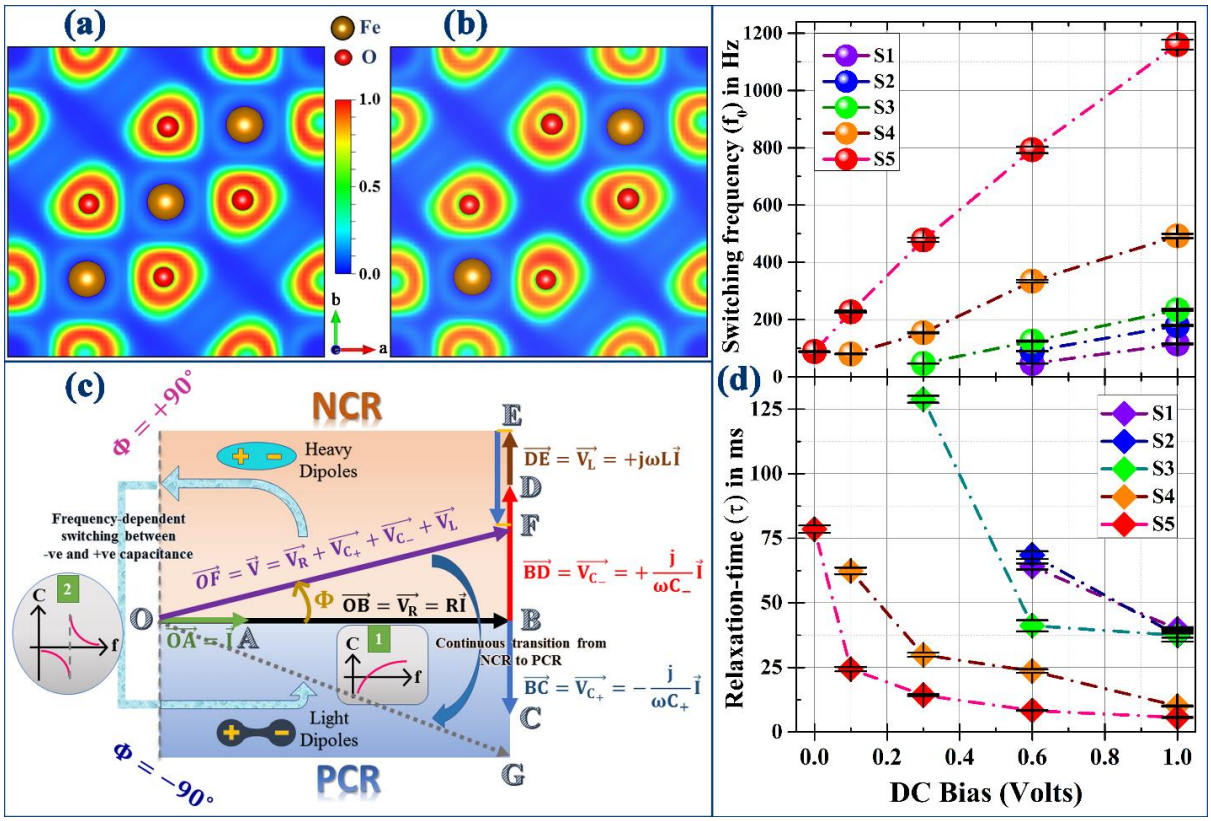

Figure 5.7 (a) ELF at (002) plane in pristine Fe_3O_4; (b) Electron cloud delocalization and drop in charge-density in the vicinity of the removed central octahedral Fe atom; (c) Schematic diagram to explain NC-switching vs continuous transition from heavy dipolar relaxation model. The two possible evolution-trajectories are shown with respective capacitance dispersions; (d) Consolidated results showing dependency of switching frequency and relaxation time on particle-size and DC bias.

5.3.3 Heavy Dipolar Relaxation Model and NC-Switching

The inner dynamics of the NC associated dipoles can be well-explained by the phasor-diagram schematics shown in Figure 5.7(c). Let $\overrightarrow{OA}$ be the current vector ($\vec{I}$). In Electrostatics

regarding MIM structures, the conduction current is considered negligible and the total electric current is due to the displacement component, related to the redistribution of bound charges.[5] The system possesses resistive, capacitive and inductive components due to grain & grain-boundary contributions, dielectric polarization and non-linear hopping of charge-carriers respectively. It also develops NC-effects related to the spontaneous non-stoichiometry present in Fe_3O_4. Let, the corresponding voltage vectors be $\overrightarrow{V_R}$, $\overrightarrow{V_L}$, $\overrightarrow{V_{C+}}$ and $\overrightarrow{V_{C-}}$ represented by the lines $\overrightarrow{OB}$, $\overrightarrow{DE}$, $\overrightarrow{BC}$ and $\overrightarrow{BD}$. The resultant voltage vector, $\vec{V} = \overrightarrow{V_R} + \overrightarrow{V_L} + \overrightarrow{V_{C+}} + \overrightarrow{V_{C-}}$ makes an angle $\Phi(\omega) = \tan^{-1}\left\{\frac{\omega L - \left(\frac{1}{\omega C_+} - \frac{1}{\omega C_-}\right)}{R}\right\}$ with $\vec{I}$. The sign of Φ depends on the parameters L, C_+ and C_-. Initially at a small frequency, let the state of the system be represented by the vector $\overrightarrow{OF}$ with $\Phi > 0$, indicating NC. At an increased value of frequency, let the system evolve to a final state: $\overrightarrow{OG}$ at PCR having $\Phi < 0$. Now, this $\overrightarrow{OF} \rightarrow \overrightarrow{OG}$ progression can take place in two paths, associated with two completely different origin.

The first one is the continuous dispersion from NCR to PCR, abundant in literature[10,13-32,35,36] caused by continual effects of contact-injection & transport, localized charge recombination, relaxed transients, interference between MWIP and hopping conduction mechanisms, detrapping of charge-carriers etc. Here Φ gradually decreases and crossing through the frequency-axis reaches PCR. This dispersion can be mathematically modelled as an L-C-R circuit, in which the state of the system passes through a point (on the real axis); where the two competing effects exactly nullify each other ($\Phi = 0$); leaving a purely resistive element. Even at this null-point, the system is perfectly stabilized. As outlined by Ershov[24] and Jonscher *et al.*,[96] this genre of NC is better appraised in the time domain. However, the association of negative-differential dielectric constant from Maxwell's equation in frequency domain: $(\sigma + j\omega\varepsilon')\vec{V}.\vec{E} = 4\pi\rho_{ext}$ involves specific information regarding the nonlinearity and 'external' charge-density (ρ_{ext}) of the system. In case of bipolar injection or trap-mediated recombination, a finite electron-hole recombination rate enclosing a small volume ($\delta V'$), generates a 'recombination current' $\left[j_r(t) \propto \left\{1 - e^{-t/\tau_r}\right\}, \frac{dj_r}{dt} > 0, \frac{d^2 j_r}{dt^2} < 0\right]$ in addition to the space charge limited current,[17] promoting an NC surge, given in terms of Fourier decomposition,

$$\Delta C_r(\omega) = \frac{1}{\delta V'} \int_0^\infty j_r(t) \cos \omega t \, dt = -\frac{\eta C_0}{1 + \omega^2 \tau_r^2}, \qquad (5.6)$$

where, η is a dimensionless parameter related to the contributing volume, C_0 is the static geometrical capacitance and τ_r is the characteristic capture/rupture time for a charge carrier getting trapped in an oppositely charged defect-state. As the capture rate is not expected to increase with bias, τ_r should not decrease with a voltage impulse $\Delta V(> 0)$, contradictory to our observations. Besides, Langevin-type bimolecular recombination[17] is not pertinent to our

system. Hence, our results do not reflect the salient characteristics of Type-I NC. Any system develops polarization either by accumulation of charges at surfaces and interfaces or by an organized alignment of accompanying dipoles. Type-I NC is all about temporal depletion of the former due to various reasons; whereas Type-II is related to the latter.

To recognize the physical mechanism behind the 2nd path, which resembles the line-shape of our capacitive dispersion, the nature of the associated dipoles needs further exploration. An ideal dipole forms when two 'point-charges' are separated by a small distance, possible for a mathematical lattice. However, in a real material, there are electron-clouds and charge-densities associated with a crystal structure, which have certain 'charge-centres' (+ve/-ve). When two opposite charge-centres get separated by a finite distance, a 'light' dipole is formed. But, if the electron-cloud is sufficiently delocalized in case of more covalent bonds due to some point-defects or doping impurities, the associated dipoles get 'heavier', in a sense their effective length (l_{eff}) contracts reasonably with respect to the geometrical length; due to shifting of the electron-density towards the centre of the bond. To demonstrate this outlook in our system, ELF in the vicinity of $V_{Fe_{oct}}^{X}$ is compared with respect to that of the pristine lattice in Figure 5.7(a) & (b). The blue to red colour scale indicates gradually increasing Pauli repulsion compared to that of the classical electron gas. As the electron cloud gets delocalized and charge-density declines in the vicinity of $V_{Fe_{oct}}^{X}$, the shifted positive and negative charge-centres cease to coincide resulting deviant localized dipoles in the system. For the same amount of external field, these 'heavy' dipoles are by definition less likely to get mobilized for sensing a reduced force/torque and thereby possess higher electrical inertia. Hence these slow dipoles lag behind the AC signal and consequently originate NC. Now, as the frequency increases, it becomes more and more difficult to follow the input signal; resulting an increase in Φ. At a limiting condition, $\Phi \to +90°, \tan\Phi \to +\infty$; indicating complete failure of the correlated dipoles to match up the input phase. Eventually, further increase in frequency makes the system go beyond $\Phi = +90°$ and crossing a divergence (indicates an infinte discontinuity in C and loss-maxima); ends up at $\Phi = -90°$ and finally settles to an acute negative Φ. Basically, these heavy dipoles fail to achieve frequency-dependent dielectric saturation, as suggested by Richert[97] and eventually encounters a switching to reach so. In this case, there is no such point in the evolution-trajectory of the system, in which it behaves like a pure resistor and here a switching takes place between NCR and PCR via a transient at a characteristic switching frequency (f_0). These features were missing in the Cole-Cole plots, as Z'' $(\sim C^{-1})$ holds no deviation for sudden colossal capacitive gain and assessed as an ineffective mean to distinguish NC switching (Type-II) from continuous transitions (Type-I). The so-called 'light' dipoles being empowered by the high frequency of the alternating signal in presence of detrapped/injected carriers start eventually following up the input sweep and transit to PCR; whereas the slow and heavy dipoles lag further behind and

consequently consumes an energy E_{flip} ($\sim f_0$) to pursue a complete flip (polarisation switching) to get into PCR. Hence, the switching-frequency (f_0) is a measure of the flipping energy required for the mobilization of the 'heavy' dipoles and relaxation-time (τ) is a measure of the flipping-kinetics. Basically, the dipoles relax according to the Debye theory before and after the flipping-point marked by the loss-maxima. The flipping energy can be deduced as: $E_{flip} \approx \frac{1}{2\tau}\int_t^{t+2\tau}\int_0^{\pi}\left|\vec{p}(\delta, l_{eff}, V, d)X\vec{E}(t')\right|d\theta\, dt'$ for the heavy dipoles with moment $\vec{p}$ in an AC field $\vec{E}(t)$. Using this model, the variation of f_0 and τ with DC bias and particle size [Figure 5.7(d)] can be explained as discussed in Table 5.3.

Table 5.3 Physical explanations of quantitative results

Sl. No.	Observations		Explanation
	Cause	Effect	
1	Increase in DC bias (V)	f_0 increases.	At higher bias field, the dipoles get stiffened to its direction and show higher tolerance against the AC sweeps, hence require larger energy to flip around.
2		τ decreases.	At higher voltage, dipoles – a construction of charges acquire higher potential energy, which helps to speed up the flipping kinetics, and consequently the net flipping-time $(t_{flip} \approx 2\tau)$ decreases.
3	Decrease in particle-size (d)	f_0 increases.	With decreasing grain-size, resistivity generally increases in semiconducting materials due to enhanced effect of grain-boundaries. A highly resistive sample is less likely to respond to a weak external field, due to substantial voltage-drop. Hence, to flip the dipoles, a larger energy needs to be supplied.
4		τ and FWHM of loss-peaks decrease.	In a domain, the 'heavy' dipoles form their own mean field[98,99] with a default orientation having optimized energy; sensitive to applied DC bias. The flipping kinetics basically compete with the mean field inside and try to reorient the associated dipoles. With a smaller domain-size, the mean-field effect weakens gradually and hence an external field can regulate faster the assembly of dipoles.

To verify this proposition, samples with NC properties are annealed at 100 °C in controlled H_2/N_2 (10:90) gas-flow (250 $cm^3\ min^{-1}$) for an hour to push off the excess oxygen and the resultant pellets either lost NC or the NCR shifted to a lower frequency out of our range, an

indicative of lightening of the correlated dipoles. Moreover near-stoichiometric MNPs synthesized in other routes exhibited no NC. This model also supports absence of any threshold bias for the manifestation of NC. For S5, NC shows at nil bias in the operating range; whereas for larger samples trend of data suggests that, f_0 is smaller than the instrumental limit. Application of bias lifts f_0 up and extends NCR to broader range; so that the capacitance eventually switches sign in the observable frequency-span. Although in this model, more covalent bonds have been attributed for the slower response, it hardly means, covalent molecules are in general more likely to demonstrate NC. Defect-driven heavy dipoles with smaller effective length incommensurate to the stream of ordinary dipoles assist persistence of NC; otherwise, ionic compounds are more liable to conceive dipolar relaxation.

5.4 Concluding remarks

Summarily, physical origin of NC is based on two mechanisms: (i) Lack of polarization or charge-accumulation at specified regions on account of extraneous time-dependent diversion of carrier-population and (ii) suspension of usual dipolar relaxation by a delocalized inertial charge-ensemble. In case of Fe_3O_4, the samples S1-S5, having a decreasing order of particle-size, intend to stabilize NC for a broader range of frequency. The same effect is accomplished by raising external DC bias. A non-stoichiometry driven heavy dipolar relaxation is attributed for this NC switching dynamics, resembling the second category. Actually, the Type-I NC corresponds to time-dependent injection/displacement/recombination currents, which pass through the system without assisting any electrical storage of energy. As continuous increment in charge-carrier density due to contact-injection or detrapping violates the fundamental assumption of non-interacting dipoles, neither Debye nor the updated models given by Cole, Davison, Havriliak and Negami fit to those observations. Contrarily, for Type-II NC, sluggish dipolar relaxation dominates over the MWIP and the relaxation-dynamics ceases only at the moment of dipole flipping. Before and after this reversal, the dipoles relax the way suggested by Debye. Furthermore, materials comprising such low-frequency stable NC (~μF) can be implemented in quantum well photodetectors, smart photovoltaic and spintronic devices to uncover new inceptions.

References

1. A. I. Khan, K. Chatterjee, B. Wang, S. Drapcho, L. You, C. Serrao, S. R. Bakaul, R. Ramesh and S. Salahuddin, *Nature Mater.*, 2015, **14**, 182.
2. D. J. Appleby, N. K. Ponon, K. S. Kwa, B. Zou, P. K. Petrov, T. Wang, N. M. Alford and A. O'Neill, *Nano Lett.*, 2014, **14**, 3864-3868.
3. P. Zubko, J. C. Wojdeł, M. Hadjimichael, S. Fernandez-Pena, A. Sené, I. Luk'yanchuk, J.-M. Triscone and J. Íñiguez, *Nature*, 2016, **534**, 524.

4. S. Salahuddin and S. Datta, *Nano Lett.*, 2008, **8**, 405-410.
5. M. Beale and P. Mackay, *Philos. Mag. B*, 1992, **65**, 47-64.
6. C. Wang, C. Zhu, G. Zhang, J. Shen and L. Li, *IEEE Trans. Electron Devices*, 2003, **50**, 1145-1148.
7. C. Zhu, L. Feng, C. Wang, H. Cong, G. Zhang, Z. Yang and Z. Chen, *Solid-State Electron.*, 2009, **53**, 324-328.
8. P. Walsh, R. Vogel and E. J. Evans, *Phys. Rev.*, 1969, **178**, 1274.
9. R. Vogel and P. Walsh, *Appl. Phys. Lett.*, 1969, **14**, 216-218.
10. V. Kytin, T. Dittrich, F. Koch and E. Lebedev, *Appl. Phys. Lett.*, 2001, **79**, 108-110.
11. M. Hoffmann, M. Pešić, K. Chatterjee, A. I. Khan, S. Salahuddin, S. Slesazeck, U. Schroeder and T. Mikolajick, *Adv. Funct. Mater.*, 2016, **26**, 8643-8649.
12. J. Muller, T. S. Böscke, U. Schröder, S. Mueller, D. Brauhaus, U. Bottger, L. Frey and T. Mikolajick, *Nano Lett.*, 2012, **12**, 4318-4323.
13. I. Mora-Sero, J. Bisquert, F. Fabregat-Santiago, G. Garcia-Belmonte, G. Zoppi, K. Durose, Y. Proskuryakov, I. Oja, A. Belaidi and T. Dittrich, *Nano Lett.*, 2006, **6**, 640-650.
14. F. Fabregat-Santiago, M. Kulbak, A. Zohar, M. Vallés-Pelarda, G. Hodes, D. Cahen and I. n. Mora-Seró, *ACS Energy Lett.*, 2017, **2**, 2007-2013.
15. A. Dualeh, T. Moehl, N. Tétreault, J. Teuscher, P. Gao, M. K. Nazeeruddin and M. Grätzel, *ACS Nano*, 2013, **8**, 362-373.
16. J. Shulman, S. Tsui, F. Chen, Y. Xue and C. Chu, *Appl. Phys. Lett.*, 2007, **90**, 032902.
17. E. Ehrenfreund, C. Lungenschmied, G. Dennler, H. Neugebauer and N. Sariciftci, *Appl. Phys. Lett.*, 2007, **91**, 012112.
18. J. Bisquert, G. Garcia-Belmonte, Á. Pitarch and H. J. Bolink, *Chem. Phys. Lett.*, 2006, **422**, 184-191.
19. H. Gommans, M. Kemerink and R. Janssen, *Phys. Rev. B*, 2005, **72**, 235204.
20. L. Pingree, B. Scott, M. Russell, T. J. Marks and M. C. Hersam, *Appl. Phys. Lett.*, 2005, **86**, 073509.
21. L. Pingree, M. Russell, T. J. Marks and M. C. Hersam, *J. Appl. Phys.*, 2006, **100**, 044502.
22. J. Bisquert, G. Garcia-Belmonte, Á. Pitarch and H. J. Bolink, *Chem. Phys. Lett.*, 2006, **422**, 184-191.
23. H. Kwok, *Solid-State Electron.*, 2003, **47**, 1089-1093.
24. M. Ershov, H. Liu, L. Li, M. Buchanan, Z. Wasilewski and A. K. Jonscher, *IEEE Trans. Electron Devices*, 1998, **45**, 2196-2206.
25. A. Perera, W. Shen, M. Ershov, H. Liu, M. Buchanan and W. Schaff, *Appl. Phys. Lett.*, 1999, **74**, 3167-3169.

26. L. Bakueva, G. Konstantatos, S. Musikhin, H. Ruda and A. Shik, *Appl. Phys. Lett.*, 2004, **85**, 3567-3569.
27. C. Godet, J.-P. Kleider and A. Gudovskikh, *J. Non-Cryst. Solids*, 2008, **354**, 2637-2640.
28. G. Parravicini, A. Stella, M. Ungureanu and R. Kofman, *Appl. Phys. Lett.*, 2004, **85**, 302-304.
29. W. Huang, J. Peng, L. Wang, J. Wang and Y. Cao, *Appl. Phys. Lett.*, 2008, **92**, 8.
30. F. Chen, J. Shulman, S. Tsui, Y. Xue, W. Wen, P. Sheng and C. Chu, *Philos. Mag.*, 2006, **86**, 2393-2398.
31. I. Mora-Sero, J. Bisquert, F. Fabregat-Santiago, G. Garcia-Belmonte, G. Zoppi, K. Durose, Y. Proskuryakov, I. Oja, A. Belaidi and T. Dittrich, *Nano Lett.*, 2006, **6**, 640-650.
32. F. El Kamel, P. Gonon, F. Jomni and B. Yangui, *Appl. Phys. Lett.*, 2008, **93**, 042904.
33. M. M. Khan, M. Zulfequar and M. Husain, *Physica B: Condens. Mater.*, 2005, **366**, 1-10.
34. M. Ilyas, M. Zulfequar and M. Husain, *Physica B: Condens. Mater.*, 1999, **271**, 125-135.
35. C. Zhu, C. Wang, L. Feng, G. Zhang, L. Yu and J. Shen, *Solid-State Electron.*, 2006, **50**, 821-825.
36. C. Wang, G. Liu, M. He and H. Lu, *Appl. Phys. Lett.*, 2008, **92**, 052905.
37. R. P. Buck, *Ann. Biomed. Eng.*, 1992, **20**, 363-383.
38. S. M. Ross, J. M. Ferrier and J. Dainty, *J. Membr. Biol.*, 1985, **85**, 233-243.
39. E. F. Owede and A. K. Jonscher, *J. Electrochem. Soc.*, 1988, **135**, 1757-1765.
40. K. S. Cole, *Cal. University of California Press*, 1968.
41. A. M. Ionescu, *Nature Nanotechnol.*, 2018, **13**, 7.
42. J. Iniguez, P. Zubko, I. Luk'yanchuk and A. Cano, *Nat. Rev. Mater.*, 2019, 1.
43. L. Tu, X. Wang, J. Wang, X. Meng and J. Chu, *Adv. Electron. Mater.*, 2018, **4**, 1800231.
44. J.-C. M'Peko, *Appl. Phys. Lett.*, 1997, **71**, 3730-3732.
45. N. Mazumder, P. Mandal, R. Roy, U. K. Ghorai, S. Saha and K. K. Chattopadhyay, *J. Appl. Phys.*, 2017, **121**, 135702.
46. F. Fabregat-Santiago, M. Kulbak, A. Zohar, M. Vallés-Pelarda, G. Hodes, D. Cahen and I. n. Mora-Seró, *ACS Energy Lett.*, 2017, **2**, 2007-2013.
47. F. Ebadi, N. Taghavinia, R. Mohammadpour, A. Hagfeldt and W. Tress, *Nat. Commun.*, 2019, **10**, 1574.
48. S. Morgan, *Trans. Electrochem. Soc.*, 1934, **65**, 109-118.
49. T. Hanai, *Kolloid-Zeitschrift*, 1960, **171**, 23-31.
50. G. Adam, *J. Chem. Phys.*, 1965, **43**, 662-669.
51. O. Alatise, N.-A. Parker-Allotey, D. Hamilton and P. Mawby, *IEEE Trans. Power Electron.*, 2012, **27**, 3826-3833.
52. Z. Liu, X. Huang, F. C. Lee and Q. Li, *IEEE Trans. Power Electron.*, 2013, **29**, 1977-1985.

53. K. Butcher, T. Tansley and D. Alexiev, *Solid-State Electron.*, 1996, **39**, 333-336.
54. A. Navrotsky, L. Mazeina and J. Majzlan, *Science*, 2008, **319**, 1635-1638.
55. Y. S. Dedkov, U. Rüdiger and G. Güntherodt, *Phys. Rev. B*, 2002, **65**, 064417.
56. J. Versluijs, M. Bari and J. Coey, *Phys. Rev. Lett.*, 2001, **87**, 026601.
57. K. Kato, S. Iida, K. Yanai and K. Mizushima, *J. Magn. Magn. Mater.*, 1983, **31**, 783-784.
58. M. Ziese, P. Esquinazi, D. Pantel, M. Alexe, N. Nemes and M. Garcia-Hernández, *J. Phys.: Condens. Matter*, 2012, **24**, 086007.
59. J. Blasco, J. García and G. Subías, *Phys. Rev. B*, 2011, **83**, 104105.
60. M. S. Senn, I. Loa, J. P. Wright and J. P. Attfield, *Phys. Rev. B*, 2012, **85**, 125119.
61. R. Kukreja, N. Hua, J. Ruby, A. Barbour, W. Hu, C. Mazzoli, S. Wilkins, E. E. Fullerton and O. G. Shpyrko, *Phys. Rev. Lett.*, 2018, **121**, 177601.
62. J. Coey and C. Chien, *MRS Bull.*, 2003, **28**, 720-724.
63. J. A. Cuenca, K. Bugler, S. Taylor, D. Morgan, P. Williams, J. Bauer and A. Porch, *J. Phys.: Condens. Matter*, 2016, **28**, 106002.
64. A. Bengtson, D. Morgan and U. Becker, *Phys. Rev. B*, 2013, **87**, 155141.
65. S. V. Ovsyannikov, V. V. Shchennikov, S. Todo and Y. Uwatoko, *J. Phys.: Condens. Matter*, 2008, **20**, 172201.
66. A. V. Smirnov and J. A. Tarduno, *Earth. Planet. Sci. Lett.*, 2002, **194**, 359-368.
67. Y. F. Krupyanskii and I. Suzdalev, *J. Phys. Colloq.*, 1974, **35**, C6-407-C406-410.
68. P. E. Blöchl, *Phys. Rev. B*, 1994, **50**, 17953.
69. G. Kresse and J. Hafner, *Phys. Rev. B*, 1993, **47**, 558.
70. G. Kresse and J. Hafner, *Phys. Rev. B*, 1994, **49**, 14251.
71. G. Kresse and J. Furthmüller, *Comput. Mater. Sci.*, 1996, **6**, 15-50.
72. G. Kresse and J. Furthmüller, *Phys. Rev. B*, 1996, **54**, 11169.
73. J. P. Perdew, K. Burke and M. Ernzerhof, *Phys. Rev. Lett.*, 1996, **77**, 3865.
74. S. Dudarev, G. Botton, S. Savrasov, C. Humphreys and A. Sutton, *Phys. Rev. B*, 1998, **57**, 1505.
75. J. Noh, O. I. Osman, S. G. Aziz, P. Winget and J.-L. Brédas, *Sci. Technol. Adv. Mater.*, 2014, **15**, 044202.
76. H. Liu and C. Di Valentin, *J. Phys. Chem. C*, 2017, **121**, 25736-25742.
77. J. Noh, O. I. Osman, S. G. Aziz, P. Winget and J.-L. Brédas, *Chem. Mater.*, 2015, **27**, 5856-5867.
78. A. Grosvenor, B. Kobe, M. Biesinger and N. McIntyre, *Surf. Interface Anal.*, 2004, **36**, 1564-1574.
79. R. Gupta and S. Sen, *Phys. Rev. B*, 1975, **12**, 15.
80. D. Wilson and M. Langell, *Appl. Surf. Sci.*, 2014, **303**, 6-13.

81. S. Lim, B. Choi, S. Y. Lee, S. Lee, H.-H. Nahm, Y.-H. Kim, T. Kim, J.-G. Park, J. Lee and J. Hong, *Nano Lett.*, 2018, **18**, 1745-1750.
82. J. Lee, S. G. Kwon, J.-G. Park and T. Hyeon, *Nano Lett.*, 2015, **15**, 4337-4342.
83. Y.-L. Lee, J. Kleis, J. Rossmeisl and D. Morgan, *Phys. Rev. B*, 2009, **80**, 224101.
84. M. Wu, X. Zhou, S. Huang, J. Cheng and Z. Ding, *Sci. Rep.*, 2018, **8**.
85. L. Zhang, I. Bredeson, A. Y. Birenbaum, P. R. Kent, V. R. Cooper, P. Ganesh and H. Xu, *Phys. Rev. Mater.*, 2018, **2**, 064409.
86. C. Zhang and P. Bristowe, *RSC Adv.*, 2013, **3**, 12267-12274.
87. J. A. Dawson, H. Chen and I. Tanaka, *ACS Appl. Mater. Interfaces*, 2015, **7**, 1726-1734.
88. D. Gilks, Z. Nedelkoski, L. Lari, B. Kuerbanjiang, K. Matsuzaki, T. Susaki, D. Kepaptsoglou, Q. Ramasse, R. Evans and K. McKenna, *Sci. Rep.*, 2016, **6**, 20943.
89. D. Kepaptsoglou, D. Gilks, K. Mckeena, Z. Nedelkoski, B. Keurbanjiang, K. Matsuzaki, T. Susaki, Q. Ramasse and V. Lazarov, *Microsc. Microanal.*, 2016, **22**, 1698-1699.
90. J. Shulman, Y.-Y. Xue, S. Tsui, F. Chen and C. Chu, *Phys. Rev. B*, 2009, **80**, 134202.
91. A. K. Jonscher, *J. Phys. D: Appl. Phys.*, 1999, **32**, R57.
92. K. S. Cole and R. H. Cole, *J. Chem. Phys.*, 1942, **10**, 98-105.
93. S. Havriliak and S. Negami, *Polymer*, 1967, **8**, 161-210.
94. M. Ali, M. Uddin, M. Khan, F.-U.-Z. Chowdhury and S. Haque, *J. Magn. Magn. Mater.*, 2017, **424**, 148-154.
95. Y. J. Kim, M. H. Park, Y. H. Lee, H. J. Kim, W. Jeon, T. Moon, K. Do Kim, D. S. Jeong, H. Yamada and C. S. Hwang, *Sci. Rep.*, 2016, **6**, 19039.
96. A. K. Jonscher, *J. Chem. Soc., Faraday Trans. 2: Mol. Chem. Phys.*, 1986, **82**, 75-81.
97. R. Richert, *Phys. Rev. E*, 2013, **88**, 062313.
98. M. Załuska-Kotur and M. Cieplak, *Europhys. Lett.*, 1993, **23**, 85.
99. D. Dunmur and P. Palffy-Muhoray, *Mol. Phys.*, 1992, **76**, 1015-1023.

6 FIELD-ENHANCED POLARIZATION IN POLYTYPE FERRIC OXIDES: CONFRONTING ANISOTROPY IN DIELECTRIC ELLIPSOID DISPERSION

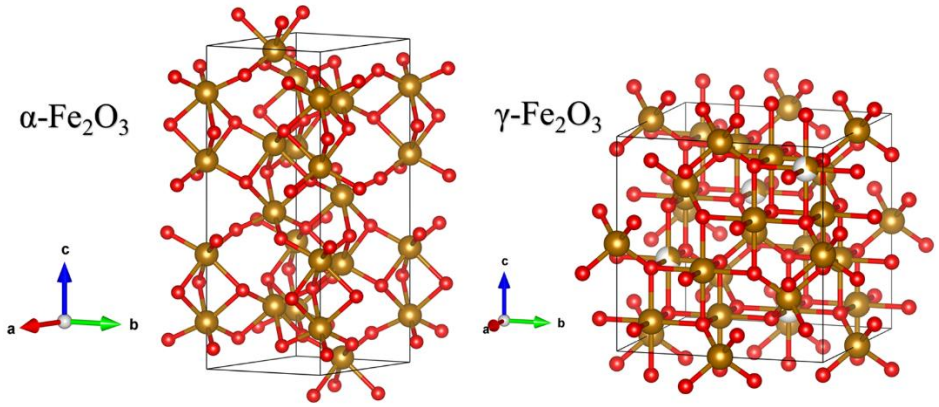

Abstract

An analytic dielectric introspection in two cardinal ferric oxide polymorphs, *viz*. hematite and maghemite, is conducted through a three-fold line of course. Firstly, DC field-dependent radio/audio-frequency impedance and dielectric spectra of polycrystalline MIM pellets; comprising near-stoichiometric (meticulously characterized) $\alpha, \gamma -Fe_2O_3$ nanoparticles, are analysed employing Cole-Davidson model, Jonscher's power law and equivalent circuitry to quantify non-Debye dipolar relaxations, small polaron hopping conduction, grain core-boundary resistivity correlations and field-driven delocalization/de-trapping of carriers. Bias-tuned low-frequency enhancement of dielectric constant via augmenting Maxwell-Wagner polarization is demonstrated for both samples, prerequisite in conquering classical energy storage bottleneck. Secondly, optical dielectric function and associated parameters are evaluated under DFT+U framework, to physically designate particular resonant absorption, dissipation, electronic polarization and decay. In doing so, a new crystallographically consistent and energetically stable; vacancy-ordered maghemite-type supercell is constructed to accomplish reasonable computational cost. Thirdly, intrinsic anisotropy in materials, sensitive to photonic excitations is foremostly videographed by simulating energy-dispersive evolution of the quadric surface to project real/imaginary dielectric tensors. The authors anticipate, this intensive technique would pictorially demonstrate anisotropic deviations in the dielectric ellipsoid, fostering materials physics over linear and nonlinear dielectrics.

6.1 Introduction

Iron oxide and oxyhydroxides contrive a fundamentally appealing class of multivalent transition metal (TM)-based compounds and composites, that present an extensive variety of coexisting magnetic, electrical, optical and optoelectronic properties against nominal cytotoxicity.[1-3] Amongst these, hematite ($\alpha - Fe_2O_3$) and maghemite ($\gamma - Fe_2O_3$) are two abundant, inexpensive; yet promising ferric oxide polymorphs. They embrace diverse applications in the fields of targeted drug delivery for hyperthermia treatment, magnetic resonance imaging, memory devices and magnetic nanofluids, magneto-mechano-electrical energy conversion, dye solar cells, Li-ion batteries, alcohol sensing and catalysis, waste water remediation *etc*.[4-22] In this context dielectric transcendence is a multifaceted asset, and persists at the forefront of devising 'bane to boon' performance.[10,12,13]

Tailoring dielectric constant and its lossless enhancement are principal objectives in order to captivate the classical energy storage bottleneck along with diversification of electrically tunable microwave equipment and miniaturized radar devices. Generally, to elevate dielectric constant of a material, the old-school technique is suitable doping, that suspends additional carriers in the system and enhances dipolar strength.[23-25] But usually, it increases defect-density, micro-strain and unwanted trap-levels in the band-structure. Besides, distinct defects can promote both *n*- and *p*-type nature in Fe_2O_3,[26,27] while stoichiometric pristine samples behave as more intrinsic semiconductors with moderate bandgap of (2.0 ± 0.2) eV and attain efficient dielectric polarization. Thus, varying external parameters is preferable to attune bulk dielectric response *i.e*., an explicit function of temperature, pressure, humidity, electric and magnetic field. In the vast literature of sublinear dielectrics, temperature-dependent description employing the Arrhenius equation and Vogel-Fulcher relation is quite abundant.[12,13,23,25,26] But, thermally activated polarization (pyroelectricity) is less useful for room-temperature applications. Meanwhile, inflicting large pressure is not only difficult (especially for thin films), but also expands defects and stress through the system; and might even cause irreversible damage.[28] Magnetodielectric effect is infrequent in piezo-ceramics and mostly feeble near room-temperature.[10,29] Many reports also discuss use of core-shell structure, variation of particle-size and calcination-temperature.[21,26,30] Nanoparticles are in fact more likely to hold larger dielectric constant due to greater surface to volume ratio of individual grains and thereby stronger surface polarization. Given such ubiquity, dielectric attributes could hardly be regulated fine enough to serve device-based applications. Therefore, small DC field-based adaptation might evince the best alternative. Moreover, effect of external bias on various frequency dispersive parameters can help in effective recognition of the underlying mechanisms. For instance, Cheng *et al*. recently reported a step-like; non-decaying electrical switching of Néel order in $Pt/\alpha - Fe_2O_3$ bilayer, induced by an anomalous spin-Hall effect.[31] Frequency response and field-

dependence of Maxwell-Wagner interfacial polarization (MWIP), non-Debye relaxations through incommensurate molecular dipoles, small polaron hopping in iron oxides through superexchange paths $\left[Fe^{(3\pm\delta)+} \leftrightarrow O^{2-} \leftrightarrow Fe^{(3\mp\delta)+}, \delta \leq 1\right]$ and related anisotropy are phenomenally different. Previously, Ang *et al*. studied 'field induced ferroelectricity' and associated coupling of soft phonon modes in quantum paraelectric perovskites, deploying single crystal or thin films.[32,33] But the anisotropic dielectric effect and intriguing loss dynamics under external field for TM-based polycrystalline systems are not fully understood yet and need further investigation.

Precise evaluation of the complex band-structure, split-off multiplets of TM ions, electronic/magnetic ordering, chemical arrangement, and double/super-exchange interactions in iron oxides very often require subtle experimental means. While first principles studies and computational modelling have handled strongly correlated electronic and spin-systems with desired accuracy and affordable computational cost in the last two decades.[34,35] Ordinary density functional theory (DFT) withstood prior challenges owing to competing phases with close ($\sim$ kJ mol^{-1}) formation energies, structures containing partially occupied states and long-range vacancy ordering, temperature-dependent structural and magnetic transformation through strongly correlated Fe 3*d* electrons, and particular loose compositions under dispersive force.[34-37] Despite; use of local spin density approximation (LSDA), pseudopotentials and hybrid functionals have quenched these discrepancies remarkably.[36-39] In this regard, Guo and Barnard have demonstrated, how choice of basis sets and density-functionals influence the energetic stability, magnetic ordering and environmentally sensitive phase transitions in five popular iron-compounds.[34] Whereas Rollmann *et al*. optimized applied pseudopotentials and regulated the on-site Coulomb interactions in hematite to validate experimental photoemission spectra and changed the forbidden gap edges from Fe(*d*-*d*) to O(*p*)-Fe(*d*).[36] Specially scavenging complex dielectric and optical functions in multivalent transition metal oxides (MTMOs); using contemporary *ab initio* methods have advanced notably and conform THz spectroscopy in terms of accuracy, accountability and versatility.[24,37,40,41] Under random phase approximation (RPA), electrons are considered to respond at the sum of macroscopic fields, induced dipole moments and screening potentials around the atomic site. Inclusively, electron localization function (ELF) is used to cultivate the ground-state atomic interactions and identify molecular dipoles, that involve topological analysis of electron density in adjacent equilibrium chemical bonds.[42] Conjunction of experimental methods with DFT hence leads to a competent dielectric benchmark of the materials of interest, over a wider range of electromagnetic spectrum.

The classical dielectric ellipsoid problem was to find the electric field $\left(\vec{E}_2\right)$ inside a homogeneous dielectric $(\overleftrightarrow{\epsilon_2})$ ellipsoid, in response to an external field $\left(\vec{E}_1\right)$ at the surrounding

medium with a different dielectric tensor ($\overleftrightarrow{\varepsilon_1}$). For an isotropic medium with charge-density ρ, the electrostatic potential, $\Omega(\vec{r}) = -\rho\left(A_x x^2 + A_y y^2 + A_z z^2\right)$ was derived by Kellogg and Mayer using elliptic co-ordinates and direct integration. However, the anisotropic case was first solved by Jones in 1945,[43] where he deduced: $\vec{E}_2 = [1 + \varepsilon_2{}^{-1} A(\varepsilon_2 - \varepsilon_1)/2\pi]\vec{E}_1$. Now-a-days, dielectric tensors are obtainable for real materials. This leads to a converse problem *i.e.*, to recreate dielectric quadric surface to contemplate the energy-evolution of anisotropy; intrinsic to the material. In this article, first synthetic procedure and basic structural characterizations are discussed. Very often in wet chemical synthesis, one of the polymorphs carry defects of the other.[44] For effective minimization of such defects, a two-step technique with controlled annealing in presence of oxygen is adopted. Next, a rigorous analysis of dielectric dispersions under external electric field is profound, followed by first principles calculations of complex dielectric parameters and ELF-dynamics. Finally, a new theoretical method is suggested, that scrutinizes the dispersive quadric surface associated with the symmetric dielectric tensor, in order to 'visualize' the anisotropy present (or induced by optical excitations) in the system. A Wolfram Mathematica program is used to animate the quadric contour as a function of energy, employing data from DFT for both hematite and maghemite. The authors expect, this novel technique can venture new realms in the theory of linear as well as nonlinear dielectrics.

6.2 Objective and methods

6.2.1 Materials and precursors

Analytical grade reagents (> 99.9% purity) are used here without manual purification. Principle solvent and precursors *viz*., diethylene glycol (DEG), polyethylene glycol (PEG; 6000 g mol^{-1}), ferric chloride hexahydrate ($FeCl_3.6H_2O$), anhydrous sodium acetate (CH_3COONa) and absolute ethanol are purchased from SIGMA-ALDRICH.

6.2.2 Synthetic procedure

Fe_2O_3 nanoparticles of the prescribed phases are synthesized using a two-step process: (i) solvothermal synthesis of spherical Fe_3O_4 nanoparticles and (ii) controlled oxidation in furnace. Firstly 1.00 g (3.70 mmol) $FeCl_3.6H_2O$, 2.50 g (30.48 mmol) CH_3COONa and 4.00 g (0.67 mmol) PEG are mixed vigorously in 40 mL DEG to prepare a homogeneous greyish yellow solution via ultrasonication for 10 min and magnetic stirring at 80 °C for 50 min respectively. Then the resultant solution is transferred into a Teflon-lined 50 mL autoclave made of stainless still and left inside a hot-air oven at 190 °C for 9 h. This process associates following reactions:

$$FeCl_3 \rightarrow Fe^{3+} + 3Cl^-$$

$$Fe^{3+} + 3OH^- \rightarrow Fe(OH)_3$$

$$Fe^{3+} + e^- \rightarrow Fe^{2+}$$

$$Fe^{2+} + 2OH^- \rightarrow Fe(OH)_2$$
$$Fe(OH)_3 \rightarrow \alpha - FeOOH + H_2O$$
$$Fe(OH)_2 + 2\alpha - FeOOH \rightarrow Fe_3O_4(\downarrow) + 2H_2O$$

After natural cooling, the black sample is precipitated and washed in absolute ethanol and deionized water (~18.2 MΩ) via respective centrifugations. Finally, the sample is dried overnight at 65 °C under rough vacuum and magnetite nanoparticles are collected.

In the second step, the powder-sample is spread onto an alumina-crucible and calcined in a tube-furnace being exposed to open air with intermediate grindings. As the temperature is elevated, magnetite first oxidizes to metastable maghemite; and eventually it turns into hematite. For maghemite synthesis, the sample is kept at 150 °C for 2 h and at 220 °C for 5 h. The black powder turns brown by the following reaction.

$$2Fe_3O_4 + \frac{1}{2}O_2 \xrightarrow{220℃} 3(\gamma - Fe_2O_3)$$

Then half of the maghemite powder is again heated to 400 °C in 2 h and kept at 500 °C for further 5 h. This turns the sample to reddish hematite for stabilizing the surface enthalpy by a crystallographic rearrangement.

$$\gamma - Fe_2O_3 \xrightarrow{500℃} \alpha - Fe_2O_3$$

For the preparation of hard polycrystalline pellets, 0.50 g of each sample is cold-pressed in a hydraulic press against 0.55 GPa pressure. Then they are further calcined at 220 °C (for maghemite) and 500 °C (for hematite) for 3 h to enhance compressive strength, truncate cracks and expel adsorbed moisture; and then quenched in air. The resultant cylindrical pellets with ≥ 95% of theoretical density, have 9.5 mm diameter and approximately 1.9 mm width. For electrical measurements, copper wires are connected in top-bottom configuration (MIM geometry) by applying adequate silver paint (Alfa Aesar). The facts that, (i) Ag is highly conducting, (ii) the electron affinity of polytype Fe_2O_3 $(3.9 - 4.9\ \text{eV})$ is close to the work-function of Ag $(4.26 - 4.74\ \text{eV})$, and (iii) the interface barrier height is small, assure formation of ohmic contacts.

6.2.3 Experimental techniques and instrumental specifications

In a Rigaku Miniflex powder X-ray diffractometer (40 kV – 15 mA), XRD data is recorded for the scattering angle range: $10° \leq 2\theta \leq 80°$ under monochromatic Cu-$K_{\alpha 1}$ radiation $(\lambda = 1.5406\ \text{Å})$ at 0.5° min^{-1} scanning speed and 0.02° step-size. The crystalline structures are then refined by the Rietveld's method in the FULLPROF program, where the line-profiles are modelled with pseudo-Voigt function. The refined unit cells can be retrieved using the VESTA software. Size and morphology of the nanoparticles are viewed in a ZEISS Sigma field emission scanning electron microscopy (FESEM) system (magnification limit 400 kX); endowed with a 5

kV electron-gun. Micro-Raman spectra are acquired from a WITec ALPHA300 RS confocal spectrometer in backscattering configuration, equipped with a solid-state monochromatic (532.3 nm) Nd:YAG laser having beam-diameter 1 μm; with laser-power set to 1 mW. In a 20 × Zeiss achromatic objective with 1800 grooves mm^{-1} holographic grating, 6 spectral acquisitions with 10 s of integration-time each are captured and averaged to compute the final spectrum for minimizing background noise. Diffuse reflectance spectra (DRS) of the powder-samples are obtained in a Shimadzu UV 3600 UV-Vis-NIR spectrophotometer for the wavelength range: 200– 2200 nm, using powder-$BaSO_4$ as a reflectance standard. X-ray photoelectron spectra (XPS) are obtained from a SPECS XPS having a monochromatic Al-K_α source ($h\nu = 1486.6$ eV) connected to a hemispherical analyzer (HSA 3500). The survey and high-resolution elemental scans are performed with pass-energy of 160 eV (step-size 1 eV) and 20 eV (step-size 0.1 eV) respectively under ultrahigh vacuum ($< 2 \times 10^{-8}\ mbar$) conditions. All spectra are calibrated by the environmental C 1s peak at 284.8 eV for charge correction. The dielectric parameters of the as-prepared polycrystalline pellets are obtained using an Agilent 4294A precision impedance analyzer with an input frequency range: 40 Hz – 110 MHz, amplitude 0.5 V and variable DC bias up-to 42 V. In this article, DC bias is everywhere given in volts for convenient numerical values. The calibration-curve for electric field in V cm^{-1} is provided below.

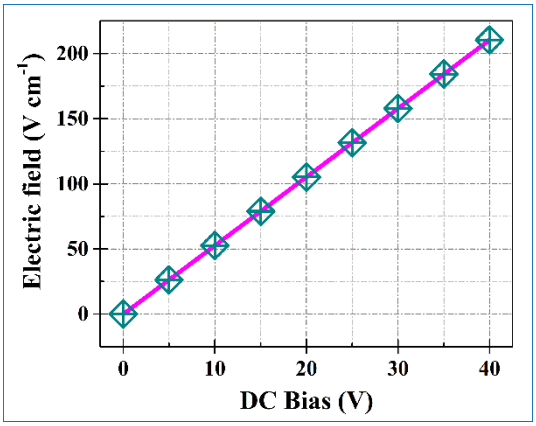

Figure 6.1 Calibration-curve for the applied electric field $[E = V/l]$ from external DC bias. Field-range: 0 – 211 V cm^{-1} against bias-range: 0 – 40 V.

6.2.4 Computational details

All first principles calculations; performed here; are based on the DFT, as implemented in the Vienna *ab initio* simulation package (VASP).[45,46] The projector augmented wave (PAW) pseudopotentials were used to describe the ion-electron interactions.[47] Under the generalized gradient approximation (GGA), the Perdew-Burke-Ernzerhof (PBE) functional was used as the exchange-correlation potential.[48] We have used primitive cells of hematite and maghemite for all electronic and optical property-related calculations with a plane wave cut-off energy of 700

eV.[49,50] In section 6.3.4, some light will be shed upon the as-constructed geometrical structure of maghemite. All the geometrical optimizations were continued, until the residual forces dropped below 10^{-5} eV Å^{-1} and the total energies converged to 10^{-6} eV. Considering the DFT+U approach; formulated by Dudarev *et al*.,[51] Meng *et al*.[52] conducted a comparative study on four iron compounds (α-FeOOH, α-Fe_2O_3, Fe_3O_4 and FeO) employing a large variation of the Hubbard U −parameter and inferred, there is no single U −value that can satisfactorily reproduce most of the structural, electronic and thermodynamic properties for the studied materials. Given such ambiguity, we used the on-site effective Coulomb potential, $U_{eff} = 5.0\ \&\ 5.5$ eV for the respective α- and γ-phases for overall consistent structural, electronic, magnetic and optical results. Explicit spin-polarization is taken into account, owing to strongly correlated Fe 3d electrons. The tetrahedron method with Blöchl corrections; was employed to determine the density of states (DOS). The optoelectronic and optical parameters *viz*. imaginary and real parts of dielectric function, electron energy loss-spectrum, absorption, reflectivity, refractive index and extinction coefficient were analyzed by using the RPA method, including the effects of local fields.[53] The detail of Γ-centered k-meshes; used to sample the first Brillouin zone during different calculations; are provided in Table 6.1.

Table 6.1 List of used k-meshes in DFT-based calculations

Calculations	Used k-mesh	
	Hematite	**Maghemite**
Geometrical optimization	20×20×20	9×9×3
Electronic property (DOS)	20×20×20	15×15×5
ELF	10×10×10	9×9×3
Optoelectronic property	10×10×10	3×3×1

6.3 Results and discussion

6.3.1 Rudimentary structural characterizations

Bragg peaks in the XRD pattern of hematite and maghemite (Figure 6.2) are matched with the JCPDS cards: 86-0550 and 39-1346, respectively. Absence of additional peaks confirms purity of the respective hexagonal (rhomb-centered, space-group: $R\bar{3}c$) and cubic (spinel, space-group: $P4_132$) phases.[27,52] The corresponding crystallite-sizes (D) are calculated from the Scherrer's equation,

$$D = \frac{K\lambda}{\beta \cos\theta} \cong \frac{0.89\lambda}{\beta \cos\theta}. \qquad (6.1)$$

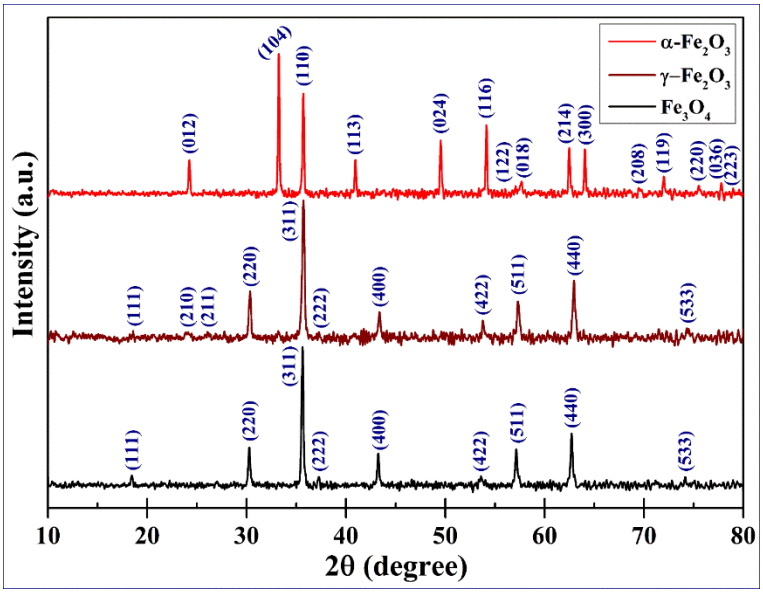

Figure 6.2 XRD patterns of hematite, maghemite and magnetite respectively. The Bragg peaks are matched with particular JCPDS cards to ensure purity of phase. The main difference in crystal structures of α- and γ-compounds is, in the former all the cations are octahedrally co-ordinated, whereas in the later three-quarters are at octahedral positions, and the rest are tetrahedrally co-ordinated.

In equation 6.1, K is a dimensionless geometric shape-factor (≈ 0.89), λ is the wavelength of incident X-ray, and β corresponds to the FWHM of the Bragg-peak located at an angle of diffraction 2θ. Considering five most intense Bragg-planes, the mean crystallite-size is noted to be 49 nm for hematite and 44 nm for maghemite. Charge neutrality of bulk maghemite structure is ensured by the arrangement and ordering of cationic vacancies. Using Rietveld refinement, the lattice parameters, strain, atomic position and occupancies are further determined (see Figure 6.3, Table 6.2) to bear out crystallographic conformation, ensuring a competent goodness of fit *i.e.*, the ratio of weighted and expected residual factors (R_{wp}/R_{exp}). Low micro-strain levels ensure applicability of Scherrer's formula. The overall parameters testify good crystallinity and stoichiometry of the as-synthesized samples. The FESEM micrographs are provided in Figure 6.4, that show much larger particles (79 & 72 nm, respectively) compared to the crystallite-sizes; hinting at the polycrystalline growth. Moreover, the morphology indicates that, hematite particles have developed substantial agglomerations due to synthesis at an elevated temperature. Nanoparticles of both the samples are nearly spherical in shape, because of the as-used surfactants during solvothermal synthesis of magnetite.

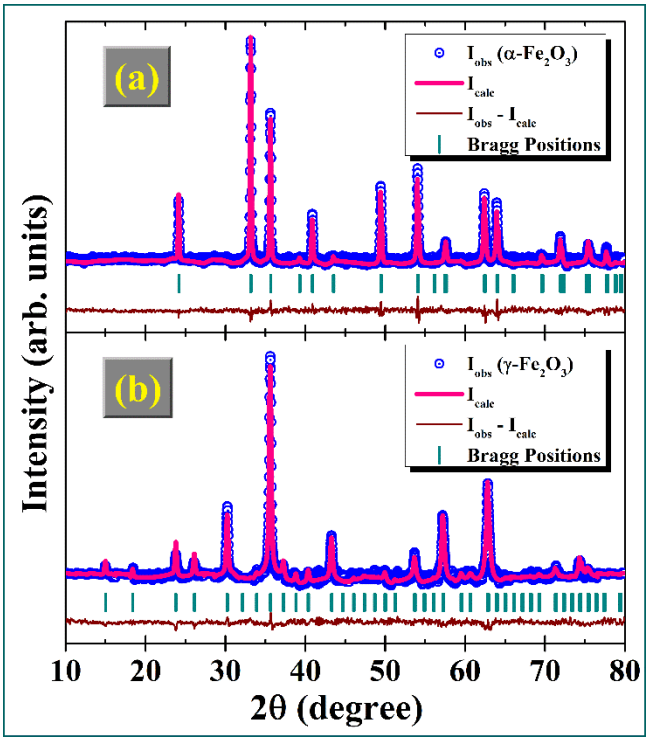

Figure 6.3 Rietveld refinement of powder XRD pattern for (a) hematite and (b) maghemite. The pink curve represents the calculated best fit obtained from FULLPROF software, against the experimental diffraction traces (open blue circles). The green vertical lines indicate respective Bragg peaks and the maroon curve shows the difference of the experimental and calculated intensities.

Table 6.2 Refined crystallographic parameters obtained from Rietveld analysis of XRD Data

Sample	Lattice Parameters	Strain (η %)	Atoms	Wyckoff sites	x	y	z	Occu-pancy	χ^2
Hematite	$a = b = 5.0397(9)$ Å; $c = 13.7587(0)$ Å; $\alpha = \beta = 90°$; $\gamma = 120°$; $V = 302.644(6)$ Å^3	0.11	Fe	12c	0.00000	0.00000	0.14483	1.000	1.67
			O	18e	0.31756	0.00000	0.25000	1.640	
Maghemite	$a = b = c = 8.3640(5)$ Å; $\alpha = \beta = \gamma = 90°$; $V = 585.126(6)$ Å^3	0.21	$Fe_{Oct}^{(1)}$	12d	0.12500	0.87500	0.12500	1.000	1.98
			$Fe_{Oct}^{(2)}$	4b	0.87500	0.87500	0.87500	0.114	
			Fe_{Tet}	8c	0.50000	0.50000	0.50000	0.813	
			$O^{(1)}$	24e	0.12500	0.12500	0.62500	0.981	
			$O^{(2)}$	8c	0.62500	0.62500	0.62500	0.994	

As XRD patterns of maghemite and magnetite are hardly distinguishable (Figure 6.2) owing to similar spinel structure,[27] Raman spectra are preferable for phase-matching. The irreducible modes of lattice-vibration at the first Brillouin zone-center for α- and γ-Fe_2O_3 are given by,

$$\Gamma_{vib}^{(\alpha)} = 2A_{1g} \oplus 2A_{1u} \oplus 3A_{2g} \oplus 2A_{2u} \oplus 5E_g \oplus 4E_u, \quad (6.2)$$

$$\Gamma_{vib}^{(\gamma)} = A_{1g} \oplus E_g \oplus T_{1g} \oplus 3T_{2g} \oplus 2A_{2u} \oplus 2E_u \oplus 4T_{1u} \oplus 2T_{2u}. \quad (6.3)$$

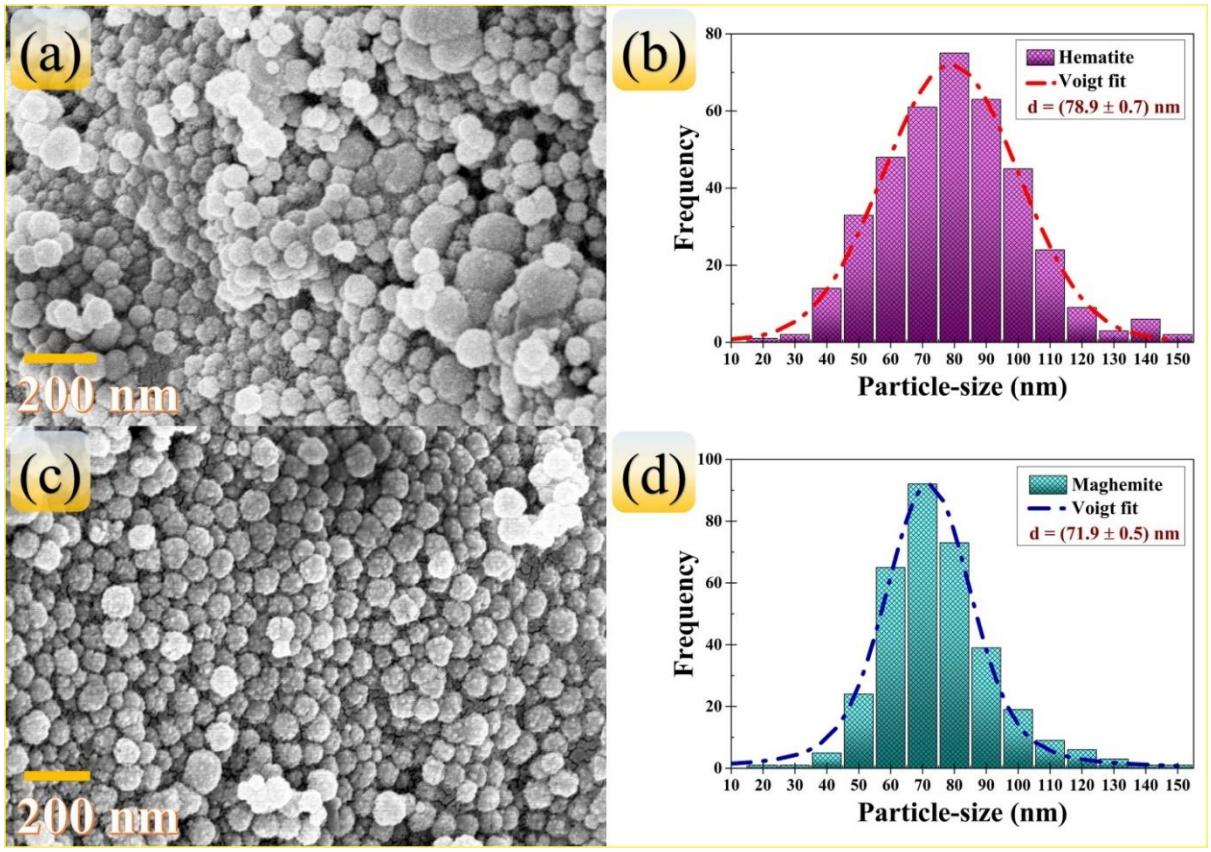

Figure 6.4 FESEM micrographs and size distribution histogram for (a,b) hematite and (c,d) maghemite nanoparticles. By fitting the respective bar charts to a Voigt function, the average particle size (d) is obtained: 79 nm for hematite and 72 nm for maghemite. For hematite, the agglomerated clusters are excluded during evaluating size distribution.

Among all the modes, acoustic A_{1u} & A_{2u} modes of hematite and T_{1g}, A_{2u}, E_u & T_{2u} modes of maghemite are optically silent,[2] some are infrared active and conserve mutual exclusiveness towards Raman spectroscopy. The identified Raman-modes in Figure 6.5(a) are: 225 (A_{1g}), 247 (E_g), 293 (E_g), 412 (E_g), 500 (A_{1g}) & 612 (E_g) cm^{-1} for hematite and 364 (T_{1g}), 499 (E_g) & 702 (A_{1g}) cm^{-1} for maghemite. The peak-positions and relative intensities conform previous reports and ensure purity of phase.[2,44] The diffused Raman peaks for γ-phase implies a weak and broad scattering response of the vacancy-dispersed spinel system.[4]

Both samples exhibit strong absorption characteristics for sub-600 nm wavelengths,[22,54] see Figure 6.5(b). The (allowed) direct bandgap (E_g) is conventionally calculated from the Tauc's plot employing the following equation:

$$(\alpha h\nu)^2 = \zeta^2(h\nu - E_g), \quad (6.4)$$

where, ζ^2 is a proportionality constant, h = Planck's constant, ν is the incident frequency and α is the absorption coefficient. From the linear extrapolation of $(\alpha h\nu)^2$ vs $h\nu$ curve, $E_g = h\nu|_{\alpha=0}$ is determined at the absorption band-edge.

In non-transparent powder materials, the principle of absorption spectroscopy fails due to high reflectance and nominal transmittance. From diffuse reflectance spectra (DRS), α is approximated by the Kubelka-Munk function $\{F(R)\}$ given by,

$$F(R) = \frac{k_m}{s} = \frac{(1-R)^2}{2R}. \tag{6.5}$$

Here $k_m = (1-R)^2$ is the molar absorption coefficient, and s is the scattering factor, numerically equal to twice the reflectance (R). The estimated optical bandgaps of the respective phases are 1.99 and 1.96 eV,[22] see Figure 6.5(c,d). These transitions correspond to $O^{2-} \rightarrow Fe^{3+}$ inter-band charge transfer.

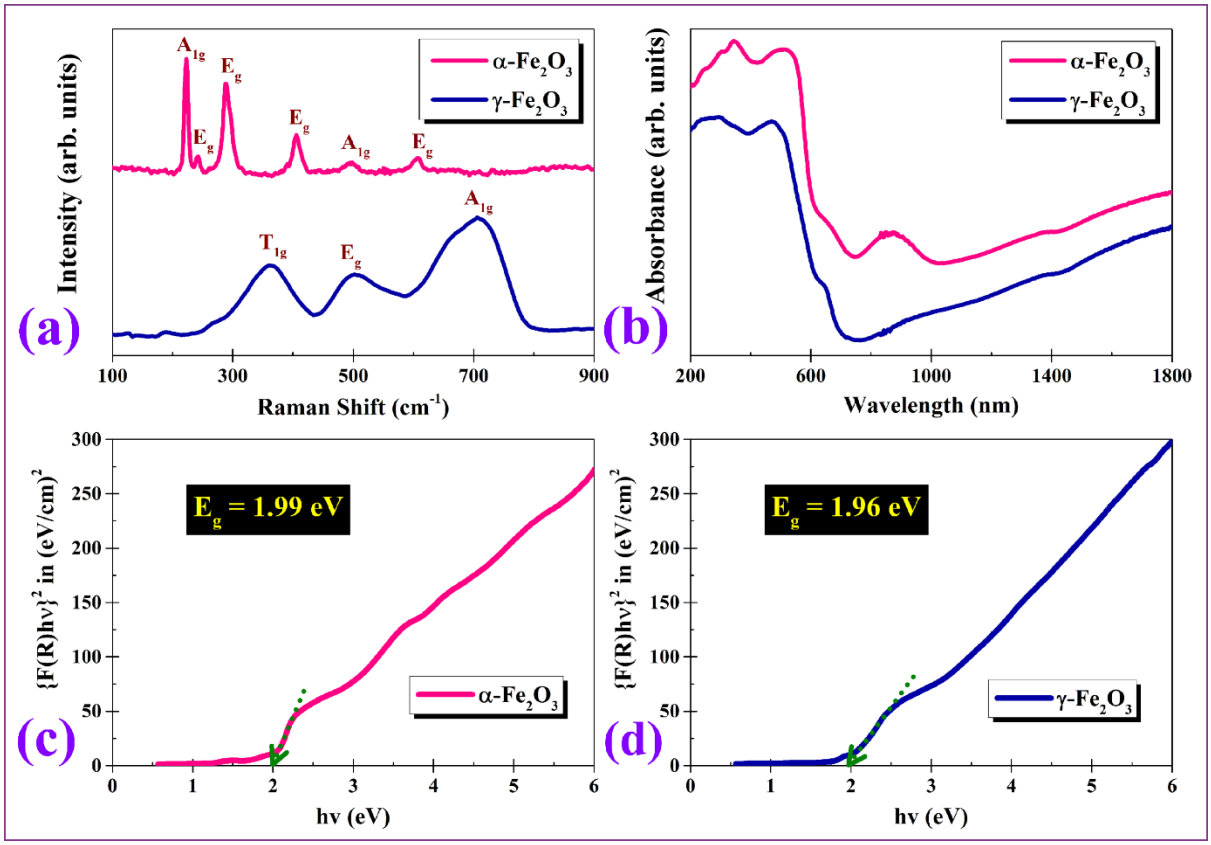

Figure 6.5 (a) Raman spectra for the two polymorphs. Continuous exposure of large (> 10 mW) laser-power transforms maghemite into the thermodynamically more stable polymorph, hematite due to significant local heating (data not shown); (b) absorbance spectra for hematite and maghemite. Optical bandgaps (E_g) are calculated employing Kubelka-Munk function {F(R)} for (c) hematite and (d) maghemite.

6.3.2 XPS analysis and compositional study

XPS is a powerful tool for systematic chemical quantification of constituent ions in particular oxidation states or crystallographic positions, inside complex MTMOs.[55] Elemental survey of photoelectron spectra [Figure 6.6(a)] revealed prominent traces of Fe (2s, 2p, 3s, 3p; accompanying an Auger peak), O (1s) and C (1s). High resolution scans of the Fe 2p and O 1s peaks were further analyzed in the CasaXPS software; employing a Shirley-type background and Voigt line-shape, for the determination of atomic proportions and distinctly bound states. Both the samples were near-stochiometric. The exact composition for hematite and maghemite were found to be $Fe_{1.94}O_3$ and $Fe_2O_{2.96}$ respectively. The gradually augmenting oxygen-rich stoichiometry is accountable, considering the successive open-air annealing from magnetite to maghemite and maghemite to hematite. The results are consistent with the atomic occupancies, determined from Rietveld refinement. Although high off-stoichiometric parameter promotes some supercapacitor and catalysis-related applications,[19,20,26] which is undesirable concerning profuse dielectric polarization.

The O 1s HR-spectra were deconvoluted into two peaks at 529.52 and 531.81 eV [$\chi^2 \leq 0.74$], in order to distinguish the contributions of lattice oxygen in Fe_2O_3 and functionalized surface,[55-57] see Figure 6.6(b). The O–Fe contribution is obviously more intense and persistent in both samples. Contrarily, the HO–C peak has notably diminished in hematite, compared to maghemite. This indicates decomposition of polyethylene glycol (capping) molecules at the outer surface at high temperature, that damaged the core-shell structure of hematite nanoparticles and stimulated agglomeration.

Table 6.3 Binding energy and FWHM of resolved peaks in Fe 2*p* photoelectron spectra

Compound	Main peak	Deconvolution and assignments		
		Components	Binding energy (eV)	FWHM (eV)
$\boldsymbol{\alpha - Fe_2O_3}$	$2p_{1/2}$	High BE multiplet	726.28 ± 0.10	3.41 ± 0.12
		Low BE multiplet	724.09 ± 0.07	2.73 ± 0.09
	$2p_{3/2}$	High BE multiplet	712.55 ± 0.08	3.25 ± 0.08
		Low BE multiplet	710.51 ± 0.08	2.39 ± 0.07
$\boldsymbol{\gamma - Fe_2O_3}$	$2p_{1/2}$	Fe_{Tet}^{3+}	726.18 ± 0.08	3.46 ± 0.11
		Fe_{Oct}^{3+}	724.27 ± 0.04	2.57 ± 0.10
	Shake-up satellite	Fe_{Oct}^{3+}	718.88 ± 0.04	0.52 ± 0.02
	$2p_{3/2}$	Fe_{Tet}^{3+}	712.85 ± 0.09	2.95 ± 0.09
		Fe_{Oct}^{3+}	710.67 ± 0.07	2.61 ± 0.06

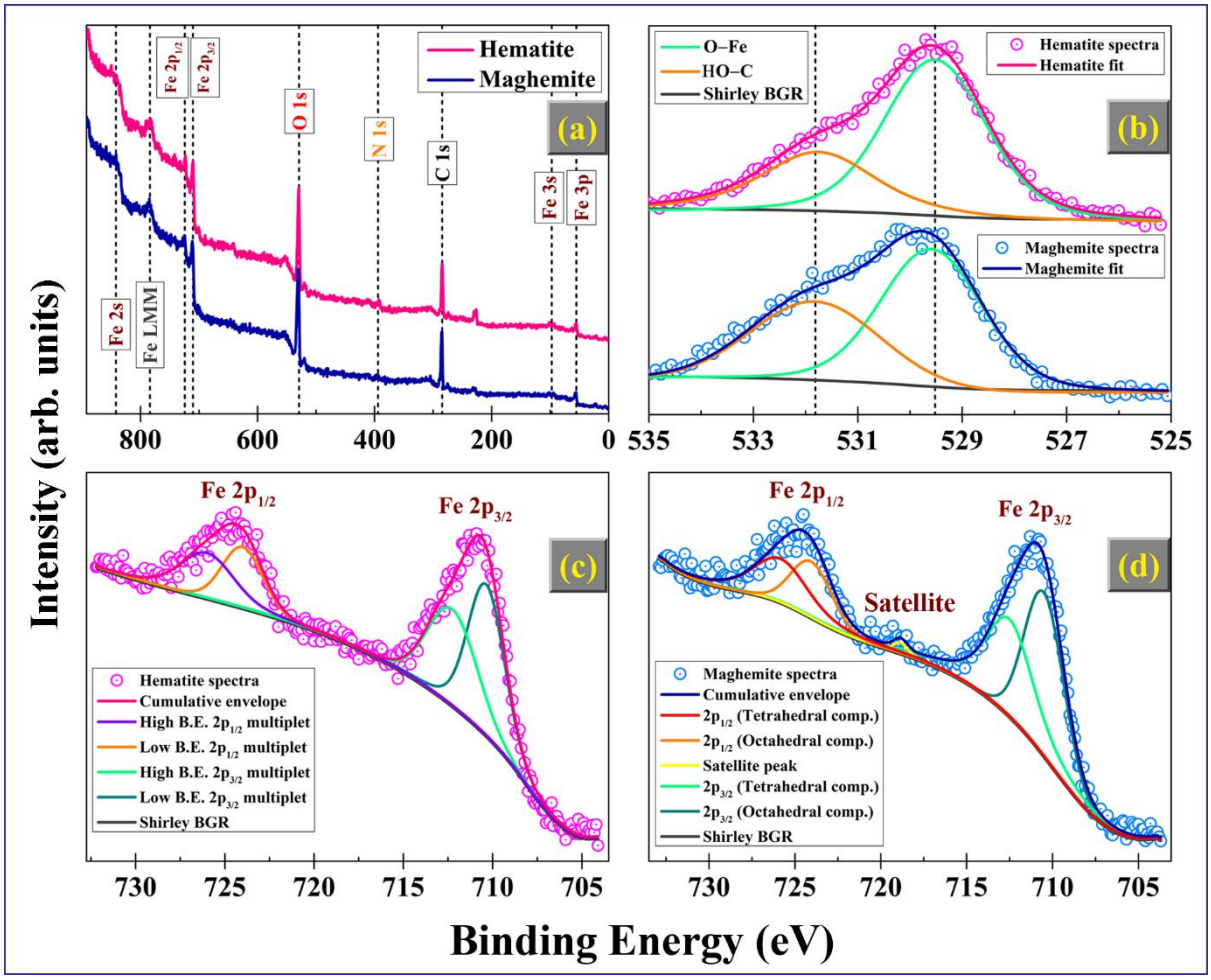

Figure 6.6 (a) XPS elemental survey scan: prominent signatures of Fe, O and C detected; (b) high-resolution O 1*s* spectra, deconvoluted to distinguish the lattice (O–Fe) and functionalized surface (HO–C) contributions; (c,d) high-resolution Fe 2*p* core-level band with respective deconvolution into various multiplets and uniquely bound crystallographic co-ordinations. Data for hematite and maghemite are presented in pink and blue colours, respectively.

The complex multiplet splitting, owing to partially filled 3d-orbitals in MTMOs and as-originated line-shape asymmetry in the Fe 2p band are extensively studied in contemporary research.[55-59] The $2p_{3/2}$ peak is stronger and narrower than $2p_{1/2}$, because it embraces a four-fold spin-orbit (j-j) degeneracy, twice to that of $2p_{1/2}$.[56,58] In high-spin iron compounds (*e.g.*, α-, γ-Fe_2O_3), these peaks develop intrinsic broadening compared to metallic iron [$Fe^{(0)}$] or low-spin ferrous species.[55] Gupta and Sen first used Hartree-Fock free ion method to associate such broadness with the electrostatic interactions and spin–orbit coupling among the 2p core-hole and unpaired 3d electrons, inclusive of the photoionized Fe-ion via crystal-field interactions.[58] Hence, the Fe 2p HR-spectra were deconvoluted to two components each for the $2p_{1/2}$ $[(724.5 \pm 0.1)\ eV]$ & $2p_{3/2}$ $[(710.9 \pm 0.2)\ eV]$ peaks, with squared deviation $\chi^2 \leq 0.85$, see Figure 6.6(c,d). In hematite, the multiplets can be fairly encapsulated to one low and one

high binding energy (BE) integrant, on account of different chemical environments[56] in terms of bulk or surface positioning or occupancy in grain core/boundaries. On the contrary, in maghemite, the tetrahedral and octahedral Fe-sites essentially possess distinct BEs. From a meticulous fit with appropriate BEs, the crystallographic occupancy is determined to be $Fe_{Oct}/Fe_{Tet} = 1.55$, close to the theoretical ratio *i.e.*, 1.67. A characteristic Fe^{3+} shake-up satellite peak (718.88 eV) is also identified in maghemite. It involves core ionization, that instantly excites a valence electron to an unoccupied orbital, known as shake excitation.[59] The details of all components in both the samples are provided in Table 6.3, that assent previous literature.[19,55-57]

6.3.3 Dielectric analysis

Formalism: Dielectric materials develop polarization in presence of an external electric field (static or alternating) due to shifting of atoms/ions. All polarization mechanisms can be classified as resonance or relaxation, depending on the frequency. Resonance occurs when the excitation frequency approaches the natural frequency of the oscillators, whereas relaxation commences subjected to the availability of time required to overcome the inertia. In the successive segments, room-temperature behaviour of a number of frequency-dispersive dielectric parameters is elaborated. These functionally complex parameters are, (i) impedance: $\hat{Z} = |Z|e^{i\theta} = Z' + iZ''$; (ii) admittance: $\hat{Y} = 1/\hat{Z} = |Y|e^{i\emptyset} = G + iB = G + i\omega C$; and (iii) dielectric constant: $\hat{\varepsilon} = \varepsilon' - i\varepsilon''$. Here, $|Z|$ & $|Y|$ are the magnitudes of impedance and admittance; Z', Z'', G, B & C represent gross resistance, reactance, conductance, susceptance and capacitance; $i = \sqrt{-1}$ and angular frequency: $\omega = 2\pi f$, f being the linear frequency in Hz. The imaginary part of dielectric constant (ε'') conveys loss/dissipation of electrical energy, while the real part (ε') emphasizes storage capability. A dielectric medium with susceptibility χ_e, develops polarization, $\vec{P} = \varepsilon_0\chi_e\vec{E}$ and displacement, $\vec{D} = \varepsilon_0\vec{E} + \vec{P} = \varepsilon_0(1 + \chi_e)\vec{E} = \varepsilon_0\varepsilon'\vec{E} = \varepsilon'_{abs}\vec{E}$. Employing capacitive dispersion:

$$\varepsilon' = 1 + \chi_e = \frac{\varepsilon'_{abs}}{\epsilon_0} = \frac{Cl}{\epsilon_0 A}, \tag{6.6}$$

Here ε'_{abs} = absolute permittivity of the material, ϵ_0 = permittivity of vacuum = 8.854×10^{-12} F m^{-1}, l = width of the pellet, and A = effective electrode area. The dissipation factor (D) or dielectric loss-tangent estimates the relaxation loss (resulting thermal dissipation) in terms of phase-lag between the input waveform and the oscillating dipoles. The defining relations are,

$$D = \tan\delta = \frac{Z'}{Z''} = \frac{G}{B} = \frac{\varepsilon''}{\varepsilon'}, \tag{6.7}$$

$$\varepsilon'' = \varepsilon' \tan\delta = \frac{Cl}{\epsilon_0 A}\tan\delta. \tag{6.8}$$

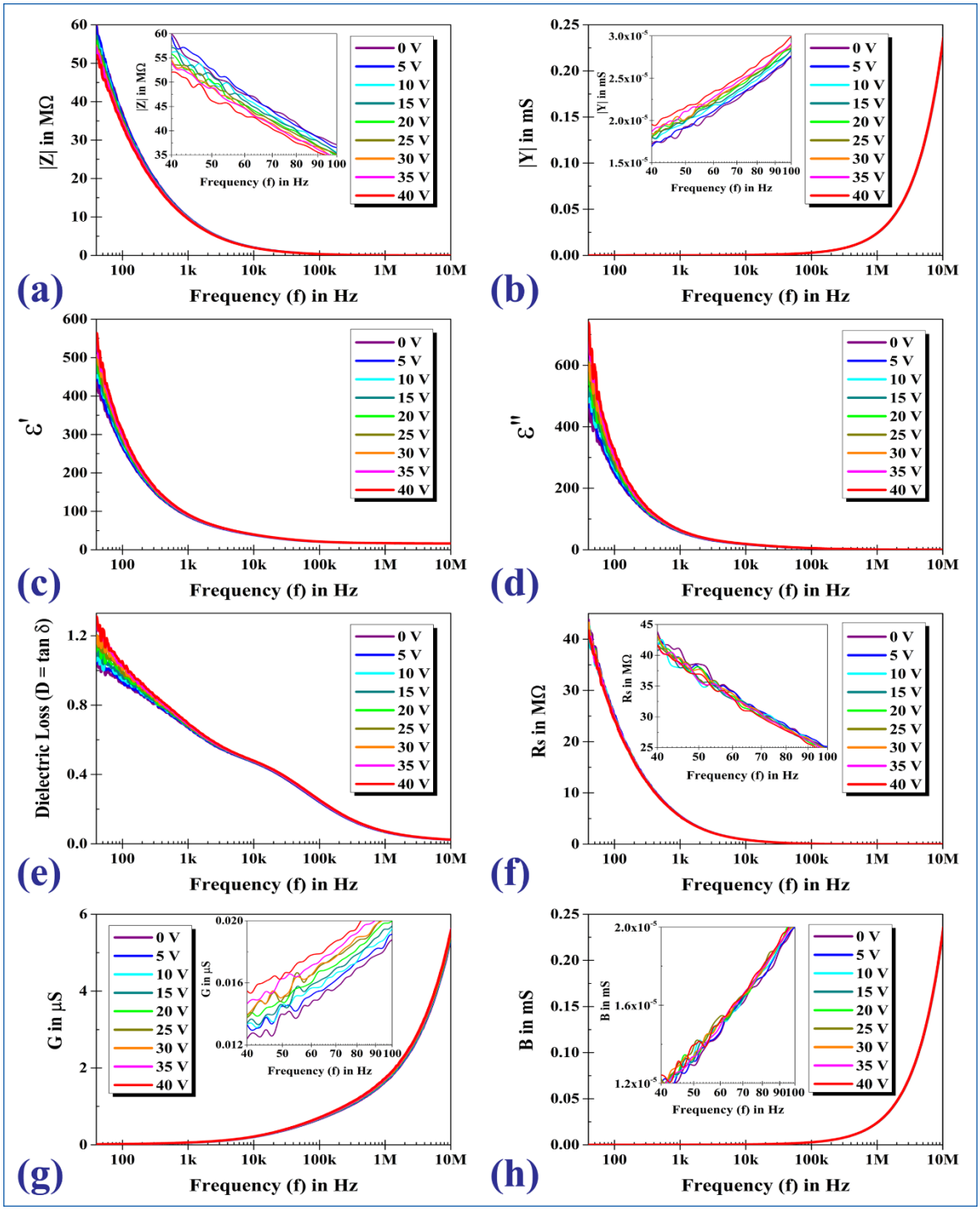

Figure 6.7 Frequency-dispersions for hematite: (a) magnitude of impedance (|Z|); (b) magnitude of admittance (|Y|); (c) real part of dielectric constant (ε'); (d) imaginary part of dielectric constant (ε''); (e) dissipation or loss-factor ($D = \tan\delta$); (f) equivalent series-resistance or ESR (R_s); (g) AC conductance (G); and (h) AC susceptance (B) for varying external bias from 0 to 40 V. In some figures, the field-dependent changes are small enough to turn down visibility. For those cases, magnified low-frequency (40 – 100 Hz) dispersions are provided in the insets.

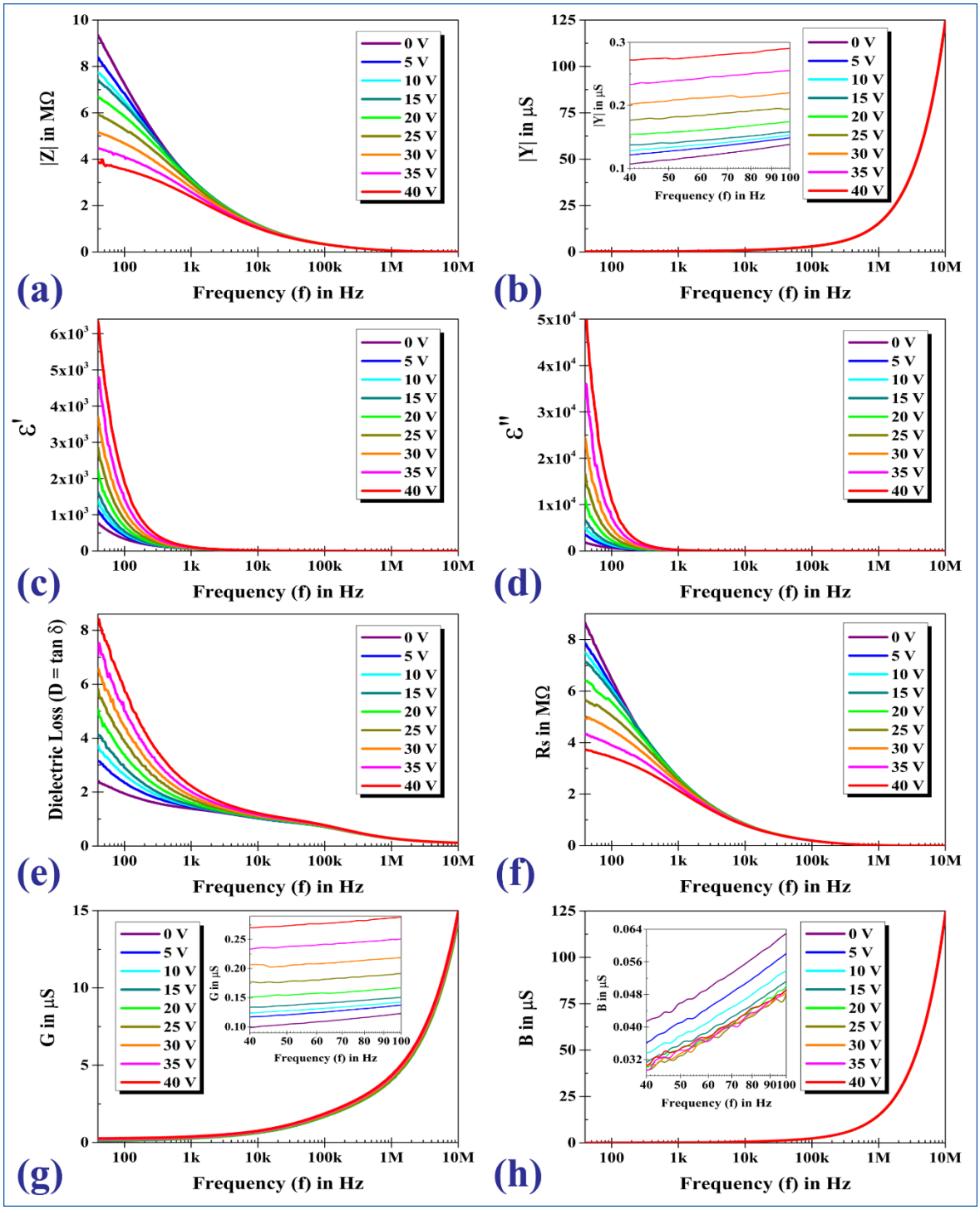

Figure 6.8 Frequency-dispersions for maghemite: (a) |Z|; (b) |Y|; (c) ε'; (d) ε''; (e) $D = \tan\delta$; (f) R_s; (g) G; and (h) B for varying 0 – 40 V external bias. The insets demonstrate magnified low-frequency (40 – 100 Hz) dispersions for difficult-to-resolve curves.

Impedance and dielectric spectra: A number of the above parameters are illustrated in Figure 6.7 and 6.8 for the α- and γ-phases against different frequency and bias conditions. Among these, $|Z|, \varepsilon', \varepsilon'', D$ & R_s rapidly decay at lower frequencies and gradually the decay-rate settles down for a pseudo-constant high frequency limit in agreement with Koop's

phenomenological theory.[60] At few tens of Hz, the dipoles easily follow the input sweeps leading to high dielectric constant and related parameters. Whereas, driving signal becomes increasingly difficult to respond at higher frequency. The associated delay in response causes the sharp decay, which is a characteristic of MWIP.[23-26,32,33,40] This is an outcome of the space-charge effect in inhomogeneous dielectric structures and polarization in the grain core–boundary interface within the nanoparticles. The grains behave as semiconductors and offer more ideal dielectric characteristics, whereas the boundaries act as insulators and its properties get influenced by defects, dislocations and traps significantly.

Conversely, $|Y|, G$ & B upsurge in higher frequencies according to Rezlescue model.[61] Admittance spectroscopy corresponds to the input AC sweeps keeping the electric displacement constant and hence can mask all low frequency electrode polarization effects (if present). Also, the results do not suffer from the influence of deep traps, since the associated release rates are $\ll 1\ s^{-1}$ and thus falls out of our operating frequency-range. In elevated frequencies, small polaron hopping conduction dominates the transport;[23-26] via exchange displacement of electrons/holes between Fe^{3+} ions and donor/acceptor sites present in the adjacent boundaries.[40,62] This is different from large polaron hopping, where conductivity drops at larger frequencies due to less mobility. Deploying the effective mass approximation on the electronic wave-function in a deformable and polarizable continuum, lattice distortion is estimated. The large polarons can polarize a greater number of neighboring sites and propagate with higher effective mass.[63]

The field dependence of the dispersions reveals another bunch of particulars. Having a much lower resistivity than hematite, maghemite shows notably greater sensitivity to similar applied bias.[64] For both samples, the low-frequency regime, dominated by the MWIP mechanism, is highly field-dependent. Whereas with increasing frequency, dielectric parameters get more reluctant towards DC bias. This is because, the dipoles vibrate too fast for the applied moderate fields to effectively align them in their direction. For obvious reasons, $|Z|$ drops and $|Y|$ elevates with electric field. Each of $\varepsilon', \varepsilon''$ & D increases with bias *i.e.*, both of the net energy storage and dissipation rise. In maghemite, a 6-8 times regular enhancement can be seen at smaller frequencies. For a superposition of multiple polarization mechanisms, the Landau-Ginzburg-Devonshire (LGD) theory and the phenomenological Johnson relation: $\varepsilon'(E) = \varepsilon'(0)/[1 + \lambda\{\varepsilon'_{abs}(0)\}^3 E^2]^{1/3}$, λ being a temperature-dependent parameter, cannot alone describe the field-dependency of the dielectric constant.[33] Some previous reports show decrease in dielectric constant of thin films under external bias on account of formation of condensing polar clusters.[32,33] Similar field-response of dielectric constant is also reported for non-ohmic contacts and electrode polarization effects in ceramic samples.[65] However, for our polycrystalline samples, (real) dielectric constant is observed to increase with bias,[66] at the cost

of greater dissipation *i.e.*, larger energy-storage proficiency along with internal heating. This particular feature is useful in devices having short-term operations, or integrated application with heat transfer appliances. Finally increasing fields enhance G associating drops in B and R_s, which is clearer for maghemite. The equivalent series resistance or ESR (R_s) outlines the net effect of bias on the grain-grain boundary constitution, which are elaborated afterwards with the scaling property of ac-conductivity. Meanwhile, the relaxation dynamics of molecular dipoles require further investigation for deeper physical insights.

The Debye relaxation theory presents the dielectric response for an ensemble of non-interacting, ideal dipoles as a function of the input frequency. However, in practice, feasible interactions with the environment and neighbouring dipoles cause asymmetric broadening of the loss-peaks.[67] The Cole-Davidson model introduces a shape-parameter: β ($0 \leq \beta \leq 1$) in the relaxation equations to describe such a nonideal dipolar ensemble, as given below:

$$\hat{\varepsilon}(\omega) = \varepsilon_\infty + \frac{\varepsilon_s - \varepsilon_\infty}{(1 + i\omega\tau)^\beta}, \tag{6.9}$$

Here, ε_s & ε_∞ are the static (saturated) and high-frequency limits. τ is the relaxation time of the oscillating dipoles *i.e.*, the minimum time taken by dipoles to orient themselves in the direction of field or to restore equilibrium position on withdrawal of the field. This equation reduces to Debye's form with a single relaxation time for $\beta = 1$.[67] Substituting, $1 + i\omega\tau = e^{i\varphi}\sqrt{1 + \omega^2\tau^2} = {e^{i\varphi}}/{\cos\varphi}$, for $\varphi = \tan^{-1}\omega\tau$; the real part of dielectric constant simplifies to:

$$\varepsilon'(\omega) = \varepsilon_\infty + (\varepsilon_s - \varepsilon_\infty)(\cos\varphi)^\beta \cos\beta\varphi. \tag{6.10}$$

The dispersion of ε' for hematite and maghemite at different bias are thus fitted to extract the parameters: $\varepsilon_s, \varepsilon_\infty, \beta$ & τ. In Figure 6.9(a,b), the fitted curves at zero and highest bias are shown for both the samples, whereas Figure 6.9(c,d) depict the above-mentioned parameters as a function of DC bias. In hematite, all four parameters monotonically increase with bias in the range $0 - 40$ V. The enhancement in ε_s & ε_∞, verifies a positive correlation of induced polarization with DC fields. As $\beta \to 1$, Debye's form becomes more relevant *i.e.*, a gradually lower deviation from the ideal nature is inflicted. Basically, in presence of a constant external field the dipoles align and act more uniformly, and this in turn increases β. However, DC fields also increase the electrical inertia of the charge-ensemble and thus, the relaxation mechanism slows down a bit under identical driving amplitude, so τ increases. Maghemite also reciprocates in a similar nature for smaller bias. But, after 10 V, ε_∞ & τ first saturate and then decrease slowly. The field-induced increase in carrier-density is likely responsible for that.[68] In most materials, lower bias helps to enhance polarization characteristics and gradual increment in external field promotes generation of free carriers in the system. Comparing Figure 6.7 and 6.8, it can be concluded that, hematite offers a much larger impedance than maghemite. Naturally, hematite can easily stand voltages up-to 40 V, while maghemite starts losing its

bound-to-free carrier ratio after 10 V. The higher electrical inertia ceases to restrict the newly generated free carriers and satisfies declining values of τ.

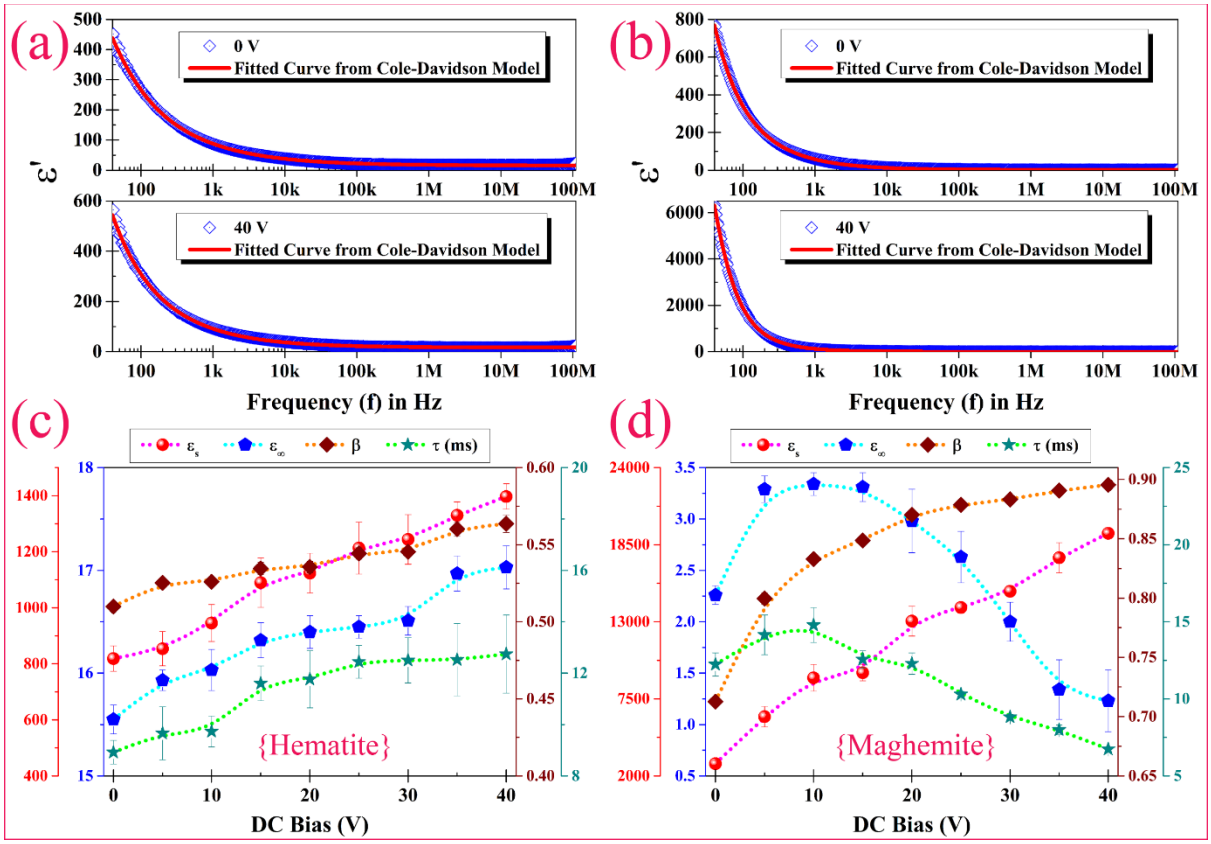

Figure 6.9 Cole-Davidson model-based fits of $\varepsilon'(f)$ at 0 and 40 V external bias for (a) hematite and (b) maghemite; bias-dependency of the extracted fitting parameters for (c) hematite and (d) maghemite. The red, blue, maroon and green scales/symbols respectively denote the variation of the parameters: $\varepsilon_s, \varepsilon_\infty, \beta$ & τ (ms). Dotted lines are guide to the eye.

Transport/insulating properties and resistance correlations of the grain core and boundaries can be efficiently probed from a retrospective analysis of Cole-Cole plots. Such a core-boundary assembly could be modelled by an equivalent circuit that consists of a couple of resistors (R) and constant phase-elements (Q), see Figure 6.10(a). Here, R_g, R_{gb} are the resistance of the grain and grain boundaries; and Q_g, Q_{gb} take care of the phase contributions of the respective subsystems.[69] The associated capacitance (C) can be determined using the relation:

$$C = R^{\left(\frac{1}{\alpha}-1\right)} Q^{\frac{1}{\alpha}}. \tag{6.11}$$

Here α is the distributing factor *i.e.*, a measure of deviation from the pure capacitive behaviour. Considering the fact that, grain cores offer lower resistance and plays a major role in transport, compared to the grain boundaries, this interlinked circuit-model is proposed to physically replicate the system. Such a circuit simulates a theoretical Cole-Cole curve, composed of two

semi-circular arcs, representing each of the $R-Q$ subsystems [Figure 6.10(b)] and assents Debye relaxations. However; in practice, very often this pair of semi-circles superpose into a single depressed semi-circle or semi-ellipse, in accordance with the Cole-Davidson model.[70] In this formalism, complex impedance has the following form:

$$\hat{Z}(f) = \frac{R_{gb} + R_g\{1 + (i.2\pi f)^{\alpha_{gb}} Q_{gb} R_{gb}\}}{1 + (i.2\pi f)^{\alpha_{gb}} Q_{gb} R_{gb} + (i.2\pi f)^{\alpha_g} Q_g [R_{gb} + R_g\{1 + (i.2\pi f)^{\alpha_{gb}} Q_{gb} R_{gb}\}]}. \quad (6.12)$$

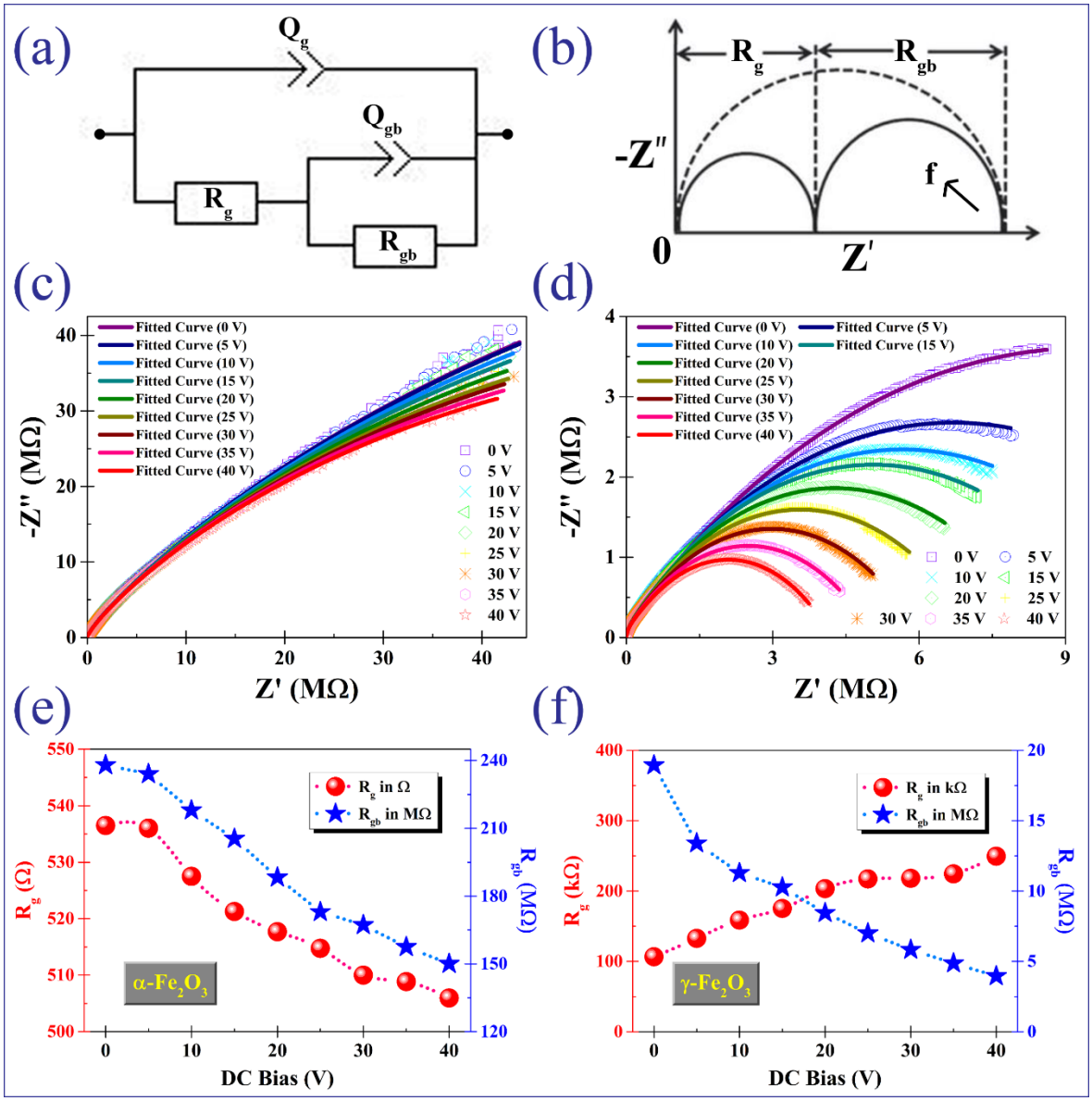

Figure 6.10 (a) A schematic of the proposed equivalent circuit-model comprising resistors and constant phase-elements; (b) theoretically simulated Cole-Cole plots for this model, depicting a pair of semicircles against the two $Q-R$ subsystems; (c,d) Cole-Cole plots (open symbols) and associated fitted curves (solid lines) at varying bias from 0 to 40 V for hematite and maghemite; (e,f) Bias-dependency of the extracted resistances of the constituent grains (R_g) and grain-boundaries (R_{gb}) for the respective samples.

The field-dependent Cole-Cole plots are hence fitted employing this circuit-model in the EC-Lab software for both the phases with satisfactory values (< 0.1) of least-squares goodness of fit, see Figure 6.10(c,d). The bias-sensitive low frequency portion manifests MWIP and might involve domain wall motion,[71] while the bias-independent high frequency region is attributed to phonon-assisted polaron hopping in the adiabatic limit. In maghemite, the Cole-Cole curves contract at a notably higher rate with bias, that admits its lower resistance than hematite. The extracted parameters R_g and R_{gb} are presented as a function of DC bias in Figure 6.10(e,f) for the respective samples. Generally, grain-boundaries contain point-defects and traps in ceramic samples. With increase in external bias, the carriers inside such potential wells get energized and de-trapped. As a result, the effective resistance decreases. For both the phases, R_{gb} is found to be a decreasing function of the bias voltage. However, the grain core may behave differently in distinct materials, depending on the polarization-mechanism, density of bound states and the energy-gap between trapped and free carriers with reference to the applied field.[72] In our case, R_g for hematite decreases with bias, while in maghemite it increases a bit. This difference in resistivity and dielectric constant of the grain core and boundary manifest MWIP. The bias-dependency of such a reorientation polarization is a function of the ratio: (R_{gb}/R_g). The fact that, the experimental data can be fitted by a model with no 'external' elements, indicates absence of noticeable electrode polarization effect.[65] Relaxation-times (τ) were calculated previously employing the Cole-Davidson model, however it can also be determined using the relation: $\tau = 1/2\pi f_{max}$, where f_{max} corresponds to the top of the Cole-Cole curves. Actually, this formula is subject to the relaxation maxima ($\omega\tau \sim 1$) in dissipation factor.[73] But for most semi-circles, the top-most point is beyond the operational frequency-range. Only a few curves of maghemite under moderate fields have their maxima in range and the corresponding τ-values agree with the data in Figure 6.9(d).

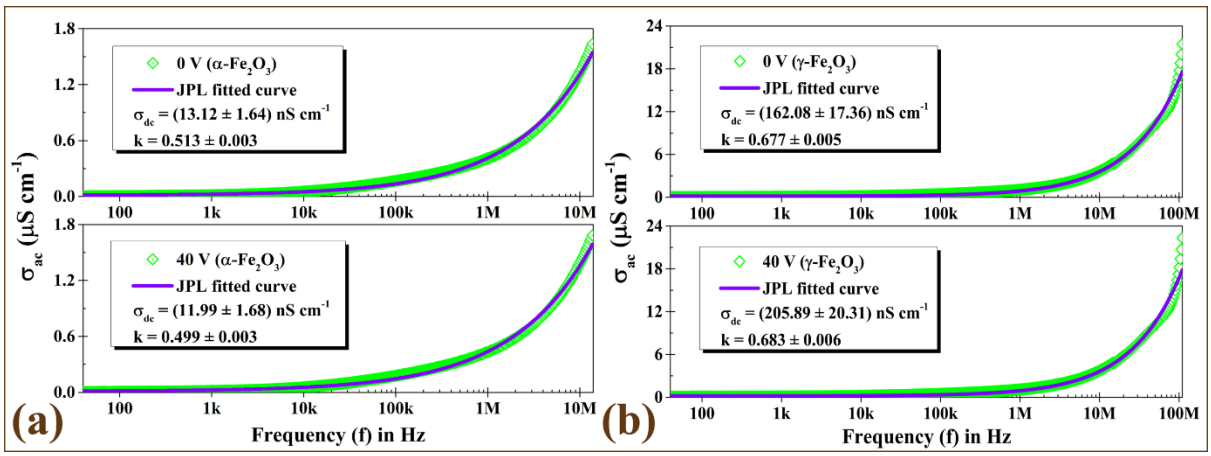

Figure 6.11 Jonscher's power law (JPL) fits of the frequency dispersive AC conductivity (σ_{ac}) at nil and 40 V external bias for (a) hematite and (b) maghemite.

The dynamics of 'available' carriers can be well-scrutinized from the dispersion of ac-conductivity:

$$\sigma_{ac} = \varepsilon_0 \varepsilon'' \omega = \varepsilon_0 \varepsilon' \omega \tan\delta = \frac{Gl}{A}, \tag{6.13}$$

σ_{ac} follows the Jonscher's power law (JPL) as given below,

$$\sigma_{ac}(\omega) = \sigma_{dc} + A\omega^k. \tag{6.14}$$

The two terms respectively represent the drift mobility of free carriers and dielectric relaxation of localized charges. Here, σ_{dc} is the extrapolated dc-conductivity, A is a constant and k is the frequency-exponent. All of them depend on the material and temperature. The temperature-dependence of k is conventionally used to determine conduction-mechanism in semiconductor samples *e.g*., overlapped polaron tunnelling, correlated barrier hopping, quantum tunnelling *etc*.[26,63,68,71] In Figure 6.11, the experimental data is fitted with JPL for the two extremum values of bias. σ_{dc} is observed to vary between 11.9 – 13.2 nS cm^{-1} for hematite and 162 – 206 nS cm^{-1} for maghemite. This involves field-induced carrier generation and mobility rise in maghemite.[74] Such kinetics incorporate de-trapping process from the octahedral vacancies of its spinel structure.[10,71] However, in hematite, polarization mechanisms dominate in the experimental bias-range. The scaling parameter, k attains a value (0.50 ± 0.02) for hematite and (0.68 ± 0.01) for maghemite. It fluctuates nominally with bias. According to Funke, $k \leq 1$ indicates translational motion of the carriers along with sudden hopping dynamics.[75]

6.3.4 First principles results

Geometrical structure: The primitive unit cell of hematite is trigonal, consists of four Fe and six O-atoms. The optimized lattice parameters are $a = b = c = 5.429$ Å and $\alpha = \beta = \gamma = 55.22°$, which are in well agreement with previous reports.

The conventional unit cell of maghemite resembles the structure of magnetite; accompanying cation-vacancies and is represented by the formula: $(Fe_8^{III})_{Tet}[Fe_{40/3}^{III} \boxdot_{8/3}]_{Oct}O_{32}^{II}$, having particular fractionally occupied Fe_{Oct}-sites. The exact theoretical structure; disregarding partial atomic occupancy; prevailed a 40 year-long debate, until in 2010; Grau-Crespo *et al*. identified the vacancy ordering by appropriate elimination of Fe-atoms from Wyckoff 4b sites.[17,76] In the 56-atom conventional cell, there are four Fe 4b sites and 8/3-unit cation vacancy. To recreate the system with commensurate crystallographic properties, they prepared a $1 \times 1 \times 3$ supercell, having twelve Fe 4b sites and 8 cation vacancies, which were distributed in the 4b positions in various combinations, unless they got the most stable coordination with minimum energy and Coulombic repulsion among the cations. However, this maghemite-type supercell has $(56 \times 3 - 8) = 160$ atoms in it and is unsuitable for extensive spin-polarized, electronic calculations.

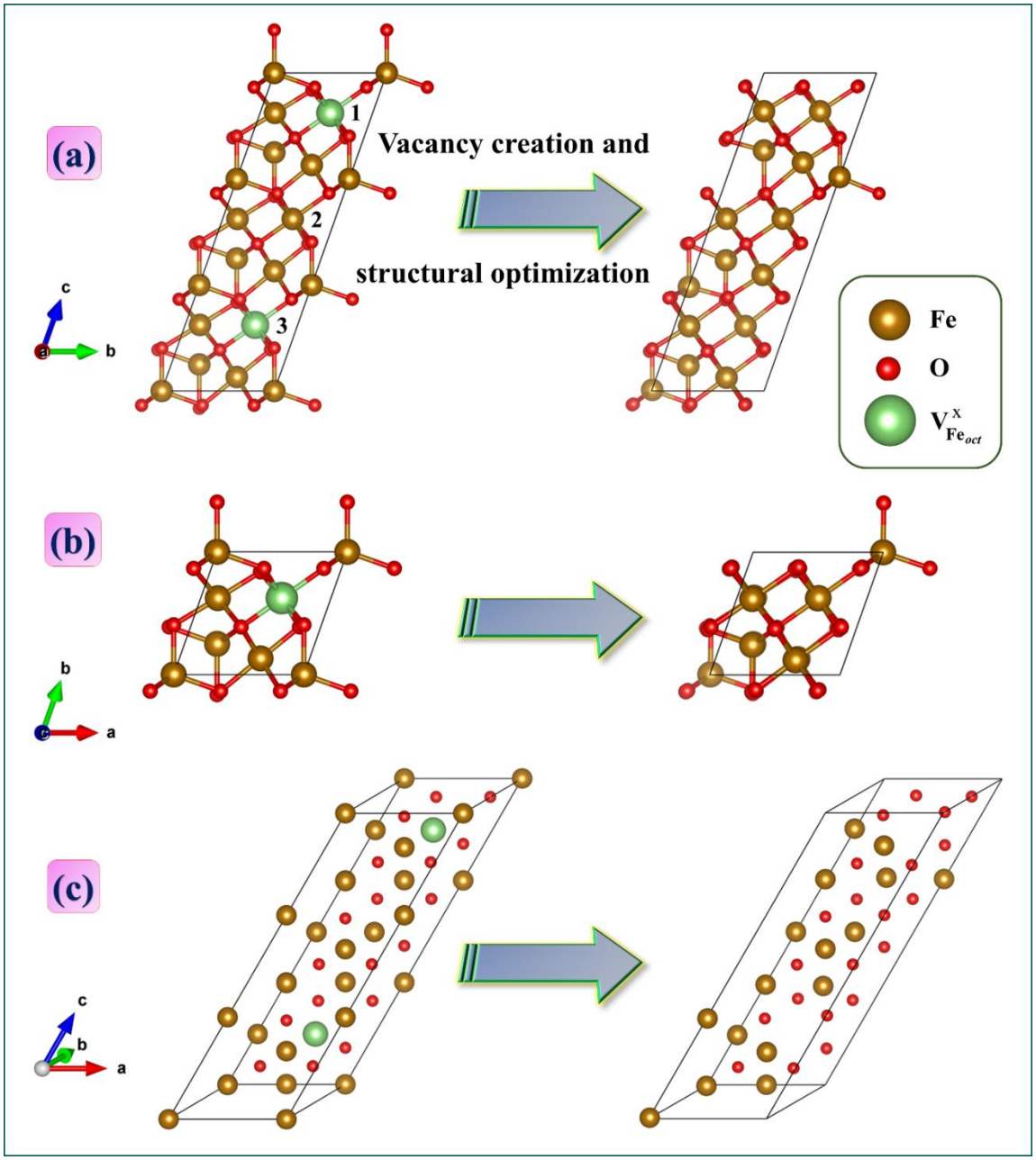

Figure 6.12 $1 \times 1 \times 3$ supercell; representative of maghemite structure, before and after particular neutral vacancy formation at (1,3) 4b-sites & structural optimization, view: (a) along a-axis, (b) along c-axis and (c) oblique line of sight. The Fe- and O-atoms are displayed as brown and red balls respectively, whereas the Fe-vacancy sites are shown by larger light green balls. During structural optimization, the atoms in the immediate neighbourhood of vacancies are seen to displace significantly for minimizing energy. As a result, some atoms at the faces of the cell (shared by two adjacent cells in the infinite array) displaced in one direction, which ceased the sharing and placed them inside only one cell. In the perpendicular view-points of (a) and (b), the vacancy formation is not visible clearly, owing to placement of identical Fe-sites, just behind the atoms to be removed. So, in (c) an oblique view is given, which clearly demonstrates the vacancy creation. However, here the bonds are not shown to make the figure unclouded.

Hence, for cost effective computations, we preferred to rebuild a feasible structure from the 14-atom magnetite primitive cell and invoked vacancies in it to follow the desired formula: $(Fe_2^{III})_{Tet}[Fe_{10/3}^{III}\ \square_{2/3}]_{Oct}O_8^{II}$. The primitive cell with one-fourth size of the unit cell, has only one Fe 4b site ($^2/_3$rd vacant). Therefore, for an analogous $1 \times 1 \times 3$ supercell composed of $(14 \times 3 - 2) = 40$ atoms, two vacancies are to be allocated among three Fe 4b sites. From energy-calculations, we found, the far arrangement (1-3) is more stable than the doubly degenerate near-combination (1-2 or 2-3), see Figure 6.12. The structure-details and calculated XRD-pattern conform experimental data.

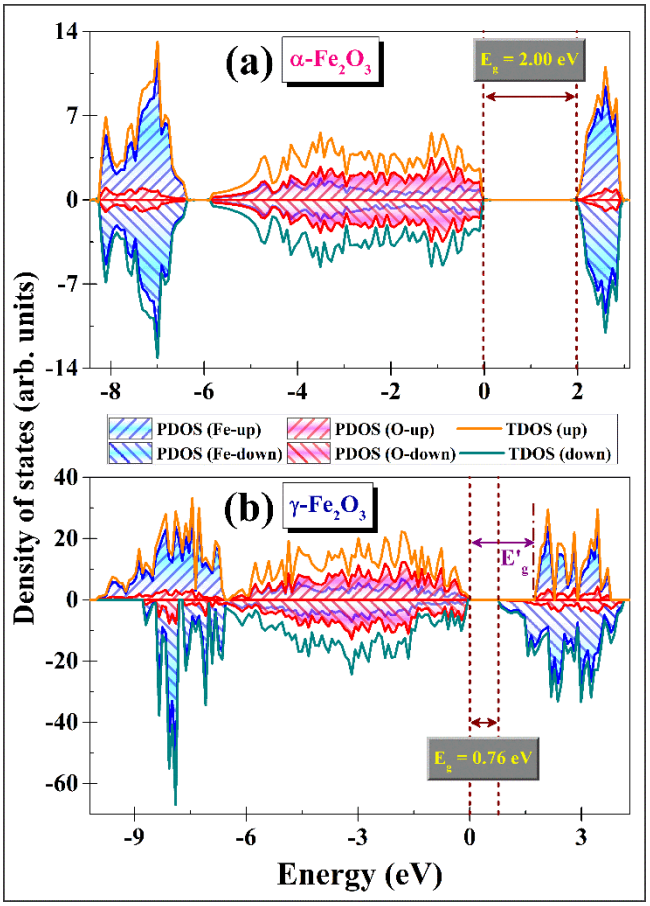

Figure 6.13 Total density of states (TDOS) and projected density of states (PDOS) apropos of contributions from Fe and O atoms; entailing up/down-spins for (a) hematite ($\alpha - Fe_2O_3$), and (b) maghemite ($\gamma - Fe_2O_3$).

Electronic and magnetic property: In Figure 6.13 and 6.14, the total and projected DOS are shown, which specify *p*-type nature in both the polymorphs. Zero and moderate spin-polarization in hematite and maghemite are indicative of the respective antiferro- and ferrimagnetic nature. In maghemite, spin-density integration inside PAW spheres of the cations yields moments: $(4.30 \pm 0.03)\ \mu_B$ for Fe_{Oct} and $(-4.17 \pm 0.01)\ \mu_B$ for Fe_{Tet} ions. The opposite alignment of octahedral and tetrahedral moments builds up the salient ferrimagnetism. Considering magnetic moments localized to the Fe sites, the total magnetization was allowed to relax and summed up to 20.0 μ_B, which inflicts high-spin Fe co-ordination.

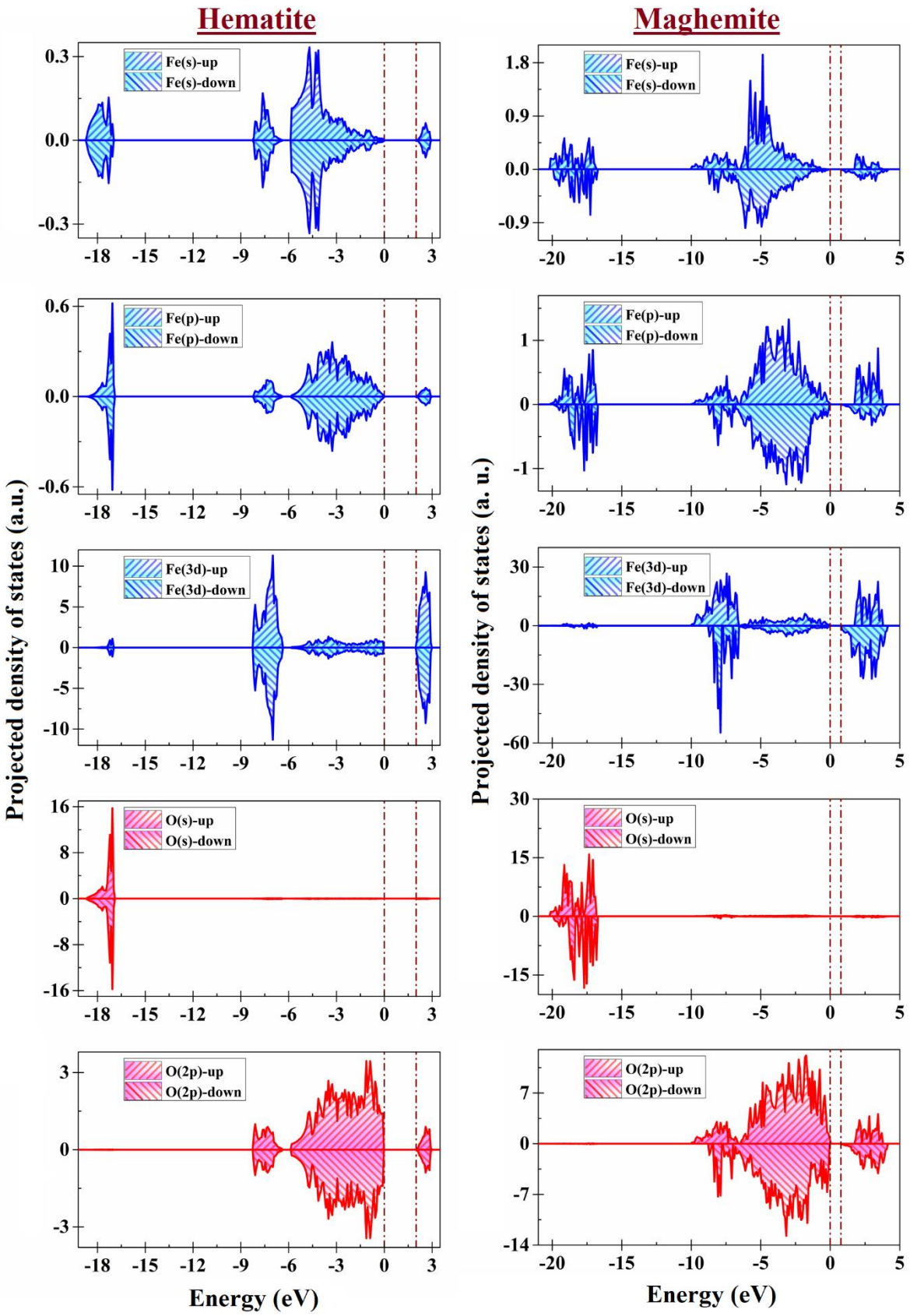

Figure 6.14 Projected density of states (PDOS) attributing Fe/O – orbital contributions in hematite ($\alpha - Fe_2O_3$) and maghemite ($\gamma - Fe_2O_3$), respectively.

The electronic band-gap for hematite and maghemite is found to be 2.00 and 0.76 eV, respectively. In hematite, the electronic bandgap agrees well with the optical gap. However, for maghemite the difference between the two gaps is noteworthy,[76] despite GGA method of DFT underestimates bandgap sometimes. The facts that, (i) maghemite is spin-polarized ($up: down = 52.6: 47.4$, considering occupied states) and (ii) the gap between valence band maximum and the minimum of (majority) up-spin conduction band; labelled as E_g' in Figure 6.13(b), accords with the optical gap well, hint at the possibility of optical transitions through these bands. The smaller number of effective bands and interactions in case of a primitive vacancy-ordered structure might also have contributed to this deviation. In Figure 6.15, ELF at particular lattice planes of the two phases is demonstrated. In maghemite, the electron cloud is notably delocalized in the immediate vicinity of the iron-vacancy [Figure 6.15(b)]. Naturally bias imparts additional carriers, that justifies its high field-dependent electrical conductivity.

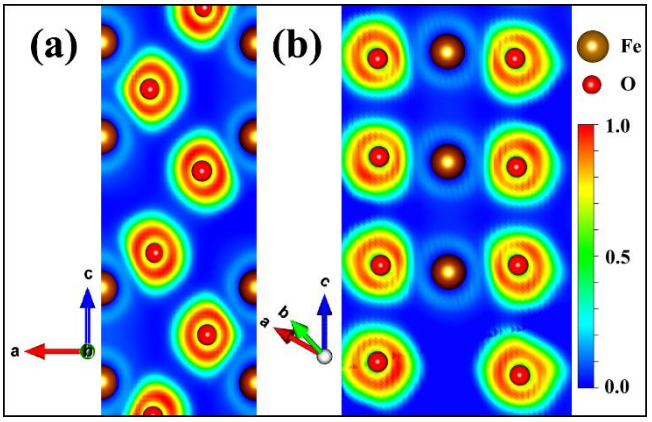

Figure 6.15 2D density maps of electron localization function (ELF) at selected planes of (a) hematite and (b) maghemite [iso-surface value = 0.5625]. The blue-to-red colour scale represents gradual increase in Pauli repulsion of the classical electron gas *i.e.*, higher charge-density cloud.

Optical and dielectric property: Dielectric function of crystalline solids involves one Drude-like intraband and an interband contributions. Taking both contributions in the matrix form of momentum operators, PAW methodology provides the following formulae for imaginary and real parts of dielectric tensor; connected through Kramers-Kronig relation, in long-wavelength limit.[53]

$$\varepsilon''_{\alpha\beta}(\omega) = \frac{4\pi^2 e^2}{\Omega} \lim_{q\to 0} \frac{1}{q^2} \sum_{c,v,k} 2w_k \delta(\varepsilon_{ck} - \varepsilon_{vk} - \omega) \langle u_{ck+e_\alpha q} | u_{vk} \rangle \langle u_{ck+e_\beta q} | u_{vk} \rangle^*, \tag{6.15}$$

$$\varepsilon'_{\alpha\beta}(\omega) = 1 + \frac{2}{\pi} P \int_0^\infty \frac{\varepsilon''_{\alpha\beta}(\omega')\omega'}{\omega'^2 - \omega^2 + i\eta} d\omega'. \tag{6.16}$$

Here, q is the incident Bloch vector, Ω is the cell-volume, c & v stand for conduction and valence band, u_{ck} is cell's periodic part for orbitals in the k −space, and P represents the principal value of the integral. The corresponding tensor-components of energy loss (L), refractive index (μ), extinction coefficient (κ) and reflectivity (R) are determined using the below formulae.

$$L_{\alpha\beta} = -Im\left(\frac{1}{\widehat{\varepsilon_{\alpha\beta}}}\right) = \frac{\varepsilon''_{\alpha\beta}}{\left(\varepsilon'_{\alpha\beta}\right)^2 + \left(\varepsilon''_{\alpha\beta}\right)^2}, \tag{6.17}$$

$$\mu_{\alpha\beta}, \kappa_{\alpha\beta} = \left[\frac{\sqrt{\left(\varepsilon'_{\alpha\beta}\right)^2 + \left(\varepsilon''_{\alpha\beta}\right)^2} \pm \varepsilon'_{\alpha\beta}}{2}\right]^{1/2}, \tag{6.18}$$

$$R_{\alpha\beta} = \left(\frac{\mu_{\alpha\beta} - 1}{\mu_{\alpha\beta} + 1}\right)^2. \tag{6.19}$$

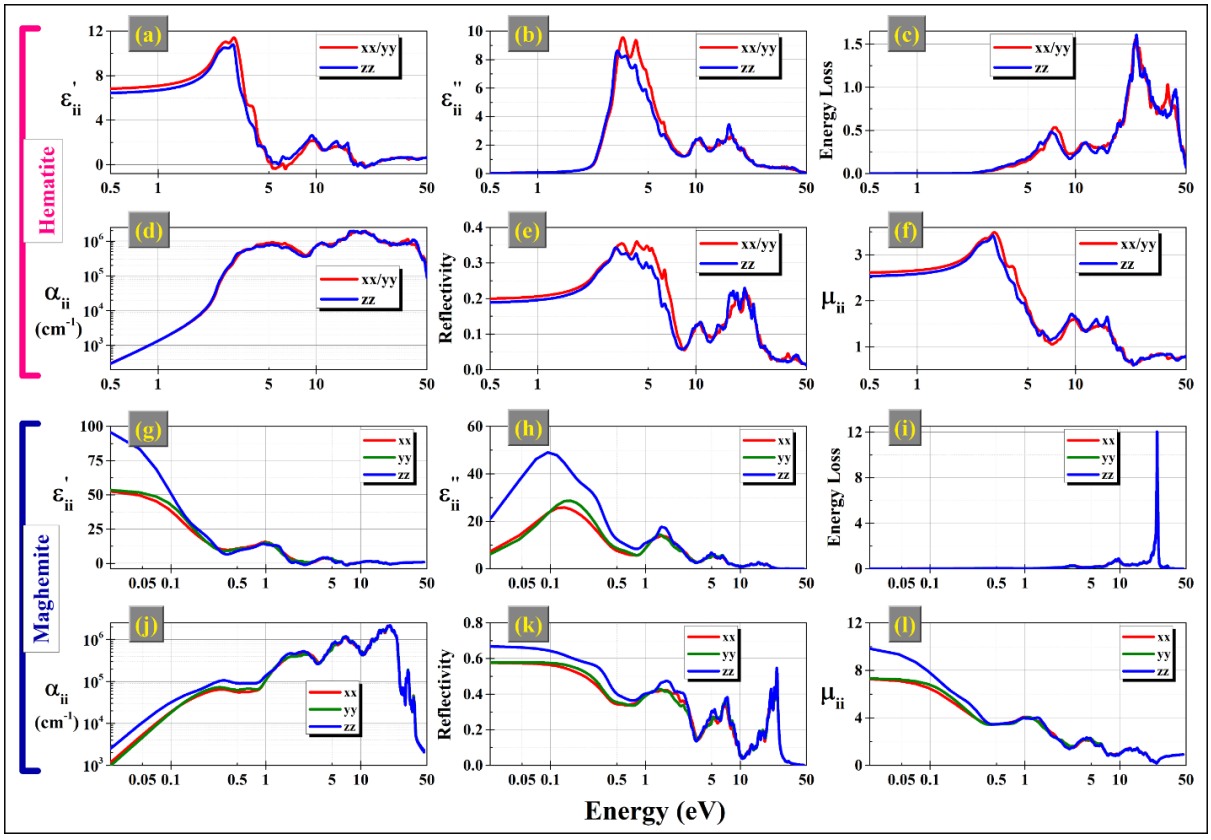

Figure 6.16 Energy-dispersion of the principle components of various tensor functions, calculated for hematite and maghemite: (a,g) real dielectric function $[\varepsilon'_{ii}; i = x, y, z]$; (b,h) imaginary dielectric function $[\varepsilon''_{ii}]$; (c,i) energy loss $[L_{ii}]$; (d,j) absorption coefficient $[\alpha_{ii}]$; (e,k) reflectivity $[R_{ii}]$; (f,l) refractive index $[\mu_{ii}]$.

In Figure 6.16, dispersion of the principal components of various dielectric tensors are displayed for the two systems. The results for hematite are consistent with previous reports.[77] The dielectric parameters of hematite possess an azimuthal symmetry $(\varepsilon_{xx} = \varepsilon_{yy} \neq \varepsilon_{zz})$,

whereas orthogonal components for maghemite are completely asymmetric, retaining obvious structural reasons. Another point is, the results so obtained from DFT reflect bulk properties, that can be significantly different from nanoparticles for obvious reasons. However, optical properties drastically vary below 50 nm and quantum confinement of electronic states (or phonons) start below 20 nm. Therefore, these first principles results can be resembled for the as-synthesized nanoparticles (>70nm).

Dynamic dielectric constant is contemplated for both electronic and optical 'excitations', as an electromagnetic wave also encompasses sinusoidal (electrical) waves, perpendicular to the direction of propagation. In case of a forced damped oscillator, ε' indicates the phase-lag between the driving (input) and response (output) frequency, which in optical experiments slows down light in a material medium by a factor μ. Whereas ε" itself is the damping factor and describes absorption of light (followed by Beer-Lambert law) and dissipation of electrical energy into heat (a high entropy variant of energy) in optical and electrical experiments, respectively.

At energies close to 5 and 2 eV, hematite and maghemite exhibit characteristic metallic behaviour such as high reflectivity, where the intraband Drude peaks of ε' changed its sign.[78] The strong anisotropy; intrinsic to the crystal structure, at lower energies not only manifested large dielectric deviations in different directions, but also obtained piecewise negative values at different regime; leading to the appearance of dielectric hyperboloids (discussed in section 6.3.5). The sign difference close to the plasma oscillation frequency features indefinite dielectric media,[78] and/or resonant absorption/dissipation. The diffused absorbance peaks (< 5 eV) owing to interband optical transitions in both polymorphs reflect complex band-properties of iron oxides.[17,52,75] Moreover, in both compounds, the energy loss maxima (characteristic of resonance phenomena in plasma oscillations) are found at quite high energies (> 20 eV); securing their dielectric and optoelectronic applicability in UV-Visible region. The multiple local maxima of the extinction coefficients correspond to the zeroes of ε', that also indicate fast photon absorption and short decay path.

6.3.5 Dielectric ellipsoid and anisotropy evaluation

Ideal dielectrics are classified as linear, homogeneous and isotropic, if the permittivity persists invariance under applied electric field, translation and rotation of space. Equations in section 6.3.3 involve scalar dielectric constant, that ensures $\vec{D}||\vec{E}$. However, in practice real materials very often lose these symmetries, resulting alteration in the directional properties of dielectric displacement $(\vec{D})$ for a given field $(\vec{E})$. Owing to favoured crystallographic orientations, permittivity is described by a 2nd rank tensor ($\overleftrightarrow{\varepsilon}$). The displacement vector component ascertains the inner product: $D_i = \varepsilon_0 \sum_j \varepsilon_{ij} E_j$, where ε_{ij} corresponds to polarization

at the 'i'-direction due to a field exerted in the 'j'-direction. The scalar product of $\vec{D}$ and $\vec{E}$ is a scalar point-function (say S) and is further reduced in the trailing matrix form.

$$\vec{D}.\vec{E} = \sum_i D_i E_i = \varepsilon_0 \sum_{i,j} \varepsilon_{ij} E_i E_j = \varepsilon_0 \begin{pmatrix} \varepsilon_{xx}E_x + \varepsilon_{xy}E_y + \varepsilon_{xz}E_z \\ \varepsilon_{yx}E_x + \varepsilon_{yy}E_y + \varepsilon_{yz}E_z \\ \varepsilon_{zx}E_x + \varepsilon_{zy}E_y + \varepsilon_{zz}E_z \end{pmatrix} \begin{pmatrix} E_x \\ E_y \\ E_z \end{pmatrix} = S, \tag{6.20}$$

When the electric field causes a polarization only in its own direction, and does not polarize the system in orthogonal directions, then all cross-terms vanish and the dielectric tensor, $\varepsilon_{ij} = \begin{pmatrix} \varepsilon_{xx} & \varepsilon_{xy} & \varepsilon_{xz} \\ \varepsilon_{yx} & \varepsilon_{yy} & \varepsilon_{yz} \\ \varepsilon_{zx} & \varepsilon_{zy} & \varepsilon_{zz} \end{pmatrix}$ diagonalizes to $\widetilde{\varepsilon_{ij}} = \begin{pmatrix} \varepsilon_{xx} & 0 & 0 \\ 0 & \varepsilon_{yy} & 0 \\ 0 & 0 & \varepsilon_{zz} \end{pmatrix}$. This manifests irrotational nature, $\vec{\nabla} \times \vec{E} = 0$ in absence of magnetic fields. Choosing $S = \varepsilon_0$ against a new unit system, the expression transforms to, $\varepsilon_{xx}(E_x)^2 + \varepsilon_{yy}(E_y)^2 + \varepsilon_{zz}(E_z)^2 = 1$ *i.e.*,

$$\left(\frac{E_x}{1/\sqrt{\varepsilon_{xx}}}\right)^2 + \left(\frac{E_y}{1/\sqrt{\varepsilon_{yy}}}\right)^2 + \left(\frac{E_z}{1/\sqrt{\varepsilon_{zz}}}\right)^2 = 1. \tag{6.21}$$

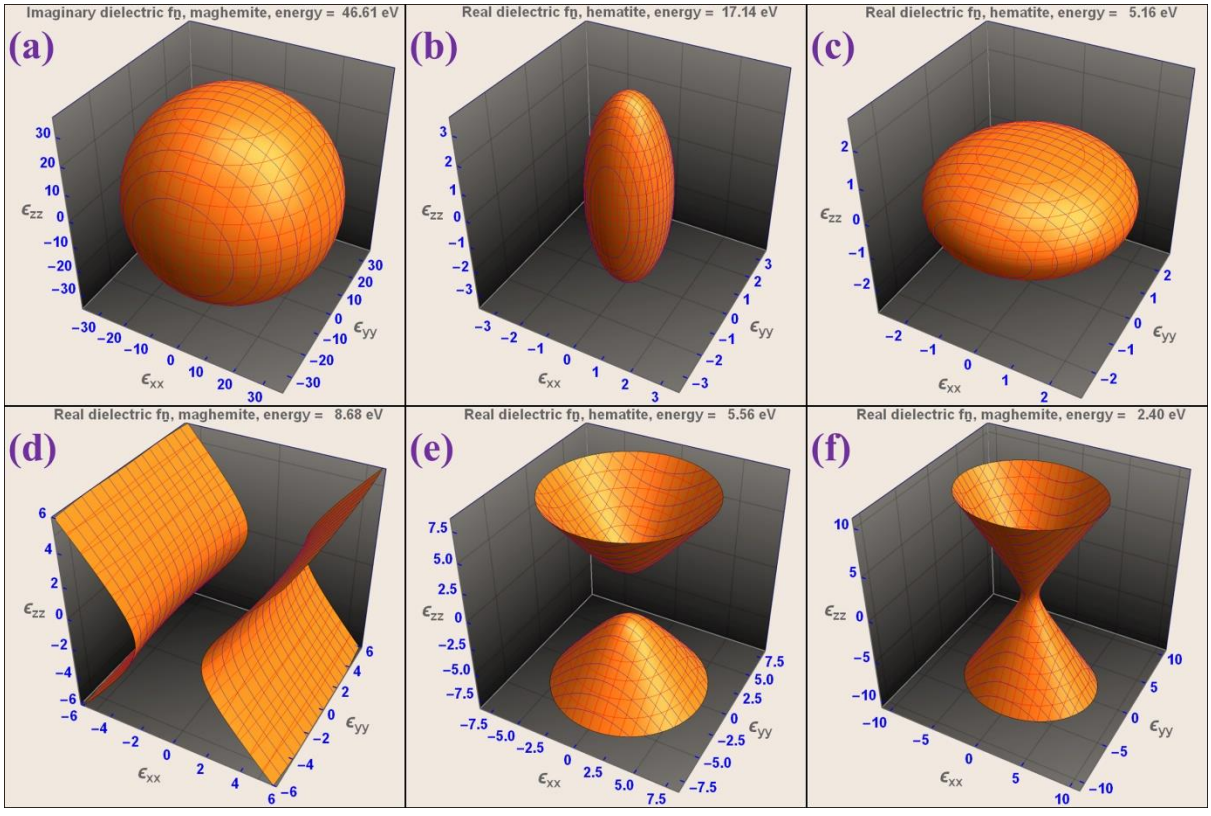

Figure 6.17 Representative quadric surface of real/imaginary dielectric tensor at particular energies: (a) sphere; (b) prolate ellipsoid; (c) oblate ellipsoid; (d,e) double-sheet (elliptic) hyperboloid with negative zz and xx-yy indices respectively; (f) one-sheet (hyperbolic) hyperboloid. For the complete energy dispersive surface evolution, please watch the supplementary video provided with the parent paper.

This equation represents the quadric surface of the dielectric tensor with semi-axes length equal to the inverse square root of the principal coefficients $\left(1/\sqrt{\varepsilon_{ii}}\,;\, i = x, y, z\right)$. Geometrically, symmetric 2nd rank tensors are represented by a 2nd degree (quadric) surface, commonly an ellipsoid, like the polarizability ellipsoid in Raman spectroscopy. However, for any $\varepsilon_{ii} < 0$, hyperboloids appear. For one, two or three negative coefficients the quadric surface respectively reshapes to hyperboloids comprising one sheet (*e.g.*, thermal expansion of plagioclase feldspar), double sheets (*e.g.*, thermal expansion of calcite under basal plane contraction) and completely imaginary exterior (*e.g.*, susceptibility of quartz/calcite). Hence, graphical representation of this surface evaluates the degree of anisotropy present in the system, as a function of excitation (photon) energy. This evolution is projected in a video. At energies close to the core bands, the surface evolves through rapid transformations to various anisotropic forms; leading to the dispersive dielectric/absorption characteristics. For higher energies, the surface slowly saturates to an isotropic spheroid. Figure 6.17 demonstrates certain representative snapshots of the quadric surface at selected energies.

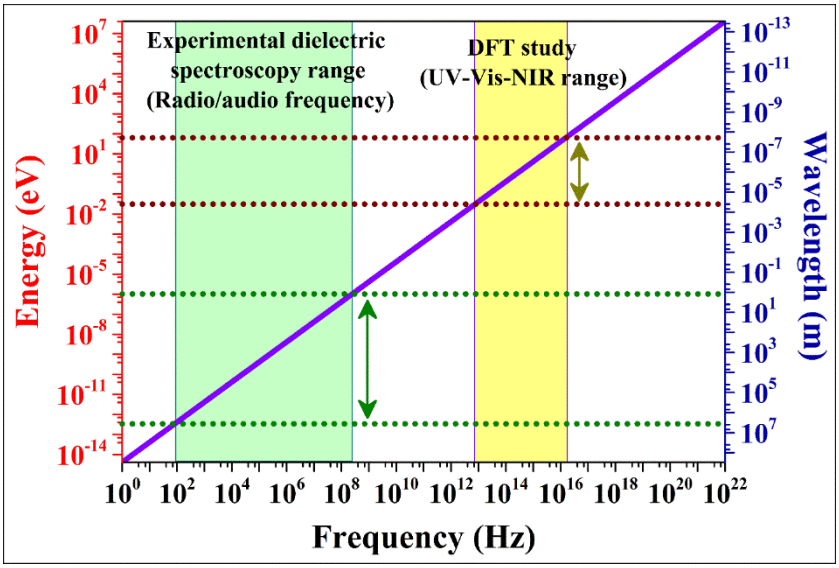

Figure 6.18 Energy or wavelength corresponding to varying frequency in electromagnetic spectrum. The green shaded region denotes the experimental dielectric spectroscopy range (radio/audio frequencies: 40 Hz – 110 MHz). The yellow shaded region indicates the computational range (0.02 – 50 eV) for DFT-based study, corresponding to UV-Vis-NIR regime. The double-headed arrows mark the associated energy and wavelength regions.

Actually, the relaxation phenomena associated with audio/radio-frequencies and UV-Vis-IR range is entirely different. The natural oscillation-frequency of a charged ensemble (ions, dipoles, interfacial layers, electrons *etc.*) has a negative correlation with its inertia. So, for a driving oscillation of the audio/radio range; the (heavy) ions, dipoles or trapped charges at the interfaces respond. On the other hand, (light) electrons respond to high-frequency optical

excitations. Here, due to comparable energy-scale with the bandgaps, resonance absorption may take place. Deviations in dielectric phenomena and mechanisms accompany distinct dependency on the driving frequency, bias field, and temperature.

6.4 Concluding remarks

Summarily, dielectric properties of hematite and maghemite were explored in both experimental and first principles framework to cultivate dipolar/interfacial polarization and optoelectronic endeavour, respectively. Various field-dependent frequency dispersions were fitted with (i) Cole-Davidson model to quantify relaxation schemes, (ii) a proposed equivalent circuit-model to determine resistance-correlations between grain core and boundaries in the midst of MWIP, and (iii) JPL to describe available carriers and small polaron hopping. Dielectric constant is tailored reversibly up-to an order by external bias, that encourages applicability in tunable energy-storage and microwave devices. In first principles investigations, a new vacancy-ordered maghemite structure is developed to ensure compatibility with heavy, spin-polarized electronic, magnetic and optical calculations. Dispersions of dynamic dielectric function and related optical parameters are emphasized; taking material-specific anisotropic fluctuations, intra- and interband transitions, plasma oscillations, resonant absorption and decay into account. Finally, the energy-dispersive quadric surface of dielectric tensor is simulated to demonstrate the degree of anisotropy present in the strongly correlated systems. This method is capable of unveiling intrinsic anisotropy in complex structures in view of dielectric and electronic polarizations.

References

1. Gupta A K and Gupta M 2005 *Biomaterials* **26** 3995-4021
2. Jubb A M and Allen H C 2010 *ACS Appl. Mater. Interfaces* **2** 2804-12
3. Parkinson G S 2016 *Surf. Sci. Rep.* **71** 272-365
4. Chertok B, Moffat B A, David A E, Yu F, Bergemann C, Ross B D and Yang V C 2008 *Biomaterials* **29** 487-96
5. Marks L 1994 *Rep. Prog. Phys.* **57** 603
6. Yavuz C T, Mayo J, William W Y, Prakash A, Falkner J C, Yean S, Cong L, Shipley H J, Kan A and Tomson M 2006 *Science* **314** 964-7
7. Sousa M, Rubim J, Sobrinho P and Tourinho F 2001 *J. Magn. Magn. Mater.* **225** 67-72
8. Itoh H and Sugimoto T 2003 *J. Colloid Interface Sci.* **265** 283-95
9. Fiorani D, Testa A, Lucari F, D'orazio F and Romero H 2002 *Physica B Condens. Matter.* **320** 122-6
10. Ali K, Sarfraz A, Mirza I M, Bahadur A, Iqbal S and Ul Haq A 2015 *Curr. Appl. Phys.* **15** 925-9

11. Kim S, Ico G, Bai Y, Yang S, Lee J-H, Yin Y, Myung N V and Nam J 2019 *Nanoscale* **11** 20527-33
12. Farooq O, Anis-ur-Rehman M and ul Haq A 2019 *J. Alloys Compd.* **786** 314-20
13. Mallikarjuna N, Manohar S, Kulkarni P, Venkataraman A and Aminabhavi T 2005 *J. Appl. Polym. Sci* **97** 1868-74
14. Miller E L, Paluselli D, Marsen B and Rocheleau R E 2005 *Sol. Energy Mater. Sol. Cells* **88** 131-44
15. Cavas M, Gupta R, Al-Ghamdi A A, Gafer Z H, El-Tantawy F and Yakuphanoglu F 2013 *Mater. Lett.* **105** 106-9
16. Wang Z, Hu X, Käll P-O and Helmersson U 2001 *Chem. Mater.* **13** 1976-83
17. Lininger C N, Cama C A, Takeuchi K J, Marschilok A C, Takeuchi E S, West A C and Hybertsen M S 2018 *Chem. Mater.* **30** 7922-37
18. Larcher D, Masquelier C, Bonnin D, Chabre Y, Masson V, Leriche J-B and Tarascon J-M 2002 *J. Electrochem. Soc.* **150** A133
19. Mirzaei A, Janghorban K, Hashemi B, Bonyani M, Leonardi S and Neri G 2016 *Ceram. Int.* **42** 6136-44
20. Abdi A and Trari M 2013 *Electrochim. Acta* **111** 869-75
21. Wang L, Lee C-Y and Schmuki P 2013 *Electrochim. Acta* **91** 307-13
22. Dhal J, Mishra B and Hota G 2015 *Int. J. Environ. Sci. Technol.* **12** 1845-56
23. Fei Y, Wang Q, Sun J, Wang S, Li T, Wang J and Wang C 2020 *Curr. Appl. Phys.* **20**(7) 866-70
24. Wang C, Wang X, Yu J, Liu Y, Dai W, Li J, Tao J and Tian W 2019 *Mater. Res. Express* **6** 105204
25. Reveendran R and Khadar M A 2018 *Mater. Chem. Phys.***219** 142-54
26. Paulose T and Abraham K 2017 *J. Optoelectron. Adv. Mater.* **19** 440-46
27. Fock J, Bogart L K, González-Alonso D, Espeso J I, Hansen M F, Varón M, Frandsen C and Pankhurst Q A 2017 *J. Phys. D Appl. Phys.* **50** 265005
28. Mitra D, Bhattacharjee S, Mazumder N, KumarDas B, Chattopadhyay P and Chattopadhyay K K 2020 *Ceram. Int.* **46** 20437-47
29. Yang L, Li J, Pu T-C, Kong M, Zhang J and Song Y 2017 *RSC Adv.* **7** 47913-9
30. Kumar V, Chahal S, Singh D, Kumar A, Kumar P and Asokan K 2018 Annealing effect on the structural and dielectric properties of hematite nanoparticles. In: *AIP Conf. Proc.*: AIP Publishing LLC) p 030245
31. Cheng Y, Yu S, Zhu M, Hwang J and Yang F 2020 *Phys. Rev. Lett.* **124** 027202
32. Ang C, Bhalla A and Cross L 2001 *Phys. Rev. B Condens. Matter.* **64** 184104
33. Ang C and Yu Z 2004 *Phys. Rev. B Condens. Matter.* **69** 174109

34. Guo H and Barnard A S 2011 *Phys. Rev. B Condens. Matter.* **83** 094112
35. Jian W, Jia R, Wang J, Zhang H-X and Bai F-Q 2019 *Inorg. Chem. Front.* **6** 2810-6
36. Rollmann G, Rohrbach A, Entel P and Hafner J 2004 *Phys. Rev. B Condens. Matter.* **69** 165107
37. Zhou Z, Shi J and Guo L 2016 *Comput. Mater. Sci.* **113** 117-22
38. Wang R B and Hellman A 2018 *J. Chem. Phys.* **148** 094705
39. Kiejna A and Pabisiak T 2012 *J. Condens. Matter Phys.* **24** 095003
40. Lunt R A, Jackson A J and Walsh A 2013 *Chem. Phys. Lett.* **586** 67-9
41. Nishiwaki M and Fujiwara H 2020 *Comput. Mater. Sci.* **172** 109315
42. Koumpouras K and Larsson J A 2020 *J. Condens. Matter Phys.* **32** 315502
43. Jones R C 1945 *Phys. Rev.* **68** 93
44. Chernyshova I, Hochella Jr M and Madden A 2007 *Phys. Chem. Chem. Phys.* **9** 1736-50
45. Kresse G and Hafner J 1993 *Phys. Rev. B Condens. Matter.* **47** 558
46. Kresse G and Hafner J 1994 *Phys. Rev. B Condens. Matter.* **49** 14251
47. Blöchl P E 1994 *Phys. Rev. B Condens. Matter.* **50** 17953
48. Perdew J P, Burke K and Ernzerhof M 1996 *Phys. Rev. Lett.* **77** 3865
49. Rollmann G, Rohrbach A, Entel P and Hafner J 2004 *Phys. Rev. B Condens. Matter.* **69** 165107
50. Blanchard M, Lazzeri M, Mauri F and Balan E 2008 *Am. Mineral.* **93** 1019-27
51. Dudarev S, Botton G, Savrasov S, Humphreys C and Sutton A 1998 *Phys. Rev. B Condens. Matter.* **57** 1505
52. Meng Y, Liu X-W, Huo C-F, Guo W-P, Cao D-B, Peng Q, Dearden A, Gonze X, Yang Y and Wang J 2016 *J. Chem. Theory Comput*. **12** 5132-44
53. Gajdoš M, Hummer K, Kresse G, Furthmüller J and Bechstedt F 2006 *Phys. Rev. B Condens. Matter.* **73** 045112
54. Lian J, Duan X, Ma J, Peng P, Kim T and Zheng W 2009 *ACS Nano* **3** 3749-61
55. Yamashita T and Hayes P 2008 *Appl. Surf. Sci.* **254** 2441-9
56. Moreira G F, Peçanha E R, Monte M B, Leal Filho L S and Stavale F 2017 *Miner. Eng.* **110** 96-103
57. Bhattacharjee S, Mazumder N, Mondal S, Panigrahi K, Banerjee A, Das D, Sarkar S, Roy D and Chattopadhyay K K 2020 *Dalton Trans.* **49** 7872-90
58. Gupta R and Sen S 1975 *Phys. Rev. B Condens. Matter.* **12** 15
59. Bagus P S, Nelin C J, Brundle C R, Lahiri N, Ilton E S and Rosso K M 2020 *J. Chem. Phys.* **152** 014704
60. Koops C 1951 *Phys. Rev.* **83** 121
61. Rezlescu N and Rezlescu E 1974 *Phys. Status Solidi A* **23** 575-82

62. Chen Z, Cvelbar U, Mozetic M, He J and Sunkara M K 2008 *Chem. Mater.* **20** 3224-8
63. Nasri S, Hafsia A B, Tabellout M and Megdiche M 2016 *RSC Adv.* **6** 76659-65
64. Yanagihara H, Myoka M, Isaka D, Niizeki T, Mibu K and Kita E 2013 *J. Phys. D Appl. Phys.* **46** 175004
65. Meeporn K, Chanlek N and Thongbai P 2016 *RSC Adv.* **6** 91377-85
66. Prakash T, Ramasamy S and Murty B 2013 *Electron. Mater. Lett.* **9** 207-11
67. Bhattacharjee S, Banerjee A, Mazumder N, Chanda K, Sarkar S and Chattopadhyay K K 2020 *Nanoscale* **12** 1528-40
68. George M, Nair S S, Malini K, Joy P and Anantharaman M 2007 *J. Phys. D Appl. Phys.* **40** 1593
69. Pal S, Das N S, Bhattacharjee S, Mukhopadhyay S and Chattopadhyay K K 2019 *Mater. Res. Express* **6** 105029
70. Bhattacharjee S, Mondal S, Banerjee A and Chattopadhyay K K 2020 *Mater. Res. Express* **7** 044001
71. Prakash T, Ramasamy S and Murty B 2011 *AIP Adv.* **1** 022107
72. Besra N, Sardar K, Mazumder N, Bhattacharjee S, Das A, Das B K, Sarkar S and Chattopadhyay K K 2021 *J. Phys. D: Appl. Phys*. **54** 175105
73. Mehraj S and Ansari M S 2015 *Physica E Low Dimens. Syst. Nanostruct.* **65** 84-92
74. Martens H, Huiberts J and Blom P 2000 *Appl. Phys. Lett.* **77** 1852-4
75. Funke K 1993 *Prog. Solid. State Ch.* **22** 111-95
76. Grau-Crespo R, Al-Baitai A Y, Saadoune I and De Leeuw N H 2010 *J. Condens. Matter Phys.* **22** 255401
77. Piccinin S 2019 *Phys. Chem. Chem. Phys*. **21** 2957-67
78. Guan S, Yang S A, Zhu L, Hu J and Yao Y 2015 *Sci. Rep.* **5** 12285

7 MANIPULATING DIELECTRIC RELAXATION VIA ANISOTROPIC FIELD DEVIATIONS IN PEROVSKITE TITANATE GRAIN–GRAIN BOUNDARY HETEROSTRUCTURE: A JOINT EXPERIMENTAL AND THEORETICAL VENTURE

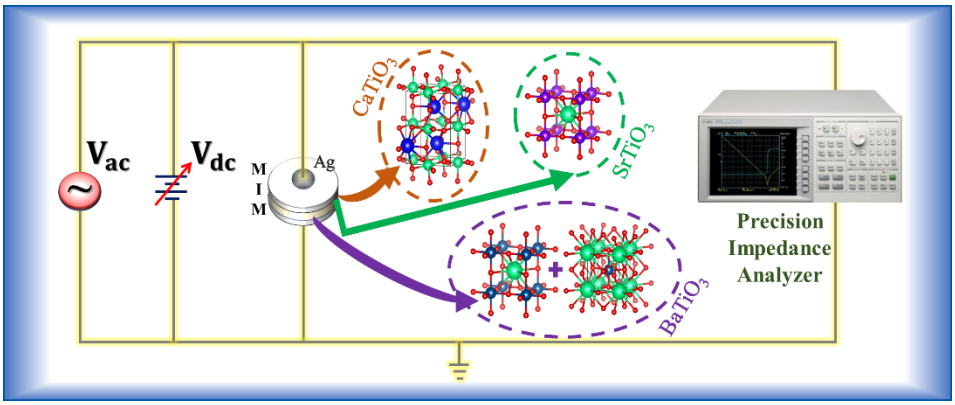

Abstract

Effect of DC field is comprehended in impedance, dielectric, admittance and modulus spectra (40 Hz–20 MHz) of solid-state synthesized, polycrystalline calcium, strontium and barium titanate nanoparticles. The phase-conformation, stoichiometry, optical and vibrational characteristics are investigated employing XRD-Rietveld analysis, DRS, FTIR and Raman spectra. The real/imaginary parts of impedance, dielectric and related functions are tailored by varying external field in the context of classical energy-storing bottleneck. The field-dependent Nyquist plots are interpreted from a proposed equivalent circuitry to quantify electrically heterogeneous, grain core-grain boundary (GC-GB) resistance correlations. Relaxation times, shape-parameters and low/high frequency limits are tailored following Cole-Davidson and Johnson's equations, that explicate Maxwell-Wagner interfacial polarization (MWIP). Using the modified Kohlrausch–Williams–Watts (KWW) equation, asymmetric broadening in modulus spectra is analysed to attune the non-Debye relaxations; free from electrode effects. Large polaron hopping conduction is scrutinized using Jonscher's power law to emphasize variable-range and correlated-barrier hopping mechanisms; comprising delocalized/de-trapped carriers. Bias-insurgence promotes Debye-relaxations, which however suspends switching of the fundamental relaxation-channel, leading to a single normalized master modulus-curve. Static dielectric tensors, Born effective charges and field-induced charge-cloud separation are enunciated via density functional theory (DFT)-framework, whereas finite element simulations

using experimentally extracted electrical parameters substantiate non-uniform and anisotropic field-diffusion within the GC-GB heterostructure.

7.1 Introduction

The emerging thrust for lead-free nanomaterials that offer an extensive variety of coexisting dielectric, piezoelectric and (relaxor or normal) ferroelectric properties along with thermal and compositional stability have promoted a plethora of investigations on alkaline-earth perovskite titanates ($ATiO_3$; A = Ca, Sr, Ba; respectively abbreviated as CT, ST and BT henceforth) and its composites or superlattices.[1-9] This garnered diverse strategies and desirable applications as electro-ceramic and inexpensive microelectronic devices *viz*., multi-layered energy storing or coupling capacitors, pyroelectric detectors, high density optical memory and radar devices, thermistors with positive temperature coefficients, bandpass filters for broadcasting and telecommunications, superior ultrasonic transducers and actuators *etc*.[9-15] The use of ultrafine grains of dielectric compounds like titanates not only improves energy density, breakdown strength and response time, but also advances miniaturized and portable electronic devices.[2,9,16,17] Apart from primary electronics, these group of materials are promising in design and development of water splitting photoelectrodes, nanophosphors (via quenching polar discontinuities), electrocatalyst and gas sensors as well, which again requires intriguing dielectric properties, tunability of conductivity bottleneck (especially photogenerated carriers and their recombination mechanism) and electro-optic coefficient.[17-21]

Amongst these three compounds, CT and ST are known to be quantum paraelectric materials.[1,6,8] The suppression of long-range ferroelectric order by quantum fluctuations accounts for the quantum paraelectric phase. Both these compounds offer to have large dielectric constant due to softening of long wavelength transverse optic phonon modes.[6] But, the difference in their dielectric permittivity is due to the tilted [TiO_6] octahedra, that prevents long-range coupling between neighbouring unit cells.[4-8] BT, which is the first perovskite-type ferroelectric discovered and studied since late 1940s, has four recognized crystal structures over a broad temperature range *viz*., rhombohedral, orthorhombic, tetragonal and cubic (such phases exist for CT and ST also at cryogenic temperatures).[6-9] The first three phases are ferroelectric with polarizations along [110], [111] & [100] direction respectively caused by an acute off-centring of the Ti^{4+} ions from the [TiO_6] octahedra, while the cubic phase is paraelectric. In the ideal cubic structure of perovskites, B (typically transition metal) ions lie at the centre of the O-octahedra and oxygen atoms are placed at the face centres, while the A cations rest at the larger 12-fold coordinated sites. Such an ideal structure assimilates various structural instabilities that involve displacement of the cations to non-centrosymmetric positions as well as rotations and (Jahn-Teller) distortion of the O octahedra.[20-23] The interplay

of particular instabilities and disorders foster transformation to lower symmetries and establish the rich variety in (anti)ferroelectrics and multiferroics. In this regard, Sai *et al*. conducted first principles studies on cubic perovskites of the form $\left(A_{1/3}A'_{1/3}A''_{1/3}\right)BO_3$ & $A\left(B_{1/3}B'_{1/3}B''_{1/3}\right)O_3$ with alternate series of monolayers having distinct cations.[22] They reported a strong variation in the strength of symmetry breaking with associated compositional perturbation, building a proficient ferroelectric nature. Liu *et al*. plumped for epitaxial $(Ba, Sr)TiO_3//Ba(Zr, Ti)O_3$ heterostructures doped with Mn in order to enhance dielectric constant and ferroelectric polarization with controlled dissipation, by optimizing thickness-ratios of deposited layers and sequencing.[23] Similar enhancements are also analysed using DFT-based approaches to confirm the effect of lattice strains, anisotropy and distortions.[24]

Dielectric spectroscopy archetypically concentrates at recognizing the very nature and origin of polarization; such as relaxation (*e.g*., orientational, interfacial) or deformational component (*e.g*., ionic, electronic) of polarizability to understand the electrical microstructure in a heterogeneous system. Basically, the accumulated charge at the interface between the grain core and boundary and an internal barrier layer capacitance (IBLC) establishes Maxwell-Wagner interfacial polarization (MWIP).[7-9,23,25] Consequently, Raevski *et al*. suggested an effective dielectric constant of the core-shell structure: $\varepsilon' = \varepsilon'_{gb}\left(t_g + t_{gb}\right)/t_{gb}$ at the low frequency regime, where ε'_{gb} is the contribution of the grain boundary (shell) and t_g & t_{gb} are the thickness of the respective parts.[26] Currently, tailoring dielectric constant, loss and conductivity are the central goals in this field and substitutional doping is the most common method for accomplishing that.[3-5,25,27] But it does not only manipulate dipolar strength or carrier-density, but also end up with increased defect-density, unwanted traps or elevated local strain. Effect of grain size, stress, A-B site stoichiometry/occupancy, humidity, calcination temperature, chemical and micro-structural variations are studied too in this regard.[9,16,17,27-30] But, enabling reversible tunability via external parameters such as pressure, temperature, electric or magnetic field is preferable for commercial or industrial use. Exerting large pressure might cause expansion of defects and stress throughout the system; and can even ensue irreversible damage.[28] Also, for most piezo-ceramics, magnetodielectric effect is feeble and infrequent at room temperature. Although pyroelectricity and other temperature-dependent alterations hardly affect room-temperature performance, they are fundamentally appealing for exploring materials physics. That is why, in the past few decades, immense research already transpired pledging Arrhenius equation, Vogel–Fulcher relation and thermally activated carrier hopping in $ATiO_3$.[3-5,8,9,18,22-25,29,31] Wang *et al*. executed comparative temperature-dependent dielectric studies in ceramic and single crystalline ST samples and observed Debye-type and relaxor-like behaviour, respectively.[18] They also correlated the multi-relaxation mechanism with the formation and dissociation of single or doubly charged oxygen vacancy clusters.

Contrastingly, field-dependent response is quite uniform and easy to operate in electrical or electronic gadgets. It helps to identify the underlying mechanisms, incommensurate molecular dipoles and non-Debye relaxations conclusively.[30-35] Ang *et al*. investigated 'field-induced ferroelectricity' and relevant couplings with soft phonon modes in some quantum paraelectric single crystal and thin films.[33,34] They in fact inferred that the Landau-Ginzburg-Devonshire (LGD) theory cannot entirely explain the properties of many polar dielectrics and thus introduced a multi-polarization mechanism, taking both extrinsic and intrinsic contributions into account. However, the effect of DC field in various dielectric parameters is still not rigorously explored for polycrystalline perovskites. Scientific literature comprises contradicting reports on modulation of dielectric constant as a function of bias.[30-36] Moreover, nanoparticles can grasp a stronger surface polarization than their bulk counterparts because of the rise in surface to volume ratio of the grains; and thereby scavenge larger dielectric constant.[9,30] Thus, a comprehensive and comparative study of bias field dependent impedance, dielectric, admittance and modulus spectra of the $ATiO_3$ family having nano-dimension is required, which is the main objective of this work.

7.2 Methodology

7.2.1 Precursors and materials

Analytical grade reagents (> 99.9% purity) were used without further purification. The raw ingredients: calcium carbonate ($CaCO_3$), strontium carbonate ($SrCO_3$), barium carbonate ($BaCO_3$) and titanium dioxide (TiO_2) powder were purchased from SIGMA-ALDRICH.

7.2.2 Synthetic procedure

Conventional solid-state method in open air was adopted to synthesize $ATiO_3$ nanoparticles. The alkaline-earth carbonates and TiO_2 powder were mixed in stoichiometric ratio and grounded thoroughly in an agate mortar for an hour to obtain homogeneous fine particles. Then the mixture was taken in an alumina crucible and calcined in a high temperature muffle furnace. In the decarbonation step, the temperature was elevated systematically to 600 °C (2 h), 800 °C (2 h) and 1000 °C (10 h). Accompanying periodic grindings, the mixture of oxides was finally sintered at 1275 °C for 6 h to obtain $ATiO_3$ phase. The average ramp-up rate was maintained at 4 °C/min, while the cooling was set to be natural. The associated reactions follow:

$$ACO_3 \xrightarrow{1000\,^{\circ}C} AO + CO_2$$

$$AO + TiO_2 \xrightarrow{1275\,^{\circ}C} ATiO_3$$

Although most experiments can be performed with the as-obtained nano-powder, dielectric characterizations manifest the best data (with low leakage conductance and associated noise) with MIM pellets. So, 0.40 g of each sample is uniaxially cold-pressed at 0.6 GPa pressure using a hydraulic press to produce polycrystalline cylindrical pellets of 9.5 mm diameter and 1.1 mm thickness. In order to truncate cracks, enhance compressive strength and density, they were further calcined at 1275 °C for an hour. The calculated densities of CT, ST and BT pellets are 3.92, 4.76 and 5.95 g cm^{-3}, respectively, which are very close to their standard densities. For electrical characterizations, thin copper wires were connected to the opposite faces of the pellets using silver paint (Alfa Aesar) to uphold MIM configuration. Formation of non-rectifying, ohmic contacts is anticipated because of (a) high electrical conductivity of silver, (b) closeness of electron affinity of the titanates to the work-function of silver, and (c) smaller interface barrier.

7.2.3 Experimental methods and instrumental specifications

XRD data is collected for the angle of diffraction: $8° \leq 2\theta \leq 85°$ in a Rigaku Miniflex powder X-ray diffractometer (40 kV–15 mA), using monochromatic Cu-K_α radiation. Scanning speed and step-interval were 0.5° min^{-1} and 0.02°, respectively. Morphological study was carried out using field emission scanning electron microscopy (FESEM, Hitachi S-4800) system at an accelerating voltage of 5 kV. FTIR absorbance was characterized in Shimadzu FTIR-8400S with a 4 cm^{-1} spectral resolution.

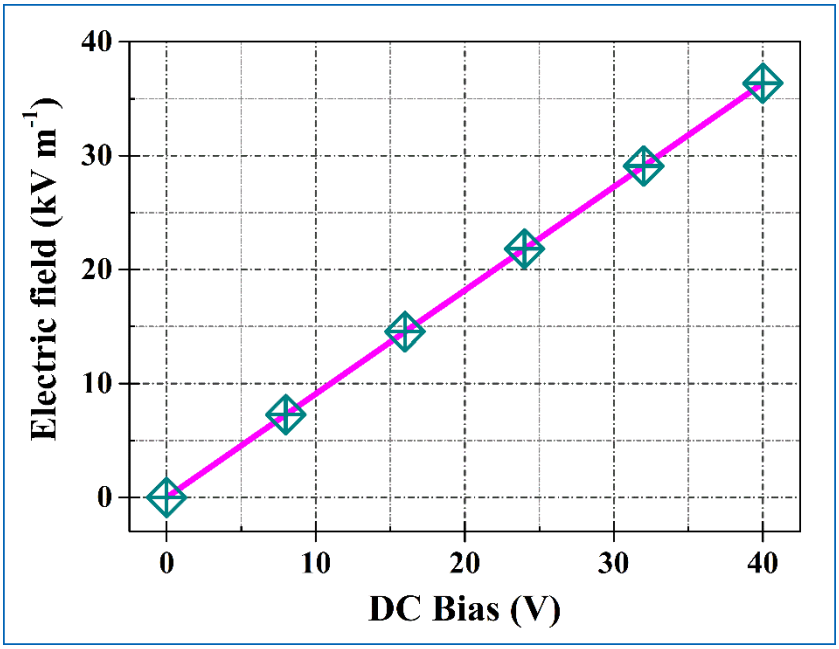

Figure 7.1 Calibration-curve for the applied electric field $[E = V/d]$ from external DC bias. Field-range: 0 – 36.36 kV m^{-1} against bias-range: 0 – 40 V.

Micro-Raman spectra were recorded in a WITec alpha300 RS confocal spectrometer under backscattering configuration, using a solid-state monochromatic (532.3 nm) Nd:YAG laser (beam-diameter 1 μm; laser-power 1 mW), 50X Zeiss achromatic objective (1800 grooves/mm holographic grating) and Peltier cooled charge coupled device (CCD). Five 15 s spectral acquisitions were averaged to compute the final spectrum (integration-time $= 15 \times 5 = 75$ s) against minimal background noise. Diffuse reflectance spectra (DRS) were captured in a Shimadzu UV 3600 UV-Vis-NIR ($200 - 2200$ nm) spectrophotometer using commercial $BaSO_4$ powder as the non-absorbing reflectance standard. All dielectric parameters were obtained from an Agilent 4294A precision impedance analyzer using 40 Hz–20 MHz input waveforms of amplitude 0.5 V under varying DC bias up-to 40 V. For convenient numerical values, bias is specified in volts throughout the chapter, although the calibration-curve of the calculated electric field in kV m^{-1} is provided in Figure 7.1.

7.2.4 Computational details for DFT-based calculations

Vienna *ab-initio* simulation package (VASP) with a plane wave basis set is used for density functional theory (DFT)-based calculations, implementing projector augmented wave (PAW) potentials. The electron exchange-correlation interaction is incorporated by applying Perdew-Burke-Ernzerhof (PBE) functional within the generalized gradient approach (GGA). The kinetic energy cut-off during all calculations is set to 600 eV and the structural relaxations are carried out until the total energy drops below 10^{-8} eV/Å. The Brillouin zone is sampled by using appropriate Γ-centered K mesh for different structures, see Table 7.1.

Table 7.1 K-mesh used for different unit cells in the DFT-based calculations

Calculations	$CaTiO_3$ ($Pbnm$)	$SrTiO_3$ ($Pm\bar{3}m$)	$BaTiO_3$ ($Pm\bar{3}m$)	$BaTiO_3$ ($P4mm$)
Effect of electric field on (110) plane	$5 \times 5 \times 1$	$6 \times 4 \times 1$	$6 \times 4 \times 1$	$6 \times 4 \times 1$
Static dielectric tensor evaluation	$7 \times 7 \times 5$	$6 \times 6 \times 6$	$6 \times 6 \times 6$	$8 \times 8 \times 6$

7.2.5 Finite element electrostatic simulations (FEES)

FEES were further conducted using the ANSYS Maxwell software to demonstrate the anisotropic build-up of electric field/flux in the GC–GB heterostructure. A miniaturized 3D model of $4 \times 4 \times 3$ semiconducting nano-cores dispersed in the grain boundary host is thus constructed and sandwiched between silver electrodes, implementing experimentally extracted electrical parameters to physically decipher the effect of unidirectional field on the nanoscopic architecture of the compounds. The dimensions are adapted as per the actual capacitive assembly in accordance to the FESEM micrographs.

7.3 Results and discussion

7.3.1 X-ray diffraction and Rietveld analysis

All Bragg peaks obtained in the XRD patterns (Figure 7.2) of the respective samples are matched with ICSD PDF cards: 01-088-0790 (CT, orthorhombic, $Pbnm$), 01-073-0661 (ST, cubic, $Pm\bar{3}m$), and 01-079-2263 (BT, cubic, $Pm\bar{3}m$), respectively. From calcium to barium compound; shift of the most intense peak to a smaller angle can be detected clearly, that suggests a gradually expanding interplanar spacing. Absence of additional peaks or deviations in the first two samples (CT and ST) confirm purity of phase. However, for BT nanoparticles, implications of a secondary tetragonal phase ($P4mm$) are found. It is well-known that, for ceramic BT samples having μm-order dimension, purely tetragonal (ferroelectric) structure survives. But, for nanoparticles, the cubic (paraelectric) phase becomes thermodynamically more stable, that may stimulate formation of mixed phase.[16]

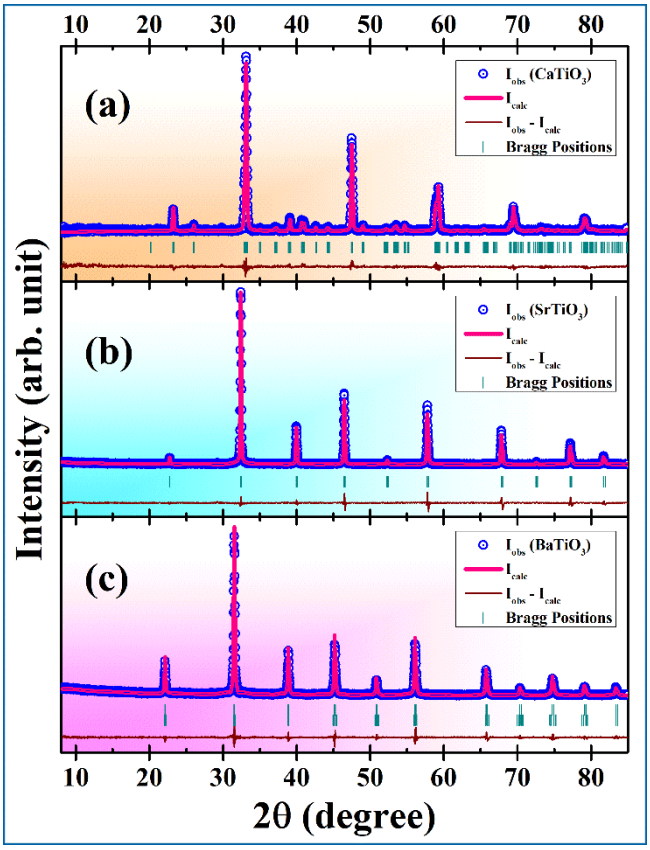

Figure 7.2 Observed (open blue circles) and refined (pink curve) powder XRD pattern for (a) CT, (b) ST and (c) BT nanoparticles. The green vertical bars represent corresponding Bragg peaks and the maroon line indicates the difference of the experimental diffraction traces to the calculated best fit.

The corresponding crystallite-sizes (D_{cryst}) are determined from the Scherrer's equation:

$$D_{cryst} = \frac{K\lambda}{\beta \cos\theta} \cong \frac{0.89\lambda}{\beta \cos\theta}. \quad (7.1)$$

Here K is a dimensionless constant, that depends on the geometry or shape of the particles, λ is the wavelength of the incident X-ray $(= 1.5406\ \text{Å})$, and β represents the FWHM of the Bragg-

peaks. Based on the five most intense peaks, mean crystallite-sizes are calculated to be 43.5, 59.2 and 48.1 nm for the respective samples. The FESEM micrographs are shown in Figure 7.3, that exhibit quite larger particles of grain size: 80-100 nm, compared to the crystallite-sizes; suggesting a polycrystalline growth. The nanoparticles develop a near-spherical morphology with moderate agglomeration as a result of high temperature sintering. The agglomeration increases more after palletization.

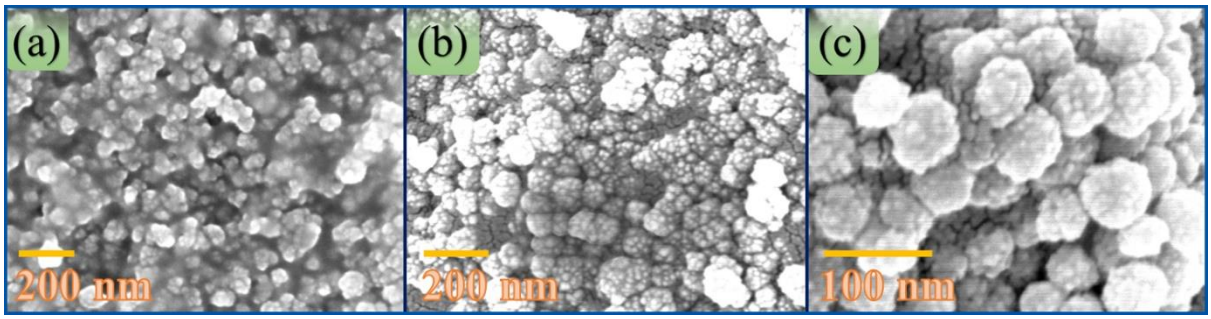

Figure 7.3 FESEM images of (a) $CaTiO_3$, (b) $SrTiO_3$, and (c) $BaTiO_3$ nanoparticles. A near-spherical morphology is detected. However, high-temperature synthesis has caused agglomeration.

Starting from the standard crystallographic information files (CIFs), the crystalline structures are refined according to the Rietveld's method deploying the FULLPROF software. A pseudo-Voigt line-profile function is considered in order to compute lattice parameters, scale factor, micro-strain, atomic positions, occupancy, isotropic thermal parameters *etc.*, see Figure 7.2 and Table 7.2. Results for CT, ST and BT nanoparticles are provided in Figure 7.2(a-c). Observed diffraction traces are shown by open blue circles, while the refined pattern is indicated by the pink curve. The green vertical bars show the positions of corresponding Bragg peaks and the maroon line represents the difference between the observed and calculated intensities *i.e.*, $(I_{obs} - I_{calc})$. Nominal internal strain in all three samples is noted, that accords use of Scherrer's formula. The consolidated parameters provided in Table 7.2 testify fine crystallinity and stoichiometry for all three samples; against a competent (< 2) goodness of fit: $\chi^2 = \left(R_{wp}/R_{exp}\right)^2$; where R_{wp} and R_{exp} are the weighted and expected profile residual factors. The quality of refinement can be verified from the following values *viz.*, CT: $R_{wp} = 3.51\%, R_{exp} = 3.43\%, \chi^2 = 1.05$; ST: $R_{wp} = 4.32\%, R_{exp} = 3.07\%, \chi^2 = 1.98$; BT: $R_{wp} = 3.97\%, R_{exp} = 2.89\%, \chi^2 = 1.89$. Although CT is purely orthorhombic and ST is purely cubic, the crystalline conformation in BT indicates a 68: 32 phase-ratio between cubic and tetragonal growth. The as-refined unit cells of the three compounds (including a mixed phase) are extracted from FULLPROF program and processed in the VESTA software to display the final crystal structures, see Figure 7.4.

Table 7.2 Rietveld analysis of XRD data: refined crystallographic parameters

Sample (Space group)	Lattice Parameters*	Strain (η %)	Atoms	Wyckoff sites	x	y	z	Occupancy	χ^2
$CaTiO_3$ ($Pbnm$)	$a = 5.3866(7)$ Å; $b = 5.4421(9)$ Å; $c = 7.6453(6)$ Å; $V = 224.125(9)$ Å^3	0.46	Ca	4c	-0.00910	0.03393	0.25000	0.500	1.05
			Ti	4b	0.00000	0.50000	0.00000	0.500	
			O1	4c	0.07108	0.47848	0.25000	0.500	
			O2	8d	0.70911	0.28952	0.03700	1.000	
$SrTiO_3$ ($Pm\bar{3}m$)	$a = b = c =$ 3.9067(0) Å; $V = 59.625(2)$ Å^3	0.63	Sr	1b	0.50000	0.50000	0.50000	1.000	1.98
			Ti	1a	0.00000	0.00000	0.00000	0.977	
			O	3d	0.50000	0.00000	0.00000	1.049	
$BaTiO_3$ ($Pm\bar{3}m$) [~68%]	$a = b = c =$ 4.0130(7) Å; $V = 64.249(4)$ Å^3	0.19	Ba	1b	0.50000	0.50000	0.50000	1.000	1.89
			Ti	1a	0.00000	0.00000	0.00000	0.974	
			O	3d	0.50000	0.00000	0.00000	1.073	
$BaTiO_3$ ($P4mm$) [~32%]	$a = b =$ 3.9999(0) Å; $c = 4.0170(0)$ Å; $V = 64.268(8)$ Å^3	0.15	Ba	1a	0.00000	0.00000	0.00000	0.961	
			Ti	1b	0.50000	0.50000	0.58388	1.409	
			O1	1b	0.50000	0.50000	0.06857	1.416	
			O2	2c	0.50000	0.00000	0.58299	1.928	

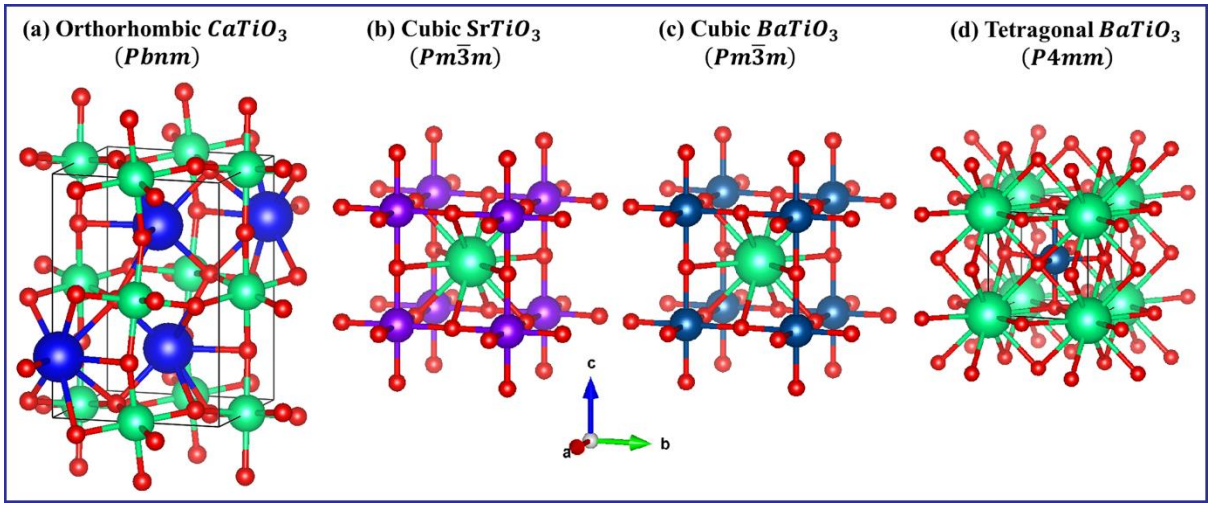

Figure 7.4 Refined crystal structure of the as-obtained phases: unit cells of (a) orthorhombic CT; (b) cubic ST; (c) cubic BT and (d) tetragonal BT. The red, green and different shades of blue-coloured balls represent oxygen, titanium and alkaline-earth metal atoms, respectively.

7.3.2 Stoichiometric assessment from energy dispersive X-ray (EDX) spectra

EDX spectra were acquired for the perovskite nanoparticles (check Figure 7.5), that demonstrate clear peaks of no elements other than the alkaline earths, titanium and oxygen. The peaks of the cations are closely spaced, but easy to resolve. To verify the elemental stoichiometry of the samples, weight and atomic %ages are determined from the spectra and

provided in Table 7.3. For all three compounds, the atomic ratio is very close to 1: 1: 3, that confirms the composition.

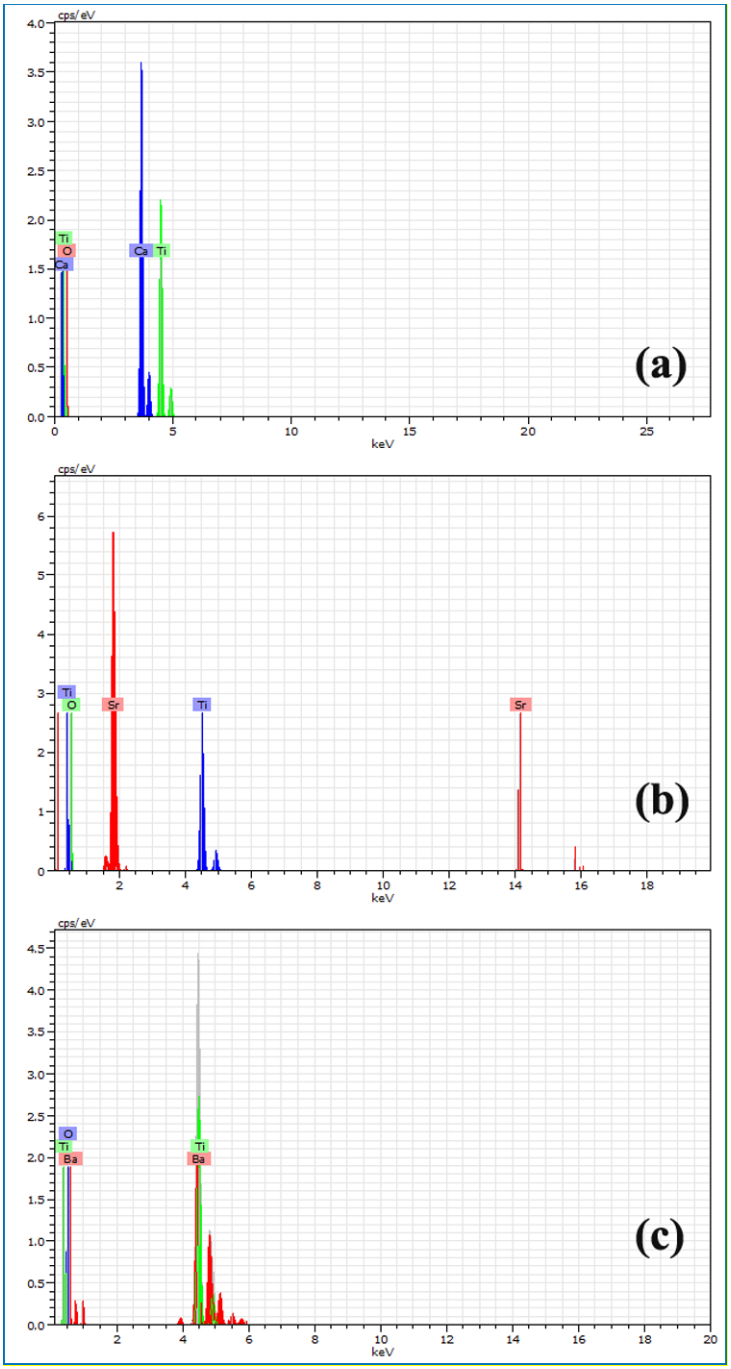

Figure 7.5 EDX spectra for (a) CT, (b) ST and (c) BT nanoparticles.

Table 7.3 Elemental weight and atomic proportions determined from EDX spectra

Elements	$CaTiO_3$		$SrTiO_3$		$BaTiO_3$	
	Wt (%)	Atom (%)	Wt (%)	Atom (%)	Wt (%)	Atom (%)
A (Ca/Sr/Ba)	31.21	21.20	48.19	20.25	55.82	18.02
Ti	33.77	19.20	25.78	19.83	21.91	20.29
O	35.02	59.60	26.03	59.92	22.27	61.69

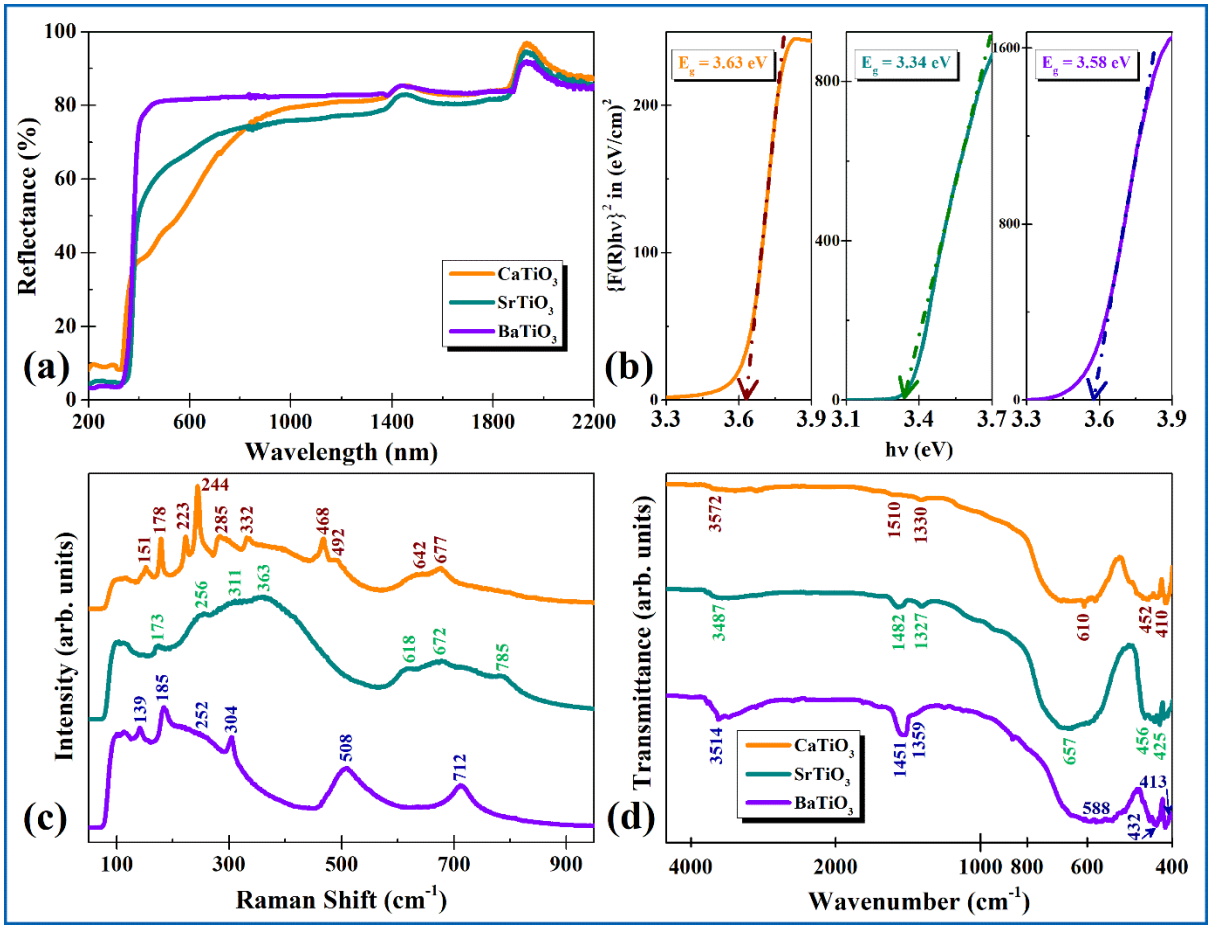

Figure 7.6 (a) Diffused reflectance spectra; (b) Tauc's plots and determination of optical bandgaps (E_g), employing Kubelka-Munk function $\{F(R)\}$; (c) Raman spectra and (d) FTIR transmittance spectra for CT (orange), ST (green) and BT (violet) nanoparticles.

7.3.3 DRS and bandgap evaluation

All three samples attain low reflectance and therefore strong absorption characteristics over $200-400$ nm incident radiation (UV), see Figure 7.6(a). For longer wavelengths, they reflect a vast majority of the incident intensity consistently, that indicates a wide gap band-structure. Conventionally the allowed, direct optical bandgap (E_g) is calculated from the Tauc's equation:

$$(\alpha h\nu)^2 = A_0(h\nu - E_g). \tag{7.2}$$

Here, h is the Planck's constant, ν is the excitation frequency and A_0 is the band tailing parameter, related to the probability of optical transitions between particular filled and vacant states. For non-transparent samples, rather than absorption spectroscopy, the absorption coefficient (α) is estimated using the following function as per Kubelka-Munk theory:

$$F(R) = \frac{k_m}{s} = \frac{(1-R)^2}{2R}, \tag{7.3}$$

where, R is the diffuse reflectance, $k_m \approx (1-R)^2$ is the molar absorption coefficient and $s \approx 2R$ is called the scattering factor. At the absorption band-edge, the extrapolated $(\alpha h\nu)^2$ vs $h\nu$ straight line estimates the bandgap: $E_g = h\nu|_{\alpha=0}$, see Figure 7.6(b). The as-determined bandgaps for calcium, strontium and barium titanate are 3.63, 3.34 and 3.58 eV, respectively.[12]

7.3.4 Raman and FTIR spectra: study of lattice vibrations

The finger-print modes of molecular vibration are further characterized via FTIR and Raman spectroscopy to confirm the phase-coordination from phonon dynamics. Considering the refined space groups, factor group analysis is conducted using VIBRATE software as per the selection rules at the Brillouin zone-center for all four phases. The irreducible modes of vibration and the IR/rotation/Raman active or optically silent modes are thereby enlisted in Table 7.4. The Raman modes in $ATiO_3$ perovskites often represent B-site disorder and loss of translation/inversion symmetries.[37]

Table 7.4 Irreducible representations: IR/rotation/Raman active and optically silent modes for different space-group or phases

	$CaTiO_3$ ($Pbnm$)	**$SrTiO_3$ & $BaTiO_3$ ($Pm\bar{3}m$)**	**$BaTiO_3$ ($P4mm$)**
Irreducible representations (Mulliken notation)	$\Gamma_{red} = 7A_g + 7B_{1g} + 5B_{2g} + 5B_{3g} + 8A_u + 8B_{1u} + 10B_{2u} + 10B_{3u}$	$\Gamma_{red} = 4T_{1u} + T_{2u}$	$\Gamma_{red} = 3A_1 + 3E$
IR active - acoustic modes (translations)	B_{1u}, B_{1u}, B_{3u}	T_{1u}	A_1, E
Rotations	B_{1g}, B_{2g}, B_{3g}	Nil	E
Raman active	$A_g, B_{1g}, B_{2g}, B_{3g}$	Nil	A_1, E
Optically silent modes	A_u	T_{2u}	Nil

As shown in Figure 7.6(c), the orthorhombic CT phase gives rise to a number of peaks at 151, 178, 223, 244, 285, 332, 468, 492, 642, and 677 cm^{-1}, that conform previous reports.[6,37] The peaks at 151 and 178 cm^{-1} are caused by the motion of A-site ions, while the peaks in the region 223-332 cm^{-1} are related to the tilting or rotations of $[TiO_6]$-$[TiO_6]$ clusters. The band observed at 642 cm^{-1} is assigned to the Ti–O symmetric stretching vibration, whereas the peaks at 468 and 492 cm^{-1} are attributed to Ti–O torsional modes, associated to the bending or internal vibration of the oxygen cage. In both the cubic phases, first order Raman scattering is completely forbidden, as mentioned in Table 7.4. For ST, two broad humps are recorded at $200-500$ and $600-800$ cm^{-1} with particular local surges.[19] They are actually indicative of second order Raman scattering, characteristic of cubic ST phase.[4] On the other hand, for BT the subsidiary tetragonal phase having a lower symmetry is strongly Raman active owing to critical changes in the selection rule and generates a number of Raman modes at

$139\ (A_1), 185\ (E), 252\ (A_1), 304\ (E - TO_3/LO_2), 508\ (A_1 - TO_3)$ & $712\ (A_1 - LO_3 + E - LO_4)$ cm^{-1}.[38,39]

FTIR spectra are displayed in Figure 7.6(d) for all three samples, which show near-similar features.[11] Strong signatures of stretching/bending vibrations of A–O and Ti–O bonds were detected along with some minute signals that describe stretching of hydroxyl groups and H–O–H bending on account of nominally adsorbed moisture at the outer surface-usual for perovskite nanoparticles. The transmittance dips are assigned in Table 7.5 with corresponding intensity levels.

Table 7.5 FTIR analysis: active modes and their assignment to particular lattice vibrations

Wavenumber (cm^{-1})			Intensity	Associated lattice vibrations
$CaTiO_3$	$SrTiO_3$	$BaTiO_3$		
410	425	413	Moderate	A–O interactions (Tetrahedral for Ca and octahedral for Sr/Ba)
452	456	432	Strong	Ti–O–Ti bending in TiO_6 octahedron
610	657	588	Strong	Ti–O stretching inside TiO_6 octahedron (broad/diffused peak)
1330	1327	1359	Weak	O–H deformation in H_2O
1510	1482	1451	Weak	H–O–H bending of adsorbed moisture
3572	3487	3514	Weak	O–H stretching

7.3.5 Ab-initio forecast from DFT

To demonstrate the effect of external electric field on the respective structures, the (110) Bragg plane is selected and a vacuum layer of 20 Å is inserted in the z-direction to avoid mutual interactions between the planes. A 0.5 eV/Å field is applied along the positive z-direction in the cell *i.e.*, perpendicular to the (110) plane. The displacement of the charge cloud pertaining the unipolar field is depicted in Figure 7.7. Such separated, diffused and delocalized charge-cloud will produce distorted relaxation kinematics for obvious reasons, that has been investigated experimentally.

The Born effective charge (Z^*) and static dielectric tensor are computed by using density functional perturbation theory (DFPT) as implemented in VASP code. The static dielectric constant (ε_∞) considering electronic contributions are found to be (i) CT: $\varepsilon_{xx} = 6.56, \varepsilon_{yy} = 6.65, \varepsilon_{zz} = 6.57$; (ii) ST: $\varepsilon_{xx} = \varepsilon_{yy} = \varepsilon_{zz} = 6.69$; (iii) BT (cubic): $\varepsilon_{xx} = \varepsilon_{yy} = \varepsilon_{zz} = 7.93$; and (iv) BT (tetrahedral): $\varepsilon_{xx} = \varepsilon_{yy} = 6.95, \varepsilon_{zz} = 6.21$, where $\forall \varepsilon_{ij} = 0$ if $i \neq j$. The Born effective charge (Z^*) relates polarization to atomic displacement *i.e.*, the change in polarization induced by periodic displacement in absence of external field. It is determined by the following relation:

$$Z^*_{\tau,ij} = \frac{\Omega_0}{e}\left(\frac{\delta P_i}{\delta u_{\tau,j}}\right)\Big|_{E=0}. \tag{7.4}$$

Here Ω_0 is the volume of the unit cell, δP_i is the change of polarisation in the i-direction, $\delta u_{\tau,j}$ is the displacement of τ^{th} atom along the j-direction and e is the electronic charge. Axe was first to propose an estimation of Z^* for ABO_3 series experimentally. It has been observed that the amplitude of Z^* deviates from static ionic charges. In our materials, Z^* of Ti and one component for O are quite larger than their static charges (+4 for Ti and -2 for O), which basically represent the mixed ionic and covalent character of the Ti-O bond.

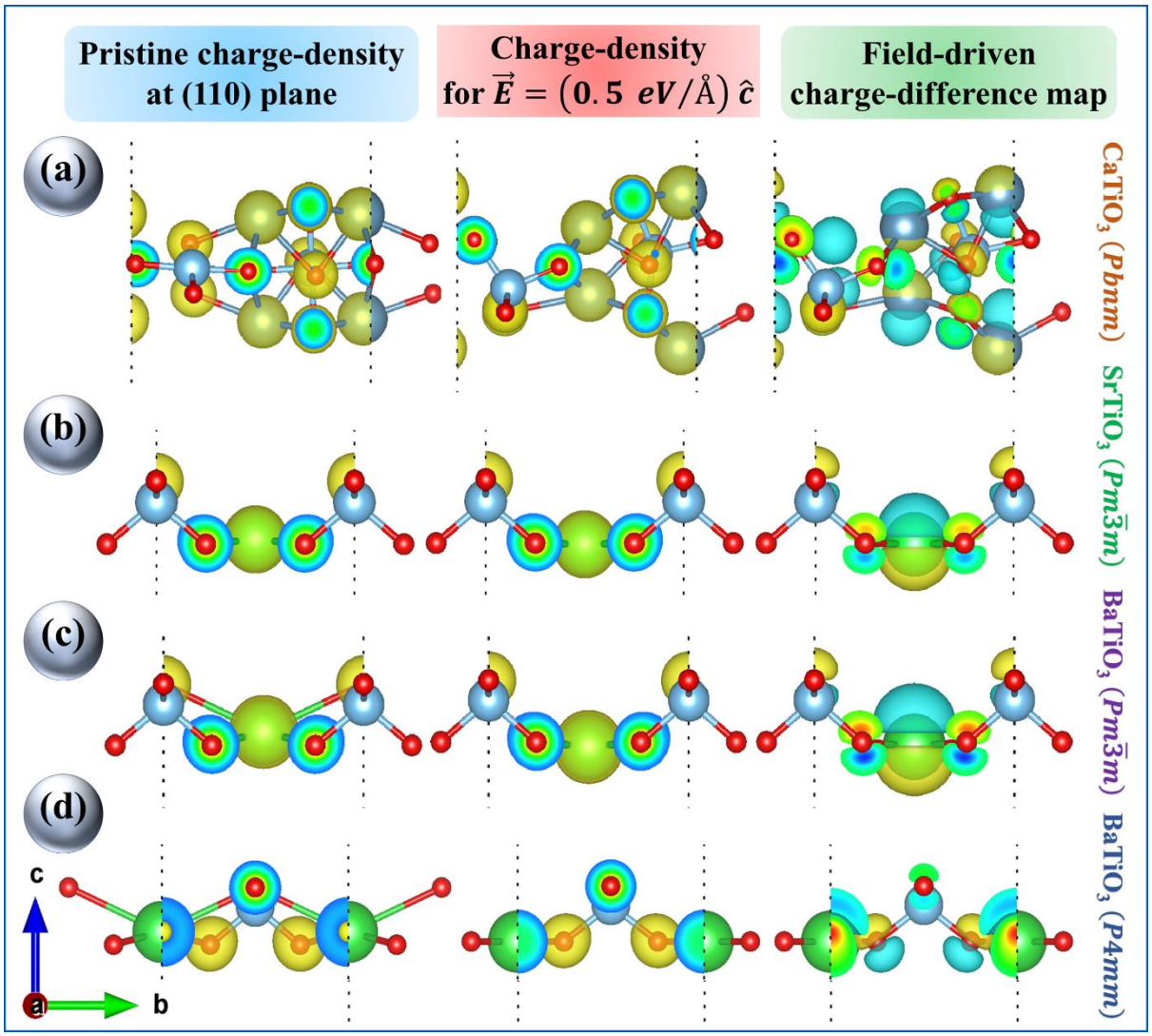

Figure 7.7 Charge-density map at (110) Bragg plane of the pristine compound (left column), under 0.5 eV/Å external electric field along c-direction (middle column) and associated charge-difference (right column) shown for (a) orthorhombic CT; (b) cubic ST; (c) cubic BT and (d) tetragonal BT. The yellow and cyan colours respectively indicate positive and negative charge accumulation under bias field.

7.3.6 Impedance and dielectric spectroscopy

Dielectric analysis involves qualitative and quantitative study of induced polarization; developed due to shifting of atoms, ions and thereby +ve/-ve charge-centers under an external static or alternating electric field. If the excitation frequency approaches the characteristic or natural frequency of the constituent oscillators, resonance occurs. Whereas relaxation takes on temporizing to overcome the electrical inertia. Frequency dispersive resonance and relaxation along with impedance spectra introspect the very nature of the constituents with distinct electrical attributes such as space-charge effects, interfacial polarization, inhomogeneous grain core/boundary structures *etc*. Complex impedance can be presented as,

$$\hat{Z} = |Z|e^{j\theta} = Z' + jZ'', j = \sqrt{-1}. \tag{7.5}$$

Here, $|Z|$ is the magnitudes of impedance, θ is the corresponding phase, Z' & Z'' are the gross resistance and reactance. The real part of complex permittivity (estimates the energy storage capability) can be calculated using the capacitance dispersion as, $\varepsilon' = Cd/\epsilon_0 A$, where C represents the capacitance of the MIM pellet of width d and effective electrode area A, $\epsilon_0 = 8.854 \times 10^{-12}$ F m^{-1} is the permittivity of free space. The dissipation factor (D) or dielectric loss-tangent emphasizes the relaxation loss due to the phase-lag of the oscillating dipoles, in reference to the input waveform, given by the following ratios:

$$D = \tan\delta = \frac{Z'}{Z''} = \frac{G}{B} = \frac{\varepsilon''}{\varepsilon'} = \frac{M''}{M'} = \frac{1}{Q_u}. \tag{7.6}$$

The terms G, B, M' & M'' respectively represent the real and imaginary parts of complex admittance and dielectric modulus (discussed in section 7.3.7 and 7.3.8); and Q_u is called the quality factor. The imaginary dielectric constant (a measure of thermal dissipation) is calculated from,

$$\varepsilon'' = \varepsilon' \tan\delta = \frac{Cd}{\epsilon_0 A}\tan\delta. \tag{7.7}$$

The frequency dispersions of the as-discussed parameters are demonstrated in Figure 7.8, 7.9 and 7.10 for all three samples under varying applied bias. The rapid and monotonic decay in lower frequencies is consistent with Koop's phenomenological theory,[40] which ultimately settles down to a quasi-constant high frequency limit under dominant electronic and atomic contributions. Below the kHz-order frequencies, the induced (dielectrics) or spontaneous (ferroelectrics) dipoles easily follow the input AC sweeps. The in-phase response allows the system to get fully polarized and develops a large dielectric constant or associated parameters. But, synchronising with the driving signal gets increasingly difficult at higher frequencies (especially for orientational polarization) *i.e.*, the input field gets reversed, before the polarization is built. The resulting delay exhibits nominal polarization and manifests the sharp decay in the dispersions, resembling the very nature of MWIP. Semiconducting grains

offer idealistic dielectric features, while properties of insulating grain boundaries are influenced by traps, dislocations and defects. Due to the dominance of grain boundaries at lower frequencies, electrons require greater energy for hopping, that substantiates the high dielectric loss.[41]

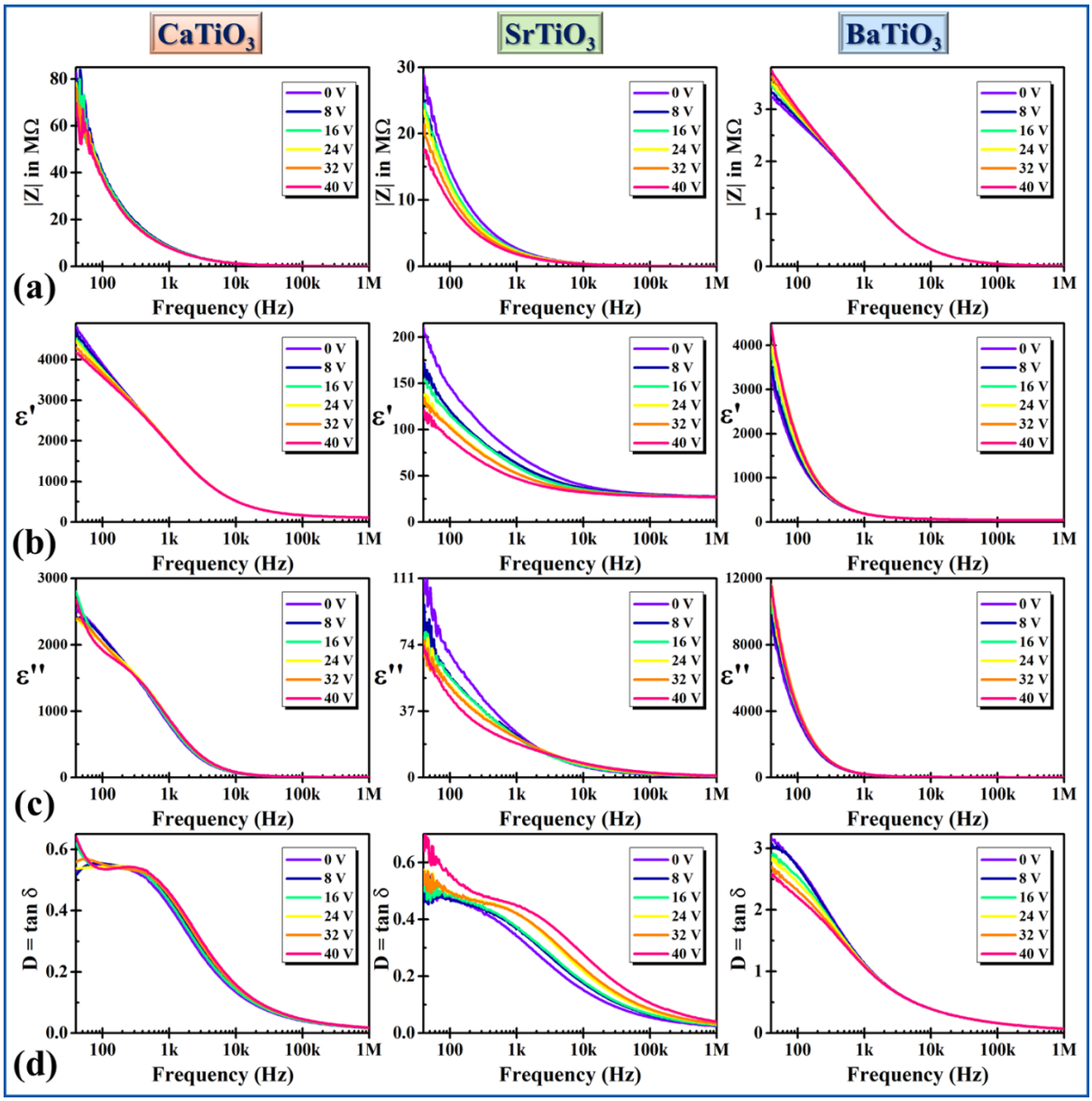

Figure 7.8 Bias-dependent frequency-dispersions: (a) magnitude of impedance ($|Z|$); (b) real part of dielectric constant (ε'); (c) imaginary part of dielectric constant (ε''); (d) dissipation or loss-factor ($D = \tan\delta$). The three columns respectively demonstrate data for CT, ST and BT. All following figures sustain this mode of presentation.

For all the dispersions, the low-frequency MWIP-dominated regime is immensely field-dependent. However, with frequency dielectric parameters gradually become reluctant to the applied field, because the dipoles vibrate so fast that the applied (moderate) field fails to align

them effectively in the appropriate direction. Having a smaller resistivity than CT, ST exhibits significantly greater sensitivity to similar applied bias. The variations of phase-angle are typically associated with the state of polarization. In both these samples, drop in $|Z|, Z'$ & R_s under increasing field is obvious. The equivalent series resistance or ESR (R_s) stipulates the net effect of unipolar field on the GC-GB assembly. This nature indicates, the release of space charges in addition to a reduction in barrier height and surge in AC conductivity.

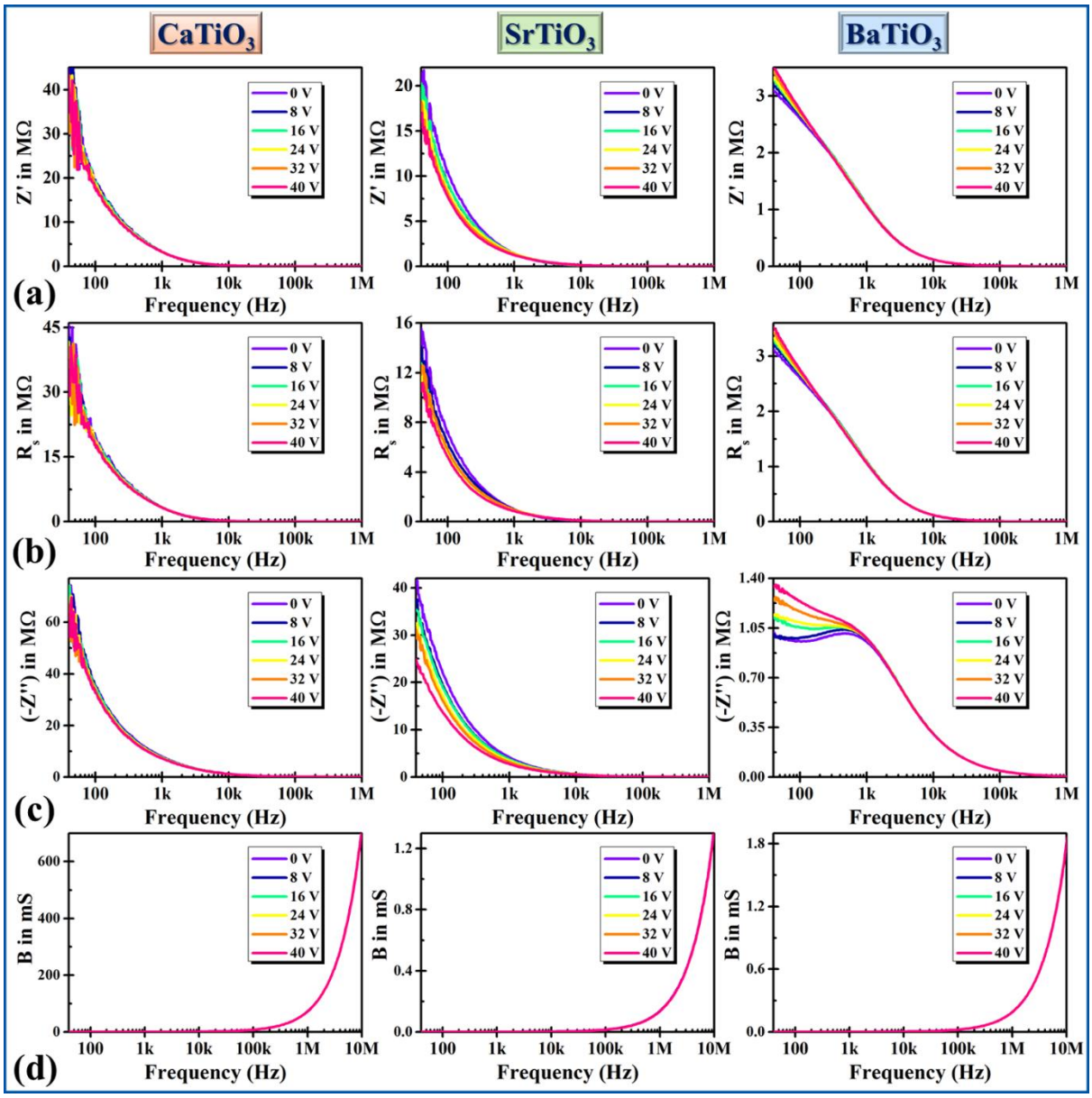

Figure 7.9 Bias-dependent frequency-dispersions: (a) real part of complex impedance (Z'); (b) equivalent series resistance or ESR (R_s); (c) negative reactance ($-Z''$); (d) susceptance (B). The three columns respectively demonstrate data for calcium, strontium and barium titanate.

Contrarily, BT displays an opposite bias-dependency in reference to CT or ST. This is because of the ferroelectric phase, which although accommodates a lesser compositional

fraction, is indeed much more electrically active than the paraelectric counterpart. The external static field builds up polarization in BT, which overshadows other responses and empowers the contribution of bound charges and resistive features. The magnitude of Z'' typically accompanies relaxation peaks at frequencies that match the hopping frequency of localized electrons. For CT and ST, the trend of data implies that, the peaks are located at very small frequencies (beyond our operating range), while the peak for BT rests near 1 kHz, which undergoes additional broadening for larger bias.

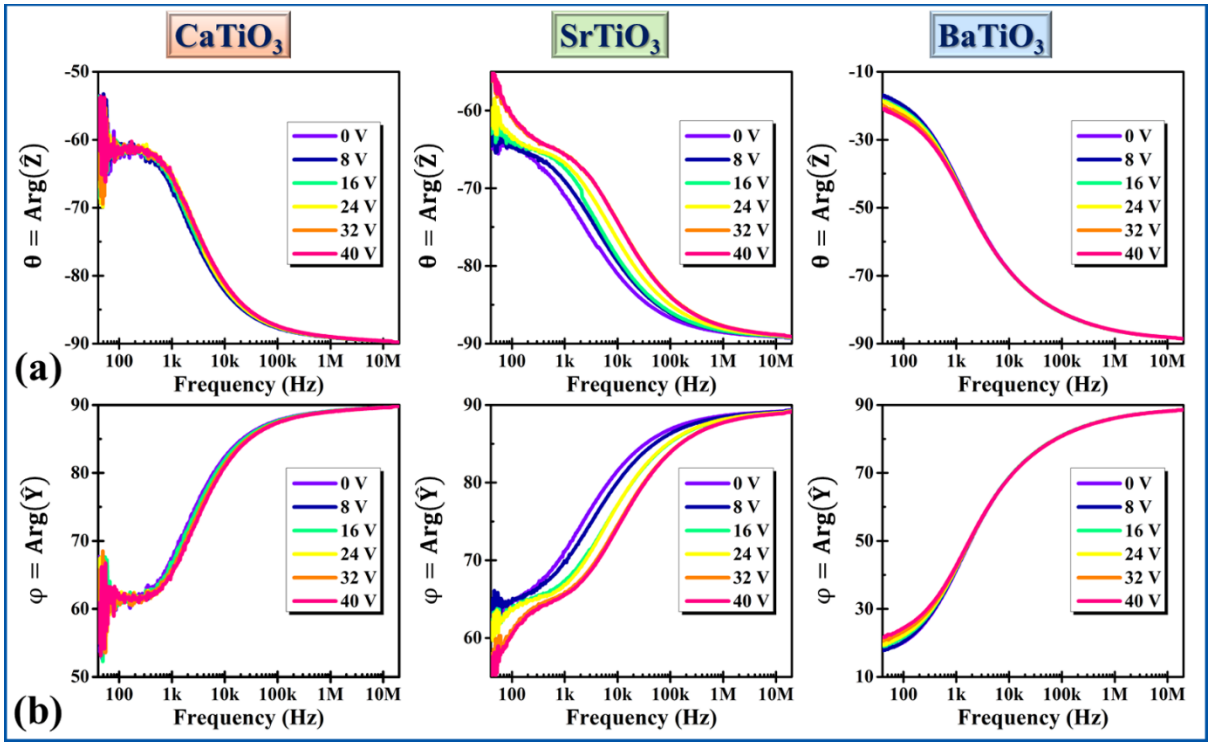

Figure 7.10 Bias-dependent frequency-dispersive phase-angles of (a) complex impedance and (b) complex admittance.

Both the dispersions of ε' & ε'' decreases with bias for CT and ST *i.e.*, the net energy storage and dissipation falls, which in turn mildly increase the loss-tangent. However, BT presents an exact opposite trend, as surface-polarization boosts up electric potential energy. For polar dielectrics, the phenomenological Johnson relation is a reasonable approximation for the bias-dependent dielectric constant:

$$\varepsilon'(E) = \frac{\varepsilon'(0)}{[1 + \lambda\{\epsilon_0\varepsilon'(0)\}^3E^2]^{1/3}}. \tag{7.8}$$

Here, λ is a temperature-dependent parameter, and $\lambda\{\epsilon_0\varepsilon'(0)\}^3E^2 < 1$ for most practical cases.[33,34] So, this nonlinear relationship behaves linearly for small to moderate range of fields, see Figure 7.11(a).

$$\frac{d\varepsilon'(E)}{dE} = -\frac{2}{3}\frac{\lambda\epsilon_0^3\{\varepsilon'(0)\}^4E}{[1 + \lambda\{\epsilon_0\varepsilon'(0)\}^3E^2]^{4/3}}. \tag{7.9}$$

The slope is negative and proportional to the applied electric field in small E limit. ST obviously offers steeper fitted lines than CT. However, if multiple polarization mechanisms superpose or condensation of polar clusters prevails, this empirical model or the simplified LGD theory fails to cumulatively explain the $\varepsilon'(E)$ behaviour. The dielectric constant is observed to increase with bias for multifaceted polarization in BT, in accordance with the smaller dissipation factor, that shows the more ordered dipolar conformation. It is especially useful in nanoelectronics, where dielectric tunability is essential against a reduced dissipation.

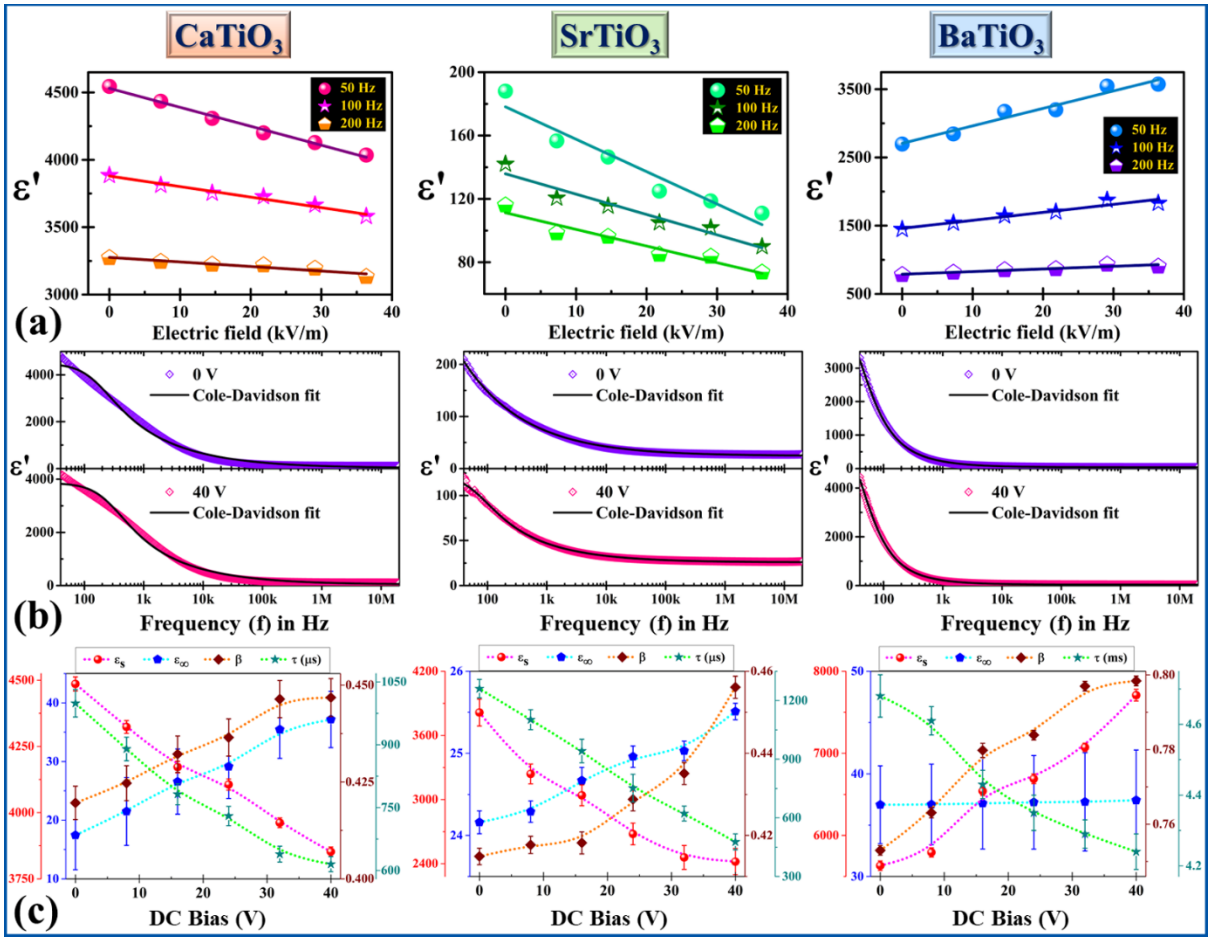

Figure 7.11 (a) Linear fits of field-dependent ε' at 50, 100 and 200 Hz input frequency; (b) Cole-Davidson model-based fitting for $\varepsilon'(f)$ dispersion under application of 0 and 40 V bias; (c) bias-dependency of the parameters, extracted from best fit: ε_s (red), ε_∞ (blue), β (maroon) and τ (green). The dotted lines are guide to the eye.

Molecular dipoles and their relaxation dynamics can be introspected using different models. The oldest is the Debye relaxation theory, that ascertains the dielectric response of an ensemble of ideal and non-interacting dipoles as a function of the excitation (angular) frequency: $\omega = 2\pi f$, f being the linear frequency (in Hz).

$$\hat{\varepsilon}(\omega) = \varepsilon_\infty + \frac{\Delta\epsilon}{1+j\omega\tau} = \left(\varepsilon_\infty + \frac{\Delta\epsilon}{1+\omega^2\tau^2}\right) - j\left(\frac{\omega\tau\Delta\epsilon}{1+\omega^2\tau^2}\right) = \varepsilon' - j\varepsilon'', \tag{7.10}$$

where, $\Delta\epsilon = \varepsilon_s - \varepsilon_\infty$ is the dielectric strength *i.e.*, the difference of saturated and high-frequency limits and τ is the relaxation time *i.e.*, the time taken by the oscillating dipoles to align themselves in the direction of the external field or the restoration time to establish equilibrium after the field is withdrawn. However, feasible interactions take place among the adjacent dipoles or with the environment in all practical cases that accompany a distribution of relaxation times and thus asymmetrically broadened loss-peaks.[42] A shape-parameter: β ($0 \leq \beta \leq 1$) is introduced in the relaxation equations of Cole-Davidson model to account such disparities:

$$\hat{\varepsilon}(\omega) = \varepsilon_\infty + \frac{\varepsilon_s - \varepsilon_\infty}{(1 + j\omega\tau)^\beta}. \tag{7.11}$$

For $\beta = 1$, Debye's form having a single relaxation time is reobtained. Substituting, $\phi = \tan^{-1}\omega\tau$ and $1 + j\omega\tau = e^{j\phi}\sqrt{1+\omega^2\tau^2} = e^{j\phi}/\cos\phi$; the simplified ε' turns up as:

$$\varepsilon'(\omega) = \varepsilon_\infty + (\varepsilon_s - \varepsilon_\infty)(\cos\phi)^\beta \cos\beta\phi. \tag{7.12}$$

The dispersions of the real dielectric constant are thus fitted for different bias using Cole-Davidson model, see Figure 7.11(b). All the extracted parameters ($\varepsilon_s, \varepsilon_\infty, \beta$ & τ) are plotted in Figure 7.11(c) as a function of bias voltage. For all three samples, τ decreases with bias, while β is seen to increase. As the steady field increases, the electric potential energy of the conjugated charge-ensemble also increases. Therefore, all relaxation mechanisms speed up resulting a monotonic increase in τ. Moreover, the steady unipolar field orients the dipoles more uniformly, which enables them to relax archetypically. So, the Debye model attains more relevance and the proper fraction β approaches unity. Now for CT and ST, ε_s decreases as prescribed by the Johnson relation, while a small but steady enhancement in ε_∞ is found. This indicates, at higher frequencies, a positive correlation persists between permittivity and external field. However, for BT, such correlation is very weak and ε_∞ remains almost bias-independent. Contrarily, ε_s monotonically increases with bias voltage for the induced polarization in agreement with the results of Figure 7.11(a). Ferroelectric nature of the tetragonal phase of BT is further verified from the $P - E$ hysteresis loops at two different field-strengths, as shown in Figure 7.12(a). The loops do not resemble ideal ferroelectric features, because the sample contains a preponderant paraelectric phase with no hysteretic property.[43] The respective remanent polarizations for the two strengths are 0.17 and 0.32 μC cm^{-2}.

The transport properties, resistivity correlations and grain core/boundary structure can be retrospectively probed by analysing Nyquist plots. Such a core-boundary constitution can be modelled with an equivalent circuit;[30,35] employing two pairs of resistors (R) and constant phase-elements (Q) as shown in Figure 7.12(b). As two distinct electrical entities *viz.*, grains and grain boundaries contribute to the dielectric properties, and the grains have significantly smaller resistivity offering greater contribution in the transport than the grain boundaries, the

attributes of the grains and grain boundaries are represented by (R_g, Q_g) & (R_{gb}, Q_{gb}). Furthermore, as grains are embedded in the grain boundary matrix, one $R-Q$ sub-network is inscribed within the other to construct such an interlinked circuit-model that renders the system physically. The capacitance (C) corresponding to an element (R, Q) can be computed given the distributing factor (α) that stands for the deviation from a pure capacitor as a result of non-Debye relaxations and asymmetric broadening.

$$C = R^{\frac{1-\alpha}{\alpha}} Q^{\frac{1}{\alpha}}. \tag{7.13}$$

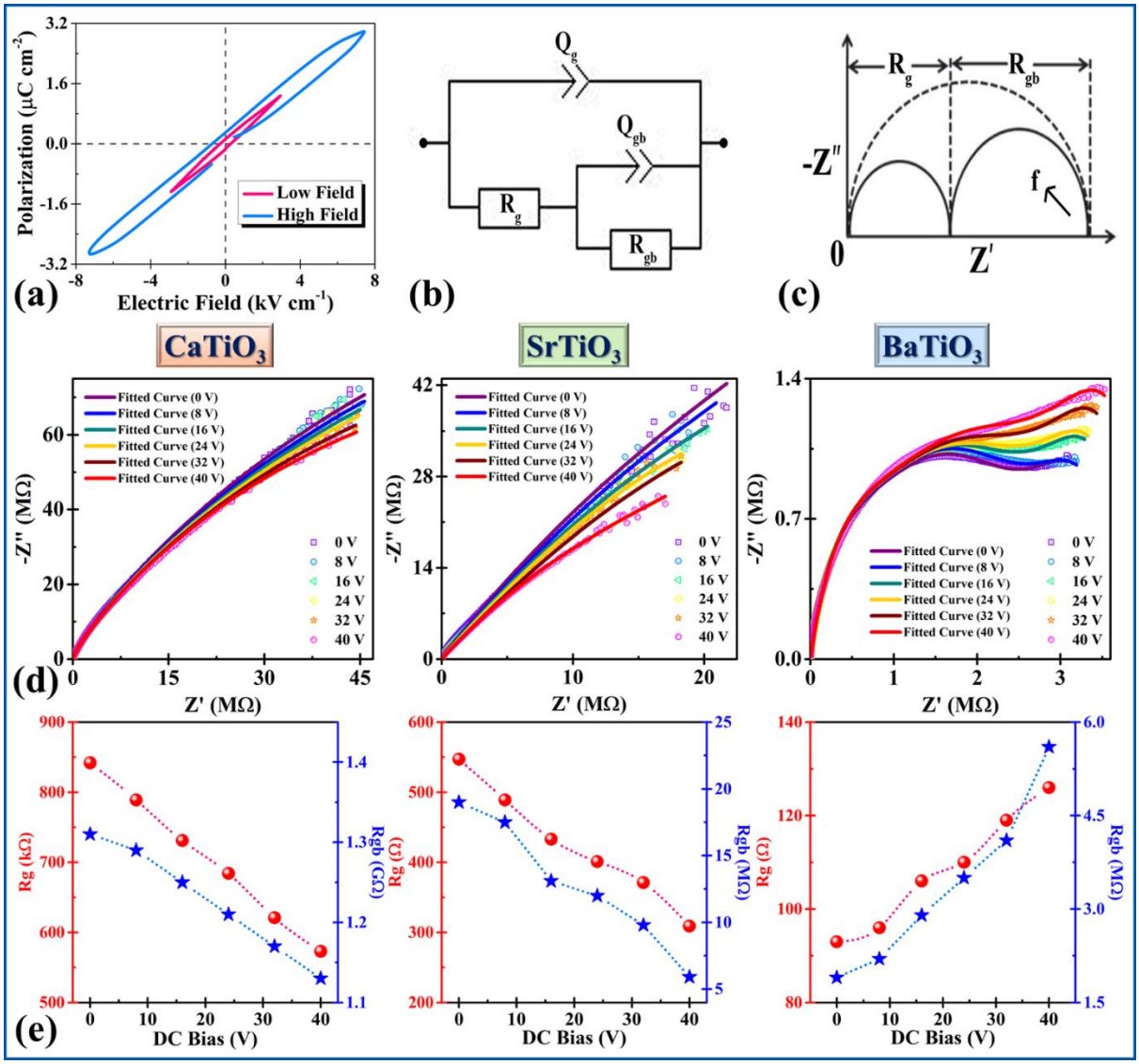

Figure 7.12 (a) $P-E$ hysteresis loops for BT under a low and a high field cycle; (b) schematic of the as-deployed equivalent circuit-model, comprising two pairs of resistors and constant phase-elements; (c) theoretical prediction of Nyquist plots from this model; (d) experimentally obtained Nyquist plots under distinct field conditions; (e) variation of R_g and R_{gb} (extracted from the fitted curves) as a function of external bias. The dotted lines are guide to the eye.

Generally, space charge effects or MWIP occurs when mobile carriers get impeded by a physical barrier *i.e.*, the grain boundary, which notably inhibits charge migration.[18,44] Subsequently, charges pile up to produce a localized polarization at the GC-GB interface. The expression for complex impedance in this formalism takes the from:

$$\hat{Z}(\omega) = \frac{R_{gb} + R_g\{1 + (j\omega)^{\alpha_{gb}} Q_{gb} R_{gb}\}}{1 + (j\omega)^{\alpha_{gb}} Q_{gb} R_{gb} + (j\omega)^{\alpha_g} Q_g [R_{gb} + R_g\{1 + (j\omega)^{\alpha_{gb}} Q_{gb} R_{gb}\}]}. \quad (7.14)$$

This model circuit simulates a Nyquist curve comprising two semi-circular arcs like Figure 7.12(c), that outlines each pair of $R - Q$ subsystems enduring Debye relaxations. But if the electrically active regions are not well-resolved or offer close credentials, the couple of semi-circles superpose and develop a single distorted semi-ellipse, that assents the Cole-Davidson model.[45]

The Nyquist plots are thus fitted against this circuit-model for various applied fields employing the EC-Lab software; ensuring satisfactory least-squares goodness of fit (< 0.1), see Figure 7.12(d). For BT, two distinct semi-circles can be recognised. The non-requirement of external elements to fit the experimental data reflects absence of any appreciable electrode polarization effect. The low frequency regime is field-sensitive and manifests MWIP involving domain wall motion.[30] However, the high frequency bias-independent region can be ascribed to phonon-assisted electron hopping at the adiabatic limit. The extracted resistances R_g & R_{gb} are plotted as a function of bias voltage in Figure 7.12(e). Typically, ceramic oxides accommodate point-defects *e.g.*, vacancies and traps. As the applied field increases, the charge-carriers trapped in such potential wells acquire electrostatic energy and eventually extricate. Subsequently, ESR drops against a smaller bound to free carrier ratio. For the pure dielectric CT/ST phases, the grain core and boundary resistances thus decrease with bias. However, BT having a ferroelectric phase delivers a countereffect, where the polarization pursuit led by bound charges predominate. Hence, the system gets more resistive with increase in bias that agrees with the dispersions of $|Z|$ & R_s.

7.3.7 Admittance spectroscopy

Achieving ideal Ohmic contacts between metal-semiconductor junction is very difficult; due to formation of insulating layers, interfacial roughness or gaps, oxidation *etc*. Hence extracted parameters from impedance and dielectric spectra are never completely devoid of error, as the unmasked low frequency declining slope is focussed. Admittance spectroscopy is a convenient tool to explore high frequency conduction mechanisms, free from electrode polarization effects. Complex admittance can be mathematically conveyed as:

$$\hat{Y} = \frac{1}{\hat{Z}} = |Y| e^{j\varphi} = G + jB = G + j\omega C, \quad (7.15)$$

where, $|Y|, \varphi, G$ & B represent the magnitude of admittance, associated phase, real (conductance) and imaginary (susceptance) parts, respectively. In Figure 7.13(a,b), parameters dominate in higher frequencies as described in Rezlescue model.[46] At lower frequencies, conductance remains insignificant and almost constant, but as the characteristic 'hopping frequency' is approached, dispersion takes place.

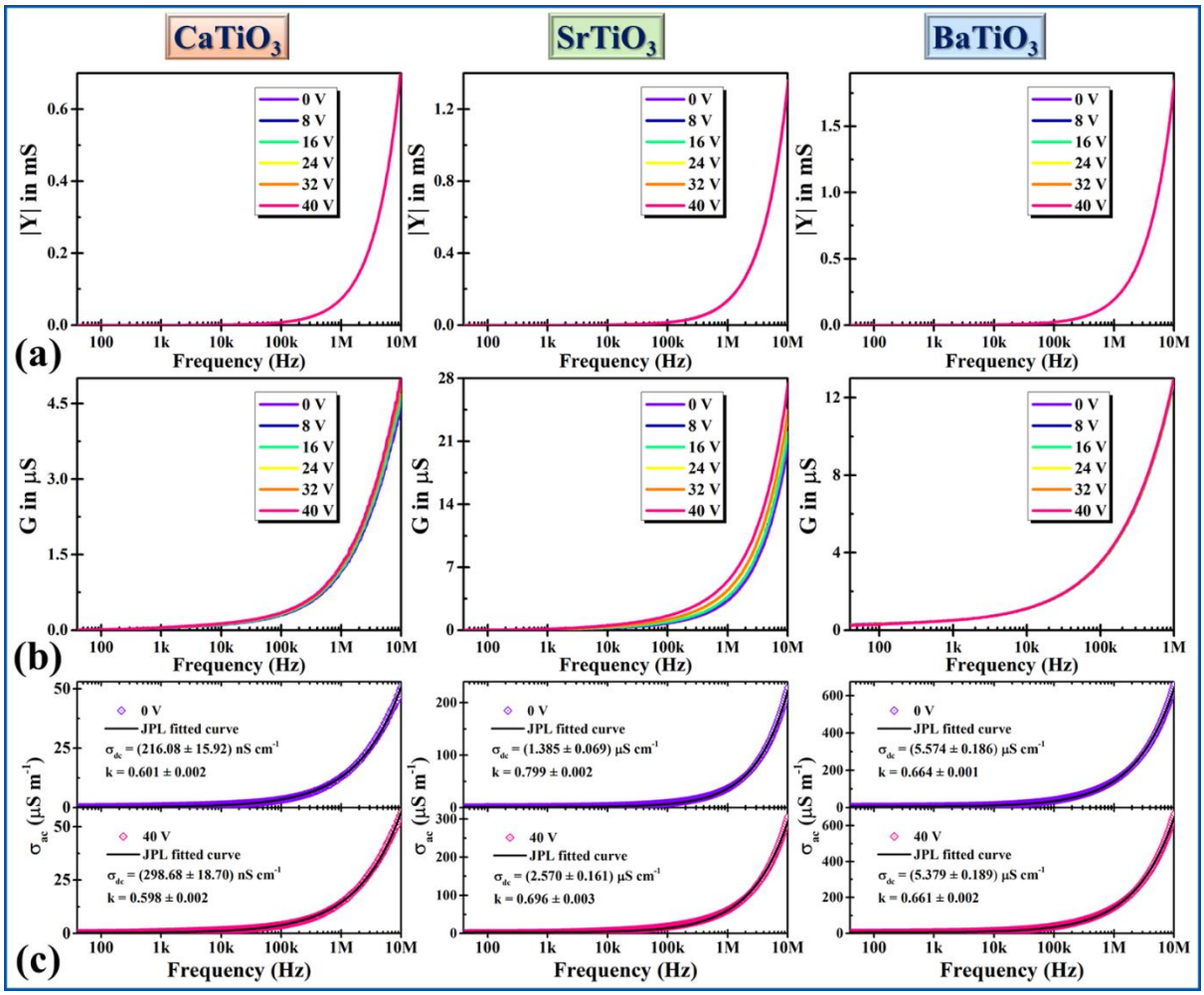

Figure 7.13 Bias-dependent frequency-dispersions: (a) magnitude of admittance ($|Y|$); (b) conductance (G); (c) Jonscher's power law (JPL) fitting of ac conductivity (σ_{ac}) at nil and 40 V applied bias.

Application of bias has very mildly increased $|Y|$ & G, and lowered B nominally for the first two samples. The field-assisted growth in carrier-density is likely responsible for this. For BT, however the trend is exactly opposite for the aforementioned reasons. Here the dispersions do not get influenced by the deep traps, as the corresponding release rates ($\ll 1\ s^{-1}$) are rejected in the operational frequency-regime. Under applied field, $3d$ electrons can hop from Ti^{3+} to Ti^{4+} ions in the family of titanates and vice versa. This multiple valency of transition metal

ions is often coupled with oxygen vacancies.[18,47] Using Kröger–Vink notation, their dynamics can be summarized as:

$$O_O^{\times} \leftrightarrow V_O^{\times} + \frac{1}{2}O_2(\uparrow)$$

$$V_O^{\times} \leftrightarrow V_O^{\bullet} + e' \leftrightarrow V_O^{\bullet\bullet} + 2e'$$

$$Ti^{4+} + e' \leftrightarrow Ti^{3+}$$

Hence, the arrangement of ions in the crystal largely controls the electron hopping mechanism and the mobility of carriers. Such mechanisms generally operate over a certain cryogenic temperature, below which all vacancy defects are 'frozen-in'.[18] At room-temperature, a significant fraction of the trapped carriers gets thermally activated and takes part in hopping and diffusion.[48] They even condense to form polar clusters, as it is energetically favorable to aggregate into clusters to reduce distortion energy.

Now, the nature of mobile carriers can be further examined by studying AC conductivity:

$$\sigma_{ac} = \varepsilon_0 \varepsilon"\omega = \varepsilon_0(\varepsilon' \tan\delta)\omega = \frac{Gd}{A}. \tag{7.16}$$

Frequency-dependence of σ_{ac} can be described by the well-known Jonscher's power law (JPL).[49]

$$\sigma_{ac}(f) = \sigma_{dc} + \sigma_0 f^n, \tag{7.17}$$

where, σ_{dc} stands for the extrapolated DC conductivity, σ_0 is a weighting constant related to the polarizability strength and n is the frequency-exponent. The first term indicates excitation of some electrons to the conduction band from a localised state and their drift mobility, while the second one represents dielectric relaxation of bound or localized charges. All these parameters depend not only on the material, but also on external field and temperature.[30,41] The exponent entails the degree of interaction between charge-carriers and the surrounding lattice. Identification of different conduction-mechanisms in semiconductors *e.g.*, correlated barrier and variable range hopping, overlapped polaron tunnelling, quantum tunnelling *etc* is based on the field and temperature dependency of n. Figure 7.13(c) displays fitting of conductivity dispersions (0 & 40 V) using JPL, and the extracted parameters are enumerated in Table 7.6.

Table 7.6 Extracted parameters from JPL fitting of frequency-dispersive conductivity

DC Bias	CT		ST		BT	
(V)	σ_{dc} (nS cm^{-1})	n	σ_{dc} (µS cm^{-1})	n	σ_{dc} (µS cm^{-1})	n
0	216.08 ± 15.92	0.601 ± 0.002	1.385 ± 0.069	0.799 ± 0.002	5.574 ± 0.186	0.664 ± 0.001
8	236.58 ± 13.11	0.601 ± 0.001	1.461 ± 0.085	0.781 ± 0.002	5.560 ± 0.153	0.664 ± 0.002
16	243.98 ± 16.00	0.600 ± 0.001	1.651 ± 0.182	0.759 ± 0.003	5.513 ± 0.154	0.664 ± 0.002
24	261.23 ± 10.16	0.599 ± 0.002	1.893 ± 0.099	0.747 ± 0.003	5.468 ± 0.205	0.663 ± 0.001
32	284.51 ± 14.12	0.598 ± 0.002	2.111 ± 0.121	0.713 ± 0.003	5.412 ± 0.201	0.662 ± 0.002
40	298.68 ± 18.70	0.598 ± 0.002	2.570 ± 0.161	0.696 ± 0.003	5.379 ± 0.189	0.661 ± 0.002

For CT and ST, DC conductivity rises with external field, while BT shows an opposite trend due to the enlarged polarisation and insubstantial delocalization of carriers. However, for all three materials, the exponent has decreased monotonically with bias. Such values of n (≤ 1) are indicative of concurrent translational and hopping dynamics of charge-carriers, according to Funke.[50,51] In his jump relaxation model (JRM), it was proposed that, the ions can make successful hops to vacant neighbouring sites for low frequency due to availability of sufficient time intervals. This gives rise to a long-range translational motion of ions, devoted to σ_{dc}. Contrarily, both successful and unsuccessful hopping take place in the high frequency regime. The jumping ions can either jump back to the initial site, or may jump to a new position for a stable relaxation. The former is considered unsuccessful, while the latter is designated as a successful hop. In the high frequency end, the ratio of successful and failed hops increases, leading to a dispersive conductivity.

For CT and ST, the respective correlated barrier hopping (CBH) and variable range hopping (VRH) model more precisely explains the exact features of conduction mechanism.[18,52,53] Here, large polaron hopping is considered responsible for the conduction, where two polarons hop over the potential barrier simultaneously between charged trap/defect states and $n(T)$ varies as:

$$n = 1 - \frac{6k_BT}{W_m + k_BT\ln(\omega\tau_0)}, \tag{7.18}$$

where, W_m is the binding energy of the carrier and k_B is the Boltzmann constant. The synergism of hopping electrons and ionized oxygen vacancies generate polaronic relaxations and evinces as-obtained field-dependency of σ_{dc} & n. Large polarons can polarize more neighbouring sites than small polarons and propagate with greater effective mass. The increase in n with bias supports that. In this model, Coulombic interactions correlate the barrier height with the inter-site separation.

7.3.8 Modulus spectroscopy

Finally, the complex electric modulus $(\widehat{\mathrm{M}})$ is studied in order to analyze the unwinding of the electric field through the space charge distribution against a fixed dielectric displacement. Macedo proposed this technique to suppress all low-frequency electrode effects completely and compute relaxation parameters of the medium seamlessly.[41,54] Considering the dielectric constant as an electrical analogue of mechanical shear modulus, $\widehat{\mathrm{M}}$ is defined by,

$$\widehat{\mathrm{M}} = \frac{1}{\hat{\varepsilon}} = \frac{1}{\varepsilon_\infty}\left[1 - \int_0^\infty e^{-j\omega t}\left\{\frac{d\psi(t)}{dt}\right\}dt\right] = \left(\frac{\varepsilon'}{\varepsilon'^2 + \varepsilon''^2}\right) - j\left(\frac{\varepsilon''}{\varepsilon'^2 + \varepsilon''^2}\right) = M' - jM'', \tag{7.19}$$

where, the function $\psi(t) = \psi(0)e^{-(t/\tau_0)^\eta}$ outlines time-evolution of the electric field inside dielectrics. The stretched exponent η is a proper fraction and τ_0 is the associated relaxation

time. The frequency-dispersive real (M') and imaginary (M'') parts are shown in Figure 7.14 for different bias-fields. M' has some inclusive features: (a) it has a nominal value in the low-frequency regime, (b) as the frequency elevates, the dispersion approaches an asymptotic maximum: $M_\infty = 1/\varepsilon_\infty$, (c) the sigmoidal nature is related to the carrier-mobility over a long range against the as-neglected electrode polarization, (d) the effect of applied field is hard to detect, instead for ST, where a small, but steady hike in M' is found.

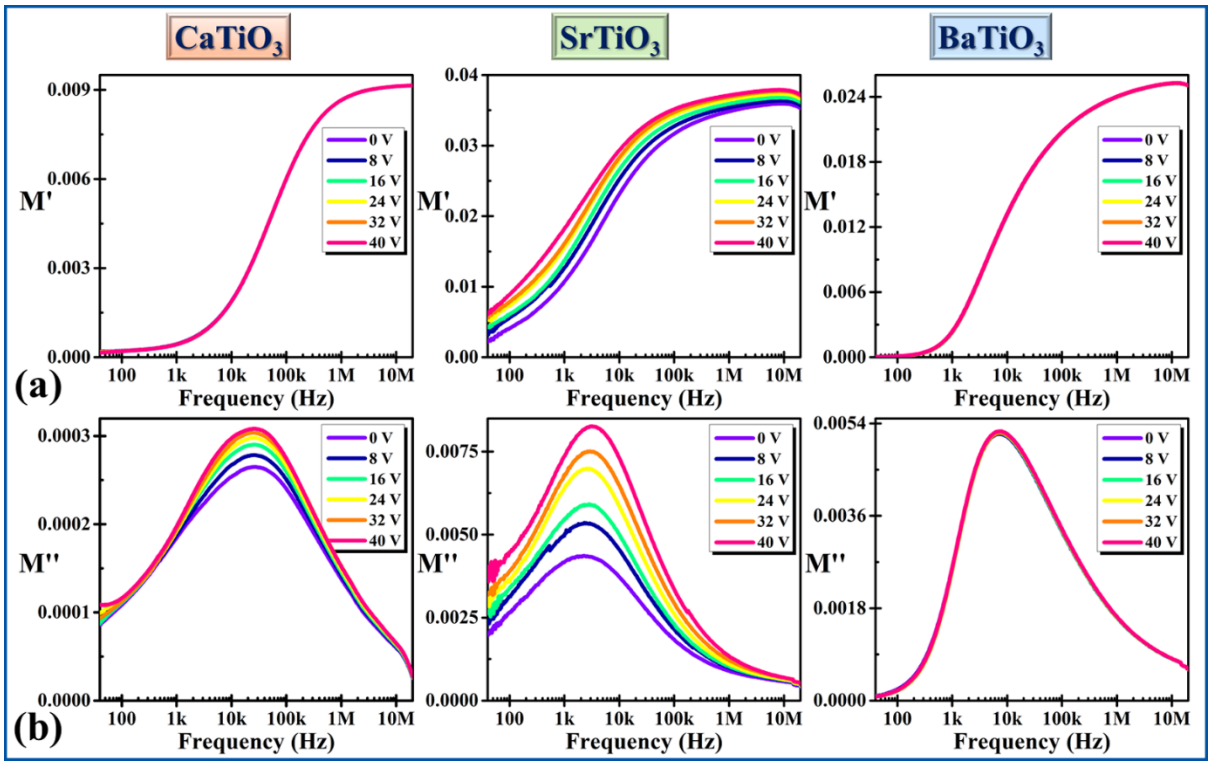

Figure 7.14 Bias-dependence of (a) real and (b) imaginary part of frequency-dispersive dielectric modulus $(\tilde{M})$.

$M''(f)$ on the other hand, exhibits a distinct and broad peak across few kHz to few tens of kHz order with perceptible bias-dependency. This is the frequency regime, where carrier-hopping in between neighbouring sites and/or carrier-motion restricted within the short range of potential wells contend over longer distances. For all three samples, the bands rise and shift towards higher frequencies with increase in applied field, although the effect is nominal for BT. As mentioned earlier, non-Debye relaxation causes asymmetric broadening of the bands, that can be further scrutinized using the modified Kohlrausch–Williams–Watts (KWW) function:

$$M''(f) = \frac{M''_{max}}{\left(\frac{1-c}{a+b}\right)\left\{b\left(\frac{f_{max}}{f}\right)^{a} + a\left(\frac{f}{f_{max}}\right)^{b}\right\} + c}. \tag{7.20}$$

Here two independent shape-parameters: a & b are used to describe the low and high frequency regime, along with a smoothing parameter (c) regarding a generalized susceptibility function,

as proposed by Bergman.[55] All $M''(f)$ dispersions are thus fitted using this model to compute a, b, c, f_{max} & M''_{max}. Fitted curves for the two extreme fields are shown in Figure 7.15(a). a, b & M''_{max} are enunciated in Table 7.7 for all samples, while the computed values of $c \approx 0$ ($< 10^{-10}$).

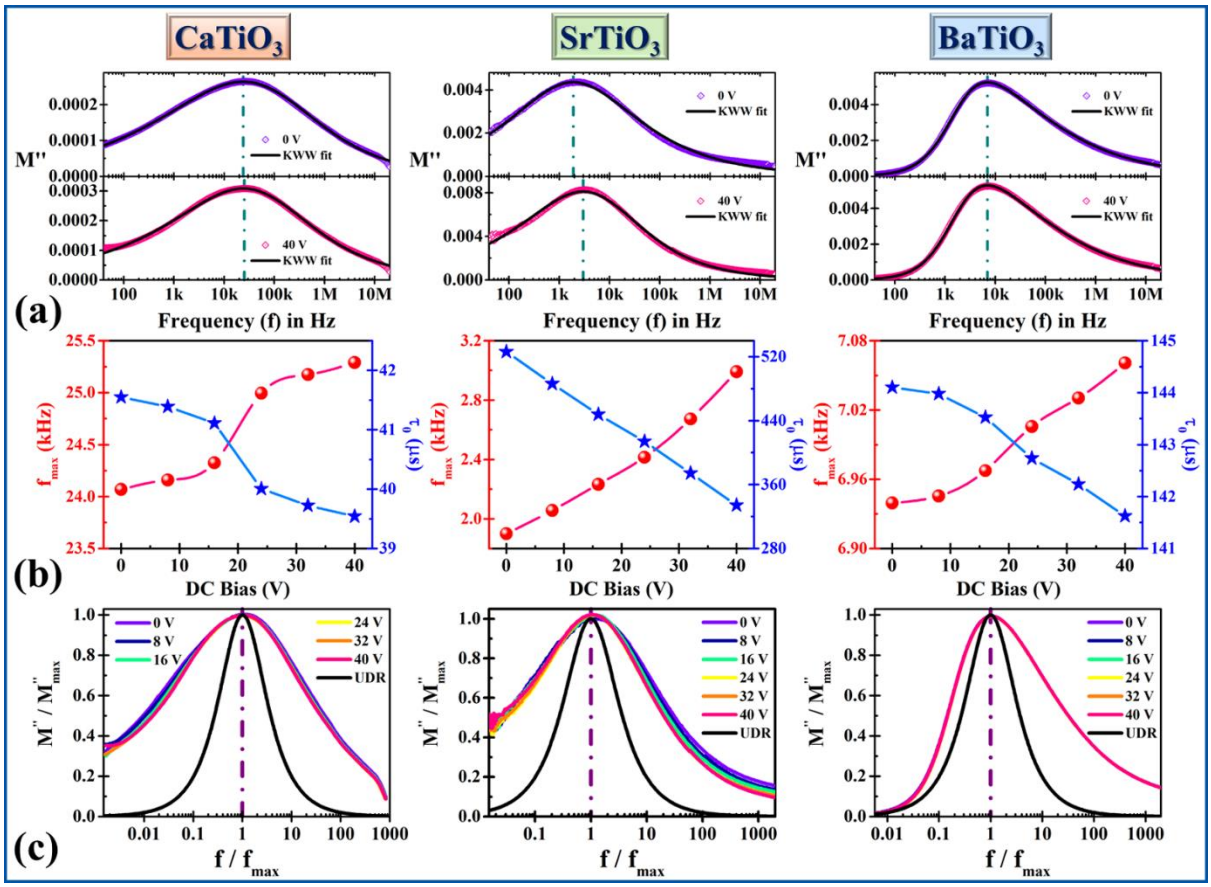

Figure 7.15 (a) Modified KWW fits for $M''(f)$ dispersion at nil and 40 V bias; (b) bias-dependency of as-obtained f_{max} & τ_0; (c) normalized imaginary electric modulus M''/M''_{max} versus f/f_{max} under varying fields in reference to the ideal Debye response (black curve).

Table 7.7 Extracted shape-parameters (a & b) and M''_{max} from modified KWW fitting of the imaginary part of frequency-dispersive electric modulus

DC Bias (V)	CT			ST			BT		
	a	b	$M''_{max} \times 10^4$	a	b	M''_{max}	a	b	M''_{max}
0	0.2184(4)	0.4079(0)	2.63(9)	0.3794(5)	0.3560(9)	0.0043(5)	1.2354(7)	0.3841(0)	0.0052(2)
8	0.2419(3)	0.4093(1)	2.77(9)	0.3930(0)	0.3868(6)	0.0052(9)	1.2487(8)	0.3842(6)	0.0052(4)
16	0.2520(3)	0.4183(3)	2.90(0)	0.4173(5)	0.4136(9)	0.0058(0)	1.2566(1)	0.3854(0)	0.0052(5)
24	0.2760(8)	0.4157(3)	2.97(1)	0.4320(3)	0.4376(2)	0.0068(5)	1.2600(6)	0.3864(1)	0.0052(7)
32	0.2840(6)	0.4181(0)	3.04(3)	0.4367(6)	0.4443(6)	0.0073(7)	1.2675(9)	0.3882(4)	0.0052(8)
40	0.3043(0)	0.4279(0)	3.08(5)	0.4471(9)	0.4695(3)	0.0080(9)	1.2746(0)	0.3884(4)	0.0052(9)

For calcium and strontium compounds, a & b are seen to increase with bias, that typically assists the ideal Debye-type properties. However, a tiny, but complex change was

recorded for BT. Here a (characterizes higher frequencies) deviates more from unity, while b (represents small frequencies) nominally increases with bias. This is because, with applied field, the dipoles reorient to mimic a more orderly structure, however the nonlinear (ferroelectric) characteristics get boosted. The characteristic relaxation time can be computed using $\tau_0 = 1/f_{max}$. Figure 7.15(b) demonstrates how f_{max} blue-shifts against bias, which eventually leads to a monotonic decrement in τ_0. It is important to emphasize that, this τ_0 is different from the τ elaborated in section 7.3.4 and Figure 7.11. The combination of dielectric, admittance and modulus spectroscopy is exceptionally powerful, because they characterize relaxation or conduction properties of distinct frequency regimes. While the first two respectively explain properties at the low and high frequency end, modulus spectra furnish information for the regime in between. The carrier dynamics and relaxation mechanisms too are distinct at different frequencies. Naturally τ_0 & τ belong to different order, although speculate similar trends against bias.

Finally, the normalized dispersion of the imaginary part $\left[\frac{M''(f)}{M''_{max}}\right]$ is plotted versus normalized frequency $\left(\frac{f}{f_{max}}\right)$ for the samples under all fields in Figure 7.15(c). The fact that, all curves nearly overlap on each other in the reduced form and can be scaled to a master curve, suggests that the fundamental dynamics of relaxation mechanism is identical under all fields.[41,53] Taking $a = b = 1$ and $c = 0$, the universal Debye response (UDR) is retrieved:

$$M''(f) = \frac{M''_{max}}{\frac{1}{2}\left(\frac{f_{max}}{f} + \frac{f}{f_{max}}\right)}. \tag{7.21}$$

In reference to UDR (FWHM = 1.144 dB), the asymmetric broadening can be clearly recognised. This FWHM has an inverse relationship with the coefficient η *i.e.*, the more the broadening, the more is the deviation of η from unity. For CT and ST, the broadening is dominated in the lower frequencies *i.e.*, the left-width is higher than the right-width in the peaks. But BT opts an opposite picture, where the curve has widened more at the high frequency side (results $a > 1$). This is speculated by the diffusive nature of the associated oscillators, that adversely respond to respective lower or higher energy excitations.

7.3.9 Electric field distribution from finite element simulation

The simulations are carried out based on a few rudimentary assumptions and propositions: (a) semiconducting grains are embedded in insulating grain boundary host and the GC-GB interface is sharply defined, (b) the distribution of grains in the dispersing medium is homogeneous and isotropic, (c) the nanocores are chosen to be spherical owing to the near-spherical morphology of our samples, (d) considering the fact that, crystallites in a polycrystalline nanoparticle polarize distinctly, the nanocore dimensions are set as per the

D_{cryst} values obtained from equation 7.1, and (e) a positive voltage is applied at the top electrode keeping the bottom electrode grounded to simulate field-conditions similar to the experimental setup, where a maximum of 40 V was applied across the sample-pellets.

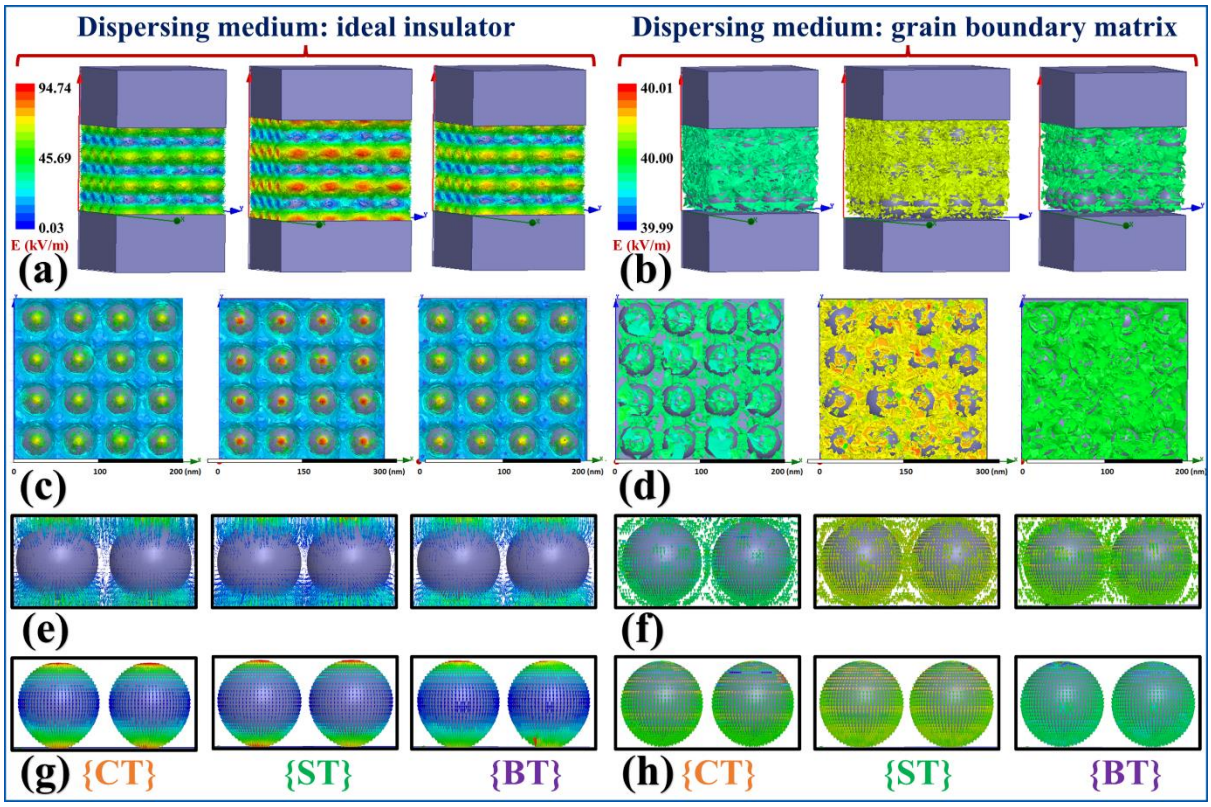

Figure 7.16 Electric field map in the GC-GB architecture depicted for the ideal insulator (left panel) and grain boundary material (right panel), serving as the dispersing medium for the three respective compounds. Magnitude of applied field: (a,b) side-view and (c,d) top-view. Magnified view for distribution of (e,f) electric field vectors outside the grains and (g,h) displacement vectors within the grains.

In theory grain boundaries are delineated as ideal insulators, however in practice they are somewhat congruent dielectric materials with much smaller conductivity due to defects and gaps. For each case, distribution of field-intensity and field/displacement vectors are illustrated in Figure 7.16. Some notable observations are: (i) in case of perfect insulator, large field-gradient is present in the vicinity of the GC-GB interface, while for the experimentally obtained grain boundary host a more uniform field-distribution can be found, (ii) the variation of electric flux is more pronounced for ST, which gradually reduces for BT and CT. This result is consistent with the experimentally realized sensitivity (ST>BT>CT) of different electrical parameters on DC bias, (iii) because of the finite conductivity of the grain boundary material, the penetration depth of the external field reduces that encompass a more realistic endeavor, (iv) for feasible GC-GB framework, the net polarization comprehends both components and interfacial

polarization develops, (v) owing to the high polarization of the grains the field-lines get weakly attracted towards them and get bent (anisotropy), (vi) the field vectors are more localized to the extreme ends (inhomogeneity) for the perfectly insulating hosts, (vii) the distribution of displacement vectors inside the grains contain their degree of polarization. So, even a homogeneous and isotropic grain distribution induces a non-uniform, anisotropic deviation at the microscopic level.[30]

7.4 Concluding remarks

Summarily, crystal structures of the as-synthesized nanoparticles were verified to be orthorhombic for CT, cubic for ST and a 68: 32 mixture of cubic and tetragonal phases for BT from Rietveld analysis. The field-dependent dielectric and impedance spectra were (a) fitted with Cole-Davidson model to understand the relaxation-dynamics and calculate relaxation times, (b) explained in the light of phenomenological Johnson relation, and (c) matched with an equivalent circuit-model that simulates Nyquist plots analogous to experimental data. The field-dependency of grain/grain-boundary resistance and associated IBLC were interpreted in accordance to MWIP and space-charge effects. Unlike CT/ST, the dielectric and ferroelectric phases in BT were seen to contest with each other, where the latter governed the outcomes and as-anticipated dielectric features were mostly suppressed. From admittance spectroscopy, the field-induced de-trapping of carriers and polaron hopping conduction were revealed. JPL-fits of Conductivity dispersions as a function of bias-voltage supported quantitative applicability of the CBH and VRH model. Finally, modulus spectra were used to characterize the non-Debye dipolar relaxations, where the subsequent variation of characteristic times, shape-parameters and asymmetric KWW broadening of $M''(f)$ peaks with bias were delineated. Theoretical results not only frame experimental background, but also establish microscopic inhomogeneity and electrical anisotropy in the GC-GB environs. A complete set of field-dependent dispersion analysis against a broad radio/audio range for this family of compounds thus offer a route-map to commendably customize diverse electrical properties in hybrid ceramics to achieve 'bane to boon' device-performance.

References

1. K.A. Müller, H. Burkard, Phys. Rev. B Condens. Mater. **19**(7), 3593 (1979)
2. L. Zhang, W. Zhong, Y. Wang, P. Zhang, Solid State Commun. **104**(5), 263-266 (1997)
3. R. Zheng, J. Wang, X. Tang, et al., J. Appl. Phys. **98**(8), 084108 (2005)
4. M. Vračar, A. Kuzmin, R. Merkle, et al., Phys. Rev. B Condens. Mater. **76**(17), 174107 (2007)
5. P. Victor, R. Ranjith, S. Krupanidhi, J. Appl. Phys. **94**(12), 7702-7709 (2003)
6. S. Qin, X. Wu, F. Seifert, A.I. Becerro, J. Chem. Soc., Dalton Trans. 19, 3751-3755 (2002)

7. T. Mitsui, W.B. Westphal, Phys. Rev. **124**(5), 1354 (1961)
8. L. Zhang, X. Wang, W. Yang, H. Liu, X. Yao, J. Appl. Phys. **104**(1), 014104 (2008)
9. B. Jiang, J. Iocozzia, L. Zhao, et al., Chem. Soc. Rev. **48**(4), 1194-1228 (2019)
10. F. Kang, L. Zhang, B. Huang, et al., J. Eur. Ceram. Soc. **40**(4), 1198-1204 (2020)
11. J.T. Last, Phys. Rev. **105**(6), 1740 (1957)
12. Y. Li, X. Gao, G. Li, G. Pan, T. Yan, H. Zhu, J. Phys. Chem. C **113**(11), 4386-4394 (2009)
13. O. Jongprateep, N. Sato, R. Techapiesancharoenkij, K. Surawathanawises, Adv. Mater. Sci. Eng. **2019** (2019)
14. S.S. Arbuj, R.R. Hawaldar, S. Varma, S.B. Waghmode, B.N. Wani, Sci. Adv. Mater. **4**(5-6), 568-572 (2012)
15. A.E. Souza, S.R. Teixeira, C. Morilla-Santos, W.H. Schreiner, P.N. Lisboa Filho, E. Longo, J. Mater. Chem. C **2**(34), 7056-7070 (2014)
16. Y.-I. Kim, J.K. Jung, K.-S. Ryu, Mater. Res. Bull. **39**(7-8), 1045-1053 (2004)
17. Maurice, R. Buchanan, Ferroelectrics **74**(1), 61-75 (1987)
18. Wang, C. Lei, G. Wang, et al., J. Appl. Phys. **113**(9), 094103 (2013)
19. H. Trabelsi, M. Bejar, E. Dhahri, et al., Appl. Surf. Sci. **426** 386-390 (2017)
20. S. Saha, T. Sinha, A. Mookerjee, J. Phys. Condens. Matter **12**(14), 3325 (2000)
21. Luo, X. Wang, E. Tian, G. Li, L. Li, J. Mater. Chem. C **3**(33), 8625-8633 (2015)
22. N. Sai, B. Meyer, D. Vanderbilt, Phys. Rev. Lett. **84**(24), 5636 (2000)
23. M. Liu, J. Liu, C. Ma, et al., CrystEngComm **15**(34), 6641-6644 (2013)
24. S. Shah, P. Bristowe, A. Kolpak, A. Rappe, J. Mater. Sci. **43**(11), 3750-3760 (2008)
25. P. Thongbai, S. Tangwancharoen, T. Yamwong, S. Maensiri, J. Phys. Condens. Matter **20**(39), 395227 (2008)
26. Raevski, S. Prosandeev, A. Bogatin, M. Malitskaya, L. Jastrabik, J. Appl. Phys. **93**(7), 4130-4136 (2003)
27. N. Giri, A. Mondal, S. Sarkar, R. Ray, J. Mater. Sci. Mater. Electron. **31**(15), 12628-12637 (2020)
28. Mitra, S. Bhattacharjee, N. Mazumder, B.K. Das, P. Chattopadhyay, K.K. Chattopadhyay, Ceram. Int. **46**(12), 20437-20447 (2020)
29. J.K. Lee, K.S. Hong, J.W. Jang, J. Am. Ceram. Soc. **84**(9), 2001-2006 (2001)
30. S. Bhattacharjee, A. Banerjee, K.K. Chattopadhyay, J. Phys. D: Appl. Phys. **54**(29), 295301 (2021)
31. H. Borkar, V. Rao, M. Tomar, V. Gupta, A. Kumar, J. Alloys Compd. **737** 821-828 (2018)
32. N. Besra, K. Sardar, N. Mazumder, S. Bhattacharjee, A. Das, B. Das, S. Sarkar, K.K. Chattopadhyay, J. Phys. D: Appl. Phys. **54**(17), 175105 (2021)
33. C. Ang, A. Bhalla, L. Cross, Phys. Rev. B Condens. Mater. **64**(18), 184104 (2001)

34. C. Ang, Z. Yu, Phys. Rev. B Condens. Mater. **69**(17), 174109 (2004)
35. S. Pal, N.S. Das, S. Bhattacharjee, S. Mukhopadhyay, K.K. Chattopadhyay, Mater. Res. Express **6**(10), 105029 (2019)
36. S. Yadav, M. Chandra, K. Singh, AIP Conf. Proc. **1953**(1), 050074 (2018)
37. H. Zheng, G.C. de Györgyfalva, R. Quimby, et al., J. Eur. Ceram. Soc. **23**(14), 2653-2659 (2003)
38. A.A. Kholodkova, M.N. Danchevskaya, Y.D. Ivakin, G.P. Muravieva, A.S. Tyablikov, J. Supercrit. Fluids **117** 194-202 (2016)
39. J. Parsons, L. Rimai, Solid State Commun. **5**(5), 423-427 (1967)
40. C. Koops, Phys. Rev. **83**(1), 121 (1951)
41. P. Sengupta, P. Sadhukhan, A. Ray, R. Ray, S. Bhattacharyya, S. Das, J. Appl. Phys. **127**(20), 204103 (2020)
42. S. Bhattacharjee, A. Banerjee, N. Mazumder, K. Chanda, S. Sarkar, K.K. Chattopadhyay, Nanoscale **12**(3), 1528-1540 (2020)
43. S. Bhattacharjee, N. Mazumder, S. Mondal, K. Panigrahi, A. Banerjee, D. Das, S. Sarkar, D. Roy, K.K. Chattopadhyay, Dalton Trans. **49**(23), 7872-7890 (2020)
44. R. De Souza, E. Dickey, Philos. Trans. Royal Soc. A **377**(2152), 20180430 (2019)
45. S. Bhattacharjee, S. Mondal, A. Banerjee, K.K. Chattopadhyay, Mater. Res. Express **7**(4), 044001 (2020)
46. N. Rezlescu, E. Rezlescu, Phys. Status Solidi A **23**(2), 575-582 (1974)
47. R.-A. Eichel, Phys. Chem. Chem. Phys. **13**(2), 368-384 (2011)
48. M.M. Bhunia, K. Panigrahi, C.B. Naskar, S. Bhattacharjee, K.K. Chattopadhyay, P. Chattopadhyay, J. Mol. Liq. **325** 115000 (2021)
49. A.K. Jonscher, Nature **267**(5613), 673-679 (1977)
50. K. Funke, Solid State Ionics **28** 100-107 (1988)
51. K. Funke, Prog. Solid State Chem. **22**(2), 111-195 (1993)
52. M. Sindhu, N. Ahlawat, S. Sanghi, A. Agarwal, R. Dahiya, N. Ahlawat, Curr. Appl. Phys. **12**(6), 1429-1435 (2012)
53. J. Liu, Q. Liu, Z. Nie, S. Nie, D. Lu, P. Zhu, Ceram. Int. **45**(8), 10334-10341 (2019)
54. T. Ghosh, A. Bhunia, S. Pradhan, S. Sarkar, J. Mater. Sci.: Mater. Electron. **31**(18), 15919-15930 (2020)
55. R. Bergman, J. Appl. Phys. **88**(3), 1356-1365 (2000)

8 LASER-INDUCED FANO ASYMMETRY, ELECTRON-PHONON COUPLING, AND PHASE TRANSITION IN LANTHANIDE SESQUIOXIDE (Ln_2O_3; Ln = Eu, Gd, Dy) NANOPARTICLES: A RAMAN SPECTROSCOPIC INVESTIGATION

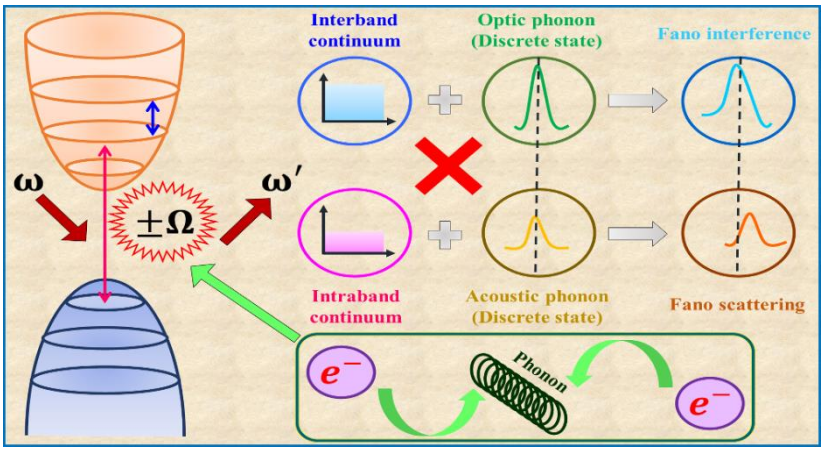

Abstract

Laser power-dependent Raman spectroscopy is deployed to probe Fano interference in asymmetrically broadened T_g modes and the associated line-shift in three technologically sound, meticulously characterized rare-earth sesquioxide systems. Group theoretical analysis is accompanied to introspect the Raman-active optic modes in cubic, monoclinic, and trigonal phases; and identify the laser heating-induced local phase transitions. With increasing laser intensity, a regular red shift and larger negative asymmetry in the Raman peaks are detected, which is attributed to the moderations in Fano scattering by the enhanced electron-phonon coupling amid the focussed photoexcited electron plasma and is illustrated using Feynman diagram. A quantitative study is thereby performed to unveil the intrinsic nature of discrete-continuum Fano resonance in the nanoparticles of interest emphasizing the high sensitivity of Raman spectra to the excitation strength, that perturbs the generic vibrational features at the Brillouin zone centre by influencing the interference conditions, force constant and length of the associated bonds compelled by tensile stress. A rising trend of the charge-phonon coupling constant (λ) with laser power validates a stronger particle-quasiparticle coupling, whereas a shorter anharmonic phonon lifetime (τ_{anh}) indicates faster interactions. Using Allen's formalism, charge density of states [$N(\varepsilon_F)$] at the Fermi level per spin and molecule is calculated, which pertains a negative regression dependence in the $\lambda N(\varepsilon_F) - \tau_{anh}$ dynamics.

8.1 Introduction

Interference between oscillators or in general, dynamical processes is archetypical and ubiquitous in physics. Systematic manipulation of the degree of such interactions involving distinct excitation pathways extends to the domain of coherence engineering.[1-3] Guiding the phase difference in discrete-continuum interference, tailoring the resonance and antiresonance conditions and the subsequent direction of asymmetric broadening in the spectroscopic line-shapes[2,4] encourage numerous applications *viz*., slow light propagation, quantum cryptography, wave transport, cyclotron resonance, magnetoelectric effect in quantum dots, development of photonic crystals, optical response of metamaterials and plasmonic lattice, *etc*.[1-3,5-10] Starting from atomic systems, the concept of Fano asymmetry in Raman spectroscopy is explored copiously for semiconductors (doped materials, thin films and devices), nanomaterials (to study the quantum confinement of phonons, electronic states or both), metamaterials and photonic systems, and even in topological Weyl semimetals.[11-22] Conventionally, the asymmetry is explained as an outcome of quantum interference between low frequency interband (intraband) transitions among the conduction and valence bands with optic (acoustic) phonons.[12,13,16-18] However, the exact factors that determine the sign of the Fano asymmetry parameter are not completely understood till date. In semiconductors, linewidth broadening towards the high frequency end (positive asymmetry) is reported to represent coupling between hole-based excitation with optical phonons, while the opposite (negative asymmetry) stipulates electron-phonon coupling and is more frequent.[14,19] Also, the incident photon energy in reference to the phonon Raman tensor values is a critical factor regarding the sign of asymmetry.[11,14,15] Presently, the objective is to understand how the system-specific description governs the generic charge-phonon interactions and the way of manipulating the same in a non-destructive manner by tuning external parameters such as pressure, temperature, electric or magnetic field; and intrinsic variables *e.g*., doping concentration in extrinsic semiconductors, particle or grain size in quantum confined systems, layer thickness and number of layers for 2D materials, thickness of ultrathin films, aspect ratio in case of nanowires *etc*.[16-18,23-29] Another critical parameter is laser power, which at smaller intensity increases only the number of events without any significant interference or alteration in the inherent nature of events. However, moderate to high laser powers can indulge significant local heating or generate photoexcited carriers with spectroscopic consequences. All these factors can alter interatomic interactions, that supports the high sensitivity of vibrational spectroscopy for probing these underlying mechanisms. Fano interference between discrete phonon and continuous electronic states may be triggered simply by the laser-induced or photoexcited charge carriers (typically, electrons).[19] The free electron plasma density rises notably with incident laser power.[16,17,30] Besides red-shifted Raman peaks and asymmetric broadening may also commence owing to the increase in

associated bond-lengths.[31] This is because, heat generated by a laser is inversely proportional to the force constant, that allows incommensurate stretching of the bonds.[30] Previously, laser power-dependent Fano asymmetry and spectral shift are qualitatively studied in some similar materials as well, like $LnFe_{0.5}Cr_{0.5}O_3$.[23] But the development of fundamental comprehension regarding the Fano effect is incomplete till date.

The most stable lanthanide (Ln)-based compounds are generally their sesquioxides (Ln_2O_3); owing to strong reactivity with oxygen.[32] Apart from a few rare-earth oxides like Pr_6O_{11}, CeO_2 or Tb_4O_7, in all other cases the sesquioxides possess trivalent lanthanide atoms in their ground state. The interesting physiochemical properties including heavy fermionic behaviour, the dense Kondo effect, high dielectric constant (useful for gate oxides in FETs), large magnetostriction (excluding Van Vleck paramagnet Eu_2O_3), and glassy property with Faraday rotation effect (beneficial for optoelectronic and photonic devices) make them useful materials,[33-36] among which we choose three technologically important candidates *viz*., Eu_2O_3, Gd_2O_3, and Dy_2O_3 nanoparticles for this study. These nanoparticles offer potential applications regarding solid-state light emitting devices (LED), dopants for tri-phosphor fluorescent lamps, high-efficiency luminescent materials and red powder activators for flat panel or plasma displays, luminescent probes in immunoassays, fuel cells, ultrafine chemical-mechanical polishing, catalytic converters, corrosion inhibitors, control rod for fast breeder reactors, rare earth magnets, magnetic refrigeration, magnetooptical recording material, *etc*.[37-40] The trivalent ions Eu^{+3}, Gd^{3+}, and Dy^{3+} respectively hold the $4f^6$, $4f^7$ and $4f^9$ electron configurations with ground states ${}^7F_0$ (half-filled), ${}^8S_{7/2}$, and ${}^6H_{15/2}$. The Raman peaks generally blue-shift with increasing number of f-electrons, because of the well-known lanthanide contraction effect. A higher effective nuclear charge across the lanthanide series due to the subsequently poor shielding ability of the $4f$ orbital pulls all electrons close to the nucleus, leading to a decreasing trend in radii of the successive rare-earth ions instead of rising number of total electrons across the period.

The sesquioxides under study crystallize in a cubic (C) phase at ambient condition, whereas with rising temperature they gradually transform to the monoclinic (B), trigonal (A), hexagonal (H), and again cubic (X) phases.[41] The most common space groups for the A, B, and C phases (relevant in this paper) are $P\bar{3}m1$ $(Z = 1), C2/m$ $(Z = 6)$, and $Ia\bar{3}$ $(Z = 16)$.[42] The molecular volume of the sesquioxides reduces with increasing cation coordination number and metal-oxygen distance in the respective C, B, and A phases. The unit cell of C phase holds a bixbyite structure containing 16 Ln_2O_3 molecules $(T_h^7, Ia\bar{3})$, where 24 Ln^{3+} ions are positioned according to the $C3_{3i}(S_6)$ symmetry.[36,39,40] However, under pressure different compounds are reported to show the direct $C \rightarrow A$, or $C \rightarrow B$ & $B \rightarrow A$ transitions depending on the state or texture (bulk powder/thin films/nanoparticles/single crystal) of the material and applied

pressure.[36,39,40,43] The free energy being a function of the aforementioned parameters often assumes the minimum for a new spatial arrangement of the constituting atoms leading to a structural phase transformation. Although the *A*-phase remains stable in colossal pressure condition, it is metastable at room temperature and immediately changes to the B (or C) structure after removal of pressure. Interestingly, moderate to high laser intensity can inflict significant local heating as well as microscopic biaxial stress within the bonds that trigger phase transformation after a threshold.[30,31,44] The crystallographic and group theoretical analysis of these phase transitions are thus fundamentally important in materials physics and chemistry.

Raman spectroscopic study is highly useful to identify local lattice fluctuation effects, charge transfer, long-range ordering, structural progressions, orbital or spin ordering *etc*. for the highly correlated rare-earth compounds.[45-51] The interpretation of asymmetrically broadened Raman peaks has always been ambiguous and significantly tricky.[52] This is because it involves diverse physical mechanisms including size contraction and quantum confinement effect, anharmonic decay of phonons in electronic Raman scattering, charge-phonon interactions in nonlinear Fano resonance, the effect of doping foreign elements or defects or lattice discontinuity that generate additional modes at the forbidden region around the Brillouin zone centre *etc*. Therefore, it is challenging to identify the intrinsic nature of Fano interaction for a particular system based on purely qualitative description of the line-shape asymmetry. Hence, a comprehensive quantitative analysis is compulsory before establishing any conclusion, which is attempted in this paper to analyse the laser power-dependent Fano asymmetry of the Ln_2O_3 nanoparticles by consolidating the theories formulated by U. Fano, M. Lax, P. B. Allen and J. C. K. Hui.[4,53-56]

8.2 Methods

Polycrystalline nano-powders of europium, gadolinium, and dysprosium sesquioxide were purchased from SIGMA-ALDRICH. Considering the analytical grade (assay $\geq$ 99.9%), no further chemical purification was performed. However, the as-received powders were ground well with a few drops of ethanol for 1 h to eliminate chunks and agglomerates. After that, the samples were calcined at 800 °C in a muffle furnace at open air for 4 h to enhance mechanical strength and to remove the possible hydroxides or adsorbed water molecules. Finally, the samples were again ground for 30 min at dry condition and stored to conduct various experiments.

XRD patterns within the scattering angle range $8° \leq 2\theta \leq 85°$ are acquired from a Rigaku Miniflex powder X-ray diffractometer (40kV–15mA) under monochromatic Cu-K_α radiation $(\lambda = 1.5406\,\text{Å})$ at 0.6° min^{-1} scanning rate and 0.02° step interval. The FULLPROF software is used to refine the crystallographic structures according to the Rietveld's method.[57]

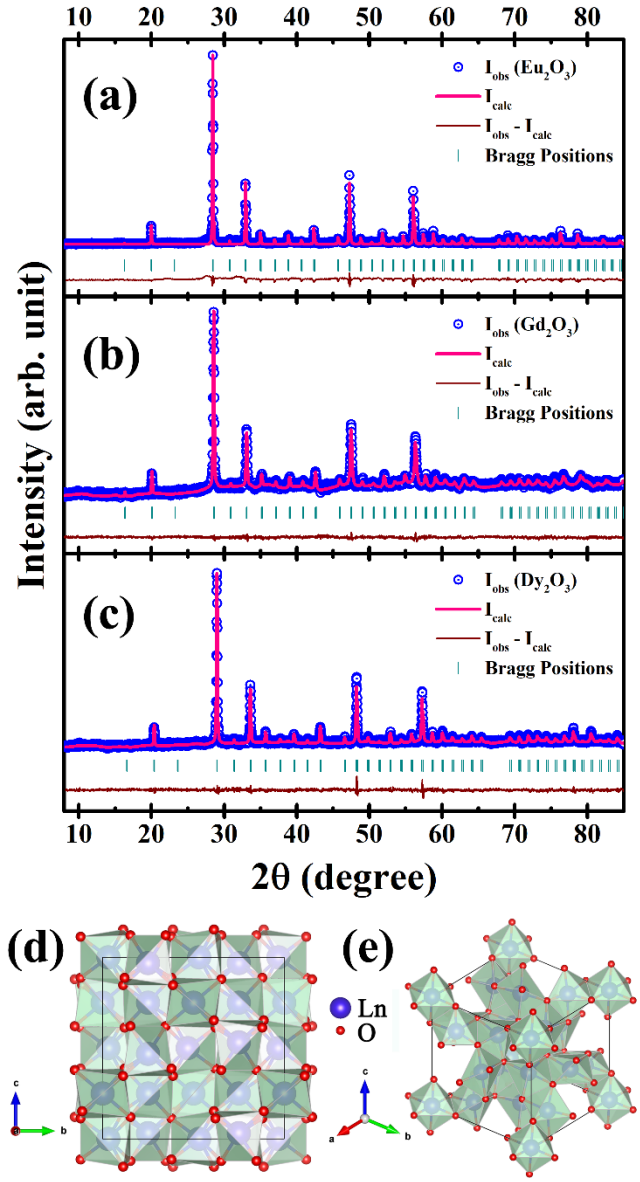

Figure 8.1 Rietveld refinement of powder XRD patterns for (a) Eu_2O_3; (b) Gd_2O_3; and (c) Dy_2O_3. The pink curve indicates the calculated best fit obtained from the FULLPROF program, against the experimentally observed diffraction traces marked with open blue circles. The vertical green bars specify the positions of the respective Bragg peaks, whereas the maroon curve represents the difference of the experimental (I_{obs}) and calculated (I_{calc}) intensities. Structure of the unit cell shown (d) along a −axis; (e) in oblique view.

Diffuse reflectance spectra (DRS) are collected from a Shimadzu UV 3600 UV-Vis-NIR spectrophotometer in 200 – 2200 nm wavelength range, using barium sulfate powder as the reflectance standard. Particle size and morphology of the samples are introspected with a ZEISS Sigma field emission scanning electron microscopy (FESEM) system equipped with an electron-gun having an accelerating voltage of 5 kV and up to 400 k × magnification. To characterize vibrational properties, Fourier transform infrared (FTIR) spectra in the range 400 – 4500 cm^{-1} are obtained from Shimadzu FTIR-8400S. Micro-Raman spectra are recorded at room temperature (20 °C) against varying laser intensity using a WITec ALPHA300 RS confocal spectrometer in backscattering configuration; connected with a solid-state monochromatic ($\lambda = 532.3$ nm) Nd:YAG laser with beam-diameter ~1 µm. Built-in holographic supernotch filters reject the Rayleigh and anti-Stokes lines without deploying polarizers. In a 50 × Zeiss achromatic objective with 600 grooves mm^{-1} (spectral resolution = 3.3 cm^{-1}) holographic

grating, 10 spectral acquisitions with 10 s of integration time each are captured and averaged to enumerate the final spectrum by minimizing the background noise. Group theoretical analysis of the various compounds and phases are carried out in the VIBRATE! software by importing the respective crystallographic information files (CIF) to identify the IR and Raman active modes.[58]

8.3 Results and discussion

8.3.1 Crystallographic, microstructural, morphological, and compositional characterization

All Bragg peaks in the XRD patterns of europium, gadolinium and dysprosium sesquioxide are matched with ICDD PDF cards: 00-043-1008, 00-043-1014, and 01-086-1327, respectively. No secondary peak is found, that confirms the pure cubic phase under space group: $Ia\bar{3}$ [206] and point group: $m\bar{3}$ (Hall: -I 2b 2c 3). From Eu_2O_3 to Dy_2O_3, the entire XRD pattern right-shifts slightly because of the lanthanide contraction-mediated reduction in interplanar spacing. The corresponding crystallite-sizes (D_{ctl}) are determined using the Scherrer's equation:

$$D_{ctl} = \frac{K\lambda}{\beta_p \cos\theta} \cong \frac{0.89 \times 0.15406}{\beta_p \cos\theta} \text{ nm.} \quad (8.1)$$

Table 8.1 Extracted crystallographic parameters from the Rietveld refinement of XRD data

Sample	Lattice parameters	Strain (η %)	Atoms	Wyckoff sites	x	y	z	Occu-pancy	χ^2
Eu_2O_3 (***C***)	$a = b = c =$ 10.8719(3) Å; $\alpha = \beta = \gamma = 90°$; $V = 1285.046(5)$ Å^3	0.02	Eu1	8b	0.25000	0.25000	0.25000	1.080	1.29
			Eu2	24d	0.96938	0.00000	0.25000	0.986	
			O	18e	0.39410	0.15400	0.38010	1.040	
Gd_2O_3 (***C***)	$a = b = c =$ 10.8246(1) Å; $\alpha = \beta = \gamma = 90°$; $V = 1268.343(2)$ Å^3	0.13	Gd1	8b	0.25000	0.25000	0.25000	1.024	1.78
			Gd2	24d	-0.03144	0.00000	0.25000	0.996	
			O	18e	0.39150	0.15240	0.38090	1.011	
Dy_2O_3 (***C***)	$a = b = c =$ 10.6644(7) Å; $\alpha = \beta = \gamma = 90°$; $V = 1212.879(9)$ Å^3	0.06	Dy1	8b	0.25000	0.25000	0.25000	1.005	1.49
			Dy2	24d	-0.03170	0.00000	0.25000	0.993	
			O	18e	0.38700	0.15300	0.37900	1.003	

In equation 8.1, K is a dimensionless constant related to the geometry or shape of the nanoparticles and β_p is the full width at half maximum (FWHM) of the corresponding Bragg peak. Considering five most intense peaks, the mean D_{ctl} is found to be 41.8, 46.4, and 56.1 nm for Eu_2O_3, Gd_2O_3, and Dy_2O_3, respectively. For more profound crystallographic information, the XRD patterns are refined according to the Rietveld's method with satisfactory goodness of fit, where the peaks are modelled with the pseudo-Voigt line profile, see Figure 8.1(a-c). The extracted profile parameters and atomic positions are enlisted in Table 8.1, and the refined structure of the unit cell is demonstrated in Figure 8.1(d,e), as obtained from the VESTA software.[59]

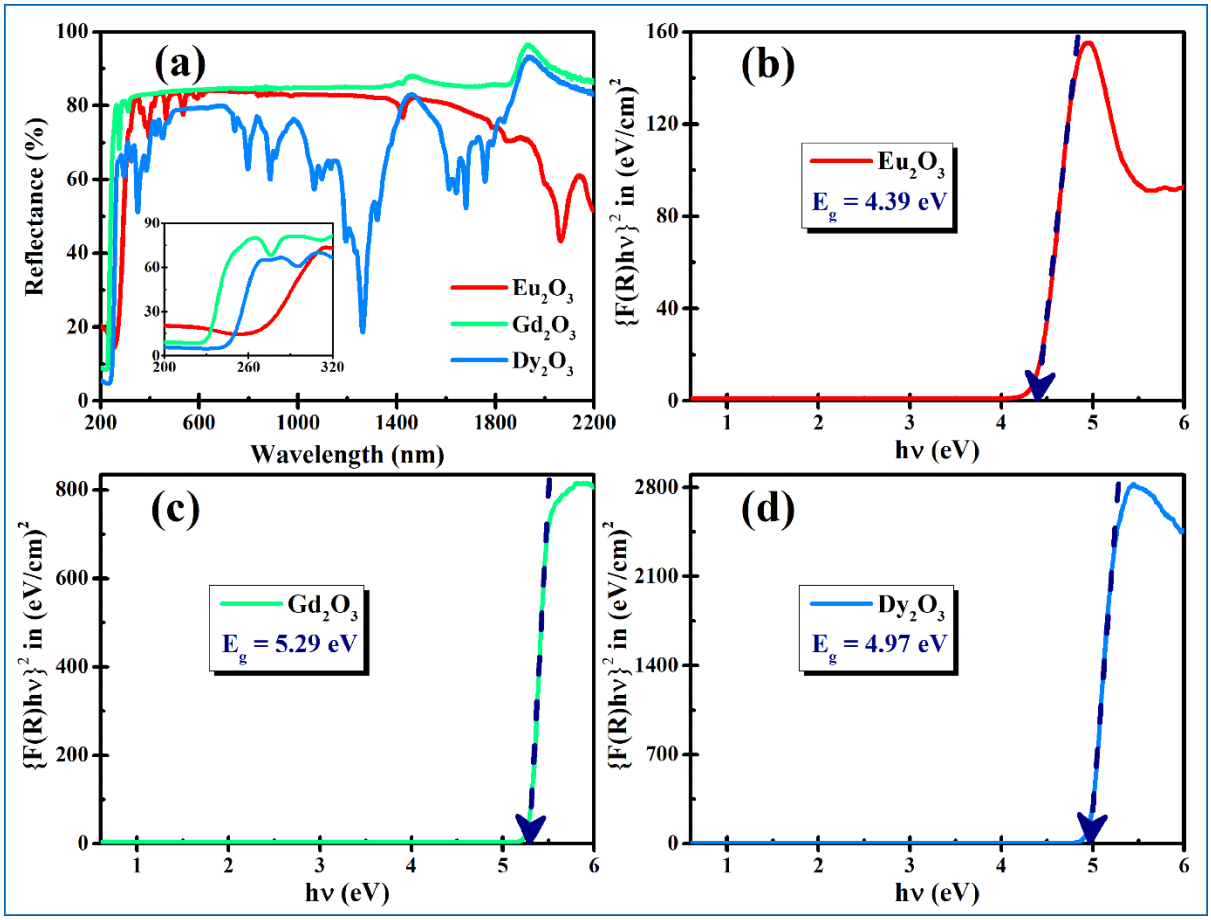

Figure 8.2 (a) Diffused reflectance spectra for the three samples. The inset shows a magnified view of the 200 – 320 nm excitation region, that comprises major optical properties of the samples. Tauc's plots are used to determine the optical bandgaps (E_g), employing the Kubelka–Munk function $\{F(R)\}$ for (b) Eu_2O_3; (c) Gd_2O_3; and (d) Dy_2O_3 nanoparticles.

DRS data of the samples are presented in Figure 8.2(a), that indicate strong absorption characteristics in the 200 – 300 nm (UV) range. High reflectivity can be found afterwards, that supports white colour of the samples. Employing the Kubelka-Munk theory, the (allowed) direct optical bandgaps (E_g) are estimated from the Tauc's plots taking the extrapolated slope at the

absorption band-edge,[60,61] as shown in Figure 8.2(b-d). The values of E_g are 4.39, 5.29, and 4.97 eV for Eu_2O_3, Gd_2O_3, and Dy_2O_3, respectively. This verifies the wide bandgap attributes of the samples. Figure 8.3(a-f) present the FESEM micrographs of all the samples at different magnification. Although the morphology is not very uniform or prominent for the samples, Eu_2O_3 can be described as nano-cubes, while both Gd_2O_3 and Dy_2O_3 can be classified as nano-reefs. The notably larger particle sizes in regard to D_{ctl} confirms the polycrystalline nature. The energy dispersive X-ray (EDX) spectra verifies the atomic composition of the samples, as provided in Figure 8.3(g-i). The stoichiometry is found to be $Eu: O = 42: 58$; $Gd: O = 45: 55$; and $Dy: O = 38: 62$ for the respective samples, which is satisfactory against the ideal atomic ratio of 2: 3 and agree with the refined occupancies.

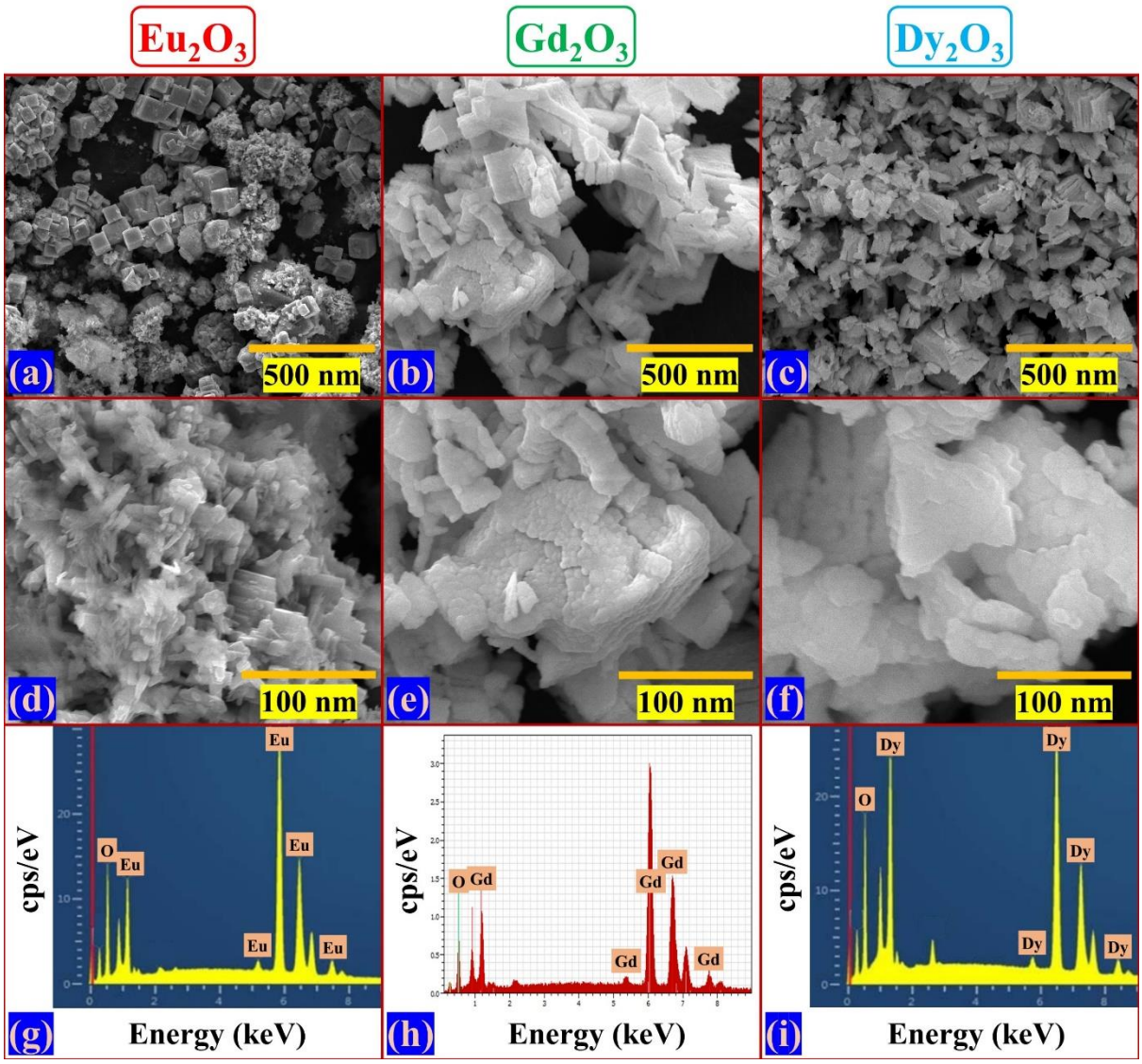

Figure 8.3 (a–c) FESEM micrographs at smaller magnification; (d–f) FESEM micrographs at higher magnification and finer resolution; (g–i) EDX spectra for the respective samples and identification of elemental signatures. The data for Eu_2O_3, Gd_2O_3 and Dy_2O_3 are presented in the three columns, respectively.

8.3.2 Introspecting lattice vibrations

The surface chemical structure and distinct finger-print modes of lattice vibration are scrutinized using FTIR and Raman spectroscopy. Figure 8.4 presents the room-temperature FTIR spectra of all three samples. The strong absorption bands detected in the range $411 - 418\ \mathrm{cm}^{-1}$ (Ln − O − Ln bending) and $536 - 554\ \mathrm{cm}^{-1}$ (Ln − O stretching) are characteristic of the cubic phase of lanthanide sesquioxides.[62,63] The comparatively weaker, but broader multiple absorption peaks in the range $1400 - 1550\ \mathrm{cm}^{-1}$ and $3420 - 3580\ \mathrm{cm}^{-1}$ for various samples are respectively attributed to the bending vibrations of H − O − H of the adsorbed water and stretching vibrations of the O − H bond.[62,64] This reflects the moisture trapping tendency of these nanoparticles.

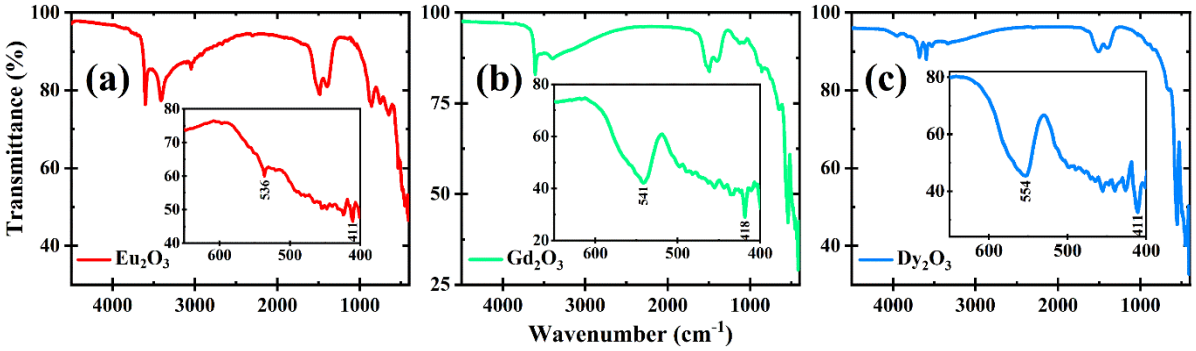

Figure 8.4 FTIR spectra for (a) Eu_2O_3; (b) Gd_2O_3; and (c) Dy_2O_3 nanoparticles. The insets show a magnified view of the region of interest ($400 - 650\ \mathrm{cm}^{-1}$).

Figure 8.5 presents the Raman spectra obtained for all three samples with the laser power varied from 0.5 to 20.0 mW. Any further increase in the laser intensity causes sample damage and hence is avoided here. With increasing laser intensity, the peaks gradually rise and red-shift with a pronounced FWHM. The more important observation is the steadily escalating (negative) Fano asymmetry. A background enhancement is also observed due to the higher thermal emission and scattering processes. Initially, at lower surface temperature, signatures of only *C* phase are detectable. But, at high enough laser power (> 6 mW), small peaks representing the *B* phase appear and grow gently. Finally compelled by even higher power (> 10 mW), the $C \rightarrow B$ phase transition is accompanied by the initiation of $B \rightarrow A$ phase transformation. Among the three compounds, Eu_2O_3 seems more sensitive to high laser power, which embarks multiple small peaks related to the *B* & *A* phases. Dilawar Sharma *et al*. have commented in this regard that, if the sample contains some traces of *B* or *A* phase at the very beginning, their transformation and growth inflate more rapidly under external influence.[36] In our case, the samples showed hardly any trace of secondary phase at ambient, that preserved the principal phase substantially until the laser power was increased to double digit values in mW.[39,40] Due to the residual heat, all data presented in this paper are recorded for increasing

power. The decreasing order data is thus excluded, which however shows that the sample is intact except for some retained phases; indicative of converse energy barrier and moderate hysteresis.[40]

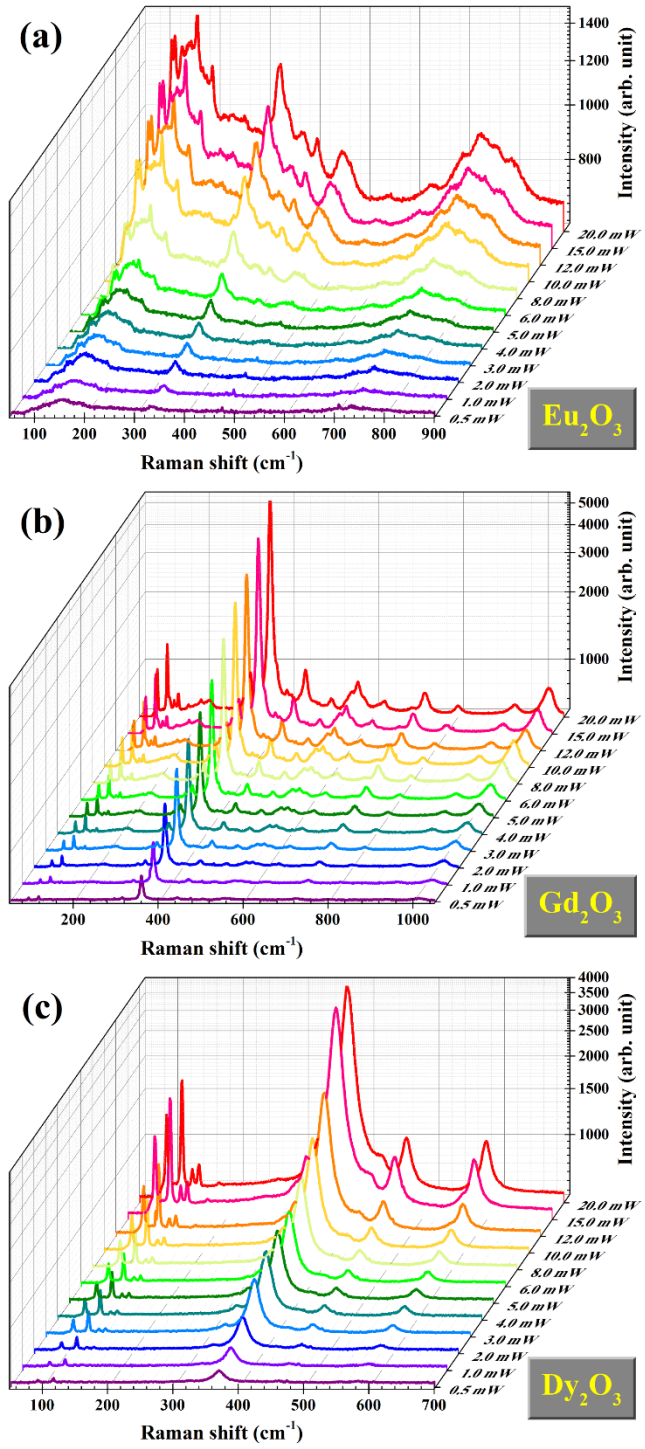

Figure 8.5 Laser power-dependent Raman spectra for (a) Eu_2O_3; (b) Gd_2O_3; and (c) Dy_2O_3 nanoparticles in 0.5 – 20 mW power range.

The irreducible phonon modes (Raman-active, IR-active or optically silent) at the first Brillouin zone center for the three phases are given by,

$$\Gamma_{vib}^{(C)} = [4A_g \oplus 4E_g \oplus 14T_g]_{Raman} \oplus [17T_u]_{IR} \oplus [5A_u \oplus 5E_u]_{Silent}, \quad (8.2)$$

$$\Gamma_{vib}^{(B)} = [14A_g \oplus 7B_g]_{Raman} \oplus [8A_u \oplus 16B_u]_{IR}, \quad (8.3)$$

$$\Gamma_{vib}^{(A)} = [2A_{1g} \oplus 2E_g]_{Raman} \oplus [3A_{2u} \oplus 3E_u]_{IR}. \quad (8.4)$$

Among the 22 Raman bands of the C phase, four A_g (symmetric stretching) modes, four doubly degenerate E_g (symmetric bending) modes and fourteen triply degenerate T_g (symmetric stretching) modes (also known as F modes) can be obtained.[33,65] Factor group theory helps to classify the optic modes into two parts: (a) modes below 250 cm^{-1} mainly comprise the internal vibrations of the LnO_6 octahedra, and (b) modes at the higher energy side of 250 cm^{-1} are predominantly engaged to translational motion of the Ln^{3+} ions.[65]

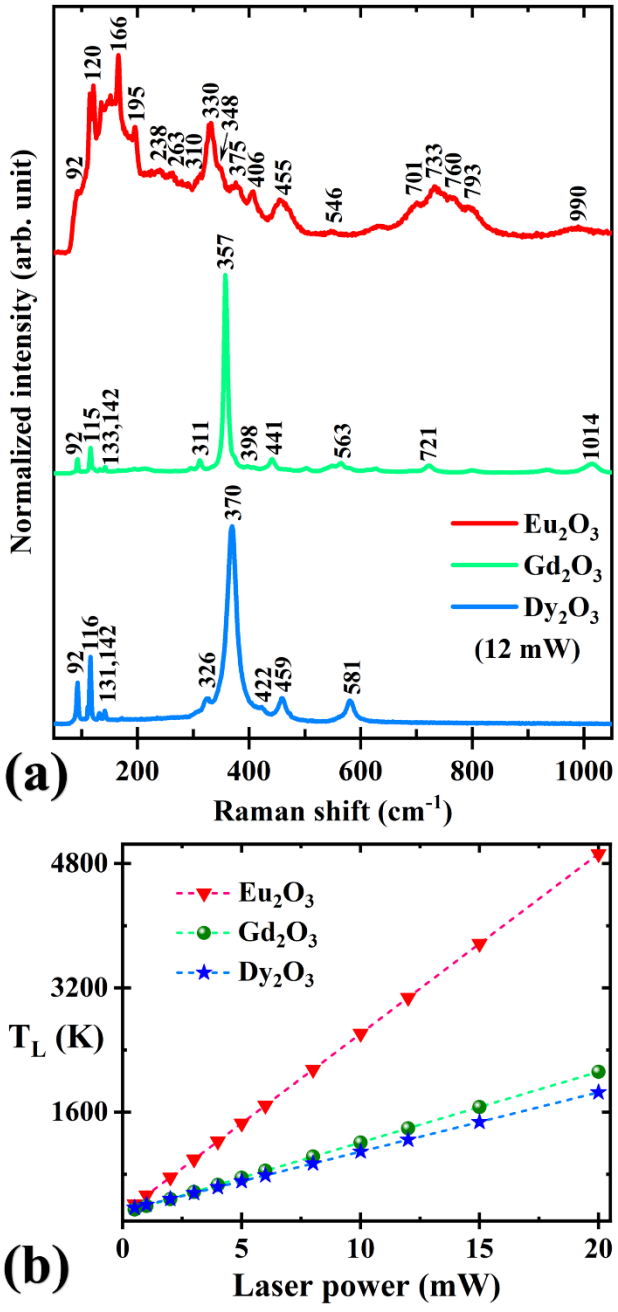

Figure 8.6 (a) Raman spectra for all the samples under 12 mW laser power. At this condition, all the three phases (A, B and C) are seen to coexist prominently. Corresponding peak positions are labeled; (b) calibration curve of Lax temperature (T_L) versus laser power in the operating range.

Table 8.2 Assignment of phase-specific Raman modes having distinct strength

Eu_2O_3		Gd_2O_3		Dy_2O_3		Assigned vibrational mode	Associated phase
Raman shift (cm^{-1})	Intensity	Raman shift (cm^{-1})	Intensity	Raman shift (cm^{-1})	Intensity		
92	Weak	92	Weak	92	Moderate	T_g	C
120	Moderate	115	Moderate	116	Moderate	A_g	C
166	Strong	133	Weak	131	Weak	$(T_g + E_g)/A_g$	C/B
195	Weak	–	–	–	–	A_g	B
238	Weak	142	Weak	142	Weak	T_g	C
263	Weak	294	Weak	326	Weak	E_g	C
310	Weak	311	Weak	–	–	$E_g/\Gamma_{el}(C_{3i})$	C
330	Strong	357	Strong	370	Strong	$T_g(+A_g)$	C
348	Weak	–	–	–	–	A_g	B
375	Weak	398	Weak	422	Weak	T_g	C
406	Moderate	–	–	–	–	A_g	B
455	Strong	441	Moderate	459	Moderate	T_g	C
546	Weak	563	Weak	581	Moderate	T_g	C
701	Weak	–	–	–	–	–	A/B
733	Strong	721	Weak	–	–	T_g	C
760	Weak	–	–	–	–	–	A/B
793	Weak	–	–	–	–	–	A/B
990	Weak	1014	Weak	–	–	CF	C

A smaller number of modes are experimentally observed in reference to the theoretical expectation likely because a few modes could superpose on each other due to close spacing, line broadening or weak factor group interactions such as the superposition of some T_g and A_g modes. The strong polarizability variation of T_g modes under external influence make them highly sensitive of alterations in vibrational characteristics. The number of phonon branches decreases in the B & A phases owing to the lesser degrees of freedom than the C phase, which indirectly helps to pronounce the LO/TO splitting. Now to assign various phonon modes of all the phases, we consider a moderate laser intensity *viz.*, 12 mW, where all the three phases (C, B & A) co-exist, but the modes related to the cubic phase are not significantly distorted yet. All peaks present at this laser power are marked in Figure 8.6(a), which are then enlisted and attributed to the corresponding phonon modes/phases in Table 8.2 with the help of group theoretical predictions and previous literature.[33,36,39,40,43] Among them, the T_g modes in the regime $330 - 370$ and $441 - 459$ cm^{-1} for different compounds are the most intense peaks, where the laser-dependent asymmetry seems prominent. These two modes will be taken into consideration for quantitative analysis with appropriate models in the forthcoming sections.

8.3.3 Evaluation of laser-induced rise in lattice temperature

Laser-induced thermal desorption (LITD), heating, annealing, and degradation of high bandgap semiconductors comprising finite heat conduction capability and attenuation factor are well-known examples, where the localized temperature rise near the point of laser implantation needs to be probed. There are primarily three methods of determining the thermodynamic surface-temperature subject to laser-induced heating: (a) using anti-Stokes to Stokes intensity ratio (I_{AS}/I_S) is a highly popular method,[30,66] especially if the intensity of the characteristic peak is very high *e.g*., silicon nanowires. The moderated Boltzmann distribution between two states with energy gap ΔE shows the following temperature dependence.

$$\frac{I_{AS}}{I_S} = \left(\frac{\omega_{el} - \omega_{inel}}{\omega_{el} + \omega_{inel}}\right)^4 exp\left(-\frac{\Delta E}{k_B T}\right). \quad (8.5)$$

Here, k_B is the Boltzmann constant, ω_{el} and ω_{inel} are the respective wavenumbers of the Rayleigh (elastic scattering) and Raman (inelastic scattering) peak. However, the major obstacle with this method is the low anti-Stokes intensity for most materials, that increases the standard deviation of the estimated temperature significantly due to low signal to noise ratio. Moreover, many spectrometers (like ours) filter out the less useful anti-Stokes lines by design, that leaves no opportunity to cultivate this technique; (b) in the quasi-harmonic approximation, the temperature-dependent wavenumber shift is entirely attributed only to the thermal expansion of the unit cell volume. Naturally, many materials manifest nominally small anharmonic effects,[66] making this strategy ineffective; (c) the third way to determine temperature involves the thermodynamic Grüneisen parameter (γ_T). The problem with this route is, one must know the thermodynamic details of the sample *e.g*., heat capacity at constant volume, isothermal bulk modulus, molar volume, coefficient of volume expansion *etc*. beforehand to calculate γ_T. Not only, extensive database of these information for various materials is unavailable, but also all the mentioned parameters vary significantly in nanomaterials. So, using information of the bulk could associate erroneous results for nanoparticles. For these reasons, we have followed the formulation suggested by M. Lax to determine the lattice temperature of the system.[53,54]

Considering a Gaussian intensity-distribution of the laser beam, $I(r) = I_0 exp\left(-\frac{4r^2}{d^2}\right)$ for a beam-diameter d and quasi-linear (or non-linear) thermal conductivity $K(T)$, the conventional heat-diffusion equation: $C\frac{\partial \mathrm{T}}{\partial \mathrm{t}} = -\vec{\nabla}.\vec{J} + G$ can be solved numerically. Here, C is the specific heat, $\vec{J} = -K(T)\vec{\nabla}T$ is the flow-vector and G is the heat source (laser in our experiment). M. Lax solved this equation for solids with thermal conductivity having a slow variation with temperature.[53,54] The boundary conditions were chosen such that, the heating is confined to an infinitesimal layer near the surface. The laser-induced local temperature increase against a

beam power P is estimated to the value $\Delta T_L = P\langle r^{-1}\rangle/2\pi K \cong P/2\sqrt{\pi}Kd$. If the ambient temperature is T_0, the final temperature at the region of interest rises to,

$$T_L(P) = T_0 + \Delta T_L(P) \cong T_0 + \frac{P}{2\sqrt{\pi}Kd}. \tag{8.6}$$

The Lax temperature gives an estimate for the maximum lattice temperature (and should not be confused with the macroscopic thermodynamic surface temperature) without taking scattering and radiation losses into account. Picking up values of thermal conductivity of the samples from previous literature,[67-69] T_L versus laser power calibration curves are obtained and plotted in Figure 8.6(b). The accuracy of this methodology is particularly appreciable for narrow laser spots focused on thermally insulating materials preserved in a controlled environment. However, for highly intense laser irradiation (power larger than a few tens of mW), this formalism will not be applicable due to fast and nonlinear variations in $K(T)$.

8.3.4 Quantitative analysis of laser power-dependent Fano asymmetry and distinct alterations in Raman modes

On top of the phonon self-energy induced linewidth, the one-phonon Raman line (discrete energy excitation) gets superimposed on the adjacent continuum of electronic states (background process). So, the coupling between these disparate excitation channels manifests an interference effect, that moderates the light scattering cross-section. The asymmetry in the Raman line-shape is indicative of these mechanisms. Therefore, a stronger coupling would accompany a more asymmetric line-shape, which can be fitted using the Breit–Wigner–Fano (BWF) function given by,[4,8,30,52]

$$I(\omega) = I_0 + S\frac{\left[q + \frac{2(\omega-\omega_b)}{\Gamma}\right]^2}{\left[1 + \left\{\frac{2(\omega-\omega_b)}{\Gamma}\right\}^2\right]}. \tag{8.7}$$

Here, S is a constant (multiplier), ω_b is the (bare) phonon frequency of the coupled Raman mode, Γ is the linewidth parameter related the FWHM of the corresponding peak, q is the Fano coefficient (ratio of the resonant and background scattering amplitudes) and I_0 takes care of the background. The quantity $|q|^{-1}$ gives a measure of the charge-phonon coupling strength. So, the BWF line-shape boils down to a symmetric Lorentzian function; only when the coupling is very weak *i.e.*, $\frac{1}{q} \approx 0$. On the other hand, resonance or antiresonance takes place for $q \to 0_{\pm}$.

Now, for a comprehensive analysis, we need to choose a few Raman modes suitable for BWF fitting at varying laser powers. To precisely recognize the asymmetry in the fitted curves and extract important parameters, the chosen modes (i) should have good enough intensity, (ii) signal to noise ratio should be high even for low powers, (iii) the Raman peak should belong to the cubic phase only, (iv) merging of close peaks or breaking of peaks should be excluded, (v)

the peak should be typically sensitive to power rise and (vi) distorted line-shapes (at any operating power) should be avoided. Based on these conditions, only the T_g modes at $330-370\ cm^{-1}$ and $441-459\ cm^{-1}$ for various samples could be considered for further calculations, which will be respectively called T_g-1 and T_g-2 henceforth. But even the T_g-1 peak of Eu_2O_3 first distorts and then breaks into two peaks after 12 mW power owing to the $C \rightarrow B$ phase transition [resulting growth of $A_g(B)$ mode], see Figure 8.7(a). Rest of the peaks are fitted with equation 8.7 for all powers as shown in Figure 8.7(b-f).

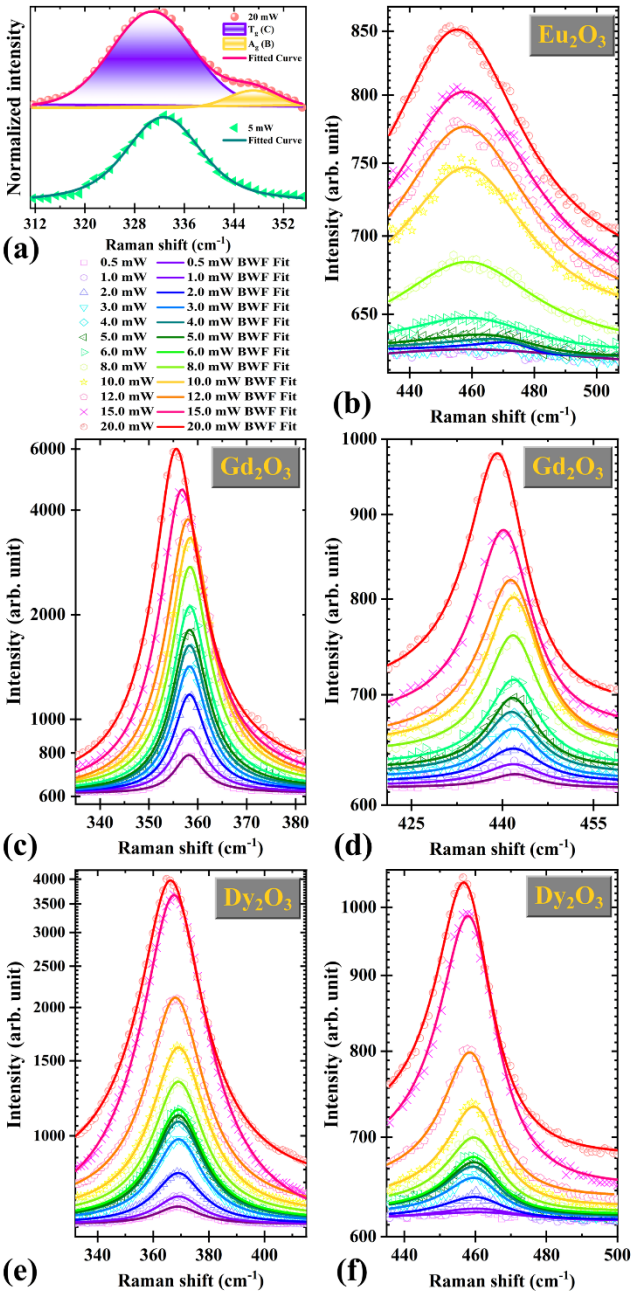

Figure 8.7 (a) Eu_2O_3 (T_g-1) peak fitted under 5 and 20 mW laser power. At higher power, an additional peak generates due to the $C \rightarrow B$ partial phase-change, which can be recognized via deconvolution. BWF fits of the (b) Eu_2O_3 (T_g-2); (c) Gd_2O_3 (T_g-1); (d) Gd_2O_3 (T_g-2); (e) Dy_2O_3 (T_g-1); and (f) Dy_2O_3 (T_g-2) modes at different laser powers between 0.5 and 20 mW.

In comparison to laser-induced lattice heating effect, anisotropic lattice disorder in these systems should be nominal and thus its effect on the spectroscopic asymmetry is

neglected in the following analysis. Due to the asymmetric line-shape, the position of the maximum intensity shifts to a position,

$$\omega_{b,max} = \omega_b + \frac{\Gamma}{2q} \begin{cases} > \omega_b, \text{if } q > 0 \\ < \omega_b, \text{if } q < 0 \\ = \omega_b, \text{if } q \to \pm\infty \end{cases}. \tag{8.8}$$

So, the positive (negative) asymmetry pushes $\omega_{b,max}$ to the high (low) energy end owing to in-phase (out-of-phase) coupling or interference.[52] In the demonstrated spectra, negative Fano asymmetry rises appreciably with increasing power for all the modes, that causes red-shifting of the bare phonon frequencies.

Traditionally, the temperature-dependent $\omega_b(T)$ and $\Gamma(T)$ are analyzed taking multiple phonon decay channels into account. But here, band transition threshold falls with the Bose-Einstein factor involved with phonon emission or absorption.[70,71] Therefore, we pick up the following relations.[52,72]

$$\omega_b(T) = \omega_0 - \frac{a}{exp\left(\frac{b\hbar\omega_0}{k_B T}\right) - 1};\ \omega_0 = \omega_b|_{T\to 0}, \tag{8.9}$$

$$\Gamma(T) = \Gamma_0 + \frac{a'}{exp\left(\frac{b'\hbar\omega_0}{k_B T}\right) - 1}. \tag{8.10}$$

Here, ω_0 and Γ_0 are the corresponding quantities at the absolute zero. The constants a, b, a', b' take care of the anharmonicity. In case of phonon softening, a is positive and vice-versa. Anharmonic effects can be significant for light atoms with large vibrational amplitudes, weak chemical bonding, and systems exposed to high temperatures.[73] These equations are conformal with the empirical Cui formulation adopted in some previous works.[52,74,75] Therefore, we fit the respective peak positions and FWHM versus T_L for various modes [Figure 8.8(a-f)] to extract ω_0 and Γ_0, which are provided in Table 8.3. In these curve fits, temperature is approximated with the values of T_L, because the nature of the curves is identical and any possible multiplier (say, s in the linear relation, $T_L = sT$) can be absorbed within the anharmonicity constants; by using them as scaling factors. Next, the phonon lifetime (τ) can be computed using the following formula.

$$\tau(T) = \frac{1}{2\pi c\Gamma(T)}, \tag{8.11}$$

c being the velocity of light in vacuum. The linewidths of a Raman peak for an ideal harmonic crystal should be infinitely narrow, that theoretically extends the phonon lifetime to forever. However, in practice, many factors like presence of impurity, defects, thermal agitation, lattice strain, Doppler broadening *etc*. disturbs the translation symmetry of the system and widens the FWHM of the elastic scattering, which evinces a significant reduction of τ.

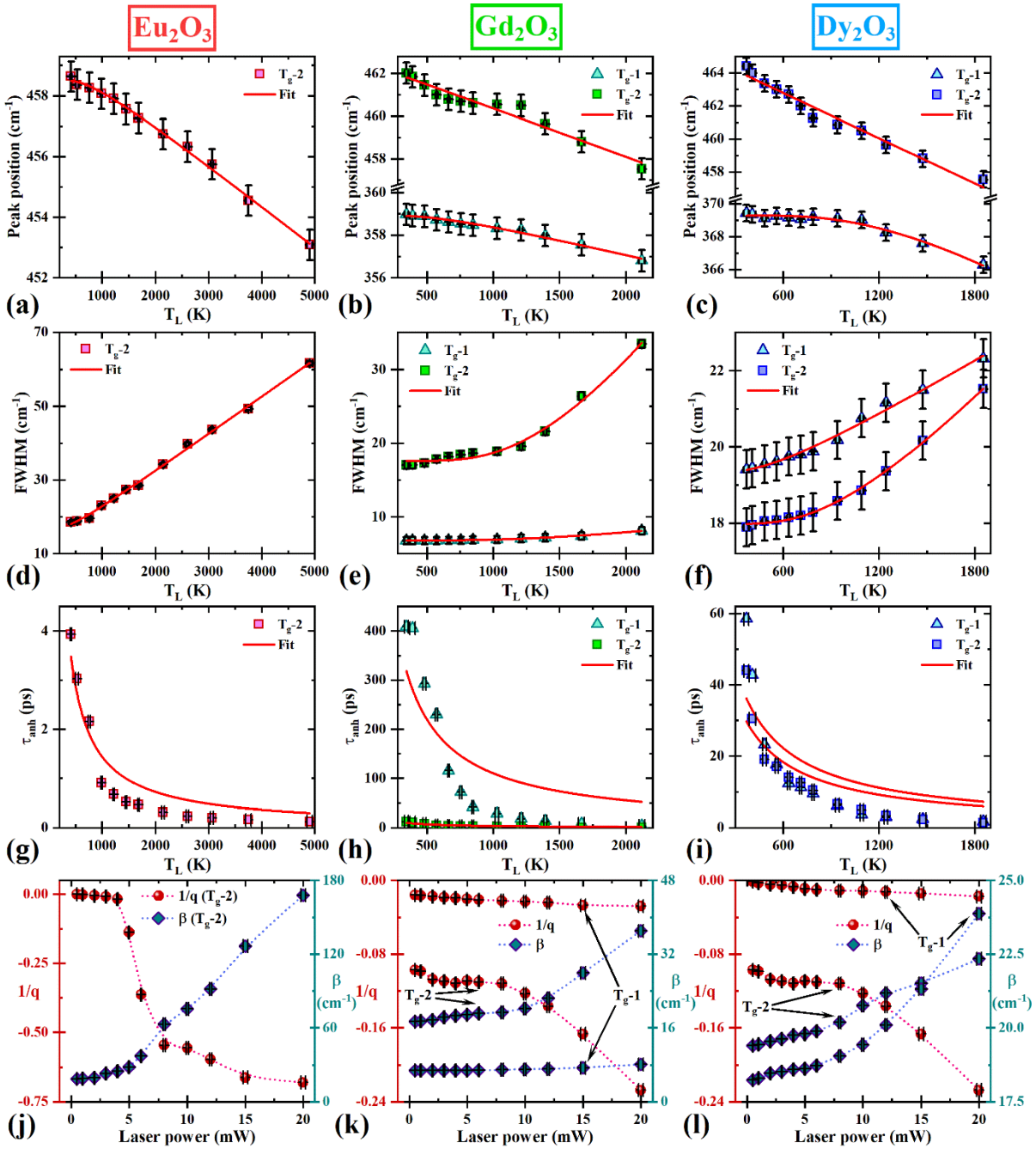

Figure 8.8 (a–c) Peak positions versus Lax temperature (T_L); (d–f) FWHM versus T_L; (g–i) anharmonic phonon lifetime (τ_{anh}) versus T_L; (j–l) $1/q$ & β versus laser power plots for all three samples. The data for Eu_2O_3 $(T_g - 2)$, Gd_2O_3 $(T_g - 1\ \&\ 2)$ and Dy_2O_3 $(T_g - 1\ \&\ 2)$ are presented in the three columns, respectively. The solid red lines represent curve fits using the associated equations, whereas the dotted lines are guide to the eye.

Subsequently, the temperature dependent phonon lifetime can be separated into two parts *viz*., the elastic component at absolute zero ($\tau_0 = 1/2\pi c\Gamma_0$) [enumerated in Table 8.3] and the thermally dispersing anharmonic part (τ_{anh}), as given below.

$$\frac{1}{\tau(T)} = \frac{1}{\tau_0} + \frac{1}{\tau_{anh}(T)} = 2\pi c\Gamma_0 + \frac{1}{\tau_{anh}(T)}, \tag{8.12}$$

$$\tau_{anh}(T) = \frac{1}{2\pi c\{\Gamma(T) - \Gamma_0\}} \cong \frac{1}{2\pi cD\left\{1 + \frac{2}{exp(\hbar\omega_0/2k_BT) - 1}\right\}}. \tag{8.13}$$

Here, D is just a fitting parameter with an inverse length dimension.[52] Higher laser power helps to speed up interactions with phonons, causing faster scattering and reduction of phonon lifetime. Figure 8.8(g-i) shows the τ_{anh} vs T_L plot, which is fitted using equation 8.13. However, the goodness of fit is not satisfactory, which can be seen in previous literature as well.[52] Hence, no parameter is extracted from the best fit and we conclude, the theory of anharmonic phonon lifetime under the effect of temperature, pressure, electric field *etc*. needs further elucidation, which however is beyond the scope of the current study. From the asymmetry parameter (q) and linewidth parameter (Γ), the net asymmetric FWHM (β) can be determined.

$$\beta = \Gamma\frac{(q^2 + 1)}{|q^2 - 1|}. \tag{8.14}$$

Figure 8.8(j-l) presents the change of $\frac{1}{q}$ (~electron-phonon coupling constant) and β as a function of laser power. At low laser intensity, $\frac{1}{q}$ is very small, that validates near Lorentzian line-shape. But, as the laser power increases, the Fano asymmetry becomes more and more negative *i.e.*, $\left|\frac{1}{q}\right|$ increases drastically for all modes. It manifests a stronger electron-phonon coupling and thereby wider asymmetric FWHM.

Table 8.3 Extracted parameters from Raman spectroscopic analysis and curve fits

Compound	Concerned Raman mode	ω_0 [cm^{-1}]	Γ_0 [cm^{-1}]	τ_0 [ps]	$N(\varepsilon_F)$ [states eV^{-1}]
Eu_2O_3	$T_g - 2$	458.95	17.15	0.31	92
Gd_2O_3	$T_g - 1$	359.09	6.74	0.79	9
	$T_g - 2$	462.08	16.58	0.32	42
Dy_2O_3	$T_g - 1$	370.08	19.32	0.27	14
	$T_g - 2$	465.52	17.77	0.30	5

The interaction between electronic excitations and vibrational modes is quite sensitive to the normal coordinates that associates crystal axes specific coupling to tailor the underlying dynamics. To analyze the mode specific electron-phonon coupling, the Allen's formulation can be adopted to monitor the dimensionless charge-phonon coupling constant (λ).[52,55,56,76]

$$\lambda = \frac{g}{2\pi N(\varepsilon_F)} \times \frac{\Gamma}{\omega_b^2}. \tag{8.15}$$

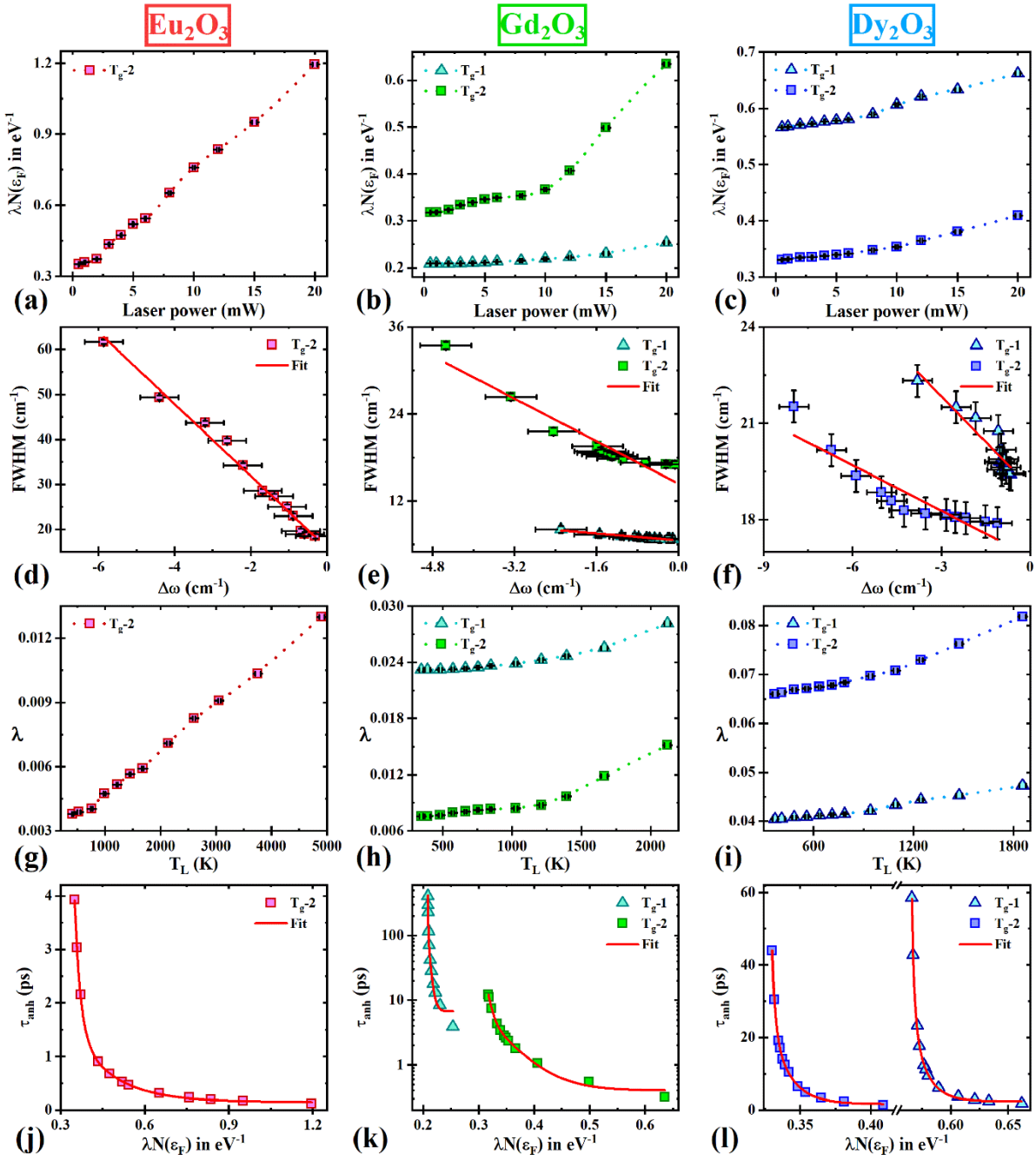

Figure 8.9 (a–c) $\lambda N(\varepsilon_F)$ versus laser power; (d–f) FWHM versus peak shift ($\Delta\omega$); (g–i) coupling constant (λ) versus T_L; (j–l) τ_{anh} versus $\lambda N(\varepsilon_F)$ plots for all three samples. The data for Eu_2O_3 $(T_g - 2)$, Gd_2O_3 $(T_g - 1\ \&\ 2)$ and Dy_2O_3 $(T_g - 1\ \&\ 2)$ are presented in the three columns, respectively. The solid red lines represent curve fits using the associated equations, whereas the dotted lines are guide to the eye.

In equation 8.15, g represents the degeneracy of the associated phonon mode and $N(\varepsilon_F)$ stands for the density of states (DOS) at the Fermi level for each spin per unit cell. This theory is applicable mainly for disordered systems including oxides, metallic nanoparticles, carbon-based structures and doped or composite ceramics, where relaxation of the conservation rules

commits for distinct wave vectors manifesting a decay of phonons.[52,70-73] From equation 8.15, $\lambda N(\varepsilon_F)$ can be calculated in eV^{-1} ($\because$ 1 cm$^{-1} \equiv 0.00012$ eV) for the triply degenerate T_g modes. The same is plotted as a function of laser power in Figure 8.9(a-c), which shows a monotonically increasing trend. Within this framework, a linear relationship between $\Gamma(T)$ and $\Delta\omega = \omega_b(T) - \omega_0$ prevails, given by the following equation.[52,76]

$$\Gamma(T) = -\frac{\pi}{2} N(\varepsilon_F)\omega_0 \Delta\omega. \tag{8.16}$$

The experimental data of $\Gamma(T)$ versus $\Delta\omega$ can be satisfactorily fitted using a straight-line equation with reasonable statistical scatter, see Figure 8.9(d-f). This validates our proposition to use Allen's model for the Ln_2O_3 system. From the slope of the line fits, $N(\varepsilon_F)$ for all the modes under investigation has been determined and the nearest integer of the same is enlisted in Table 8.3. Imposing these values upon $\lambda N(\varepsilon_F)$, we calculate and plot λ as a function of T_L in Figure 8.9(g-i). The coupling constant rises with laser power or lattice temperature expectedly, that manifests greater interference cross-section and more asymmetric Raman line-shape. Now, to obtain a formally complete description of charge-phonon dynamics, we combine the equations 8.13 and 8.15 to reach the following identity.

$$\tau_{anh} \times \lambda N(\varepsilon_F) = \frac{g}{4\pi^2 cD} \times \frac{\Gamma}{\omega_b^2}\left\{1 + \frac{2}{exp(\hbar\omega_0/2k_BT) - 1}\right\}^{-1}. \tag{8.17}$$

Figure 8.9(j-l) presents τ_{anh} versus $\lambda N(\varepsilon_F)$ plots, which are fitted with a double exponential decay function. The competent goodness of fit validates presence of two entities (electrons and phonons) or excitation channels involved in the particle-quasiparticle coupling. Any further investigation demands the insertion of thermal expansion-based terms, which is unnecessary for lanthanide sesquioxides at this range of power.

The laser-induced heating effect directly tailors the force constant of the associated bonds and their respective bond-lengths. The wavenumber of a particular Raman peak and the associated force constant (k) are related according to the following equation.

$$\omega_b = \frac{1}{2\pi c}\sqrt{\frac{k}{\mu}}. \tag{8.18}$$

Here, the reduced mass (μ) for the Ln– O bonds can be calculated from the atomic weight of the corresponding lanthanide and oxygen atom.

$$\mu = \frac{M_{Ln}M_O}{M_{Ln} + M_O}. \tag{8.19}$$

So, force constants with varying peak positions for all modes are computable deploying the couple of equations. Furthermore, the laser excitation can induce a relative residual biaxial stress (ε) within the system. It can be determined from the empirical formula involving shift of the Raman peak ($\Delta\omega$) and the pressure coefficient (α).[44,77]

$$\varepsilon = \pm \frac{\Delta\omega}{\alpha} \text{ GPa.} \tag{8.20}$$

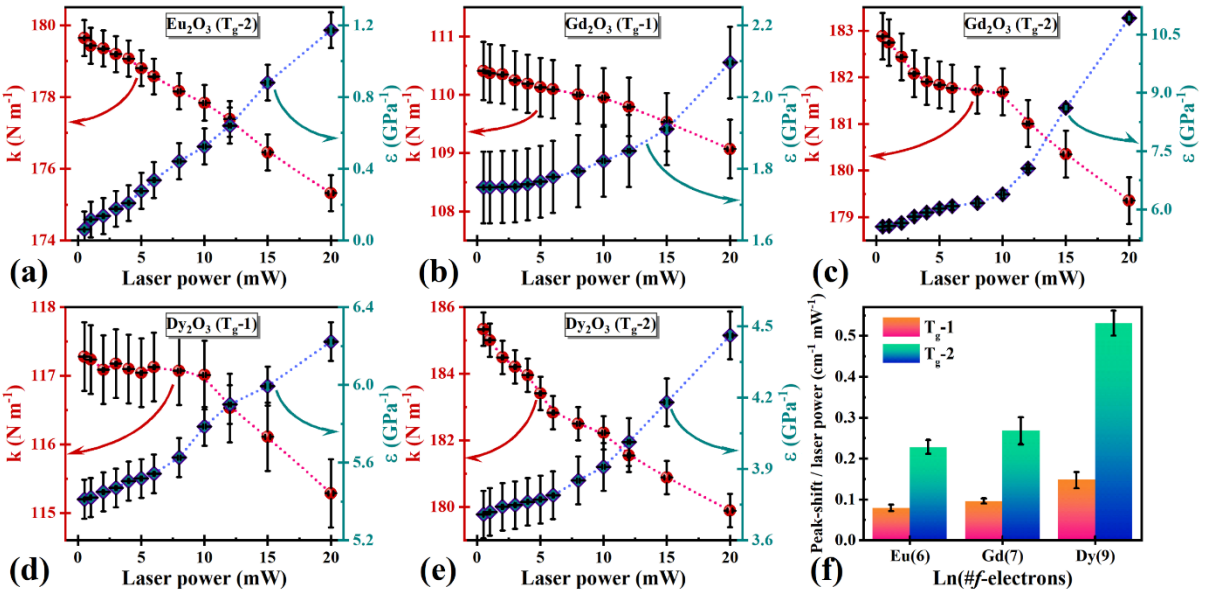

Figure 8.10 Force constant (k) [shown with reddish symbols and left scale] and relative residual biaxial stress (ε) [shown with greenish symbols and right scale] as a function of laser power for (a) Eu_2O_3 $(T_g - 2)$; (b) Gd_2O_3 $(T_g - 1)$; (c) Gd_2O_3 $(T_g - 2)$; (d) Dy_2O_3 $(T_g - 1)$; and (e) Dy_2O_3 $(T_g - 2)$ modes; (f) comparison of peak-shift per unit increase in laser power (in the low power regime) for the $T_g - 1$ and $T_g - 2$ modes versus number of f-electrons in the corresponding lanthanide atom.

In equation 8.20, the sign of $\Delta\omega$ can be both positive (implies shift of peaks to a higher wavenumber as a result of compressive stress) or negative (indicates shift of peaks to a lower wavenumber being compelled by tensile stress). To plot the relative stress for different modes, we collected the values of mode-specific pressure coefficients (defined as the Raman shift per unit external pressure) in units of cm^{-1} GPa^{-1} for each compound from a previous study.[36] Figure 8.10(a-e) demonstrates the dependence of k and ε on laser power. Higher laser power inflicts a stronger tensile stress upon the bonds,[44] that eventually reduces the force constant or weakens the related bonds. Low lying f-electron states (might vary for distinct lanthanides owing to the unique electronic band structure) can couple with the vibrational states to alter the interaction potential, that adjusts the curvature of the potential well, drops the force constant and lowers the frequencies.[65,78] Finally, peak-shift per unit increase in laser power (considering the low intensity linear regime) for both $T_g - 1$ and $T_g - 2$ modes is plotted in Figure 8.10(f) against different lanthanides with 6, 7 or 9 f-electrons. It is clearly noticeable that, the shift hikes significantly when the f-electrons increase in number. It not only substantiates the role of lanthanide contraction regarding this trend, but also frames a predictability over these

properties for other Ln_2O_3 systems, which are not explored in this paper. Besides, the broadening can also be influenced by the proximity of f-electron states near the Fermi level.[65] Similar dependence on the number of f-electrons is reported in a pressure-dependent study for a series of lanthanide sesquioxides.[36]

8.3.5 A perspective on various concepts related to Fano interactions

Quite similar to the concept of Brillouin scattering at low frequency region, various phenomena based on Fano scattering takes place at the nanoscale. Having lower energy than the optic phonons, acoustic phonons may interfere with the interband continuum. But it will be hardly observable as per the Raman line-shape asymmetry is concerned. Optic phonons (described in this paper) can interact more effectively with the interband transitions leading to clear signs of Fano asymmetry. But, intraband transitions and optic phonons hold extensive energy mismatch leading to noncompliance of the interference conditions. Nevertheless, acoustic phonons can easily interact with intraband transition manifesting Fano scattering-induced asymmetry in the Raman line-shape. Regarding the effect of size on quantum confined phonon response in silicon nanostructures, Yogi *et al*. recently demonstrated how the electronic continuum of nonradiative transitions can be extracted by subtracting the known symmetric line-shape from the Fano scattered asymmetric lines of discrete acoustic phonons.[16,17] In fact, silicon nanowires are among the most decorated materials, which are opted for temperature-dependent Raman investigation taking the effects of phonon confinement, anharmonic potential, and lattice stress into account.[79-84]

Figure 8.11 schematically briefs these concepts along with the Feynman diagram. Here ω and ω' indicate the wavenumbers of the incident and scattered photons, while Ω represents the contribution of the phonons. Each vortex of the Feynman diagram denotes either a particle-particle or a particle-quasiparticle interaction *viz*., electron-photon and electron-phonon interactions in our case. If $|\rho\rangle$ and $|\varkappa\rangle$ stand for the respective phonon state and electronic continuum, and $\widehat{H}$ represents the corresponding Hamiltonian, the following equations can be written according to Fano's initial treatment.

$$\langle\rho|\widehat{H}|\rho\rangle = E_\rho, \tag{8.21}$$

$$\langle\varkappa|\widehat{H}|\rho\rangle = V_{\varkappa\rho}, \tag{8.22}$$

$$\langle\varkappa'|\widehat{H}|\varkappa\rangle = E_\varkappa\delta(E_{\varkappa'} - E_\varkappa). \tag{8.23}$$

If the phonon energy E_ρ lies within the energy span of the electronic continuum $(E_\varkappa)$,[23] the interaction between $|\rho\rangle$ and $|\varkappa\rangle$ may lead to a renormalized hybrid or mixed state $|\zeta\rangle$ given by,

$$|\zeta\rangle = m|\rho\rangle + n\int \varkappa\, \mathrm{d}E_\varkappa. \tag{8.24}$$

Here, the orthonormality condition applies on m and n. The Raman tensor components will take up the frequency-dependent asymmetry, when evaluated over the $|\zeta\rangle$ space. The expression for asymmetry parameter is given below.[27,28]

$$q = \frac{\langle\zeta|\hat{T}|0\rangle}{\pi E_{\varkappa}\langle\varkappa|\hat{T}|0\rangle}. \tag{8.25}$$

Here, $\hat{T}$ is the transition matrix, and $|0\rangle$ is the ground state.

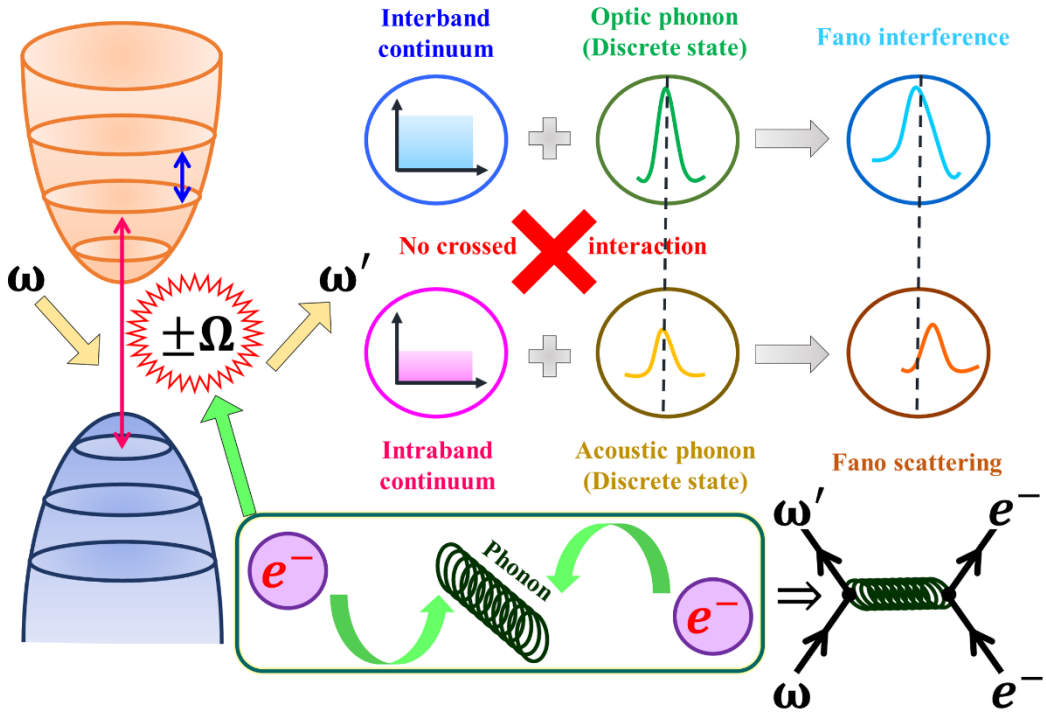

Figure 8.11 Schematics indicating various mechanisms concerning electronic-discrete Fano interactions in interband or intraband transitions influenced by electron-phonon (optic/acoustic) coupling and the associated Feynman diagram. The electron plasma or the phonon or both may be confined in particular fine nanostructures.

As shown in Figure 8.8(a-c), all Raman modes downshift with different nonlinearity against rising laser power or temperature. Several factors can influence the temperature dependence of Raman shift, such as charge-phonon (in semiconductors, both electrons and holes can contribute into it) and phonon-phonon interactions, change in bond-lengths as well as relative stress due to thermal expansion of the lattice or anharmonic effects *etc*. Some researchers have also considered the quartic-order contributions of the anharmonic phonon-phonon interactions to analyze the intense first order Raman spectrum for silicon.[70,81,84,85] Because charge-phonon coupling inevitably leads to the peak-frequency renormalization with temperature, the functional form of Einstein's approximation regarding gap renormalization can be invoked. In fact, many physical mechanisms *e.g*., crystal disorder, interaction of phonons with charge carriers or spins, as well as other phonons and even the effect of crystal fields can

result phonon damping. Material-specific anisotropic electronic and phonon-based deviations can be an important contributor too.[22,86,87] However, the effect of disorder, crystal field interactions, and incommensurate magnetic ordering are predominantly ignored in this study considering high lattice temperature and lesser defects.

Quantum confinement of phonons in nanomaterials is another reason behind asymmetric broadening and red-shifting of the Raman lines. Richter *et al*. first proposed the idea of phonon confinement in ultrasmall nanoparticles or ultrathin films in 1981.[88] Afterwards, a modified phonon confinement model (MPCM) was also suggested,[89-91] that predicts the following expression for intensity of nanoparticles of size L,

$$I(\omega, L) = \frac{4\pi A \rho_{BE}(\omega)}{L^3} \int_{2\pi-1}^{2\pi+1} \frac{\left[\frac{\sin(q_k/2)}{4\pi^2 - q_k^2}\right]^2 \left(\frac{\Gamma}{2}\right)}{[\omega - \omega'(q_k)]^2 + \left(\frac{\Gamma}{2}\right)^2} dq_k, \tag{8.26}$$

where, $\rho_{BE}(\omega)$ and q_k are the Bose–Einstein occupancy and reduced wave-vector. The constant A and the dispersion relation for $\omega'(q_k)$ depend on the specific material and dimensionality.[52] In the present study, the phonon mean free path is likely not greater than the crystallite size, which is larger than 40 nm for all nanoparticles. Therefore, the likelihood of confinement effect in the broadening can safely be disregarded. Thus, the results presented in this article predominantly reflect an amalgamation of laser-induced heating effects, emergence of charge plasma composed of photoexcited electrons and associated electron-phonon coupling *i.e*., a monotonically increasing function of excitation intensity. The methodology presented in this work can be further extended to different families of oxides, ceramics and nanoparticles that uphold interesting electronic, magnetic, optical or lattice vibrational properties or go through structural or metal-nonmetal phase transition. Apart from distinct rare-earth sesquioxides, transition metal oxides and Mott transition oxides *e.g*., VO_2, Cr_2O_3 *etc*. can be interesting candidates in this regard.[92-97]

8.4 Concluding remarks

Nanoparticles of three rare-earth sesquioxides *viz*., Eu_2O_3, Gd_2O_3, and Dy_2O_3 are selected for laser power-dependent Raman spectroscopic investigation in connection with Fano scattering. The samples are examined with powder X-ray diffraction pattern refined by Rietveld's method, diffuse reflectance spectroscopy (DRS), electron microscopy, energy dispersive X-ray (EDX) analysis, and Fourier transform infrared spectroscopy (FTIR) spectroscopy to establish purity of cubic phase at room temperature, absence of notable structural defects, nominal micro-strain, wide bandgap nature, nanoscopic morphology, satisfactory stoichiometry, and characteristic vibrational attributes. While acquiring Raman spectra, the Lax formulation is used to compute the (local) lattice temperature at the laser spot

under varying excitation power. The interference of discrete optic phonon modes with the (interband) electronic continuum in the midst of the photoexcited electron plasma delivers the negative line-shape asymmetry in the T_g modes. Being inflicted by intense excitation, red-shift in peak positions, increase in full width at half maximum (FWHM), drop in phonon lifetime, rise in the electron-phonon coupling constant or $\left|\frac{1}{q}\right|$ *etc*. are quantitatively analysed in the light of theories proposed by Fano and Allen *et al*. for the rare-earth species with distinct $4f$-electrons. An improved representation of Allen's formulation is proposed to explore the $\lambda - \tau_{anh}$ interplay, which serves as a robust alternative of the traditional calculations involving the charge-phonon coupling matrix in the context of Fano asymmetry. The basic limitation of this idea lies in the merging of Allen's formulation with Lax's theory (although it has worked satisfactorily for Ln_2O_3 nanoparticles in the operating power range), that may fail for larger laser powers and for some compounds having high thermal conductivity, or if the same varies nonlinearly with temperature. Furthermore, the as-considered microscopic rise of lattice temperature near the laser spot can be incommensurate to the surface temperature dynamics or gradient-like spread for many materials. Nevertheless, the external parameter-mediated noncorrosive tuning of constructive or destructive interference among competing resonance channels can be useful in electronic, photonic and communications engineering as well as in the physics of vibrations.

References

1. M. V. Rybin, A. B. Khanikaev, M. Inoue, K. B. Samusev, M. J. Steel, G. Yushin, and M. F. Limonov, Phys. Rev. Lett. **103,** 023901 (2009).
2. Y. Chen, L. Chen, K. Wen, Y. Hu, and W. Lin, J. Appl. Phys. **126,** 083102 (2019).
3. A. N. Poddubny, M. V. Rybin, M. F. Limonov, and Y. S. Kivshar, Nat. Commun. **3,** 1 (2012).
4. U. Fano, Phys. Rev. **124,** 1866 (1961).
5. C. Wu, A. B. Khanikaev, and G. Shvets, Phys. Rev. Lett. **106,** 107403 (2011).
6. A. Faraon, I. Fushman, D. Englund, N. Stoltz, P. Petroff, and J. Vučković, Nat. Phys. **4,** 859 (2008).
7. P. T. Valentim, J. P. Vasco, I. J. Luxmoore, D. Szymanski, H. Vinck-Posada, A. M. Fox, D. M. Whittaker, M. S. Skolnick, and P. S. S. Guimaraes, Appl. Phys. Lett. **102,** 111112 (2013).
8. S. V. Dordevic, G. M. Foster, M. S. Wolf, N. Stojilovic, H. Lei, C. Petrovic, Z. Chen, Z. Q. Li, and L. C. Tung, J. Phys. Condens. Matter **28,** 165602 (2016).
9. K. Kobayashi, H. Aikawa, S. Katsumoto, and Y. Iye, Phys. Rev. Lett. **88,** 256806 (2002).
10. B. Luk'Yanchuk, N. I. Zheludev, S. A. Maier, N. J. Halas, P. Nordlander, H. Giessen, and C. T. Chong, Nat. Mater. **9,** 707 (2010).

11. B. G. Burke, J. Chan, K. A. Williams, Z. Wu, A. A. Puretzky, and D. B. Geohegan, J. Raman Spectrosc. **41,** 1759 (2010).
12. F. Cerdeira, T. A. Fjeldly, and M. Cardona, Solid State Commun. **13,** 325 (1973).
13. F. Cerdeira, T. A. Fjeldly, and M. Cardona, Phys. Rev. B **8,** 4734 (1973).
14. S. Piscanec, M. Cantoro, A. C. Ferrari, J. A. Zapien, Y. Lifshitz, S. T. Lee, S. Hofmann, and J. Robertson, Phys. Rev. B **68,** 241312 (2003).
15. D. Olego and M. Cardona, Phys. Rev. B **23,** 6592 (1981).
16. P. Yogi, S. Mishra, S. K. Saxena, V. Kumar, and R. Kumar, J. Phys. Chem. Lett. **7,** 5291 (2016).
17. P. Yogi, S. K. Saxena, S. Mishra, H. M. Rai, R. Late, V. Kumar, B. Joshi, P. R. Sagdeo, and R. Kumar, Solid State Commun. **230,** 25 (2016).
18. M. Chandrasekhar, J. B. Renucci, and M. Cardona, Phys. Rev. B **17,** 1623 (1978).
19. V. Magidson and R. Beserman, Phys. Rev. B **66,** 195206 (2002).
20. H. Xu, M. Zhao, Z. Chen, M. Zheng, C. Xiong, B. Zhang, and H. Li, J. Appl. Phys. **123,** 203103 (2018).
21. A. Bhardwaj, V. Sridurai, N. M. Puthoor, A. B. Nair, T. Ahuja, and G. G. Nair, Adv. Opt. Mater. **8,** 1901842 (2020).
22. K. Zhang, T. Wang, X. Pang, F. Han, S.-L. Shang, N. T. Hung, Z.-K. Liu, M. Li, R. Saito, and S. Huang, Phys. Rev. B **102,** 235162 (2020).
23. A. Kumar, O. V. Rambadey, H. Rai, and P. R. Sagdeo, J. Phys. Chem. C **126,** 5403 (2022).
24. J. Bak, U. Venkateswaran, C. L. Mak, R. Sooryakumar, and B. T. Jonker, J. Phys. Chem. Solids **56,** 563 (1995).
25. M. Wang, A. Krasnok, T. Zhang, L. Scarabelli, H. Liu, Z. Wu, L. M. Liz-Marzán, M. Terrones, A. Alù, and Y. Zheng, Adv. Mater. **30,** 1705779 (2018).
26. T. Cao, C. Wei, R. E. Simpson, L. Zhang, and M. J. Cryan, Sci. Rep. **4,** 1 (2014).
27. V. Dwij, B. K. De, S. Tyagi, G. Sharma, and V. Sathe, Phys. B: Condens. Matter **620,** 413265 (2021).
28. V. Dwij, B. K. De, and V. G. Sathe, in *Electric field tuning of the Fano resonance in BaTiO3*, 2021 (IEEE), p. 1.
29. S. Wang, Q. Cheng, J. Lv, and J. Wang, J. Appl. Phys. **128,** 034501 (2020).
30. A. Sunny, A. Thirumurugan, and K. Balasubramanian, Phys. Chem. Chem. Phys. **22,** 2001 (2020).
31. Y. Zhang, C. X. Harris, P. Wallenmeyer, J. Murowchick, and X. Chen, J. Phys. Chem. C **117,** 24015 (2013).
32. G.-y. A. Gy and N. Imanaka, Chem. Rev. **98,** 1479 (1998).

33. J. Łażewski, M. Sternik, P. T. Jochym, J. Kalt, S. Stankov, A. I. Chumakov, J. Göttlicher, R. Rüffer, T. Baumbach, and P. Piekarz, Inorg. Chem. **60,** 9571 (2021).
34. N. Singh, S. M. Saini, T. Nautiyal, and S. Auluck, J. Appl. Phys. **100,** 083525 (2006).
35. S. Ohmi, C. Kobayashi, I. Kashiwagi, C. Ohshima, H. Ishiwara, and H. Iwai, J. Electrochem. Soc. **150,** F134 (2003).
36. N. Dilawar Sharma, J. Singh, A. Vijay, K. Samanta, S. Dogra, and A. K. Bandyopadhyay, J. Phys. Chem. C **120,** 11679 (2016).
37. M. H. Cho, D. H. Ko, K. Jeong, S. W. Whangbo, C. N. Whang, S. C. Choi, and S. J. Cho, Thin Solid Films **349,** 266 (1999).
38. M. Hong, J. Kwo, A. R. Kortan, J. P. Mannaerts, and A. M. Sergent, Science **283,** 1897 (1999).
39. N. Dilawar, S. Mehrotra, D. Varandani, B. V. Kumaraswamy, S. K. Haldar, and A. K. Bandyopadhyay, Mater. Charact. **59,** 462 (2008).
40. N. Dilawar, D. Varandani, S. Mehrotra, H. K. Poswal, S. M. Sharma, and A. K. Bandyopadhyay, Nanotechnology **19,** 115703 (2008).
41. M. Zinkevich, Prog. Mater. Sci. **52,** 597 (2007).
42. S. Jiang, J. Liu, C. Lin, X. Li, and Y. Li, J. Appl. Phys. **113,** 113502 (2013).
43. N. D. Sharma, J. Singh, S. Dogra, D. Varandani, H. K. Poswal, S. M. Sharma, and A. K. Bandyopadhyay, J. Raman Spectrosc. **42,** 438 (2011).
44. R. Roy, N. Mazumder, G. S. Kumar, H. Mamgain, U. K. Ghorai, D. Sen, and K. K. Chattopadhyay, J. Raman Spectrosc. **47,** 845 (2016).
45. S. Khamlich, B. D. Ngom, C. K. Kotsedi, K. Bouziane, E. Manikandan, and M. Maaza, Surf. Rev. Lett. **21,** 1450001 (2014).
46. H. E. A. Mohamed, K. Hkiri, M. Khenfouch, S. Dhlamini, M. Henini, and M. Maaza, J. Opt. Soc. Am. A **37,** C73 (2020).
47. K. Kaviyarasu, N. Matinise, N. Mayedwa, N. Mongwaketsi, D. Letsholathebe, G. T. Mola, N. AbdullahAl-Dhabi, M. Valan Arasu, M. Henini, and J. Kennedy, S. Afr. J. Chem. Eng. **26,** 49 (2018).
48. M. Maaza, B. D. Ngom, M. Achouri, and K. Manikandan, Vacuum **114,** 172 (2015).
49. B. T. Sone, E. Manikandan, A. Gurib-Fakim, and M. Maaza, J. Alloys Compd. **650,** 357 (2015).
50. S. Bhattacharjee, A. Banerjee, N. Mazumder, K. Chanda, S. Sarkar, and K. K. Chattopadhyay, Nanoscale **12,** 1528 (2020).
51. S. Bhattacharjee, S. Mondal, A. Banerjee, and K. K. Chattopadhyay, Mater. Res. Express **7,** 044001 (2020).

52. N. Mazumder, P. Mandal, R. Roy, U. K. Ghorai, S. Saha, and K. K. Chattopadhyay, J. Phys. Condens. Matter **29,** 375701 (2017).
53. M. Lax, J. Appl. Phys. **48,** 3919 (1977).
54. M. Lax, Appl. Phys. Lett. **33,** 786 (1978).
55. P. B. Allen, Solid State Commun. **14,** 937 (1974).
56. P. B. Allen and J. C. K. Hui, Zeitschrift für Physik B Condensed Matter **37,** 33 (1980).
57. J. Rodríguez-Carvajal, Physica B Condens. Matter **192,** 55 (1993).
58. A. M. Glazer, J. Appl. Crystallogr. **42,** 1194 (2009).
59. K. Momma and F. Izumi, J. Appl. Crystallogr. **44,** 1272 (2011).
60. P. Kubelka and F. Munk, Z. Tech. Phys. **12,** 259 (1931).
61. D. Mitra, S. Bhattacharjee, N. Mazumder, B. K. Das, P. Chattopadhyay, and K. K. Chattopadhyay, Ceram. Int. **46,** 20437 (2020).
62. M. Salavati-Niasari and J. Javidi, J. Clust. Sci. **23,** 1019 (2012).
63. H. E. A. Mohamed, K. Hkiri, M. Khenfouch, S. Dhlamini, M. Henini, and M. Maaza, J. Opt. Soc. Am. A **37,** C73 (2020).
64. X. Jiang, L. Yu, C. Yao, F. Zhang, J. Zhang, and C. Li, Materials **9,** 323 (2016).
65. K. A. Irshad, T. R. Ravindran, V. Srihari, and K. K. Pandey, J. Mol. Struct. **1128,** 325 (2017).
66. O. N. Shebanova and P. Lazor, J. Raman Spectrosc. **34,** 845 (2003).
67. B. H. Justice and E. F. Westrum Jr, J. Phys. Chem. **67,** 345 (1963).
68. R. Gilblas, T. Sentenac, D. Hernandez, and Y. Le Maoult, Infrared Phys. Technol. **66,** 70 (2014).
69. R. Dargis, D. Williams, R. Smith, E. Arkun, R. Roucka, A. Clark, and M. Lebby, ECS J. Solid State Sci. Technol. **1,** N24 (2012).
70. M. Balkanski, R. F. Wallis, and E. Haro, Phys. Rev. B **28,** 1928 (1983).
71. A. Debernardi, S. Baroni, and E. Molinari, Phys. Rev. Lett. **75,** 1819 (1995).
72. S. F. Wu, P. Richard, X. B. Wang, C. S. Lian, S. M. Nie, J. T. Wang, N. L. Wang, and H. Ding, Phys. Rev. B **90,** 054519 (2014).
73. B. Monserrat, N. D. Drummond, and R. J. Needs, Phys. Rev. B **87,** 144302 (2013).
74. J. B. Cui, K. Amtmann, J. Ristein, and L. Ley, J. Appl. Phys. **83,** 7929 (1998).
75. M. S. Liu, L. A. Bursill, S. Prawer, K. W. Nugent, Y. Z. Tong, and G. Y. Zhang, Appl. Phys. Lett. **74,** 3125 (1999).
76. Z. V. Popović, Z. D. Dohčević-Mitrović, N. Paunović, and M. Radović, Phys. Rev. B **85,** 014302 (2012).
77. A. F. Azevedo, E. J. Corat, N. F. Leite, N. G. Ferreira, and V. J. Trava-Airoldi, Mater. Res. **6,** 51 (2003).

78. M. W. Urban and B. C. Cornilsen, J. Phys. Chem. Solids **48,** 475 (1987).
79. Y. Chen, B. Peng, and B. Wang, J. Phys. Chem. C **111,** 5855 (2007).
80. R. Gupta, Q. Xiong, C. K. Adu, U. J. Kim, and P. C. Eklund, Nano Lett. **3,** 627 (2003).
81. T. R. Hart, R. L. Aggarwal, and B. Lax, Phys. Rev. B **1,** 638 (1970).
82. A. A. Shklyaev, V. A. Volodin, M. Stoffel, H. Rinnert, and M. Vergnat, J. Appl. Phys. **123,** 015304 (2018).
83. A. Jorio and R. Saito, J. Appl. Phys. **129,** 021102 (2021).
84. D. R. Abujetas, J. J. Sáenz, and J. A. Sánchez-Gil, J. Appl. Phys. **125,** 183103 (2019).
85. S. Banerjee, D.-I. Kim, R. D. Robinson, I. P. Herman, Y. Mao, and S. S. Wong, Appl. Phys. Lett. **89,** 223130 (2006).
86. S. Bhattacharjee, A. Banerjee, and K. K. Chattopadhyay, J. Phys. D: Appl. Phys. **54,** 295301 (2021).
87. S. Bhattacharjee, R. Sarkar, P. Chattopadhyay, A. Banerjee, N. S. Das, D. Das, and K. K. Chattopadhyay, Appl. Phys. A **128,** 1 (2022).
88. H. Richter, Z. P. Wang, and L. Ley, Solid State Commun. **39,** 625 (1981).
89. I. H. Campbell and P. M. Fauchet, Solid State Commun. **58,** 739 (1986).
90. S. Bhattacharjee, N. Mazumder, S. Mondal, K. Panigrahi, A. Banerjee, D. Das, S. Sarkar, D. Roy, and K. K. Chattopadhyay, Dalton Trans. **49,** 7872 (2020).
91. A. C. A. Silva, E. S. F. Neto, S. W. da Silva, P. C. Morais, and N. O. Dantas, J. Phys. Chem. C **117,** 1904 (2013).
92. M. Maaza, D. Hamidi, A. Simo, T. Kerdja, A. K. Chaudhary, and J. B. K. Kana, Opt. Commun. **285,** 1190 (2012).
93. J. B. K. Kana, J. M. Ndjaka, P. O. Ateba, B. D. Ngom, N. Manyala, O. Nemraoui, A. C. Beye, and M. Maaza, Appl. Surf. Sci. **254,** 3959 (2008).
94. M. Maaza, O. Nemraoui, C. Sella, and A. C. Beye, Gold Bull. **38,** 100 (2005).
95. S. Khamlich, E. Manikandan, B. D. Ngom, J. Sithole, O. Nemraoui, I. Zorkani, R. McCrindle, N. Cingo, and M. Maaza, J. Phys. Chem. Solids **72,** 714 (2011).
96. J. B. K. Kana, J. M. Ndjaka, B. D. Ngom, N. Manyala, O. Nemraoui, A. Y. Fasasi, R. Nemutudi, A. Gibaud, D. Knoesen, and M. Maaza, Thin Solid Films **518,** 1641 (2010).
97. S. Khamlich and M. Maaza, Energy Procedia **68,** 31 (2015).

9 GRAND CONCLUSION AND FUTURE PROSPECTS

9.1 Cumulative summary of the as-investigated works

In this thesis, so far, indigenous nanomaterials have been identified with some general traits such as, (a) all materials are lead-free and thus are excluded from being classified as environmentally hazardous substance. Some of them are completely non-toxic and biodegradable in nature, whereas a few possess nominal cytotoxicity; (b) all the materials are multifunctional *i.e.*, they offer multifaceted applications in diverse domains. Therefore, a comprehensive investigation and appropriate manipulation of their properties can lead to development of cutting-edge nanotechnology; and (c) all these materials hold rich and interesting physiochemical attributes, which are fundamentally appealing in condensed matter physics and materials sciences.

In the 4th to 8th chapter of this thesis, distinct concluding remarks are already asserted in great detail, however the objective of the present chapter is to summarize in a simpler language the key aspects, that are known from this thesis. The conclusions are consolidated in the following points.

I. The predominant thrust in materials research and nanotechnology is to attain a fastidious control over extensive physical (magnetism, polarizability, band-structure, luminescence, electron-phonon interactions, quantum effects, *etc.)* as well as chemical (dispersibility, crystallinity, reactivity, effective surface area, Zeta-potential, *etc*.) characteristics in a nutshell to frame state-of-the-art multifunctional devices. In the work explained in chapter 4, size-modulated functionalized core-shell Fe_3O_4 nanoparticles (bulk to quantum regime) are synthesized via a novel, cost-effective and highly reproducible strategy to critically attune the as-stated nanoscale properties. Systematic acclimatization of optical bandgap over the entire visible spectrum, enhancing surface-charge by an order, determination of effective mass of excitons from Brus equation fit, an incongruous contest between ferrimagnetism and superparamagnetism, short-range electron-phonon coupling and phonon confinement-induced Fano asymmetry in Raman line-shape *etc*. are the key-highlights of this article. We conclude from this work that, the physical and chemical properties of magnetite

nanoparticles with core-shell structure can be easily tuned in order to achieve desired benchmark for multifaceted applications including MRI contrast agents and magnetic hyperthermia-based use case.

II. To demonstrate the technical benefit of this diverse manipulation in exclusive physio-chemical properties, Fe_3O_4 is also incorporated in PVDF, a well-known model host-matrix for lead-free mechanical energy harvester. The impact of size of the dopant/additive on piezo-response of PVDF-based nanocomposites is scrutinized comprehensively for the first time to explicate interface-engineered energy-inclusive applications of hybrid devices. This work exhibits superior piezo performance owing to intense ion-dipole and dipole-dipole interactions. It has also been illustrated by high relative permittivity and glowing bunch of red, green, and blue LEDs. Apart from size-dependent properties and piezoelectric applications, some interesting non-trivial DC bias-dependent dielectric properties are investigated in this thesis, which are mentioned in the coming points.

III. The double-well energy landscape in Landau description of ferroelectrics predicted mathematical possibility of negative capacitance (NC), which today has been well-implemented in overcoming fundamental limits of power dissipation suggested by Boltzman tyranny. However, classical electrodynamics do not include any theory related to NC in non-ferroelectric materials. Since 1969, after the first official report in amorphous chalcogenide films, there are numerous observations of NC in an extensive variety of materials, among which at least forty cases are not at all related to parasitic effects or erroneous measurement protocol; and severely represent material properties. Absence of strong and pre-defined theoretical grounds compelled researchers to explain the observations using versatile and apparently uncorrelated ideas. But there ought to be some generalized mechanisms associated, which we have attempted to explore. The work explained in chapter 5 of this thesis demonstrates, a persistent low-frequency NC dispersion in size-modulated non-stoichiometric magnetite $\left[Fe_{3(1-\delta)}O_4\right]$ nanoparticles under the application of moderate positive DC bias. To the best of the authors' knowledge, nanoparticle size-effect on NC is precisely ventured in non-ferroelectrics for the first time. Moreover, a comprehensive model (Heavy dipolar relaxation model) using phasor diagrams is discussed to characterize frequency dispersive NC to construct a universal and generalized theory. This work thus facilitates the mathematical framework of updating the universal Debye relaxation (UDR) in order to counter both negative and positive capacitance dispersions and also tries to establish the general grounds of distinct models in the non-ferroelectric NC genre.

IV. Iron oxides and oxyhydroxides have long been playing a pivotal role in the fundamental as well as applied physics; trailing a plethora of optoelectronic, magnetic and dielectric phenomena, some of which are described in the as-discussed works. Next, we focus on nanoscopic dielectric activity of two promising ferric oxide (Fe_2O_3) polymorphs *viz*., hematite and maghemite with a three-fold approach and objective. Firstly, impedance and dielectric spectroscopy is used for experimental study. Regulating radio/audio-frequency dielectric polarization is a formidable challenge in classical energy management bottleneck and thus a DC field-controlled, reversible enhancement of dielectric constant for energy-storage and microwave devices is realized. Various frequency-dispersions are also fitted employing Cole-Davidson model, equivalent circuitry and Jonscher's power law (JPL) under varying DC fields to extract physical insight of non-Debye dipolar relaxations, small polaron hopping conduction, grain core-boundary resistivity correlations manifesting Maxwell-Wagner interfacial polarization and field-driven de-trapping of carriers.

V. Next, first principles investigation and simulations for energy-dispersive anisotropy evaluation were carried out. The theoretical structure of maghemite met a 40-year long debate, until in 2010, when the vacancy ordering involving Wyckoff 4b Fe-sites and constructed a 160-atom supercell was identified. However, such a large system is unsuitable for spin-polarized optoelectronic investigations. Therefore, we built a new 40-atom structure with maghemite-type crystallographic conformation, which is feasible for heavy computations. From DOS, p-type nature and antiferromagnetic/ferrimagnetic high-spin ordering of the respective polymorphs are noted and ELF-dynamics displayed delocalized electron cloud near Fe_{Oct} vacancies in maghemite. Finally, dynamic dielectric function and related optical parameters are emphasized, taking material-specific anisotropic fluctuations, intra- and interband transitions, plasma oscillations, resonant absorption, and decay into account.

VI. The intrinsic anisotropy present in complex structures can be estimated from the deviations in principle components of the dielectric tensor. The energy-dispersive quadric hypersurface of dielectric function is simulated and videographed using relevant DFT data to demonstrate the degree of anisotropy present in the systems. This is the first time, anisotropic deviations of dielectric ellipsoid are displayed for real materials, that can venture new realms in the theory of linear and nonlinear dielectrics.

VII. Emerging lead-free alkaline-earth perovskite titanate and its composites offer an extensive variety of coexisting dielectric, piezoelectric and (relaxor or normal) ferroelectric properties along with thermal and compositional stability. So, they have long been playing a pivotal role in the fundamental as well as applied physics; trailing a

variety of optoelectronic, catalytic, magnetic and dielectric phenomena. Temperature-dependent dielectric relaxation and conductivity studies are extensively studied in the literature, but a comprehensive and comparative field-dependent study is essential. Hence, the work from chapter 7 opts for a rigorous analysis of the nanoscopic dielectric response and effect of DC field is comprehended in impedance, dielectric, admittance, and modulus spectra (40 Hz–20 MHz) of solid-state synthesized MIM pellets. The phase-conformation, stoichiometry, optical and vibrational characteristics of polycrystalline calcium, strontium and barium titanate nanoparticles are investigated employing Rietveld analysis of powder XRD patterns, DRS, FTIR and Raman spectra. From Rietveld analysis, the respective crystal structures are verified to be orthorhombic for $CaTiO_3$, cubic for $SrTiO_3$ and a 68:32 mixture of cubic and tetragonal phases for $BaTiO_3$. The field-dependent dielectric and impedance spectra are (a) fitted with Cole-Davidson model to understand the relaxation-dynamics and calculate relaxation times, (b) explained in the light of phenomenological Johnson relation, and (c) matched with an equivalent circuit-model that simulates Nyquist plots analogous to experimental data. The field-dependency of grain/grain-boundary resistance and associated IBLC are interpreted in accordance with MWIP and space-charge effects. The dielectric and ferroelectric phase in $BaTiO_3$ contest with each other, where the ferroelectric phase governs the outcomes and as-anticipated dielectric features (like $CaTiO_3$ or $SrTiO_3$) are mostly concealed. From admittance spectroscopy, the field-induced de-trapping of carriers and large polaron hopping conduction are revealed. Conductivity dispersions are fitted employing JPL and the quantitative results as a function of bias-voltage supported particular applicability of the CBH and VRH model. Finally, modulus spectra are used to characterize the non-Debye dipolar relaxations using the KWW function and the subsequent variation of characteristic times, shape-parameters, and asymmetric broadening of $M''(f)$ peaks with bias are discussed.

VIII. Static dielectric tensors, Born effective charges and charge-cloud separation under external electric field are enunciated via density functional theory (DFT) framework, whereas finite element simulations using experimentally extracted electrical parameters substantiate non-uniform and anisotropic field diffusion within GC-GB heterostructure, concurring experimental findings. Our results bring up a complete set of field-dependent dispersion analysis against a broad radio/audio range for this family of compounds and therefore offers a route-map to commendably manipulate or customize various electrical properties in composite ceramics to achieve 'bane to boon' device-performance.

IX. Raman spectroscopic study is highly useful to identify local lattice fluctuation effects, charge transfer, electron-phonon coupling, long-range ordering, structural progressions, phase transitions, orbital or spin ordering, *etc*. Laser-induced heating generates a photoexcited chunk of electron plasma while acquiring Raman spectra, that can be used to tune electron-phonon coupling framework. The line-shape asymmetry in Raman spectrum regarding Fano scattering is thus manifested by the moderated interference between the electronic continuum and discrete phonon modes. Rare-earth sesquioxide nanoparticles are important materials due to potential applications regarding solid-state LEDs, dopants for tri-phosphor fluorescent lamps, high-efficiency luminescent materials, red powder activators for flat panel or plasma displays, fuel cells, ultrafine chemical-mechanical polishing, catalytic converters, control rod for fast breeder reactors, rare-earth magnets, magnetic refrigeration, *etc*. These compounds are thus ideal testbeds not only for encouraging fundamental understandings of Fano resonance, group theoretical or crystallographic study of phase transitions, and heating or anharmonic effects on spectral broadening; but also, for controlling the intrinsic vibrational attributes by a non-destructive *ex situ* method to stimulate technological aspects. A quantitative study is thereby performed to unveil the intrinsic nature of Fano resonance in Eu_2O_3, Gd_2O_3, and Dy_2O_3, emphasizing the high sensitivity of Raman spectra on the intensity of excitation, that perturbs the generic vibrational features by influencing the interference conditions, the force constant and length of the associated bonds compelled by tensile stress. This is the main subject of chapter 8.

X. The interference of discrete optic phonon modes with the (interband) electronic continuum amid the photoexcited electron plasma delivers the negative line-shape asymmetry in the T_g modes. Being inflicted by intense excitation, red-shift in peak positions, increase in FWHM, drop in phonon lifetime, rise in the electron-phonon coupling constant or $\left|\frac{1}{q}\right|$ *etc*. are quantitatively analysed in the light of theories proposed by Fano and Allen *et al*. for the rare-earth species with distinct $4f$-electrons. A rising trend of the charge-phonon coupling constant (λ) with laser power shows a stronger particle-quasiparticle coupling, whereas a shorter anharmonic phonon lifetime (τ_{anh}) indicates faster interactions. Using Allen's formalism, charge density of states [$N(\varepsilon_F)$] at the Fermi level per spin and molecule is calculated, which pertains a negative regression dependence in the $\lambda N(\varepsilon_F) - \tau_{anh}$ dynamics. The external parameter-mediated noncorrosive tuning of constructive or destructive interference among competing resonance channels can be useful in electronic, photonic and communications engineering as well as in the physics of vibrations.

Therefore, the as-investigated materials can be used in energy storage, conversion or harvesting devices, microwave and radar systems, electromagnetic interference shielding technology, sensors, transducers and actuators, *etc*. Furthermore, the products would be non-toxic and environmentally green.

9.2 Scope for future projects

There are some future plans and projects that can add new horizons to this journey of exploring the physics of technologically sound lead-free nanomaterials, that include optoelectronic applications of materials showing photoionic conductivity, thermoelectric applications using high entropy materials, phonon anomalies, multiferroic aspects of mixed tetragonal tungsten bronze ceramics, *etc*. Some of these work plans are briefly delineated below.

I. Tetragonal tungsten bronze (TTB) oxides with the general formula $(A_1)_n(A_2)_{6-n}(B_1)_{6-n}(B_2)_{4+n}O_{30}$ $(n = 3,4,5)$ are important dielectric materials and undergo ferroelectric phase transitions.[1-7] This transition is controlled by the modulation of oxygen octahedra, which depends on the cationic radius on the A-site. The TTB structure has interconnected octahedra that create channels with three, four, and five-fold pseudo-symmetry. This can host a variety of cations. Certain niobium oxides of formula $A_2LnFeNb_4O_{15}$ (A = Ba, Sr, Ca and Ln = La, Pr, Nd, Sm, Eu, Gd) with TTB structure exhibit spontaneous electric and magnetic order in specific temperature ranges.[1-5] Neodymium, samarium, and europium-based TTB compounds are ferroelectric with Curie temperature between $320 - 440$ K, while the praseodymium and gadolinium compounds are relaxors below 170 and 300 K, respectively.[5] All of them, except lanthanum, exhibit magnetic hysteresis loops at room temperature. These materials show potential for room-temperature composite multiferroics due to the presence of both ferroelectric and magnetic hysteresis loops.

II. High entropy perovskites (HEPs) are a class of crystalline materials with a perovskite crystal structure, where multiple cations are randomly distributed to ensure a highly disordered crystal structure.[8-11] These materials have recently gained interest in thermoelectric applications due to small phonon mean free path, high electrical conductivity and low thermal conductivity. One such base material for interesting high entropy perovskites is $LaMO_3$, where M is a transition metal, such as Cr, Mn, Fe, Co, Ni, Cu, *etc*. By accommodating multiple transition metals together at the same Wyckoff site, entropy can be maximized and phonon mean free path can be shortened. Basically, the thermoelectric figure of merit is directly proportional to the electrical conductivity and inversely proportional to the thermal conductivity. Thus,

by decreasing phonon mean free path by multiple accommodation at the M site, and increasing electrical transport by doping a heterovalent atom at the La site, both the conditions can be fulfilled leading to excellent thermoelectric properties. On the other hand, DFT is a useful computational method that can be deployed to study the electronic structure, transport and vibrational properties of these materials. DFT calculations can help in predicting the thermoelectric properties of high entropy perovskites, such as the Seebeck coefficient and power factor, which are important for evaluating their potential as thermoelectric materials. In addition, it can be used to optimize the composition and doping strategies for enhancing the thermoelectric performance of these engineered materials.

III. Phonon anomalies are deviations in the dispersion of phonons (quantized lattice vibrations), from the normal behaviour predicted by linear lattice dynamics theory. These anomalies arise due to the interaction between the lattice vibrations and electrons, magnons, or other degrees of freedom in the solid. Phonon anomalies can have fundamental implications in understanding the electronic, magnetic, and thermal properties of materials, as well as technical applications in materials engineering and design. One of the well-known phonon anomalies is the Kohn anomaly,[12,13] named after Walter Kohn, who predicted it in 1959. The Kohn anomaly occurs when the energy of a longitudinal acoustic phonon at the zone boundary of a simple cubic lattice approaches zero, leading to a divergence in the electronic response function. This divergence is related to the nesting of the Fermi surface, and can lead to instabilities such as charge density waves or superconductivity in some materials. The Kohn anomaly has been observed experimentally in several materials, including simple metals, semiconductors, and transition metal dichalcogenides. The observation of the Kohn anomaly provides valuable information on the electronic and phonon properties of these materials, and has implications for their potential use in electronic and energy applications.

IV. Doped cerium oxide (CeO_2) has shown promise as a photoionic conductor, where the transport of both electrons and oxygen ions is facilitated by photoexcitation.[14,15] This phenomenon has opened up new opportunities for optoelectronic applications, such as photovoltaics, gas sensing, and photocatalysis. Temperature-dependent DC conductivity measurements in presence of ultraviolet light can add valuable information in such research. Also, DC bias-dependent impedance spectroscopy can be highly useful in this regard to probe thin films. Doping with different cations can tune the optoelectronic properties of CeO_2 and enhance its photoionic conductivity. For example, doping with transition metals can introduce electronic states within

the bandgap, which can promote photoexcitation and increase the concentration of oxygen vacancies, thus enhancing the oxygen ion conductivity. In addition, the photoionization process can also generate free electrons, which can contribute to the electronic conductivity of the material. This dual conductivity, both ionic and electronic, makes doped CeO_2 a promising material for various optoelectronic applications.

V. BWF profiling of suspended graphene nanosheets on periodic nanopillars can help to deduce Fano asymmetry parameter, electron-phonon coupling strength, phonon lifetime, and image the tensile stress over the surface. This methodology of analysing asymmetric deviation in Raman modes can be extended to other 2D materials, as well.

All the new projects are planned and will be executed with the same underlying philosophy of employing non-toxic materials in diverse applications by exploring and manipulating various physiochemical properties that they hold.

References

1. D. C. Arnold and F. D. Morrison, *J. Mater. Chem.*, 2009, **19**, 6485-6488.
2. E. Castel, M. Josse, D. Michau and M. Maglione, *J. Condens. Matter Phys.*, 2009, **21**, 452201.
3. E. Castel, P. Veber, M. Albino, M. Velázquez, S. Péchev, D. Denux, J.-P. Chaminade, M. Maglione and M. Josse, *J. Cryst. Growth*, 2012, **340**, 156-165.
4. J. Gardner, F. Yu, C. Tang, W. Kockelmann, W. Zhou and F. D. Morrison, *Chem. Mater.*, 2016, **28**, 4616-4627.
5. M. Josse, O. Bidault, F. Roulland, E. Castel, A. Simon, D. Michau, R. von Der Mühll, O. Nguyen and M. Maglione, *Solid State Sci.*, 2009, **11**, 1118-1123.
6. Y. J. Wu, Z. J. Hong, Y. Q. Lin, S. P. Gu, X. Q. Liu and X. M. Chen, *J. Appl. Phys.*, 2010, **108**, 014111.
7. X. Zhu, M. Fu, M. C. Stennett, P. M. Vilarinho, I. Levin, C. A. Randall, J. Gardner, F. D. Morrison and I. M. Reaney, *Chem. Mater.*, 2015, **27**, 3250-3261.
8. C. Oses, C. Toher and S. Curtarolo, *Nat. Rev. Mater.*, 2020, **5**, 295-309.
9. A. Kumar, D. Dragoe, D. Berardan and N. Dragoe, *J. Materiomics*, 2023, **9**, 191-196.
10. P. Zhang, Z. Lou, M. Qin, J. Xu, J. Zhu, Z. Shi, Q. Chen, M. J. Reece, H. Yan and F. Gao, *J. Mater. Sci. Technol.*, 2022, **97**, 182-189.
11. Y. Zheng, M. Zou, W. Zhang, D. Yi, J. Lan, C.-W. Nan and Y.-H. Lin, *J. Adv. Ceram.*, 2021, **10**, 377-384.
12. S. Piscanec, M. Lazzeri, J. Robertson, A. C. Ferrari and F. Mauri, *Phys. Rev. B*, 2007, **75**, 035427.

13. F.-H. Liu, W. Fu, Y.-H. Deng, Z.-B. Yuan and L.-N. Wu, *Appl. Phys. Lett.*, 2021, **119**, 091901.
14. R. T. Dirstine, R. N. Blumenthal and T. F. Kuech, *J. Electrochem. Soc.*, 1979, **126**, 264.
15. T. Defferriere, D. Klotz, J. C. Gonzalez-Rosillo, J. L. M. Rupp and H. L. Tuller, *Nat. Mater.*, 2022, **21**, 438-444.

“We are just an advanced breed of monkeys on a minor planet of a very average star. But we can understand the Universe. That makes us something very special.”

– Stephen Hawking

“The important thing is not to stop questioning. Curiosity has its own reason for existence. One cannot help but be in awe when he contemplates the mysteries of eternity, of life, of the marvelous structure of reality. It is enough if one tries merely to comprehend a little of this mystery each day.”

– Albert Einstein

“An expert is a person who has made all the mistakes that can be made in a very narrow field.”

– Neils Bohr

“Scientists have become the bearers of the torch of discovery in our quest for knowledge.”

– Stephen Hawking

Jadavpur University, 2023